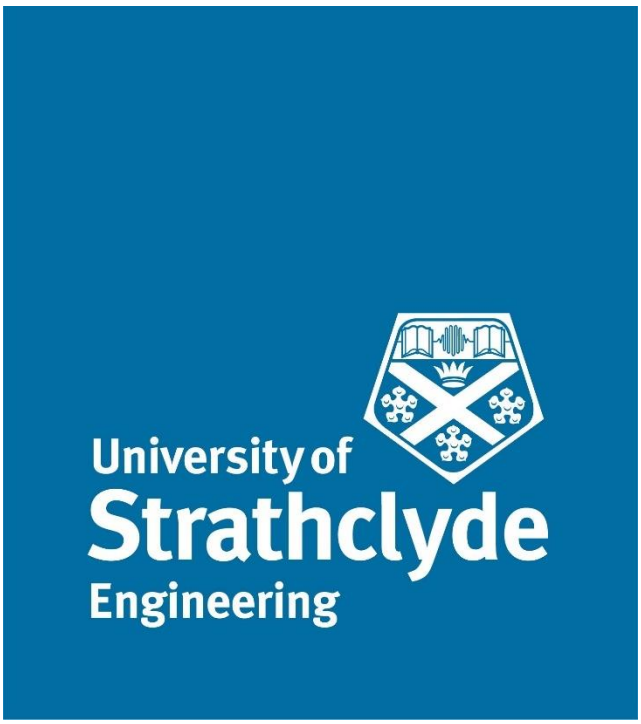

Investigation of key challenges facing aerogel composites development through multiscale approach

A thesis in fulfilment of the requirements for the degree of Doctor of Philosophy

By

Mariusz Kucharek

Department of Mechanical and Aerospace Engineering

University of Strathclyde

Glasgow

UK

2021

Declaration of Authenticity and Author's Rights

This thesis is the result of the author's original research. It has been composed by the author and has not been previously submitted for examination which has led to the award of a degree.

Signed:

Date:

Acknowledgements

I would like to express my gratitude to my supervisor Dr Liu Yang for his constant support during my PhD. I appreciate his expertise and all the necessary guidance allowing me to independently proceed with this investigation. Additionally, I would like to thank him for the financial support which made this PhD happens in the first place.

I am also thankful for all the help provided to me by the various members of the Advanced Composites Group. Without them, the time in the lab would not be as enjoyable.

As well as my fellow PhDs in the Advanced Composites Group, I would also like to thank the Advanced Materials Research Laboratory staff. Especially James Gillespie for his help with all the mechanical testing and James Kelly for his aid in microscopy and sample manufacturing. Special thanks also go to Dr Fiona Sillars, Dr Tiziana Marrocco and Dr Maider Olasolo for their technical support.

I wish to also thank Dr Paul Baker of Glasgow Caledonian University for providing me with the time and opportunity to work with his heat flow meter.

I also thank the Engineering and Physical Science Research Council for their financial support as a part of DTP grant.

I would like to express special gratitude to my parents and brother, whose support helped me keep going with this study.

Finally, my greatest appreciation and gratitude go to Agnieszka for her unwavering support and belief in me.

Publications

Some results presented in the following thesis have been published over the course of this PhD project in the following journal articles and conference contributions.

M. Kucharek, W. MacRae and L. Yang. Investigation of the effects of silica aerogel particles on thermal and mechanical properties of epoxy composites. Composites Part A: Applied Science and Manufacturing 139 (106108).

M. Kucharek, L. Yang and K. Wang. Assessment of insulating package performance by mathematical modelling. Packaging Technology and Science 33 (2). pp. 65-73.

K. Wang, L. Yang and M. Kucharek. Investigation of the effect of thermal insulation materials on packaging performance. Packaging Technology and Science.

M. Kucharek and L. Yang. Investigation of aerogel-fibre interface. 5th International Conference on Mechanics of Composites, Lisbon, Portugal, 1-4 July 2019.

M. Kucharek and L. Yang. Comparison of interatomic potentials for thermal analysis of porous silica structures via molecular dynamics simulation. Under Review.

Abstract

The aerogel particulate and fibre reinforced composites are becoming more and more popular due to their exceptional properties, nevertheless, they do face a range of challenges that need to be overcome for wider applications. The main ones include a lack of understanding of the interactions between aerogels and reinforcing fibre materials, lack of appropriate models to predict their performance, and finally, lack of property database, allowing for an informative selection of aerogel composites as a viable alternative to other materials. The primary goal of this work is to tackle those challenges and provide a better fundamental understanding of some cases of aerogel composites.

In order to fulfil the thesis' goals, the aerogel influence on the various thermal and mechanical properties of epoxy and vinyl ester polymers were investigated. By incorporating various weight contents and sizes of silica and polyimide aerogel particles into these polymers, their thermal conductivity, compressive properties, and other thermomechanical properties in these particle-filled polymers have been evaluated. Overall, created composites presented a significant decrease in thermal conductivity, while the introduction of porous particles deteriorated composite mechanical response. Additionally, micromechanical testing of the interface between aerogel and fibre reinforcement has been performed for the first time to understand their bonding ability. By designing a method to deposit an aerogel droplet surrounding the fibre, the microbond tests were enabled, and the results revealed poor adhesion between aerogel and selected fibre type in general.

In addition to the experimental part, this study also focused on modelling aerogels and aerogel composites, which provided insight into the interactions between aerogels and most common reinforcement materials using a multiscale approach. As a result, the nanoscale analysis using molecular dynamics allowed to estimate thermal and mechanical properties of low density silica and polyimide. What is more, the aerogel-fibre interfacial properties values have also been obtained though modelling. Finally, the microscale model was used to model the thermal and mechanical properties of epoxy composites. A close match between experimental and modelled thermal conductivity and compressive modulus of epoxy combined with low density silica or polyimide particles has been achieved by incorporating the nanoscale properties into the micromechanical model.

Contents

Nomenclature

Symbol	Definition
A	Contact area between materials
AFM	Atomic force microscopy
AHEW	Amine hydrogen equivalent weight
a_i	Acceleration of particle i
AMBER	Assisted Model Building with Energy Refinement
ASTM	American Society for Testing Materials
BAX	Bisaniline-p-xylidene
BET	Brunauer-Emmett-Teller
BJH	Barrett, Joyner, Halenda
b_{ij}	Bond order measurement
B_{ijk}	Strength of three-body interactions
BISGMA	(Bisphenol A-glycidyl methacrylate
BKS	Beest Kramer van Santen
BPDA	Biphenyl-3,3′,4,4′-tetracarboxylic dianydride
CFs	Carbon fibres
CHARMM	Chemistry at Harvard Macromolecular Mechanics
C_{ijk}	Three-body saturation parameter
CMCs	Ceramic matrix composites
CO_2	Carbon dioxide
CTE	Coefficient of thermal expansion
D	Fibre diameter
DETA	Diethylenetriamine
DGEBA	Diglycidyl ether of bisphenol-A
D_{ij}	Strength of the charge–dipole attraction forces
$\Delta\Lambda_{\sigma\pi}$	Change of sample length
DMA	Dynamic mechanical analysis
DMBZ	2,2′-dimethylbenzidine
DT	Temperature difference
E	Total energy

$E_{aerogel}$	Total energies of aerogel sample in separate state
E_{angle}	Energy components for angle bending
$E_{assembly}$	Total energy of combined samples
E_{bond}	Energy components for bond stretching
E_c	Elastic modules of composite material
E_{coa}	Energy components for three body conjugation term
E_{conj}	Energy components for four body conjugation term
$E_{coulomb}$	Energy components for nonbonded Coulomb interactions
EEW	Epoxide equivalent weight
$E_{H\text{-}bond}$	Energy components for hydrogen bond interactions
E_i	Young's modulus of material phase i
E_{lp}	Energy components for lone pair energy interactions
E_m	Elastic modules of matrix material
E_{nb}	Energy components for non-bonded interactions
E_{over}	Energy components for over coordination
E_{pen}	Energy components for penalty energy
$E_{reinforcenment}$	Total energies of reinforcement sample in separate state
$E_{torison}$	Energy components for torsional interactions
E_{triple}	Energy components for triple bond energy correction
E_{under}	Energy components for undercoordination
EVA	Ethylene-co-vinyl acetate
E_{val}	Energy components for angle energy
$E_{vdWaals}$	Energy components for van der Waals interactions
f	Fractional density
f1, f2, and f3	Phase angles
f_A	Function representing three-body interactions
f_C	Smooth cut-off function
FCC	Face-centred cubic
FEA	Finite element analysis
F_i	Force exerted on particle i
f_R	Function representing two-body interactions

FRP	Fibre-reinforced plastics
FTIR	Fourier transform infrared spectroscopy
GUI	Graphic user interface
H_2O	Hydrogen peroxide
H_2SO_4	Sulfuric acid
HCl	Hydrochloric acid
HDT	Heat distortion temperature
HF	Hydrogen fluoride
H_{ij}	Strength of the short-range repulsion forces
HNO_3	Nitric acid
IFSS	Interfacial shear stress
ILSS	Interlaminar shear strength
InP	Indium phosphide
ISO	International Organization for Standardization
IUPAC	International Union of Pure and Applied Chemistry
j_i	Dihedral angle
k	Calibration coefficient
k	Stress concentration factor
k_B	Boltzmann constant
K_q	Angle coefficient
K_r	Bond coefficient
L	Initial length of a specimen
l	Pull-out distance
LAMMPS	Large-scale Atomic/Molecular Massively Parallel Simulator
LCTE	Linear coefficient of thermal expansion
l_{eb}	Fibre embedded length
LJ	Lennard–Jones
L_x	Dimensions of the simulation box along x-axis
L_y	Dimensions of the simulation box along y-axis
m-CT	Micro-computed tomography
MD	Molecular Dynamics

MEKP	Methyl ethyl ketone peroxide
m_i	Mass of particle i
MIP	Mercury Intrusion Porosimetry
MMCs	Metal matrix composites
MMM	Multiscale material modelling
$MoSi_2$	Molybdenum disilicide
N	Number of atoms
n	Unit vector along the displacement
Na_2SiO_3	Sodium silicate
NaCl	Sodium chloride
N_{piece}	Number of atoms in the piece
N_{swap}	Cumulative number of atom swaps
OAPS	Octa(aminophenoxy)silsesquioxane
ODA	4,4′-oxydianiline
OPLS-AA	Optimized potentials for liquid simulations all-atom
OVITO	Open Visualization Tool
P	Pressure
PAA	Poly (amic acid)
PBCs	Periodic boundary conditions
P_c	Critical pressure
PDA	Polydiacetylene
PDMS	Poly(dimethylsiloxane)
PEEK	Polyether ether ketone
PET	Polyethylene terephthalate
phr	Parts per hundred
PI	Polyimide
PLA	Polylactic acid
PMCs	Polymer matrix composites
PMF	Potential of mean force
PPDA	P-phenylene diamine
ppm	Parts per million

pppm	Particle-particle particle-mesh
PSD	Pore size distribution
PVB	Polyvinyl butyral
PVOH	Poly(vinyl alcohol)
PWD	Pine wood dust
Q	Relaxation of the friction dynamics
q_{eq}	Equilibrium bond angle
q_i	Atomic charges of particle i
Q_{in}	Fixed energy flux
q_j	Atomic charges of particle j
R(t)	Position of the centre of mass of the pulled atoms at the given time step
R_0	Starting centre of mass of pulled atoms
RDF	Radial Distribution Function
ReaxFF	Reactive force field
r_{eq}	Equilibrium bond length
R_f	End position of the displaced material centre of mass
r_i	Position of particle i
r_{ij}	Distance between neighbouring i and j atoms
RNEMD	Reverse Non-Equilibrium Molecular Dynamics
$ScCO_2$	Supercritical carbon dioxide
SEM	Scanning electron microscopy
SFFT	Single fibre fragmentation test
SFPoT	Single fibre push-out test
SFPT	Single fibre pull-out test
SiO_2	Silicon dioxide
T	Temperature
T	Thickness
TA	Thermal Analysis
TAB	1,3,5-triaminophenoxybenzene
TAPOB	1,3,5-tris(4-aminophenoxy)benzene
T_c	Critical temperature

T_c	Thermal conductivity
TEGDMA	Triethylene glycol dimethacrylate
TEM	Transition electron microscopy
TEOS	Tetraethyl orthosilicate
T_g	Glass transition temperature
TiO_2	Titanium dioxide
TMA	Thermomechanical analysis
TMCS	Trimethylsilyl chloride
UA	United-atom
UFF	Universal Force Field
$U_{ij}^{(2)}$	Two-body type of interactions
$U_{ijk}^{(3)}$	Three-body potential
V	Volume
v	Volume fraction of filler added
V	Potential energy of the whole system
V_0	Pore volume of aerogel particles
V_1, V_2, and V_3	Coefficients in the Fourier series
v_{cold}	Velocities of lowest energy atoms
v_{hot}	Velocities of highest energy atoms
Vinf	Filled pore volume fraction
vol%	Added volume ratio of silica aerogel
W	Sample width
W_A	Thermodynamic work of adhesion
w_{ij}	van der Waals interactions
wt%	Mass fraction
Z_i	Effective charge
α_m	Linear coefficient of thermal expansion
γ_{LV}	Surface free energy of the liquid-vapour interface
γ_{SL}	Surface free energy of the sliquid-solid interface
γ_{SV}	Surface free energy of the solid-vapour interface
θ	Sensitivity factor

λ	Thermal conductivity
λ_1	Screening lengths for a Coulomb force
λ_4	Screening lengths for a charge–dipole forces
λ_c	Thermal conductivities of composite
λ_f	Thermal conductivities of filler
λ_m	Thermal conductivities of epoxy
μ	Chemical potential
ρ	Density of composite
$\rho_{polymer}$	Density of polymer
ρ_{silica}	Density of silica
σ	Stress imposed on the sample
σ_c	Strength of composite
σ_m	Strength of matrix material
τ	Coupling parameter controlling scaling of the MD system
χ	Interface cohesion term
ς	Fictitious dynamic variable

List of figures

List of tables

1 Introduction

1.1 Background

The term "aerogel" describes various materials derived from organic, inorganic or hybrid molecular precursors created during a sol-gel process jointly with the utilisation of appropriate drying techniques to maintain three-dimensional and highly porous structure resulting in material porosity of even up to 99% [1]. The begging of aerogels is dated back to 1931, when Kistler synthesised the first inorganic, silica aerogel [2]. Kistler based his experiment on the observation carried by Graham in 1864, who had successfully replaced a water part of silica gel with alcohol (organic solvent) and Butschli in 1896, who did the same with gelatine [3]. During his experiments, Kistler managed to synthesise aerogels using various materials other than silica, including tungstic, ferric, aluminium, stannic oxide and nickel tartrate, and some organic ones like gelatine, agar, nitrocellulose or egg albumin. In addition, in his attempts to create rubber aerogels, a variety of solvents used during supercritical drying was tested, such as propane, ethyl ether, and liquid CO_2 [2]. Despite the first silica aerogel being produced by Samuel Kistler in 1931, research into these highly porous solids was not widespread until much later due to the long and complex production process required [4]. It was not until Stanislaus Teichner found in what year that aerogels porous network could store rocket fuel that aerogels research and development began to grow [4]. Since then, the number of created aerogels was steadily increasing. In their work Woignier, Phalippou and Zarzycki expanded the knowledge regarding aerogels silicate while Teichner explored the simple and binary oxides aerogels [5, 6]. In 1989 Pekala has undertaken a different path and created aerogel with resorcinol-formaldehyde, which was then subjected to pyrolysis for the creation of carbon aerogel [7, 8]. As indicated by Figure 1-1, the interest in aerogels has been rapidly growing over the last decades. Current research focuses on making aerogel production more cost-effective as well as developing new aerogel types such as sulphated zirconia, TiO_2, or exotic chalcogenide aerogels [9-12]. In addition, many studies have been analysing testing methods to correctly analyse the mechanical, thermal, and optical properties of created materials [12-21]. Finally, the investigations aiming at the implementation of aerogel materials into commercial applications have also unlocked aerogel potential in many industrial sectors such as containment of nuclear waste, energy storage devices, metal casting moulds, CO_2 trapping, chemical sensors, water-repellent coatings, acoustic transducers, adsorption of pollutants etc. [12, 19-23].

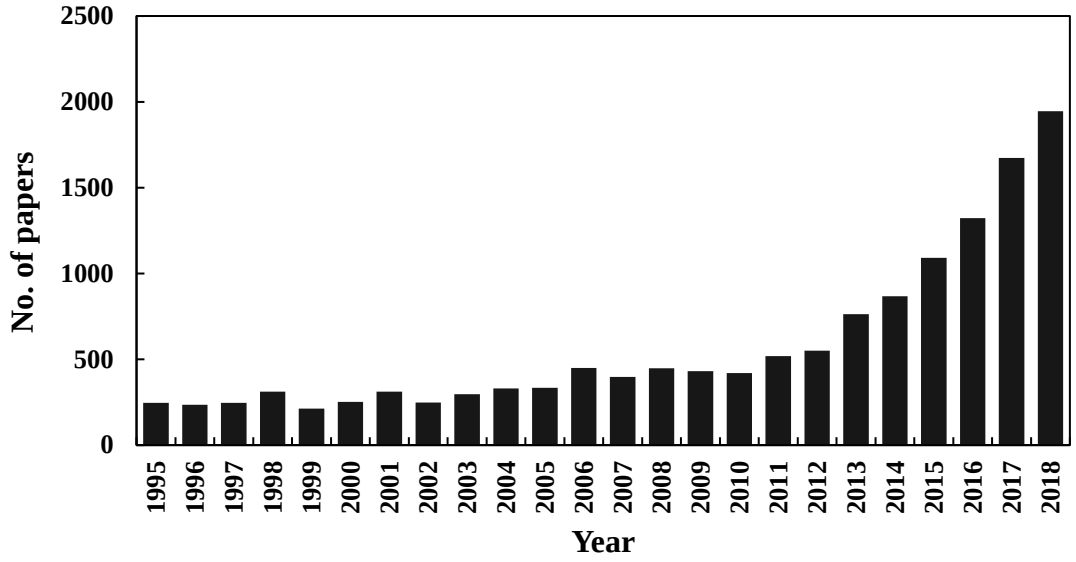

Figure 1-1 Number of articles published regarding "aerogels" over the last 23 years (ScienceDirect Database).

Nowadays, superior insulators are becoming increasingly relevant in low-carbon and energy efficient development. As global issues such as depletion of fossil fuels, an increasing population and global warming become more prevalent, novel solutions to conserve energy loss are widely investigated [1, 2]. With numerous companies successfully commercialising aerogel products (including Aspen Aerogels Company, Cabot Corp., American Aerogel Corp., etc.), aerogels are become a viable solution to tackling some the global issues [12, 24-26]. Silica aerogel, the leading representative of the aerogel family, is an extremely lightweight (2 g/cm^3), highly porous material (typical porosity) with one of the lowest documented thermal conductivities of 15 - 40 $mWm^{-1}K^{-1}$ [3]. It proves to be an ideal insulating material, however, its brittle nature hinders the utilisation of silica aerogel in multiple applications. Therefore, a significant amount of effort has been put into strengthening the aerogels and mitigating their highly brittle nature. It involves the combination of aerogels with more durable materials allowing the structural weaknesses to be overcome while providing superior thermal properties. The most common approach is based on synthesising the aerogel with fibre reinforcement, resulting in the creation of aerogel blankets [27, 28]. Others attempt to exploit aerogels natural properties and develop the superior thermal characteristics of materials through the incorporation of silica aerogel particles [29-32]. Silica aerogel/epoxy composites are one example that can offer exceptional improvements to thermal conductivity while retaining desirable mechanical properties [33]. Despite these potential solutions based on composites concept, aerogel composites also face significant challenges. The main one being a lack of understanding of the interactions between aerogels and reinforcing materials in

aerogel blankets or polymeric materials in aerogel filled resins. Such a knowledge gap prevents us from utilising aerogel composites to their full potential, and the dusty nature of aerogel blankets resulting from low interfacial adhesion between aerogel and fibrous reinforcement can be used as a prime example. The other issues faced by aerogel composites include lack of appropriate models to predict their performance and lack of properties' database allowing for an informative selection of aerogel composites as a viable alternative to other materials.

1.2 Aims and objectives

As discussed above, the aerogels are still emerging materials, and in order to fully utilise their superior properties, a wide range of challenges still have to be overcome. Aerogels incorporation into composite materials seems to be the most promising approach forward. Nevertheless, it is substantially hindered by the lack of understanding of interactions between different constituents. Therefore, the primary goal of this thesis is to provide a better insight into the interactions between aerogels and the most common reinforcement materials using multiscale modelling and experiment. Additionally, the influence of aerogel on the various properties of polymer matrices is also investigated, allowing for the broader incorporation of aerogel materials into future projects. To fulfil the goal of this thesis, the following objectives have been formulated:

1) To experimentally investigate the effect of aerogel particles on the mechanical and thermal properties of some most common resin materials, including epoxy and vinyl ester.
2) To investigate the interfacial adhesion of aerogel fibrous composites using micromechanical testing methods.
3) To use the multiscale modelling approach to study silica and polyimide aerogels' thermal and mechanical properties and their interactions with reinforcement materials.

Even though a certain amount of research has already been devoted to assessing the properties of aerogel composites either experimentally or through modelling means, the following thesis introduces a great deal of novelty by focusing on the interface between the aerogel and reinforcing materials. As a result, the thesis includes the following innovative investigations that have not been seen in the literature:

- The micromechanical testing of aerogel-fibre adhesion
- The molecular dynamics study of polyimide aerogel properties
- The molecular dynamics study of thermal and mechanical properties of aerogel composites interface.

- The analysis of the wide range of thermomechanical properties of epoxy and vinyl ester resin filled with aerogel particles.

1.3 Outline of thesis

Chapter 2 presents the fundamental background focusing on the materials used during this study and the multiscale modelling approach.

Chapter 3 gives the results of the mechanical and thermal testing of aerogel filled polymers.

Chapter 4 discusses the micromechanical investigation of silica and polyimide aerogel adhesion to various reinforcement fibres.

Chapter 5 presents the nanoscale investigation of low density silica and polyimide thermal and mechanical properties and their interactions with reinforcement materials via molecular dynamics modelling.

Chapter 6 presents the microscale modelling of epoxy composites incorporating the results obtained from the nanoscale investigation.

Chapter 7 summarises the main findings of this thesis and suggests future work in this area.

2 Fundamental background

This chapter introduces the fundamental overview of two main topics of interest for this study. It commences with an overview of aerogels and aerogel composites. As a result, the history and synthesis of silica and polyimide aerogels have been analysed, followed by the description of aerogel particulate and fibrous composites including the reinforcement materials used for their preparation. The second part of this chapter focuses on the theoretical background of multiscale modelling. It also highlights the basics of simulation methods used in this study including molecular dynamics and finite element analysis. These above topics are presented as a separate chapter as they provide overlapping common ground for more than one of the subsequent chapters.

2.1 Materials overview

2.1.1 Aerogel

2.1.1.1 Silica aerogel

As mentioned before, the silica aerogel was the first aerogel ever synthesized. Kistler's initial attempts to create aerogel were conducted with the use of sodium silicate and hydrochloric acid to create the gel.

$$Na_2SiO_3 + 2HCl + (x\text{-}1)H_2O \rightarrow SiO_2{\cdot}xH_2O + 2NaCl \qquad \text{Eq. 1}$$

To remove the water from the gel, Kistler utilised simple drying techniques; nevertheless, the resulting lattice collapsed due to the surface tensions and capillary forces. In the subsequent attempts, the samples were exposed to high pressure, and the critical water temperature was reached. Afterwards, under constant temperature, the pressure was lowered, resulting in the vapour leaving the pores without damaging the lattice [2]. With the supercritical drying process in place, Kistler faced another issue as the silica network reacted with supercritical water. To overcome this problem, the liquid was replaced with ethanol which was non-reactive and required less demanding conditions for supercritical drying. On the other hand, the liquid replacement technique appeared to be highly time-consuming. Due to the complex manufacturing process, aerogel development was suspended for few decades until 1985, when Pajonk and Teichner used it to store rocket fuel [34]. Resulting aerogels have characteristics of high porosity, large surface area, low density and excellent thermal insulating properties combining the features desired by many industrial sectors. The investigation carried out by Fritz and Jain revealed that the thermal conductivity of the silica aerogel could be as low as 17 mW/mK, making it a potential solution for thermal insulation applications [35]. Nevertheless,

such intriguing features of silica aerogel result from the high porosity of the material and impose significant limitations upon the practical use of aerogels. Their mechanical performance is significantly hindered by the low intrinsic tensile strength of porous amorphous silica and the low density. As shown by previously conducted experiments by Woignier and Groß, the elastic modulus and tensile strength of silica aerogel can be up to four times lower than values for silica glass [5, 36, 37]. The silica aerogel has found an application in many scientific applications such as: radioluminescent devices, inertial confinement fusion or shock wave studies at high pressures [38-40].

It is often accepted that the synthesis of silica aerogel can be divided into 3 main steps, including gel preparation, solvent exchange and drying. During the gel preparation process, the solid nanoparticles are dispersed through solution and connected to form a structure of particles across the whole substance. In order to obtain the gel, the first step includes the creation of sol by diluting silicon derivative such as silicon alkoxides, tetramethoxysilane or tetraethoxysilane; the last two have been successfully used in the creation of monolith silica aerogel [41]. A wide selection of solvents has previously been used, such as alcohols, dioxane, acetone or tetrahydrofuran. However, it is worth mentioning that alcohols can reduce the hydrolysis rate by taking part in an esterification reaction [42]. The hydrolysis process can result in various materials' properties depending on used parameters with, the most crucial factor being Si: H_2O ratio. Much research work was conducted to establish an optimum ratio, and in general, the agreement was that the increase in water concentration would decrease the gelation time as the chemical reactions were accelerated [43, 44]. The next step of the gelation process, condensation, occurs in the presence of a catalyst with three main approaches of acid catalysis, base catalysis and two-step catalysis (including a different catalyst during hydrolysis and condensation) [42]. Through experimental methods, significant differences between these catalysis approaches were detected. In acid catalysis, randomly branched silica chains were created in sols, while in base catalysis, the uniform structure is obtained within sol. Acid catalyst usually incorporate HCl, H_2SO_4, HNO_3, HF, oxalic, formic and acetic acids, while base one uses dilute ammonia [45, 46].

Aging is the second step of silica aerogel synthesis and it aims to strengthen the silica links created during the gelation process to avoid pore collapse during further steps of the synthesis [47]. During this stage two main strengthening processes take place, which substantially influences the final internal structure of the silica aerogel [42]. The first one includes neck growth between neighbouring silica particles due to precipitation of dissolved silica onto necks, which are the weakest links in the pearl-necklace structure created by silica

nanoparticles. The second phenomenon incorporates precipitation of dissolved silica onto larger particles of formed silica network [42]. Both processes are driven by differences in solubility of the material within the mixture. As a result, smaller particles with high solubility tend to precipitate onto necks (area of low solubility due to the geometry) and larger particles' surface (area of low solubility due to the particle size). On the other hand, the excessive ageing time can lead to reverse dissolution of previously precipitated particles (so-called "ripening mechanism"), resulting in the coarsening of the structure [42]. If the aerogel synthesis process includes either supercritical CO_2 or ambient drying the solvent exchange become necessary. It can be performed alongside ageing or shortly afterwards, however solvent exchange conditions such as the chemical composition or temperature of the solvent can significantly affect the aerogel structure. As a result, in the past many studies were conducted investigating the effect of solvents upon material properties. Titulaer et al. and Chou and Lee measured the effect of solvents on surface area and indicated a close relation between the polarity of the solvent and resulting surface area [48]. Haereid et al. correlated the strength and stiffness of wet gels to the ageing time, temperature and pH of the solvent [49, 50]. Finally, Smitha et al. looked into the effect of solvent onto porosity of the resulting silica aerogel and reported that using solvent with 80% of tetraethyl orthosilicate (TEOS) gave the lowest bulk density and shrinkage of the sample while providing the highest surface area and pore volume [51].

Drying is the final step in silica aerogel preparation, during which the solvents are being removed, leaving a solid porous structure. It has been widely recognised that drying is the most crucial of all the synthesis steps and it is driven by capillary stresses occurring when a transition from liquid to gas state takes place within the pores. Even though siloxane bonds have a partially covalent character, making them more resistant to drying effects than other oxide gels, the stresses within structure can reach up to 200 MPa causing cracks and pore collapse. Multiple drying techniques have been developed to replace a liquid part of the gel with gas and thus obtain lighter material. However, the change in the drying process also affects the internal structure of the materials. As a result, multiple additional materials, such as xerogels and cryogels, were defined as presented in Figure 2-1.

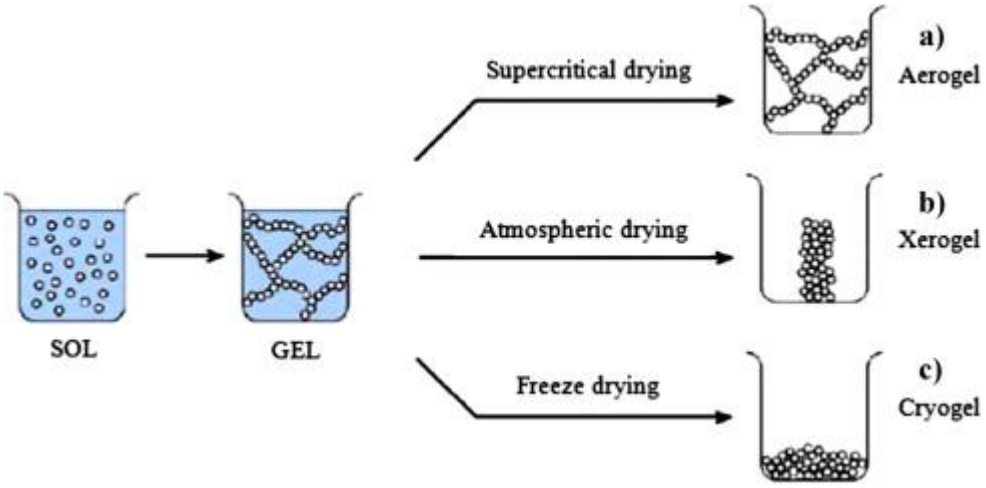

Figure 2-1 Types of material obtained as a result of various drying techniques [52].

Following the IUPAC definition, xerogel is an "open network formed by the removal of all swelling agents from a gel" and is obtained by drying the gel under atmospheric conditions [53]. Other variation of this method, the atmospheric pressure drying (APD) incorporates placement of the gel/solvent mixture at the elevated temperatures in order to accelerate the drying process. Quite frequently the multi-step drying approaches are being used with each step gradually increasing temperature until reaching desired temperature. During the drying process, the capillary stresses reduce the volume of the sample to 30% (or less) of starting gel volume. Cryogels are created by freezing gel or precursor solution in the so-called freeze-drying [54]. However, this process has some drawbacks as the resulting lattice might be distorted or destroyed due to the nucleation and/or growth of solvent particles [55]. Finally, the most popular materials, aerogels, are created by replacing liquid components with gas during supercritical drying. Such a process includes heating the gel substance above the critical temperature of the solvent (T_c) while being exposed to critical pressure (P_c) of the solvent present in the material pores. This approach reduces pressure on aerogel walls and mechanical tension in entrapped liquid. As a result, the liquid-gas replacement can be conducted without collapse of the gel structure [12]. In case of silica gels submerged in ethanol solvent the process of supercritical drying with the use of CO_2 includes the following steps. Firstly, the silica gel fully surrounded by the solvent is placed in the autoclave which is then pressurised to 5-6 MPa while the temperature of the system is lowered to 5-10°C [56]. Liquid CO_2 is then introduced into the vessel in order to commence the replacement of the ethanol. Afterwards, the autoclave system is then heated and further pressurized until reaching critical temperature and pressure of the CO_2. In order to ensure complete removal of the solvent, such conditions are maintained for various time depending on the silica gel geometrical features such as shape or thickness.

Finally, the CO_2 is being released in a controlled manner until reaching ambient pressure marking the end of the aerogel synthesis process [56].

2.1.1.2 Polyimide aerogel

Organic aerogels have proven to provide significantly different properties than their inorganic counterparts [57]. They present improved mechanical properties, however, they do not perform well at elevated temperatures due to low thermal and dimensional stability [58]. In order to tackle these issues, the polyimide aerogel has been developed by scientists from NASA's Glenn Research Centre [59]. The resulting material presents outstanding properties with its strength exceeding 500 times the most popular silica aerogel while maintaining low thermal conductivity, low density, and manufacturing simplicity [59, 60]. In addition, polyimide aerogel is neither fragile nor dusty like silica aerogels and can be manufactured in the form of thin films providing flexible wrapping insulation. Polyimide aerogel has been incorporated into multiple space applications such as space suits insulation or landing applications, as well as filtering and high-performance sports applications [61, 62].

Currently, most processes used for the synthesis of polyimide aerogel follow similar steps as silica aerogel preparation, including gel formation, solvent exchange, and drying [61]. There are two main types of aerogel formations being reported, including linear and crosslinked ones. The linear polyimide aerogels have been traditionally synthesized using dianhydrides and diamines dissolved in polar aprotic solutions with the poly (amic acid). Following the addition of dehydrating agent, the chemical imidization leads to polyimide gel formation [61]. Alternatively, a dianhydride and a diisocyanate can be used without the addition of the dehydrating agent, as presented by Chidambareswarapattar et al. [63]. Although the cost of the latter method is lower due to the lower temperatures required, it also produces aerogel with inferior properties compared to samples produced with the usage of diamine [58].

Crosslinked polyimide aerogel is the second type of polyimide aerogel that recently has been extensively investigated. It has been reported that crosslinked gels present a much lower shrinkage of less than 20% (compared to up to 60% for linear aerogels) due to their structure comprising a three-dimensional network [61]. The synthesis of crosslinked gels commences with the solution of excessive dianhydrides monomer and diamines monomer in polar aprotic solutions to obtain a poly (amic acid) solution (PAA). Next, the crosslinker with equal quantities of amino and anhydride such as 1,3,5-triaminophenoxybenzene (TAB) or octa(aminophenoxy)silsesquioxane (OAPS) is added to initiate the crosslinking process and produce polyimide gel [58]. The resulting gel is no longer soluble in the reaction solvent and thus it has to be submerged into ethanol or acetone to remove the remaining reaction solvent.

Following the solvent exchange, the PI gel undergoes a drying process using the same drying techniques as described in the silica aerogel section [61].

Most of the research in polyimide aerogel focuses on the investigation of gel formation and drying upon the final properties of created aerogels. Guo et al. prepared PI aerogel with biphenyl-3,3′,4,4′-tetracarboxylic dianydride (BPDA), bisaniline-p-xylidene (BAX) and OAPS crosslinker, finalised with drying procedure using supercritical carbon dioxide ($ScCO_2$) [64, 65]. Resulting material exhibited low thermal conductivity (14 mW/m K), low density (~ 0.1 g/cm^3) and high surface area (230-280 m^2/g) [64, 65]. Meador et al. synthesised a wide range of polyimide aerogels, replacing OAPS crosslinker with cheaper 1,3,5-triaminophenoxybenzene (TAB) [66]. In their study, BPDA and benzophenone-3,3′,4′4′-tetra-carboxylic dianhydride (BTDA) dianhydrides were combined with multiple diamines such as Polydiacetylene (PDA), 4,4′-oxydianiline (ODA), and 2,2′-dimethylbenzidine (DMBZ), providing insight into how monomers' structures impact the morphology and macroscopic properties of Pi aerogels [66]. The lowest shrinkage (20%) and density (0.14 g/cm^3) together with the highest porosity (above 90%) have been recorded for samples prepared with BTDA and DMBZ. On the contrary, the poorest results have been achieved for BPDA and p-phenylene diamine (PPDA) combination. By manufacturing thin films, the mechanical properties of Pi aerogels have also been measured with tensile strength of films in the range of 4-9 MPa [66]. Finally, the PI aerogel samples presented high thermal stability with a glass transition temperature of 270 - 340°C, and the thermal decomposition temperature was ranging between 460 and 610°C [66].

Especially in the case of silica aerogel, a significant amount of effort has been put into improving their mechanical performance and mitigating their highly brittle nature. It involves the combination of aerogels with more durable materials allowing the structural weaknesses to be overcome while providing superior thermal properties. The most common approach is based on synthesizing the aerogel with fibre reinforcement, resulting in the creation of aerogel blankets [27, 28]. Others attempted to develop the superior thermal characteristics of various materials by incorporating silica aerogel particles into them or creating hybrid aerogel structures [29-32]. The following literature review will focus on the description of particulate reinforced composites and the polymers used in further parts of this study. In addition, it will discuss the fibrous composites and the fibre types used during microbond tests.

2.1.2 Particulate reinforced composites

Particulate composites are defined as materials formed with at least one material starting in the particles phase being dispersed in a matrix consisting of a second material. The examples of such materials can be found everywhere around us with examples such as paints (combination of solvent, opaque particle and polymer), porcelain (mixed oxide ceramic crystals and glass phases) or brake pads (mix of graphite, metals, and ceramics) [67].

Particulate composites cannot be considered a modern discovery. Examples of intentional addition of particles to other materials have been noticed through almost whole known human history. One of the earliest examples come from China and it is a porcelain dinnerware dated to be almost 3500 years old. As a result of a combination of oxide minerals with water, thick paste was obtained and formed into desired shapes, followed by firing in charcoal kilns [68]. Another early example was discovered in South America around 300 BC, where Incas were fusing gold and platinum powders in temperatures reaching even up to 1100°C. The combined material later was subjected to forging and annealing processes to form everyday objects such as needles, spoons, fish hooks and jewellery [67, 69]. In Europe, examples of ancient particulate composites can be still found in Rome and, most precisely in Roman concrete used for the construction of more significant buildings. The cement was formed by incorporating brick fragments, stones, sand, volcanic ash, and limestone reinforcement with calcium, silica and water. Recent studies revealed that cured hydrated calcium-silicate formed crystals ranging in size from 2 to 30 μm which bonded remaining ingredients [70, 71]. All previously mentioned examples impacted further development of particulate composites leading to extensive development of this type of materials in the last 100 years. With the multitude of material combinations used to customize specific material, the polymer, metal and ceramic composites become the three most commonly used types [67, 72-74].

Matrix is a homogeneous material connected throughout the structure of composite. It provides the medium and covers the particles from mechanical and/or environmental damage, and transfers the loads imposed on composite [75]. When considering the matrix material, particulate composites can be divided into three main categories with polymer matrix composites (PMCs), metal matrix composites (MMCs) and finally ceramic matrix composites (CMCs), as presented in Figure 2-2. As it can be expected, the selection of the matrix material influences the methods used for manufacturing, mechanical behaviour, and properties of created material. As a result, the selection of matrix material is crucial in composite design [76].

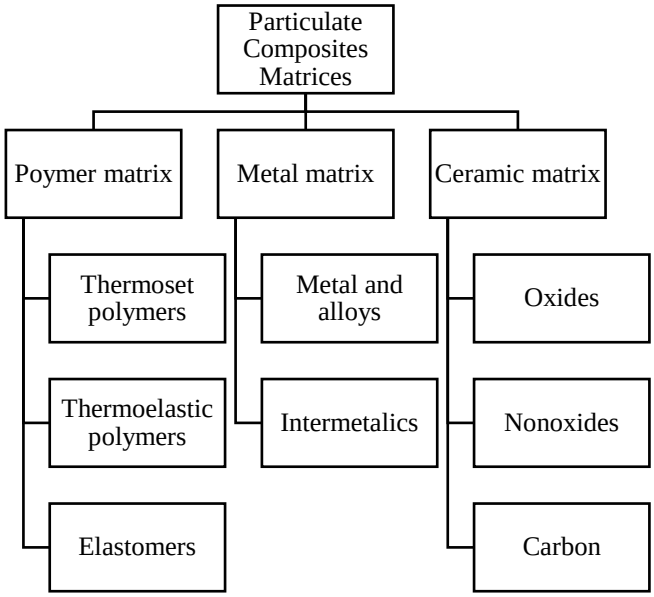

Figure 2-2 Classification of matrix materials used for particulate composites [70].

The polymer matrices are further divided into subgroups, including thermoset polymers, thermoplastic polymers and elastomers. The PMCs carries many advantages such as high specific strength and modulus, high damage tolerance and good fatigue resistance. Nevertheless, polymer-based materials are only suitable to be used for applications with relatively low service temperatures of up to 350°C [77]. Since the research conducted in this work will include only polymer-based composites, more detailed discussion of this matrix type will be presented in further parts of the chapter.

Metallic and alloy matrices are most often used when high-temperature resistance is required, as they can withstand even up to 1200°C [70]. A vast majority of metals and their alloys can be utilised for composites manufacturing. However, the most common ones include lightweight metals such as aluminium, titanium or magnesium. These composites are frequently used in aerospace applications where both extremely high durability and low weight are necessary [78, 79]. The other type of metallic matrix, so called intermetallic matrices, involve combination of two or more metallic or semi metallic elements which exist together as homogeneous substance. Atomic level differences such as long-range ordering and fixed stoichiometry distinguish them from other alloys. Resulting materials have impressive mechanical properties at elevated temperatures due to the restriction of the dislocations movement, nevertheless at the cost of extremely low ductility [80]. The representative of intermetallic materials is molybdenum disilicide ($MoSi_2$), frequently used as a heating element of furnaces [76, 79].

Ceramic matrix composites cover a broad range of inorganic materials (not including metallic materials), often requiring high-temperature processes [81]. The main advantage of ceramic matrices is high (compared to other matrix types) resistance to heat, abrasion, wear and chemical reactions. However, these benefits are offset by typically poor tensile and impact properties and low ductility, leading to catastrophic failures. The most important CMCs include silicon carbide, mullite or sodalime glass [81, 82].

2.1.2.1 Aerogel filled composites

Due to the various exceptional properties, the materials from the aerogel family have been identified as a desirable filler for particulate composites. Most often, the composites comprise different aerogel particles of varying sizes and shapes embedded into a polymer matrix structure. Figure 2-3 briefly summarise the aerogel and polymer combinations found in the recent research \\Salimian, 2018 #315//.

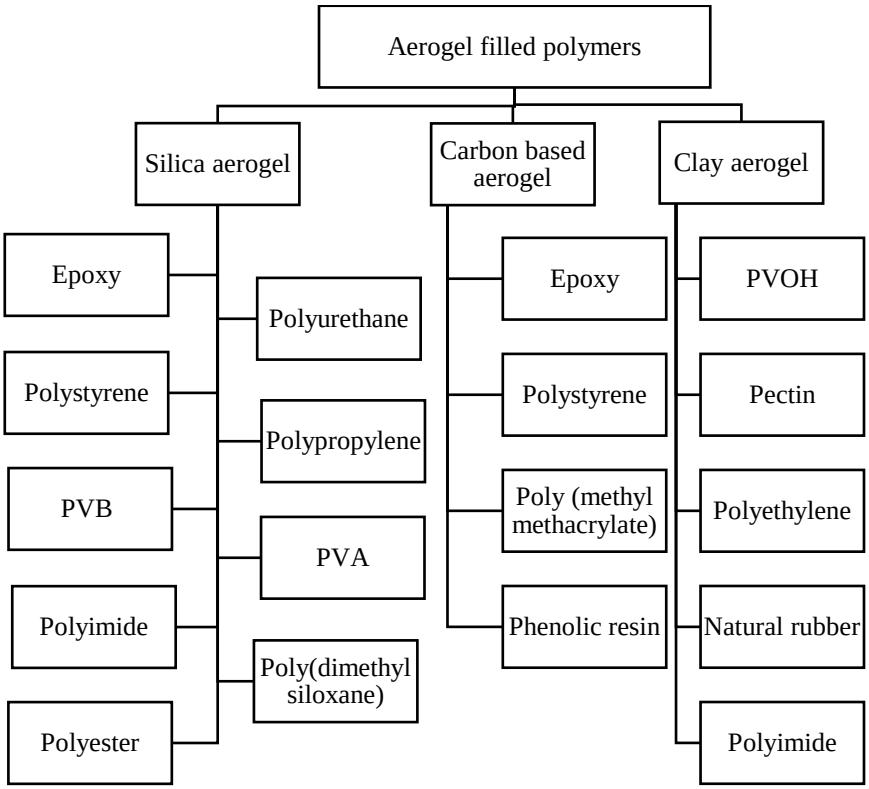

Figure 2-3 Summary of studies about aerogel filled polymers divided by aerogel type.

By analysing the literature, it can be noticed that most research focused on investigating the potential benefits of using silica aerogel particles. This is due to the superiority of its properties compared to other aerogels and the fact that it is the first aerogel being synthesized and commercialised. A number of investigations have been launched in characterising the properties of silica aerogel particles mixed with various polymers, with epoxy remaining the

most popular one [24, 30-32, 83-94]. The majority of such studies have evaluated the impact of silica aerogel particles on epoxy thermal properties mainly due to the interest from the industry, wide availability, and resins' ease of use [86]. Nevertheless, those investigations have mainly focused on mechanical properties of aerogel-filled composites and did not exploit the full potential they can provide in terms of thermal properties [85, 91, 95].

Another type of widely used polymer filler is clay aerogel. It is combined with a broad range of water-soluble polymers such as poly(vinyl alcohol) (PVOH), natural rubber or poly(amide-imide) [96-100]. The addition of organic polymer components allows clay aerogels to exhibit better mechanical properties than silica aerogel. However, such characteristics are strongly dependent upon the composition, microstructure and processing parameters [96, 99]. Also, the utilisation of specific polymers (such as pectin) results in complete biodegradability of the material. Combined with excellent mechanical properties and a cheap manufacturing process, clay-based aerogels are being noticed as a replacement of unrecyclable polymer foams in insulation and packaging areas [96, 97].

Finally, the effect of carbon-based aerogel has also been investigated with prominent representatives of this type of aerogels, including graphene aerogel, aerographite and carbon aerogel [86, 101-103]. With similar physical properties to other aerogel types, carbon aerogels attract attention mainly due to the extremely high electrical conductivity [104-106]. These outstanding properties of carbon aerogels find application in multiple industrial areas such as solar energy collection, electrochemical devices or catalyst support. Mostly combined with similar resin systems as silica aerogel, carbon-based aerogels allow for higher mechanical properties, including tensile strength and fracture toughness, on the other hand significantly increasing thermal conductivity values [107-110].

2.1.2.2 Polymers

The word "polymer" indicates a substance comprised of molecules with long sequences of one or more types of atoms or group of atoms connected using primary bonds (most often covalent) [111]. The molecules building polymer are called "macromolecules", and they are formed in the process of linking together monomer molecules through the chemical process known as polymerization. As a result of polymerisation, multiple types of skeletal structures of polymers can be achieved, leading to different properties of synthesized materials. The simplest form of skeletal structure is the "linear" one, and it can be described as a chain with two ends able to link with other macromolecules. Other types include cyclic (ring) polymers which do not possess free ends. Branched polymers include lengthy side chains connected to the main chain at a branch point. Finally, network polymers being able to create three-dimensional structure

by joining with all neighbouring chains (crosslinking). Both branched and network polymer can be synthesized through polymerisation or, most common by crosslinking previously created shorter chains. The skeletal structure has been proved to have a significant impact on the properties of materials. As a result, the melting temperature of linear polyethylene is about 20°C higher than branched polyethylene. In addition, the crosslinking density of breached and network polymers was investigated with high crosslinking density materials presenting higher mechanical properties [112].

The majority of commercially available polymers are organic due to the presence of a covalent compound of carbon, and Figure 2-2 presents the most common classification of polymers by separating them into three groups, including thermoplastics, thermosets and elastomers.
Thermoplastic polymers (also referred to as plastomers) are plastics that can be shaped in a specific temperature range, however, this process is reversible. As a result, after solidification, the change in shape is possible by reheating the material to its meting temperature, unless thermal degradation occurs. Examples of thermoplastics include polyethylene and nylon [113]. Completely different behaviour is presented by thermoset polymers that create three-dimensional cross-linked structures, making it impossible for further alteration of the material shape. The leading representatives of this family of plastics are commonly used epoxy and polyester resins [114]. Elastomers can change their dimensions elastically under tensile or compressive stress but return to their initial state when stress is removed. The main reason behind such behaviour is very weak intermolecular forces and glass transition temperature below room temperature. Elastomers are most frequently used for the manufacturing of tyres or rubber seals [77].

2.1.2.2.1 Epoxy resin

The discovery of epoxy resins is dated to 1909 by Prileschajew [115]. They belong to the group of the thermosetting resin and are characterised by the presence of oxirane or epoxy ring in their molecular chain in a form presented below [116]:

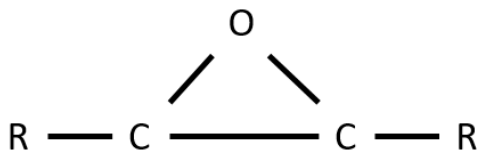

Figure 2-4 Epoxy ring molecular form [115].

Properties of epoxy resins strongly dependent upon the type of epoxy and curing agent used. Three main classes of epoxides being used nowadays include phenolic glycidyl ethers, aromatic glycidyl amines and cycloaliphatics [115]. The oxirane groups present in epoxy monomers can react with various curing agents such as amine-type, alkali, anhydrides, and catalytic curing agents [117]. The following description of the epoxy curing process will focus on the cross linking behaviour of epoxy mixed with amine agents due to the use of such hardeners in further experimental and simulation studies. As a result, during the curing process, the polyaddition reaction happens as the epoxy ring open when being affected by active hydrogen in the curing agent. Afterwards, the nitrile group of curing agent and previously created hydroxyl group form the amide structure [118]. Initially, curing tends to form linear epoxy chains; however, it leads to crosslinking of formed chains as the reaction progresses. As a result, the molecular weight rapidly increases due to the linking of not only epoxy and amine monomers but also long chain segments. Finally, curing process leads to formation of an infinite a cross-linked 3 dimensional network of polymer chains and solid structure of epoxy [118].

Epoxy resins present excellent mechanical properties (due to the high degree of cross-linking), good heat and chemical resistances and high adhesiveness to many substrates (excellent wetting properties) [119]. As a result, epoxies are widely used as general-purpose adhesives, composite reinforcing materials, high-performance coatings, and encapsulating materials [115].

2.1.2.2.2 Vinyl ester resin

Vinyl ester resin is a thermosetting matrix initially introduced to the industry in 1965 by Shell Chemical Company [120]. Chemically vinyl ester is quite similar to polyester incorporating backbone and multiple terminal ester groups but with different location of reactive sites (only two at the end of the chain) [121]. The main backbone of the vinyl ester can be obtained from epoxide, polyester, urethane or other resin systems, however, one derived from epoxy resins are of the most significant importance for industry [122]. In such vinyl ester, the synthesis is obtained by esterification of epoxy resin and unsaturated carboxylic acid (such as acrylic, methacrylic, terephthalic, or fumaric acid) [121]. Further, the diester is being diluted in a reactive solvent such as styrene (30-40% solid content) and finally cured by the addition of organic peroxide [123]. During the curing process, the free radical copolymerization of styrene with terminal reactive groups occurs, leading to creating a three-dimensional network of the polymer [123]. Due to the slow diffusion of catalyst through the polymer, the complete cure

is difficult to achieve while under atmospheric conditions [124]. As a result, post-curing at elevated temperature has to be accomplished to achieve full material strength [124].

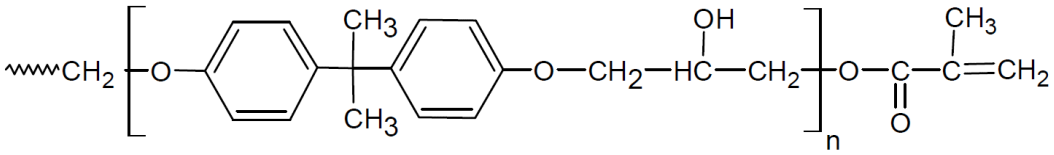

Figure 2-5 Monomer system of vinyl ester resin derived from Bisphenol A diglycidyl ether [125].

Vinyl esters present significant advantages over other polymer systems. Long molecular chains of vinyl esters can absorb loading shocks resulting in higher toughness and resilience compared to polyester[122]. In addition, the vinyl ester incorporates fewer ester groups that are especially susceptible to water degradation by hydrolysis, thus providing higher resistance to water and other chemicals [125]. Finally, having low vinyl functionality vinyl ester has minor shrinkage upon cure and lower peak exothermic temperatures [122]. Due to all mentioned advantages, vinyl esters are often selected to be used in marine, building, transportation and military applications [124].

2.1.3 Fibre-reinforced composites

Most frequently, fibrous composites consist of three main components: the discontinuous or dispersed phase in the form of fibres, the matrix used as the continuous phase, and the interphase region. For the reinforcement to be considered a fibre, it needs to have a high ratio between length and the cross-sectional dimension, also called the aspect ratio. Overall, the fibrous composites can be defined by the geometry of the reinforcement used. In the case of the aligned composites, the fibres face the same direction and the material properties are highly anisotropic. In addition, based on the aspect ratio of the fibres, two subgroups can also be introduced. As a result, the composites incorporating infinite aspect ratio fibres are called 'continuous', while the usage of short fibres with low aspect ratio results in the manufacturing of ‘discontinuous' composites [126]. Another type of fibrous composites is termed ‘random’ and comprises short fibres randomly orientated across the sample. Rather isotropic characteristics and lower price compensate for the lower mechanical properties of such composites. Finally, the woven reinforcements are used for the preparation of laminated structures. In this case, the fibres are turned into organised fabrics providing much easier handling and better mechanical performance [127]. Another type of categorising fibrous composites includes the matrix material used, and such a classification system is presented in Figure 2-6.

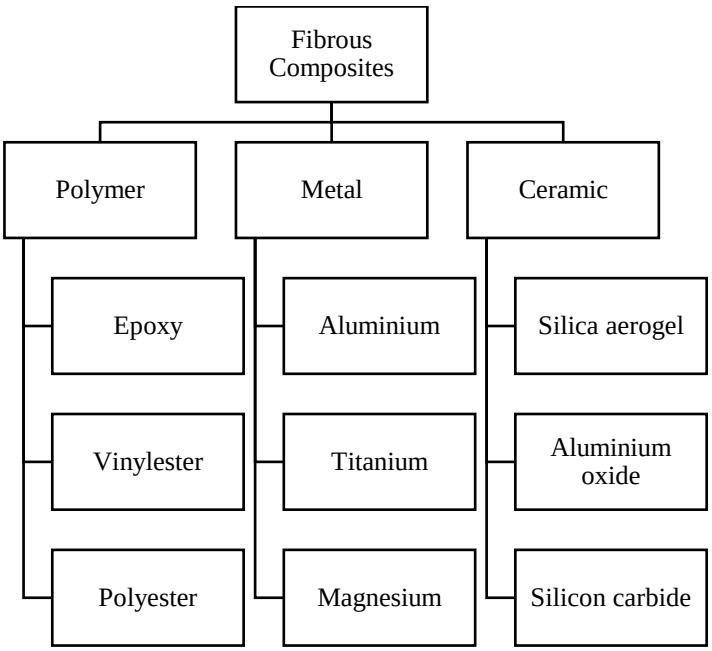

Figure 2-6 Classification of matrix materials used for the manufacturing of fibre reinforced composites.

Fibre-reinforced plastics (FRP) are probably the most frequently manufactured type of fibrous composites in which polymer matrix is being reinforced with fibres [128]. Most frequently utilised polymer resins include epoxy, vinyl ester and polyester, with the glass, carbon and aramid fibres used for their reinforcement. The resulting composites present superior strength to weight ratio and are increasingly important in aerospace, automotive, and construction industries [113].

Metal matrix composites (MMC) provides the advantage of mixing the properties associated with the metallic matrix, such as ductility and toughness, with those of the ceramic reinforcement, including high strength and stiffness [129]. Most frequently utilised fibrous reinforcements are carbon, SiC, and several oxide fibres, with polymeric and organic fibres not being able to withstand the temperatures required for MMC fabrication. Those materials are of particular interest to the aerospace industry, with multiple aluminium matrix composites being used in aeroplane production [129].

Finally, the ceramic matrix composites (CMCs) are a particular type of composite incorporating fibre and matrix, both of which are ceramic type. By combining different materials, CMCs presents high-temperature resistance combined with low density and greater fracture toughness and thermal shock resistance [130]. The fibres used for CMCs requires a polycrystalline structure in order to withstand temperatures of up to 1000°C. As a result, the most often used reinforcements include carbon, silicon carbide, alumina or mullite fibres. Such

ceramics composites are primarily utilised in high-temperature environments and can be found in turbine blades, high-performance braking systems or rocket propulsion components [81].

2.1.3.1 Aerogel blankets

Aerogel types of material have also been incorporated into fibre reinforced composites, mainly in the form of aerogel blankets, which now contributes to almost 70% of the total aerogel market [131]. They are manufactured by submerging the fibrous blanket into the aerogel solution before it gels and following the desired aerogel synthesis process. The resulting material presents thermal properties similar to pure aerogel, nevertheless, a significant increase in tensile properties can be expected [132]. Even though the current research in the aerogel field focuses on various aerogels, similarly as particulate composites, silica aerogel becomes the most frequently used aerogel type for the production of insulation blankets. Table 2-1 presents the commercially available silica aerogel blankets, the reinforcement type used and claimed thermal conductivity values.

Table 2-1 Examples of commercially available silica aerogel blankets with the reinforcement type used and claimed thermal conductivity values included [133].

Commercial name	**Manufacturer**	**Fibrous reinforcement**	**Thermal conductivity [mW/mK]**
Therma Wrap	Cabot	Polyester and PET	23
Cryogel x201	Aspen aerogel	Polyester and glass fibre	14
Pyrogel HPS	Aspen aerogel	Glass fibre	14
Spaceloft	Aspen aerogel	Fibre glass	15
SACB-0-X	Joda	Fibre glass	16
SACTT-X	Joda	Ceramic fibre	16

When analysing Table 2-1, it can be noticed that the silica aerogel has been combined with a wide range of fibrous reinforcement, including glass, PET or ceramic fibres. Regardless of the type of fibre used, all the composites provide high thermal resistance mainly due to the material's low fibre volume and internal structure. Typical blanket includes fibres coated in aerogel and large voids in between the coated fibres. According to the manufacturer, there is no contact between neighbouring fibres inside the aerogel blanket composites, reducing the heat conduction through solid aerogels [132]. Also, the aerogel particles on the fibre surface reduce the void spaces between fibres and thus the gas conduction heat transfer of the porous materials. In addition, other superior properties have been found, such as perfect sound insulation, high fire retardation and even air purification capabilities [132]. Even though the

silica aerogel blankets provide a wide range of benefits, they do possess certain drawbacks. Due to being manufactured with amorphous silica, most commercially available aerogel blankets are prompt to produce high quantities of dust particles. Nevertheless, both the International Agency for Research on Cancer and the Occupational Safety and Health Organization has reported aerogel particles not harmful to human health [133].

Currently available aerogel blankets are mainly used as thermal insulation material in many aerospace and construction applications. Multiple cases of incorporating such materials into oil and gas pipelines or building walls have been reported, resulting in much lesser energy losses. In addition, recently, aerogel blankets have also been used by the textile industry, with Oros using them as a base for their high-performance outdoor outfits. Additionally, the aerogels were used in a space application with the aerogel parts being included in multiple space rovers such as the 2003 “Spirit and Opportunity” made by NASA [132-134].

2.1.3.2 Fibre reinforcements

The classification of fibre reinforcements by origin is presented in Figure 2-7.

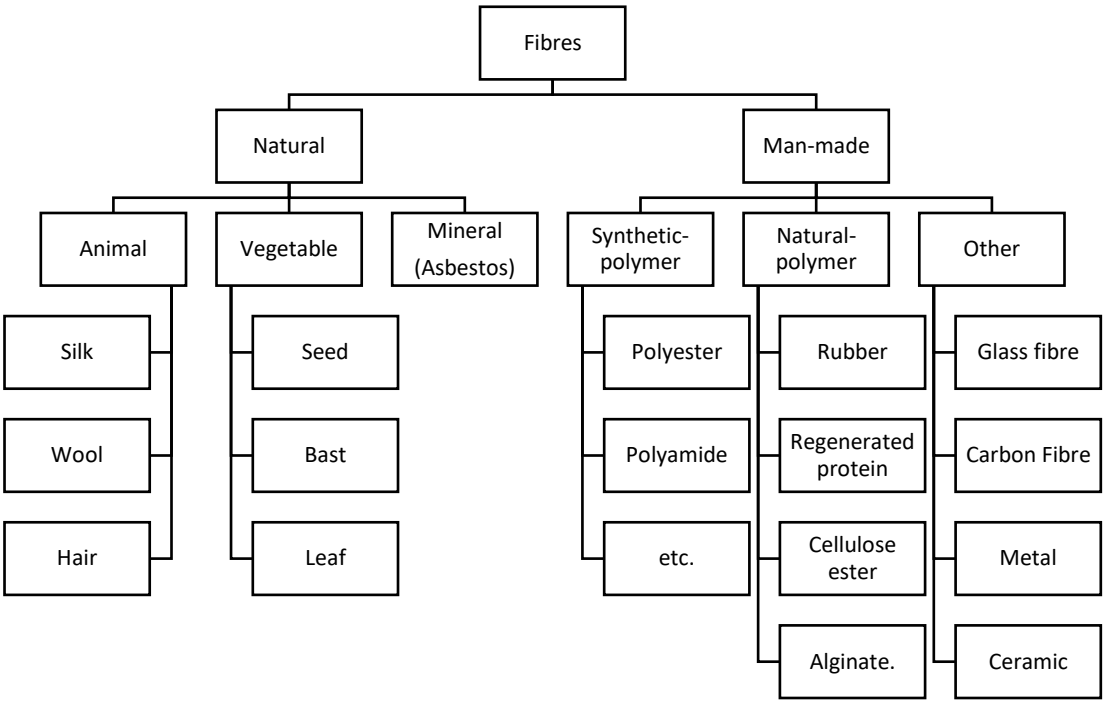

Figure 2-7 Classification of fibre reinforcements by origin [135].

Fibre reinforcements combined with various matrices provide enhanced properties of the resulting composite materials [136]. Due to their shape, they are the most popular type of composite reinforcements providing materials with superior strength and stiffness while maintaining low density [76]. Such properties result from the three most important characteristics: small diameter to grain size ratio, high aspect ratio, and a very high degree of flexibility [137]. Currently, multiple types of fibres are being used, however, the most common classification divides them by their origin [135]. Even though the fibres occur naturally, the following review will focus only on man-made fibres as they are most widely used in the production of aerogel composites, including the most popular ones such as glass, carbon, and PET fibres.

2.1.3.2.1 Glass fibre

Glass fibre can be simply described as a material incorporating many small diameter fibres of glass. Initially used in 1893 by Edward Drummond Libbey to create a silk and glass fibre fabric, it quickly has been introduced to mass production in the form of glass wool [138]. Nowadays, most of the glass fibre is produced using a technique in which raw materials such as sand, clay, colemanite etc., are being heated and mixed in a furnace, further draw into a form of fibre using bushings [139]. Even though silica become the main constituent of glass fibre, the addition of other materials led to the creation of multiple types of glass fibres such as E-glass (alumoborosilicate glass) providing superior electrical insulation, type C (calcium borosilicate glass) providing superior chemical resistance and type D (borosilicate glass) with low dielectric constant [138, 139]. Typically created glass fibres have a diameter in a 3.8 – 20 μm range and are processed into two major geometry groups. These include continuous fibres mainly incorporated into yarns and textiles and discontinuous fibres used in the form of blankets or batts [140].

2.1.3.2.2 Carbon fibre

Carbon fibres (CFs) have been manufactured for the first time in 1880 by Thomas Edison to be used in incandescent electric lamb [141]. The fibres exhibit superior properties with high tensile modulus and strength, fatigue strength, and high thermal conductivity [142]. Previously carbon fibres were manufactured by carefully controlled pyrolysis of organic-based fibres. Most recently they are produced through carbonization of organic polymers (e.g. polyacrylonitrile) drawn into long strands resulting in fibres made of more than 92 wt% of carbon in the nongraphic state [141]. Currently, there are few types of carbon fibres being manufactured, and they are categorised according to their tensile modulus and strength. The categories include general-purpose (GP), high strength (HS), intermediate modulus (IM), or

high modulus (HM) fibres. However, the properties of CFs vary for different manufacturers [141]. CFs usually have a diameter between 5 – 10 μm and similarly as glass fibre is available in continuous and chopped forms. Due to the high cost of carbon fibres, they are mainly used in aerospace, defence and automotive industries [128].

2.1.3.2.3 PET fibre

Polyethylene terephthalate (PET) fibres represent chemical fibres and, more specifically, polyester fibres [135]. Manufactured for the first time in 1934 by E. W. Spanagel due to condensation of ethylene diglycol and therephthalic acid PET is gaining more interest [143]. As a result of being a thermoplastic polymer, PET fibres can be reused (re-melted), which is frequently used in a manufacturing process and makes it a perfect candidate for a recyclable reinforcement material [127]. Most often, PET fibres are being manufactured using continuous polymerisation or previously granulated polymer (batch process), during which initially dried and melted polymer pellets are being extruded through a spinneret [143]. The diameter of created fibres ranges between 12 – 25 μm, and the properties of created fibres strongly depend on the parameters used during the manufacturing process. Even though the manufacturers tailor properties of PET fibres according to customer demand, in general, PET fibres exhibit low hardness, rigidity and strength but has a significant ductility and impact strength, which are often required in insulation materials and garments [127].

2.2 Multiscale material modelling

Multiscale material modelling (MMM) is defined as a modelling approach incorporating at least two modelling techniques with varying length and times scales [144]. As presented in Figure 2-8, there are many approaches to simulate materials with the most common methods, including atomistic modelling, mesoscale modelling and engineering and process unit design [144].

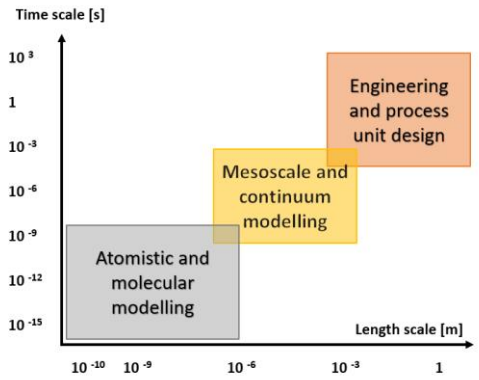

Figure 2-8 Representation of multiscale modelling techniques and approximate range of time and space they cover [144].

Regardless of the simulation techniques used, there are two main approaches to categorise multiscale modelling based on the connection between the modelling techniques. They are hierarchical and hybrid methods. The hierarchical approach is based on the utilisation of separate models connected through defined parametric coupling. In contrast, hybrid approach models are concurrently analysing different spatial regions of the same simulation [144].

The hierarchical approach has been reviewed by many research studies, including Espinosa et al., Weinberger et al., or Schmauder et al. [145-147]. They often highlighted the difficulty of providing correct coupling mechanism and creating the linkage between the nanoscale and higher scale simulations [145-147]. Although there are currently many ways of linking the material properties obtained at different scales, many researchers failed to implement them. For example, Johnston et al. have utilised a hierarchical approach to investigate carbon fibre and epoxy composites [148]. In their work, the author implemented a molecular dynamics study to model the mechanical properties (transverse modulus and tensile strength) of the fibre/polymer interfacial region. Afterwards, those properties have been incorporated into the microscale simulations without any coupling mechanism allowing for the analysis of the failure mechanics. Another approach of multiscale modelling has been presented by Chandra et al., who implemented a hierarchical coupling methodology. In their work he has transfer data between molecular dynamics at the nanoscale and discrete dislocation dynamics at the microscale. In addition, obtained results were further introduced into the crystal plasticity framework at the mesoscale. The resulting model allowed to assess the plasticity in the coper crystal under uniaxial tension. Nevertheless, the author highlighted that the proposed modelling system possesses certain limitations as it can simulate only crystal FCC materials [149]. A few other hierarchical investigations have been conducted, with the consensus that more reliable coupling mechanisms are needed for more accurate MMM.

The hybrid multiscale methods have been described by Scheibe et al. [150], Wang et al. [151] and Giessen et al [152]. In general, such models identify a crucial fraction of the overall simulation domain and utilise the small-scale fractional model with high resolution to analyse it. The output of such analysis is directly linked to a large-scale model with coarse resolution investigating the remaining portion of the overall domain. This method allows for a detailed analysis of material structure while maintaining a moderate need for computational resources. Other terms such as “adaptive algorithms” or “multi-physics modelling” have also been used to describe the hybrid methods. A great example of hybrid analysis is presented by Lidorikis et al. [153]. In their work, Si_3N_4 film in contact with pure Si was modelled. In this case, the interfacial region was investigated via molecular dynamics simulations while the remaining solids being analysed through finite element analysis. Both models have been joined by using

a hand-shaking scheme. By utilising the hybrid approach, they managed to investigate the atomistical induced stress distributions and reduced computational time by 75% compared to the purely atomistic approach [153].

The multiscale material modelling performed in this thesis employs the hierarchical approach and uses two different scale modelling techniques as presented in Figure 2-9. This approach was selected due to due to much easier implementation strategy allowing to use already existing software packages without the need to create complex coupling mechanisms.

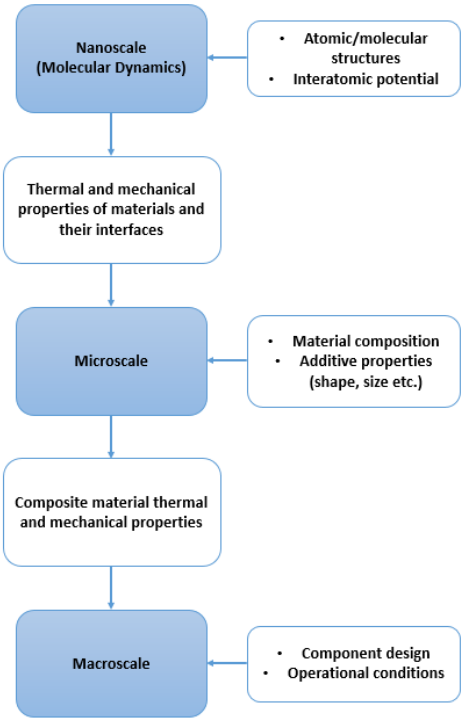

Figure 2-9 The schematical representation of multiscale material modelling approach used in this study.

It involves with the molecular dynamics simulation with the introduction of atomistic structures and interatomic potentials in order to predict thermal and mechanical properties of aerogel materials. In addition, it incorporates the modelling of the interface between aerogels and reinforcement materials allowing for a calculation of its' thermal and mechanical properties. Afterwards, the obtained data are inputted into a microscale model based on a finite element analysis. When supplemented by a higher scale input parameter, including material composition or properties of additive materials, it allows to predict mechanical and thermal properties of particulate composite materials. Afterwards, such data can be introduced to macroscale models without explicitly modelling the internal structure of the composite material. The section 2.2.1 discusses the theory behind modelling techniques used in analysing the aerogel-filled composites.

2.2.1 Molecular dynamics background

Molecular Dynamics (MD) is a computational simulation allowing for the investigation of the physical movement of atoms or molecules [154]. The method is based on numerical solutions of classical equations of motion (Newton's equations) describing the trajectory of an atom movement as well as its position, velocity and acceleration as a function of time [155]:

$$F_i = m_i a_i \quad \text{Eq. 2}$$

$$F_i = -\nabla_i V \quad \text{Eq. 3}$$

$$\frac{dV}{dr_i} = m_i \frac{d^2 r_i}{dt^2} \quad \text{Eq. 4}$$

where F_i is a force exerted on particle i, m_i is a mass of particle i, a_i is an acceleration of particle i and V is the potential energy of the whole system. As a result, Newton's equations can relate the derivative of the potential energy of the atoms to the change in their position (r_i) with time (t) [155]. The potential energy of atoms and force acting between particles is calculated using molecular mechanics force fields or interatomic potentials. Following the calculation of such microscopic observables, it is possible to convert them into macroscopic properties such as pressure or energy via methods of statistical mechanics [156].

Molecular Dynamic simulations have multiple ways to determine the position of the particles at future time steps. The most common ones include [154, 157-160]:

a) Verlet method – the velocity of atoms is not required in the calculation of future position
b) Velocity Verlet method – both current position and velocity of the particle are necessary to determine the position of the particle in the future
c) Leapfrog method – scheme calculates velocities at time $t + 0.5\Delta t$ and position at time $t + \Delta t$ effectively leaping over each other.

The procedure of using the Velert method can be described in a few steps, as presented in Figure 2-10.

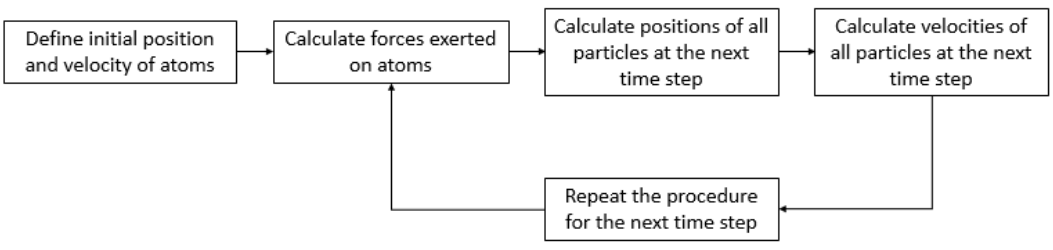

Figure 2-10 Most common simulation procedure for the velocity Velert method [154].

2.2.1.1 Force field and potential functions

In molecular dynamics, the force field is described as the form and parameters of a mathematical function used to calculate the potential energy of the analysed system. Both equations and parameters are obtained from quantum mechanical calculations and experimental work [161]. All of the force fields are divided into three main groups, including all-atom force fields (incorporate parameters for every atom type in the simulation), united-atom force fields (define hydrogen and carbon atoms in methyl and methylene structures as a single interaction centre) and coarse-grained force fields (simplified model in which molecular models substitute atomistic details) [154, 162].

In standard force field equations, the total energy (E_{total}) of the systems comprises of bonded (E_{bonded}) terms(including covalent bonds) and nonbonded ($E_{nonbonded}$) terms describing long-range electrostatic and van der Waals forces [163, 164]:

$$E_{total} = E_{bonded} + E_{nonbonded} \quad \text{Eq. 5}$$

Further expansion of energy terms yield:

$$E_{bonded} = E_{bond} + E_{angle} + E_{dihedral} \quad \text{Eq. 6}$$

and

$$E_{nonbonded} = E_{electrostatic} + E_{van\ der\ Waals} \quad \text{Eq. 7}$$

Except for the function form to calculate each of the mentioned parameters, the force field would include a set of parameters including atomic mass, partial charge for individual atoms, bond lengths, bond angles, and dihedral angles for pairs and effective spring constant for each potential [154]. A slightly different approach is being used for interatomic potentials. They describe interactions between atoms in the form of a parameterized bond-order function, instead of using many-body expansions of potential energy in bond lengths and angles as an underlying principle. As a result, such an approach introduces many-body effects and chemical bonding into a pair potential [154, 156, 165].

In the following study, a number of different potentials have been used. BKS, Tersoff, and Vashishta were used to simulate silica aerogel and amorphous silica, while OPLS-AA and ReaxFF potentials were utilised to simulate organic compounds [165-170].

2.2.1.1.1 BKS

BKS potential is a two-body potential described by the equation below:

$$V(r_{ij}) = \frac{q_i q_j}{r_{ij}} + A_{ij} e^{-B_{ij} r_{ij}} - \frac{C_{ij}}{{r_{ij}}^6} \quad \text{Eq. 8}$$

where r_{ij} represents the distance between neighbouring i and j atoms, q_i and q_j are their atomic charges and A_{ij}, $B_{ij,}$ and C_{ij} are constants specified for a particular pair of atoms. Equation 8 describes both long-range Coulombic interactions (first term) and short-range attraction and repulsion of atoms (respectively second and third term) [170]. The cut-off distance for all interactions was set up to be 8 Å. Beyond that distance. The Coulombic interactions were computed by particle-particle particle-mesh (pppm) solver in the Large-scale Atomic/Molecular Massively Parallel Simulator (LAMMPS). Firstly, the solver maps the atom charge onto a 3-D mesh, then uses 3-D Fast Fourier Transforms to compute the Poisson's equation on the mesh, and finally interpolates electric fields from the points included within mesh back to the atoms. In order to achieve the required accuracy, the relative root-mean-square error in per-atom forces was not expected to increase beyond 0.0001 [171].

Nevertheless, modelling silica aerogel samples requires the creation of amorphous silica in the first place. The subsequent heating and cooling of the silica and oxygen atoms can lead to atoms approaching each other too closely, resulting in nonphysical behaviour. Since BKS potential is not capable of addressing close repulsive forces [172], the additional '24-6' Lennard–Jones (LJ) term was introduced to the previous equation resulting in the final version of the potential to be:

$$V(r_{ij}) = \frac{q_i q_j}{r_{ij}} + A_{ij} e^{-B_{ij} r_{ij}} - \frac{C_{ij}}{{r_{ij}}^6} + 4\varepsilon_{ij}\left[\left(\frac{\sigma_{ij}}{r_{ij}}\right)^{24} - \left(\frac{\sigma_{ij}}{r_{ij}}\right)^{6}\right] \qquad \text{Eq. 9}$$

where additional parameters ε_{ij} and σ_{ij} are respectively: the depth of the potential well and the distance at which the inter-particle potential is zero [173]. In the simulated system, three different atom pairs are present: Si-Si, Si-O and O-O. Parameters used to simulate those pairs are presented in Table 2-2.

Table 2-2 Parameters used for simulating silica aerogel using BKS potential [174].

Parameter	Si-Si	Si-O	O-O
$\boldsymbol{A_{ij}}$ [eV]	0.0	18,003.7572	1388.7730
$\boldsymbol{B_{ij}}$ [Å^{-1}]	0.0	4.87318	2.760
$\boldsymbol{C_{ij}}$ [eV Å^6]	0.0	133.5381	175.0
$\boldsymbol{\varepsilon_{ij}}$ [eV]	13.20	1.12×10^{-2}	4.78×10^{-4}
$\boldsymbol{\sigma_{ij}}$ [Å]	0.40	1.35	2.20
$\boldsymbol{q_{Si}}$ [e]	2.4		
$\boldsymbol{q_O}$ [e]	-1.2		

2.2.1.1.2 Tersoff

The Tersoff method describes a three-body potential, including an angular contribution of the force. This potential and its parameters were selected to fit experimental and theoretical values measured for both existing and predicted silicon arrangements. It has been widely used in recent studies regarding, e.g. silicon, carbon or germanium [167, 175, 176]. The potential energy of a system is calculated using the following set of equations:

$$E = \frac{1}{2}\sum_{i}\sum_{j\neq i} V_{ij} \quad \text{Eq. 10}$$

$$V_{ij} = f_C(r_{ij})[f_R(r_{ij}) + b_{ij} f_A(r_{ij})] \quad \text{Eq. 11}$$

$$f_C(r) = \begin{cases} 1 & : \quad r < R - D \\ \frac{1}{2} - \frac{1}{2}\sin\left(\frac{\pi}{2}\frac{r-R}{D}\right) & : \quad R - D < r < R + D \\ 0 & : \quad r > R + D \end{cases} \quad \text{Eq. 12}$$

$$f_R(r) = Ae^{-\lambda_1 r} \quad \text{Eq. 13}$$

$$f_A(r) = -Be^{-\lambda_2 r} \quad \text{Eq. 14}$$

$$b_{ij} = (1 + \beta^n {\zeta_{ij}}^n)^{-\frac{1}{2n}} \quad \text{Eq. 15}$$

$$\zeta_{ij} = \sum_{k\neq i,j} f_C(r_{ik}) g(\theta_{ijk}) e^{[{\lambda_3}^m (r_{ij} - r_{ik})^m]} \quad \text{Eq. 16}$$

$$g(\theta) = \gamma_{ijk}\left(1 + \frac{c^2}{d^2} - \frac{c^2}{[d^2 + (\cos(\theta) - \cos(\theta_0))^2]}\right) \quad \text{Eq. 17}$$

where, f_C is a smooth cut-off function used to reduce the range of potential and thus reduce required computational resources. Further functions, f_R represents two-body interactions while f_A is responsible for three-body interactions. Function b_{ij} corresponds to the bond order measurement, including terms that aim to limit the range of interactions to the first neighbouring shell. By introducing this function, it was possible to introduce the dependency of the local environment on the atom bonds' strength (strength is lowered with an increasing number of neighbours). The ζ_{ij} term calculates effective coordination number of atom i taking into account the distance between two neighbouring atoms r_{ij} and r_{ik} and the bond angle θ.[167]

2.2.1.1.3 Vashishta

Vashishta and co-workers have managed to create a potential incorporating combined two-body and three-body potentials. It calculates screened charge-dipole, screened Coulombic, repulsive and dispersion interactions, including bond-angle energy using Stillinger-Weber potential [166]. The Vashishta potential have been used in recent studies primarily to simulate inorganic compounds such as SiO_2 or InP [166, 177], where the following set of equations calculates the energy of the atomistic system:

$$U = \sum_{i}^{N}\sum_{j>i}^{N} {U_{ij}}^{(2)}(r_{ij}) + \sum_{i}^{N}\sum_{j\neq i}^{N}\sum_{k>j,k\neq i}^{N} {U_{ijk}}^{(3)}(r_{ij}, r_{ik}, \theta_{ijk}) \quad \text{Eq. 18}$$

$${U_{ij}}^{(2)}(r) = \frac{H_{ij}}{r^{\eta_{ij}}} + \frac{Z_i Z_j}{r} e^{\frac{-r}{\lambda_{1,ij}}} - \frac{D_{ij}}{r^4} e^{\frac{-r}{\lambda_{4,ij}}} - \frac{W_{ij}}{r^6}, r < r_{c,ij} \quad \text{Eq. 19}$$

$$\begin{aligned} &{U_{ijk}}^{(3)}(r_{ij}, r_{ik}, \theta_{ijk}) \\ &\quad = B_{ijk} \frac{[\cos(\theta_{ijk}) - \cos(\theta_{0ijk})]^2}{1 + C_{ijk}\,[\cos(\theta_{ijk}) - \cos(\theta_{0ijk})]^2} \\ &\quad \times\ e^{(\frac{\gamma_{ij}}{r_{ij} - r_{0,ij}})} e^{(\frac{\gamma_{ik}}{r_{ik} - r_{0,ik}})}, r_{ij} < r_{0,ij},, r_{ik} < r_{0,ik} \end{aligned} \quad \text{Eq. 20}$$

where: ${U_{ij}}^{(2)}(r)$ describes all two-body type of interactions, H_{ij} determines the strength of the short-range repulsion forces, Z_i is an effective charge, D_{ij} specifies the strength of the charge–dipole attraction forces, w_{ij} describes van der Waals interactions, and λ_4 and λ_1 are respectively screening lengths for a charge–dipole and Coulomb forces. Furthermore, ${U_{ijk}}^{(3)}$ defines the three-body potential, including spatial and angular dependencies described by B_{ijk} (strength of three-body interactions) and C_{ijk} (three-body saturation parameter)[166]. A detailed description of the parameters and values used in mentioned equations was described by Branicio [177].

2.2.1.1.4 OPLS-AA

OPLS-AA (optimized potentials for liquid simulations all-atom) force field is an improved version of the original OPLS force field developed by Prof. William L. Jorgensen. The initial model utilised a partially united-atom (UA) approach, while the all-atom model introduces more flexibility in terms of charge allocation and torsional energetics [168, 169, 178, 179].

The total energy of the system in the OPLS-AA force field comprises four energy components such as bond stretching (E_{bond}), angle bending (E_{angle}), torsional ($E_{torison}$) and non-bonded interactions (E_{nb}).

$$E = E_{bond} + E_{angle} + E_{torsion} + E_{nb} \quad \text{Eq. 21}$$

The following equations represent the bond stretching and angle bending terms:

$$E_{bond} = \sum\nolimits_{bond} K_r(r - r_{eq})^2 \quad \text{Eq. 22}$$

$$E_{angle} = \sum\nolimits_{angles} K_\theta(\theta - \theta_{eq})^2] \quad \text{Eq. 23}$$

where, K_r and K_θ factors are respectively bond and angle coefficient, r_{eq} is equilibrium bond length and θ_{eq} is equilibrium bond angle. The majority of force constants are acquired from the AMBER all-atom force field; however, to improve accuracy, some were taken from the CHARMM force field [169, 180, 181]. The torsional energy term is the sum of the following expression for all dihedral angles:

$$E_{torsion} = \sum_i \frac{{V_1}^i}{2}[(1+\cos(\varphi_i + f_i 1)] + \frac{{V_2}^i}{2}[(1-\cos(2\varphi_i + f_i 2)] + \frac{{V_3}^i}{2}[(1-\cos(3\varphi_i + f_i 3)] \quad \text{Eq. 24}$$

where V_1, V_2, and V_3 are the coefficients in the Fourier series, φ_i is the dihedral angle, and f1, f2, and f3 are phase angles. Finally, the nonbonded interactions used by OPLS-AA constitute Lennard-Jones terms with the addition of Coulomb charge terms.

$$E_{nb} = \sum_i^a \sum_j^b [\frac{q_i q_j e^2}{r_{ij}} + 4\epsilon_{ij}(\frac{{\sigma_{ij}}^{12}}{{r_{ij}}^{12}} - \frac{{\sigma_{ij}}^6}{{r_{ij}}^6})]f_{ij} \quad \text{Eq. 25}$$

where r_{ij} represents the distance between neighbouring i and j atoms, q_i and q_j are their atomic charges. Parameters. ε_{ij} and σ_{ij} are respectively: the depth of the potential well and the distance at which the inter-particle potential is zero. Nonbonded interactions are calculated only if three or more bonds separate the atoms, and 1,4 interactions will be weakened by a fudge factor (f_{ij}) of 0.5. In any other cases f_{ij} will be equal to 1 [169].

2.2.1.1.5 ReaxFF

Reactive force field (ReaxFF) is a bond order-based force field created by Adri van Duin et al. Initially created in 2001 for hydrocarbons; the force field gained much interest due to its ability to perform fully reactive simulations of large scale systems [165]. The overall system energy is defined by the following equation [182]:

$$\begin{aligned} E_{system} = {} & E_{bond} + E_{lp} + E_{over} + E_{under} + E_{val} + E_{pen} + E_{coa} + E_{C2} \\ & + E_{triple} + E_{tors} + E_{conj} + E_{H-bond} + E_{vdWaals} \\ & + E_{Coulomb} \end{aligned} \quad \text{Eq. 26}$$

As it can be noticed, Reax Force Field included much more partial energies than standard potentials mentioned beforehand. Instead, introducing (with different functional forms) previously known energy components such as bond energies (E_{bond}), torsional energies (E_{tors}) or nonbonded Coulomb ($E_{Coulomb}$) and van der Waals ($E_{vdWaals}$) interactions it also includes more complex partial energies to account for: lone pair energy (E_{lp}), over coordination (E_{over}), undercoordination (E_{under}), angle energy (E_{val}), penalty energy (E_{pen}),

three (E_{coa}) and four (E_{conj})body conjugation term, hydrogen bond interactions (E_{H-bond}), correction for C_2 (E_{C2}) and triple bond energy correction (E_{triple}) [165, 182]. All functional forms describing components of system total energy were documented in Chenoweth et al. work [182].

What makes the Reax force field so popular is the possibility of simulating chemical reactions due to the terms related to the bond order concept enabling the breakage and creation of bonds [183, 184]. Other non-reactive force fields are only capable of stretching/twisting bonds due to interaction with other atoms. In addition, Reax tends to be more general, with parametrisation being conducted for a wide range of materials such as polymers, ion batteries, hydrocarbon reactions and many more [165, 185, 186]. Best fitting force field parameters can be achieved through global optimization techniques, including using the latest parametrization tools like ADFtrain and CMA-ES [183].

2.2.1.2 Ensemble

An ensemble can be described as a collection of many systems presenting a similar macroscopic (or thermodynamics) state but under a different microscopic state. Since classical thermodynamics is not interested in the behaviour of individual particles but rather the averaged properties of a macroscopic sample, an ensemble approach has to be used [154]. As a result, instead of investigating the time development of all particles in an analysed volume, a very large number of copies of the system with specified microscopic properties are created. Afterwards, the values are being averaged, and following the ergodic theorem, they equal the time average calculated by investigating the time evolution of the initial system. However, it should be highlighted that volumes created in the ensemble are not identical on the molecular level, but they do share specific thermodynamic properties [154-156, 187]. Within molecular dynamics, four most ensembles have been used most extensively.

1) Canonical ensemble (NVT) – number of atoms (N), volume (V) and temperature (T) are kept constant [188, 189].
2) Microcanonical ensemble (NVE) - number of atoms (N), volume (V) and total energy (E) are kept constant [190].
3) Isothermal-isobaric ensemble (NPT) - number of atoms (N), pressure (P) and temperature (T) are kept constant [191].
4) Grand canonical ensemble (μVT) – chemical potential (μ), volume (V) and temperature (T) are kept constant [192].

2.2.1.3 Thermostating

Thermostating is defined as an act of controlling the temperature of atoms during a molecular dynamics simulation. It is of particular importance as the averaged velocities of particles may lead to a slightly different temperature value than required, with the main reason for such behaviour is an energy exchange between kinetic and the potential energies [154]. The microcanonical ensemble is mainly used in classic molecular dynamics due to total energy control [154]. However, to create more experimental environment, the ensembles with controlled temperature are also used. As a result, several thermostating techniques have been determined to control particles' velocity (and thus the system's temperature), including the most frequently used: Nosé–Hoover and Berendsen thermostats [154, 193].

a) Berendsen thermostat

The Berendsen thermostat rescales the velocities of atoms in order to control the temperature of the system. The required temperature is achieved by coupling the system with an external heat source with a specified temperature (T_0) [194, 195]. As a result, the particles' velocities are scaled over time, and the rate of change of temperature is related to the difference in temperature between the system and the source [194]:

$$\frac{dT(t)}{dt} = \frac{1}{\tau}(T_0 - T(t)) \qquad \text{Eq. 27}$$

The coupling parameter τ controls the scaling of the system, and the change in temperature between the following time steps is calculated by:

$$\Delta T = \frac{\delta t}{\tau}(T_0 - T(t)) \qquad \text{Eq. 28}$$

Finally, the scaling factor for atoms' velocities is:

$$\lambda^2 = 1 + \frac{\delta t}{\tau}(\frac{T_0}{T_1} - 1) \qquad \text{Eq. 29}$$

where T_1 is the temperature of the system at the analysed time step.

The Berendsen thermostat is suitable for the microcanonical ensemble for which the temperature fluctuations will continue to grow until the required value is achieved. However, the system will not provide a correct canonical ensemble, especially for small systems (below a few hundred atoms) [162]. Overall, the Berendsen thermostat is used for its efficiency but is often combined with the Nosé-Hoover thermostat, allowing for correct atom trajectories fulfilling canonical ensemble requirements [154].

b) Nosé-Hoover thermostat

Nosé-Hoover thermostat has a slightly different approach to thermosetting as it limits the impact of an external heat reservoir to just an extra degree of freedom of the system. It is considered a fictitious dynamic variable (ς), which is physically similar to friction, which accelerates or decelerates particles until reaching the desired temperature [188, 189]. The following equations of motion have been introduced by Nosé-Hoover thermostat [195]:

$$m_i \frac{d^2 r_i}{dt^2} = f_i - \varsigma m_i f_i \qquad \text{Eq. 30}$$

$$\frac{\partial \varsigma(t)}{\partial t} = \frac{1}{Q}\left[\sum_{i=1}^{N} \frac{v_i^2}{2} - \frac{3N+1}{2} k_B T\right] \qquad \text{Eq. 31}$$

where, m_i and v_i are respectively a mass and velocity of a particle and f_i is a force applied to particle, Q represents the relaxation of the friction dynamics, N is a number of degree of freedom, k_B is Boltzmann constant, and T representing system desired temperature.

Nosé-Hoover thermostat determines the temperature of the investigated system; thus, the temperature fluctuates in the vicinity of the target value but does not reach it completely [196]. Similarly, the energy of the system is not steady. If the thermostat multiplier, ς, becomes positive, the heat is removed from the system while added when it falls below zero. The overall multiplier average value is 0 since no eternal force acts on the system [193, 197].

2.2.1.4 Periodic boundary conditions

The most commonly used boundary conditions for equilibrium MD simulations are periodic boundary conditions (PBCs), which enable simulation of an "infinite" system with the use of its small part named "unit cell" [154]. As presented in Figure 2-11, the central cell (modelled simulation region) is surrounded by virtual cells created by replicating a central cell to effectively simulate a continuous large system [163].

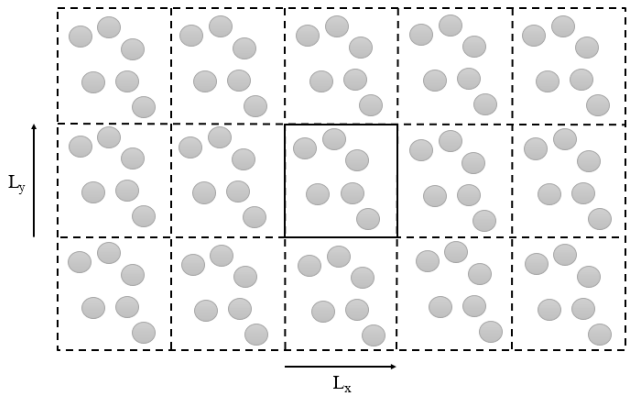

Figure 2-11 Schematically representation of periodic boundary conditions with grey spheres representing atoms within each unit cell.

Under such boundaries, the particles are allowed to interact across the boundary and leave the simulation volume on one side and re-enter it on the other side [155]. However, the original cell size has to be large enough to avoid unphysical topology. In the case of the too-small simulation volume, particles could be affected by their own representation in neighbouring virtual cells, leading to unphysical dynamics [198].

The opposite approach which allows particles to only interact within the cell is introduced using other boundary conditions such as fixed boundaries [199-201]. Also called non-periodic boundaries, they do not allow atoms to interact and move across boundaries. Instead, atoms are being deleted after crossing the boundary [200]. Other types of fixed boundaries, such as repulsive boundary, atomistic rigid walls and atomistic semi-rigid walls boundaries, apply repulsive forces as atoms get closer to the boundary [199].

2.2.1.5 LAMMPS

Large-scale Atomic/Molecular Massively Parallel Simulator (LAMMPS) is a molecular dynamics code focusing on material modelling. Developed in 1995 by Steve Plimpton from Sandia National Laboratories, LAMMPS is open-source software, and its usage is covered by the terms of the GNU General Public License [202].

LAMMPS was developed to simulate various systems, including atomic, polymeric, solid-state granular, coarse-grained, or macroscopic systems, under a broad range of boundary conditions and force fields [202]. Created to support parallel computing LAMMPS allows to simulate up to a billion particles by integrating Newton's equations of motion. It analyses particles mainly using a short-range interaction mode. However, additional long-range interactions can also be incorporated [203]. In addition, LAMMPS introduced a few interesting options for more meaningful and faster simulations. Firstly, to maintain the physical behaviour of the particles, LAMMPS incorporates a neighbour list that analyses the nearby atoms and prevents unphysical local densities [202]. Secondly, to speed up simulation using parallel computing, software utilizes spatial-decomposition techniques, resulting in a split of the simulation domain into equally computationally costly parts and assigning them to separate processors [202]. In order to maintain the connection between parts, processors communicate between each other and store "ghost" atom information for atoms located nearby their sub-domain [204].

2.2.2 Background of finite element analysis

Finite element analysis (FEA) is essential widely used technique for engineering design and analysis. It analyses the impact of external factors such as forces, heat, fluid flow or other

physical effects onto the defined products [205-208]. FEA works by discretising the modelled object into finite elements and then solving physical governing equations, often partial differential equations in nature, using a numerical approach to predict the behaviour of each element. All of the elements are then integrated to meet boundary conditions that constrain the whole object [205, 207].

The term, Finite Element Analysis, was used for the first time in 1960 by Clought, who used the FEA to investigate the stress distribution over the aircraft wings [206, 208]. However, the history of FEA technique can date back to 1941 and it originates from the need to find a solution for complex elasticity and structural analysis problems in engineering [205, 207, 208]. Hrennikoff and Courant are considered the authors of the first two publications in the field of finite element analysis, and even though their approaches are substantially different, they both carry a resemblance to the current FEA methods. In 1941, Hrennikoff divided a continuous domain with the use of lattice analogy, while in 1943 Courant managed to find the torsional deflection of a hollow shaft by decomposing the cross-section area into a set of triangles followed by the incorporation of piecewise shape functions for the results interpolation [205]. As computational capacity keeps improving over the past decades, the FEA has become available for a wide range of applications, including stress distribution, heat transfer, and fluid flow [205, 206, 208].

2.2.2.1 Advantages and limitations of FEA

FEA can simplify the product design process and provide an easier way to realise design concept. However, it has certain disadvantages, and it is up to the user to identify the potential benefits FEA can provide.

Firstly, FEA significantly reduces the cost of the product design phase as it allows to simulate the investigated idea without the need for costly experimental investigation. Additionally, it provides design flexibility. It can investigate engineering systems using a wide range of analysis methods including solid mechanics, dynamics, thermal, fluid flows and electrostatic and by allowing to simulate the design under hazardous, destructive, or impractical load conditions [205, 206, 209]. The FEA also provides a certain advantage over other computational methods as it can work with complex boundary and loading conditions, including cases such as over constraints in solid mechanics or application of time-dependent loads [207, 210]. On the other hand, the FEA can only provide an approximate solution for an analysed situation and not a closed-form analytical solution due to the fundamental techniques it incorporates. FEA also incorporates certain inherent errors because of numerical computations or the idealization of models [205, 211]. Finally, the FEA is strongly susceptible

to operator error as it heavily relies on the user to provide detailed inputs and to validate and verify the simulation results [205].

Overall, the FEA has gathered significant interest from the industry and research community mainly due to its flexibility and ease of use. As a result, it is not surprising that it has been incorporated into various engineering investigations.

2.2.2.2 Application of FEA

Even though the detailed FEA requires considerable computational power to generate an accurate system response, the FEA tools have been widely used to assist the product design and development processes [205, 208, 212, 213]. By incorporating a FEA into the product development process, the designers can identify the issues with a new idea and introduce necessary improvements. The FEA has been successfully incorporated into the following engineering scenarios [205, 206, 210, 212, 214, 215]:

- Structural analysis –investigate the stress and displacement under static loading conditions.
- Modal analysis – investigate the natural frequencies and mode shapes of the analysed design.
- Fatigue analysis – investigate the impact of cyclic loading on the analysed design.
- Thermal analysis – investigate the thermal behaviour of the design by incorporating major heat transfer methods such as conduction, convection, and radiation.
- Conjugate thermal analysis – investigate thermal behaviour between solid domain and adjacent fluid flow.
- Manufacturing analysis – investigate the impact of manufacturing processes on processed material.
- Flow simulation – investigate the flow of liquid or gas in a controlled environment.
- Fluid structural interactions – investigates the impact of surrounding fluid flow onto the analysed object.
- Failure analysis – investigate the possible reasons for structure failure under design conditions.

2.2.2.3 Modelling procedure

Even though the FEA analysis allows for a broad range of investigation, the principles of operation are the same for all analysis type. As a result, in FEA, the investigated volume is divided into smaller parts called “elements”, which are further assembled through the interconnection of points named “nodes” [205, 212, 213, 216, 217]. During the FEA

simulations, the behaviour of each element is determined by the behaviour of surrounding nodes. In general, the FEA procedure incorporates six steps, as presented in Figure 2-12 [210].

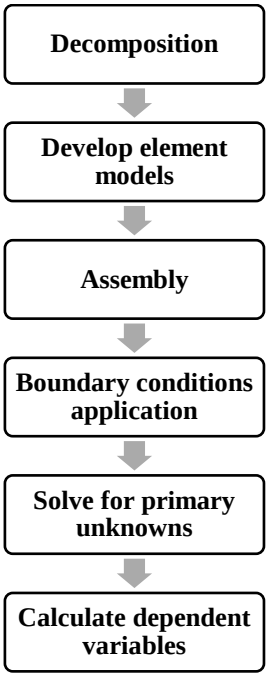

Figure 2-12 Procedure used during FEA modelling [205].

As presented in Figure 2-12, the FEA incorporates numerous steps. The first step of FE modelling is decomposition during which, the analysed object is discretized into finite elements or shapes, and the nodes surrounding each element are defined. In addition, during this stage, the elements and element/node relations are being defined, allowing to derive interpolation functions used to evaluate the element behaviour based on the nodal values [212]. The second step of FE analysis aims at the development of element models. As a result, the analysis type is being specified based on the objectives of the analysis.

Furthermore, the design variables are identified, and the mathematical model relying on governing differential equations is defined and translated into element models by various approximation methods [205, 212, 216]. Next, during the assembly step, the global coordinate system is created for the whole model. In order to achieve it, the elements under local coordinate systems are translated into elements under global coordinate system followed by an assembly of all elements into a single system model. Afterwards, the user-specified boundary conditions allow to define the external environment's effect on the analysed system. Following, implementation of adequate boundary conditions, the model is being solved for primary unknowns [205, 206]. During this stage, the large quantities of linear equations are being solved using mathematical algorithms to derive an approximate value of primary

unknowns. Finally, based on the solution of the linear equations, the dependent variables are being calculated based on the constitutive model of materials [205, 207].

Following the development of commercial FEA codes, the implementation of FEA methods become much more manageable. Even though the FEA incorporates multiple steps, most of them are processed by the software, with the user required to input only minimal information to run the simulations successfully. In addition, the graphic user interface (GUI) has been widely adopted into commercial FEA products, enabling quicker and more accurate interference within all the solving stages [205, 206].

2.2.2.3.1 Mesh

Decomposition is also called a "meshing process". It is performed to fit the created substructures into computer memory and reduces the computational time by balancing the workload among each processor. As proven by previous investigations, the quality of domain division can significantly influence the computing time of FEA [205, 218]. In order to successfully reduce computational time, the user should always try to minimize the number of interface nodes. However, also analyse the model dependency on the element number by running statistical analysis. In order to fit the wide range of FEA types, numerous mathematical algorithms for domain partitioning have been derived previously, including recursive graph bisection [198, 205, 219]. The mesh type used for FEA can be categorised based on multiple features such as discretization, analysis type, time dependence or dimensions, as presented in Figure 2-13.

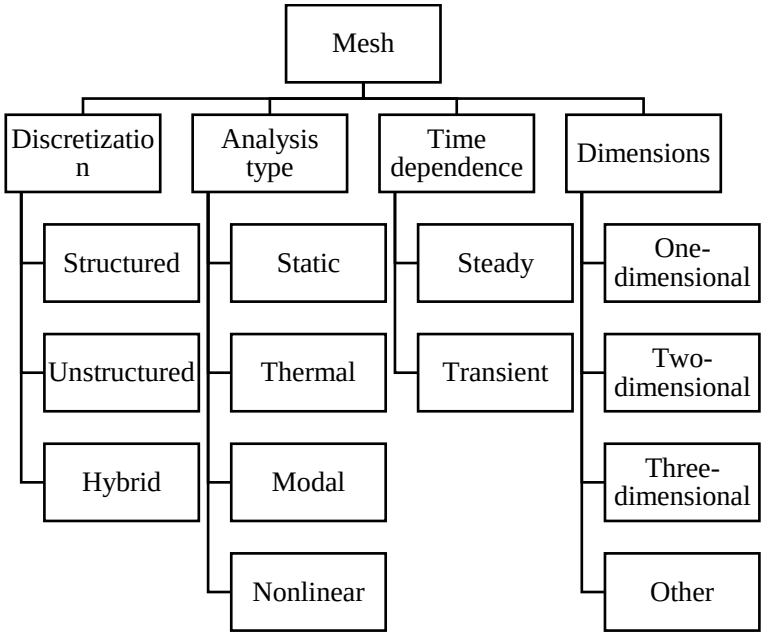

Figure 2-13 Mesh categorisation method [205].

The mesh types based on the discretization method are probably the most crucial division related to the number of elements surrounding the internal node. Such number is constant across the whole continuum in structured mesh, allowing mesh connectivity to be calculated and not stored explicitly. Such an approach reduces the computational time significantly [205, 219]. On the other, hand in the unstructured mesh, the number of elements around the nodes is different, which enable a more accurate representation of complicated geometric features but at the price of increased computational time. The hybrid mesh is the most widely used and incorporates both structured and unstructured mesh regions allowing for a combination of benefits of both techniques [205, 220, 221]. The other interesting mesh categorisation is based on the mesh dimension. The one-dimensional mesh is represented by a line and most frequently is used to analyse the truss structures, long shafts, or beams. Two-dimensional mesh uses the triangular and quad shapes and allows for analysis of sheets or panels frequently used in autobody or aeroplane bodies. Three-dimensional mesh has the most significant shape variation as it can include the tetrahedral, hexahedral, pyramid, pentahedral and many other shapes [205, 209, 219]. Most frequently used for the analysis of solid bodies across all ranges of analysis. Finally, the remaining mesh types are used to idealise the mechanical or thermal elements in FEA simulations and describe features like a point element mass for centralized gravity load or point element spring as a for various loads. The remaining mesh categorisation includes time and analysis type dependency, mainly predefined by the simulation goals [205].

2.2.2.3.2 Governing equations

A finite element analysis can be used only if the analysed problem can be described by a mathematical model in which the differential equations govern the system response. Most of the problems analysed using FEA are governed by the physical principles of conservation, including mass, momentum and energy conservation [205, 217]. Those principles can be described in the form of partial differential equations and are named the governing equations [212, 213]. Depending on the engineering systems analysed, the different governing equations can be incorporated into FEA and the examples are presented in Table 2-3.

Table 2-3 FEA analysis type and examples of governing equations used [205].

Analysis type	Governing equations basics
Solid mechanics	Hooke’s Law
Dynamics	Lagrange's Equation
Thermal	Fourier law Newton's law of convection Stefan–Boltzmann law of radiation
Electromagnetics	Maxwell's equations Gauss' law for electricity Faraday's law of induction Ampere's law
Fluid mechanics	Law of conservation of mass

2.2.2.3.3 FEA formulation

In order to solve the governing equations, a multitude of approaches for FEA formulation has been derived. The most common ones include direct formulation, minimum total potential energy formulation and weighted residual formation, all of which are briefly described below [205, 206, 212, 213].

The direct formulation is used to solve a simple problem, and most often, it provides an understanding of underlying concepts. It is based on the basics of engineering principles and incorporates balance of forces while applying statistics to derive the equations for finite elements. It is the only formulation that provides the approximated solutions by directly deriving them from the governing equations [205, 208]. Most frequently used for a one-dimensional problem, this formulation is easy to introduce and does not require extensive computational resources, but it provides physical insight into finite element analysis. For example, the direct formulation can model the spring system, various shaft loading scenarios or simple heat transfer cases [205, 206, 212].

According to other physical principles, the behaviour of an engineering system can be correlated with one or a few scalar quantities, including energy, momentum, and mass [206, 222]. The minimum total potential energy formulation derives from the fact that the energy can be transferred between various bodies. However, it can never be destroyed. The minimum total potential energy formulation is a more complex formulation method based on the total potential energy of the system and primarily used for a solid mechanics problem [206, 222].

According to this formulation, to achieve a stable system, the system's total potential energy must reach its minimum when the displacement at the equilibrium position occurs [205].

Finally, the last discussed formulation, weighted residual formulation, assumes the approximate solution to tackled governing differential equations [206, 223, 224]. As a result, under this formulation, an initial guess solution is implemented into differential equations; however, it is rarely an exact solution. Some residuals or errors still occur in most cases, and the following iterative process is adjusting the solution to minimise the residual error [206, 223, 224]. Few methods can be used to minimise the residual functions, including Collocation method, Subdomain method, Galerkin method or Least Square method. None of them provides a clear advantage over the others, and it is up to the user to select the most suitable one. The weighted residual formulation is the most generic and flexible formulation used for most FEA tasks, including beam bending or heat conduction in solid cases [205, 206, 223, 224].

2.2.2.3.4 Verification and validation of FEA results

Verification and validation of FEA is a crucial step allowing us to understand obtained results fully. Even though both terms are frequently used interchangeably, their definitions differ in finite element analysis. As a result, verification mainly investigates the mathematical approach and software used during the finite element analysis. On the other hand, validation looks at how accurate the obtained results are [213, 214, 225].

Verification allows ensuring that the mathematical model behind conducted FEA is correct. In general, the main aspects of FEA verification on the user side includes the confirmation that obtained solution presents an acceptable level of error. In order to confirm it without the need for experimental work, error estimation techniques are being used. The main type of error estimation includes the priori or posteriori error estimation depending on whether the estimation was performed before or after simulation was solved [214, 226]. They both often incorporate the solution of a simplified problem to detect potential bugs in the system or inappropriate physics used. Nevertheless, the verification does not describe how well the model represents the physical reality but rather evaluate the mathematical error present [214, 225].

Validation, on the other hand, detects how well the model captures the investigated system's physical behaviour. This often requires a direct comparison between the experimental and simulation results [214, 226]. Such an approach is described by the validation pyramid as presented in Figure 2-14.

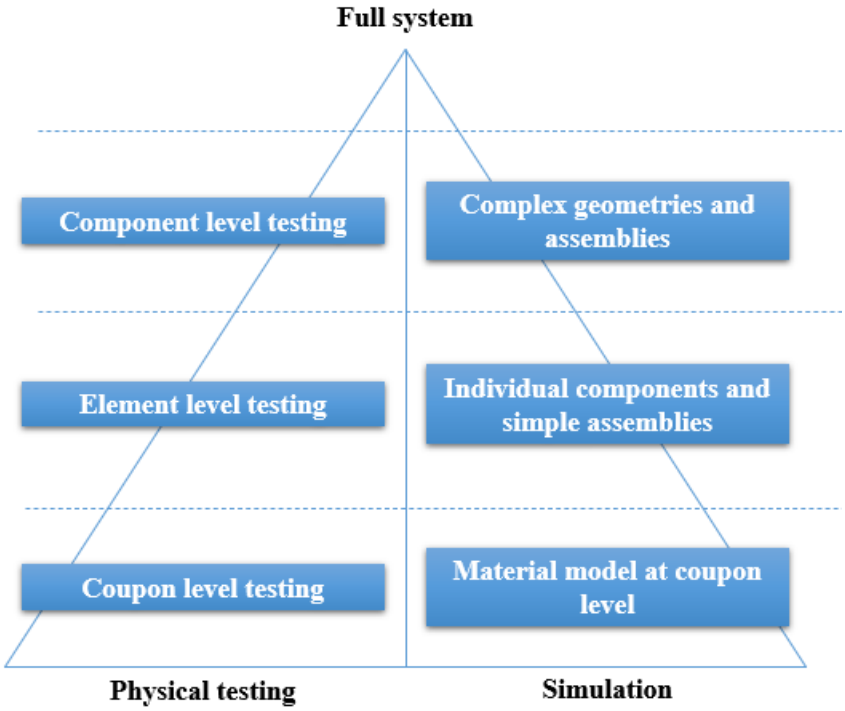

Figure 2-14 The validation pyramid [214].

As it might be noticed, the model suggests starting from the low complexity cases and adjusting the simulation model until achieving a good match with the experimental results. The initial stage of such investigation often requires coupon level testing to confirm the properties of materials used. With the increasing complexity of the simulation model, a more demanding testing method are required [214, 225, 226].

2.2.2.4 ANSYS

ANSYS has been selected for the finite element analysis within this work. It is a general-purpose finite element software that allows for multiple simulations, including solid mechanics, heat transfer, fluid mechanics, electromagnetics, and acoustics [206, 227]. ANSYS is a commercially available software; however, for this study, a student version has been used with the simulations run in the main module of ANSYS/Mechanical. ANSYS also incorporates an intuitive graphical interface to share the results between various simulations directly and quickly access current simulations, input values, results, and manuals [206, 228]. Nowadays, multiple industry branches widely use ANSYS, including mechanical, civil, aerospace, electrical, and chemical engineering [206, 227-229].

2.3 Conclusions

In this chapter, the material overview and fundamental multiscale background have been discussed. Mentioned topics have been presented as a separate part of the thesis as they do provide an overlapping literature review for more than one of the upcoming chapters.

The materials overview includes the presentation of all materials used in this study, focusing on aerogels and aerogel composites. As a result, the history and synthesis of silica and polyimide aerogels have been analysed, followed by the description of aerogel particulate and fibrous composites and the reinforcement materials most frequently used for their preparation. When investigating aerogel composites a silica aerogel seems to be the most popular choice for either particulate or fibrous composites, mainly due to the wide availability. Other aerogels are being used scarcely which could be attributed to the lack of the adequate commercialisation. Additionally, for particulate composites, a significant bias towards polymer and especially epoxy-based composites can be noticed with little work being done for other types of matrix materials. Overall, the aerogel composites are still relatively niche subject and an investigation of thermal and mechanical properties of wider range of aerogels and reinforcements could provide a better overview for potential users.

The second part of this chapter focuses on the theoretical background of multiscale modelling. It provides an overview of the current multiscale material modelling approaches, including hybrid and hierarchical approaches. This study employs the hierarchical approach and uses two different scale modelling techniques including molecular dynamics and finite element analysis. The former has been used to obtain thermal and mechanical properties of bulk aerogel materials as well as the interface between aerogels and reinforcement materials. Afterwards, the obtained data are inputted into a microscale model based on a finite element analysis, which supplemented by a higher scale input parameter allows to predict mechanical and thermal properties of particulate composite materials. The basics of both of simulations methods has also been introduced in this chapter. Regardless of the approach used a significant difficulty in relating the material properties between different scales is still the main issue of the multiscale material modelling. Even though multiple coupling mechanisms have been already developed, there is still a lack of a clear method allowing for an accurate multiscale modelling.

3 Thermomechanical characterisation of aerogel particulate composites

This chapter investigates the effect of the addition of aerogel particles to polymer resins on their thermally insulating properties and compressive properties. For this study, both silica and polyimide aerogel particles have been used as fillers for epoxy and vinyl ester resins. To preserve the pores in the aerogels, the delayed mixing method was developed by analysing viscosity changes during the resin curing stages and the influence of resin viscosity on the thermomechanical properties of aerogel-filled resin composites was evaluated. This approach identified a cost-effective method of introducing aerogel particles to a liquid matrix while maintaining aerogel porous structure. Additionally, various thermal and mechanical properties were investigated to provide insight into crucial design parameters of aerogel-filled resin composites. It is also the first time that a combined effect of varying aerogel particle size and loading on the polymer resin composites was extensively studied. Table 3-1 gives a summary of the material properties investigated in this work as well as the techniques used for property characterisation.

Table 3-1 Summary of investigated properties of created aerogel filled polymers and techniques used for measurements.

Material Property	Testing Technique	Equipment used
Thermal conductivity	Heat flow meter method	TA Instruments Fox 50
Compressive properties	Compression test	50kN Instron 5969
Linear thermal expansion coefficient	Thermomechanical analysis (TMA)	TA Instruments Q400
Heat distortion temperature	Dynamic mechanical analysis (DMA)	TA Instruments Q800
Glass transition temperature	Dynamic mechanical analysis (DMA)	TA Instruments Q800

3.1 Literature review

3.1.1 Manufacturing of aerogel filled polymer composites

When dealing with aerogel-filled composites it seems that one of the most challenging parts is their manufacturing. Compared to other filler materials, it requires additional measures preventing the destruction of the internal aerogel structure. As a result, a few most common manufacturing techniques have been identified and described below [33, 88, 91, 93].

The most frequently utilised manufacturing method includes dispersing aerogel particles in the desired matrix's liquid form and casting it in a mould, with multiple researchers such as Basri, Kim or Mazlan previously utilising it [32, 91, 230, 231]. However, this method was reported to raise serious issues during composites manufacturing, which involves filling the aerogel pores or their collapse under the curing stresses [88, 92]. In response, multiple methods have been incorporated to prevent such scenarios and fully benefit from aerogel particles' addition to plastic matrices. Firstly, Gupta et al., as well as Maghsoudi & Motahari, have used a standard mixing technique with a high viscosity resin, enabling the production of a composite that had a slightly lower density than the plastic matrix [87, 91]. A slightly different approach was used by Krishnaswamy et al., who purposely delayed the addition of aerogel particles to resin/hardener mixture [88]. They have investigated the morphology, optics and thermal character of aerogel-epoxy composites by increasing the resin viscosity to the point where aerogel pores were no longer infiltrated following mixing. However, it was found under microscopy that the physical destruction of the aerogel particles had occurred due to epoxy curing shrinkage. Such destruction indicated a larger surface area of the particle through which the resin could now enter the aerogel interior pore network [88]. Another manufacturing technique utilised to preserve the aerogel pores from resin infiltrations was presented by Kim et al. [91]. In this work, aerogel was submerged in ethanol before mixing with epoxy and the whole mixture was hot-pressed under elevated temperature and pressure resulting in total evaporation of ethanol and preservation of aerogel pores. However, even though this method allows for preserving the aerogel pores, it is worth mentioning that it also results in high cost and hazardous manufacturing conditions [91]. On the contrary, Ge has dropped the idea of dispersing aerogel in a liquid matrix and instead used the powdered epoxy and dry mixing technique [93]. As a result, combined aerogel and epoxy powders have been processed in the hot press resulting in only partial infiltration of aerogel pores [93]. Finally, it is also worth mentioning that other methods of incorporating aerogel into plastic resin are being developed all the time. YG Kim proposed one of the most recent solutions, manufacturing polyvinylidene

fluoride nanofibers filled with silica aerogel [21]. The fibres with a porous internal structure possessed a low thermal conductivity as well as high flexibility and fire retardation [21].

3.1.2 Microstructure of aerogel filled polymer composites

It can be noticed that the purpose of all alterations to known manufacturing methods was to preserve the internal aerogel structure during composite processing. Only when the aerogel particles had been introduced to the matrix in an intact form, their actual effects on the matrix's thermal and mechanical properties could be evaluated. As a result, multiple research pieces have investigated the microstructure of created composites to describe phenomena such as heat transfer or stress gradients. Most often, the researches use scanning electron microscopy (SEM), transition electron microscopy (TEM), FTIR, elemental mapping or micro-computed tomography (m-CT).

m-CT and elemental mapping were used for the non-destructive imagining of aerogel particle distribution within the matrix. Using both methods, Cho et al. were able to visualize the arrangement of silica aerogel particles inside the polyurethane matrix, proving possible homogeneous distribution at 30 vol% loadings [232]. Elemental analysis was also used by Allan et al., who have investigated the distribution of silica aerogel in poly ethylene-co-vinyl acetate (EVA) nanocomposite [233]. Again, he was able to prove the homogenous distribution of the particles. However, he discovered that it was challenging to detect Si in composites with less than 10% volume fraction. On the other hand, composites with a high volume fraction of aerogel particles were prompt to aggregate and form clusters. Overall, both methods were proven to successfully define the internal structure of aerogel filled composites [77]. Nevertheless, due to the resolution, they could not identify the aerogel particles' internal structure.

To overcome this issue, SEM or TEM was used to capture the aerogel particle's internal structure after composite formation. By preparing samples in three different ways (wet, dry and dual mixing), Kim et al. were able to capture the destruction of aerogel porous structure when the wet mixing technique was used [234]. The infiltration of pores resulted in higher thermal conductivity and density values of the final composite. On the other hand, remaining manufacturing was proven not to affect aerogel structure adversely [45]. Similarly, Zhao et al., Halim et al. and Maghsoudi et al. used SEM to prove successful preservation of aerogel structure is prepared silica aerogel/epoxy [83, 87, 94]. A slightly different approach was used by Ge et al., who incorporated TEM into their analysis of silica aerogel/epoxy nanocomposite [93]. They have compared internal structures of silica aerogel particles added to epoxy resin via dry and wet mixing. They have discovered that for dry mixing the nanopores of the silica

aerogel have been penetrated by the resin, but the 3D net structure remained intact, while wet mixing caused both pore infiltration and destruction of the whole structure [93].

Finally, FTIR spectra have been used to analyse whether the chemical bonding occurs between the aerogel particles and the matrix. As a result, epoxy with a wide range of volume fractions of silica aerogels particles has been investigated by Zhao et al. [83]. For combined materials, Zhao has discovered peaks at 3,440 and 1,100 cm^{-1} representing respectively hydrophilic functional groups (OH) and absorption band of C–O–C. Also, the disappearance of peak at 940 cm^{-1} implied the reaction between Si-OH and C–OH bonds through ring-opening of epoxy resulting in the creation of Si–O–C bonds. The resulting functional group between the silica aerogel and the epoxy resin was expected to preventing the epoxy chain from moving and improving the heat distortion temperature (HDT) of created composite. Halim et al. have done a similar investigation for unsaturated polyester samples and found that not a single of the silica aerogel characteristic peaks was represented in the composite FTIR spectrum [94]. By detailed investigation of obtained spectrums, they have managed to identify a bit wider vibration band around 3600 cm^{-1} possibly suggesting the existence of hydrogen bonding between silica aerogel and unsaturated polyester resin [94].

3.1.3 Properties of aerogel filled polymer composites

3.1.3.1 Thermal properties

When analysing the scientific work in the field of aerogel-filled polymers, it can be noticed that thermal conductivity among all of the thermal properties seems to gain the most interest. It was proven that the addition of aerogel particles could significantly lower the thermal conductivity of matrix material with the epoxy resin and silica aerogel particles being the most commonly researched combination [32, 91, 92].

Kim et al. have investigated the effect of three different types of silica aerogel particles on epoxy resin [91]. In their study, they have used standard silica aerogel particles as well as plasma treated and ethanol filled ones. By incorporating standard particles, he has managed to lower epoxy resin's thermal conductivity from 275 $mWm^{-1}K^{-1}$ to 110 $mWm^{-1}K^{-1}$ when using 25 vol% of aerogel [92]. However, a further increase in aerogel quantity yielded no additional decreases in thermal conductivity values. In the case of plasma-treated particles, the thermal conductivity has dropped even lower to 90 $mWm^{-1}K^{-1}$ for 25 vol% of aerogel, but when additional aerogel was included, thermal conductivity started to increase. For both particles, the values of thermal conductivities and obtained trends have been attributed to the liquid resin's aerogel pores being infiltrated. Finally, the best results have been achieved using

ethanol-filled particles allowing thermal conductivity of 60 and 45 $mWm^{-1}K^{-1}$ for samples with 25 vol% and 75 vol% aerogel loading respectively [91].

Ge et al., by using dry mixing method of silica aerogel and epoxy powder managed to achieve low thermal conductivity of 44 $mWm^{-1}K^{-1}$ for 90 vol% [93]. In addition to room temperature measurement, they have explored silica aerogel-filled composites' thermal conductivity at elevated temperatures. It was revealed that composites with high silica aerogel volume fraction are much more stable than pure epoxy with similar thermal conductivity values at 25 and 200 °C. Additionally, Ge was able to increase serviceability temperature up to 250 °C by using 80 vol% of silica aerogel [93]. Finally, except for the experimental work, he compared his work with the most common theoretical models presenting a close match [93].

Zhao et al. studied the thermal properties of silica aerogel/epoxy composites and discovered that at 60 wt% aerogel particles, the thermal conductivity of 105 $mWm^{-1}K^{-1}$ was achieved, in addition to an increased serviceability temperature [83]. Two sizes of aerogel particle were used (200 μm and 2000 μm) to produce composites, and it was concluded that the addition of larger aerogel particles resulted in lower thermal conductivity and a higher martens heat distortion temperature [83].

In other studies, Krishnaswamy et al. looked into the possibility of the addition of silica aerogel particles at a different time of resin curing [88]. By adding aerogel particles after 1.5 hrs from the creating resin/hardener mixture the authors have created composites presenting a 13.3% decrease in thermal conductivity when 3 wt% silica aerogel particles were added [88]. Also, Maghsoudi & Motahari investigated silica aerogel and epoxy composites. Their revealed that the addition of 3 wt% aerogel decreased the T_c from 195 to 74 $mWm^{-1}K^{-1}$ [87].

The effect of silica aerogel particles on other matrix systems has also been measured. Halim et al. investigated the impact of three different particle sizes (powder, granules and beads) with the same 30 vol% loadings on thermal and mechanical properties of unsaturated polyester composites [94]. Their work revealed a decrease in thermal conductivity values by 11%,57% and 61% for respective powder, granules and bead. The higher effectiveness of larger particles has been proven by lower thermal conductivity values and higher thermal stability compared with unfilled resin. Nevertheless, the authors stressed the need for aerogel pore preservation during manufacturing [94].

Kim et al. tried a combination of silica aerogel particles with epoxy and polyimide resin [92]. In the case of epoxy resin, they have managed to lower thermal conductivity values from 225 $mWm^{-1}K^{-1}$ to 112 $mWm^{-1}K^{-1}$ when adding 25 vol% without any further reduction with more

aerogel. On the contrary, for the polyimide aerogel, they achieved a nonlinear trend and lowered conductivity values with increasing aerogel content [92]. It was deducted that the multi curing process allowed to preserve aerogel pores successfully and lowered thermal conductivity values from 500 $mWm^{-1}K^{-1}$ to 30 $mWm^{-1}K^{-1}$ with 50 vol% aerogel content [92].

Other research led by Cho and Lee included a mixture of silica aerogel with respectively polyurethane and poly(dimethylsiloxane) (PDMS) matrices, achieving respectively 80% and 85% decreases in thermal conductivity of both materials and further highlighting the importance of aerogel pore preservation [30, 232]. On the other hand, Prasad et al. investigated sisal/polylactic acid (PLA) combined with nanometre size silica aerogel particles up to 2 wt% [84]. This study observed that particles' addition impacted the interfacial adhesion between fibres and matrix, resulting in improved thermal stability [84]. Finally, Kim et al. summarised the principles of heat transfer in polymer/aerogel composites and the most important physical factors impacting their thermal conductivity [90].

3.1.3.2 Mechanical properties

To find a balance between aerogel-filled composites' thermal and mechanical properties, it is necessary to investigate how porous particles' addition affects various mechanical properties such as tensile strength, impact strength, flexural strength, hardness, fracture toughness. Even though aerogel composites' mechanical properties are not as commonly investigated as thermal ones, several studies have mainly focused on either tensile or compressive testing.

Gupta et al. analysed the interaction between aerogel particles and the epoxy matrix in a mechanical context. It was found that a high viscosity resin resulted in poor binding while a low viscosity resin invaded the aerogel pores [235]. Specimens were created using a heated high viscosity resin, which enabled the production of a composite with slightly lower density than the plastic matrix and improved mechanical characteristics [235]. By subjecting samples to compression, Gupta has studied their deformation and fracture behaviour finding compressive failure strain of over 25% for samples with 20–30% aerogel by volume. In addition, the increase in compressive modulus and decrease in yield strength was recorded. The latter was attributed to the early crack initiation due to the aerogel porous inclusions.

Similar results were also observed by Salimian et al., who investigated the structure-property relationship in epoxy nano-composites filled with silica aerogel [85]. In their study, the addition of 6 wt% of aerogel particles has improved the mechanical properties significantly with increases of 35%, 62% and 126% in respectively elastic modulus, tensile strength and toughness. Two main mechanisms of mechanical properties improvement have been

identified. Firstly, it was suggested that the introduction of the polymer networks into the aerogel mesopores increased the composite toughness by limiting the crack propagation and deflection [85]. The second reason was plastic deformation which absorbed energy (resulting in higher toughness of composite) by forming voids, cavities, and debonding effects at the crack tip.

Kim et al. have used the silica aerogel particles for both glassy and rubbery state of epoxy resin [91]. In the rubbery epoxy nanocomposites, a strong correlation between aerogel loading and mechanical properties has been found. By increasing the aerogel content, Kim has improved the tensile modulus values, tensile strength, toughness and elongation leading to respectively 2.7, 6.3, 2.1, and 6.3 times improvement at 7 wt% [91]. A much smaller improvement has been recorded for the glassy nanocomposites for which the addition of the same quantity of aerogel particles resulted in only a 10% increase in mentioned properties. The improvement of mechanical properties has been attributed to the strong interfacial interactions and adhesion between the epoxy and silica mesophase [91].

G. S. Kim & S. H. Hyun focused their study on the mixture of silica aerogel and PVB, however, in their case the addition of aerogel particles has significantly decreased the modulus of rupture of the composite material from 46.5 MP to 0.15 MP when increasing aerogel volume fraction from 30% to 90% [32]. The authors have also observed the difference in the modulus of rupture of composites using dry mixing and wet mixing technique. The former was higher and such behaviour was linked with the integration of PVB into aerogel particles using wet mixing [234].

A slightly other approach was used by Mazlan et al., who growth carbon nanotubes on the surface of highly porous silica aerogel using chemical vapour deposition technique [230]. Further addition of up to 2.5 wt% of enhanced aerogel particles to the epoxy matrix resulted in increased flexural strength by 30% compared to pure epoxy. In addition, flexural modulus increased by about 50% for the same aerogel loading. The improvement was justified by the high stiffness of the filler particles contributing to the reinforcement effects, good adhesion between particles and matrix and finally better dispersion of enhanced particles in the matrix used [230].

Finally, Venkata Prasad et al. investigated sisal/polylactic acid combined with nanometre size silica aerogel particles up to 2 wt% [84]. This study observed that particles' addition impacted the interfacial adhesion between fibres and matrix, resulting in tensile strength and modulus increase; on the other hand, the flexural strength decreased. By altering the fibre interface by adding aerogel particles, authors improved the thermal stability and mechanical properties of

created composites and identified the opportunity to use the silica aerogel particles as an additive in biodegradable composites [84].

3.1.3.3 Thermomechanical properties

The addition of silica aerogel particles to polymer matrices affects both the resin's thermal and mechanical properties. However, to fully understand the newly created materials thermomechanical analysis can describe material properties during heating or cooling. Techniques most commonly used to investigate aerogel-filled composites include dynamic mechanical analysis (DMA) or thermomechanical analysis (TMA) and determine a range of properties such as glass transition temperature or thermal expansion coefficient.

Kim et al. looked into the storage modulus and glass transition temperature of glassy epoxy-aerogel nanocomposites [91]. In their study, they has discovered a significant increase in storage modulus with an increase of aerogel content. As a result, storage modulus has increased from 2083 MPa to 2746 MPa with an addition of 5 wt% of aerogel. On the other hand, the glass transition temperature of created composites maintained the same at the level of 102 °C [91].

Salimian et al. also have investigated the silica aerogel and epoxy composites under DMA. Their study revealed that the inclusion of 6 wt% of aerogel particles increased epoxy's storage modulus at 45 °C from 0.93 to 1.03 GPa [85, 86]. Based on the loss factor, they measured an increase in glass transition temperature by 5.2 °C compared to unfilled epoxy. Such an increase in measured thermomechanical properties was attributed to the mechanical anchoring of the epoxy polymer chains by particle included. As a result of limiting the epoxy chain movement, the storage modulus and glass transition temperature values were increased [85, 86].

Du et al. manufactured numerous silica aerogel and epoxy composites via the sol-gel method with aerogel content ranging from 0 to 100 wt% [236]. Their studies focused on DMA analysis and revealed that for both storage and loss modulus the addition of 0.1 wt% of aerogel particles yielded the best results with the highest values of both parameters but further addition of aerogel led to a steady decrease in properties values. Contrary to previously discussed studies, they achieved an impressive increase in the glass transition temperature [236]. By adding 10 wt% of aerogel particles, T_g of epoxy increased to almost 85 °C compared to 45 °C for pure epoxy. Similarly, as in the case of Salimian, this study links the thermomechanical properties with interfacial effect and anchoring of epoxy chins. On the other hand, the author also considers other justifications, including adsorption of polymer into aerogel particles and pores destruction [236].

Lee et al. have investigated storage modulus and the glass transition temperature of silica aerogel particles and poly(dimethylsiloxane) matrix [30]. Interestingly two different manufacturing method were used, one allowing to preserve aerogel pores and the other purposely infiltrating them. Following DMA, it was found that samples with impregnated pores presented an increase in storage modulus values with an increasing quantity of aerogel while samples with preserved pores showed a reversed trend. On the other hand, neither type of samples presented a change in the matrix's glass transition temperature [30].

Finally, Halim and Yajid added plain and core-shell silica aerogel particles to evaluate their impact on unsaturated polyester's thermomechanical properties [94]. The difference between both types of aerogel particles was mainly due to the accessibility to the pores as plain particles had open pores while shell particles had all pores enclosed. The conducted study revealed that the addition of both types of particles resulted in lower values of storage and loss modulus and no improvement in the glass transition temperature of polyester. Nevertheless, plain particles usage resulted in lower thermal insulation and a higher density of resulting composites than shell particles [94].

3.1.4 Conclusions of the literature review

Aerogel filled polymers are increasingly gaining attention in the scientific world with a wide variety of combinations of different aerogel and matrix types being investigated. Nevertheless, before those materials are fully implemented in industrial applications few challenges still have to be resolved. Currently, the main issue remains to preserve aerogel pores through the manufacturing process to achieve the full benefits of incorporating aerogel particles in the polymer matrix. Up to date, many researchers have been looking into and modifying current wet and dry mixing techniques to prevent filling the aerogel pores or their collapse under curing stresses. In addition, competitive and more elaborate methods such as ethanol pore filling have been proven to also yield positive results.

Moreover, the effects of aerogel particles on multiple material characteristics are yet to be determined. As a result, a series of attempts to characterise aerogel particles' effect on polymer matrices has been undertaken. It was proven that the introduction of aerogel particles can significantly lower polymer thermal conductivity and improve flame retardancy. What is more, the presence of aerogel particles was allowed to achieve higher values of storage modulus as well as glass transition temperature as a result of limiting the movement of polymer main-chain motion. On the other hand, the impact of aerogel particles upon the mechanical characterisation of aerogel filled polymers is still debated in the literature. Some researchers suggest that the addition of aerogel particles could introduce possible strengthening

mechanisms and increase the composite toughness by limiting the crack propagation and deflection, while others advocate the weakening effect of brittle, porous inclusions.

3.2 Experimental

3.2.1 Materials

The epoxy resin and hardener were purchased from Easy Composites Ltd. The resin was a mixture of bisphenol-A-epoxy resin and Epichlorohydrin-formaldehydephenol polymer (trade name IN2 Epoxy Infusion Resin) both with molecular weight equal to or less than 700 g $mole^{-1}$. A cycloaliphatic amine-based hardener (trade name AT30 Slow Hardener) was used as the curing agent.

Acquired vinyl ester resin is a bisphenol-A based vinyl ester urethane resin, dissolved in styrene with a trading name Atlac 580 and styrene content in 25-50% range. In addition, a Methyl ethyl ketone peroxide (MEKP) hardener (Butanox M50) was used as catalyst to complete the curing process.

The silica aerogel particles produced by Enersens were sourced from Aerogel UK Ltd. In total 4 different batches of different particle sizes were purchased with the largest particle size of 100 µm, 500 µm, 1250 µm and 3500 µm (trade name of particles was respectively Kwark®XP100, Kwark®XP500, Kwark®GS and Kwark®GL). These aerogels have a nominal density between 40 and 80 kg/m^3, porosity above 95%, a specific surface area of 850 m^2/g and pore diameter between 5 and 12 nm. An examples of silica aerogel particles is shown in Figure 3-1.

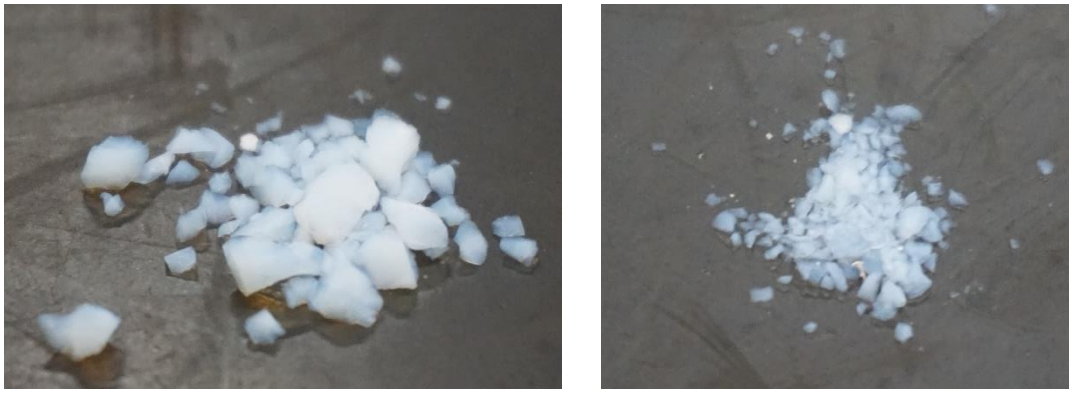

Figure 3-1 3500 µm (left) and 100 µm (right) silica aerogel particles used in this study.

Finally, organic polyimide aerogel particles were acquired from Blueshift Materials Inc. and included a single batch of particle size below 100 µm (trade name AeroZero®). According to the manufacturer, the aerogel has a nominal density between 150 and 200 kg/m^3, a specific

surface area of 850 m²/g and a pore diameter ranging from 5 to 12 nm. An example of polyimide aerogel particles in presented in Figure 3-2.

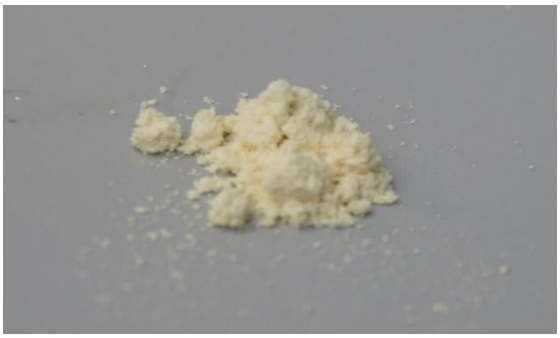

Figure 3-2 Example of polyimide aerogel particles used in this study.

3.2.2 Sample Preparation

3.2.2.1 Aerogel-filled epoxy

Figure 3-3 presents the silica aerogel and epoxy composite preparation steps.

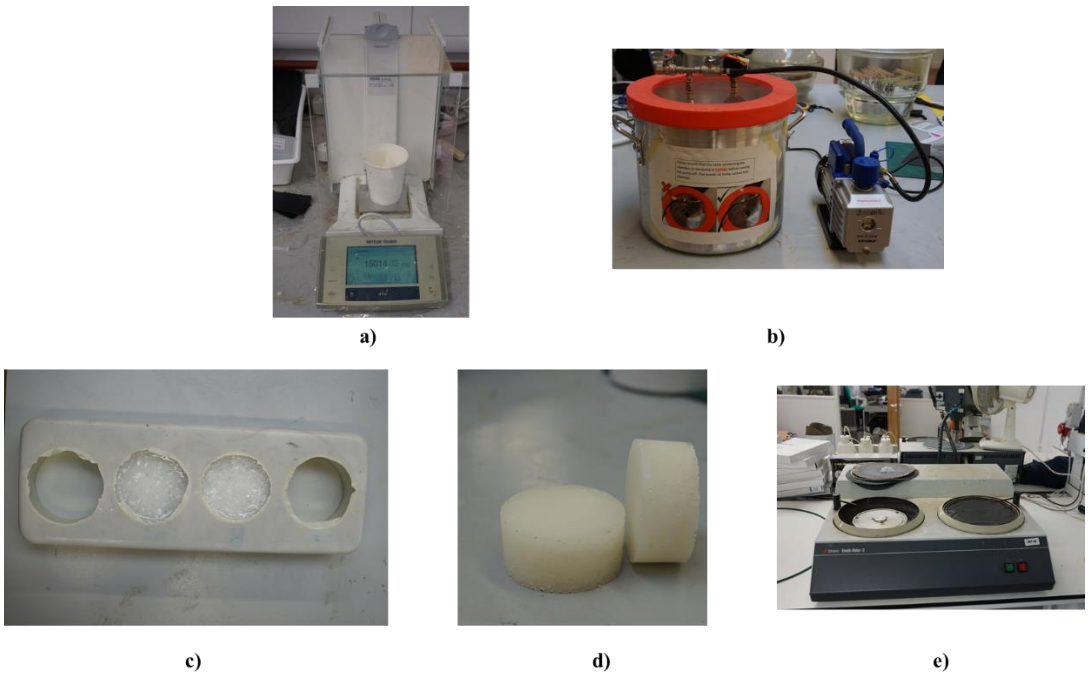

Figure 3-3 Aerogel/epoxy composite preparation steps.

Aerogel/epoxy composites were fabricated using a delayed wet mixing technique. Initially, a weight ratio of 100 parts of resin and 30 parts of hardener were measured using microscale as presented in Figure 3-3a. For most of the samples a 50 g of resin and 15 g of hardener have been used as this quantity was sufficient for preparation of two thermal conductivity samples or six compression samples. Resin and hardener were combined using manual stirring for 5

minutes, and the mixture was subsequently degassed under vacuum for 10 minutes. The degas chamber setup is presented in Figure 3-3b. Afterwards, the mixture was left to cure under the room condition in order to increase its' viscosity and then 0-5 wt% of aerogel particles of various sizes were added to the resin. Such a range of aerogel weight percentage was used as further addition of aerogel particles created too thick mixture preventing any further processing of the mixture. The composite mixture was then poured into silicon moulds coated with release agent (Figure 3-3c) and left to cure at room temperature for 24 hours. Once removed from the silicon mould the samples were subjected to the post-curing process at 60°C for 6 hours. All aerogel/epoxy composites were machined and polished using wet sanding setup presented in Figure 3-3e to the sample dimension required for various tests. Finished samples for both thermal and mechanical testing are presented in Figure 3-4.

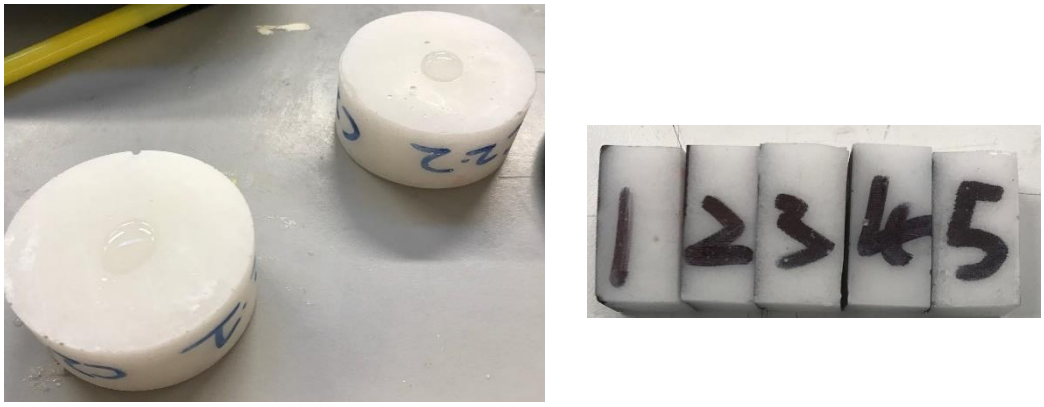

Figure 3-4 Photo of thermal (left) and compression (right) samples used during the study. Samples were prepared with epoxy resin and 100 μm silica aerogel particles.

3.2.2.2 Aerogel-filled vinyl ester

Vinylester composites were also manufactured using a delayed wet mixing technique, however, due to the styrene fumes being released from the resin, all following actions were conducted under a fume cupboard with as little contact with uncured material as possible. Firstly, a weight ratio of 100 parts of resin and 1.5 parts of hardener has been combined using manual stirring for 5 minutes with the subsequent degassing process under vacuum for 10 minutes. Afterwards, the mixture was left to pre-cure under room conditions for various periods until 0-5 wt% of aerogel particles were stirred into the resin. The composite mixture was then poured into silicon moulds coated with release agent and was left to cure at room temperature for 48 hours followed by post-curing at 100°C for 3 hours. Finally, aerogel/vinyl ester composites were machined to the sample dimension according to the test standards.

3.2.3 Gas adsorption

To investigate the pore structure represented by particles gas adsorption measurements were conducted using a Micromeritics ASAP2420 Surface Area and Porosity Analyser. Surface area, pore volume and average pore size were determined via analysis of the cryogenic nitrogen adsorption/desorption isotherm. Approximately 0.1 g of aerogel particles was subject to a degas cycle of 30 min at 50 °C, followed by 120 min at 110 °C, at a pressure of 10 mHg. This process removed any residual solvent or surface contaminants from the samples. Degassed samples subsequently underwent a 40 point adsorption cycle between the relative pressures of 0.01 and 1, followed by a 30 point desorption cycle between the relative pressures of 1 and 0.1. Sample temperature was maintained at a constant value of -196 °C throughout the experiment using a liquid nitrogen bath. The total pore volume is calculated from the amount of gas adsorbed when reaching 0.99 relative pressure mark, while the specific surface area is obtained using the BET (Brunauer-Emmett-Teller) method. Finally, pore size distribution and average pore size have been measured by the BJH model used to analyse the adsorption isotherms. Even though this method has been incorporated in this study it is necessary to highlight that other researchers suggest that due to limitations and underlying assumptions the BJH method produces large error when charactering the pore size distribution and thus is unable to accurately describe the mesopores [237]. The example adsorption/desorption curve is presented in Figure 3-5 below.

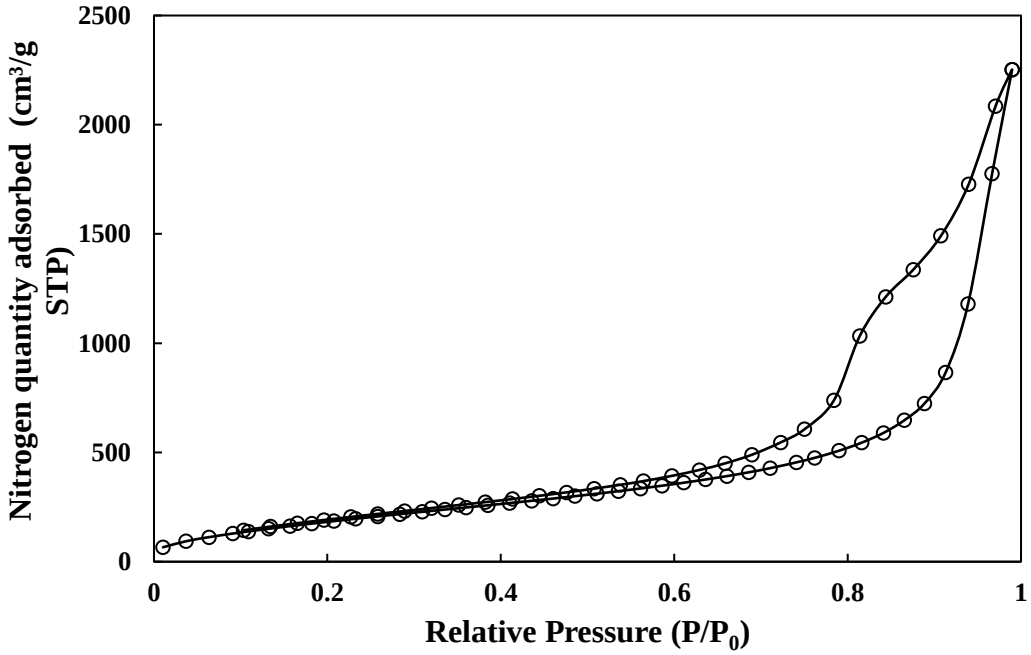

Figure 3-5 Typical adsorption/desorption curve produced during BET analysis.

3.2.4 Viscosity measurement

The viscosity measurement of both resins is essential for assessing the correct time for the addition of aerogel particles to preserve their pores and achieve the lowest possible thermal conductivity. An in-house prepared rotational viscometer (which required a manufacturing of rotational spindle using 3D printing) was used to measure the viscosity of the resin. All the measurements were conducted at room conditions using at 300 rpm constantly monitoring the torque required for the spindle (25 mm diameter) to skim the surface of the resin. Afterwards, the torque (T) has been related to resin viscosity (τ) using:

$$\tau = \frac{T \times 2 \times h}{r^4 \times \pi \times \omega} \qquad \text{Eq. 32}$$

where, h is a height of a fluid between the spindle and the bottom of the container, r is a radius of the spindle and ω is angular velocity of the spindle. The viscometer setup is presented in Figure 3-6.

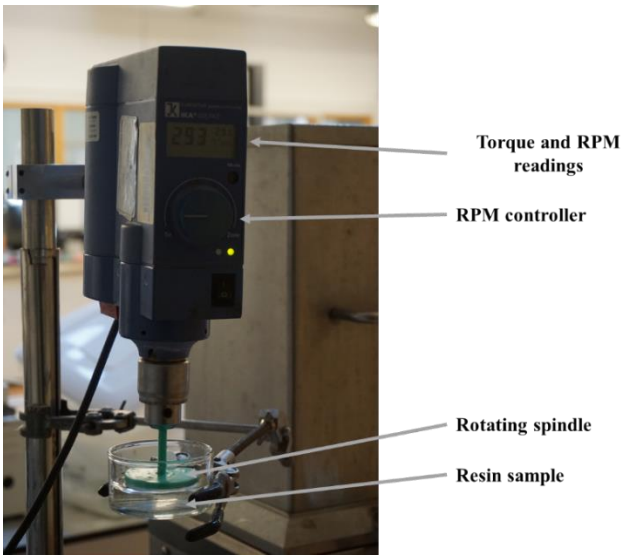

Figure 3-6 Image of viscosity measurement setup.

For both resin systems, 15 batches were prepared each comprising 65 g of resin and hardener mixture. Such quantity was selected for study as it was sufficient to produce a single thermal sample or a complete set of mechanical samples. Afterwards, one of each resin samples was placed underneath the viscometer to measure viscosity changes as a function of time, while the remaining samples were mixed with 2 wt% aerogel particles at specific intervals of time. After all the samples had been cured as described in 3.2.2, samples were tested to obtain the thermal conductivity and their bulk density was calculated through measured sample weight and volume.

With a focus on further investigating the pore infiltration level, the filled pore volume fraction (V_{inf}) was calculated, representing a volume ratio of the filled pores to the original unfilled pores. This factor can help assess the number of pores being destroyed by resin infiltration during the manufacturing process, with a 100% ratio indicating complete infiltration and 0% meaning all pores have been preserved. In order to calculate filled pore volume fraction, the following calculations have been used [85]:

$$V = \left(\frac{100}{vol\%}\right) \times \left(\frac{1}{\rho} - \frac{1}{\rho_{polymer}}\right) + \frac{1}{\rho_{polymer}} - \frac{1}{\rho_{silica}} \quad \text{Eq. 33}$$

$$V_{inf} = \frac{V_0 - V}{V_0} \times 100 \quad \text{Eq. 34}$$

where ρ, $\rho_{polymer}$ and ρ_{silica} are densities of respectively composite, epoxy resin (1.16 g cm^{-3}) and β-Cristobalite silica (2.18 g cm^{-3}) [238]. Additionally, $vol\%$ represents added volume ratio of silica aerogel and V_0 is a pore volume of particles obtained from gas adsorption analysis.

3.2.5 Particle size and distribution

As only the maximum diameter of aerogel particles was available from the supplier, a more detailed analysis of particle size was required to investigate the size effect. As a result, FASEP - the System for Fibre Length Analysis has been used and the setup is presented in Figure 3-7.

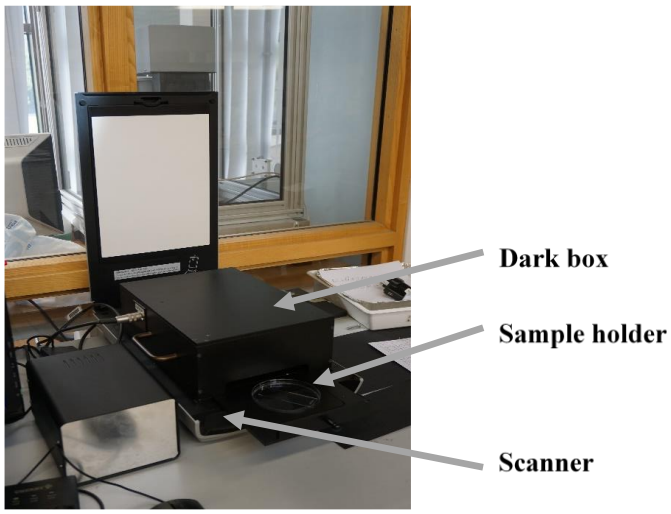

Figure 3-7 Setup used for the Fibre Length Analysis.

Even though, this system has been previously used to only measure the geometry of various types of fibres, it was successfully optimised to analyse an aerogel particle. As a result, 0.1 g of aerogel particles were dispersed in 100 ml of acetone with additional glycerine and stirred for 5 minutes using a magnetic stirrer at 500 rpm. Afterwards, a part of the solution was transferred onto a glass plate and dried out to avoid particle agglomeration. Such technique

was used in order to separate the particles, nevertheless it is quite possible the acetone impregnated the pores and during drying could cause a pore collapse resulting in size shrinkage. Then, prepared samples were positioned in the dark field box of an DM FASEP fibre length measurement as presented in Figure 3-7. Dark box was located on the top of a high-resolution scanner (Canon ScanoScan 9000F) with a resolution of 10.52 μm per pixel, which allowed to capture high quality 2D image of a sample as presented in Figure 3-8. Further those images were analysed using an Image Pro macro of the IDM FASEP fibre length measurement system, allowing the identification of particles as small as 10 μm. In the case of irregularly shaped particles, the system uses an algorithm based on the Hough Transformation. It draws an ellipse around the particle and report its length and diameter which are later used to assign particle to specific categories. All available aerogel samples were tested under the same procedure.

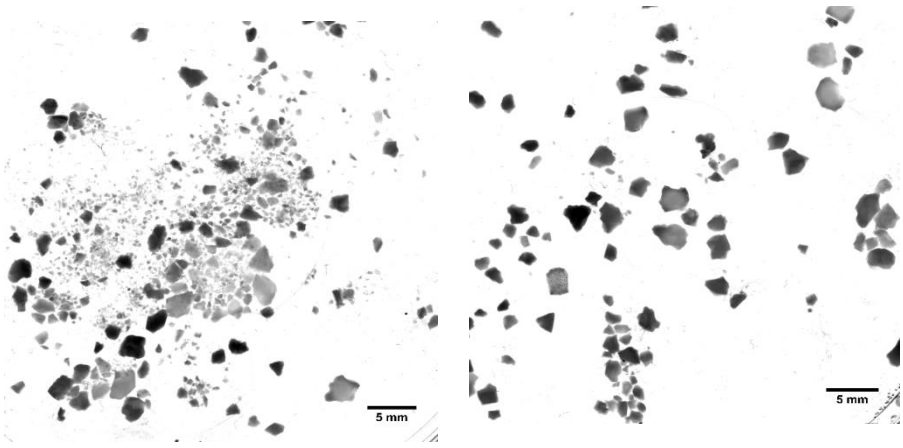

Figure 3-8 Scanned images of 1250 μm (left) and 3500 μm (right) silica aerogel particles.

To more clearly presents the size difference and provide an indication of particles' shapes and texture the optical microscopy images have been captured using Olympus BX51 microscope under transmitted light in brightfield with a magnification between 20 and 100.

3.2.6 Scanning electron microscopy

Scanning electron microscopy (SEM) was used to investigate the internal structure of both virgin aerogel particles and aerogel particles incorporated within the polymers. All the SEM imagining has been conducted using HITACHI SU-6600 machine. In order to proceed with scanning the samples have been attached to the SEM mount using a double-sided carbon tape and then coated with a layer of gold to improve the electrical conductivity of the samples. Following the placement of the mount within scanning chamber the images were taken using accelerating voltage between 5 kV and 15 kV and the magnification of up to 100k. In case of aerogel particles incorporated into polymer matrix the samples have been obtained by cutting

out the part of the composite from the centre of a larger samples using a band saw. It is suspected that preparation of the sample could affect aerogels' internal structure, nevertheless such measures were required to prepare a sample with adequate size to fit SEM.

3.2.7 Thermal conductivity measurement

TA Fox50 heat flow meter was used to measure the thermal conductivity of aerogel composites by following ASTM C518. This method requires a sample to be sandwiched between hot and cold plate in order to induce the heat flux which is latter used to calculate thermal conductivity of the sample using Fourier's law for one-dimensional heat conduction at a steady state. All test specimens were cast using a silicone rubber mould and they had cylindrical geometry with a diameter of 51 mm and a thickness of 25.4 mm. To minimise the effect of any surface defects, a silicon thermal paste with thermal conductivity of 15.7 w/mK was applied to both horizontal surfaces of each sample. Upon placement of the sample inside Fox50 the temperature of hot and cold plate was set to be 25 °C and 15° C respectively. Afterwards, the machine controlled the input of electrical energy to both plates until the heat flux stabilized. Only at that point the steady state has been achieved and the measurement could commence. In order to fulfil the requirement of the measurement standard at least two samples for each aerogel/polymer blend were tested.

Due to limited access to Fox50, the TC3000E thermal conductivity meter was also used as an alternative for thermal conductivity measurements. It utilizes the transient hot-wire method and follows ASTM D5930 − 17 standard. According to this technique the thermal conductivity is measured by analysing the increase in the samples' temperature when it is heated by a thin hot wire. In order to utilise this method, the sensor needs to be surrounded by the material, thus previously created cylindrical samples were cut in the middle and polished using sandpaper to provide a tight contact with the sensor. Afterwards the sensor was placed in between both material pieces and a 500 g mass was placed on top of the whole assembly to ensure no movement and appropriate contact between sensor and the sample as presented in Figure 3-9. During most of the measurement, recommended settings has been used with a voltage of 1V and 10 seconds measurement time.

Figure 3-9 a) TC3000E thermal conductivity meter sensor b) setup of the thermal conductivity measurement. Sampel used was a vinyl ester filled with 2 wt% 1250 μm aerogel particles.

3.2.8 Mechanical testing

Compression tests according to ASTM D695 were undertaken to evaluate the effects of the aerogel addition on compressive properties of the polymer specimens. An Instron 5969 series universal testing system, fitted with a 50 kN load cell and equipped with a video extensometer, was used to load rectangular samples with the dimensions of 12.7×12.7×25.4 mm at a constant rate of 1.3 mm/min at 20 °C. At least 5 samples for each aerogel/polymer blend were tested and a typical stress/strain curve is presented in Figure 3-10.

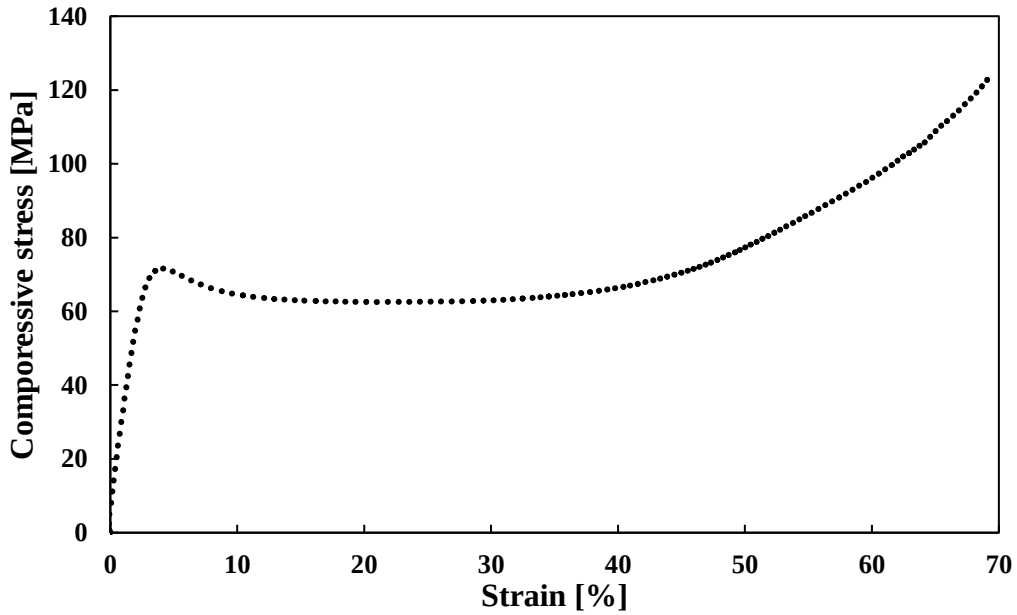

Figure 3-10 Average stress-strain curves for epoxy filled with 1 wt% 100 μm aerogel particles.

3.2.9 Thermomechanical analysis

Thermomechanical analysis (TMA) was conducted to measure the effects of aerogel particles' addition on the polymer matrix's linear coefficient of thermal expansion (CTE) and glass transition temperature (T_g). All measurements were conducted according to the ASTM E831 – 19 standard using TA Instruments Q400 Thermomechanical Analyzer. During the measurement, a sample of 5×5×5 mm was placed under the silica expansion probe exerting 100 mN of force. Afterwards, the temperature ramp was executed at a rate of 5 °C/min from 0 to 200 °C providing the expansion vs temperature graph as presented below. At least 3 samples have been tested for each materials combination and an example of a displacement-temperature graph generated by TMA is presented in Figure 3-11.

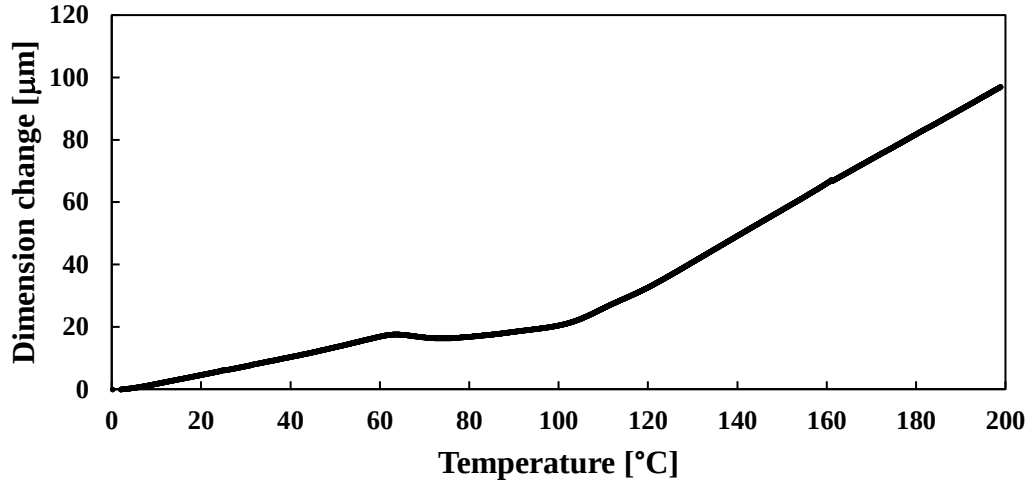

Figure 3-11 Example of a displacement-temperature graph generated by TMA for a vinyl ester filled with 1 wt% 100 µm aerogel particles.

Finally, the mean CTE was calculated using the following equation:

$$\alpha_m = \frac{\Delta L_{sp} \times k}{L \times \Delta T} \qquad \text{Eq. 35}$$

where L is an initial length of a specimen at room temperature, ΔL_{sp} is a change of sample length across the desired temperature range, k is a calibration coefficient and ΔT represents the temperature difference for which the coefficient is being measured. In this work, the results for sample dimension change in a temperature range of 0-50 °C were used to calculate the CTE. On the other hand, the glass transition temperature was determined at the cross section point of two tangential lines drawn along the first major discontinuity in the dimensional change and temperature graph.

3.2.10 Dynamic mechanical analysis

To investigate the impact of aerogel particles on viscoelastic properties of both epoxy and vinyl ester, the dynamic mechanical analysis has been conducted using TA Instruments Q800. heat distortion temperature (HDT) and glass transition temperature (T_g) have been examined following ASTM D648 and ASTM D7028 standards.

In case of heat deflection temperature, the samples were moulded to the size of 60×12.6×3.2 mm and were subjected to a 3-point bending test with a span length of 50 mm. In order to comply with the standard and apply the stress of 0.455 MPa to the sample the preload force was calculated for each sample based on its geometrical features using the equation below:

$$F = \frac{2}{3} \times \frac{\sigma \times T^2 \times W}{L} \qquad \text{Eq. 36}$$

where σ is the required stress on the sample, T, W and L are respectively thickness, width and length (50 mm in this case) of the tested sample. Following the preload application, the temperature inside the chamber was raised from 25 to 200 °C at a rate of 5 °C/min and the displacement as a function of temperature was recorded. Afterwards, the HDT was identified at an intersection point between linear portions of the graph before and after large sample deflection as shown in Figure 3-12.

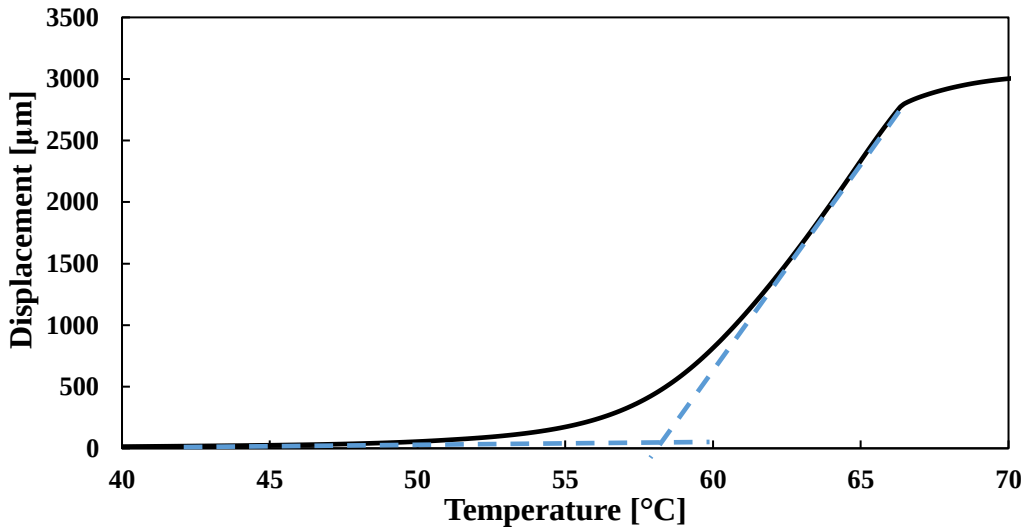

Figure 3-12 Example displacement-temperature graph produced by DMA for epoxy filled with 1 wt% 1230 µm aerogel particles with HDT determined at the intersection point of two dashed lines.

In addition to HDT measurement, samples of the same dimensions were also used in DMA 3-point bending setup to measure glass transition temperature. However, this time the experimental settings were altered. As a result, the settings included heating rate of 2°C/min between 25°C to 150°C, the oscillating frequency of 1 Hz, the amplitude of 50 µm, static pre-load of 0.1 N and force track of 105%. The resulting graph included the changes in storage

modulus, loss modulus and damping index (tan δ) as presented in Figure 3-13. T_g was obtained by identifying the maximum value of loss modulus.

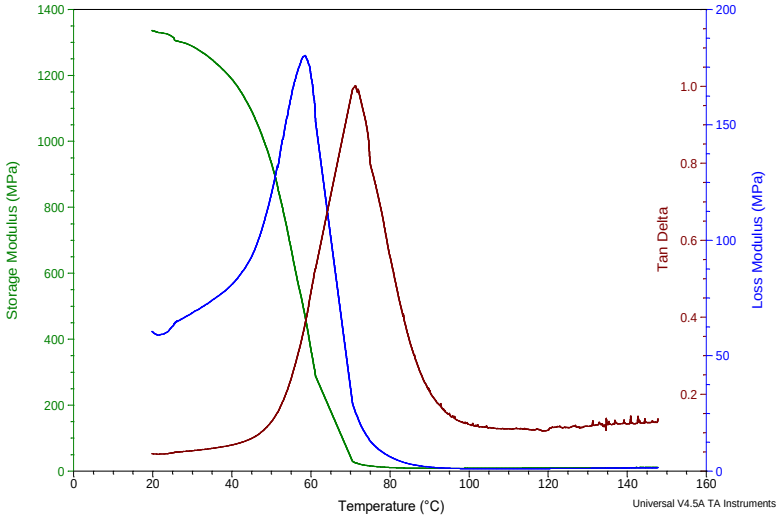

Figure 3-13 Example graph produced by DMA presenting dynamic mechanical parameters as a function of temperature for epoxy filled with 1 wt% 1230 μm aerogel particles.

3.3 Results and discussion

3.3.1 Particle size distribution

3.3.1.1 Silica aerogel

Figure 3-14 presents the size distribution of silica aerogel particles as received from the supplier.

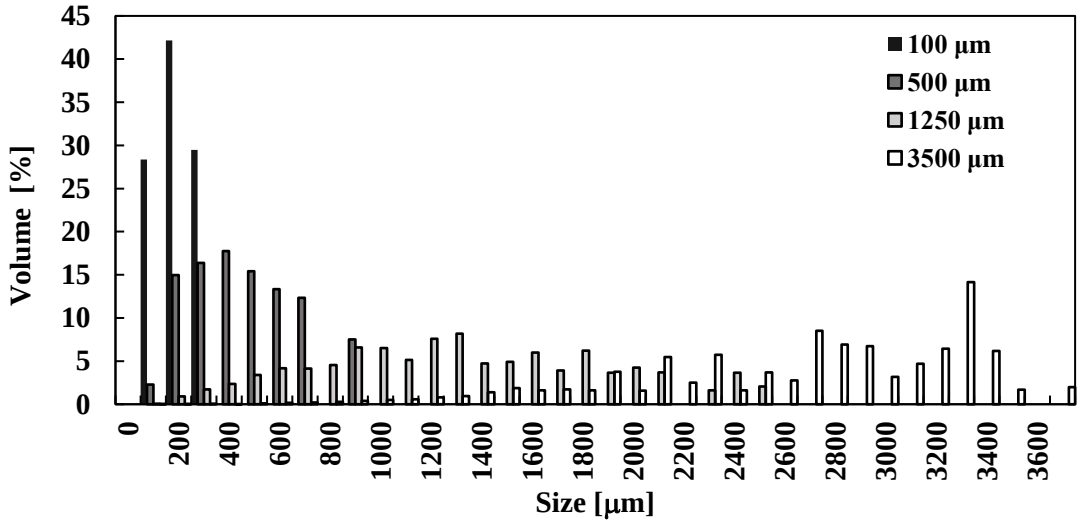

Figure 3-14 Silica aerogel particle size distribution.

The results show that the single value of the particle size given by the supplier only covers the upper range of particles. Also, due to transportation and handling, it is anticipated that the particles size could be further reduced. It can also be noticed that most tested particles present a normal distribution except the largest particles that exhibit negatively skewed distribution. The average particle diameters are 85, 202, 601 and 1233 μm for 100, 500, 1250 and 3500 μm particle batches. Since particles of aerogel were produced by grinding the shape of particles was irregular and independent of the particle size as presented in Figure 3-15.

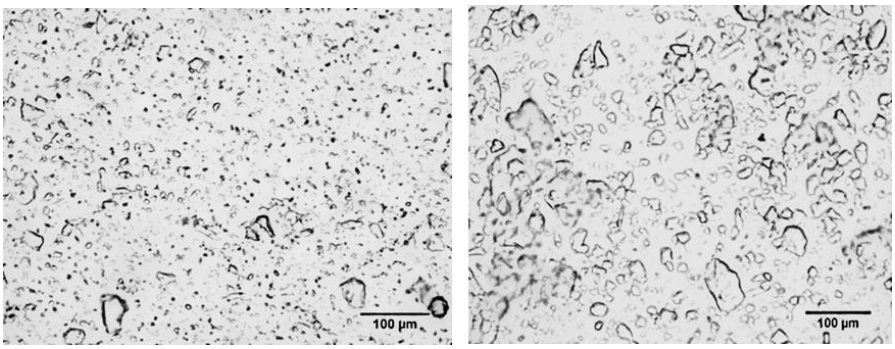

Figure 3-15 Microscopic images of 100 μm (left) and 200 μm (right) silica aerogel particles.

3.3.1.2 PI aerogel

A single size of polyimide aerogel particles has also been characterised with their size distribution presented in Figure 3-16.

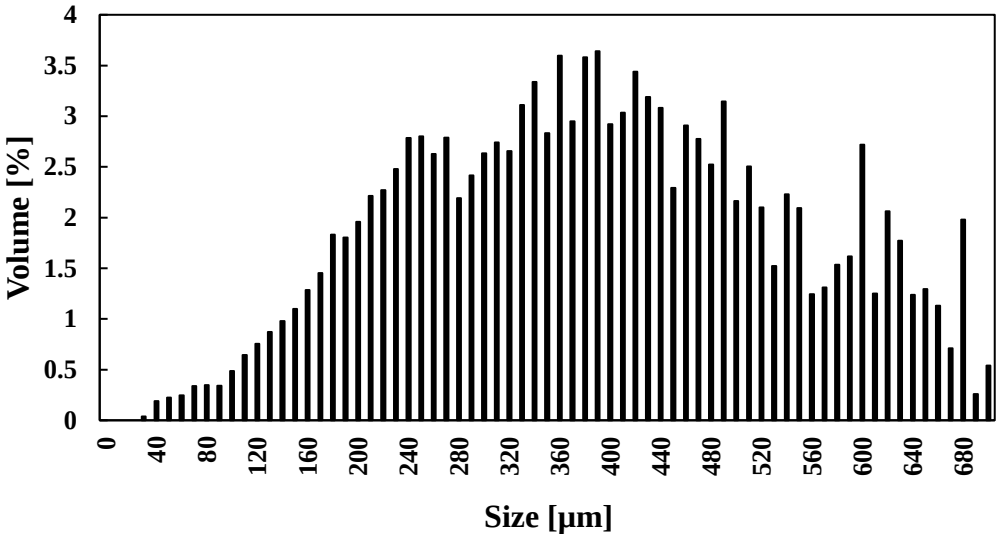

Figure 3-16 Polyimide aerogel particle size distribution.

The polyimide aerogel particles follow the normal distribution with an average diameter value of 183 µm. In addition, it covers the wide range of particle size (up to 700 µm), and in terms of particle size they are most similar to the 500 µm silica aerogel particles. Nevertheless, when comparing particles' shape, a significant difference can be noticed, as seen in Figure 3-17. PI aerogel has a spongy type of particles when compared to the angular one presented by silica aerogel. Because both types of particles have been manufactured through grinding, the shape difference can be associated with the diverse composition of both materials with polyimide, an example of organic aerogel and silica inorganic ones.

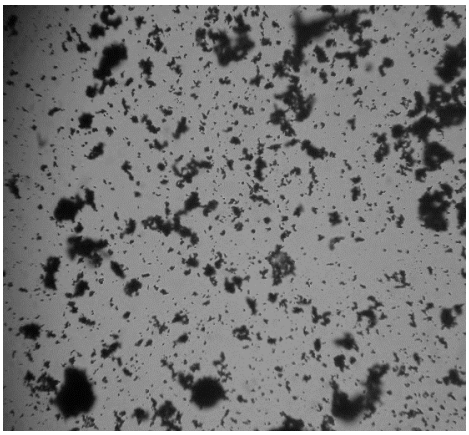

Figure 3-17 Microscopic images polyimide aerogel particles.

3.3.2 Aerogel pore characteristics

3.3.2.1 Silica aerogel

Nitrogen adsorption and desorption have been used to characterise the internal pore structure of pure silica aerogel particles. The isotherms obtained are presented in Figure 3-18.

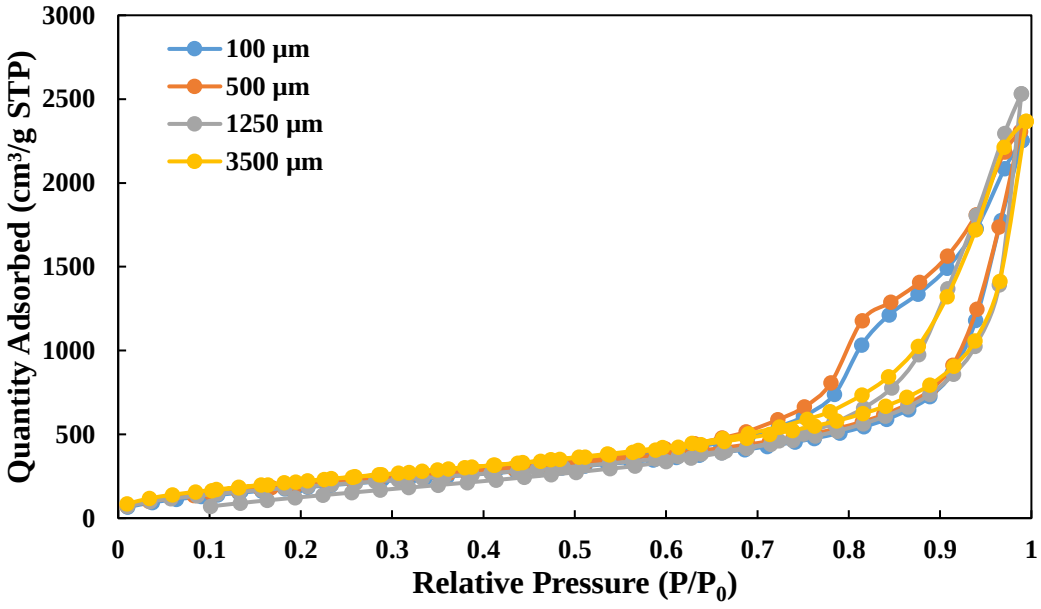

Figure 3-18 Nitrogen adsorption and desorption isotherms of silica aerogel particles.

All aerogel particles present a similar type IV isotherm indicating mesoporous material with a pore diameter in a 2 – 50 nm range. However, a slight difference in hysteresis loop width of small (100 and 500 µm) and larger particles (1250 and 3500 µm) can be noticed in a 0.7 – 0.9 relative pressure range. The increase in hysteresis loop width in case of smaller particles can results from the higher variation in pore diameters than larger particles. It is possible that due to grinding of silica aerogel particles into their final size the outside portion of particles' pores has been altered leading to creation of more various pore distribution. This effect would not be as severe in case of larger particles as even after grinding they still maintain a significant particle core of uniform internal structure. Nevertheless, the shape of all hysteresis loops also suggests condensation of the gas inside pores at low-pressure ranges, with further mono and multilayers formation at higher pressure [239]. In addition, the type IV hysteresis in Figure 3-18 also implies the presence of spherical pores with walls made of mesoporous silica. BET results are summarised in Table 3-2.

Table 3-2 Pore characteristics of silica aerogel particles obtained from BET analysis.

Silica aerogel				
Particle size [nm]	100	500	1250	3500
BET surface area [m^2/g]	761.42	811.49	750.19	881.52
BJH adsorption average pore width [nm]	17.16	16.58	19.63	16.44
BJH desorption average pore width [nm]	13.43	12.84	16.17	14.27
Cumulative pore volume (cm^3/g)	3.47	3.55	3.88	3.65

The specific surface area of aerogels is significant with an average value of 801 m^2/g, indicating the material's high porosity. The adsorption pore width of all samples varies between 1.7 nm to 70 nm, with an average of 17.5 nm and a cumulative pore volume of 3.55 g/cm^3. These pore characteristics suggest a high-quality aerogel with varying particle sizes having little impact on porous structure.

3.3.2.2 PI aerogel

Nitrogen adsorption and desorption have also been used to characterise polyimide aerogel samples' internal pore structure. The resulting isotherm is presented in Figure 3-19.

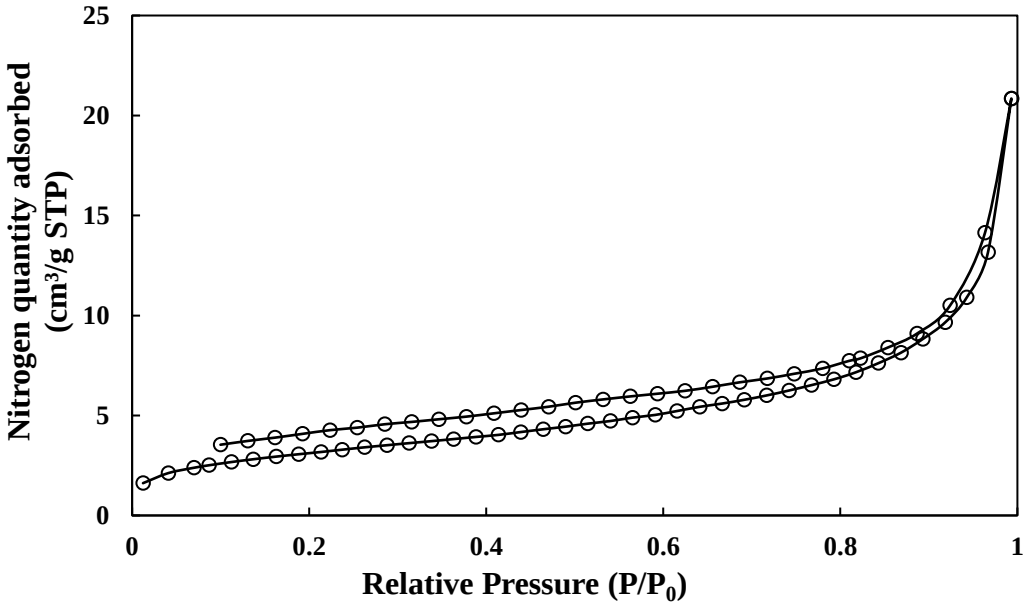

Figure 3-19 Nitrogen adsorption and desorption isotherms of polyimide aerogel particles.

Similarly, as in the case of silica aerogel, the type IV isotherm is obtained, indicating mesoporous material with a pore diameter in a 2 – 50 nm range. However, significant differences can be noticed, starting with a much lower quantity of nitrogen absorbed and a much smaller gap between adsorption and desorption isotherms. Also, the type III hysteresis

loop is present indicating the existence of flaky particles forming slit-like pores [239]. The BET properties, such as surface area and pore volume are summarised in Table 3-3.

Table 3-3 Pore characteristics of polyimide aerogel particles obtained from BET analysis.

PI Aerogel	
Particle size [nm]	183
BET surface area [m²/g]	11.29
BJH adsorption average pore width [nm]	13.67
BJH desorption average pore width [nm]	11.40
Cumulative pore volume (cm³/g)	0.030

It can be noticed that PI aerogel particles present a significantly lower specific surface area values with an average value of 11.29 m²/g. Together with a cumulative pore volume of 0.03 g/cm^3 they suggest low porosity of the material than silica aerogel counterparts. Nevertheless, both materials share a similar pore size, as for polyimide aerogel the adsorption pore width varies between 1.7 to 68 nm with an average value of 13.67 nm. According to the manufacturer, the aerogel has a nominal density between 150 and 200 kg/m^3 and which could indicate porosity in a region of 87 and 93%.

3.3.3 Matrix rheological behaviour

3.3.3.1 Epoxy resin

Figure 3-20 presents the measured shear viscosity of pure epoxy resin as a function of time after the hardener's addition.

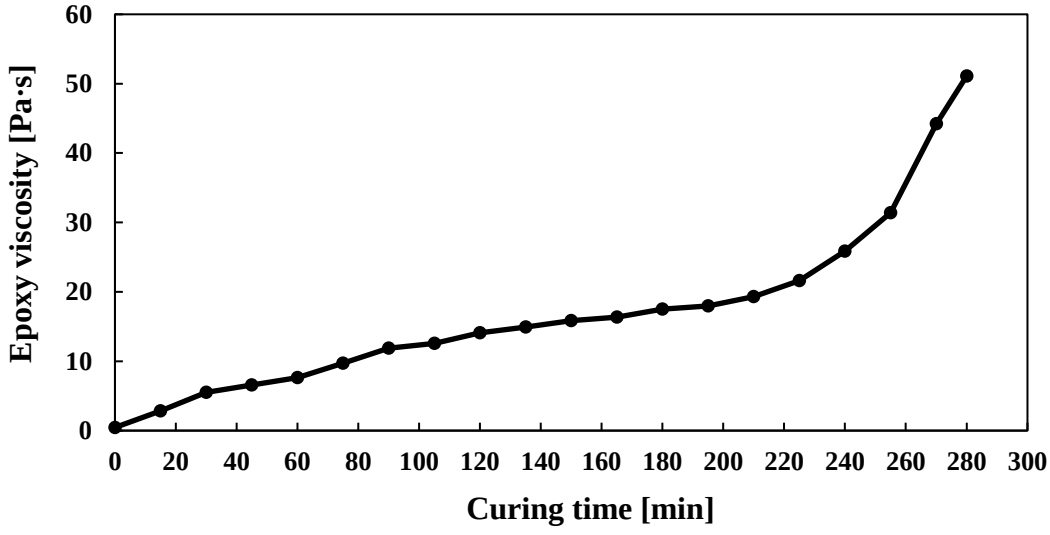

Figure 3-20 Evaluation of epoxy viscosity over curing time.

Overall, it took over 4 hours to cure the epoxy beyond the point when further measurements were impossible, with gelation point occurring around 3.5 hr mark. An initial average viscosity

growth of 0.078 Pa·s per minute was detected before the gelation point, followed by a rapid increase at a rate of 0.831 Pa·s per minute afterwards.

3.3.3.2 Vinyl ester resin

Figure 3-21 presents the measured shear viscosity of pure vinyl ester resin as a function of time after the hardener's addition.

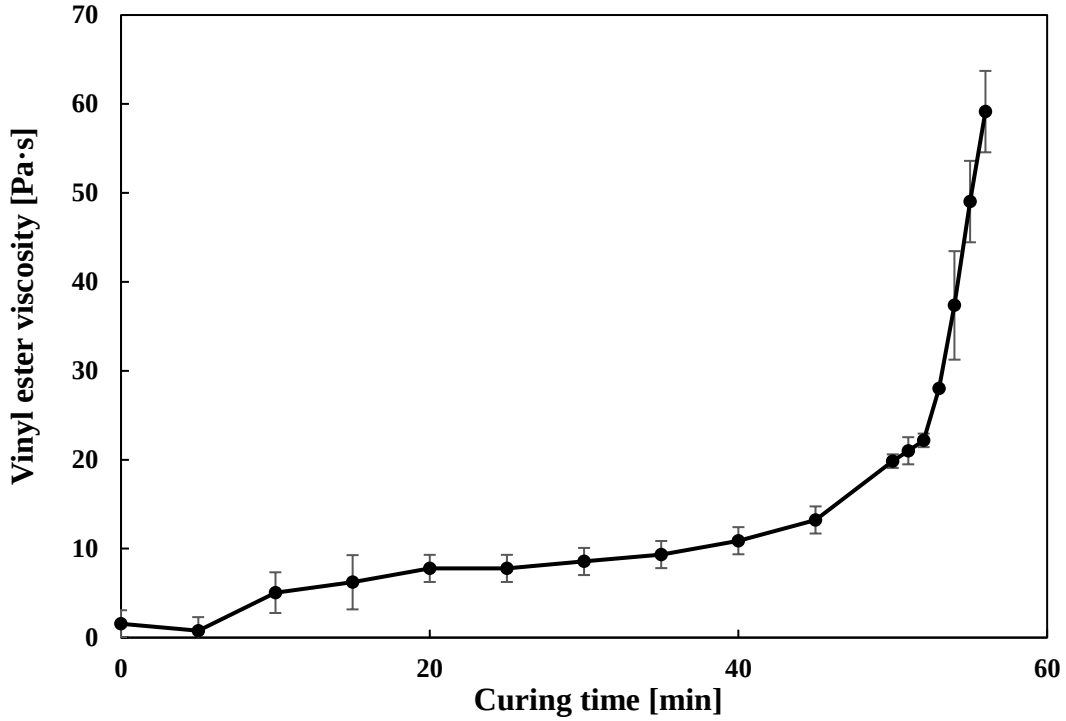

Figure 3-21 Evaluation of vinyl ester viscosity over curing time.

As can be noticed, vinyl ester was reacting much quicker than epoxy with less than an hour required to cure the sample. Gelation point occurred around 45 min mark and an initial average viscosity growth of 0.196 Pa·s per minute was detected before gelation point, followed by an extremely rapid increase at a rate of 6.753 Pa·s per minute afterwards.

3.3.4 Effect of resin viscosity

3.3.4.1 Density

3.3.4.1.1 Epoxy resin

Multiple composites have been created alongside the viscosity measurements by introducing 2 wt% 1250 μm silica aerogel particles at a specific polymer curing time. Figure 3-22 presents the change in silica aerogel/epoxy composites density over time of aerogel addition during epoxy curing.

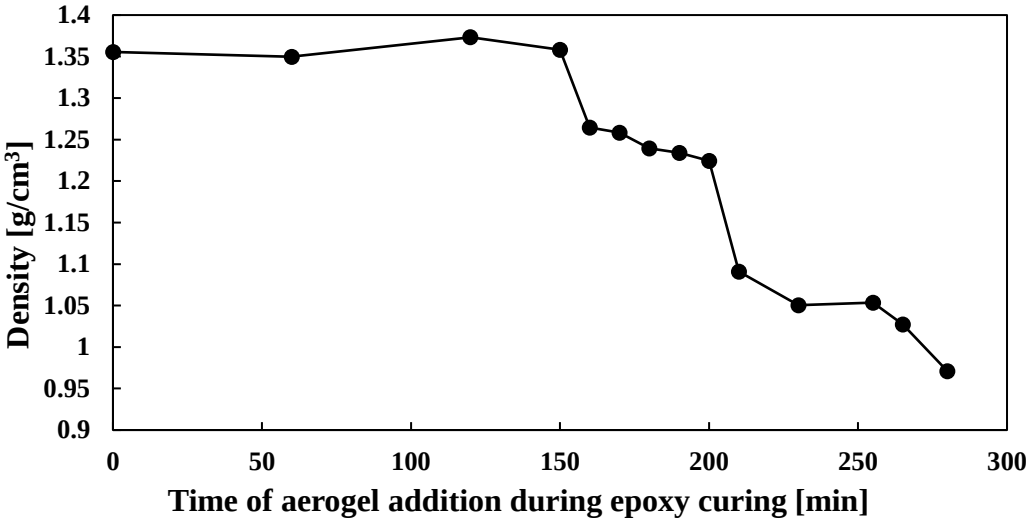

Figure 3-22 Change in silica aerogel/epoxy composites density over time of aerogel addition during epoxy curing. The composites have been created with the use of 2 wt% 1250 μm aerogel particles.

As reflected by Figure 3-22, the addition of aerogel particles shortly after the resin/hardener mixture's preparation resulted in no reduction in the composites' density. It was only after reaching 160 minutes mark when the density of created samples started to decline, leading to a 28% decrease after 280 minutes. Afterwards, the addition of silica aerogel particles become impossible due to the further crosslinking of the epoxy system producing a thick mixture, restricting uniform distribution of particles across the samples, also trapping significant volume of air pockets in the process. To fully understand the occurring phenomenon, Figure 3-23 was created incorporating both densities of created samples and viscosity of resin when particles were added.

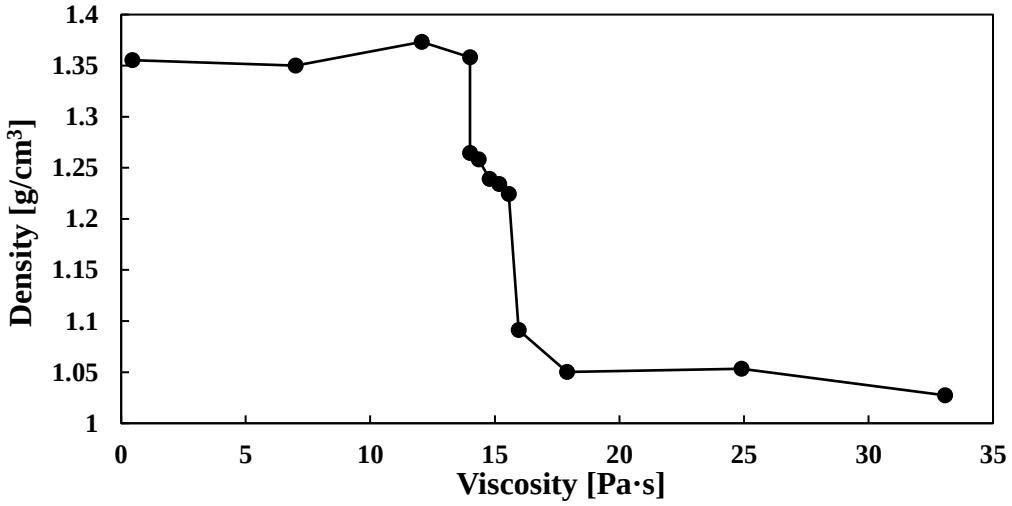

Figure 3-23 Change in silica aerogel/epoxy composites density over resin's viscosity at which particles were added. The composites have been created with the use of 2 wt% 1250 μm aerogel particles.

Data included in Figure 3-23 indicates a sharp drop in composites density when particles were added to the epoxy resin with a viscosity of 14 Pa·s. After reaching 18 Pa·s the decrease in density was significantly hindered, however still present. Such change in density can occur due to diminishing the pore infiltration of resin into the aerogel structure. However, other less desirable factors such as the introduction of air pockets to the composite must be considered. To validate the effect of mechanical stirring during resin curing additional test was conducted during which resin was stirred at different time intervals but without adding any aerogel particles. Nevertheless, no changes in density were recorded for created samples.

3.3.4.1.2 Vinyl ester resin

Figure 3-24, presents the change in silica aerogel/vinyl ester composites density over time of aerogel addition during vinyl ester curing.

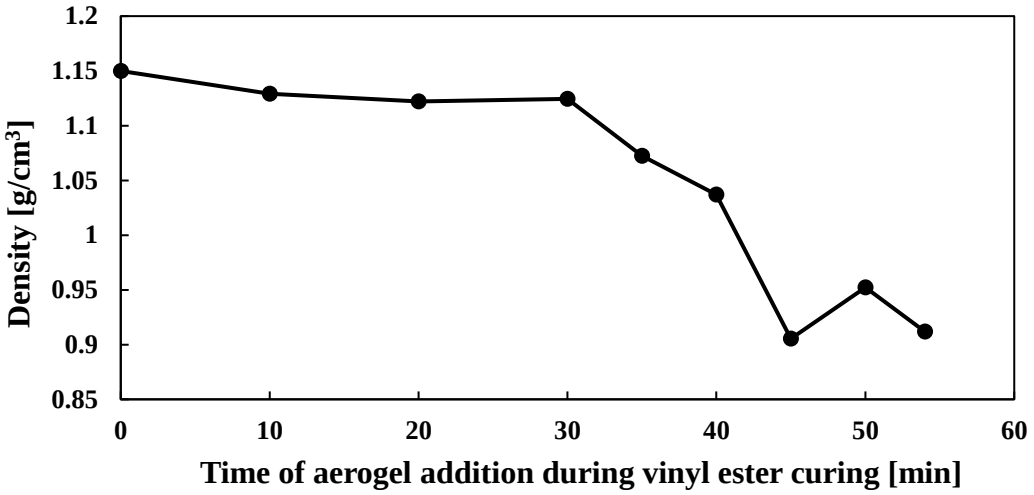

Figure 3-24 Change in silica aerogel/vinyl ester composites density over time of aerogel addition during vinyl ester curing. The composites have been created with the use of 2 wt% 1250 μm aerogel particles.

As presented in Figure 3-24, the incorporation of aerogel particles right after preparation of the resin/hardener mixture resulted in a minor reduction in density of the composites, only after reaching 30 minutes mark when the density of created samples started to decrease finally leading to a 20% decrease after 55 minutes. Beyond that point, silica aerogel particles' addition becomes difficult due to the vinyl ester resin mixture's elevated thickness. Such behaviour restricted the uniform distribution of particles across the samples, additionally trapping a significant volume of air pockets inside the composite during the mixing process. To further understand the effect of vinyl ester viscosity on the density of created composited, Figure 3-25 was created incorporating both densities of created samples and viscosity of resin at the moment when particles were added.

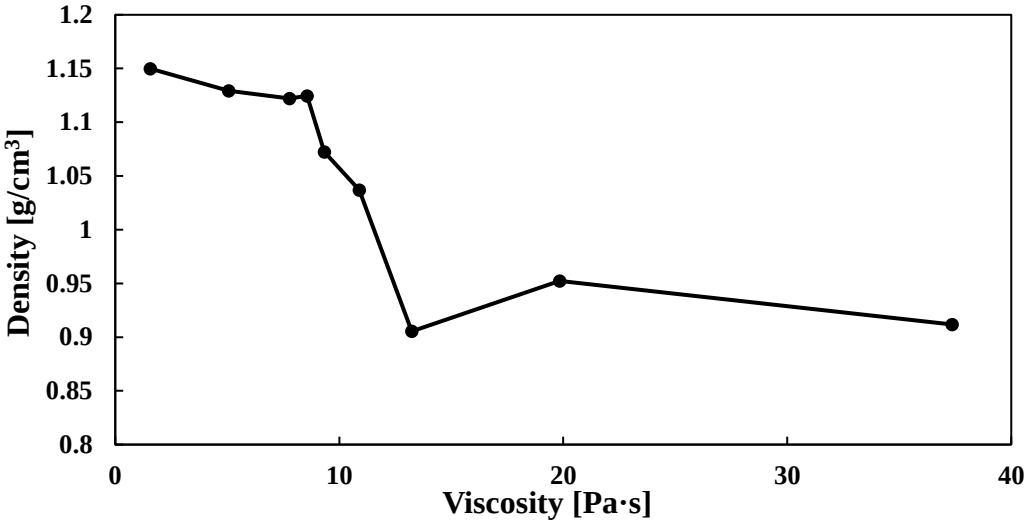

Figure 3-25 Change in silica aerogel/vinyl ester composites density over resin's viscosity at which particles were added. The composites have been created with the use of 2 wt% 1250 μm aerogel particles.

Data presented in Figure 3-25 indicates a slight yet steady decrease in composite density (when using low viscosity resin mixture) followed by a sharp drop when particles were added to the vinyl ester resin with a viscosity of 10 Pa·s. When reaching 13 Pa·s the decrease in density was almost halted, leading to the conclusion that such change in density can occur due to reducing infiltration of the aerogel pores by the vinyl ester. Similarly, as in epoxy composites, the introduction of air pockets to the composite must also be considered. To confirm no effect of mixing on the polymer properties, the additional test was conducted during which resin was stirred at different time intervals without adding any aerogel particles. Afterwards, no changes in density were recorded for created samples.

3.3.4.2 Thermal conductivity

Similarly, as in the case of density measurements, the thermal conductivity of samples created by the addition of aerogel at different polymer cure time has been tested.

3.3.4.2.1 Epoxy resin

Figure 3-26 and Figure 3-27 presents thermal conductivity values as a function of respectively time and viscosity of polymer at the moment when particles were added.

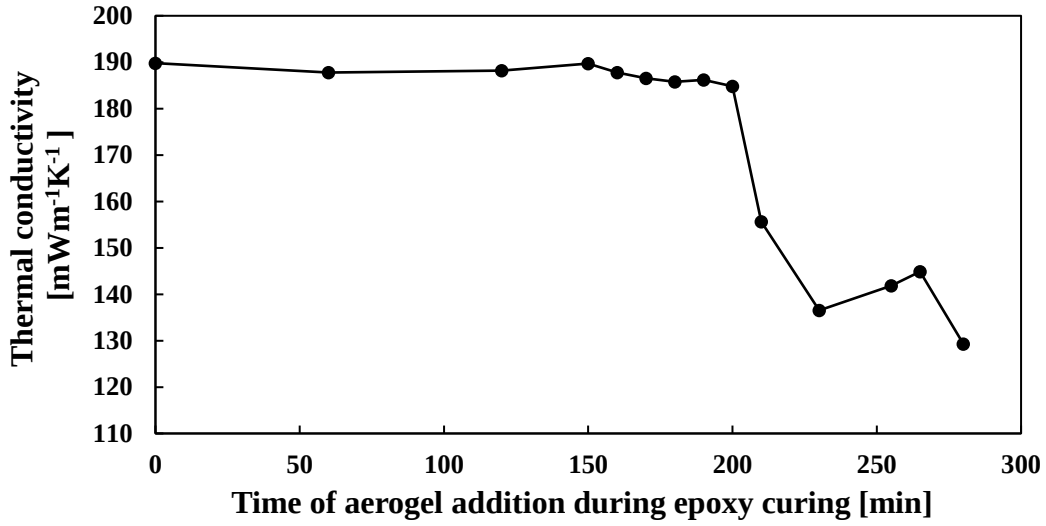

Figure 3-26 Change in silica aerogel/epoxy composites thermal conductivity over time of aerogel addition during epoxy curing. The composites have been created with the use of 2 wt% 1250 μm aerogel particles.

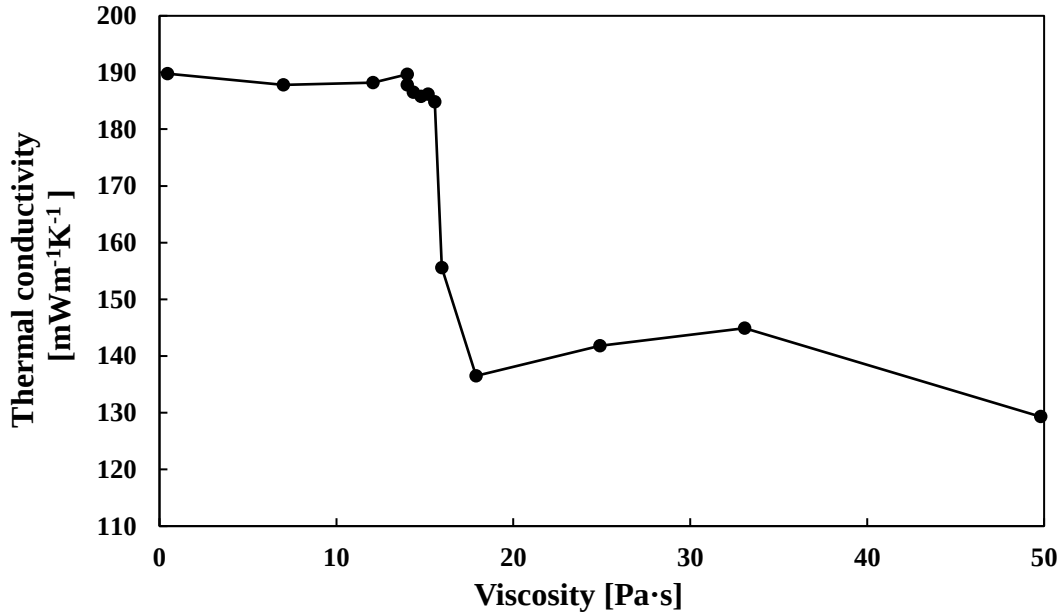

Figure 3-27 Change in silica aerogel/epoxy composites thermal conductivity over the resin's viscosity at which particles were added. The composites have been created with the use of 2 wt% 1250 μm aerogel particles.

The results regarding thermal conductivity presented in Figure 3-26 and Figure 3-27 mostly follow a similar trend as observed in density variation. The thermal conductivity showed slight variation around the pure epoxy value of 190 $mWm^{-1}K^{-1}$ when the aerogel particles were mixed with the resin at the viscosity below 14 Pa·s. Between 14 and 18 Pa·s a sharp conductivity drop was recorded, leading to the 32% decrease in composite thermal conductivity for the sample prepared with the highest viscosity resin.

3.3.4.2.2 Vinyl ester resin

Figure 3-28 and Figure 3-29 presents thermal conductivity values as a function of respectively time and viscosity of vinyl ester at the moment when particles were added.

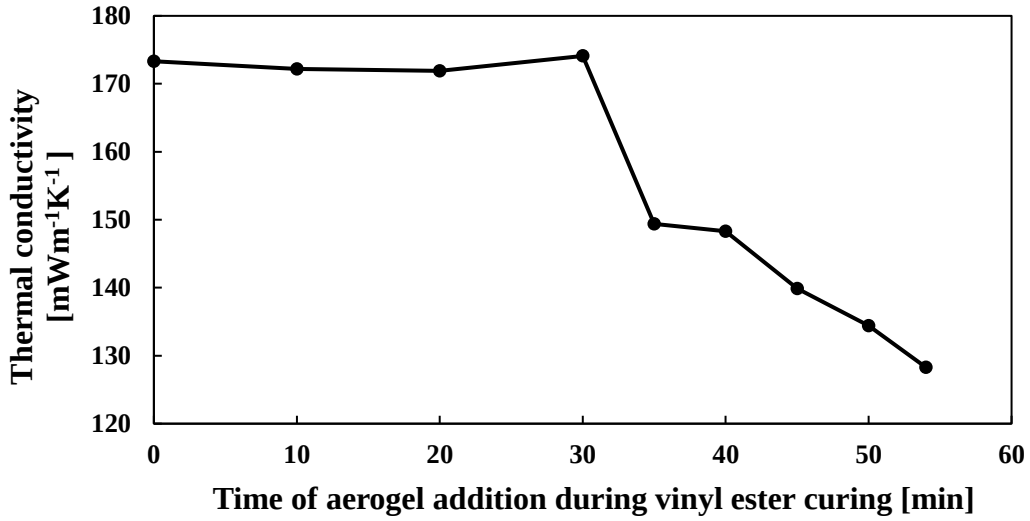

Figure 3-28 Change in silica aerogel/vinyl ester composites thermal conductivity over time of aerogel addition during vinyl ester curing. The composites have been created with the use of 2 wt% 1250 μm aerogel particles.

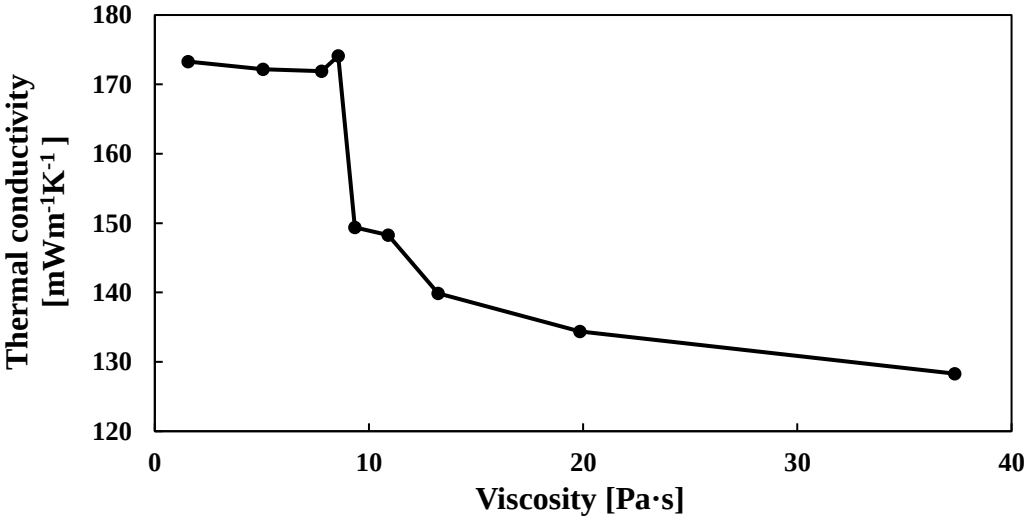

Figure 3-29 Change in silica aerogel/vinyl ester composites thermal conductivity over the resin's viscosity at which particles were added. The composites have been created with the use of 2 wt% 1250 μm aerogel particles.

As indicated by Figure 3-28 and Figure 3-29, samples prepared with low viscosity vinyl ester resin do not significantly affect the composite thermal conductivity and oscillate slightly below the Tc value of pure vinyl ester (170 $mWm^{-1}K^{-1}$**)**. It is only between 10 Pa·s and 13 Pa·s when a sharp drop in Tc was recorded, followed by a steady decrease afterwards. Overall, a 30%

decrease in thermal conductivity value has been achieved by using a high viscosity vinyl ester resin.

3.3.4.3 Discussion

Figure 3-30 correlates the thermal conductivities and densities of all epoxy and vinyl ester samples prepared by adding the aerogel particles to the resin systems with different viscosity.

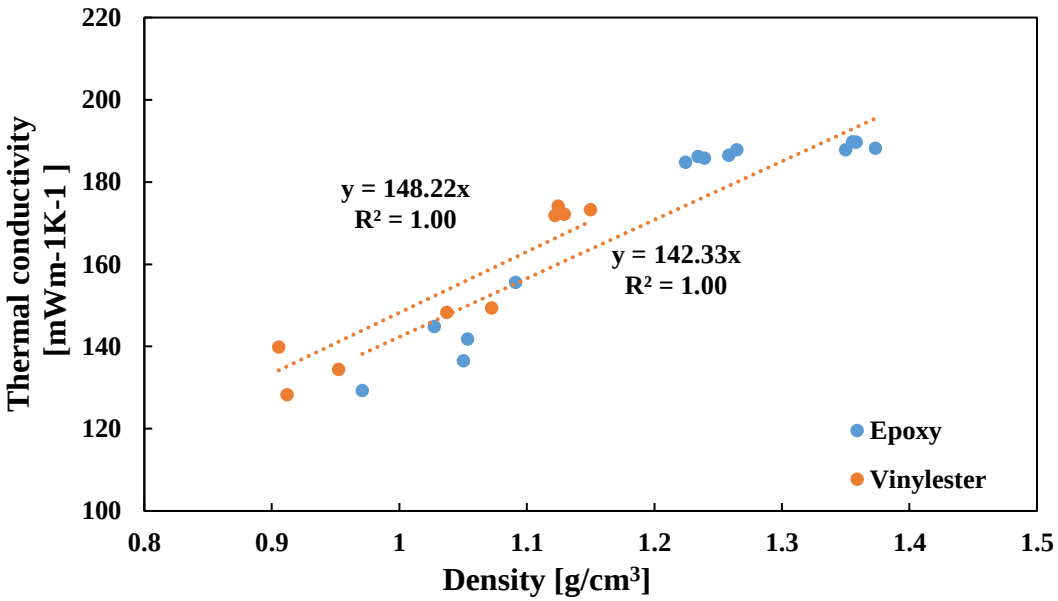

Figure 3-30 Thermal conductivity of epoxy/ vinyl ester and silica aerogel composites as a function of density.

As presented in Figure 3-30, in case of both epoxy and vinyl ester composites the thermal conductivity is directly correlated with the density of the sample and decreases with decreasing density values. It is suspected that when low viscosity resin was used during sample preparation, a high degree of aerogel pore infiltration occurred. Such behaviour is believed to destroy the internal, nanoporous structure of aerogel thus increasing the density of the composite and diminishing all potential benefits aerogel particles can contribute to the material thermal properties. Nevertheless, by using partially cured resins, its molecules might be large enough not to infiltrate aerogel pores resulting in preservation of the air pockets within the particles and reducing the thermal conductivity of the created composite. With a focus on further investigating the level of pore infiltration the filled pore volume fraction was calculated (using Eq. 33 and Eq. 34) and presented in Figure 3-31 and Figure 3-32 as a function of time of aerogel addition during respectively epoxy and vinyl ester curing.

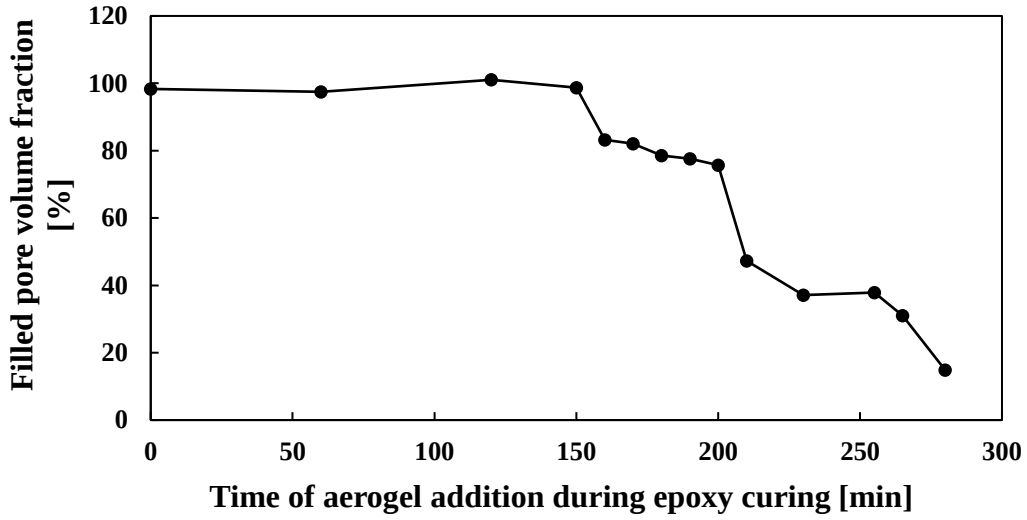

Figure 3-31 Change in the filled pore volume fraction of composite material created by adding 2 wt% 1250 μm particles over time of aerogel addition during epoxy curing.

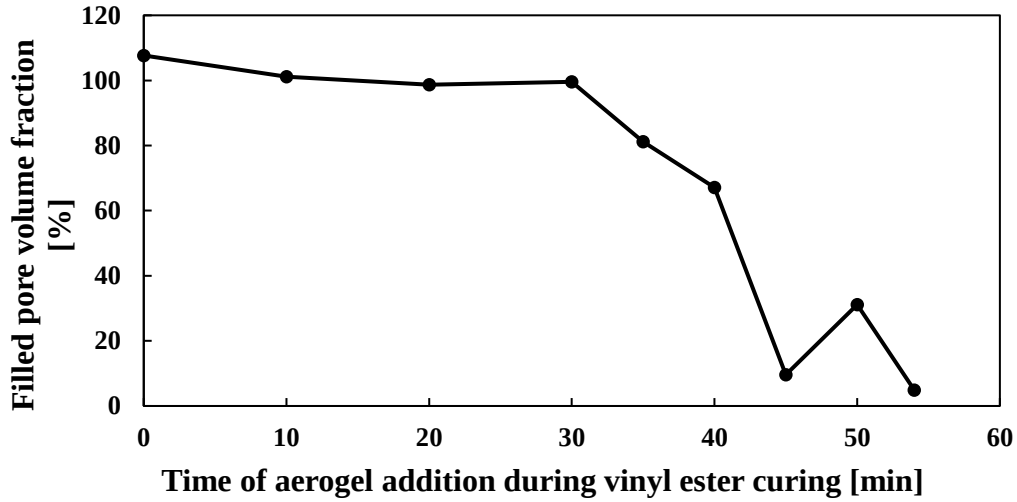

Figure 3-32 Change in the filled pore volume fraction of composite material created by adding 2 wt% 1250 μm particles over time of aerogel addition during vinyl ester curing.

As presented in the figures above, the usage of low viscosity resin systems can lead to complete infiltration of aerogel pores. The elevation of resin viscosity leads to a gradual decrease in filled pore volume fraction, but even with delayed addition of aerogel particles on average, 10% of pores are being infiltrated for both epoxy and vinyl ester resins. To further support this thesis, SEM images of aerogel particle added to epoxy resin at different curing stages has been taken and presented in Figure 3-33.

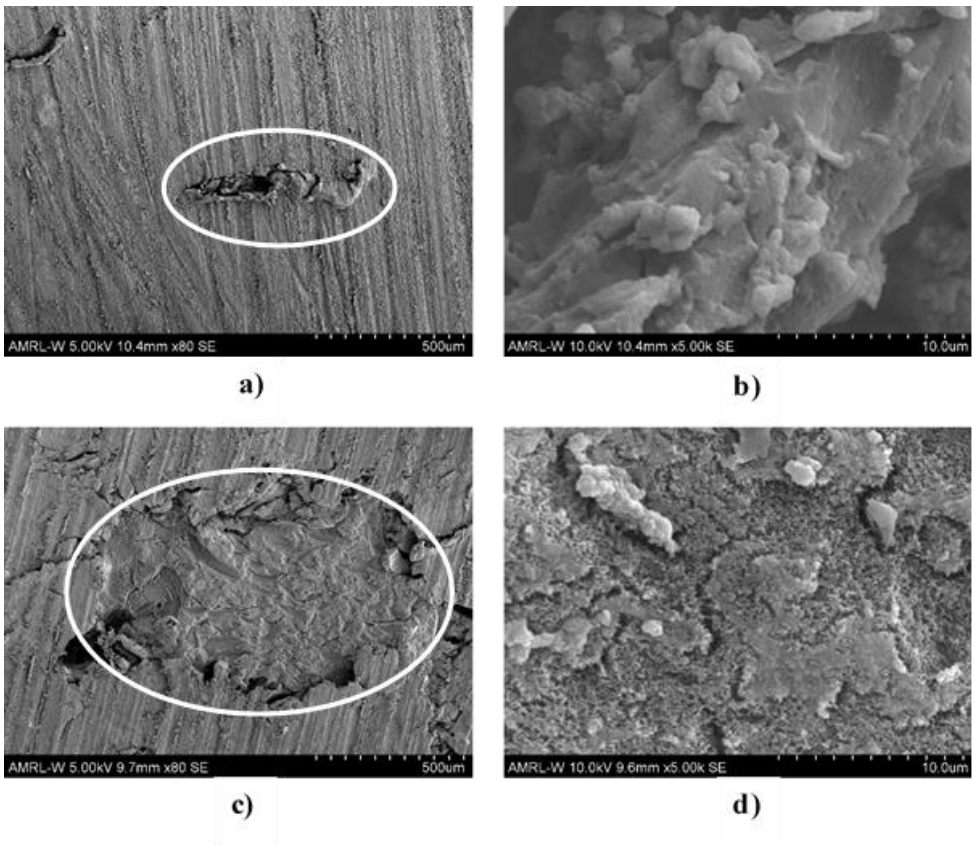

Figure 3-33 SEM images of silica aerogel particles submerged in epoxy resin. (a) aerogel particle (designated by the white circle) surrounded by epoxy resin with aerogel addition at the beginning of curing, (b) 5000x magnification of aerogel particle added in the epoxy.

First of all, the difference in the inclusions' volume can be noticed in Figure 3-33a and Figure 3-33c. Even though similar size particles have been used, in the case of particle submerged at the beginning of the curing process, the inclusions are significantly smaller than the other sample. Furthermore, higher magnification images revealed differences in the internal structure of inclusions with the monolithic and porous structure presented in respectively Figure 3-33b and Figure 3-33d. All the above points led us to believe that in the case of immediate silica aerogel addition, pores have been infiltrated by epoxy resin. Also, the destruction of internal structure led to silica aerogel particles' collapse, effectively reducing possible advantages to material thermal properties.

Since it is aerogel pores that affect the composites' properties, it is more meaningful to assess the effect of filled pore volume fraction on density and thermal conductivity. As a result, the density of composites normalised to the unfilled resin density as a function of calculated volume fraction of filled pores are shown in Figure 3-34.

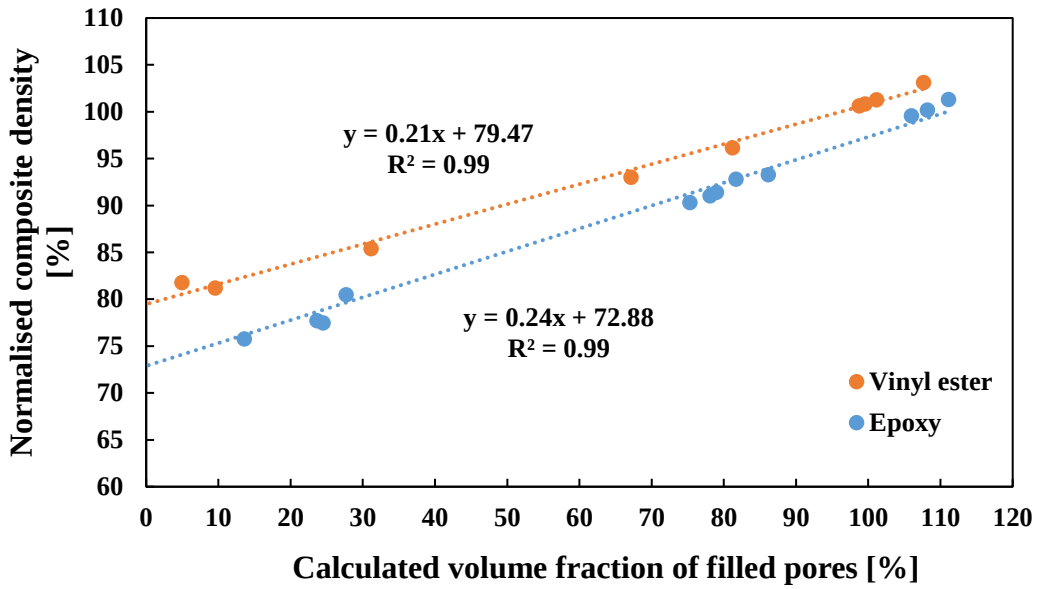

Figure 3-34 The impact of volume fraction of filled pores in aerogel/polymer composites on composites density normalised to unfilled resin density.

As presented in Figure 3-34, the normalised composite density decreases linearly with decreasing volume fraction of filled pores. Additionally, it suggests that a percentage of unfilled resin weight of nearly 73% and 80% would be achieved by incorporating respectively epoxy and vinyl ester with 2 wt% addition of silica aerogel particles, whose pores had not been filled at all. Notably, if using the rule of mixture to calculate the normalised composite density for each mixture, a result of 76% (epoxy) and 79% (vinyl ester) can be obtained. Since the rule of mixture estimates an upper boundary of the composite properties, a close fit to the experimental data collected was achieved. It is also worth noticing that a higher density of epoxy resin was the leading cause behind lower normalised composite density for the same volume fraction of filled pores than a vinyl ester. Also, vinyl ester presents a slightly lower decrease in density with changes in the volume fraction of filled pores. Such behaviour might result from higher curing shrinkage of vinyl ester imposing larger stresses on brittle aerogel structure during manufacturing and causing more significant pore collapse than in the case of epoxy [240]. Furthermore, the effect of pore infiltration on composite thermal conductivity has been analysed and presented in Figure 3-35.

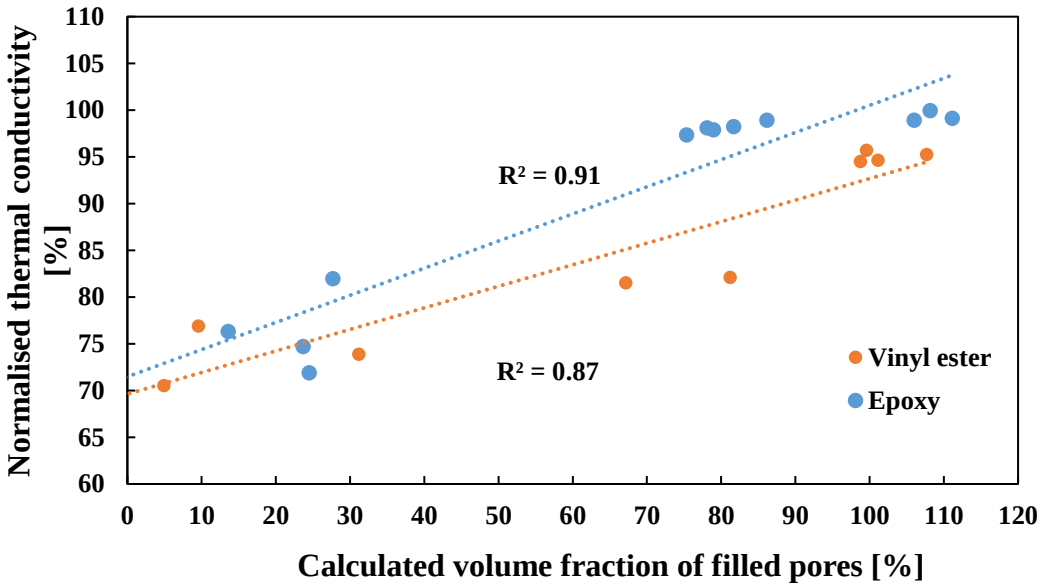

Figure 3-35 Effect of volume fraction of filled pores on composites normalised thermal conductivity to unfilled resin density.

Figure 3-35 presents that both composites' normalised thermal conductivity decreases with decreasing volume fraction of filled pores. Additionally, it indicates that the addition of 2 wt% of silica aerogel particles might reduce the thermal conductivity values of epoxy and vinyl ester by respectively almost 30% and 29% if no pores are being infiltrated by liquid resin. The proper match with theoretical data can also be confirmed, as both values are within the range calculated using parallel and series model which provide respectively upper and lower boundaries of thermal conductivity of two-component systems [241, 242]. Figure 3-35 also indicates the higher impact of pore infiltration on epoxy resin, which might be contributed to the higher thermal conductivity value of pure epoxy resin. By filling aerogel pores the epoxy resin increases its volumetric presence and elevate thermal conductivity more than vinyl ester. Those results suggest that pore infiltration is more severe to the samples created with the higher thermal conductivity matrix material. As a result, more careful manufacturing steps have to be undertaken.

The analysis of both thermal conductivity and density data leads to the conclusion that the delayed mixing technique allows for incorporating hollow arrears within the resin structure, decreasing both density and thermal conductivity. It is quite possible that low viscosity resin is being able to infiltrate aerogel pores effectively leaving the silica skeleton surrounded by resin. When, in some cases, it might be a desirable outcome, to achieve a reduction in the matrix's thermal conductivity, the porous structure of aerogel needs to be preserved [85]. Similar behaviour was observed by Lee et al., who had noticed a decrease in thermal

conductivity only when pores were preserved [30]. By considering the analysis above, it was finally concluded that to utilise the potential of aerogel particles fully, the delayed curing method would have to be selected for manufacturing the remaining samples.

3.3.5 Effect of aerogel particles on polymer density

3.3.5.1 Epoxy resin

Figure 3-36 plots the density values of aerogel/epoxy composites at different weight fractions.

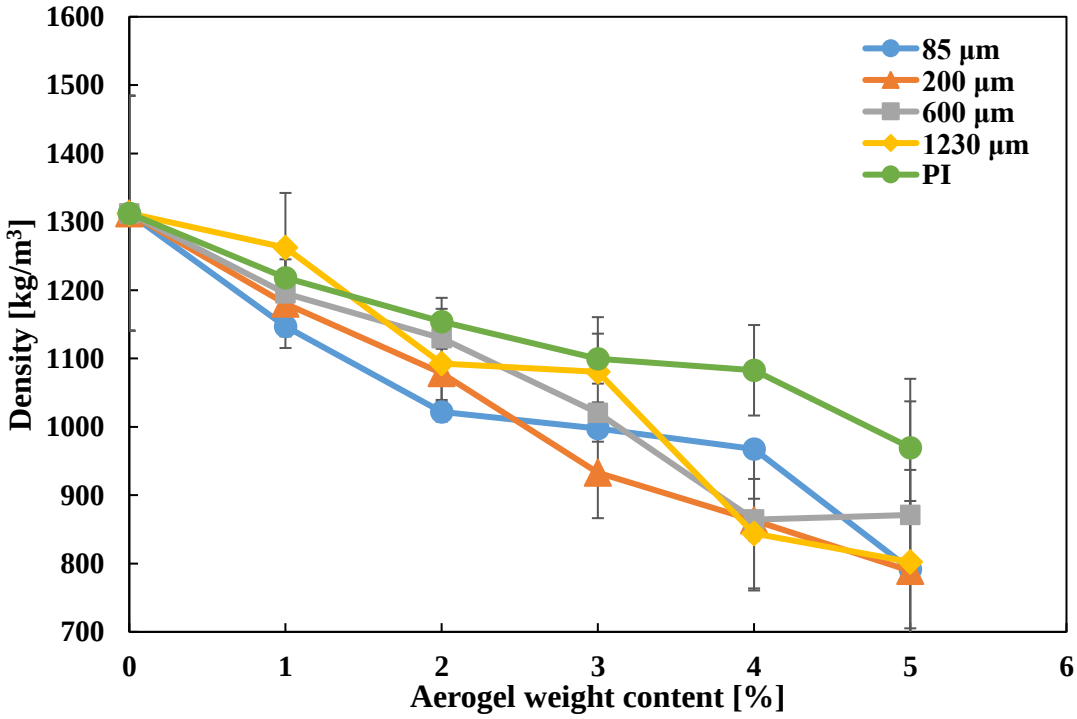

Figure 3-36 Density of aerogel/ epoxy composite with varying aerogel content and particle sizes.

As presented in Figure 3-36, the addition of aerogel particles to epoxy resin reduces the polymer samples' density linearly. The addition of respectively 1, 2, 3, 4 and 5 wt% of aerogel particles resulted in an average density reduction of respectively 9.5, 19.25, 25.5, 33.9 and 39.6%. Furthermore, Figure 3-36 implies that the aerogel particle size has a little impact on the composite material's final density. In general, smaller particles (85 µm) allowed to achieve the most significant decrease in density for the lower loading scenarios (up to and including 2 wt%). On the other hand, large particles (especially 1230 µm) presented lower density values in composites with aerogel loading above 3 wt%. Nevertheless, the densities of composites manufactured with all particle size tend to converge at a similar value for a 5 wt% loading case. Figure 3-36 also presents a much smaller impact of polyimide particles upon composites density. Starting with 2 wt%, the polyimide samples present higher density values that all other

silica counterparts with the difference enlarging with increasing aerogel loading. As a result, the addition of 5 wt% of particles resulted in only 26% lower density than pure epoxy.

3.3.5.2 Vinyl ester resin

Figure 3-37 presents the density values of aerogel/vinyl ester composites at different weight fractions.

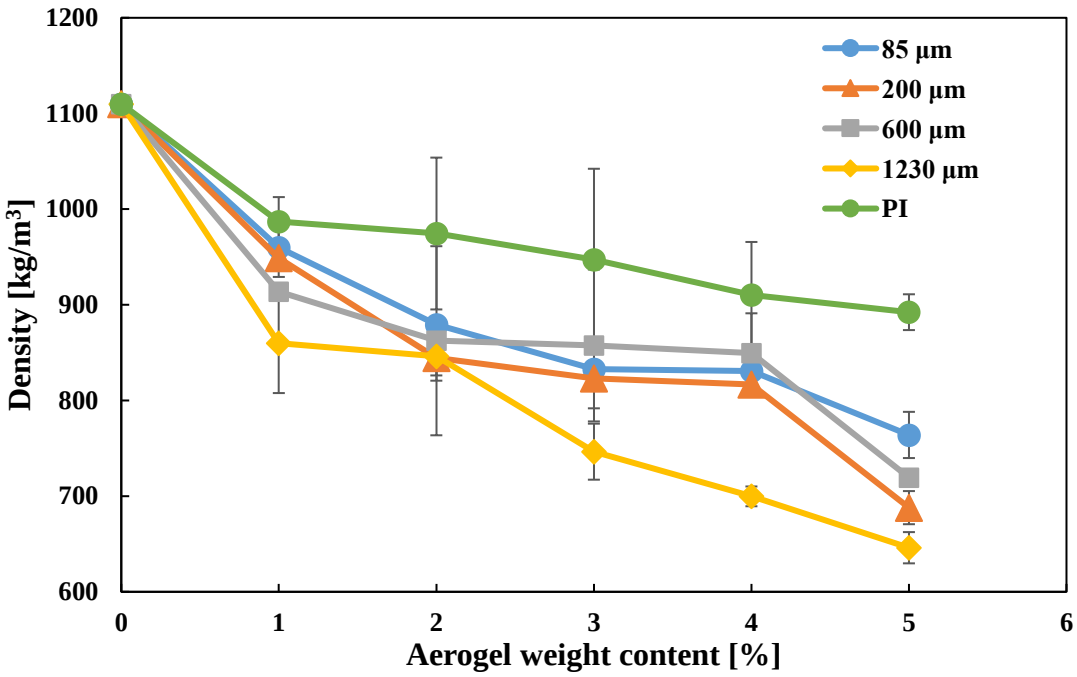

Figure 3-37 Density of aerogel/ vinyl ester composite with varying aerogel content and particle sizes.

As indicated by Figure 3-37, the addition of aerogel particles to vinyl ester resin reduces the density of the polymer samples linearly, with the addition of 1, 2, 3, 4 and 5 wt% of aerogel particles resulting in an average density reduction of respectively 16.5, 21.8, 25.1, 27.5 and 34.4%. By analysing the impact of the aerogel particle size upon the vinyl ester density it can be noticed that larger particles tend to provide lower density values in all measured aerogel loading scenarios. In addition, when reaching 5 wt% aerogel loading, the values of composite densities present wide discrepancy with the lowest value of 646 kg/m^3 for 1230 µm particles and the highest of 764 kg/m^3 for 85 µm particles. Finally, even though both aerogel systems have proven to follow the same trend, the addition of polyimide aerogel tends to produce higher density values that its silica counterpart across all of the loading scenarios. The highest discrepancy occurs at 5 wt% when PI aerogel composites have only 20% lower density than a pure vinyl ester.

3.3.5.3 Discussion

Data presented in Figure 3-36 and Figure 3-37 indicated that the addition of aerogel particles to epoxy and vinyl ester resins reduces their densities. As can be expected, the main reason behind such behaviour is the introduction of low density and porous inclusions such as aerogel particles into the matrix. Also, measured average density of pure epoxy was higher than expected from the datasheet (1.31 g/cm^3 vs 1.15 g/cm^3), which could be attributed to the high measurement error introduced by the method used. Figure 3-38 plots the average percentage density reduction as a function of aerogel loading for composite samples manufactured with various aerogel type and particle size.

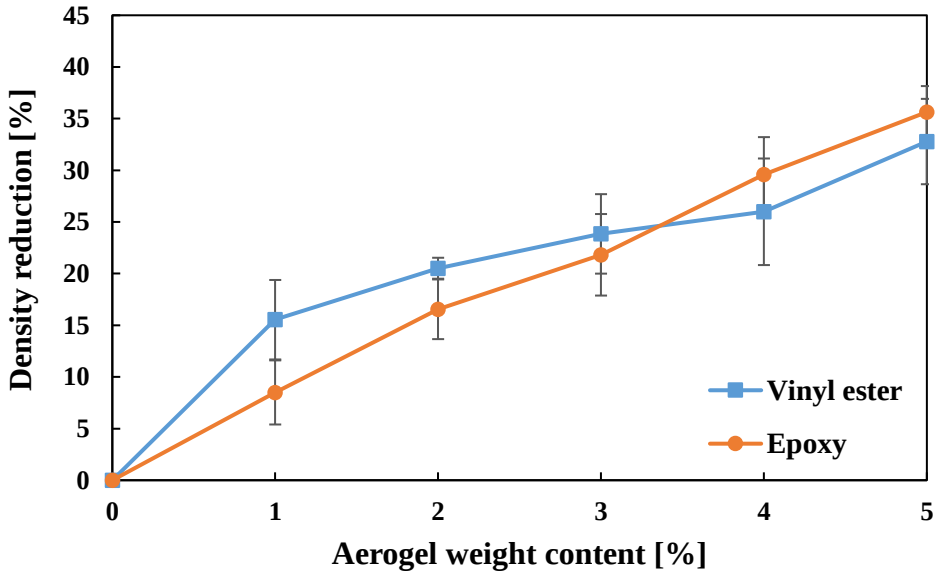

Figure 3-38 Average reduction in polymer density as a function of aerogel loading. Values have been calculated for all particle size and aerogel type composites.

As presented in Figure 3-38, the addition of aerogel particles to both types of resin results in similar reduction in polymer density with 33% and 36% average density reduction at 5 wt% for respectively vinyl ester and epoxy. The almost identical impact of aerogel particles on both materials can be attributed to the similar initial density of both resin systems with the minor differences most likely occurring due to some aerogel pore infiltration or inclusion of tiny air pockets within the matrix during manufacturing process. Moreover, it is also beneficial to investigate the effect of particle size on density changes. Figure 3-39 presents the average reduction in polymers density as a function of aerogel loading. This time the average density reduction value of composites made with the same particle size has been considered.

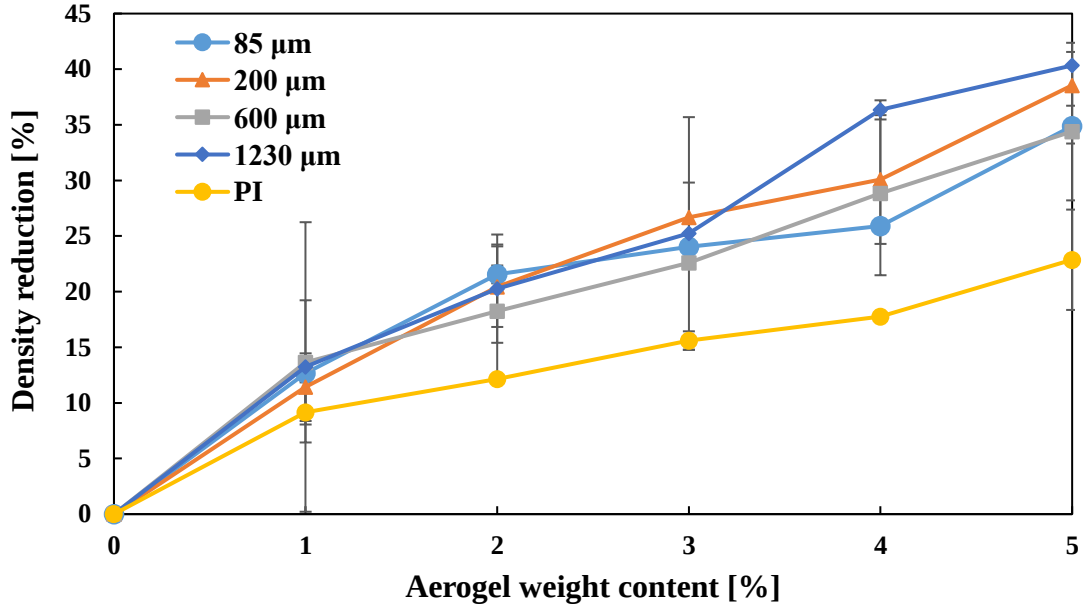

Figure 3-39 Average reduction in polymer density as a function of aerogel loading. Values have been calculated for composites manufactured with both resin types.

Figure 3-39 indicates that silica aerogel particle size has a little impact on the composite density values. Even though some discrepancies between density reduction for different particle size are present at each aerogel weight content, they are not statistically significant to enable to draw a confident correlation linking the aerogel particle size and composite density. Nevertheless, Figure 3-39 reveals that the impact of polyimide particles upon resins densities is significantly lower when compared with silica counterparts and above 1 wt% loading the addition of PI aerogel particles reduces the polymers density to the lesser extent. Such behaviour might occur due to the lower pore volume of polyimide aerogel particles (as presented in 3.3.2.2). As such PI particles introduce lower quantity of voids into polymer structure in comparison to the silica aerogel particles and thus cannot provide the same degree of density reduction.

3.3.6 Effect of aerogel particles on polymer thermal conductivity

3.3.6.1 Epoxy resin

Figure 3-40 presents aerogel/epoxy composites' thermal conductivity as a function of different aerogel weight fractions.

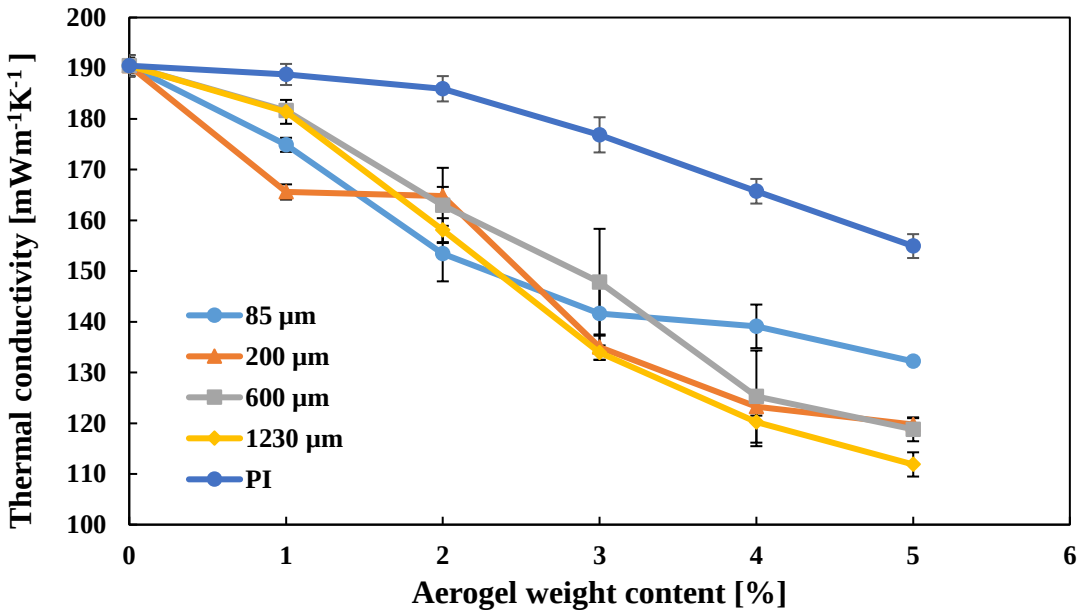

Figure 3-40 Thermal conductivity of aerogel/ epoxy composites with varying particle size and loading.

Firstly, when analysing Figure 3-40, it can be seen that the thermal conductivity is dependent on both the quantity of silica aerogel as well as the aerogel particle size. The incorporation of silica aerogel in the epoxy matrix reduced the composites' thermal conductivity as aerogel loading increased. As a result, 1 wt% of aerogel provides an average of 6% thermal conductivity reduction increasing to up to 33% reduction with the addition of 5 wt%. The least changed specimen was found to be the sample incorporating 1 wt% 1230 µm silica aerogel granules, resulting in thermal conductivity of 175.5 $mWm^{-1}K^{-1}$. On the other hand, the best reduction was obtained through the addition of 5 wt% 1230 µm, which significantly reduced the composite's thermal conductivity to 112 $mWm^{-1}K^{-1}$ (a reduction of 40%). In general, thermal conductivity and aerogel weight content seem to be correlated linearly independently from the different particle sizes investigated in this work. However, for 85 µm diameter particles there appears to be a somewhat different behaviour with the significant thermal conductivity decrease up to 3 wt% while further additional of silica aerogel presents only minor changes. Also, even though the PI aerogel samples follow a similar trend compared with silica aerogel composites, this aerogel brings much lower thermal conductivity reduction. It can be noticed that each respective loading samples manufactured using PI aerogel have the lowest rate of Tc reduction with only a 19% drop when adding 5 wt% of particles.

Figure 3-41 presents the thermal conductivity of the aerogel/epoxy composite as a function of density. As expected, for both types of aerogels the conductivity rises as the density increases

and they correlate well in a linear fashion with an r-squared value of 0.92 and 0.85 for respective silica and PI aerogel. The same trend lines also indicate that the silica aerogel has a more considerable impact on composite thermal conductivity with a slope gradient of 143 compared to 111 in the case of polyimide aerogel.

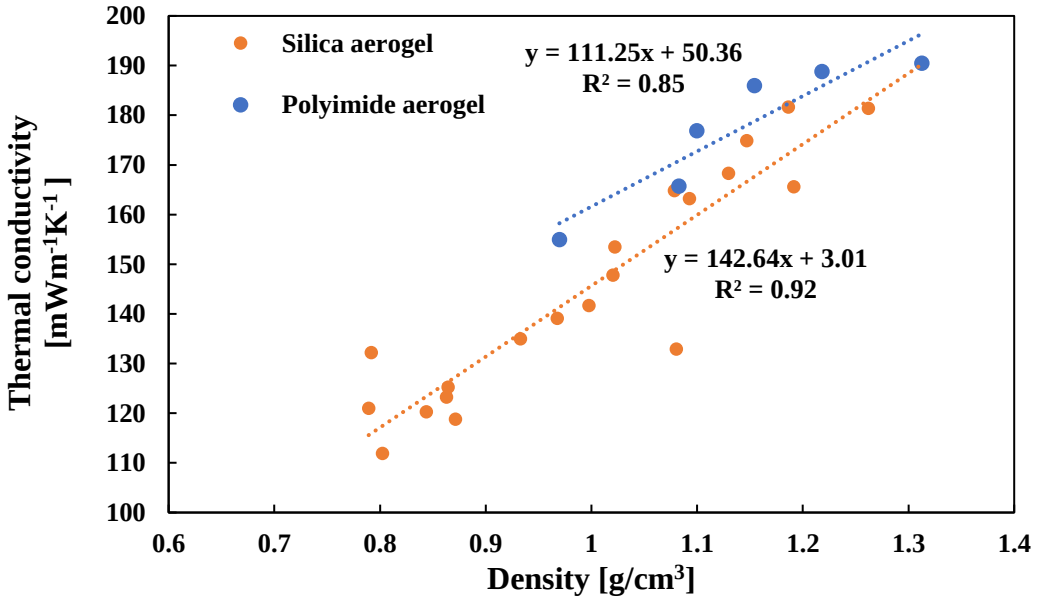

Figure 3-41 Thermal conductivity of aerogel/epoxy composite as a function of composite density.

3.3.6.2 Vinyl ester resin

Due to the restricted access to the Fox 50 heat flow meter, vinyl ester samples have been tested using a TC3000E thermal conductivity meter. To provide a direct comparison between both results Figure 3-42 was created presenting a difference in thermal conductivity values measured using both pieces of equipment.

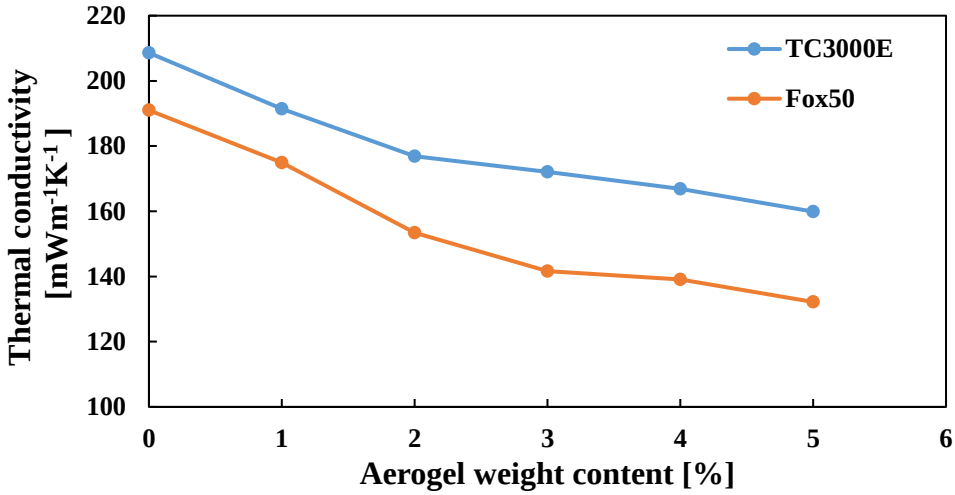

Figure 3-42 Comparison between thermal conductivity values of 85 µm silica aerogel and epoxy composites measured using both Fox5o and TC3000E.

As it can be noticed, TC3000E is producing on average 13% higher Tc values than Fox50 across the whole investigated aerogel weight content range. Thus, it was decided to introduce a correction factor for further thermal conductivity measurement. The resulting aerogel/vinyl ester composites' thermal conductivity as a function of different aerogel weight fractions is presented in Figure 3-43.

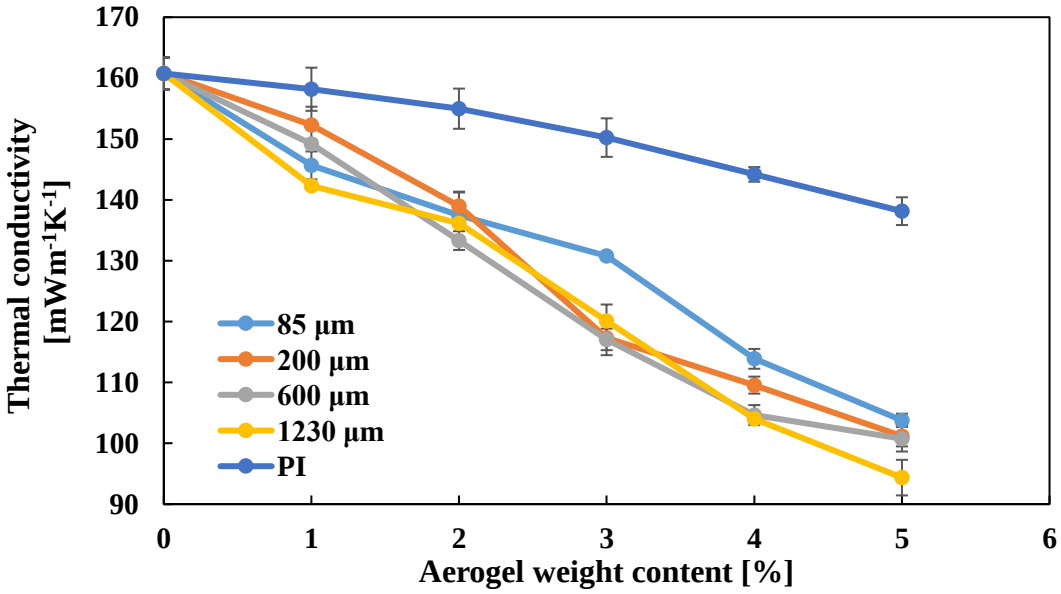

Figure 3-43 Thermal conductivity of aerogel/ vinyl ester composites with varying particle size and loading.

The analysis of Figure 3-43 reveals that vinyl ester resin's thermal conductivity is also dependent on both the quantity of silica aerogel and the aerogel particle size. The addition of silica aerogel reduced the composites' thermal conductivity as aerogel loading increased. As a result, 1 wt% of aerogel provides an average of 9% thermal conductivity reduction increasing to up to 34% reduction with the addition of 5 wt%. The least changed specimen was found to be the sample incorporating 1 wt% 1250 µm silica aerogel granules, resulting in thermal conductivity of 149 $mWm^{-1}K^{-1}$. On the other hand, the best reduction was obtained through the addition of 5 wt% 1230 µm, which greatly reduced the composite's thermal conductivity to 94 $mWm^{-1}K^{-1}$ (a reduction of 41.3%). Overall, the correlation between thermal conductivity and aerogel loading seems to be linear for all of the different particle sizes investigated in this work. However, starting with 3 wt% the smallest particles present lower thermal conductivity reductions than larger particles. The vinyl ester composites manufactured with PI aerogel follow the same linear trend decreasing thermal conductivity with higher aerogel content. However, similarly as in the case of epoxy composites, PI aerogel's addition brings much less of an impact in terms of thermal conductivity reduction. It can be noticed that each respective loading samples manufactured using PI aerogel have the lowest rate of Tc reduction with only

a 20% drop when adding 5 wt% of particles. Finally, Figure 3-44 was created to correlate the thermal conductivity of aerogel/vinyl ester composite with their density. As predicted, the incorporation of both types of aerogels results in an increase in conductivity as the density increases and they correlate well in a linear fashion with an r-squared value of 0.72 and 0.98 for respectively silica and PI aerogel.

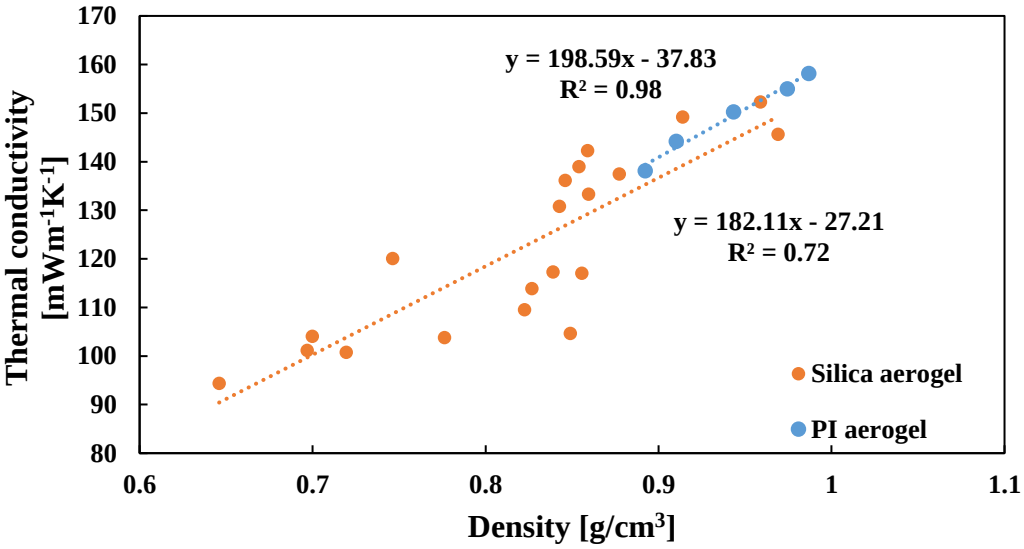

Figure 3-44 Thermal conductivity of aerogel/vinyl ester composite as a function of composite density.

3.3.6.3 Discussion

Figure 3-45 plots the average reduction in polymer thermal conductivity as an aerogel loading function for all particle size and aerogel type composites.

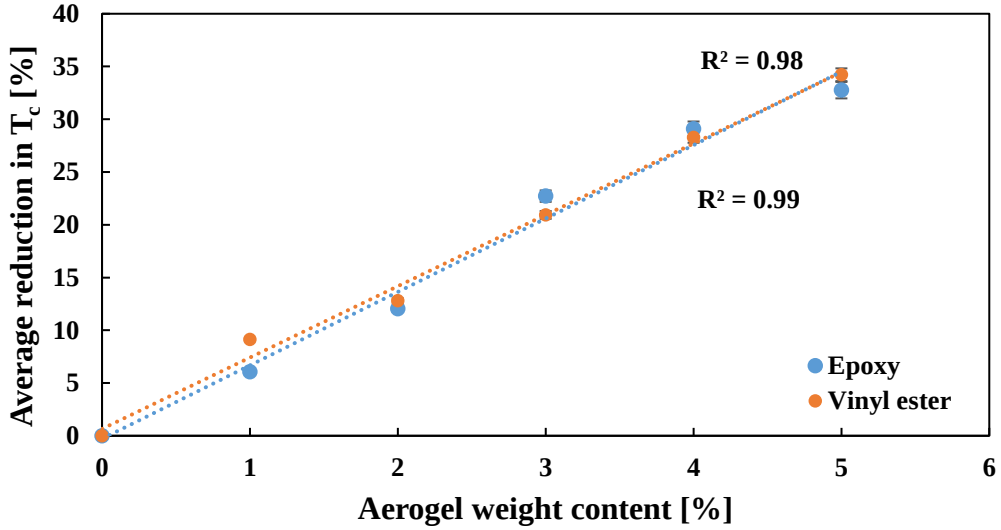

Figure 3-45 Average reduction in polymer thermal conductivity as a function of aerogel loading. Values have been calculated for all particle size and aerogel type composites.

Unsurprisingly, the addition of aerogel particles to both vinyl ester and epoxy resin reduce their thermal conductivity values. Such behaviour can be explained by analysing the core-shell

unit cell model based on the three main heat transfer methods within the nanocomposites [243]. As a result, solid conductivity is reduced by the extremely low thermal conductivity of aerogel particles. Both polyimide and silica are poor conductors of heat and due to the high porosity of aerogels most of the volume occupied by the particles is filled with air resulting in even better insulation. In addition, dispersed particles create a barrier for energy transfer and reduce the number of direct paths through the composite, effectively limiting the heat transfer. Secondly, the air inside aerogel pores might contribute to gas convection heat transfer. However, such a heat transfer method can be almost completely neglected due to pores' encapsulation within the polymer structure. In addition, the previously proven size of aerogel pores is less than the mean free path of gas molecules, limiting their vibration and random movement [244]. On the other hand, introducing aerogel pores within the polymer structure allows for radiative thermal transport within the material. As a result, heat exchange between pore walls occurs and even though it is not relevant at room temperature increasing temperature will only enlarge this phenomenon [245]. It is believed that the combined effect of all the mentioned factors leads to a significant decrease in thermoset resin systems' thermal conductivity values. Also, both resins present an almost identical correlation between composite thermal conductivity and aerogel loading, which can be attributed to similar T_c values of pure resins and similar interaction with aerogel particles. On the other hand, Figure 3-46 includes the average reduction in polymer thermal conductivity as a function of aerogel loading for composites manufactured with both resin types.

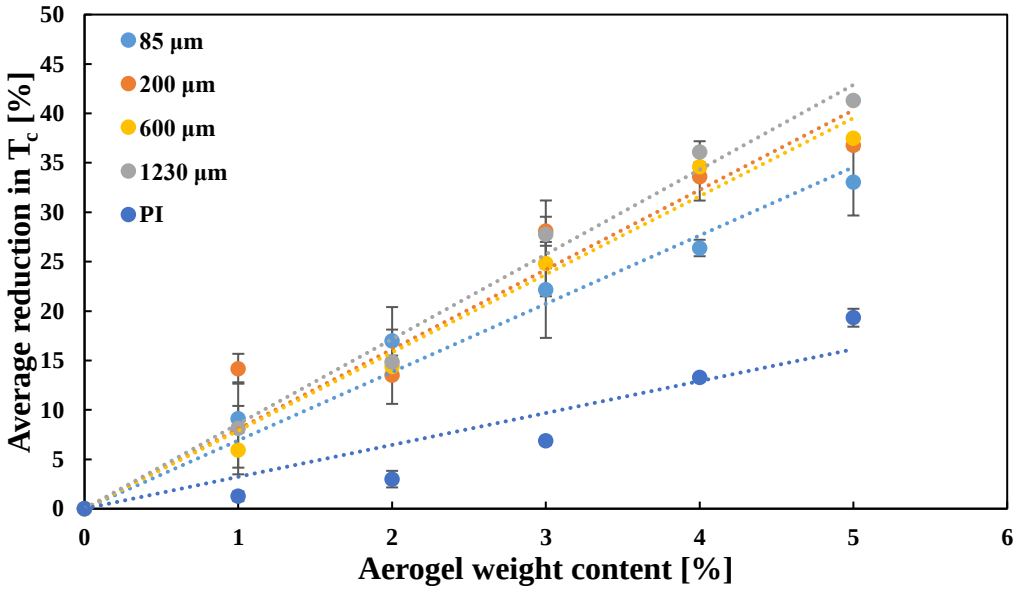

Figure 3-46 Average reduction in polymer thermal conductivity as a function of aerogel loading. Values have been calculated for composites manufactured with both resin types.

Figure 3-46 indicates that the smaller silica particles tend to be more efficient in reducing resin systems' thermal conductivity for a low aerogel loading only. On the other hand, samples manufactured with larger particles achieve lower thermal conductivity values when adding more than 1 wt% of the particles. Two competing mechanisms may explain this behaviour. Firstly, the number of particles introduced to the resin can affect heat transfer in filled resin. Dispersed particles create a barrier for energy transfer and reduce the number of direct paths through the composite, hence lowering the thermal conductivity. Smaller particles can better implement such benefit as larger quantities of particles are present in the same weight fraction system. In contrast, larger particles possess a lower number of granules in the composite in the same volume, resulting in more aerogel-free paths through the epoxy. This leads to a lesser reduction in thermal conductivity. However, the effect is negated by the usage of higher loadings of aerogel [93]. Another critical factor negating aerogel properties is the infiltration of aerogel pores by the resin. Despite delaying particles' addition until reaching the desired viscosity of epoxy, a degree of pore infiltration still occurs, reducing the quantity of aerogel, contributing to thermal conductivity reduction. This effect is more detrimental for smaller particles due to their higher surface-to-volume ratio resulting in more filled pores than larger particles at a given weight fraction. With increasing aerogel content, this factor's effect may gradually outweigh the effect of the absolute number of aerogel particles in the resin and cause smaller particles to bring about less impact on decreasing conductivity. While this hypothesis requires further work to verify, the results shown in Figure 3-46 seem to suggest that aerogel particle size should at least be considered as one of the critical parameters for designing aerogel filled composites. Moreover, Figure 3-46 presents PI aerogel particles' inferiority in reducing the epoxy and vinyl ester resin systems' thermal conductivity compared to the silica counterpart. Such behaviour can be explained by analysing the material properties described by the BET in previous chapters. By analysing those, it can be noticed that PI aerogel has much lower both BET surface area and cumulative pore volume indicating lower porosity of the material. Assuming that the reduction of resin thermal conductivity is mainly achieved by encapsulating the air inside aerogel pores, PI aerogel's lower porosity is adversely affecting its ability to lower thermal conductivity values. Even the usage of pore preservation techniques during manufacturing stages does not help as PI aerogel cannot introduce the same degree of a barrier for energy transfer and reduce the number of direct paths through the composite.

3.3.7 Effect of aerogel particle on polymer compressive properties

3.3.7.1 Epoxy resin

Figure 3-47 plots compressive stress-strain curves of 85 μm silica aerogel/epoxy composites at different weight fractions.

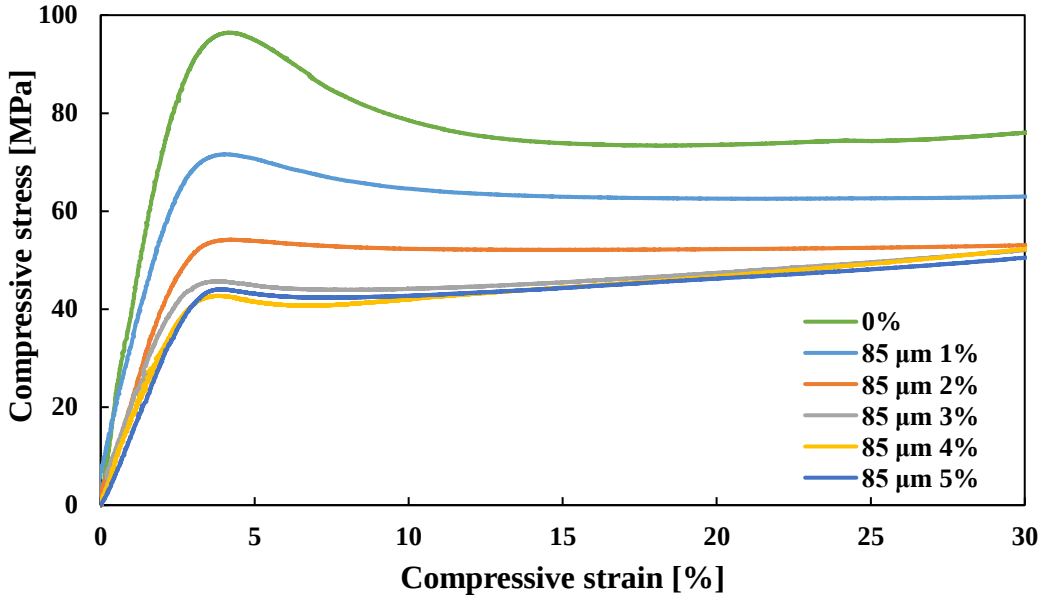

Figure 3-47 Typical compressive stress-strain curves for silica aerogel/epoxy composite at different weight fractions of 85 µm aerogel particles.

The addition of aerogel particle can significantly affect the mechanical behaviour of the epoxy. The neat resin exhibits a distinct yield point after initial linear behaviour and strain hardening at large deformation. In contrast, the resins doped with silica aerogel particles tend to develop a less distinct yield point. It can also be noticed that incorporating the resin with the silica aerogel can make the resin more brittle and less stiff simultaneously. Figure 3-48 give the yield compressive stress as a function of an aerogel content.

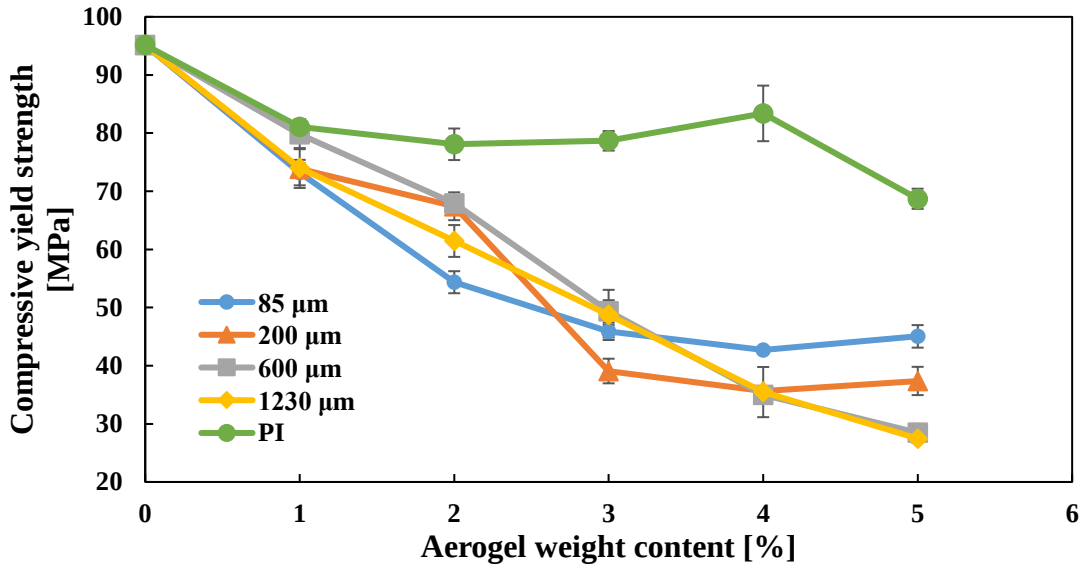

Figure 3-48 Compressive yield strength of aerogel/ epoxy composite with varying aerogel content and particle sizes.

Figure 3-48 shows that compressive strength decreases with increasing loading of aerogel particles. However, both aerogel types follow various trends. After initial drop when adding 1

wt% the polyimide aerogel composites maintain relatively steady compressive strength slightly decreasing after adding 4 wt% of aerogel. On the other hand, a noticeable more significant decrease in compressive strength is measured for composites incorporating silica aerogel particles for which compressive strength is decreasing following exponential (for smaller particles) and linear (for larger particles) trend. In the case of smaller particles, the plateauing in compressive properties decrease can be noticed starting at 3 wt%. At the same time, larger particles are presenting a relatively linear decreasing trend. As a result, the introduction of 5 wt% particles leads to a relative decrease in compressive strength (compared with neat epoxy) of 50, 55, 70 and 71% for 85, 200, 600 and 1230 µm particle size respectively. The introduction of PI aerogel particles achieved a much smaller impact on the compressive properties of epoxy resin. Following the initial decrease in compressive yield strength after adding 1 wt% of particles, the values seem to decrease slightly with the lowest compressive yield strength of 69 MPa at 5 wt%.

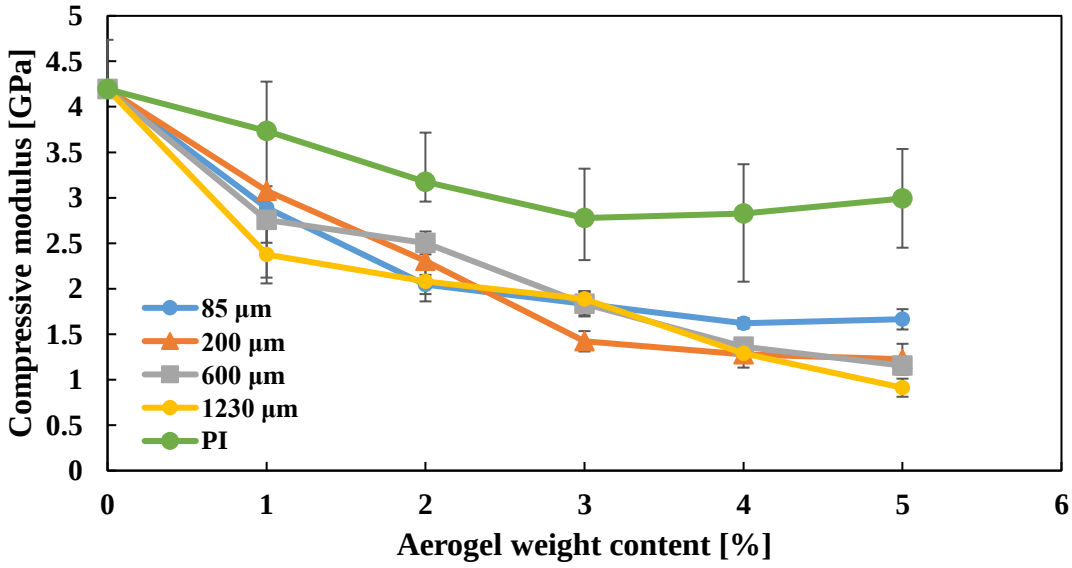

Figure 3-49 Compressive modulus of aerogel/ epoxy composite with varying particle size and loading.

Similarly, as in the case of compressive strength, the compressive modulus also decreases after the addition of aerogel particles. Silica aerogel particles cause a constant decrease in compressive modulus, presenting a greater impact than was observed in strength values with a 70% average drop at 5 wt%. Polyimide aerogel composites follow the same trend as their silica counterparts. However, it affects compressive modulus to a lesser extend with only a 25% decrease at 5 wt%. Moreover, it should be highlighted that the particle size has a small impact on composite compressive modulus and the differences between modulus values of composites manufactured with various particle size are not statistically significant to enable to draw a confident conclusion. However, as in the case of compressive yield strength, PI

aerogel's addition yields a much smaller impact upon the epoxy resin's compressive modulus. An initial linear decrease in modulus results in the lowest value of 2.7 GPa at 3 wt%, followed by a certain degree of a strengthening mechanism with increasing aerogel content. Figure 3-50 shows the compressive yield strength against the composite density for both silica and polyimide aerogel.

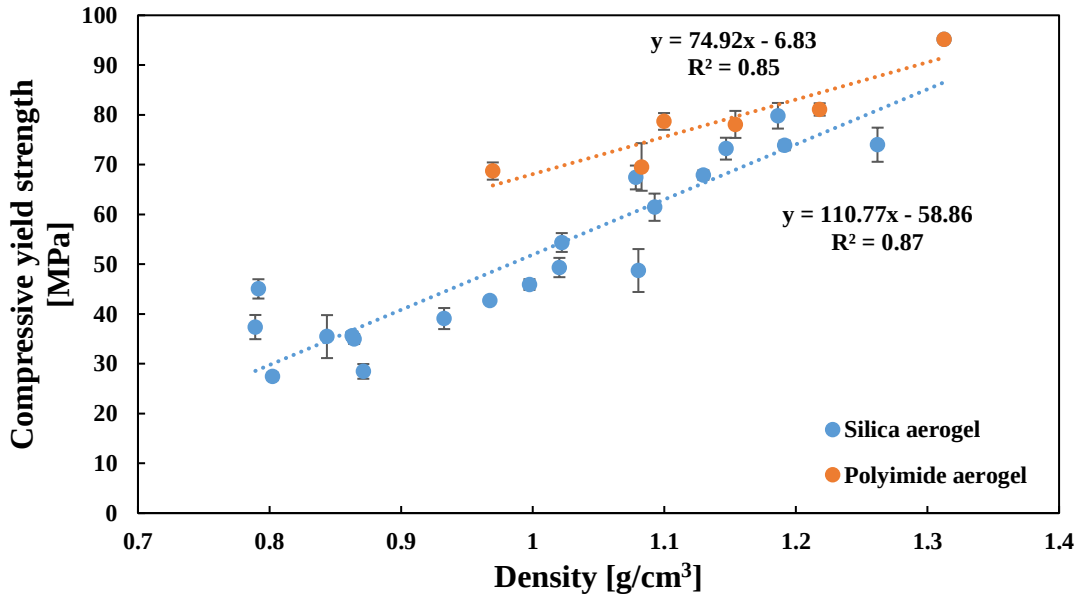

Figure 3-50 Compressive yield strength of aerogel/epoxy composite as a function of composite density.

As expected, for both aerogel types, the yield strength increases with material density following a linear trend line with an r-square value of 0.87 and 0.85 for respective silica and polyimide aerogels. Nevertheless, silica aerogel composites present a higher impact on the composite compressive properties with a slope value of 32% higher than one presented by PI aerogel composites. Following the initial goal of finding the correlation between aerogel-filled composites' thermal and compressive properties

Figure 3-51 was created which attempts to combine the compressive yield strength with aerogel/epoxy composites' thermal conductivity with all four groups of particle sizes. For silica aerogel composites, a strong linear relation (r-squared value of 0.96) was found between these two parameters despite particle size differences. What is more, the PI aerogel composites fit well within such trend line regardless of differences in density correlation. Nevertheless, in both cases, caution should be taken before further extrapolating this relationship outside the investigated data range.

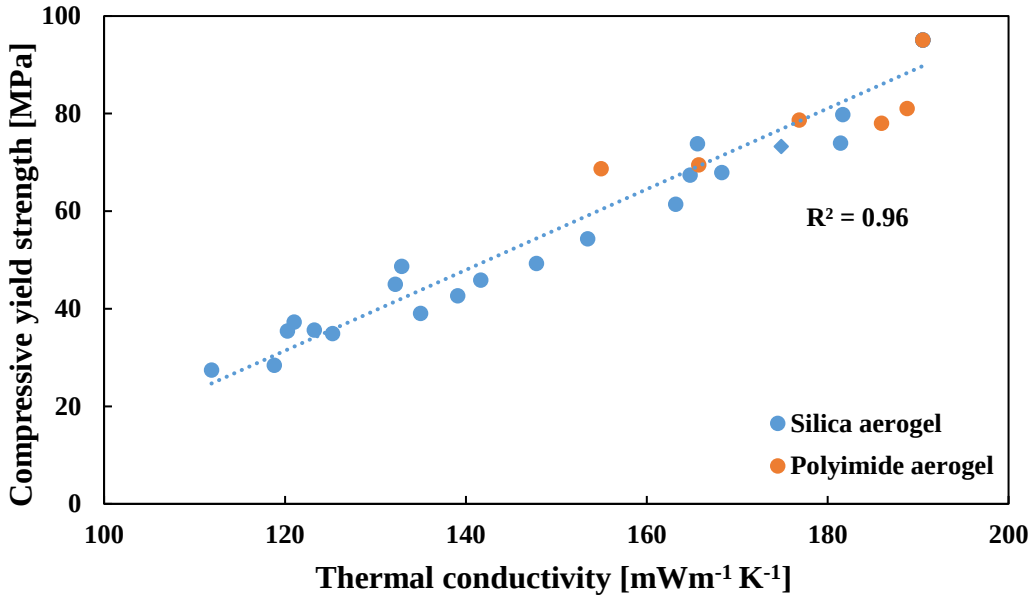

Figure 3-51 Correlation between thermal conductivity and compressive strength of aerogel filled epoxy.

3.3.7.2 Vinyl ester resin

Figure 3-52 plots compressive stress-strain curves of 85 µm silica aerogel/vinyl ester composites at different weight fractions.

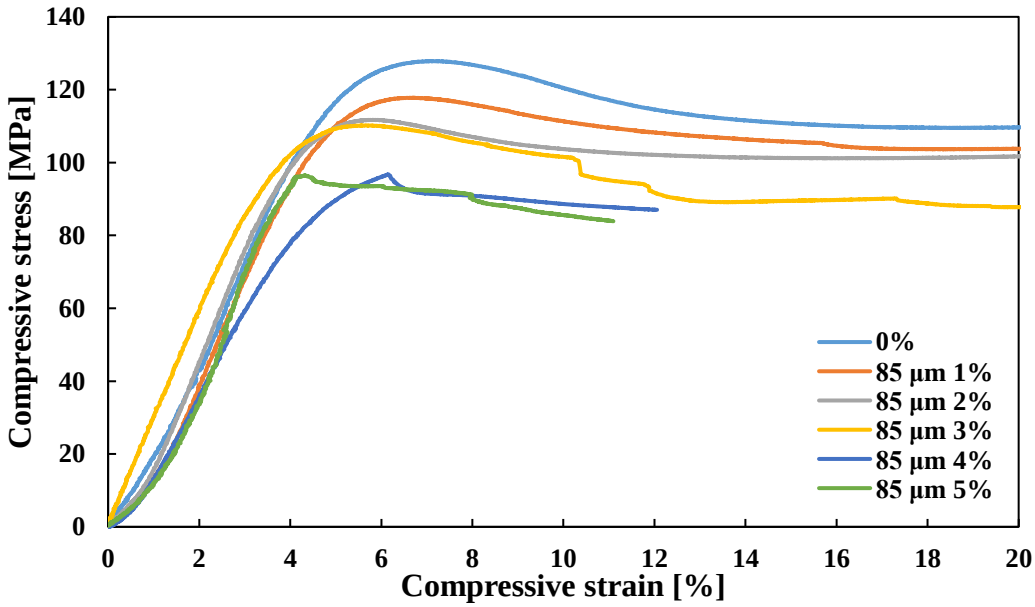

Figure 3-52 Typical compressive stress-strain curves for silica aerogel/vinyl ester composite at different weight fractions of 85 µm aerogel particles.

Figure 3-52 indicates that the addition of aerogel particles can substantially change the vinyl ester's compressive behaviour. First of all, unfilled resin presents a clear yield point after initial linear behaviour. The addition of aerogel particles diminishes this effect and composites

manufactured with the addition of particles tend to develop a less distinct yield point. Figure 3-53 was plotted to provide compressive stress at yield against aerogel content and different particle sizes.

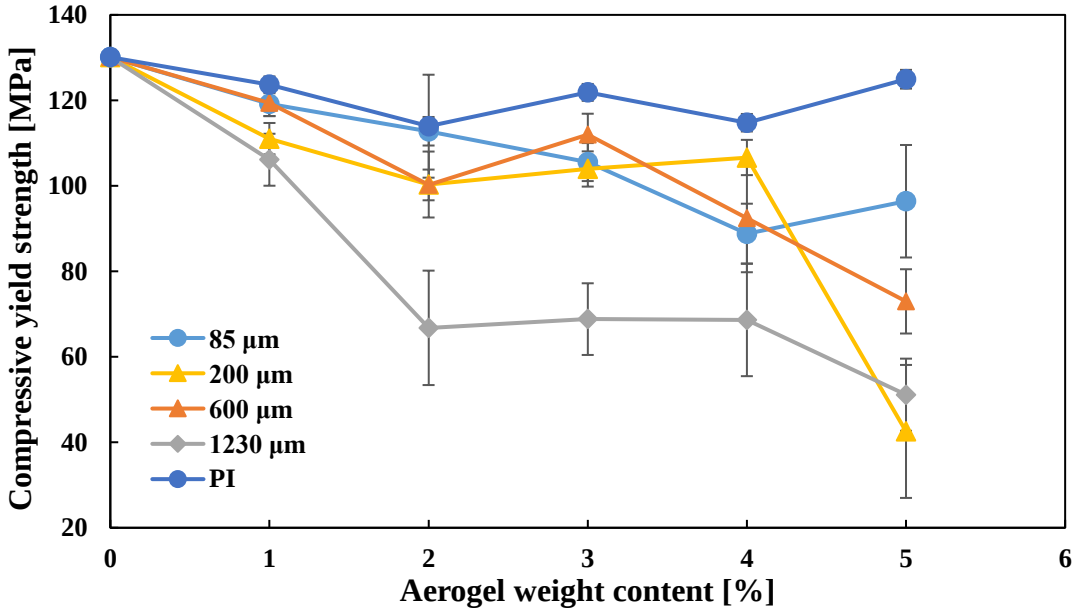

Figure 3-53 Compressive yield strength of aerogel/ vinyl ester composite with varying aerogel content and particle sizes.

Figure 3-53 indicates that the addition of the silica aerogel particles to vinyl ester resin decreases its compressive yield strength. The samples manufactured with silica aerogel's addition present a weakening effect, nevertheless two different behaviours can be noticed. For low and medium size particles added a similar, linear trend relating the yield strength and aerogel content was found on the other hand the largest particles caused a considerable performance drop at low aerogel content while stabilising afterwards. As a result, the introduction of 5 wt% particles lead to a relative decrease in compressive strength (compared with neat vinyl ester) of 31, 44 and 60% for 85, 600 and 1230 µm. However, Figure 3-53 also reveals an outlier for the sample prepared with 5 wt% of 200 µm, which decrease compressive strength by 67%. Such significant decrease could be linked to the manufacturing defects which might deteriorate the compressive performance of the samples. On the other hand, polyimide aerogel presents only a slight decrease of 12% in vinyl ester compressive property at 2 wt% of aerogel addition and higher aerogel content presents either similar results or even slight strengthening effect. Figure 3-54 was plotted to provide compressive modulus against aerogel content and different particle sizes.

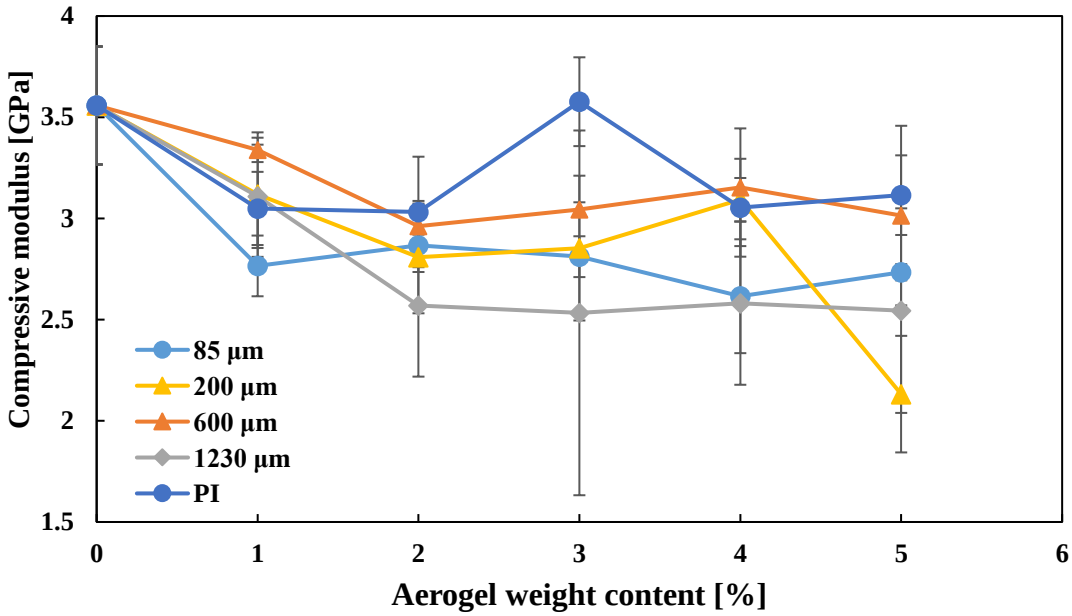

Figure 3-54 Compressive modulus of aerogel/ vinyl ester composite with varying particle size and loading.

Figure 3-54 presents that similarly as in the case of compressive strength, compressive modulus also decreases with the addition of aerogel particles. Nevertheless, the trend is substantially different, with composites experiencing higher modulus decrease at a range of up to 2 wt%., stabilising until 5 wt%. Opposite to what has been seen in case of compressive strength, the composites prepared with polyimide aerogel particles also follow this trend, presenting a similar level of modulus deterioration. However, the sample prepared with 3 wt%., polyimide aerogel particles is the only sample presenting strengthening effect. Such behaviour could be caused by the destruction of aerogel internal structure during sample manufacturing process. Similar effects have been presented in previous studies which were able to strengthen the polymer matrix by adding aerogel particles but infiltrating their pores [33]. What is more, it should be highlighted that the results does not imply strong impact of particle size on the compressive modulus of created composites. Additionally, similarly as in the case of compressive strength an outlier for the sample prepared with 5 wt% of 200 µm has been detected presenting a 40% decrease in compressive modulus of the vinyl ester. Again, it is suspected that material defects introduced during sample manufacturing could be responsible for such behaviour. Overall, both Figure 3-53 and Figure 3-54 imply, that the larger quantity of aerogel added, the lower stress and strain required for the material failure suggesting that the aerogel can make the resin simultaneously more brittle and less stiff. Figure 3-55 includes the compressive yield strength against the composite density for both silica and polyimide aerogel.

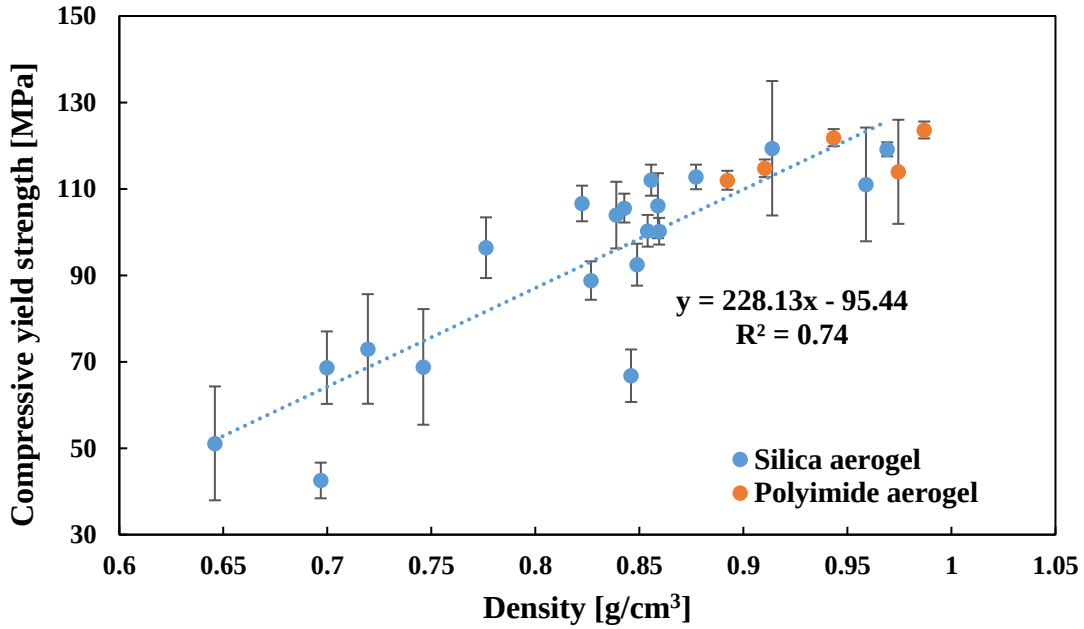

Figure 3-55 Compressive yield strength of aerogel/vinyl ester composite as a function of composite density. The line fitting is based on only silica aerogel data.

As expected, for both aerogel types, the yield strength increases with material density following a linear trend line with an r-square value of 0.74. In addition, the polyimide aerogel particles seem to provide a similar correlation. However, due to the lack of low-density samples their impact on compressive yield strength cannot be evaluated. To correlate thermal and compressive properties of aerogel-filled composites, Figure 3-56 was created, including compressive yield strength as a function of thermal conductivity of vinyl ester composites.

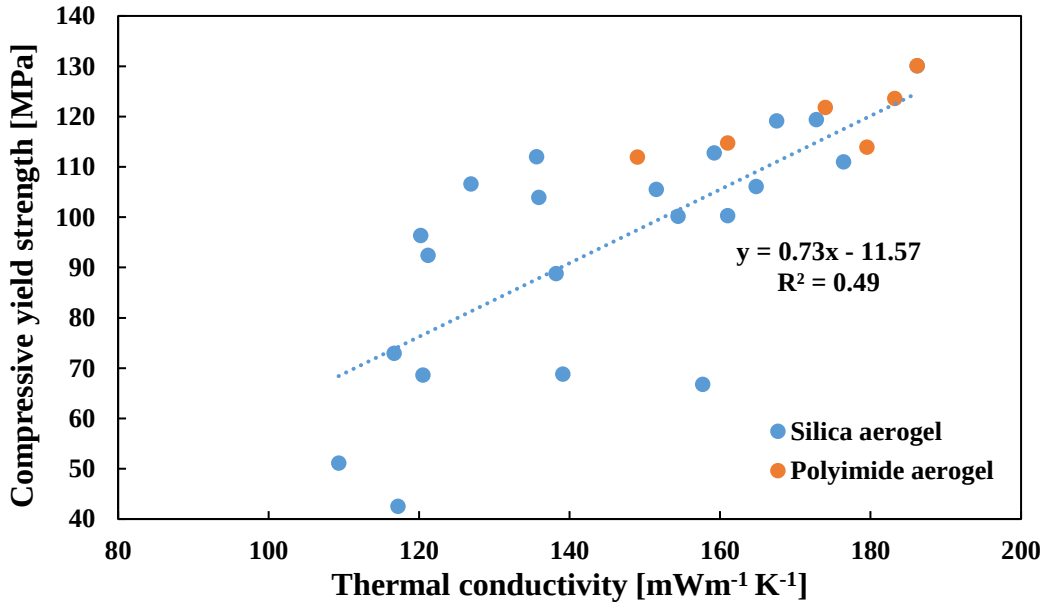

Figure 3-56 Correlation between thermal conductivity and compressive strength of aerogel filled vinyl ester. The line fitting is based on only silica aerogel data.

For silica aerogel composites, a linear relation (r-squared value of 0.49) was found between these two parameters. The results' dispersion was mainly caused by 1230 μm particles diverging from the trend line while the best fit being provided by smaller particles. Also, the PI aerogel composites seem to fit well within the drawn trend line, especially when compared with composites made with small silica aerogel particles. Again, in both cases caution should be taken before further extrapolating this relationship outside the investigated data range.

3.3.7.3 Discussion

Figure 3-57 plots the average reduction in polymer compressive yield strength as a function of different aerogel contents. The data for this graph has been obtained by averaging the reduction in polymer compressive yield strength of all particle sizes and aerogel types used in this study.

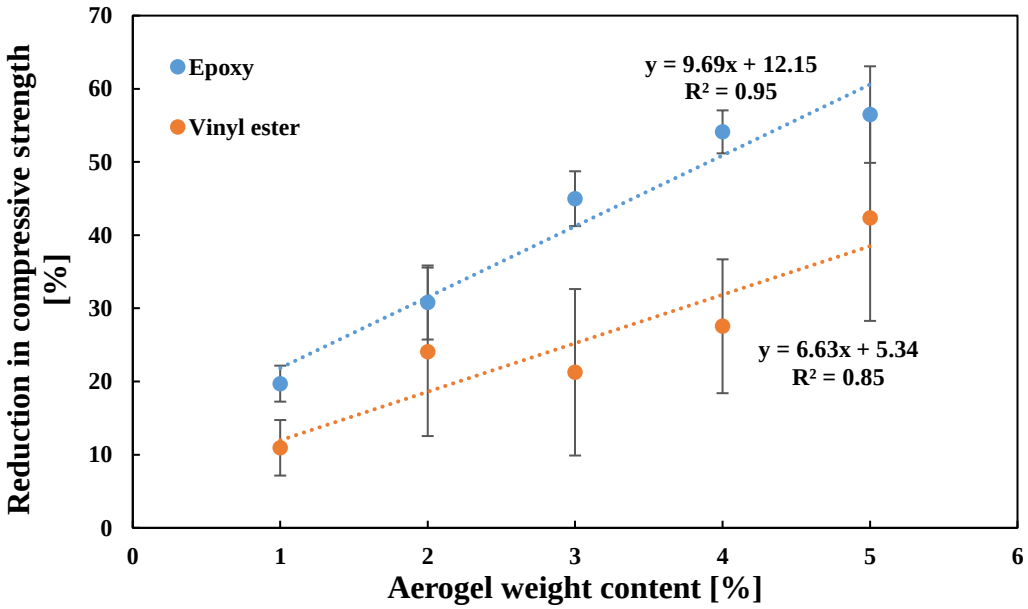

Figure 3-57 Average reduction in polymer compressive strength as a function of aerogel loading. Values calculated for all particle size and aerogel type composites.

It reveals that the compressive yield strength of aerogel-filled composites decreases with increasing aerogel content for the range of particle sizes investigated in this work. Such correlation is anticipated as porous silica aerogels have much lower mechanical properties than tested resin systems [246, 247]. As a result, the introduction of air-filled porous particles into a coherent structure of a matrix is expected to lower the compressive strength. In addition, the aerogel particles should be treated as irregularities in the geometry and the material with respect to the continuum resin phase. They became the stress raiser in the resin causing premature failure of the resin. Interestingly it is epoxy resin being affected by the addition of

aerogel particles to a larger extent than vinyl ester resin. Especially for the higher loading, the reduction in epoxy's compressive strength can be as twice higher as the vinyl ester value. It is speculated that a few reasons might be responsible for such difference. Firstly, epoxy resin has a significantly lower curing volume shrinkage of 1-5% compared to vinyl ester with 7-10% shrinkage [240, 248]. As a result, during the curing process stronger residual stresses occur in case of vinyl ester which might cause larger quantity of aerogel pores to collapse. In addition, the same stresses could result in higher mechanical interlocking between matrix and the material resulting in stronger particle bonding and better load carrying capacity. Both phenomena would lead to a superior compressive property of aerogel filled vinyl ester composites. Secondly, a significantly higher value of compressive strength for pure vinyl ester can be a reason for such discrepancies. Even with the introduction of aerogel particles, stronger load-bearing polymeric structure remains in the case of vinyl ester resin allowing for superior compressive properties. Finally, it was previously found that the incorporation of particles might reduce the polymer matrix cross-linking by preventing polymeric chains' movement until reaching elevated temperatures [249]. It can be speculated that due to the much quicker curing process as well as post-curing at higher temperatures vinyl ester has achieved a higher curing degree thus resulting in superior mechanical properties. To investigate the effect of particle size on compressive properties, Figure 3-58 shows an average reduction in polymers compressive yield strength as a function of aerogel loading of all particle sizes for both silica and PI aerogel composites.

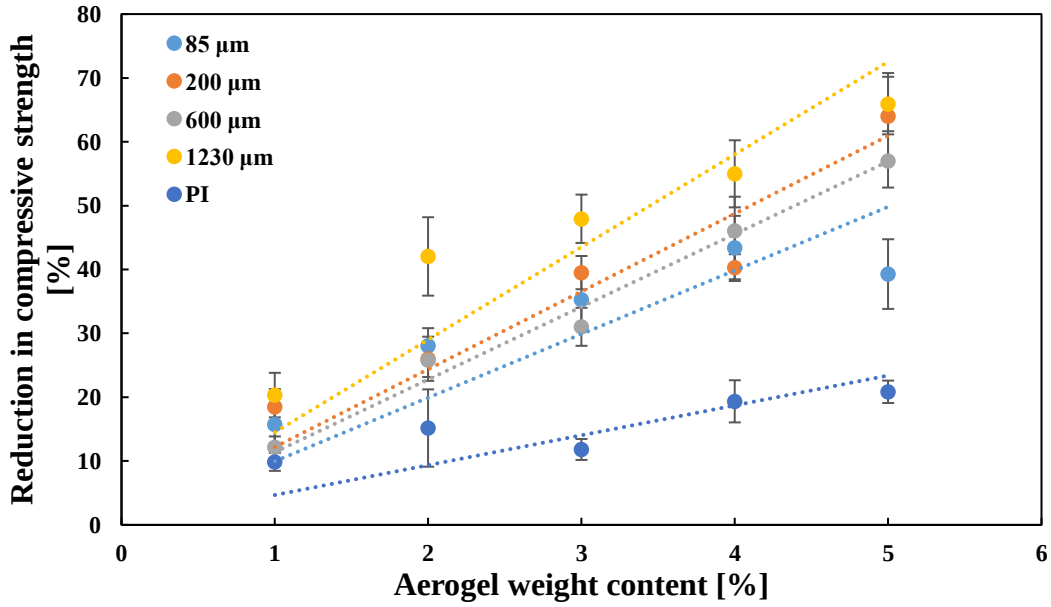

Figure 3-58 Average reduction in polymer compressive strength as a function of aerogel loading. Values have been calculated for composites manufactured with the same size of aerogel particles for epoxy resin.

Figure 3-58 indicates that regardless of the size of silica aerogel particles used the composites' properties follow the same trend with decreasing compressive strength when increasing aerogel content. Moreover, the composites manufactured with different size of silica aerogel particles still achieve rather similar compressive strength reduction and further statistical analysis revealed no direct connection between the aerogel particle size and compressive properties of the composite. On the other hand, as in case of thermal conductivity, the composites created with PI aerogel particles present a much smaller reduction in compressive properties than silica ones. Such behaviour can be again attributed to both the internal and external structure of PI aerogel particles. Firstly, because PI aerogel particles have significantly lower pore volume, they are anticipated to exhibit much higher mechanical properties than silica aerogel and do not cause a weakening effect to such a high degree. Secondly, particles' external shape is more rounded (as presented in Figure 3-17) most likely not causing stress concentration to the same degree as irregular and sharp silica aerogel particles. Finally, the PI aerogel particles added to the resin systems were relatively small, thus as presented by analysis of different particle size their effect would not be as detrimental as if larger particles would be added. To directly compare the effect of aerogel particle addition to both resin systems on mechanical and thermal properties, Figure 3-59 has been created.

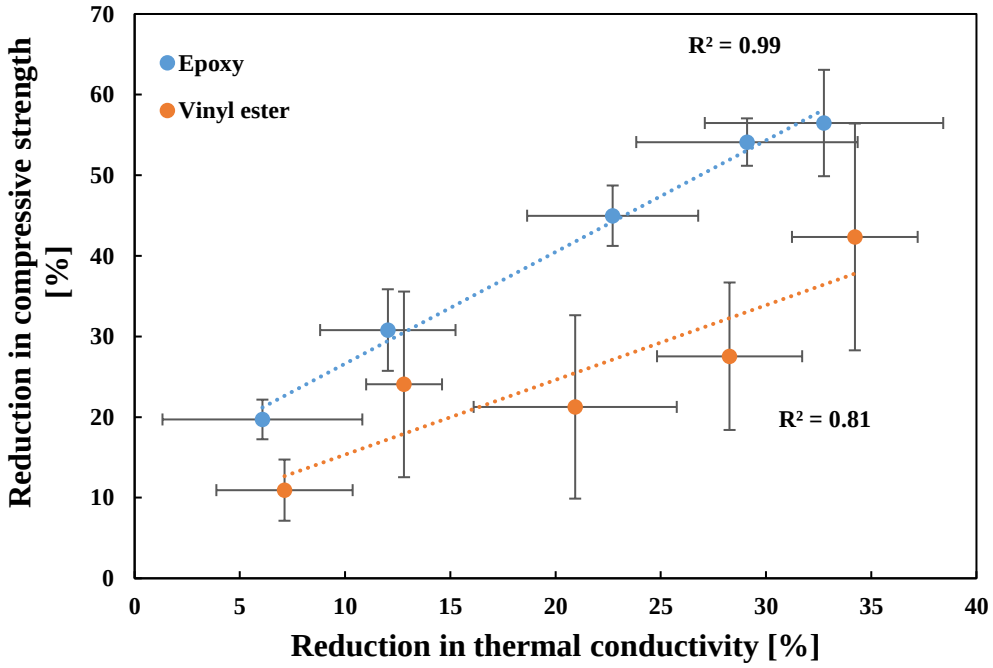

Figure 3-59 Correlation between average reduction in polymer compressive strength and a reduction in thermal conductivity. Values have been calculated for all particle size and aerogel type composites.

Figure 3-59 indicate the possibility of enhancing the thermal insulating properties of both epoxy and vinyl ester resin by introducing aerogel particles. Simultaneously, the addition of

aerogel deteriorates the compressive properties of epoxy resin and those materials are more likely to be used in scenarios with limited external loading applied to them. By investigating both thermal and mechanical properties, as presented in this work, the opportunity for careful balancing of those properties has been created. Future users of composites made with aerogel, epoxy and vinyl ester can now select a combination best suiting their needs, hopefully leading to greater usage of this particular lightweight insulation material.

3.3.8 Effect of aerogel particle on polymer coefficient of thermal expansion

3.3.8.1 Epoxy resin

Figure 3-60 presents the thermal expansion (CTE) coefficient of aerogel and epoxy composites at room temperature.

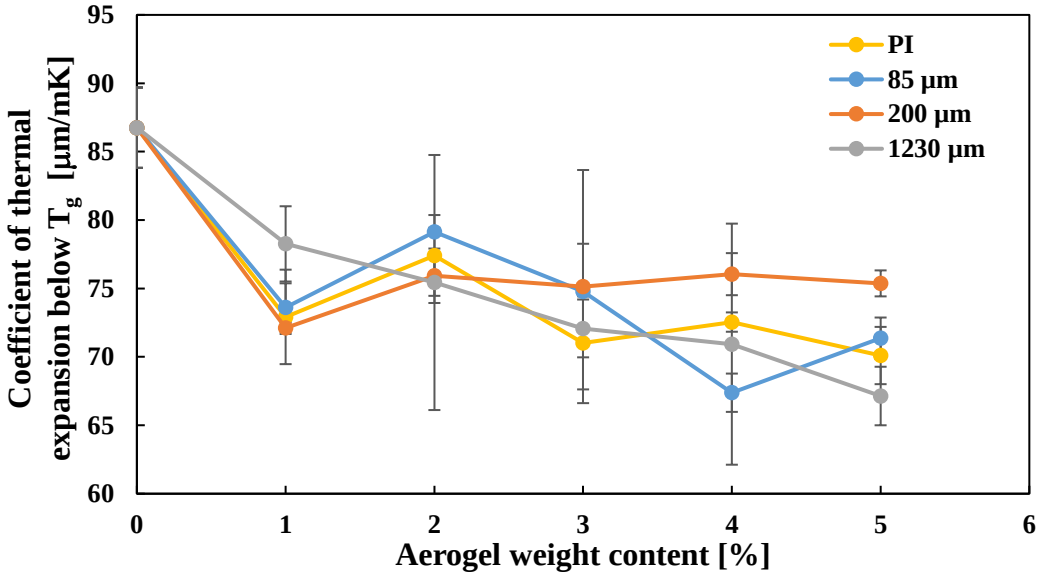

Figure 3-60 Coefficient of thermal expansion at room temperature of aerogel/ epoxy composite with varying particle size and loading.

As it can be noticed in Figure 3-60, the addition of aerogel particles tends to decrease epoxies' coefficient of thermal expansion. The largest change in CTE is achieved by adding only 1 wt% of particles resulting in the average reduction of the property by 15%. The addition of larger quantities of aerogel particles further decreases the coefficient of thermal expansion, however, to a lesser extent. For example, when incorporating 5 wt% of the aerogel, the CTE was only reduced by 19%. The size of the particles added seems not to affect the CTE values. Finally, both silica and PI aerogel seems to have a similar effect on epoxy thermomechanical properties. To analyse the effect of aerogel particles on the coefficient of thermal expansion above T_g, Figure 3-61 has been plotted.

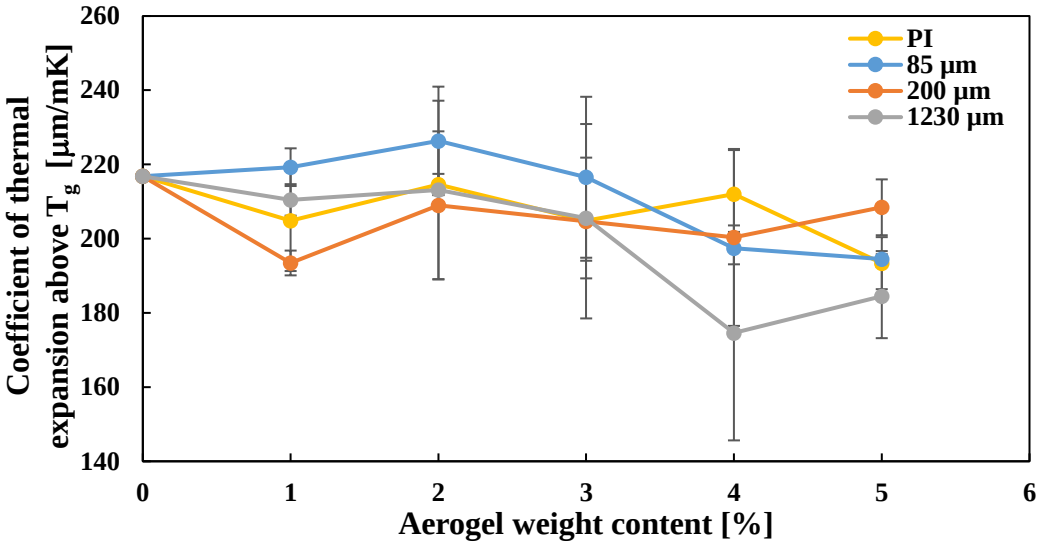

Figure 3-61 Coefficient of thermal expansion above glass transition temperature of aerogel/ epoxy composite with varying particle size and loading.

Firstly, it can be noticed that due to exceeding glass transition temperature the coefficient of thermal expansion increased by more than 200%. The figure also presents that for epoxy resin above glass transition temperature a trend can be noticed with a coefficient of thermal expansion decreasing with increasing aerogel content. What is more, the effect of aerogel particles on the thermomechanical property has diminished with only a 10% average reduction in CTE at the highest aerogel loading. Finally, the statistical analysis has revealed lack of impact of particle size on CET values. Figure 3-62 attempts to correlate the coefficient of thermal expansion above and below T_g with the density of aerogel/epoxy composites.

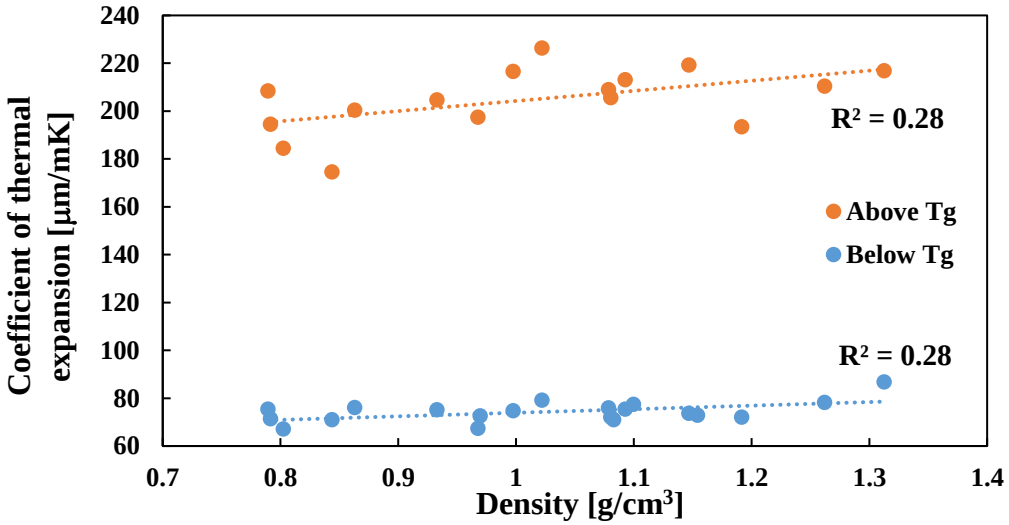

Figure 3-62 Coefficient of thermal expansion at above and below T_g of aerogel/epoxy composite as a function of composite density.

As it can be noticed, the coefficient of thermal expansion decreases with decreasing composites' density however, a relatively weak linear relation (r-squared around 0.3) was

found between both. Such a weak correlation could result from the resin not being completely cured at the experiment time, even though the manufacturer post-curing procedure has been followed. This could lead to the lower thermal stability of polymer and larger than expected discrepancies in results.

3.3.8.2 Vinyl ester resin

Figure 3-63 and Figure 3-64 present the effects of aerogel particle size and loading on the vinyl ester coefficient of thermal expansion composites at room temperature and beyond the polymer's glass transition temperature.

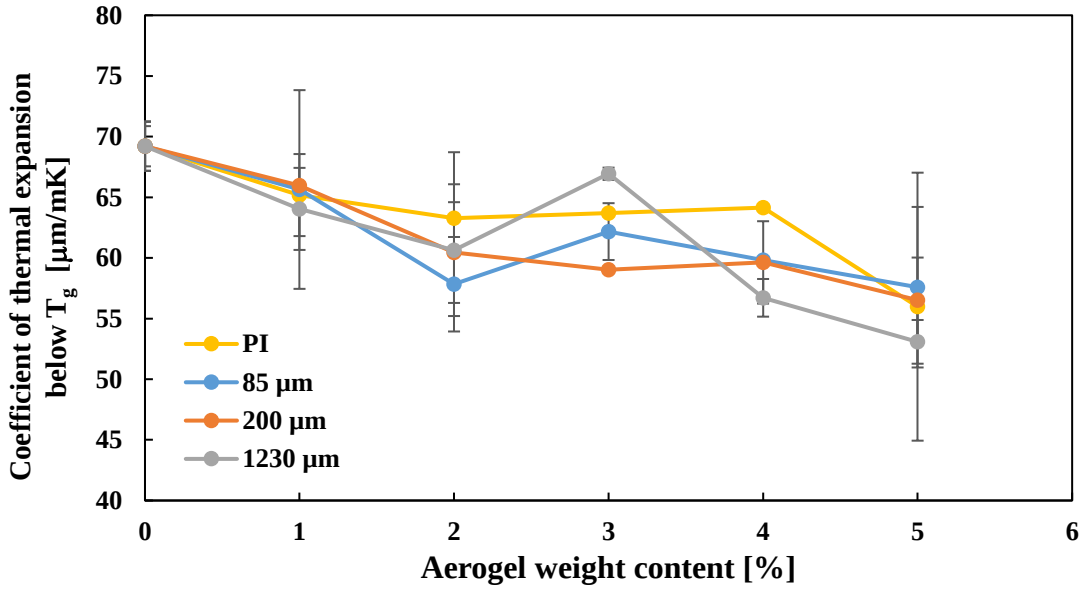

Figure 3-63 Coefficient of thermal expansion at room temperature of aerogel/ vinyl ester composite with varying particle size and loading.

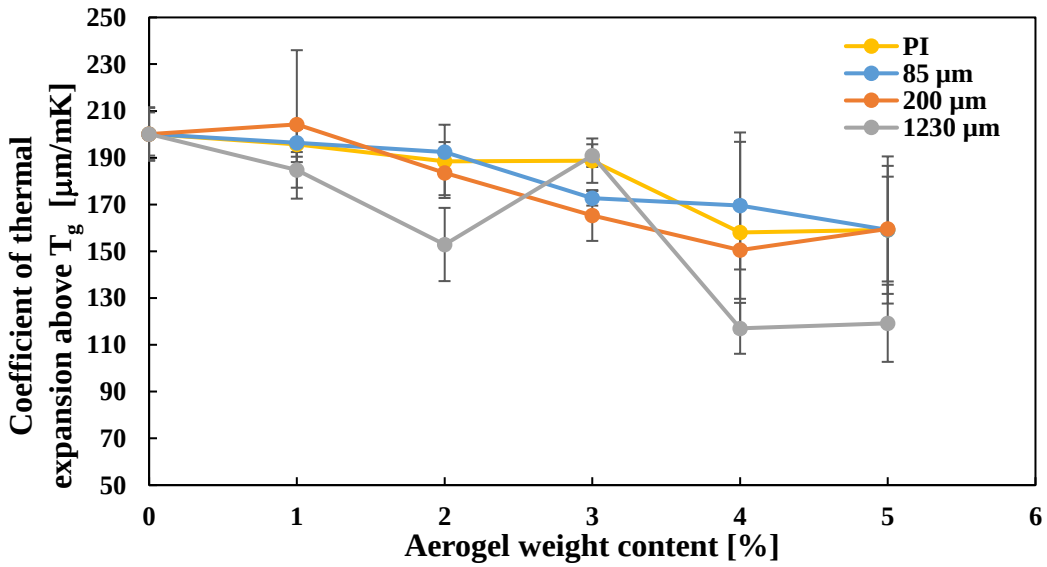

Figure 3-64 Coefficient of thermal expansion above T_g of aerogel/ vinyl ester composite with varying particle size and loading.

As shown in Figure 3-63, the addition of aerogel particles decreases the coefficient of thermal expansion of vinyl ester at room temperature. The addition of 1, 2, 3, 4 and 5 wt% aerogel resulted in average CTE reduction (across all particles used) of 5, 11, 8,12 and 19% presenting a relatively linear trend. In addition, the particle size seems not to affect the CTE values. Finally, PI aerogel's addition tends to produce composites with similar CTE values for 1 and 5 wt% scenarios. However, slightly higher values can be observed for the middle range loading scenarios. Even though upon reaching the glass-state of created composites, the value of the coefficient of thermal expansion increases drastically by almost 300%, a similar trend of decreasing CTE with increasing aerogel content can be noticed as presented in Figure 3-64. As a result, the addition of up to 5 wt% of aerogel particles resulted in a 25% reduction in CTE values. Finally, polyimide aerogel samples follow an identical trend as silica particle ones. Again, the correlation between the coefficient of thermal expansion and vinyl ester composites density was drawn and presented in Figure 3-65.

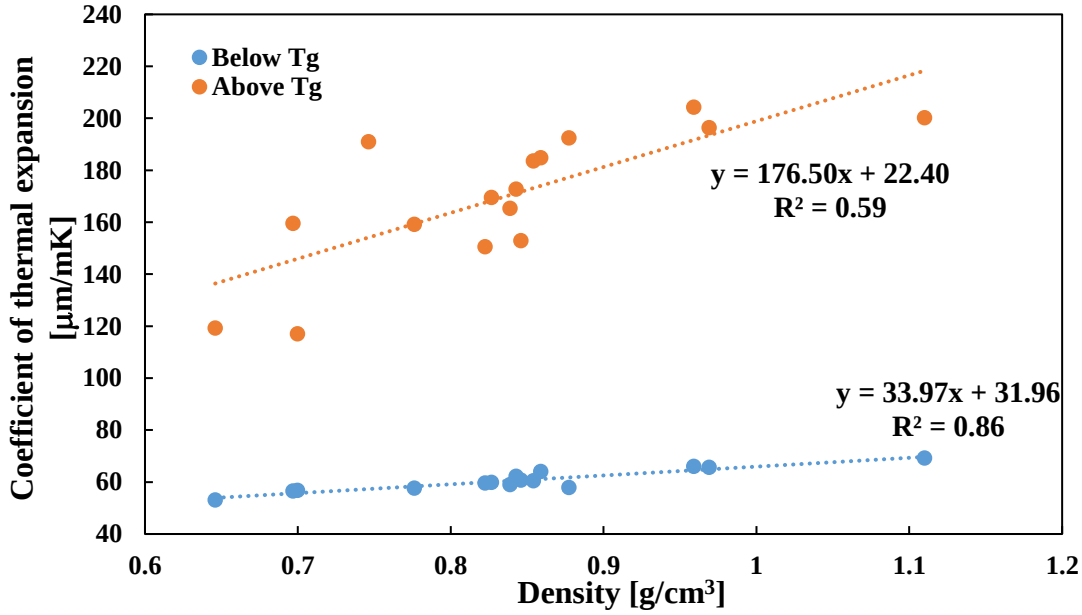

Figure 3-65 Coefficient of thermal expansion at above and below T_g of aerogel/vinyl ester composite as a function of composite density.

Figure 3-65 presents the values of the coefficient of thermal expansion above glass transition temperature and at room temperature correlated with the density of aerogel/vinyl ester composites with all groups and types of particle sizes used. As can be seen, a strong linear relation (r-squared 0.86) was found between density and coefficient of thermal expansion at room temperature. However, caution should be taken before further extrapolation of this relationship outside the investigated data range. On the other hand, a slightly lower r-squared value (0.59) has been found for thermal expansion's coefficient beyond glass transition

temperature. Such a weak correlation is most likely due to lower stability of vinyl ester beyond T_g and variations in CTE values between composites manufactured with a different particle size as presented in Figure 3-65.

3.3.8.3 Discussion

Figure 3-66 presents a reduction in thermal expansion coefficient as a function of aerogel loading for both resin systems at room temperature and glassy-state.

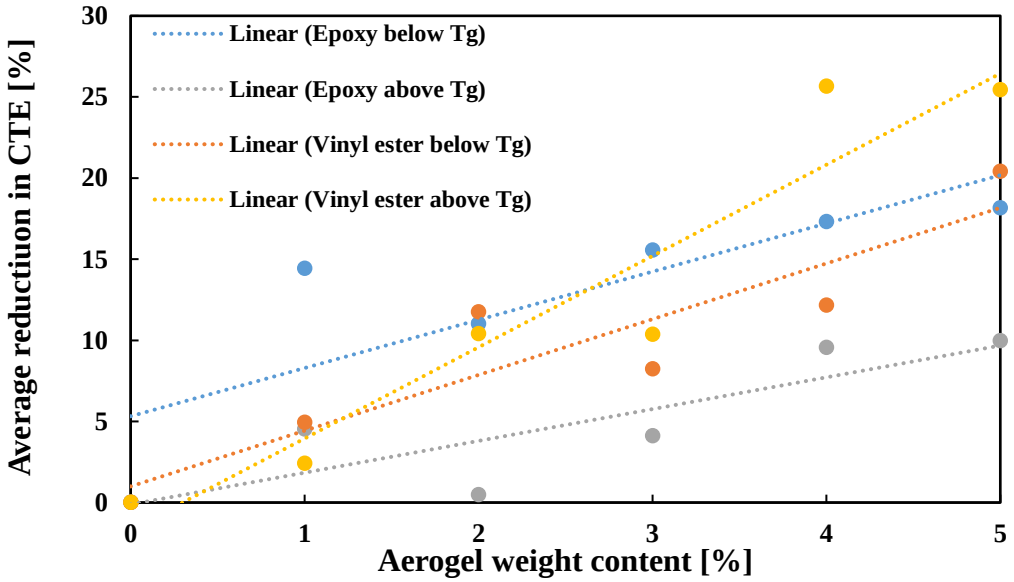

Figure 3-66 Trend lines presenting reduction in coefficient of thermal expansion as a function of aerogel loading for both resin systems at room temperature and glassy-state.

By analysing the results presented in Figure 3-66, it can be concluded that in the case of both epoxy and vinyl ester resin, their coefficients of thermal expansion decrease with increasing particle content. It is expected behaviour due to multiple factors. Firstly, the intrinsic CTEs of the aerogels is significantly lower than both resin systems [29]. Gross and Fricke reported that the linear thermal expansion of silica aerogel, in standard atmospheric conditions, is in a range of $40\times10^{-6}\ K^{-1}$. However, with reduced mobility of air molecules (or their lack) CTE value decreases to values as low as $2\times10^{-6}\ K^{-1}$ [250]. Thus, replacing higher expansion material with aerogel results in decreasing CTE values. Secondly, the interface region between resin and aerogel particles also plays an important role. An investigation led by Kiba et al. revealed that the resin which infiltrated pores of aerogel particles seems to have almost completely restricted mobility in the presence of excessive thermal energy. They have also suggested that complete infiltration of aerogel pores can stabilise a wide range of polymers. As a result, the introduction of aerogel particles further reduces the mobility of polymer chains around them and thus, an increasing aerogel content can result in decrease of CTE values. Figure 3-66 also indicates that

the impact of aerogel particles on epoxy resin was greater than for vinyl ester, especially at lower aerogel loadings. This finding can be contributed to the higher molecular mobility and lower curing temperatures of epoxy resin, both of which reduces its resistance to elevated temperatures. As such, the replacement of matrix with more thermally stable aerogel particles carries higher impact on less thermally stable epoxy resin. Nevertheless, with increasing aerogel loading the difference between both resin systems diminished resulting in similar CTE reduction at 5 wt%. A reduction in epoxy CTE values has also been achieved by Wong et al., who have investigated the effect of silica particles on the epoxy system. In their work they have managed to decrease the CTE to an even larger degree, which might be attributed to the usage of silica particles which have even lower coefficient of thermal expansion that aerogel particles [251].

The sudden increase in both polymers' thermal expansion coefficients above the glass transition temperature is expected mainly due to the free movement of polymers segments at elevated temperatures [252]. Similarly, as at the room temperature, both polymers follow the same trend with reducing coefficient values with increasing aerogel weight content. However, above T_g significant differences in reduction magnitude can be observed. The vinyl ester presents a linear trend resulting in higher CTE reduction than epoxy for each loading scenario. In addition, a 25% reduction in CTE value has been achieved at 5 wt% aerogel loading for vinyl ester samples while epoxy's CTE was reduced by only 10% for the same scenario. Such behaviour can be associated with different filler/ resin interactions. By using both silane-treated and untreated filler it was previously shown by Soderholm that the chemical bond between filler and resin plays a minor role in lowering the coefficient of thermal expansion [253]. On the other hand, he suggested that the bond between both materials is formed during resin polymerisation and is dependent on the curing shrinkage [253]. Such hypothesis could explain the differences between the reduction in CTE value of epoxy and vinyl ester resins. As previously stated, epoxy resin has a significantly lower curing volume shrinkage of 1-5% compared to vinyl ester with 7-10% shrinkage [240, 248]. On the other hand, as presented by Hamama, the shrinkage stresses are also directly dependent upon the modulus of the polymer, which in this case is higher for the epoxy resin (as presented in 3.3.7)[254]. As a result of impact of both polymer modulus and shrinkage strain, it is difficult to clearly assess which resin would form stronger mechanical interactions with aerogel particles. However, higher reduction in thermal expansion coefficient above glass transition temperature might suggest that higher constraint of polymer chains was achieved in case of viny ester samples. The combined effect of particle size on the thermal expansion coefficient at room temperature for vinyl ester system has been presented in Figure 3-67. Similar trend can be observed for epoxy

system, however averaging over data from two different resin systems was deemed inappropriate due to their different thermomechanical behaviour.

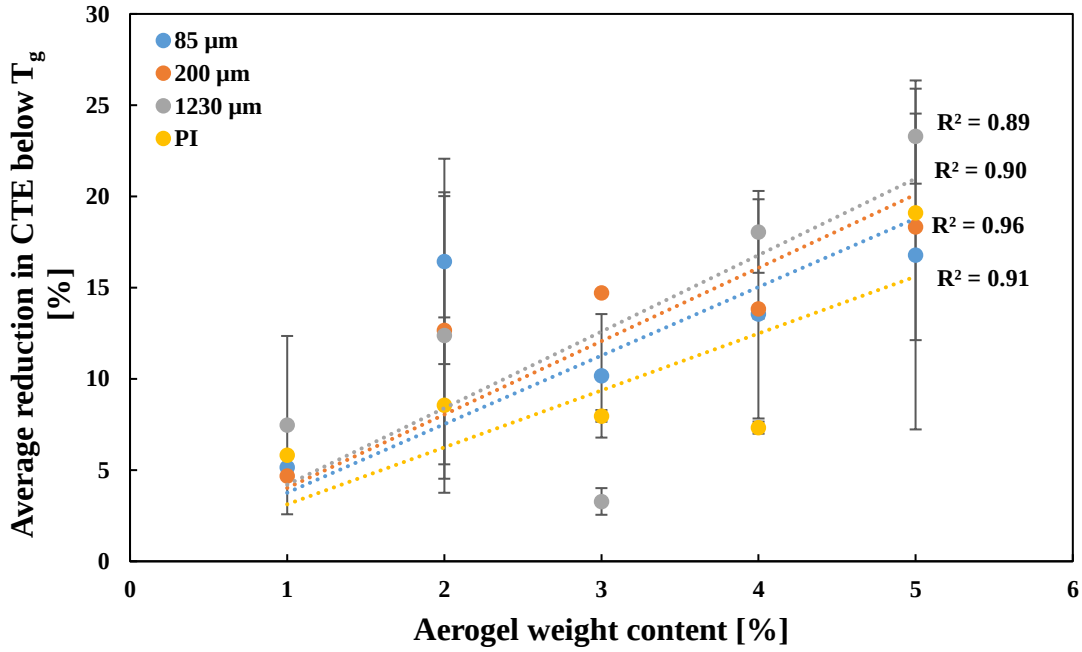

Figure 3-67 Trend lines presenting reduction in coefficient of thermal expansion at a room temperature as a function of aerogel loading for different particle size used. Values have been calculated for composites manufactured with vinyl ester.

As it can be noticed the addition of silica particles to the vinyl ester resin allows to reduce its CTE by even more than 20% when incorporating 5 wt% of the aerogel. Nevertheless, no statistically significant differences between CTE values of composite prepared with different particle size can be identified. As a result, it seems that regardless of the particle size used the silica aerogel affects the coefficient of thermal expansion of vinyl ester in the same manner. On the other hand, the impact of particle size on CTE reduction was previously investigated by Jang et al., who have tested epoxy/SiO_2 composites and found that smaller particles resulted in lower CTE values [255]. Nevertheless, their study covered only composites with filler volume fraction up to 1.63%, which cannot give much perspective for high aerogel loading scenarios. Additionally, regardless of the different material and particle shape the PI aerogel particles reduces CTE of vinyl ester in a similar way as the silica aerogel particles. More results can be drawn for coefficients of thermal expansion above the glass transition temperature as presented in Figure 3-68.

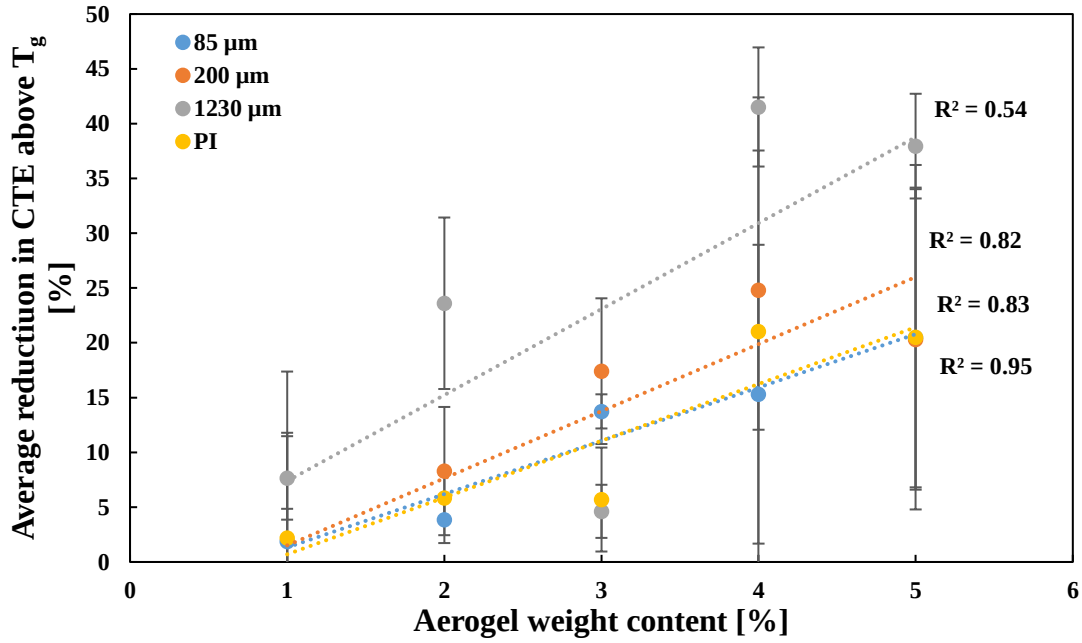

Figure 3-68 Trend lines presenting reduction in coefficient of thermal expansion above T_g of the vinyl ester as a function of aerogel loading for different particle size used.

Figure 3-68 presents that above T_g the CTE of vinyl ester decreases with increasing particle loading, nevertheless, due to the high variation in obtained data it is difficult to determine whether particle size has any impact on the CET value of manufactured composites. Similarly, as in room temperature case the polyimide aerogel particles seem to impact thermal expansion's coefficient to the same extent as the silica aerogel particles. Such finding can be explained by the similar thermal expansion coefficient of both aerogel types (and as low as 8 $\times 10^{-6}\,K^{-1}$) and comparable size distribution as presented in particle size analysis in 3.3.1[256]. As a result, the effects of both introduction of low CTE areas and polymer chain interlocking yield a similar impact on the CTE reduction.

3.3.9 Effect of aerogel particle on polymer glass transition temperature

3.3.9.1 Epoxy resin

Previous analysis of coefficient of thermal expansion has also enabled the measurement of the glass transition temperature of created composites. Figure 3-69 presents the glass transition temperature (T_g) of epoxy composites create with various silica and polyimide aerogel particles.

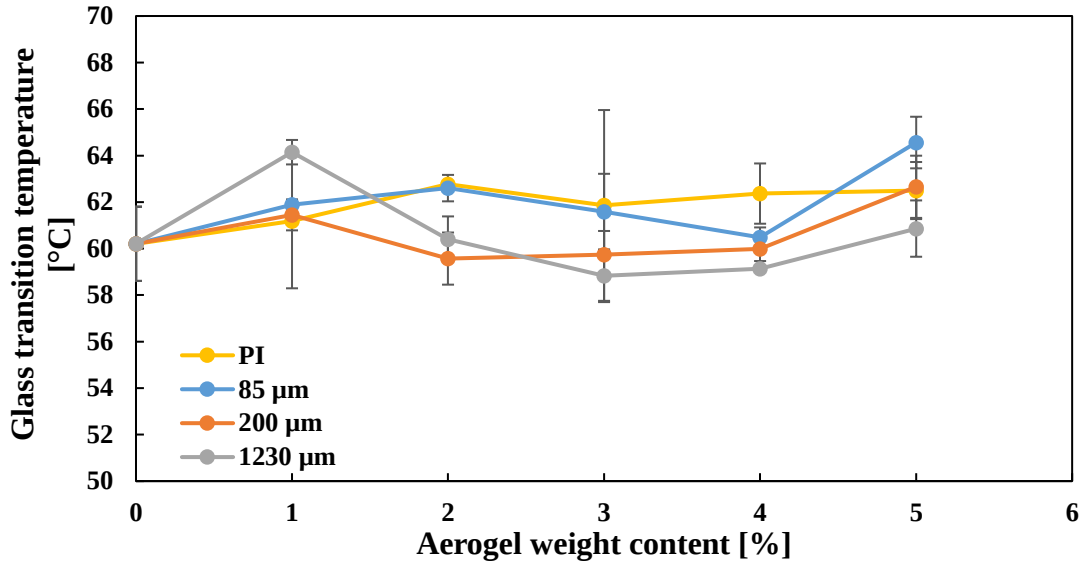

Figure 3-69 Glass transition temperature of aerogel/ epoxy composites based on TMA measurements.

The TMA analysis presents that the addition of aerogel particles to the epoxy resin has minor effect on its glass transition temperature, with a slight increase in T_g values at low aerogel loading followed by a constant or sometimes decreasing values when increasing aerogel content. Additionally, the statistical analysis has indicated no significant changes which might suggest different impact of aerogel type or particle size on epoxy's glass transition temperature. To further investigate aerogel impact on polymer T_g the DMA analysis was performed with Figure 3-70 and Figure 3-71 presenting the glass transition temperature of aerogel/epoxy composites based on respective storage and loss modulus. Please notice that no statistical analysis has been performed for these measurements due to the use of only single test specimen for each sample.

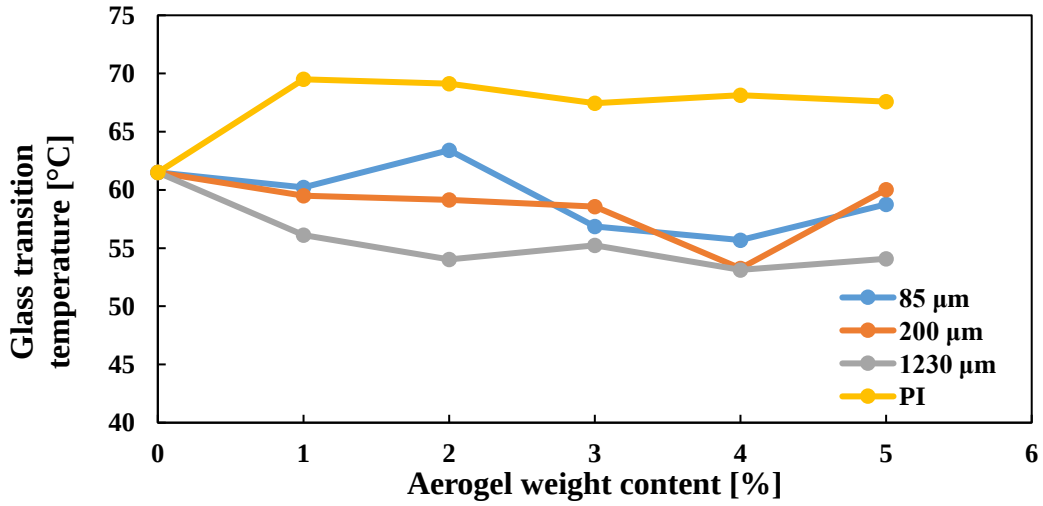

Figure 3-70 Glass transition temperature of aerogel/ epoxy composites based on storage modulus measurements.

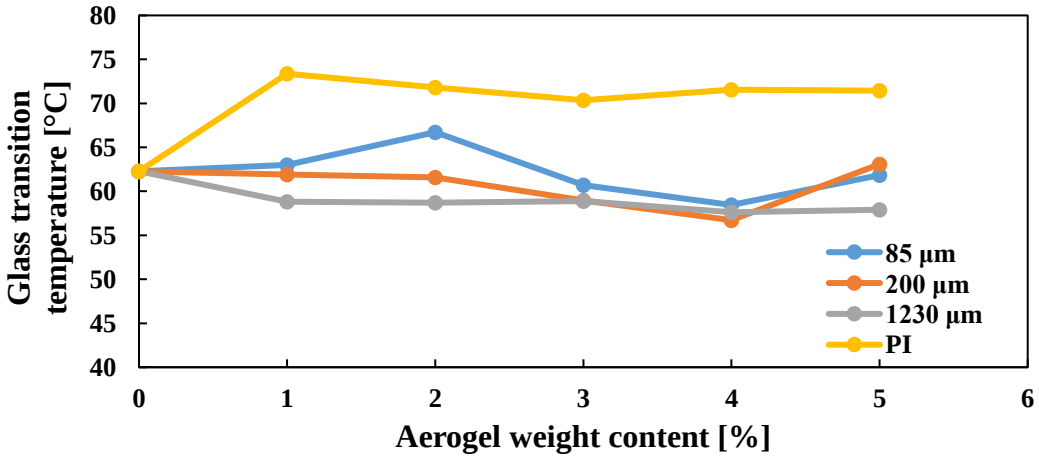

Figure 3-71 Glass transition temperature of aerogel/ epoxy composites based on loss modulus measurements.

Glass transition temperature obtained by analysis of storage modulus is assumed to be the most conservative and the results reflect that with the lowest. Starting with an initial value for neat epoxy of 61.5 °C each of the aerogel types tends to affect epoxy resin differently. Firstly, the samples manufactured with the addition of PI aerogel record a significant increase in glass transition temperature (13% increase) with the addition of 1 wt%, followed by a slight decrease with additional loading. On the other hand, all silica aerogel particles tend to decrease epoxy's glass transition temperature with a slight sign of increase at the highest loading. Slightly higher T_g values were obtained by analysis of loss modulus as presented in Figure 3-71. However, regardless of the value differences an identical impact of silica aerogel particles on the glass transition temperature was noticed with epoxy's T_g values slightly decreasing with increasing silica aerogel content. Following the presentation of obtained glass transition temperatures, mechanical properties at a glassy state have also been investigated. As a result, Figure 3-72 have been created presenting storage modulus at the glassy state of aerogel/epoxy composites.

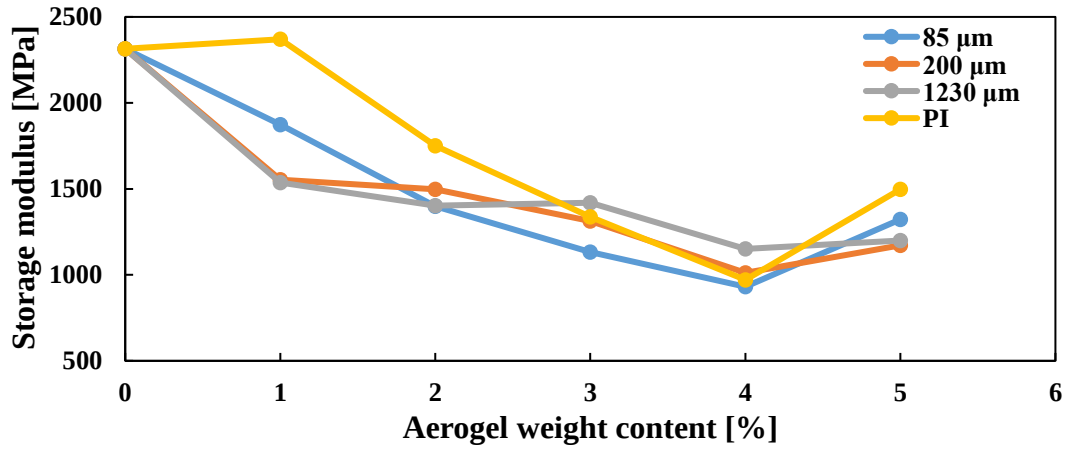

Figure 3-72 Storage modulus of aerogel/epoxy composites at glassy state.

By analysing Figure 3-72, it can be seen that the addition of aerogel particles to epoxy resin significantly decrease the storage modulus of the tested material. In the case of silica particles, the addition of 1 wt% can reduce loss modulus by almost 30% followed by a steady decrease until 5 wt% when a sign of strengthening effect can be noticed. No impact of particle size can be noticed. A similar trend can be observed for PI aerogel samples. However, in their case an initial straightening mechanism can be spotted at 1 wt% with further reduction until reaching 5 wt%. A similar observation can be drawn for loss modulus as presented in Figure 3-73.

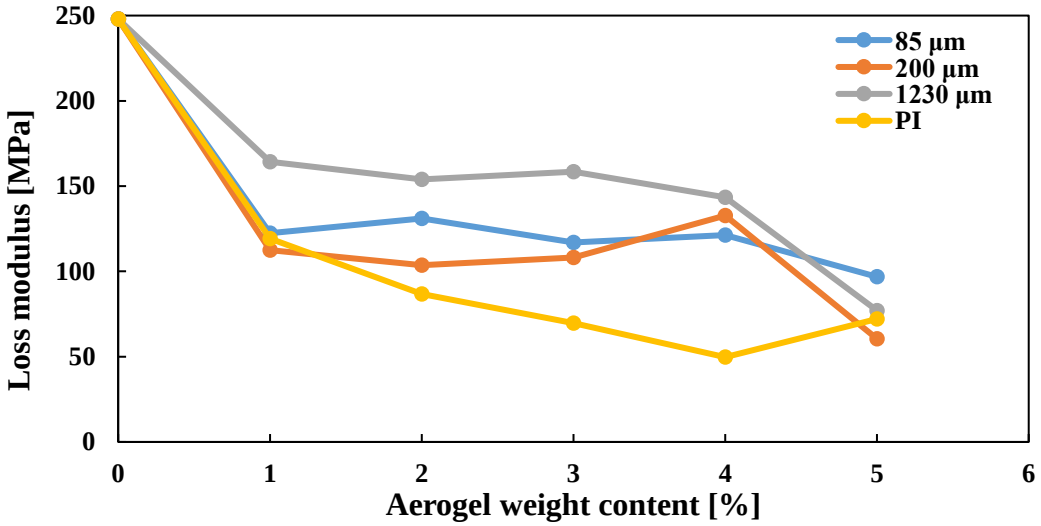

Figure 3-73 Loss modulus of aerogel/epoxy composites at glassy state.

Figure 3-73 indicates that the addition of aerogel particles is detrimental to loss modulus. The loss modulus exponentially correlates with aerogel loading with the largest drop at 1 wt% and aerogel particles' further addition leading to values stabilisation. In addition, Figure 3-73 reveals a possible dependency of particle size upon loss modulus reduction with smaller particles presenting lower loss modulus values until reaching 5 wt% when all values converge at a similar level. Also, PI aerogel samples present a significant drop in loss modulus at 1 wt%, followed by a constant decrease with increasing loading resulting in much higher loss modulus reduction than silica aerogel counterparts.

3.3.9.2 Vinyl ester resin

Similarly, as in the case of epoxy composites the TMA results have been used to identify the glass transition temperature of vinyl ester composites prepared with the addition of silica and polyimide particles. Figure 3-74 has been created to correlate the T_g values with the aerogel weight content of various silica and polyimide aerogel particles.

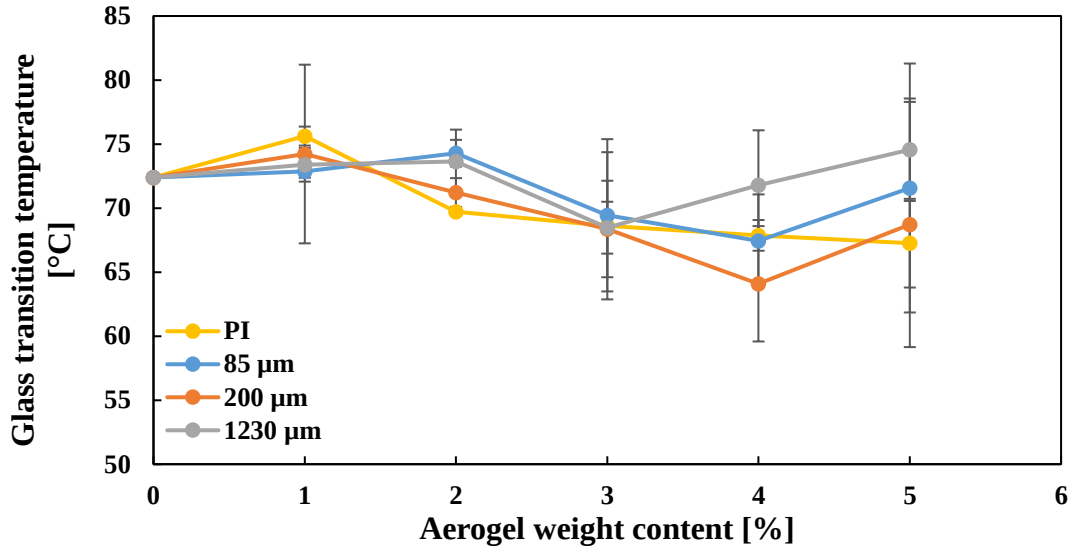

Figure 3-74 Glass transition temperature of aerogel/vinyl ester composites based on TMA measurements.

Figure 3-74 presents that the addition of aerogel particles to the vinyl ester yields similar results as in case of epoxy composites with initial increase of polymer's glass transition temperature followed by the constant deterioration with increasing aerogel content. Additionally, it seems that all the particle regardless of the type and size carry similar impact on the vinyl ester T_g. To investigate the impact of aerogel particle on vinyl ester properties further the DMA analysis was performed and Figure 3-75 was created presenting the glass transition temperature of aerogel/vinyl ester composites based on storage modulus. Again, no statistical analysis has been performed for these measurements due to the use of only single test specimen for each sample.

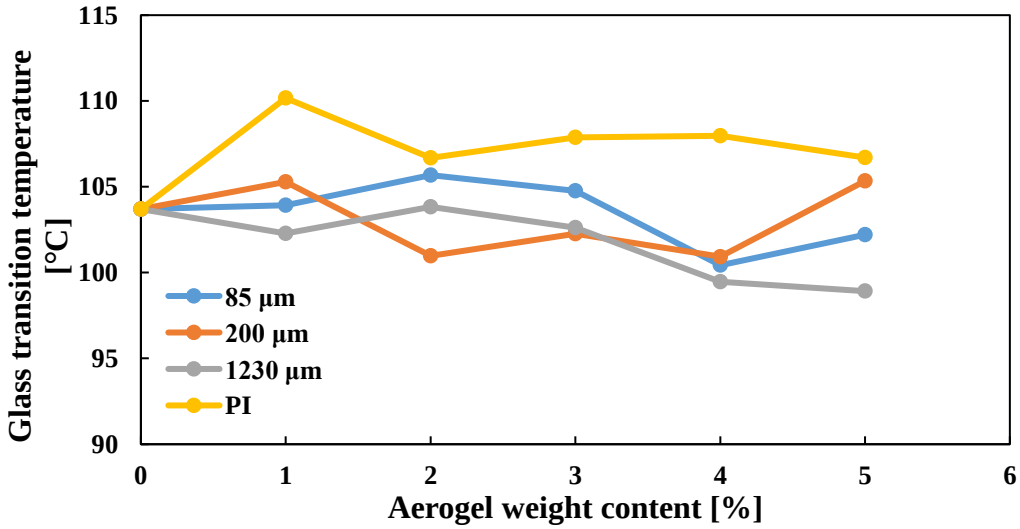

Figure 3-75 Glass transition temperature of aerogel/vinyl ester composites based on storage modulus measurements.

The analysis of Figure 3-75 indicates that PI aerogel significantly impacts vinyl ester's glass transition temperature. By incorporating 1 wt% of PI aerogel particles, the T_g has been increased by 16% with a slight drop in the value with larger particles quantities. In the case of silica aerogel particles only a slight change in T_g has been recorded with the most significant increase of 4% achieved at 2 wt% followed by a slight decrease in case of higher loadings. Also, little effect of particle size on glass transition temperature was observed. Different behaviour can be seen when analysing glass transition temperature obtained by loss modulus measurements as presented in Figure 3-76.

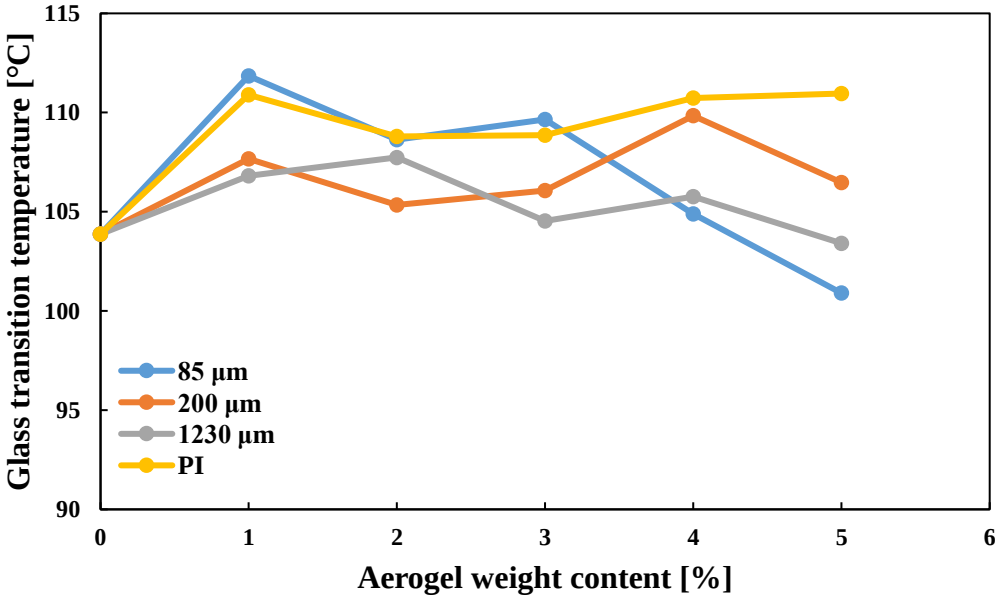

Figure 3-76 Glass transition temperature of aerogel/ vinyl ester composites based on loss modulus measurements.

In this case all composites prepared with silica aerogel particles achieve the highest T_g at low loading scenarios (1 or 2 wt%) followed by a drop below the neat vinyl ester values. On the other hand, PI aerogel particles increased vinyl ester glass transition temperature significantly and no major decrease was noticed with increased aerogel loading. Following the analysis of obtained glass transition temperatures, the analysis of mechanical properties at a glassy state has been conducted. As a result, Figure 3-77 and Figure 3-78 have been created presenting both storage and loss modulus at the glassy state of aerogel/vinyl ester composites.

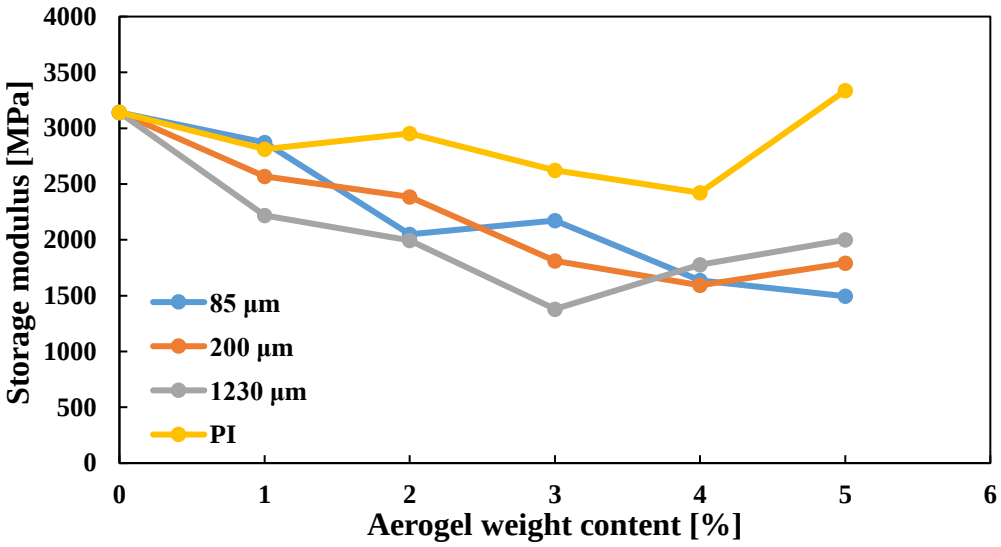

Figure 3-77 Storage modulus of aerogel/vinyl ester composites at glassy state.

Figure 3-77 reveals that the addition of aerogel particles to vinyl ester resin decreases the tested material's storage modulus. In the case of silica particles, the linear decrease has been noticed between 1 and 4 wt% as a result of which over 40% decrease in storage modulus was recorded. Interestingly the sign of stiffening was observed at 5 wt%. Samples with PI aerogel particles followed a very similar trend. However, the decrease was much less impactful with a maximal decrease in storage modulus of 23%. Again, the increase in storage modulus was recorded at 5 wt%, however the rate of the increase might suggest the point is an outlier. Such behaviour could results from infiltration of aerogel pores by the liquid resin or non-homogenous nature of the sample. A similar observation can be drawn for loss modulus data as presented in Figure 3-78.

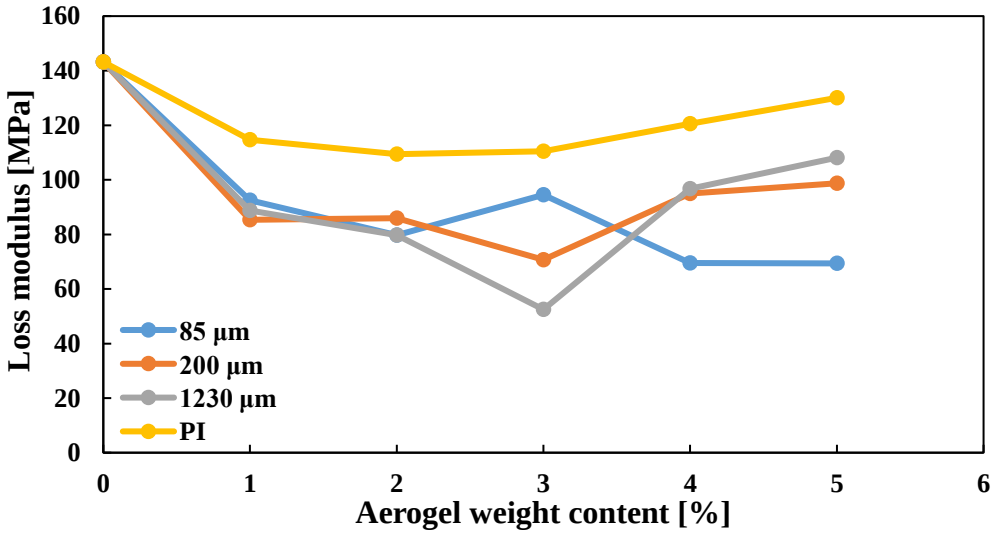

Figure 3-78 Loss modulus of aerogel/vinyl ester composites at glassy state.

Aerogel particles' addition is detrimental for loss modulus with the largest drop of 43% at 3 wt%. Further addition of aerogel particles leads to an increase in composites loss modulus of most samples except for the one with 85 μm silica aerogel particles used. Similarly, as in the case of storage modulus, PI aerogel samples follow the same trend. However, in their case reduction in loss modulus is much smaller than in the case of silica aerogel particles achieving only a 24% reduction at 2 wt% followed by a steady increase with increasing aerogel content.

3.3.9.3 Discussion

Obtained glass transition temperature values for pure epoxy and vinyl ester resin are within an expected range. As provided by manufacturer datasheets, the T_g of epoxy is 92 – 98 °C and 132 °C for vinyl ester. Even though the number seems to be much higher than the values obtained in this work it should be noted that different measurement techniques as well as post-curing techniques for both polymers have been implemented in order to obtain such values. The following discussion focuses on glass transition temperatures obtained through TMA measurements and the analysis of storage modulus using DMA, as it provides the most conservative results. When comparing results obtained by both measurement techniques it can be noticed that DMA tends to produce higher values of glass transition temperature (especially in case of vinyl ester samples) than TMA. Similar observation has been presented in multiple previous works which indicated that the difference in T_g values obtained from DSC, TMA, and DMA methods may differ by more than 25 °C. The author of mentioned works associated such large discrepancies with various size of the specimen used as well as different methodology and instrumental mechanisms associated with data acquisition [257, 258]. To further compare the impact of aerogel particles on the glass transition temperature measured using both thermomechanical analysis techniques, Figure 3-79 was created and presents the average change in absolute values of glass transition temperature as a function of silica aerogel loading.

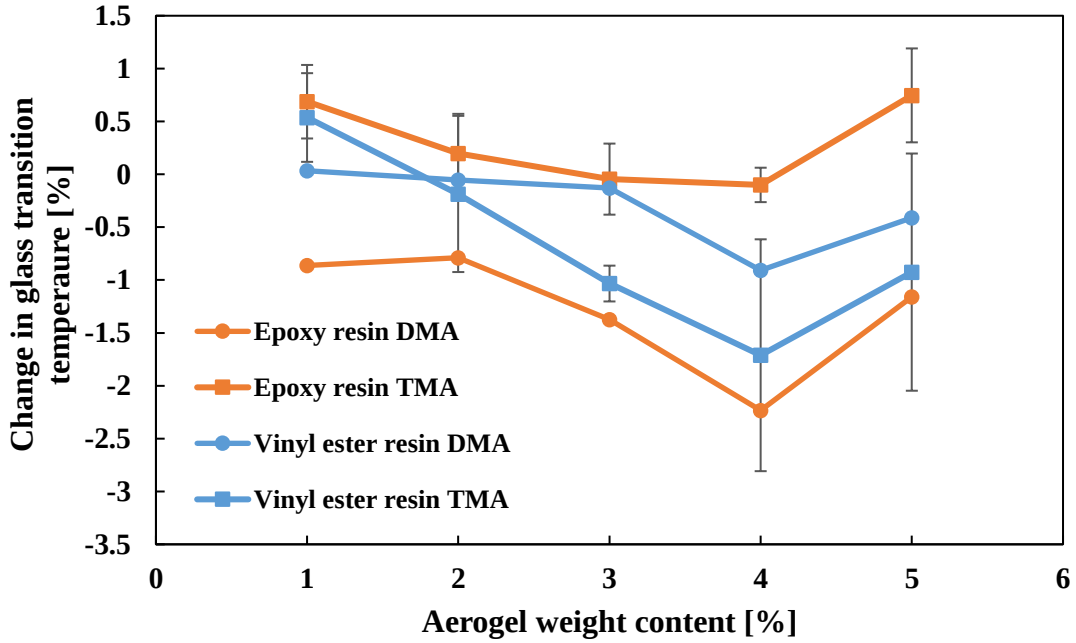

Figure 3-79 Average change in glass transition temperature as a function of silica aerogel loading. The values have been obtained by averaging TMA and DMA results in absolute temperature for different silica aerogel particle sizes.

Figure 3-79 presents further differences between T_g values obtained by using TMA and DMA. Firstly, the TMA indicates that the addition of low quantities of aerogel particles can increase the glass transition temperature of both epoxy and vinyl ester (around 1% increase), while the DMA results suggest that the aerogel particles can only decrease T_g. The different impact of particles addition on polymer T_g when using different measurement techniques was previously presented in the literature. When investigating the impact of Al_2O_3 nanoparticles on the DGEBA- based epoxy Jiang et all, used DSC, TMA and DMA to detect the glass transition temperature of created composites [259]. As a result, authors detected various level of decrease in T_g when using DSC and TMA, while DMA presented increase in T_g values. Such findings were attributed to uneven heating rates, various arrangement of temperature sensors and the influence of sample sizes leading to lag in the measured temperature of the sample [260]. Further analysis of epoxy's glass transition temperature using all three measurement techniques by Cassel and Twombly revealed that the best correlation between thermomechanical techniques can be achieved when using the same heating rate [261]. Surprisingly, regardless of the initial impact of the particles, for both polymer types TMA and DMA results follows the same trend with decreasing T_g values with increasing aerogel content until reaching 5 wt% when the increase in recorded. Such trend was previously reported in the literature. Preghenella et al., who investigated silica particles' effect on the epoxy matrix, noticed a decrease in T_g with increasing silica content [249]. They suggested that particles'

addition reduces the polymer matrix cross-linking by preventing the complete matrix curing until reaching temperatures which also cause polymer degradation. Also, the increase in T_g at higher silica loadings has been attributed to the superior physical immobilization of polymer chains around the particles' surface [249]. Following the second DMA run using the same samples, much higher T_g values have been recorded and the degrading impact of particles has been minimised [249]. A similar trend but different reasoning has been proposed by Liu et al., who suggested the plasticizing effect of the silica particles and elevated free volume of epoxy to be the main reason behind T_g lowering [262-264]. The effect of aerogel particles on both polymer systems' storage and compressive modulus has been presented in Figure 3-80.

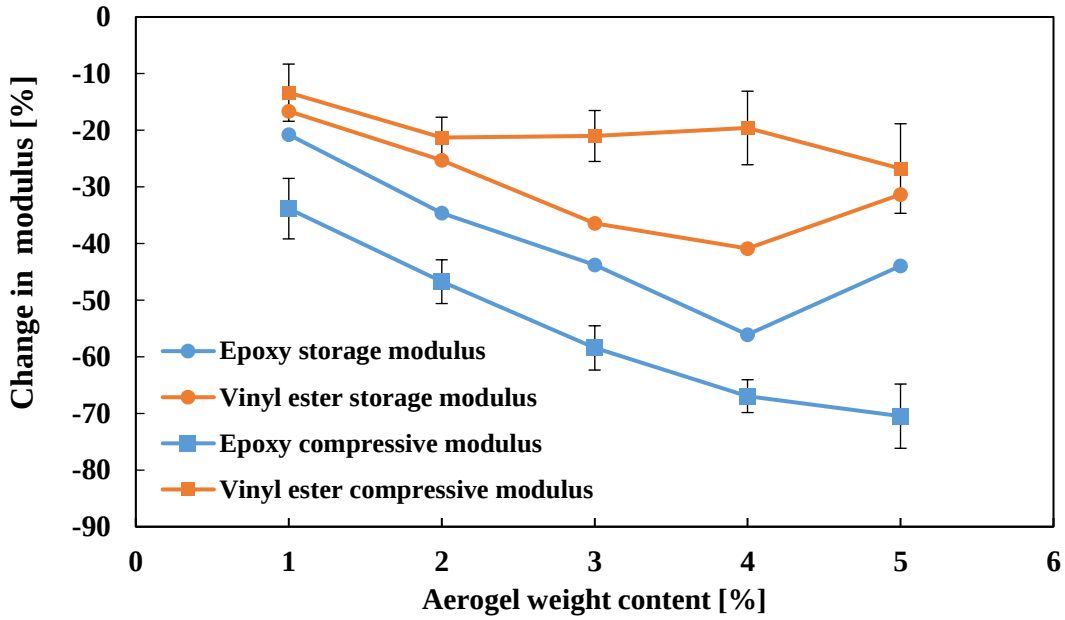

Figure 3-80 Average change in storage and compressive modulus as a function of silica aerogel loading. The values have been obtained by averaging results for different silica aerogel particle sizes. Compressive modulus data are presented in 3.3.7.

As indicated by Figure 3-80, both epoxy and vinyl ester resin's storage and compressive modulus decrease drastically with increasing aerogel content. Overall, the addition of aerogel particles softens the materials and has a detrimental effect on polymer composites' mechanical properties. Again, the lower degree of polymer cure caused by particles' introduction could be responsible for such behaviour. By reducing the crosslinking of polymer chains the materials become softer thus reducing both modulus values. Nevertheless, different behaviour for both properties can be noticed for 5 wt% samples with the storage modulus increasing and compressive modulus decreasing further. Some authors suggested that at higher aerogel loading the particles (resistant to temperature impact) affect the surrounding polymers chains by anchoring and preventing them from dislocation leading to increase in storage modulus

[249]. The same effect would not be detected for the compressive modulus as the measurement is conducted in absence of elevated temperatures. Similarly, as in case of compressive properties the impact of aerogel particles on storage modulus is substantially larger for the epoxy resin. Again, it can be speculated that due to the much quicker curing process as well as post-curing at higher temperatures vinyl ester has achieved a higher curing degree thus resulting in superior mechanical properties. Further analysis focuses on the impact of aerogel type on epoxy's' glass transition temperature has been investigated and plotted in Figure 3-81. Similar trends can be observed for vinyl eester system, however averaging over data from two different resin systems was deemed inappropriate due to their different thermomechanical behaviour.

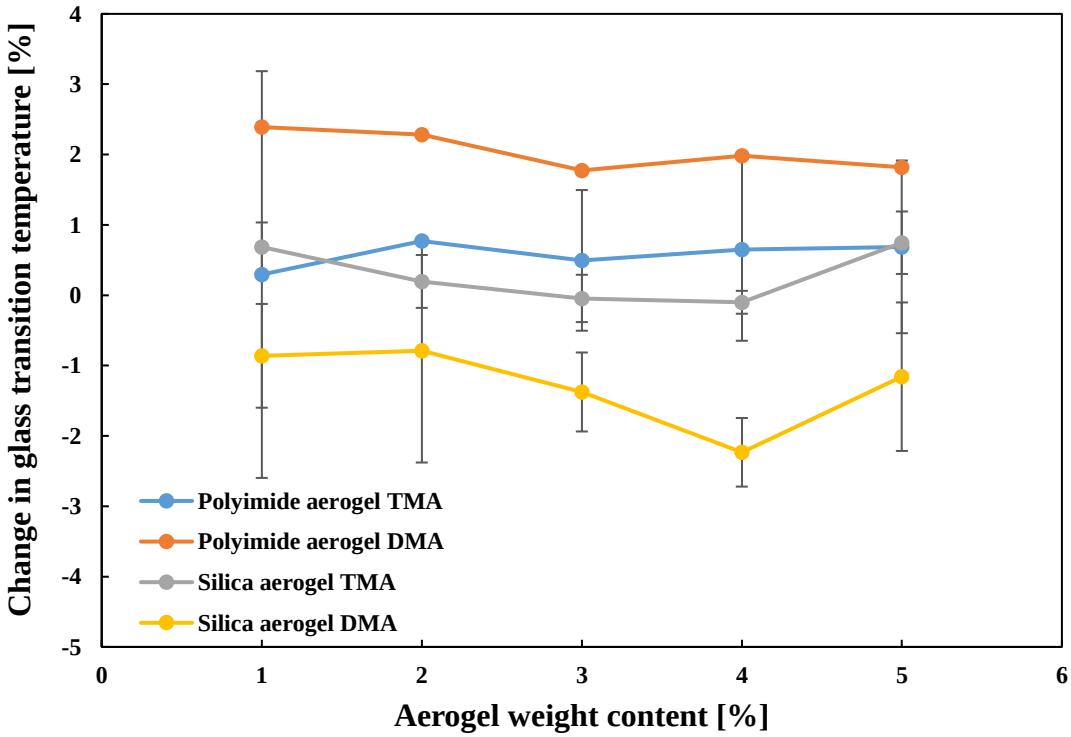

Figure 3-81 Change in glass transition temperature as a function of aerogel loading for different particle size used. Values have been obtained for composites manufactured with epoxy resin.

Figure 3-81 does not include results for composites manufactured with different size of silica aerogel particles as conducted statistical analysis has not indicated strong correlation between the particle size and change in polymer's glass transition temperature. On the other hand, substantial difference can be detected between composites prepared with silica and polyimide aerogel particles as the addition of the latter particles increased T_g of both epoxy resin regardless of the measurement technique used. As such for DMA it provides around a 2% increase in T_g values at 1 wt% followed by an inverse relationship afterwards. In case of TMA,

0.3% increase is recorded for 1 wt% which further increase with addition of larger quantities of polyimide aerogel. Increase in T_g values is mainly attributed to the creation of strong interfacial interaction between the polymers and polyimide molecules. Caused by not only high specific surface area (due to a low diameter of PI particles) but mainly due to a large polarity in the polyimide molecules, the interface severely constraints the polymer molecules' chain motion [265]. Improvement in T_g values has also been observed by Chen et al., who have used polyimide fibres in order to reinforce epoxy resin [265]. The analysis of particle size's impact has also been conducted for storage modulus with results presented in Figure 3-82.

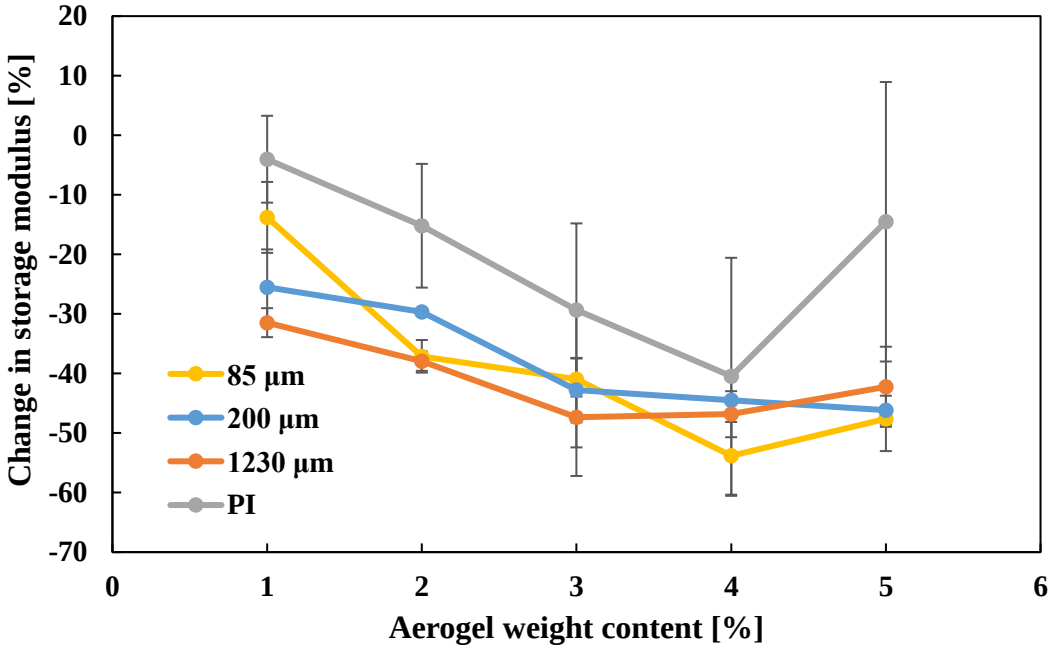

Figure 3-82 Change in storage modulus as a function of aerogel loading for different particle size used. Values have been obtained for composites manufactured with epoxy resins.

The change in storage modulus of aerogel filled composites has been presented in Figure 3-82 and it can be noticed that the particle size yield little impact on the value of the change in storage modulus. Similarly as in the previous thermomechanical analysis the statistical analysis has not presented a significant differences which might indicate that using different silica aerogel particle sizes can impact polymers' storage modulus in a different way. However, Figure 3-82 also indicates that despite different behaviour seen in glass transition analysis, PI aerogel particles also reduce the storage modulus of polymers used. Nevertheless, due to much stronger interfacial interactions between PI and polymers the reduction in storage modulus is significantly lower than for silica counterparts.

3.3.10 Effect of aerogel particles on polymer heat distortion temperature

3.3.10.1 Epoxy resin

Figure 3-83 plots DMA displacement curves for silica aerogel/epoxy composite at different weight fractions of 1230 μm aerogel particles.

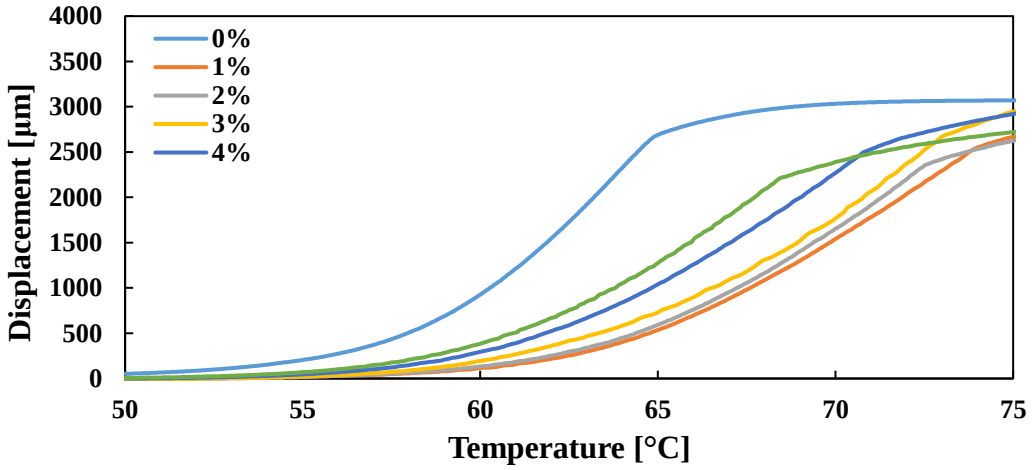

Figure 3-83 Typical DMA displacement curves for silica aerogel/epoxy composite at different weight fractions of 1230 μm aerogel particles.

The addition of aerogel particles can significantly affect the thermo-mechanical behaviour of the epoxy resin. Pure resin exhibits much higher displacement under the same stress over the whole temperature range, indicating lesser thermal stability and lower heat distortion temperature. The addition of aerogel particles increases the HDT values and it is the addition of 1 wt% of aerogel particles that affect the composite property to the greatest extent. On the other hand, further addition of particles reduces the HDT towards the neat resin value. As a result, Figure 3-84 gives a heat distortion temperature of aerogel/epoxy composite with varying particle size and loading.

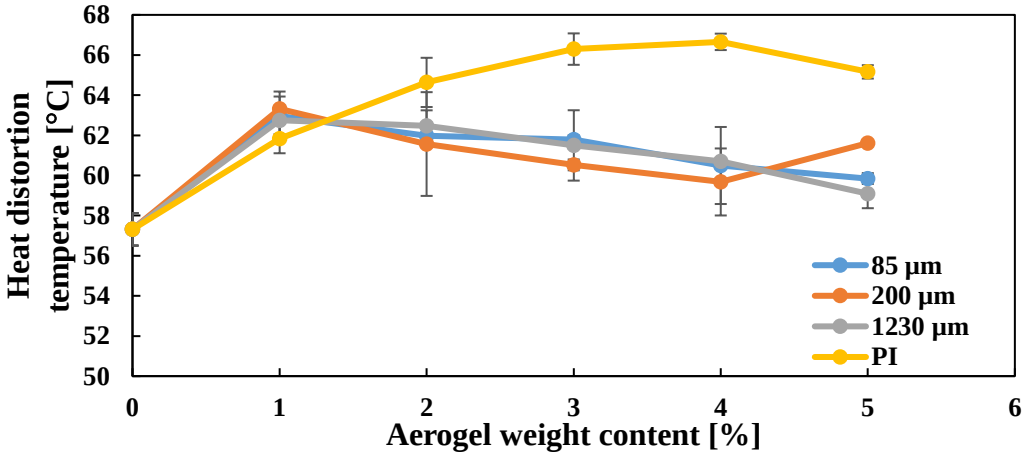

Figure 3-84 Heat distortion temperature of aerogel/epoxy composite with varying particle size and loading.

Figure 3-84 shows that for silica aerogel particles, heat distortion temperature reaches its highest with 1 wt% of aerogel particles. Further addition of aerogel particles results in a decrease in HDT in a linear fashion. Also, data suggest that incorporating different particle size does not affect the heat distortion temperature to a great extent. In the case of analysed silica aerogel particles, the HDT values are relatively close with larger particles producing slightly lower HDT values for the highest loading scenario. On the other hand, a significantly different trend is presented by composites manufactured with PI aerogel. Firstly, the increase in HDT is 6% greater than for silica aerogel. Also, the presented trend is different and the addition of aerogel particles up to 4 wt% increase the heat distortion temperature, followed by a slight decrease afterwards. Overall, the addition of 85 µm, 200 µm,1230 µm and PI particles resulted in a maximum HDT increase of respectively 10 %, 10.5 %, 9,5 % and 16 %.

3.3.10.2 Vinyl ester resin

Figure 3-85 plots DMA displacement curves for silica aerogel/vinyl ester composite at different weight fractions of 1230 µm aerogel particles.

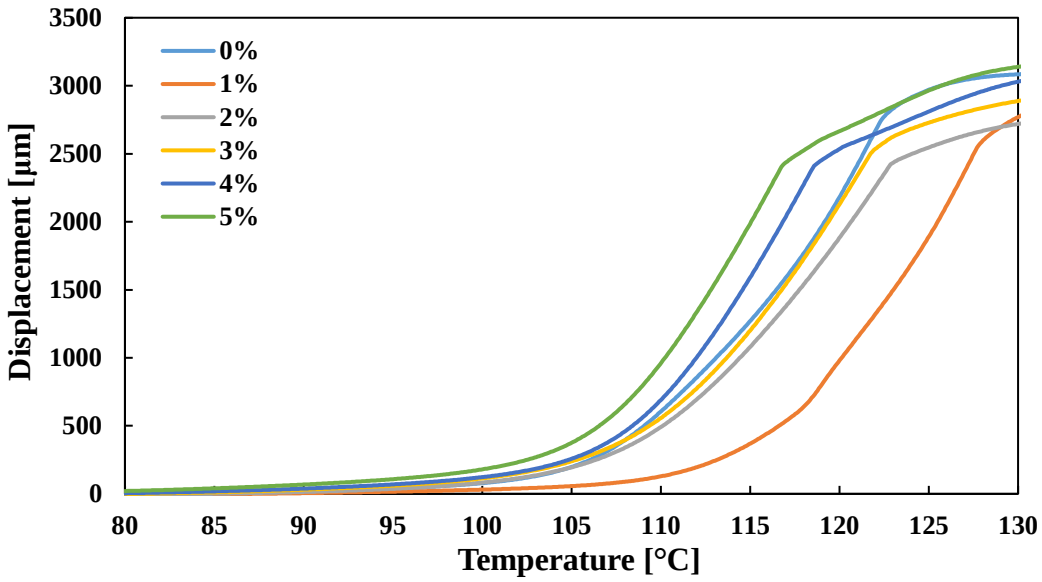

Figure 3-85 DMA displacement curves for silica aerogel/vinyl ester composite at different weight fractions of 1230 µm aerogel particles.

Similarly, as in the epoxy resin case, it might be noticed that the addition of aerogel particles can significantly affect the vinyl ester resin's thermos-mechanical behaviour. However, in this case, only the addition of a low quantity of aerogel particles increases the heat distortion temperature. Incorporation of 3 wt% or higher of aerogel results in HDT decreases below that of neat vinyl ester resin making the composites even less thermally stable. As a result, Figure

3-86 gives a heat distortion temperature of aerogel/vinyl ester composite with varying particle size and loadings.

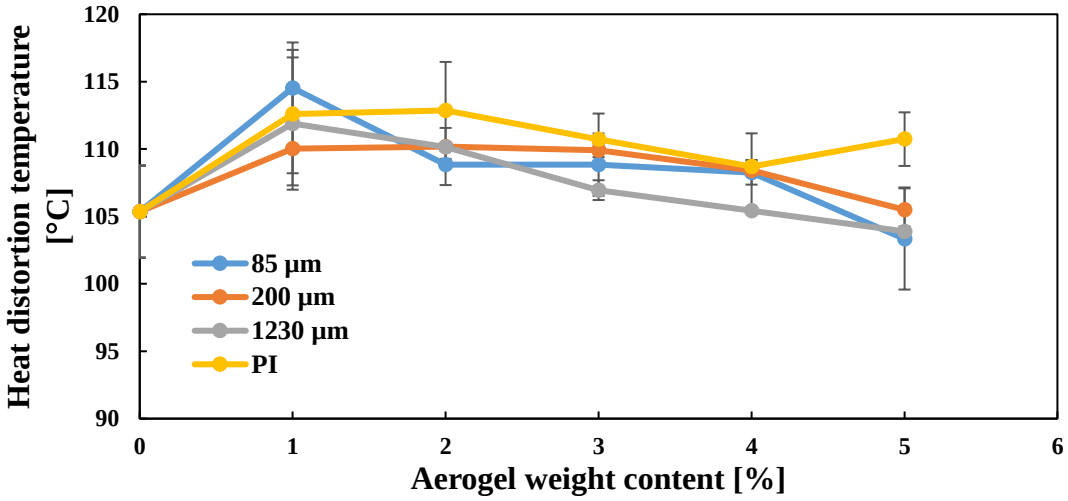

Figure 3-86 Heat distortion temperature of aerogel/vinyl ester composite with varying particle size and loading.

Figure 3-86 presents the highest HDT values for vinyl ester composites after adding 1 wt% of aerogel particles. An increase in the aerogel loading only reduces the heat distortion temperature with most composites achieving below neat vinyl ester value at the highest aerogel loading. Moreover, the graph suggests no direct relation between the HDT and used particle size. Contradicting to the observations for epoxy composites, the addition of PI aerogel to vinyl ester resin seems to produce results similar to one achieved for silica aerogel. Even though the maximum HDT value is achieved at 2 wt% and in general PI composites tend to have higher HDT values across the whole loading range, the difference is not as significant as in the previous case. Overall, the addition of 85 µm, 200 µm,1230 µm and PI particles resulted in a maximum HDT increase of respectively 8 %, 4.5 %, 6,2 % and 7 %.

3.3.10.3 Discussion

Following the DMA analysis, it was found that the pure epoxy and vinyl ester have different heat distortion temperatures of respectively 57 °C and 105 °C. Those results are not surprising, especially when vinyl ester compares well with the data provided by resin manufacturers (115 °C). In the case of epoxy system rather large discrepancy can be noticed between measured (57 °C) and provided data (82 °C), however as stressed in the datasheet more elaborate post-curing technique has been incorporated by the manufacturer in order to achieve such high thermal resistance. Figure 3-87 presents the average change in polymer heat distortion temperature as a function of aerogel loading.

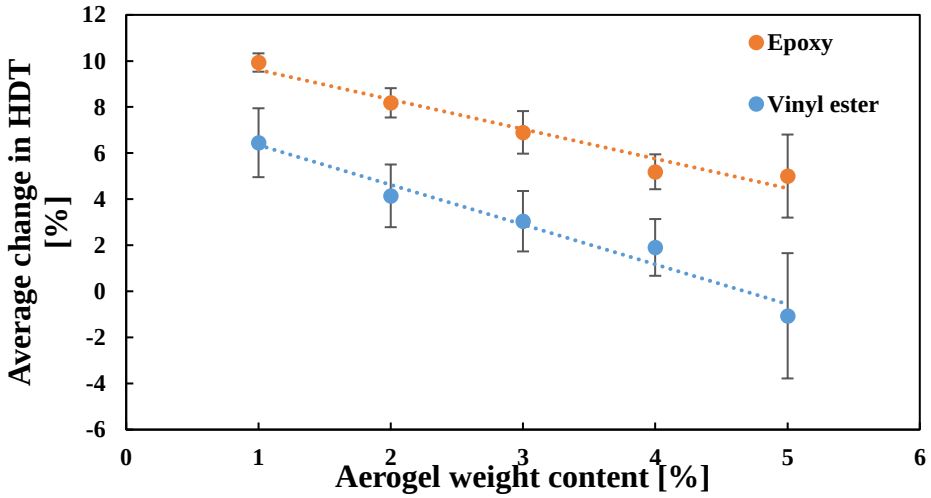

Figure 3-87 Average change in polymer heat distortion temperature as a function of aerogel loading. Values have been calculated for all silica aerogel particle size composites.

As it can be noticed in Figure 3-87, both resins systems present a similar response to the introduction of the aerogel particles with HDT increasing at low loading scenarios with a further addition of particles leading to a linear decrease in HDT. The highest heat deflection temperature values have been achieved for 1 wt% resulting in a 6% and 10% HDT increase for respectively vinyl ester and epoxy. Since HDT is principally a function of sample stiffness and T_g, presented HDT values correlate much better with the T_g results obtained through TMA which suggested the increase in polymers' glass transition temperature following the addition of aerogel particles. As a result, by adding aerogel particles to the polymer matrix, extremely high thermal resistance areas are created due to aerogels' intrinsic properties. Those areas are resistant to temperature impact and affect the surrounding polymers chains by anchoring, preventing their dislocation and thus increasing T_g values of the polymers. On the other hand, as presented in 3.3.7 and 3.3.9, the aerogel particles due to their brittleness tend to have a detrimental effect on polymer mechanical properties of created composites. As such the initial improvement in the HDT values is linearly decreasing as the composites become less stiff. Additionally, the HDT does not indicates any improvement at 5 wt% (as presented in storage modulus values) suggesting constant decrease in composite stiffness as reflected by compressive data. When comparing both resin systems, the aerogel particles causes on average a 4% higher increase in HDT for the epoxy resin. This finding can be contributed to the presence of multifunctional methacrylate polymeric backbone in vinyl ester chain resulting in higher thermal resistance of vinyl ester resin composites. As a result, the introduction of aerogel particles carries less impact on more thermally stable vinyl ester resin. To better understand the effect of aerogel particles on polymer matrices, Figure 3-88 has been created presenting a change in heat distortion temperature of epoxy resin as a function of aerogel

loading for different particle size used. Similar trend can be observed for vinyl ester system, however averaging over data from two different resin systems was deemed inappropriate due to their different thermomechanical behaviour.

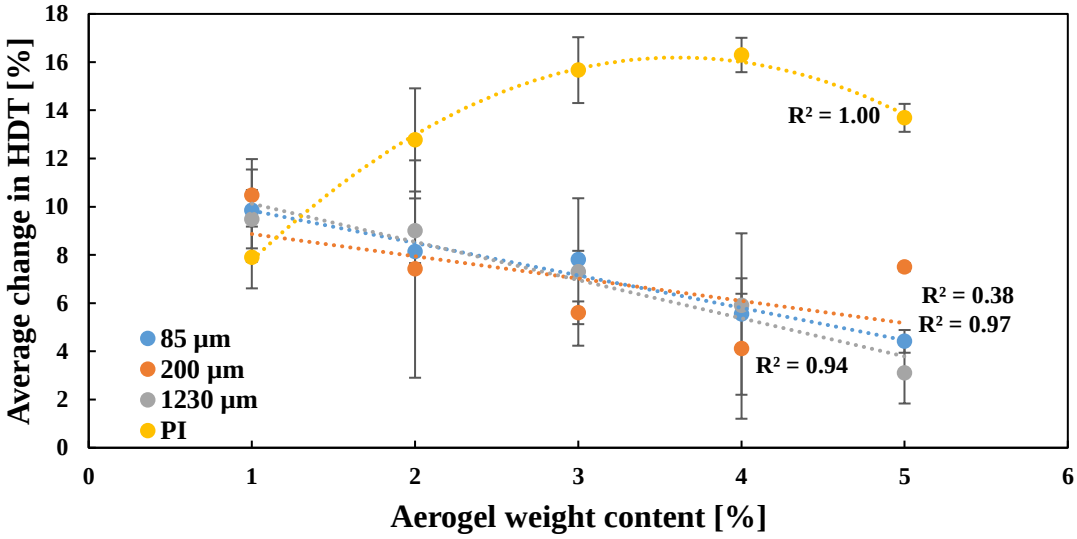

Figure 3-88 Trend lines presenting a change in heat distortion temperature as a function of aerogel loading for different particle size used. Values have been calculated for composites manufactured with epoxy resin.

Figure 3-88 indicates that the addition of various size of silica aerogel particles yields similar impact on the heat deflection temperature of the epoxy resin and the statistical analysis has failed to identify a correlation between the size of aerogel particles used and their impact on HDT. On the other hand, the introduction of PI aerogel particles has achieved significantly different results, as they provide a larger increase in the heat distortion temperature than any of the silica particles. The trend has been substantially shifted with increasing HDT reaching its peak at a relatively high loading scenario of 3 wt%. Further addition of particles caused HDT decrease, possibly indicating the initiation of linearly decreasing trend as in the case of silica particles. Such outstanding thermomechanical performance of PI aerogel composites correlates well with the T_g results presented in previous section. As a result of much higher increase in glass transition temperature and lower degradation of storage and compressive moduli, the PI aerogel composites were also able to achieve much more substantial increase in HDT than any silica aerogel counterparts.

3.4 Summary

In this chapter, the effects of silica and polyimide aerogel particles on epoxy and vinyl ester resins have been evaluated. Conducted work investigates the impact of varying the size and loading of aerogel particles on thermoset resins' thermal, compressive, and thermomechanical

properties. Following the literature review it was found that pore infiltration by liquid resin is the main cause of not utilising aerogel particles to their full capabilities. Thus, the impact of resin viscosity on density and thermal conductivity of resulting composites has been measured and it was found to play a crucial role in avoiding pore invasion during the mixing stage of the composite preparation process. By careful analysis of resins viscosity as a function of time, a novel delayed curing production technique was developed and used to prepare silica aerogel reinforced epoxy composites. It allowed to avoid aerogel pore infiltration and destruction and utilize all the advantages aerogel can provide.

The addition of silica aerogel particles facilitated a significant reduction in epoxy and vinyl ester thermal conductivity, providing approximately a 40% reduction in thermal conductivity of both when a particle loading of 5 wt% was applied. Such a large decrease in thermal conductivity of composites has been contributed to the extremely low thermal conductivity of aerogel particles. As such, when dispersed through the matrix, the particles reduce the number of direct paths through the composite and create a barrier for the energy transfer. Additionally, it was found that 1230 μm silica particles tend to reduce thermal conductivity the most, while polyimide aerogel particles had negligible effects.

The superior thermal properties were also associated with a decrease in compressive strength and Young's modulus. It was found that the compressive yield strength and compressive modulus of the aerogel filled composites decrease with increasing aerogel content resulting in as much as 56% reduction in compressive properties of epoxy and 42% of vinyl ester. Such detrimental loss in mechanical properties was expected mainly due to the low mechanical performance of aerogel and the introduction of stress concentrations at the particle resin boundaries. Finally, the results indicate no impact of silica aerogel particles size on the final compressive properties of the composite material. On the other hand, similarly as in the case of thermal conductivity, the composites created with PI aerogel particles present a much smaller reduction in compressive properties than silica ones.

The coefficient of thermal expansion was another property investigated during this study. To create a full picture of how aerogel affects the CTE values, measurements below and above glass transition temperature have been taken. It was revealed that in the case of both epoxy and vinyl ester resin, their coefficients of thermal expansion decrease with increasing particle content. The main reason behind such behaviour was low intrinsic CTEs of the aerogels. Additionally, it was speculated that the interfacial region between resin and aerogel particles restricted the mobility of polymers chains in the presence of excessive thermal energy. For coefficients of thermal expansion above glass transition temperature large discrepancy was

recorded between both resin systems with vinyl ester presenting a much larger CTE reduction. It was deducted that due to the curing shrinkage, stronger mechanical interactions have been formed for the vinyl ester resulting in a better constraint of material at higher temperatures. Finally, regardless of the particle size and aerogel type used the composites presented similar CTE reduction degree.

While analysing the glass transition temperature of aerogel filled polymers both TMA and DMA techniques has been used. Surprisingly both measurement techniques presented opposite results with TMA indicating that the addition of low quantities of aerogel particles can increase the glass transition temperature of both epoxy and vinyl ester while the DMA results suggested that the aerogel particles can only decrease T_g. Such difference was attributed to uneven heating rates, various arrangement of temperature sensors and the influence of sample sizes leading to lag in the measured temperature of the sample. Different behaviour was found for polyimide aerogel with both TMA and DMA indicating increase in T_g following the addition of such particles. Due to much better compatibility polyimide particles managed to create a strong interfacial bond with polymers and increase T_g of both epoxy and vinyl ester. Regardless of aerogel type the addition of particles reduced the storage modulus of polymer resins.

In the case of heat distortion temperature both resins systems present a similar response to introducing aerogel particles with HDT increase at low loading scenarios and further addition of particles leading to a linear decrease in HDT. It is suspected that two contradicting mechanisms are responsible for such behaviour. The addition of aerogel introduces areas of extremely high thermal resistance anchoring polymer chains and preventing them from dislocation. On the other hand, the aerogel particles tend to have a detrimental effect on polymer composites' mechanical properties which become more prevailing with increasing aerogel content and thus leads to linear decrease in HDT. Finally, PI aerogel particles' introduction has achieved significantly different results as a larger increase in heat distortion temperature than any of the silica particles has been achieved.

4 Mechanical characterisation of Aerogel/Fibre interface

This chapter focuses on characterising the silica and polyimide aerogel adhesion to various fibrous reinforcements. In order to achieve the main objective of this chapter, a new testing procedure was developed for the deposition of aerogel microdroplets on the surfaces of glass, carbon, and PET fibres. The visual observation of microdroplet formation during various aerogel synthesis stages made it possible to quantify cure shrinkage or pore collapse. Alongside the microbond sample preparation, the bulk silica and polyimide aerogel samples were also created and their internal structure was tested using the Brunauer, Emmett and Teller (BET) and Mercury Intrusion Porosimetry (MIP) methods.

The microbond technique was selected as a micromechanical testing method to measure the aerogel-fibre interfacial shear stress (IFSS) in this study, and the samples were subjected to visual inspection and AFM scanning upon test completion. The micromechanical analysis revealed superior adhesion of polyimide aerogel to all tested fibre types, mainly attributed to lower porosity and larger residual stresses. Finally, the samples prepared with carbon fibre resulted in the largest IFSS values, mainly connected with its geometrical features such as high surface roughness and small diameter. However, microbond limitations were also highlighted as potential sources of variation in IFSS values between aerogels and different fibres.

4.1 Literature Review

This literature review provides a background to the mechanical characterisation of aerogel and fibre interface. It commences with the description of complex interactions mechanisms occurring at the fibre and matrix interface, followed by a description of micromechanical techniques used to quantify the interface adhesion. Finally, due to the fact that there has not been a study investigating the micromechanical interfacial properties of any aerogel/fibre composite a limited discussion in assessing the impact of matrix porosity on the other composite systems has been also presented.

4.1.1 Matrix-fibre interface

The interface in fibrous composites is defined as a common surface between fibre and matrix that maintains coherent structure of the composite and enables the effective transfer of loads between constituents [266]. The properties of such interface, either physical or chemical, are related to surface characteristics of specific fibre and matrix system, and they can be related in continuous or in a stepwise manner. This indicates that the interphase can be seen as a distinctive physical region which incorporates not only the fibre/matrix contact area but also neighbouring sections of the fibre and the matrix [267]. However, the interfacial properties

are highly variable and are affected by various parameters such as atomic arrangement, fibre topography, molecular conformation and chemical composition of fibre and the matrix. As a result, the interface characteristics are unique for each fibre and matrix combination [266]. In order to describe and analyse the stress transferability of the interface, the term 'adhesion' is often used. This term is a simplified way of describing otherwise complex interactive mechanisms occurring at the fibre and matrix interface. The fibre-matrix adhesion is generally accepted as a combination of various interfacial interactions such as adsorption and wetting, electrostatic attraction, interdiffusion, chemical bonding, and mechanical interlocking [266-268].

Wetting of fibres occurs during the production stage of fibre reinforced composites when a solid fibre is covered by a liquid or molten resin, creating a solid-liquid interface [269, 270]. It has been previously shown that wetting has a substantial impact on the properties of the final composites and inadequate wetting of the fibres can generate pores on the interface of fibre and solidified matrix. Such can later act as material flaws, subsequently reducing its' mechanical properties [266]. The adhesion due to wetting is based on short-range atomistic interactions between the fibre and matrix electrons. Nevertheless, such forces are only developed when the atoms of both materials are within the cut off range, usually in a range of few angstroms. This type of adhesion can be quantitatively expressed in terms of the negative work of de-adhesion using the Dupre equation [266]:

$$W_A = \gamma_{SV} + \gamma_{LV} - \gamma_{SL} \qquad \text{Eq. 37}$$

Where W_A is the thermodynamic work of adhesion, γ_{SV}, γ_{LV}, and γ_{SL} represent respectively the surface free energy of the solid-vapour, liquid-vapour, and liquid-solid interface. Using Young's equation, Dupre equation can be applied to model a liquid drop on the flat surface of a solid [270]:

$$W_A = \gamma_{SL} + \gamma_{LV}\cos(\theta) \qquad \text{Eq. 38}$$

With θ representing the contact angle as presented in Figure 4-1. Finally, both equations can be combined into Young-Dupre equation, which allows determining work of adhesion using contact angle measurements [266, 270-277]:

$$W_A = \gamma_{LV}(1 + \cos(\theta)) \qquad \text{Eq. 39}$$

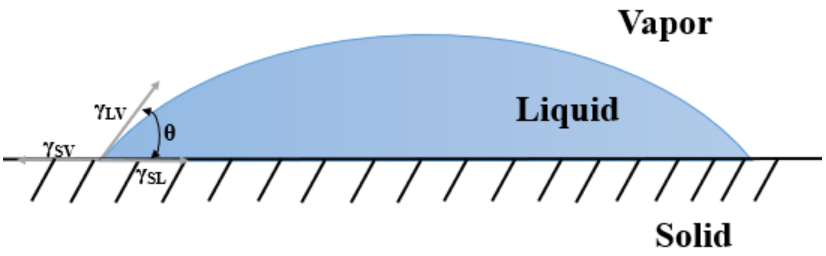

Figure 4-1 Application of Dupre equation to the model of a liquid drop on the flat surface of a solid [266].

Interdiffusion is another important interfacial mechanism responsible for adhesion between fibres and the matrix. It occurs when atoms or molecules from both materials combine across the interface and create an interpenetrating network [266, 267]. Due to the substantial thickness of the created interpenetrating network, it is considered a separate phase with chemical and physical properties, which are a combination of matrix and fibre properties. Additionally, the strength of bonds created by the interdiffusion is strictly related to the atomistic properties of the phenomena, such as the molecular entanglement degree, quantity of molecules involved, and the strength of the intermolecular forces present [268, 278].

Electrostatic attraction is one of the weaker mechanisms contributing to fibre and matrix adhesion. It occurs when across the interface, the difference in electrostatic charge between the fibre and the matrix is present [267]. This phenomenon can be responsible for creating attraction bonds between both materials. Nevertheless, the strength of such bonds is highly dependent on the charge density [268]. As such, electrostatic attraction cannot be considered as a significant constituent of the adhesion mechanism and can be even further reduced by discharging in the presence of a strongly polar solvent, such as water. On the other hand, the application of coupling agents to the fibre surface substantially increases electrostatic attractions [266-268].

Chemical bonding is the most widely accepted mechanism for bond creation between the fibre and matrix [279-281]. Multiple theories are identifying the chemical phenomenon as the primary source of adhesion. For example, the physical adsorption theories rely on either Van der Waal's forces or the reaction between an acid and a base. In contrast, others identify primary covalent bond across the interface to be responsible for the physical interactions between the two constituents [267]. As a result, a wide range of coupling agents has been produced to enhance the chemical bonding between compatible chemical groups on the fibre surface and within the matrix. Such coupling agents are often applied to the fibre surface during the manufacturing stage as a part of chemical sizing [266-268].

Mechanical bonding is the last interfacial interaction contributing to fibre-matrix adhesion and is mainly based on the mechanical interlocking between both materials. It arises from the interactions between asperities on both sides of the interface and is often connected with the surface roughness and friction forces [266]. As such, the strength of this interaction is much stronger in the most common loading mechanism of longitudinal shear rather than transverse tension. It is widely accepted that the quality of mechanical binding between fibre and the matrix depends on the fibre surface roughness and the fibres' wettability [266]. In addition, except for geometrical aspects of mechanical bonding, internal stresses present within the composite can influence adhesion due to mechanical bonding. Such stresses are often related to the mismatch of thermal expansion coefficients between the thermoset composite constituents during heating or cooling, which results in the creation of the compressive radial residual thermal stresses [282-286]. The combination of surface geometrical features and internal stresses is assumed to restrict interfacial sliding [267].

4.1.2 Micromechanical characterisation of fibre-matrix interface

Previous studies have proven a significant impact of interface properties on the mechanical characteristic of fibrous composites. Thus, it became important to analyse and quantify the interaction between matrix and fibrous reinforcement [267, 287]. As a result, a wide range of testing techniques has been developed, with the two main groups being micromechanical and macromechanical testing. Distinguished by the nature of samples and the scale of testing, the micromechanical techniques involve a single fibre sample and aim at direct measurements of the interfacial properties [267, 287]. On the other hand, the macromechanical methods incorporate bulk composite specimens and measure interlaminar/intralaminar properties, which are later used to derive interfacial properties. In addition, both testing techniques often focus on measuring the interfacial shear strength (IFSS) between the matrix and composites, which represents the shear stress required to produce shear failure at the interface [267]. This section, however, will focus only on micromechanical testing techniques including single fibre microbond, pull-out, fragmentation push-out and push-in tests.

The microbond test is one of the most popular testing methods to measure the interfacial shear strength values and was first introduced by Miller et al. in 1987 [288]. It involves the shearing of a small matrix droplet from the surface of a single fibre in the presence of external forces. The resulting maximum force is later used to calculate the IFSS value by relating it to the sample's geometrical features such as embedded length or droplet diameter [267, 287]. Nevertheless, this testing technique suffers from a few limitations, mostly resulting from the nature of samples and testing procedures used. As a result, the scientists highlighted the need

for producing consistent samples in terms of size and the symmetry around the fibre to reduce the scatter among the results. In addition, some studies also suggested the dependency of the mechanical interface properties on the sample size. By changing the droplet diameter, the concentration of the curing agent within the matrix can be affected, and the impact of the variation in fibre sizing can be enlarged [288, 289]. Multiple studies have been devoted to measuring the impact of sample features and testing parameters (such as vice angle and gap size) on the microbond results [290, 291]. Regardless of the limitations posed, the microbond test is still widely used in the research community due to its' sensitivity and production of results comparable to the full laminate composites [267, 283, 285, 286, 292-296].

The single fibre pull-out test (SFPT) is similar to the microbond test, with the main difference being the scale and geometry of the tests. In SFPT, the single fibre is embedded in the matrix plates or discs, resulting in a significantly larger embedded interfacial area than in the microbond case [297]. Upon the fixture of a matrix, a tensile force is applied to the fibre until the full debond of the fibre is achieved. The IFSS value is later calculated using maximum recorded force and embedded area. The SFPT is widely used for the fibre reinforced thermoplastic composite, however other matrix systems have also been investigated via this technique [298-300]. Similarly, to the microbond test, the SFPT also presents certain issues around the sample preparation (straight alignment of the fibre) and the measurement itself (inaccuracy in embedded length measurements). As a result, a series of studies have analysed the accuracy and suitability of this technique [301-304].

A single fibre fragmentation test (SFFT) can also be used to quantify the adhesion between the fibre and the matrix. In principle, the test requires tensile stress to be applied to the sample, which includes a fully embedded single fibre. The stress is transferred to the fibre through the interfacial shear strength until the tensile strain is high enough to fracture the fibre. Further increase in the stress value results in subsequent fibre fractures until all the fibre parts reach the critical fibre length and become too short to fracture any further [305]. The combination of critical fibre length, fibre diameter and fibre strength is then used to calculate the average interfacial shear strength. The main drawbacks of this technique involve its' susceptibility to the impact of the fibre sizing on the interphase region chemistry and lack of data reduction parameters enabling to link the changes in surface chemistry and mechanical properties of created composites [305, 306]. Even though the fragmentation test has been widely used to measure the interfacial properties of natural fibre and carbon fibre composites [307-310].

The single fibre push-out test (SFPoT) is another technique used to measure the mechanical properties of fibre and matrix interface. It requires a tungsten carbide punch to apply the force

onto the fully embedded fibre until it is completely pushed out of the matrix [311]. The resulting load response allows measuring the debonding energy of the interface between the matrix and the behaviour of the fibre following the interface failure. Due to the way the load is applied to the fibre, this method is mainly used for metallic matrix or intermetallic matrix composites testing [47, 312-314]. Small fibre size and difficulty in preparing required specimens are the main reasons for little work done with other composites.

The single fibre push-in test is the last technique used to measure the adhesion between a single fibre and matrix. Such test is performed by applying the load to an individual fibre embedded in the matrix until achieving the fracture of the interface. Following the test, the IFSS value can be calculated from the critical load measured at the onset of interface failure through the shear-lag model [315-317]. Previous studies focused on investigating the qualitative values of ceramic, metal and polymer composites. Additionally, the investigation of the glass fibre and epoxy composites revealed the similarity of IFSS values derided by the means of the push-in and the pushout tests [317].

As presented before, each of the testing methods presents certain positives and negatives when it comes to interface analysis, both of which are strongly dependent upon the composite's constituents. Nevertheless, it should be highlighted that there is still a major discussion regarding the accuracy of the micromechanical testing techniques and how physical the obtained results are when scaled up to the macro-level [318, 319]. For the purpose of this study the microbond test was chosen to be the most suitable testing technique as the deposition of aerogel droplets around the fibres was found to produce the most uniform samples and largest handling flexibility compared to other methods described in this section.

4.1.3 Impact of matrix porosity on interfacial properties

At the moment of writing this thesis, there has not been a published study investigating the micromechanical interfacial properties of any aerogel/fibre composite. As a result, there is no clear reference point for this study. Nevertheless, limited work has been conducted in assessing the impact of matrix porosity on the other composite systems.

Such investigation often focuses on the impact of porosity on macromechanical properties such as interlaminar shear strength (ILSS) mainly due to its' sensitivity to the void presence and the easiness of sample preparation [320-323]. Even though those investigations rarely discuss the failure mechanism caused by the presence of voids, the consensus is reached that by increasing the pore volume within the composites, its mechanical and interlaminar properties are deteriorating. On this scale, pores are identified as stress concentration points

whin enable crack creation and then propagation within the matrix resulting in simple or multiple shear failure. However, there is still a debate regarding the magnitude of the impact, as various material combinations and testing techniques result in significant discrepancies [322]. For instance, Costa et al. have detected an almost 35% decrease in interlaminar shear strength of carbon/epoxy composite with only 5.6% of the void content [322]. On the other hand, Mouritz claims only a 12% reduction for the same void content in the glass fibre and polyester resin [320]. Thomason has tested a wide range of fibre and polymer combinations, highlighting the impact of material properties on the void effects [324]. In addition, few theoretical models have also been derived to predict the fracture stress of composites with the presence of voids, all indicating inferior mechanical properties with increasing void content [325-327].

Much less work has been done to evaluate the impact of pores or voids on the microscale interfacial properties of fibrous composites. Ali and Singh have used the pull-out test to investigate the interfacial properties of glass fibre and gypsum plaster [328]. By altering the water/plaster ratios, they were able to control the porosity of the matrix materials and have shown a decrease in resulting pull-out forces when higher porosity samples were used. In addition, the authors correlated the porosity of the matrix and the critical length of embedment, allowing to utilise the ultimate strength of the fibre in each scenario [328]. A similar trend has also been observed by Sarıdağ et al., who achieved lower pull-out strength values of glass fibre posts when increasing the porosity of cement matrix [329]. Both studies suggest that the increase in matrix porosity results in deterioration of composites' interfacial shear strength. Nevertheless, due to the investigation's length scale, it is extremely difficult to correlate such behaviour with any particular change in the failure mechanism. However, it can be suspected that if the high porosity of the matrix material is also present at the interfacial region, it can reduce the adhesion area between the fibre and the matrix, effectively limiting the number of chemical interactions and mechanical interlocking between them. Such a hypothesis can be somehow supported by analysing the reversed scenario when high porosity reinforcements are combined with a solid matrix. As presented by Nganga et al., who have combined porous E-glass-fibre tissue and photopolymerisable resin system [330]. The resulting push-out forces were almost doubled when the porosity was increased from 10% to 60%, and the higher level of mechanical interlocking between the composite constituents was given as the main reason for such occurrence [330].

4.1.4 Conclusions of literature review

The properties of the interface between the constituents of the fibrous composites have been proved to significantly affects the overall performance of the resulting material. They are based on interfacial interactions such as adsorption and wetting, electrostatic attraction, interdiffusion, chemical bonding, and mechanical interlocking, all of which contribute to interfacial adhesion. As a result, a wide range of testing techniques has been developed to evaluate the mechanical properties of the interfaces, with the two main groups being micromechanical and macromechanical testing. Both testing techniques focus on measuring the interfacial shear strength (IFSS) between the matrix and composites, representing the shear stress required to produce shear failure at the interface. Finally, many studies have proven the negative impact of matrix porosity on interlaminar and interfacial properties of fibrous composites. With the increasing presence of porosity, the interlaminar and interfacial shear strengths have been significantly reduced. However, the composite constituents' properties were the primary factor determining the extent of changes.

4.2 Experimental

4.2.1 Fibrous reinforcement

The fibres used in this investigation included:

- Glass fibre - water-sized (bare) 1200 tex E-glass fibre manufactured by Owens Corning from a 2000-hole pilot bushing.
- Polyethylene terephthalate (PET) fibre - Airbleed 10 manufactured by Aerovac Systems Keighley Ltd.
- Carbon fibre – unsized 12k HexTow AS4C carbon fibre supplied by Hexcel, Duxford, UK.

Those fibres have been selected as each one of them covers different fibre diameters range with carbon, glass and PET fibres having an average diameter of respectively 6 μm 18 μm and 45 μm.

4.2.2 Aerogel synthesis

In order to fully control the manufacturing of the aerogel samples, both silica and polyimide aerogels were synthesised in the Advanced Composites Group laboratory using the procedure described in the following sections.

4.2.2.1 Silica aerogel

In order to have better control over the gelation time, the two-step catalysis process described by Jia et al. was used in the preparation of the silica aerogel, as presented in Figure 4-2 [331]. This process has been selected in order to completely control the gelation time of SiO_2 hydrosol and thus develop a method allowing to deposit hydrosol droplet around the fibres. A sodium silicate solution was diluted with distilled water using 1:4 volume ratio. Afterwards, under constant stirring (on a magnetic stirrer) at 500 rpm, a 6 mol/L solution of hydrochloric acid was added until the solution has reached the pH value of 2. A 1 mol/L solution of ammonium hydroxide was then added until reaching a pH value between 3 and 3.5. After pouring the hydrosol into the desired mould, the gelation process was completed after 1 hour. Then 24 hour ageing of the hydrogel was performed under atmospheric conditions followed by a solvent exchange including a submersion of the hydrogel sample in ethanol and n-hexane for 24 hour respectively to obtain an alcogel. Next, surface treatment was carried out by adding the alcogel samples into a TMCS: n-hexane solution mixed with the volume ratio of 1:1 for 24 hour at room temperature. Finally, the sample was dried under an ambient pressure for 4 hour at each temperature of 60 °C, 80 °C, 100 °C and 120 °C, completing the creation of a silica aerogel sample [331].

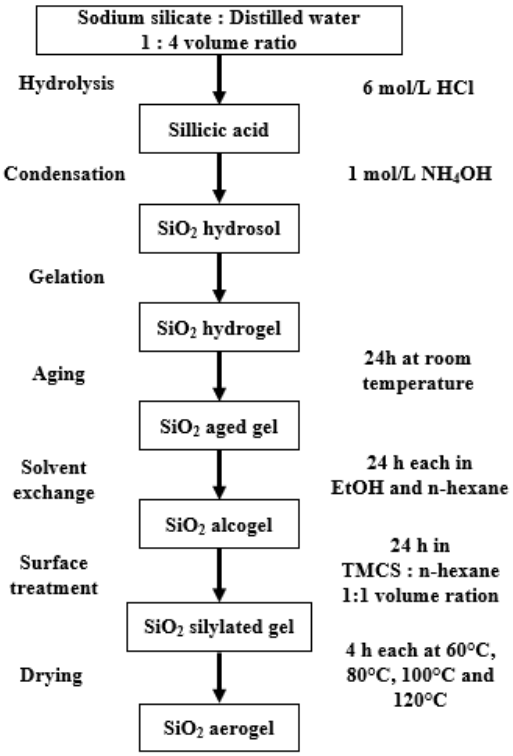

Figure 4-2 Schematical representation of the silica aerogel synthesis process [331].

The chemicals used in the silica aerogel synthesis were all sourced from VWR International. They included sodium silicate in aqueous solution (Si 26.6 wt%, SiO_2 8 wt%) as a precursor, 30% hydrochloric acid (VWR Chemicals) as acid catalyst and 28% ammonia solution (VWR Chemicals) as a base catalyst. Furthermore, 96% ethyl alcohol (Acros Organics) and 95% n-hexane (VWR Chemicals) were used as exchanging solvents, while trimethylchlorosilane (produced by Merck KGaA) was a silylating agent.

4.2.2.2 Polyimide aerogel

The synthesis of polyimide aerogel was a much less complicated process and involved preparation of the polyamic acid by mixing dimethyl sulfoxide (DMSO) with dibenzoylmethane (DMB), octadecylamine (ODA) and 1,3,5-tris(4-aminophenoxy)benzene (TAPOB) in a chemical reactor. Due to the proprietary claim, no further information regarding polyamic acid synthesis can be included. Imidization of the polyamic acid was carried outwith the addition of 2-methylimidazole and benzoic anhydride into the polyamic acid, as presented in Figure 4-3. The solution was then transferred into the desired mould, and the gelation process usually took about 20 minutes later, followed by a 24 h ageing under the room conditions. Afterwards, the sample was moved into acetone solution for 24 hour solvent exchange. Finally, the polyimide alcogel was dried under an ambient pressure for 1.5 hour at 200 °C and 12 hour at 300 °C, creating a final polyimide aerogel sample.

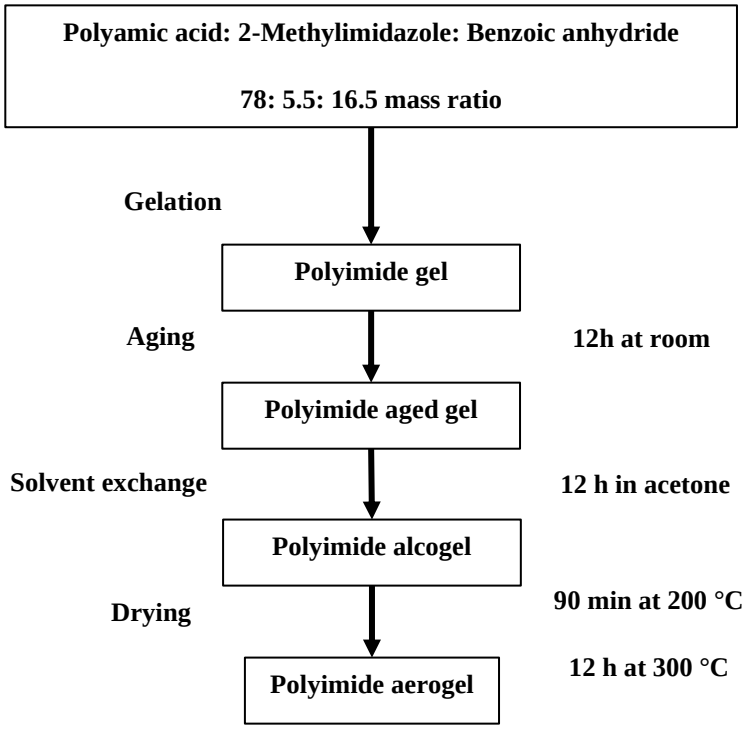

Figure 4-3 Schematical representation of the polyimide aerogel synthesis.

The chemicals used in the polyimide aerogel synthesis were all sourced from VWR International and included 2-methylimidazole (Merck) and benzoic anhydride (Acros Organics). Furthermore, 99% acetone (VWR Chemicals) was used as exchanging solvent.

4.2.3 Characterisation of aerogel internal structure

Following the synthesis of aerogel samples, their internal structure was investigated to validate and assess their usefulness for studying aerogel-fibre interface. Three testing methods included mercury intrusion porosimetry, gas adsorption and gas pycnometer.

4.2.3.1 Mercury intrusion porosimetry

To investigate the pore size, pore-volume, bulk/apparent density and porosity of created aerogels, a mercury intrusion porosimetry (MIP) was conducted using Quantachrome poremaster 60 and following the standard ASTM UOP578 – 11. During the test, a sample was placed in a pressurised chamber, filled with mercury. Next, pressure was gradually increased, forcing the mercury to intrude into aerogel pores. As pressure increased, smaller and smaller pores were invaded, resulting in inter-particle pores and the intra-particle pores being filled with mercury. For this investigation, a low-pressure station was used to impose a maximum of 250 MPa pressure for pore size measurements ranging from over 1100 µm micron to 0.0064 µm pore diameter. The example data plot produced by MIP is presented in Figure 4-4. The figure includes a logarithmic differential pore volume distribution as a function of pore diameter, which reveals the pore size distribution of tested sample. By presenting data in such fashion a more detailed overview of internal structure of the material can be achieved rather than by stating the total porosity or average pore size.

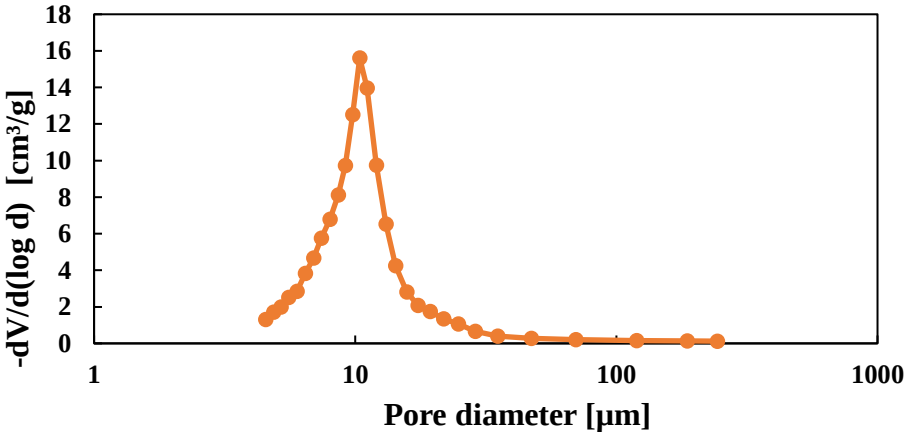

Figure 4-4 Example of MIP pore distribution of polyimide aerogel synthesised in this study.

4.2.3.2 Gas adsorption

For the description of gas adsorption technique please refer to the Section 3.2.3.

4.2.3.3 Gas pycnometer

Another technique allowing to measure the total porosity of various materials is gas pycnometer, which measures a volume of solid samples of any shapes. The equipment measures a pressure difference by expanding a known quantity of gas into respectively an empty chamber and sample-filled chamber. The pressure difference between two chambers and the measured volume of the empty gas chamber can determine sample volume using Boyle's Law. Afterwards, the skeletal density of the sample can be calculated by dividing the mass of the sample by the volume obtained through pycnometer. Finally, by using equation below a porosity (φ) can be related to the ratio between the bulk (ρ_b) and skeletal density (ρ_s).

$$\varphi = (1 - \frac{\rho_b}{\rho_s}) \times 100 \qquad \text{Eq. 40}$$

In this study, the MicroUltraPycnometer 1202 produced by Quantachrome provided a skeletal density of aerogel samples. The ISO12154:2014 standard was followed, and a gas pressure of 20 psi was used.

4.2.4 Single fibre tensile test

Single fibre tensile test was carried out by following the ASTM C1557-03. A paper card frame was prepared using 250 g/m^2 grade paper, as presented in Figure 4-5. Afterwards, the double-sided tape was placed about 10 mm from the edge of the cut-out window. Individual fibres were separated from their fibre bundle and laid across the cut-out window before being attached to both pieces of tape. Next, the Loctite Gel Superglue was applied to the fibre around the window edge, permanently attaching it to the paper frame. 20 mm gauge length was selected for this study, and at least 30 single fibre samples was prepared for each test.

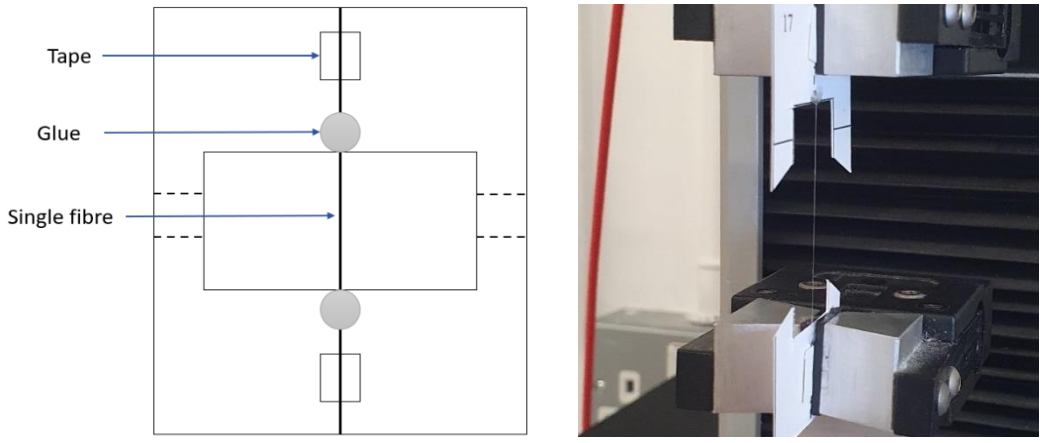

Figure 4-5 Left: Schematical representation of single fibre tensile test sample. Right: Single fibre tensile sample during the test.

Following the placement of fibres within paper frames, the diameter of each fibre was measured. As a result, each fibre was photographed using an Olympus GX51 optical microscope under 50 magnification (as presented in Figure 4-6), and ImageJ software was used to measure fibre diameter. Again, the assumption about the circularity of measured fibres was used for simplicity. Nevertheless, it should be highlighted that such assumption is more appropriate for glass fibres which presents circular and constant cross section across the fibre length. In case of carbon and PET fibres such simplification can introduce an error into the evaluation of fibre modulus and strength due to the possible uneven polygonal cross-sections.

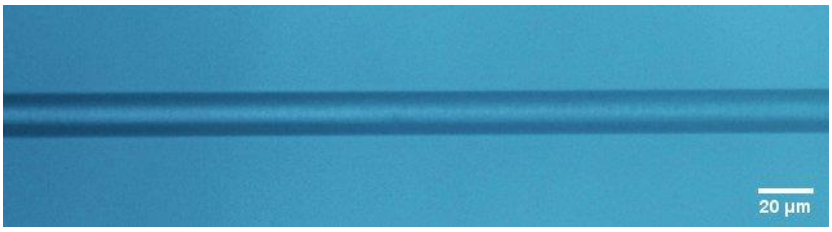

Figure 4-6 Image of glass fibre captured using Olympus GX51 optical microscope.

A tensile test of a single fibre was conducted using Testometric M250-2.5CT equipped with a 5 N load cell. The strain rate of 1.5 %/min under room conditions was used, and the experimental set-up of the tensile test is presented in Figure 4-5.

4.2.5 Microbond sample preparation and testing

Microbond test requires a aerogel droplet of a micro-scale size to be formed around a single fibre. In order to achieve this, some adjustments had to be introduced, and the sample preparation and testing techniques are discussed in the sections below.

4.2.5.1 Silica aerogel microdroplet

The preparation of microbond samples commenced with deposition of cement drops on the especially prepared polyamide frame covered with a non-sticking tape as presented in Figure 4-7. The cement used was a premixed, quick drying aluminium oxide cement. Before cement drops were allowed to dry the single fibre has been manually selected from the fibre bundle, stretched across two drops and pushed into the cement. Afterwards, the cement was left to solidify for 4 hrs at room temperature, however the process could be shortened to 20 min by placing the samples into oven at 80 °C. Once the cement solidified, the fibre has been cut in the middle creating two separated fibres. It is important to highlight that an attempt have been also made to deposit the fibres onto metal washers, however due to the corrosive properties of chemicals used in further steps of the aerogel synthesis this idea was abandoned.

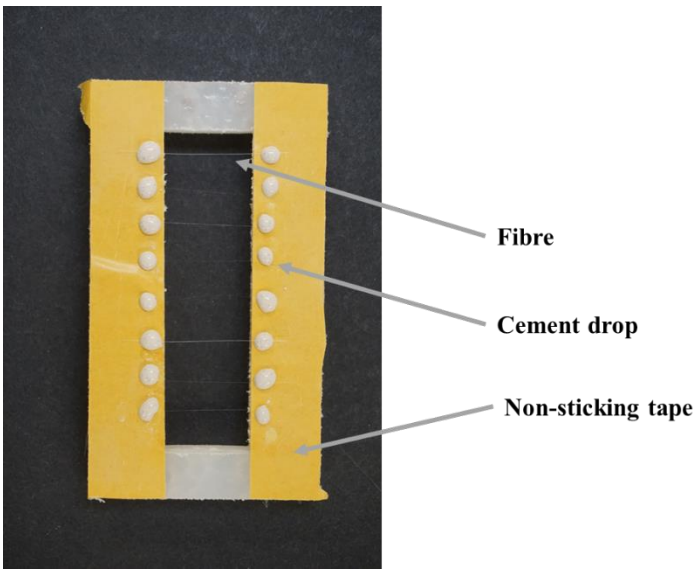

Figure 4-7 Polyamide frame setup used to prepare single fibre specimens.

Following the preparation of single fibre specimens, the preparation of the aerogel solution was required. After the mixing of sodium silicate solution with hydrochloric acid and ammonium hydroxide, the solution was left to thicken for 5 to 10 minutes (depending on the pH value of the solution) otherwise the aerogel sol droplets would fall off or slide along the fibres. Once the hydrosol viscosity was sufficient to create strong enough surface tension, the droplets of SiO_2 hydrosol were deposited on single fibre samples as presented in Figure 4-8.

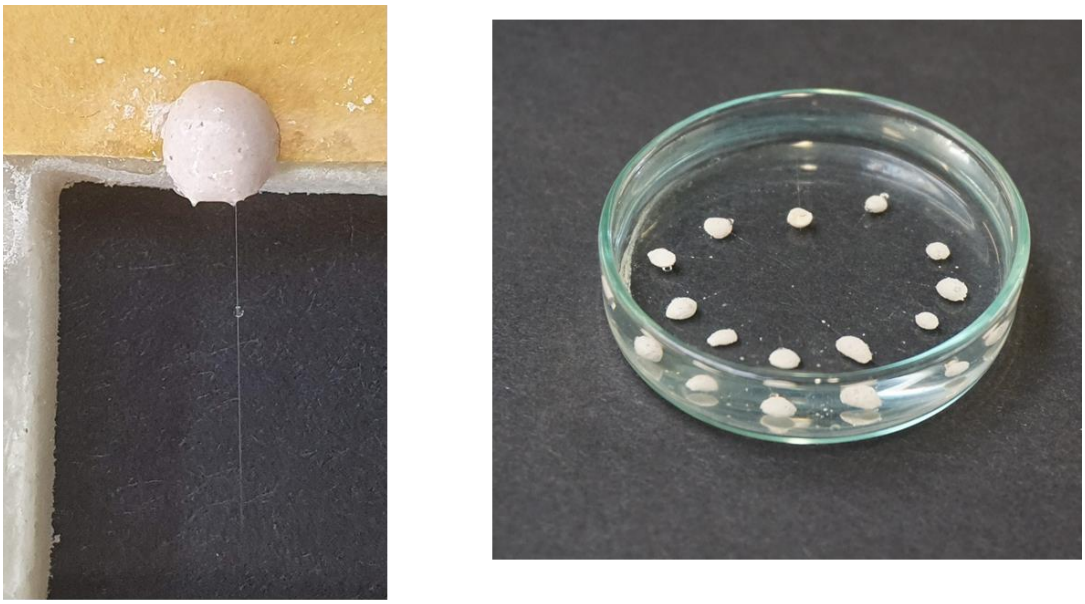

a) **b)**

Figure 4-8 a) SiO_2 hydrosol droplets deposited on the glass fibre, b) glass petri dish used for the movement of the sample between different stages of solvent exchange.

It was achieved by repeatedly dipping and removing the fibres from the hydrosol solution. Following the creation of the droplets, the samples were let to cure for 2 – 5 min before being moved into an ethanol bath, even though the bulk silica aerogel synthesis process required a 24 hrs curing time. Such a decision was caused by the small volume of hydrogel droplets deposited on the fibres. Together with large surface-to-volume ratio, the droplets tend to dry out once left in ambient conditions for more than 5 min (depending on the initial droplet size). If the time at ambient conditions was exceeded the complete collapse of aerogel structure was observed and the deposition of silica crystals on the fibre surface occurred. Further steps of solvent exchange and surface treatments have been conducted as described in the aerogel synthesis procedure in 4.2.2.1. However, when moving the samples from respective solvent exchange solutions they have never been removed from the aqueous environment. Instead, the shallow glass petri dish containing samples still submerged in the ethanol has been directly placed in larger container filled with n-hexane. Such approach allowed to reduce the manual handling of the samples and avoid possible drying of the sample during the move. Finally, following the surface treatment, the samples were placed in a sealed jar and moved to the oven for drying. All the samples were dried under an ambient pressure for 4 hours at each temperature of 60 °C, 80 °C, 100 °C and 120 °C. Once samples were prepared the cement drops were glued to the paper cards with a circular hole so they could undergo the microbond test. An example of aerogel microbond sample is shown in Figure 4-9**Error! Reference source not found.**, please be aware the images presented in this chapter are to illustrate the sample preparation process only and represent various samples.

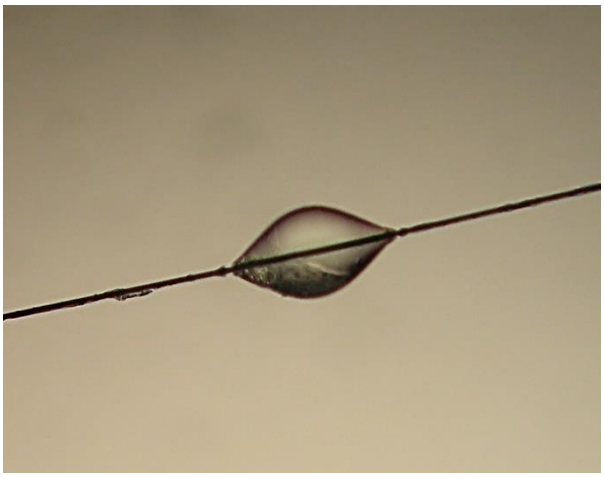

Figure 4-9 Silica aerogel microbond sample deposited on a carbon fibre.

Even though the droplets were successfully deposited around the fibres, certain issues might still affect their suitability for the microscale testing. The first one regards the effect of the

aggressive chemicals used during the silica aerogel synthesis on the fibres' surface, as all fibres were placed for 24 hrs in ethanol, n-hexane and TMCS. As presented by Son et al., a submersion of PET fibres in the pure ethanol for even 30 min roughened the surface of the fibre [332]. Additionally, Lee and Jang treated glass fibre in the ethanol for 24 hrs which removed some sizing from the glass fibre surface and weaken the adhesion force between glass filaments [333]. Although, the combined impact of all mentioned chemicals on the glass, carbon or PET fibre surface has not been tested, it is possible that they might affect the physical as well as the chemical properties of fibres' surface. Nevertheless, the fibres would most likely undergo a similar treatment during a production of a bulk silica aerogel blankets, as such the effects of these chemicals would also be present in a bulk material. Another issue regards the difference between the droplet properties and the aerogel's macroscale properties. Previous studies on the polymer samples have shown that using small quantities of the matrix material to create a microbond samples can possibly alter the chemistry of the material. Strong correlation between droplet size and the amount of curing agent was found, resulting in varying matrix properties [351]. Such property difference due to the scale difference could be even more substantial for the aerogel samples as most likely it would not only change the chemical composition of the material but also the impact of each synthesis step on the internal structure of the aerogel. As such, smaller size of the samples produced for the microbond test could improve solvent exchange and increase the ratio of the material subjected to the surface treatment. Overall, it is highly possible that by using substantially smaller aerogel quantities than for the manufacturing of a bulk aerogel blankets a significantly different internal structure of the material could be achieve and thus the sample might not correctly replicate the macroscale properties of the silica aerogel.

4.2.5.2 Polyimide aerogel

Due to the lack of corrosive chemicals in polyimide aerogel synthesis, the single fibre was attached to two washers using double-sided tape. Afterwards, the cement was used to attach the fibre to the washer permanently as presented in Figure 4-10. Then the cement was left to solidify for 4 hrs at room temperature, however the process could be shortened to 20 min by placing the samples into oven at 80 °C. Following cement solidification, the fibre was cut in the middle to produce two separated fibres.

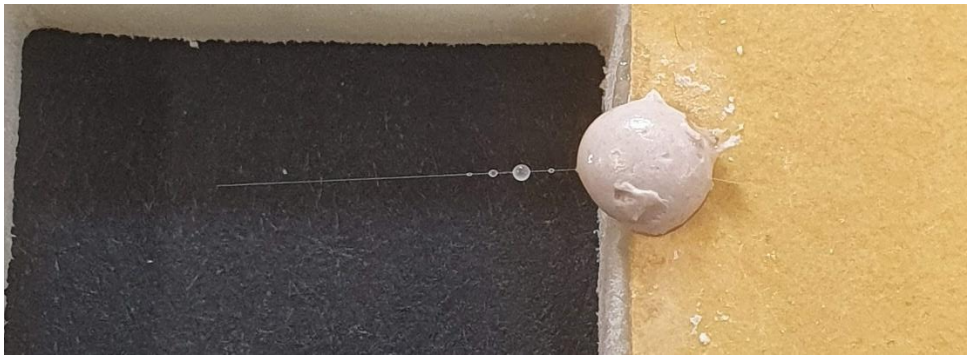

Figure 4-10 PI aerogel solution deposited on glass fibre.

Following the preparation of single fibre sample the PI sol has been prepared according to the 4.2.2.2. As a result, the 2-methylimidazole and benzoic anhydride were added into the polyamic acid and in order to prepare a full set of 30 samples a 10 ml of the sol was sufficient. Due to the lower viscosity of PI sol it was possible to deposit the droplets on the fibre immediately after mixing the chemicals. Thus, prepared fibrous samples were repeatedly dipped and removed from polyimide solution until the droplets have been formed. Afterwards, the sample was left to age for 12 hour in room conditions and then fully submerged into acetone solution for 12 hour in order to perform single solvent exchange. Once removed from the acetone, the polyimide alcogel was dried under at a room temperature for 1 hr. This step differs from procedure recommended for a bulk material preparation as it caused a significant degradation of the droplets. As a result, when incorporating elevated temperatures as recommended in the case of bulk materials the droplets has experienced a gradual shrinkage finally leading to separation of the droplet from the fibre. Together with a black discoloration emerging on the sample, both signs suggested the occurrence of thermal degradation of the sample. The polyimide aerogel sample created in the described process is presented in Figure 4-11.

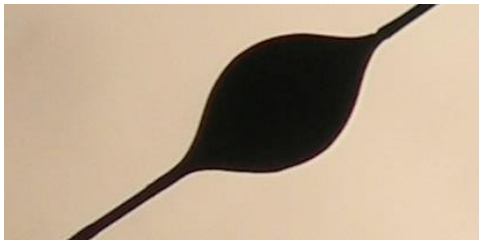

Figure 4-11 Polyimide aerogel sample deposited onto glass fibre.

4.2.5.3 Microbond testing

Following the creation of microbond samples, the images of droplets were taken using Olympus BX51 microscope, and ImageJ software was used to measure fibre diameter (D_f), droplet diameter (D_d) and embedded fibre length (L_{eb}) as presented in Figure 4-12.

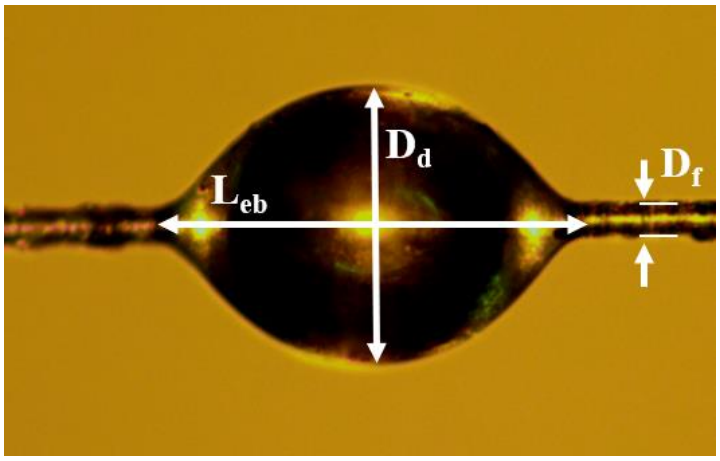

Figure 4-12 Example of PI aerogel droplet on GF with dimensions measured for microbond test.

The microbond tests were conducted using Instron 3342 universal testing machine equipped with a 10 N load cell. Either washer or card frame was suspended on the hook above shearing blade, and adjustable shear blades were moved until just being in contact with the fibre. Afterwards, the height of the droplet was adjusted to be directly under the blades, as presented in Figure 4-13.

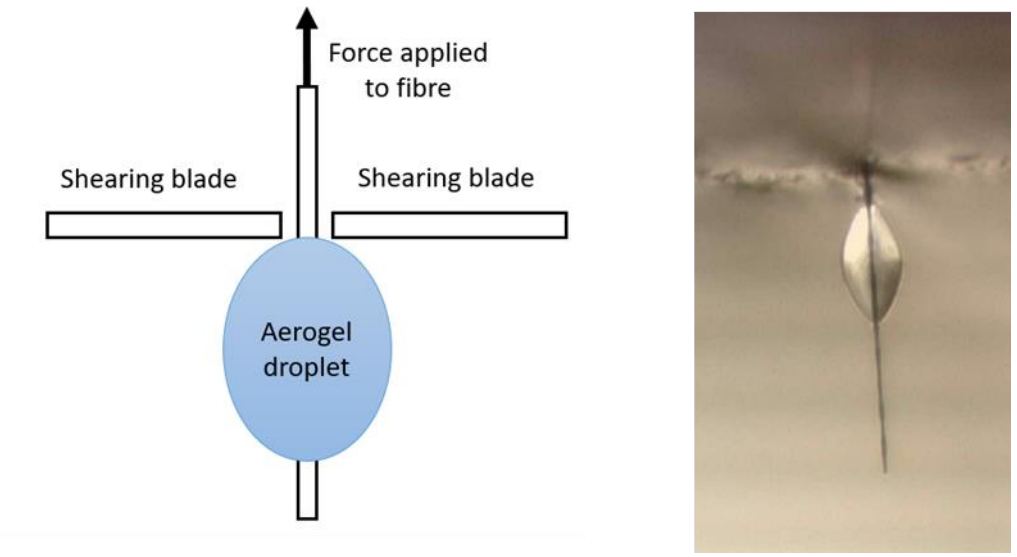

Figure 4-13 Left: schematic representation of microbond test. Right: the actual image of the microbond test.

When the test commenced, a fibre displacement speed of 0.1 mm/min was used, leading to the droplet being sheared off the fibre by blades. During the microbond test, the shear force was constantly recorded as a function of displacement as presented in Figure 4-14.

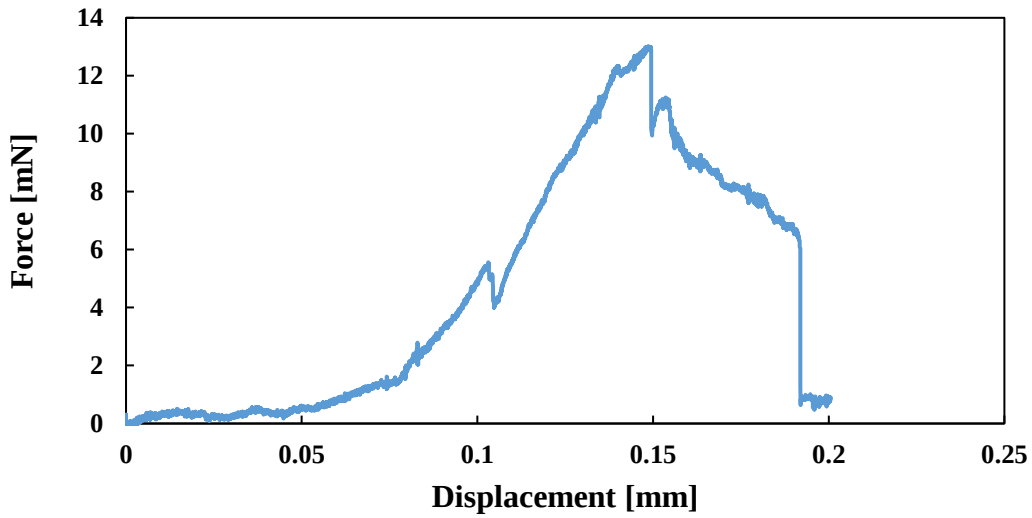

Figure 4-14 Example of force and displacement graph produced during microbond test.

Once the force reached a peak, a full debond of the droplet from the fibre is achieved. Followed by a steady shear force decrease until the test was completed. The sample was constantly observed during the test duration using a 45x magnification microscope with a DCM140 video camera. Finally, an apparent interfacial shear strength (IFSS) was calculated using the following equation:

$$IFSS = \frac{F_{max}}{\pi D l_{eb}} \qquad \text{Eq. 41}$$

Fmax is the highest force achieved during the microbond test, D is a fibre diameter, and l_{eb} is fibre embedded length.

4.2.6 Image analysis

Three different image techniques have been used to visually inspect the aerogel samples and fibre interface throughout this study. They include optical microscopy, scanning electron microscopy and atomic force microscopy.

4.2.6.1 Optical microscopy

To capture the diameter of fibres used and the shape and size of the created aerogel droplet, the optical microscopy images of aerogel samples were captured using Olympus BX51 microscope under transmitted light in brightfield with a magnification of 10 as presented in Figure 4-15.

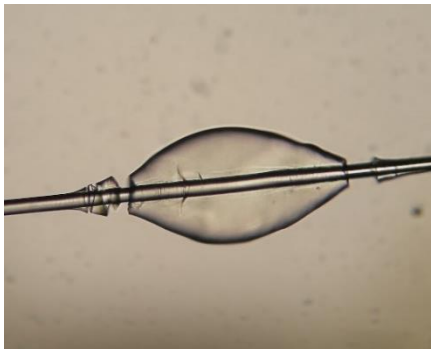

Figure 4-15 The example of silica aerogel droplet deposited on glass fibre obtained by optical microscopy.

4.2.6.2 SEM

Scanning electron microscopy (SEM) images were taken to capture the external and internal structure of aerogel samples and the deboned fibre surface following the microbond testing, as presented in Figure 4-16. The samples were initially coated with a layer of gold, and images were taken using 15 kV accelerating voltage in a HITACHI SU-6600 machine.

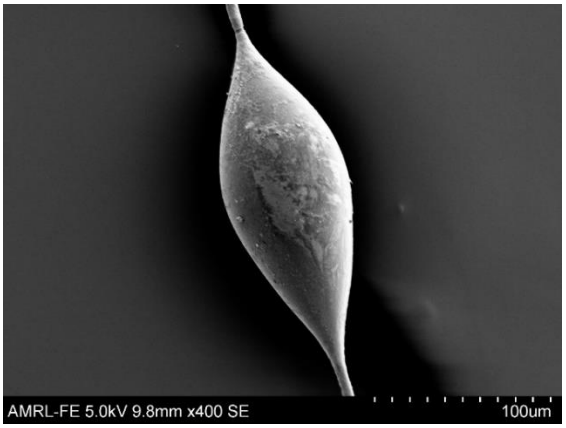

Figure 4-16 The example of silica aerogel droplet deposited on glass fibre obtained by SEM microscopy.

In addition, while performing the SEM imagining, the Oxford Inca Wave 700 Microanalysis System with Energy + Software was used to perform elemental analysis. As a result, the fibre surface previously embedded in the droplet was analysed following the microbond test to identify any remaining aerogel residuals.

4.2.6.3 Atomic force microscopy

Atomic force microscopy (AFM) was used to investigate the surface topography of single fibre by the Bruker Innova instrument. Fibre surface before and after the microbond test was analysed to identify any remaining aerogel residuals and quantify any change to fibre surface roughness. In order to overcome the issues associated with fibre analysis, such as curvature

and micro-scale dimensions, a single fibre was taped to a scanning disc using double-sided tape and imaging was conducted in tapping mode using a low-force probe provided by the machine manufacturer. The Novo Drive software was used to capture and post-process the images as presented in Figure 4-17.

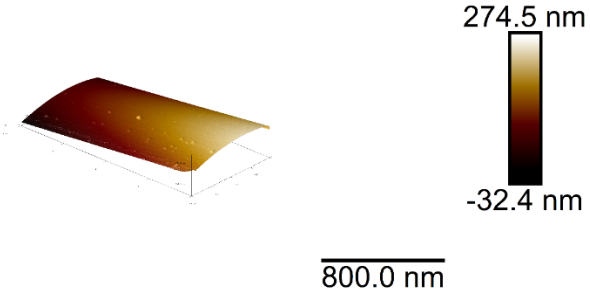

Figure 4-17 The example of glass fibre surface obtained by the AFM scanning.

4.3 Results and discussion

The effect of fibre reinforcement type on aerogel adhesion was measured in this work using the microbond test. Before this can be achieved, the mechanical properties of fibrous reinforcements were measured using a single fibre tensile test. Later the visual inspection of microbond droplet formation was conducted and followed by measuring internal properties of bulk aerogels. Finally, with all the information about sample constituents, micromechanical testing is performed alongside visual inspection of tested samples.

4.3.1 Single fibre characteristics

Table 4-1 presents tensile strength and Young's modulus of the fibres used during this study.

Table 4-1 Tensile strength and modulus of fibres used for the aerogel interface study together with their confidence limits.

	Tensile strength [GPa]	**Tensile strength 95% confidence limits [GPa]**	**Young's modulus [GPa]**	**Young's modulus 95% confidence limits [GPa]**
Glass fibre	0.94	0.14	55.74	2.87
PET fibre	0.27	0.03	5.28	0.56
Carbon fibre	4.07	0.57	208.42	21.11

It can be seen from Table 4-1 that carbon fibre has the highest tensile strength and Young's modulus, followed glass and PET fibres. Obtained results are slightly lower than experimental results from other studies or manufacturer data [334]. This can result from the lack of sizing in case of glass and carbon fibres and fibre damage created during the fibre manufacturing process (e.g. roving) or handling during sample preparation. Additionally, the PET fibres have undergone extra postproduction steps to turn them into blankets, reducing their mechanical

performance even more. Even though the PET fibres present the lowest strength and modulus values, it is compensated by a high ductility with up to 50% of failure strain. It should also be highlighted that all the fibres have been stored for many years before being used in this project, which could also affect their mechanical properties. Especially in case of glass fibre previous studies suggested lowering of the fibre modulus due to the slow moisture diffusion into the glass fibres resulting in 20% reduction from the initial modulus after 25 years [335]. Considering expected low IFSS values for all three types of fibre, the results in Table 4-1 suggest that the strength of these fibres should be high enough to avoid fibre breakage during microbond testing. The prevention of fibre breakage during the microbond test is critical as it was previously shown that the this can cause artificial bias in the microbond results [336]. Figure 4-18 shows the SEM images of surfaces of all fibre used in this study.

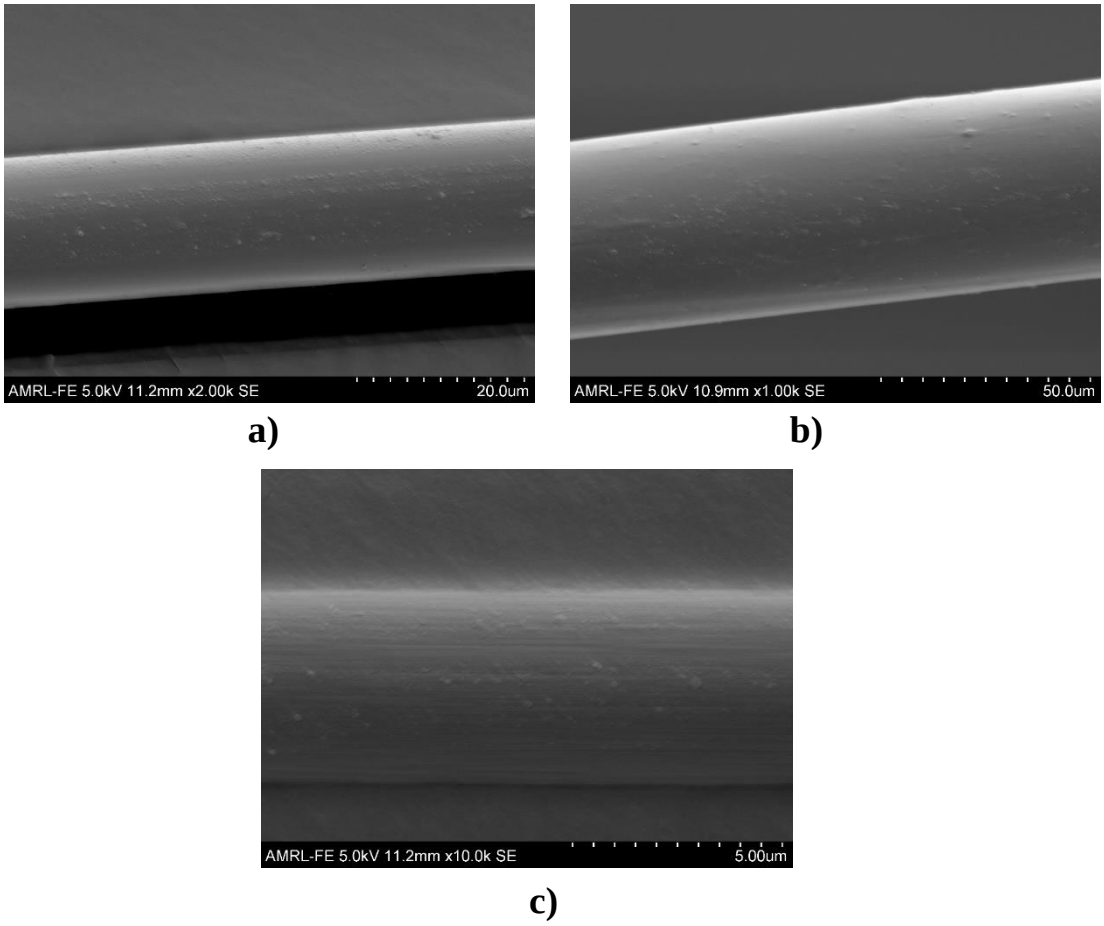

Figure 4-18 SEM images of fibres used for the aerogel interface study. Images presents a) glass fibre b) PET fibre and c) carbon fibre.

The images reveal that both glass and PET fibres have relatively smooth surface. On the other hand, the carbon fibre surface is marked with multiple groves. As previously reported, they originated from the manufacturing process during which phenomena such as double diffusion,

stretching, the effect of interfacial tension and surface crystallisation caused surface deformation [337, 338]. Finally, some impurities can be noticed on all fibre surfaces. In case of PET fibre, it might be a binder used to prepare a fibrous blanket, however, presence of impurities on unsized glass and carbon fibres can also indicate fibre contamination during the sample preparation process or inadequate fibre storage. Similar observations can be derived from the Figure 4-19, which includes AFM scans of fibres used for the aerogel interface study.

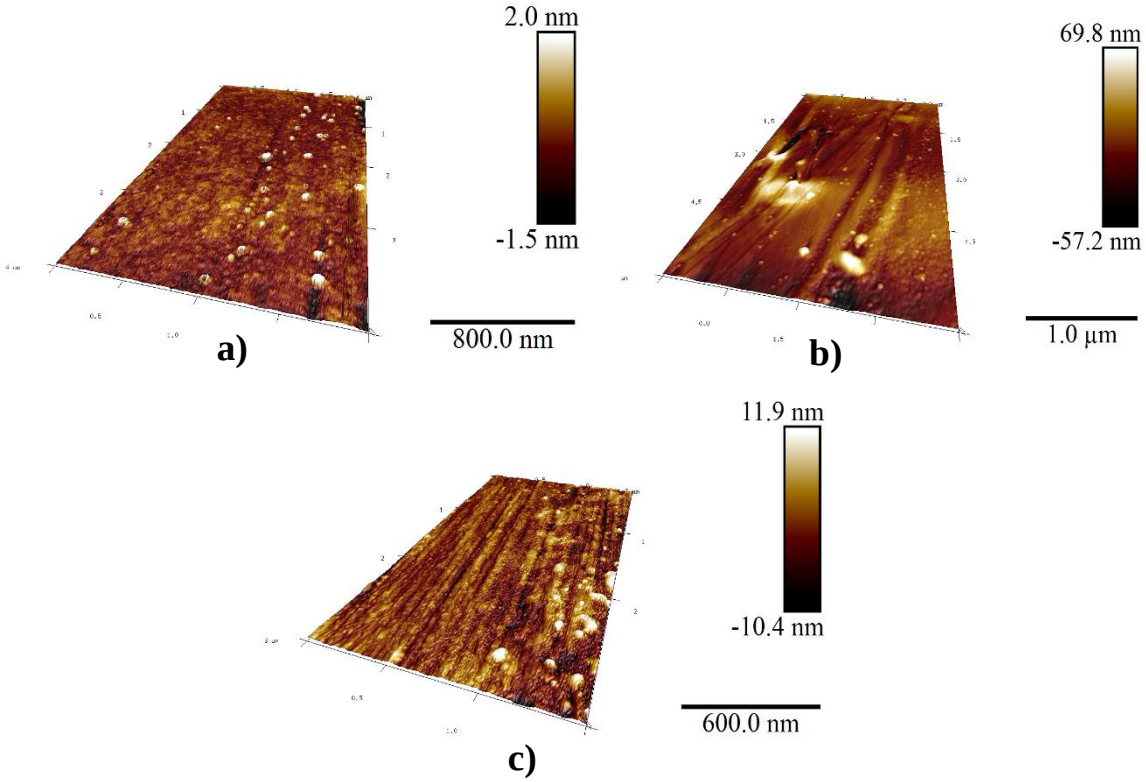

Figure 4-19 AFM scans of fibres used for the aerogel interface study. Images presents a) glass fibre b) PET fibre and c) carbon fibre.

Firstly, the significant difference in the topography of surfaces can be noticed. Glass fibre surface has a heterogeneous topography of "hills" and "valleys" with a height variation of less than 3.5 nm. The surface of PET fibres presents a similar topography. Nevertheless, wide groves stretching along the sample are also present, and they contribute to the largest height variation among tested fibres exceeding 100 nm. Similar topography was also recorded by Xu et al., and the large height variations were identified as a defect during fibre manufacturing [339]. Finally, the carbon fibre surface presents fine striated wrinkles and grooves with a height difference of around 20 nm. Such topography can often be found for a wet spun untreated carbon fibre presented by Sun et al. [340]. The corresponding roughness of scanned

surfaces was also measured with the average surface roughness of 0.25, 6.60 and 2.32 μm for glass, PET, and carbon fibres.

4.3.2 Microbond sample formation

4.3.2.1 Silica aerogel

Since it was the first time the aerogel microbond samples were prepared, a careful visual inspection of droplets formation on the fibre surface were performed. Following the deposition of the silica aerogel droplets on the glass fibre surface, the microbond sample was moved into the ethanol using tweezers to avoid drying out. Figure 4-20 presents the behaviour of silica aerogel droplet during the solvent exchange process. Due to the translucent nature of the constituents, the use of a microscope with transmitted light allows for the analysis of the sample's internal structure.

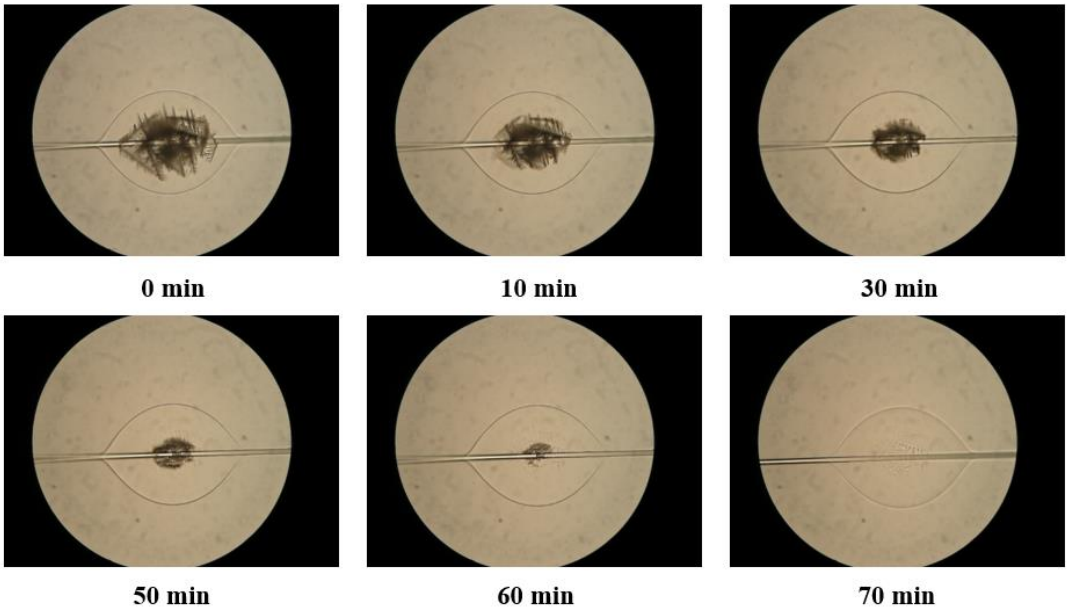

Figure 4-20 Silica aerogel and glass fibre sample submerged in the ethanol. Time under the images indicates the time since the beginning of the solvent exchange process.

As indicated by Figure 4-20, during the previous step of aerogel synthesis, a crystalline structure is formed around the fibre. This structure gradually diminishes with the progress of the solvent exchange and completely disappears after 70 minutes in ethanol. Additionally, the changes in aerogel droplet size were noticed and presented in Figure 4-21.

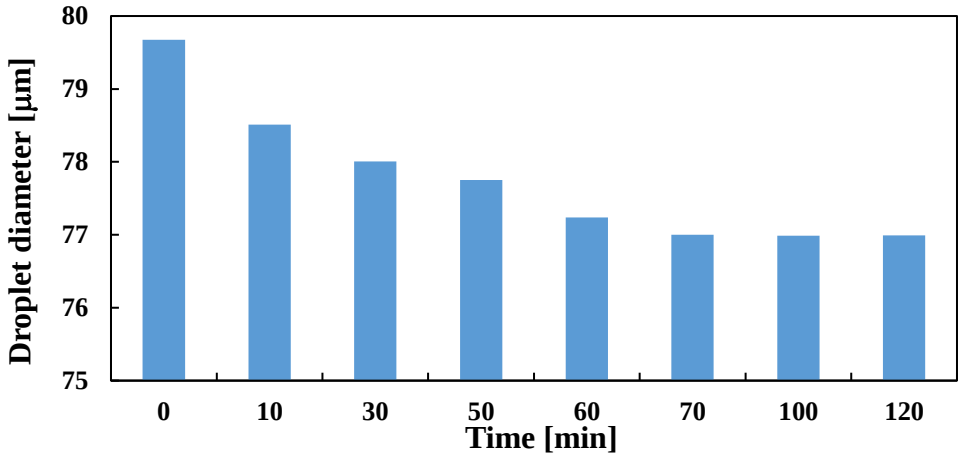

Figure 4-21 The diameter of silica aerogel droplet during ethanol solvent exchange.

During the ethanol solvent exchange time, the droplet diameter shrinkage is observed. It results in 5% decrease in droplet diameter during the first 70 minutes of solvent exchange. Afterwards, no significant changes in droplet size or internal structure are happening. The possible explanation for the growth of crystals inside silica aerogel samples can be found by analysing the nucleation mechanisms in liquid-solid systems. It assumes that the gel in the primary amorphous phase is not in an equilibrium state. The equilibration reactions constantly change the primary phase into the secondary amorphous phase, which is later converted into crystalline zeolite [341]. Each consecutive phase is increasingly ordered from the previous one. Currently, there are two distinctive ideas of how the zeolites are being formed. The first assumes that the amorphous gel includes small soluble species causing the zeolite crystals to grow by a solution-mediated mechanism [341]. The second one proposes that the zeolite lattice is formed via an ordering of the gel if no precipitation of solution occurs [341]. Both mechanisms are possible in the current situation as presented crystals can result from either spontaneous ordering of silica gel or the presence of fibre which can act as an impurity initiating crystal nucleation [341]. There was only one single previous silica aerogel study that showed a similar finding, and it was shown that the presence of such structures inside silica gel is not deteriorating the properties of the final material [342]. Due to the presence of a sample in a liquid environment, drying cannot be responsible for the change in droplets' size. Nevertheless, such occurrence could be attributed to the fact that the aerogel can still be undergoing the ageing phase with progressing sample densification. On the other hand, the replacement of water inside the sample with ethanol could result in pore collapse due to the surface tension present during this process.

Following the solvent exchange in ethanol, the sample has been moved to the n-hexane solution. As a result, the shallow glass petri dish containing samples still submerged in the

ethanol has been directly placed in larger container filled with n-hexane. Such approach allowed to reduce the manual handling of the samples and avoid possible drying of the sample during the move. Figure 4-22 includes the images of silica aerogel droplets submerged in an n-hexane solution.

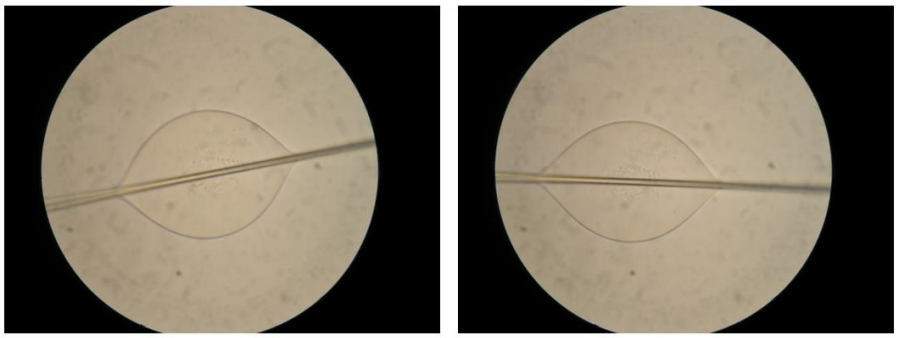

Figure 4-22 Silica aerogel and glass fibre sample submerged in the n-hexane. Time under the images indicates the time since the beginning of this solvent exchange stage.

As presented in Figure 4-22, after 24 hour in n-hexane solution, no visible changes occurred inside the sample. Nevertheless, a 5.2% reduction in droplet diameter was recorded. On the other hand, no difference in embedded length was recorded. Due to the extended time within both ethanol and n-hexane solutions, the aerogel ageing process is most likely finished and does not affect the material anymore. As a result, these measurements support the idea that the surface tension during the replacement of solvents inside the sample is responsible for the diminishing droplet diameter. In addition, it is suspected that the fibre/aerogel interactions at the interface are responsible for maintaining the embedded length constant. Afterwards, the sample has been placed inside n-hexane and TMCS solution to carry out the surface treatment process.

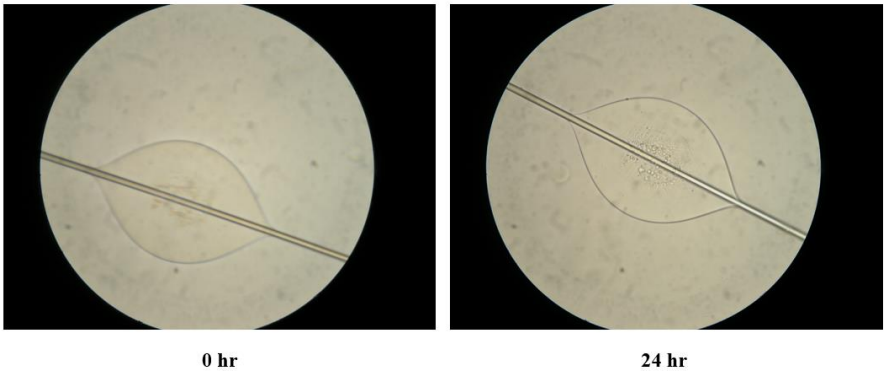

Figure 4-23 Silica aerogel and glass fibre sample submerged in the n-hexane and TMCS solution. Time under the images indicates the time since the beginning of the surface treatment process.

Following the 24 hours in surface treatment solution, the sample does not present any droplet diameter or embedded length changes. The strengthening effects of the TMCS can explain such behaviour. As previously reported in the literature, the surface treatment process can introduce the hydrophobic nature of the silica aerogel and strengthen its internal structure [343]. Wu et al. have shown that the surface modification strengthened the backbone of silica aerogels by increasing pore/water displacement promotion. Subsequently, it resulted in superior thermal and hydrophobic stabilities of created materials [343]. Additionally, by including the n-hexane in a surface treatment solution, it can be expected that much lesser surface tension forces are being induced inside the sample. The combined effects of both factors can be responsible for the lack of droplet sizes reduction. Figure 4-23 also revealed small droplets being formed on the aerogel droplet surface. Since they were not present in any previously aerogel synthesis step, it can be concluded that those droplets might contain the remnants of water still present within the sample or surrounding liquid. Following the surface treatment, it formed into droplets and settled onto the droplet surface. As the last step of aerogel synthesis, the aerogel droplet was removed from the aqueous environment and dried under room conditions, as presented in Figure 4-24.

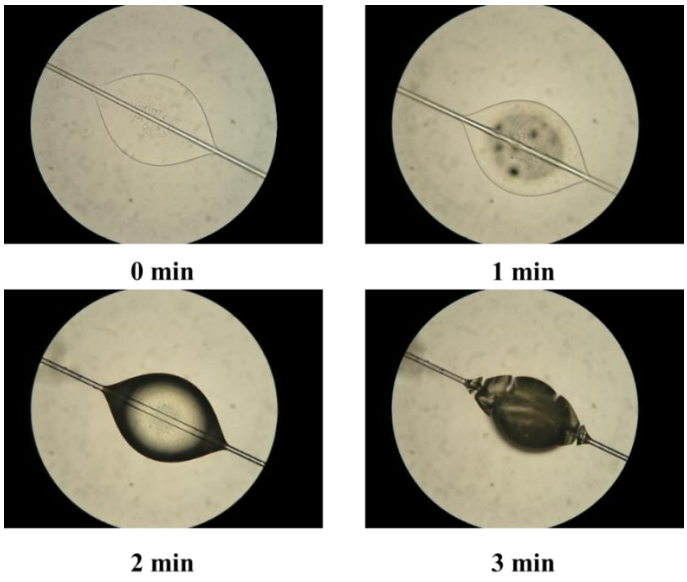

Figure 4-24 Drying of silica aerogel and glass fibre sample under room conditions. The drying time is presented underneath the images.

Figure 4-24 presents the drying behaviour of silica aerogel droplet when removed from the surface modification solution. It shows that the drying process is relatively quickly with only 3 minutes required to evacuate the solvent from the droplet inside. As a result of drying, the droplet diameter decreases by 17%, and multiple cracks are formed across the sample. Even though the embedded length remains unchanged, the separation of the meniscus from the rest

of the droplet can also be observed. The deformation and mechanical damage of the droplet are primarily caused by the capillary pressure occurring during drying. As shown by Scherer and Smith, capillary pressure can reach even up to 200 MPa, and its' magnitude is strongly dependent on multiple parameters such as the pore size and strength of the wet gel and the solvent used [344]. Such internal stresses induced are sufficient to damage the brittle structure of the aerogel's and to reduce such stress, complex drying methods are often used. It is also worth highlighting that in this study, the sample behaviour during the drying step depends on the initial size of the droplet. As presented in Figure 4-25, droplets with smaller diameters were mostly crack free and maintained their translucent nature. Even though the shrinkage and meniscus separation were still present, smaller droplets maintain their shape and symmetry around the fibre.

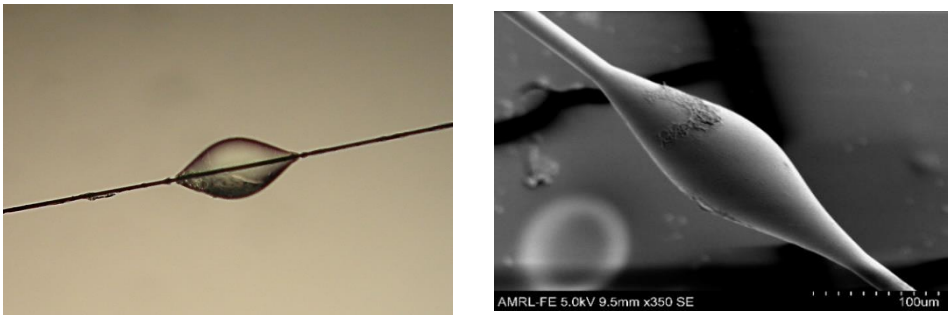

Figure 4-25 Dried polyimide aerogel droplets. Images captured with optical microscopy and SEM.

4.3.2.2 PI aerogel

A similar observation has also been performed for the preparation of polyimide aerogel microbond samples. Following the deposition of polyimide aerogel solution onto the glass fibre, the sample was left to age under room conditions as presented in Figure 4-26.

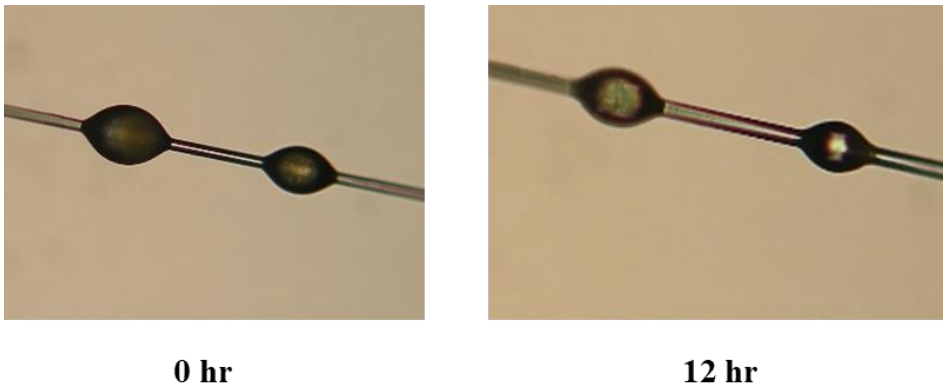

Figure 4-26 Polyimide aerogel microdroplets around glass fibre. Time under the images indicates the time since the beginning of the ageing process.

Due to the non-translucent properties of the polyimide aerogel, it is impossible to comment on the internal behaviour of the material. Nevertheless, during ageing, the aerogel droplets

underwent a significant shrinkage, with the diameter and embedded length decreasing by almost 30%. Such a high shrinkage is not unusual in the case of polyimide aerogels. Guo et al. have synthesised a wide range of polyimide aerogels with varying rigid diamine content and experienced shrinkage between 10 and 40% [64]. Especially the samples, including PPDA, has been proven to be vulnerable to ageing shrinkage. Additionally, the shrinkage has been attributed to multiple effects such as solvent interactions, chain rigidity, and chain packing [64]. Following ageing, the samples have been placed inside the acetone solution to commence the solvent exchange process as presented in Figure 4-27.

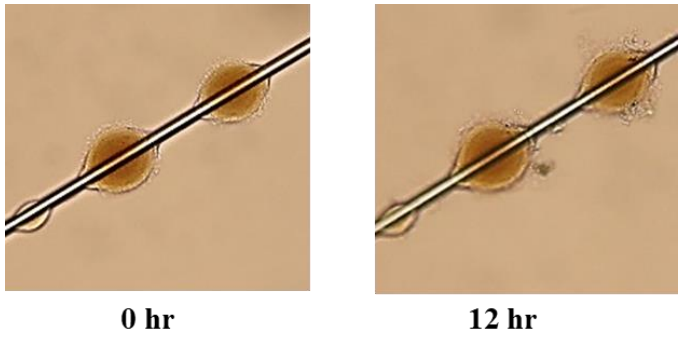

Figure 4-27 Polyimide aerogel and glass fibre sample. Time under the images indicates the time since the beginning of the solvent exchange process.

Following the infiltration of aerogel pores with acetone, the droplets have become more translucent and exhibited characteristic for polyimide yellow shade. Nevertheless, no major changes in droplet structure nor size have been noticed over 12 hours of solvent exchange. Finally, the polyimide aerogel samples were removed from the acetone bath and left to dry at a room temperature. The change in droplet diameter as a function of drying time is presented in Figure 4-28.

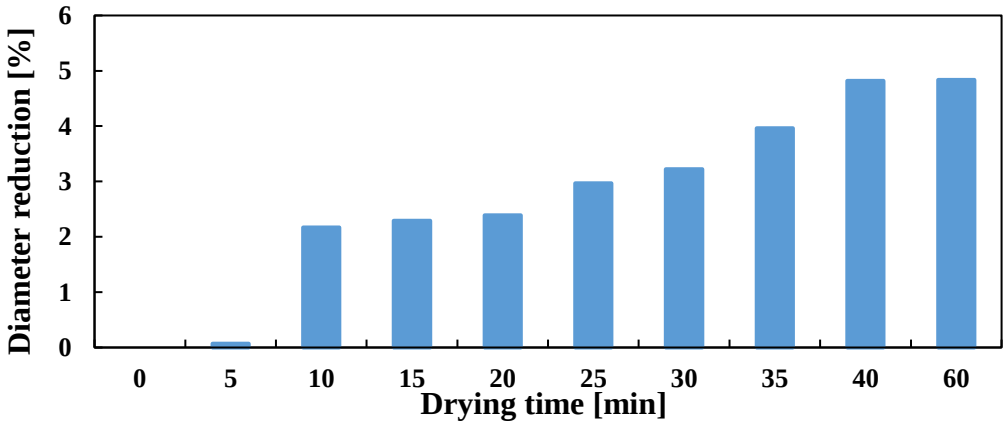

Figure 4-28 Polyimide aerogel droplet diameter reduction as a function of drying time at room conditions.

The removal of samples from the acetone environment did not cause a significant shrinkage as it happened in the case of silica aerogel. The droplet diameter decreased by only 5% following the first hour of drying with little impact afterwards. The lack of pore collapse during this aerogel synthesis stage can result from the stronger internal structure of the polyimide aerogel's. In addition, larger pores are expected in polyimide aerogels [345]. If true for this case, it could provide much easier paths for solvent evacuation, resulting in lesser capillary pressures induce during drying. Dried polyimide droplets are present in Figure 4-29.

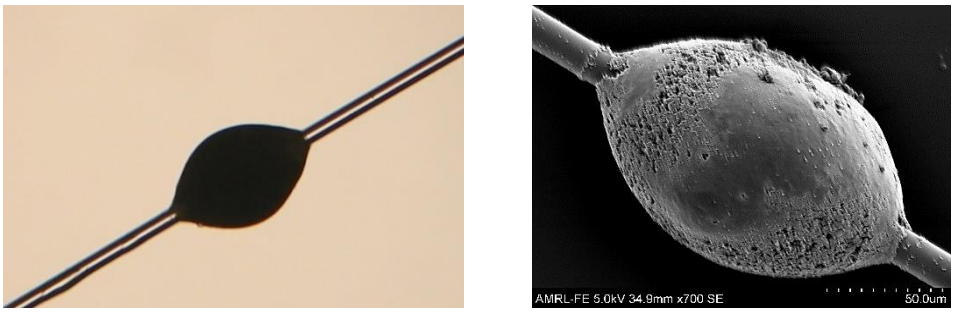

Figure 4-29 Dried polyimide aerogel droplets. Images captured with optical microscopy and SEM.

4.3.3 Aerogel internal structure

In order to provide as close as possible comparison between microbond and bulk samples the same sol which was used to produce microbond samples has been also used to produce bulk aerogel specimens. Those samples were tested to investigate the internal structure of synthesised aerogels using mercury intrusion porosimetry and gas adsorption/desorption techniques. The direct comparison between microbond and bulk samples would be mostly invalid due to the sizes difference. Nevertheless, the following investigation was still conducted to validate the aerogel synthesis methods and prove the synthesis of aerogel structures. As a result, Figure 4-30 presents the MIP pore distribution both aerogels.

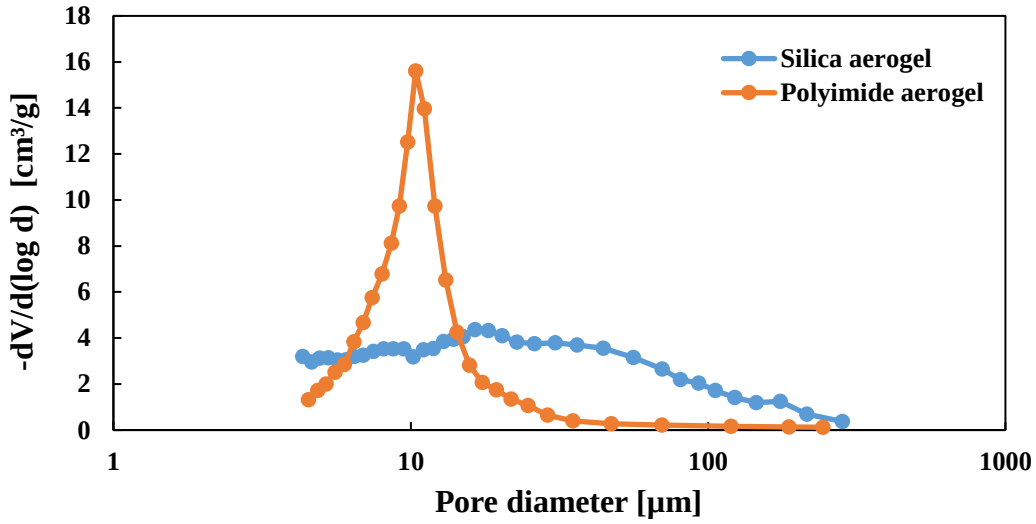

Figure 4-30 MIP pore distribution of bulk silica and polyimide aerogel synthesised in this study.

The MIP results suggest that both silica and polyimide aerogels have pores in a μm range of 15.33 and 10.04 μm average pore size. Such a large pore size is mainly caused by the usage of low-pressure MIP (up to 50 psia) due to equipment limitation. As a result, it could not test the aerogel samples at high pressure (up to 33,000 psia) and penetrate the smaller pores in a nanometre range. Despite of this, the MIP investigation has managed to produce information that might help understand bulk properties of the materials, as presented in Table 4-2. The results indicate that both aerogel types have low-density values. Nevertheless, especially for silica aerogel, low values of porosity and surface area were measured. Again, it is suspected that the lack of proper pore penetration is mainly responsible for such findings. The polyimide aerogel seems to be less affected by low MIP pressure, implying a larger pore size or a more open pore nature facilitated the mercury penetration.

Table 4-2 MIP results of silica and polyimide aerogel synthesised in this study.

	Silica aerogel	**Polyimide aerogel**
Bulk (Particle) Density [g/cm³]	**0.10**	**0.19**
Apparent Density [g/cm³]	**0.15**	**0.22**
Surface Area m²/g	**1.34**	**1.66**
Intrusion average pore size [μm]	**15.33**	**10.04**
Extrusion average pore size [μm]	**19.75**	**23.49**
MIP porosity [%]	**50.80**	**80.37**
Skeletal density [g/cm³]	**1.61**	**-**
Pycnometer porosity [%]	**93.7**	**-**

Even though the MIP provided only approximate result in this study, many previous studies have found the excessive capillary pressure imposed during MIP testing can result in pore collapse and subsequent alteration of the internal aerogel structure, resulting in inaccurate results [346]. For both aerogels, it is expected that the density and porosity of the materials should probably be respectively lower and higher than the measured values in Table 4-2. In order to further test silica aerogel porosity, a pycnometer has been used to measure material skeletal density. Obtained skeletal density of 1.61 g/cm³ is significantly lower than expected value of 2.17 g/cm^3 corresponding to amorphous silica. Previous studies on silica aerogels which also reported lower skeletal density values attributed this phenomenon to presence of methoxy groups on the surface of the aerogel particles. Such groups prevent the adequate penetration of aerogels' porous internal structure by the helium resulting in higher measured volume (and thus lower skeletal density) than the real one [347]. Following density based calculations (relating bulk and skeletal densities) the porosity exceeding 90% was obtained. In addition, to provide a better overview of aerogels' internal structure, nitrogen adsorption was also used, with Figure 4-31 presenting obtained isotherms.

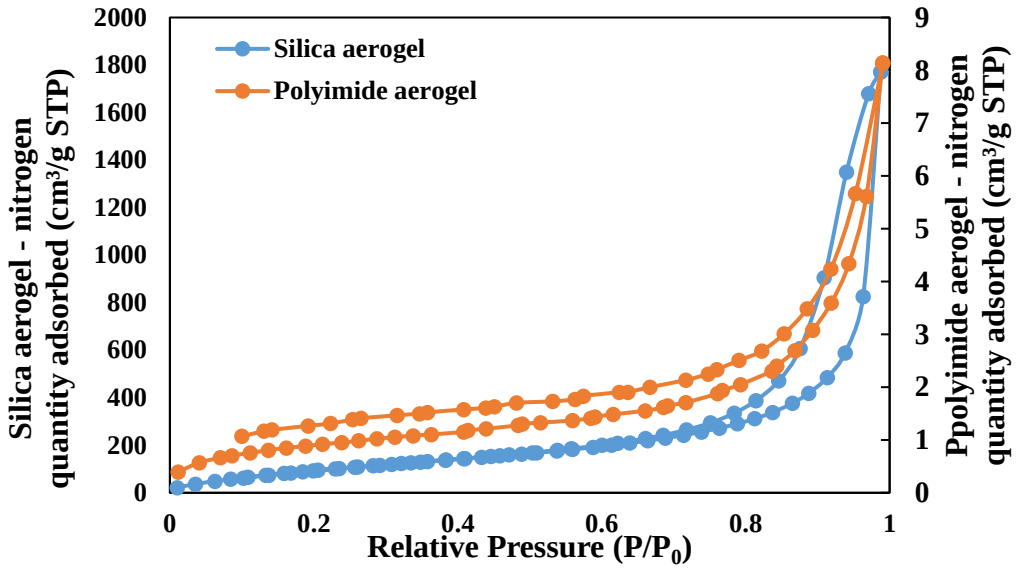

Figure 4-31 Nitrogen adsorption and desorption isotherms of silica and polyimide aerogel synthesised in this study.

Silica aerogel presents a type IV isotherm indicating mesoporous material with a pore diameter in a 2 – 50 nm range. The shape also suggests condensation of the gas inside pores at low-pressure ranges, with further mono and multilayers formation at higher pressure [239]. Similarly, the polyimide aerogel also presents the type IV isotherm. However, significant differences can be noticed, starting with a much lower quantity of nitrogen absorbed and a much smaller gap between adsorption and desorption isotherms. Additionally, the shape of both hysteresis loops suggests a different type of pores present in both materials. As a result, type IV hysteresis in the case of silica aerogel implies the presence of spherical pores with walls made of mesoporous silica. On the other hand, the type III hysteresis loop is present in polyimide aerogel, suggesting flaky particles forming slit-like pores [239]. Finally, the BET results for both aerogels are summarised in Table 4-3.

Table 4-3 BET results of silica and polyimide aerogel synthesised in this study.

	Silica aerogel	**Polyimide aerogel**
BET Surface Area [m²/g]	431.00	3.32
BJH Adsorption average pore width [nm]	23.75	18.35
BJH Desorption average pore width [nm]	19.21	14.20
Cumulative Pore Volume (cm³/g)	2.73	0.012

The specific surface area of silica aerogel is significant, with an average value of 431 m²/g, indicating the material's high porosity. The adsorption pore width of all samples varies between 1.7 nm to 80 nm, with an average of 19.21 nm and a cumulative pore volume of 2.73 g/cm^3. On the other hand, PI aerogel presents significantly lower specific surface area values with an average value of 3.32 m²/g. Together with a cumulative pore volume of 0.012 g/cm^{3,}

they suggest lower material porosity than silica aerogel counterparts. Also, PI aerogel presents a smaller pore size with the adsorption pore width varying between 1.7 to 48 nm and an average value of 18.35 nm. It is worth noticing that the BET results obtained for synthesised aerogels are lower than the results for the commercially purchased aerogel particles as presented in the previous chapter. Multiple factors such as different synthesis, various drying or altered post processing could influence this difference. However, overall surface area and pore size values are in a similar range and thus it is believed good quality aerogel has been synthesized. In addition to both analyses, the SEM images of silica and polyimide aerogels have been captured and presented in Figure 4-32.

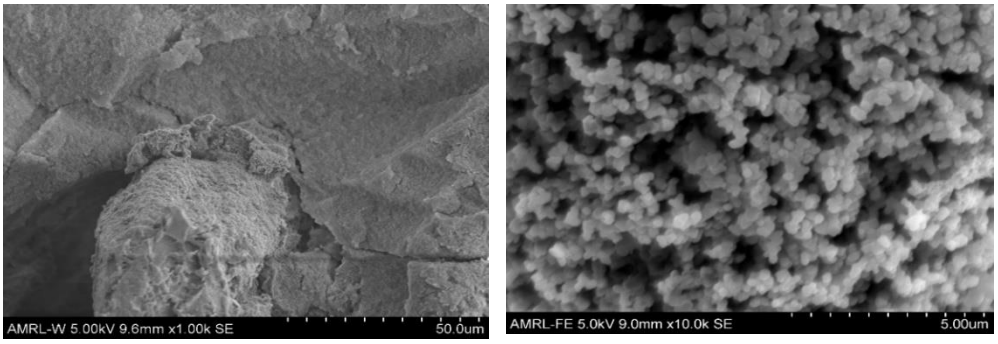

Figure 4-32 SEM images of synthesised aerogel internal structure. The image on the left presents silica aerogel, and the image on the right polyimide aerogel.

As it can be noticed in Figure 4-32, both aerogel types present quite different internal structure. In the case of silica aerogel, spherical nano-sized silica particles form a typical three-dimensional network with meso-sized pores present. On the other hand, polyimide aerogel presents a coarser structure with micron-sized features. Guo et al., who have synthesised a polyimide aerogel using a mixture of DMBZ and ODA diamines [79], observed a similar structure. In addition, by investigating the sample under even larger magnification, the formation of hierarchical pore structures with finer pores structure inside a coarser framework has also been proven. Such structure was attributed to the macro-phase separation during the gelation process. It is possible that a similar internal structure has been achieved in this study as this idea corresponds well with nanometre range pores detected by BET [348].

4.3.4 Impact of reinforcement type on aerogel adhesion

Following the successful creation of aerogel microbond samples using glass, carbon, and PET fibres, the aerogel-fibre adhesion was characterised via the microbond method. Afterwards, a series of post-testing, fibre surface inspections were performed to better understand the mechanisms behind the aerogel adhesion to various fibres.

4.3.4.1 Silica aerogel

A typical force and displacement graph for silica aerogel and glass fibre microbond test is presented in Figure 4-33.

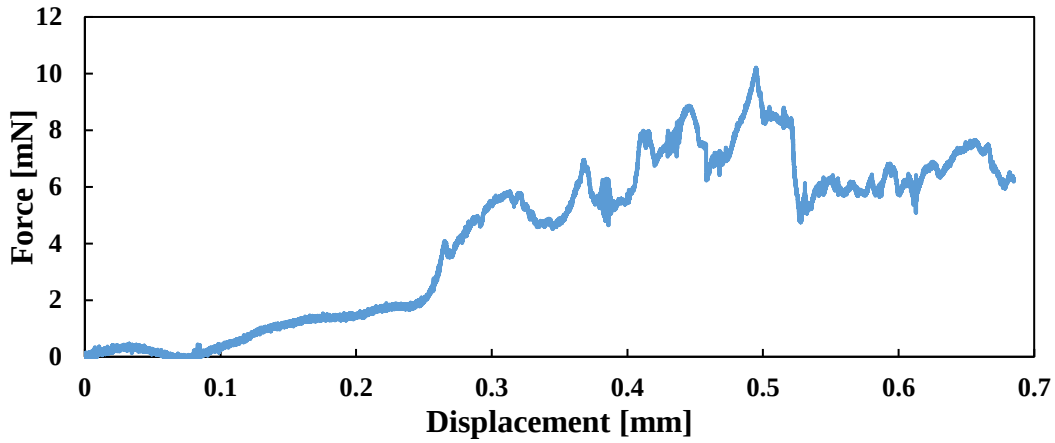

Figure 4-33 Example of load vs displacement plot of silica aerogel and glass fibre sample produced during microbond test.

The presented plot indicates a very noisy behaviour of the test and there is a lack of neat linear load–extension curve. This might result from the brittle nature of the aerogel, causing droplet cracking or shearing blade penetration with increasing load. After reaching the point of maximum force which is also considered the point of debonding, the samples presented constant or sometimes even increased dynamic friction. However, sharp force drops were also recorded in the case when the whole droplet falls off the fibre. The tested microbond samples are presented in Figure 4-34. The SEM image revealed a substantial indentation in the droplet caused by the blade edges, most likely highlighting the brittle nature of the sample. In addition, the cracks across the droplet can be noticed, which following the visual inspection of the droplets were most likely created during sample drying stage. On the other hand, optical microscopy suggested the creation of internal cracks perpendicular to the fibre surface.

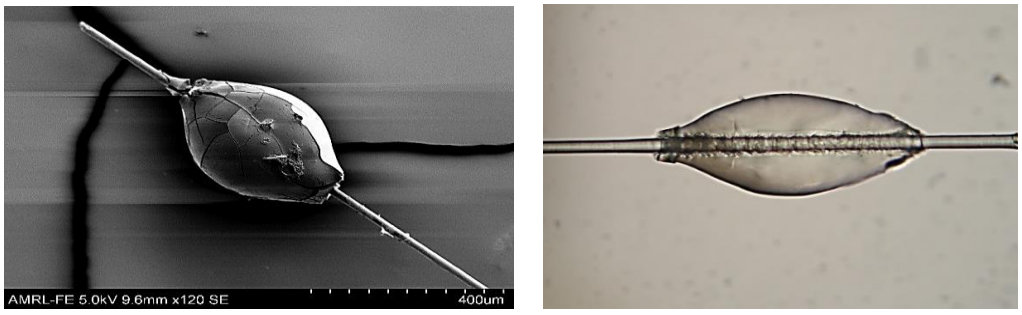

Figure 4-34 Post microbond silica aerogel droplets. Images captured with optical microscopy and SEM.

Figure 4-35 presents a plot of peak force vs interfacial area for the data set obtained with glass, carbon, and PET fibres in silica aerogel via the microbond method.

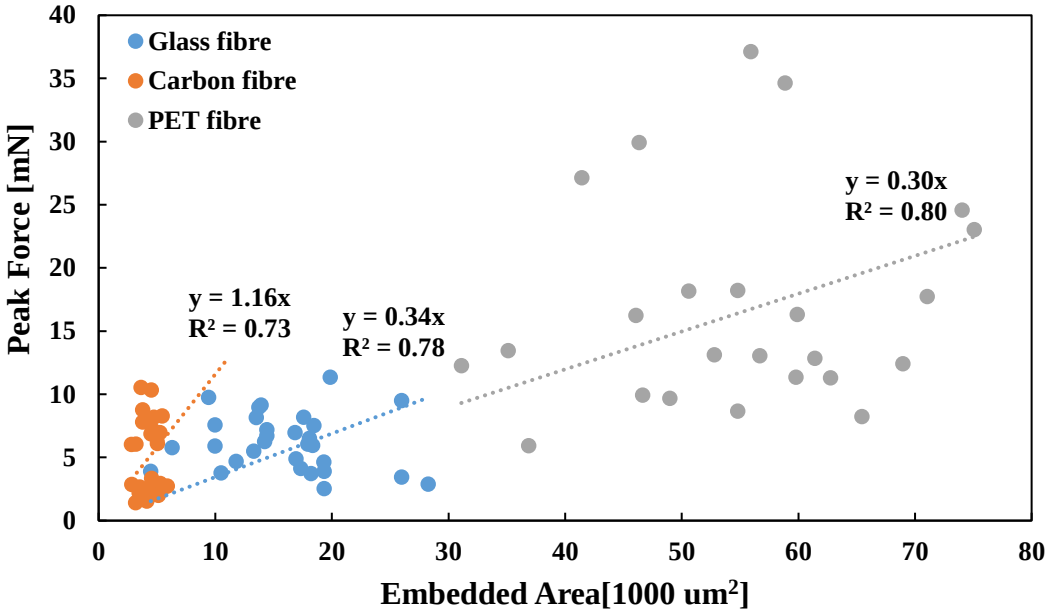

Figure 4-35 Plot of peak force vs embedded area measured for silica aerogel on glass, carbon and PET fibres using microbond test.

By fitting a linear trendline to the data and forcing it to go through the origin, the IFSS values of 0.34, 1.16 and 0.3 MPa have been measured for silica aerogel combinations with respective glass, carbon, and carbon PET fibres. Even though the R^2 values for all data sets are higher than 0.7 the datapoints present a relatively large scatter. In addition, it needs to be highlighted that due to the significantly varying fibre diameter, the datasets for respective fibre types cover different regions of the embedded area spectrum, with PET forming the largest interfacial regions and carbon fibre the smallest. Upon completion of the microbond testing, the samples have been inspected under the SEM, and the images of fibre surfaces post the microbond test can be seen in Figure 4-36.

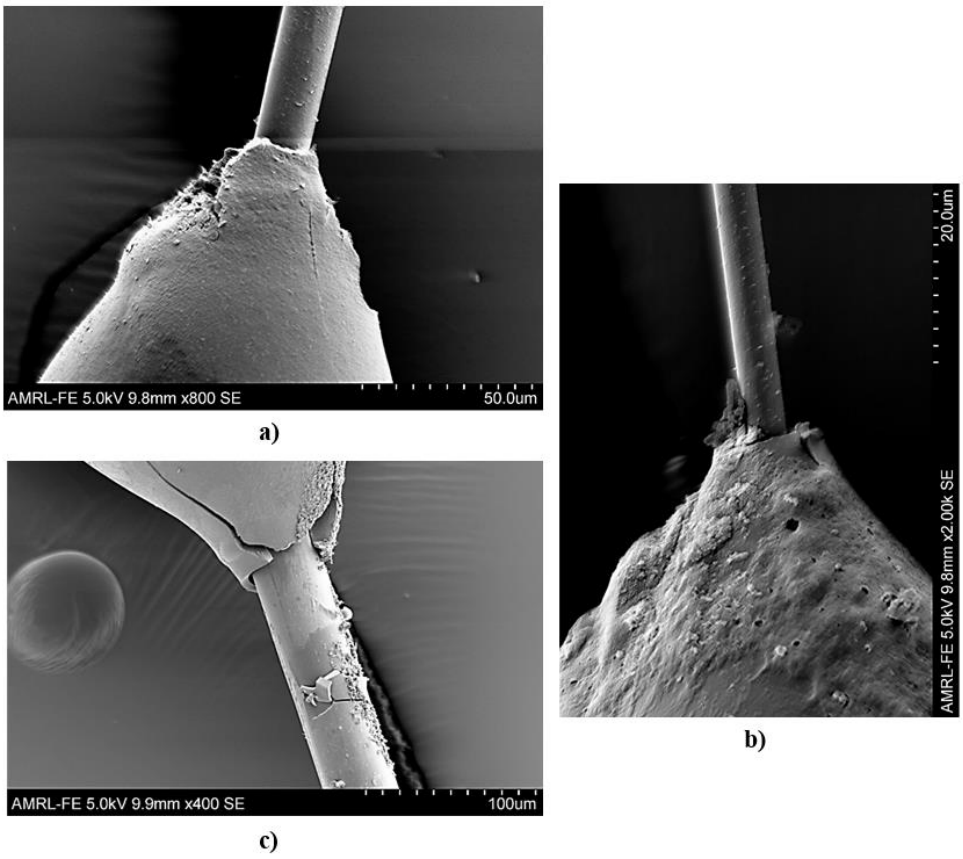

Figure 4-36 SEM images of fibre surfaces post the microbond test. Images presents a) glass fibre b) carbon fibre and c) PET fibre.

The microscopy inspection shows a significant residue left on the fibre surface post the interfacial testing. Further magnification of such residual as presented in Appendix A reveals its' porous structure similar to structures previously seen inside the silica aerogel. Additionally, the elemental analysis performed alongside SEM imaging revealed silica presence and elevated presence of oxygen on the surface of organic fibres. The results of the elemental analysis can be seen in Appendix A. Such findings suggest that it might be the material failure and not interface failure, responsible for separating the fibre and aerogel droplets. The results of AFM phase scanning presented in Figure 4-37 seems to provide similar evidence and suggest that regardless of the initial fibre surfaces, they all present similar features post microbond testing. As a result, the increase in phase voltage to a similar level is observed for all fibres. In addition, the surfaces of the fibres underwent a significant alteration, with multiple circular inclusions present across tested areas. The shape and voltage values could imply that similar material is present on all fibres, most likely silica aerogel. Regardless of the similarities, the fibres managed to maintain some of their original features, and for example, carbon fibre groves are still visible. Additionally, the surface roughness of tested fibres

increased significantly with the average surface roughness of 0.69, 6.96 and 9.30 μm for, respectively, glass, carbon fibres and PET. The AFM topography images can be seen in Appendix A. Even though such change could be caused by mechanical damage to the fibre surface by the shearing blades, it could also support the idea of silica aerogel residue presence on the fibre surfaces.

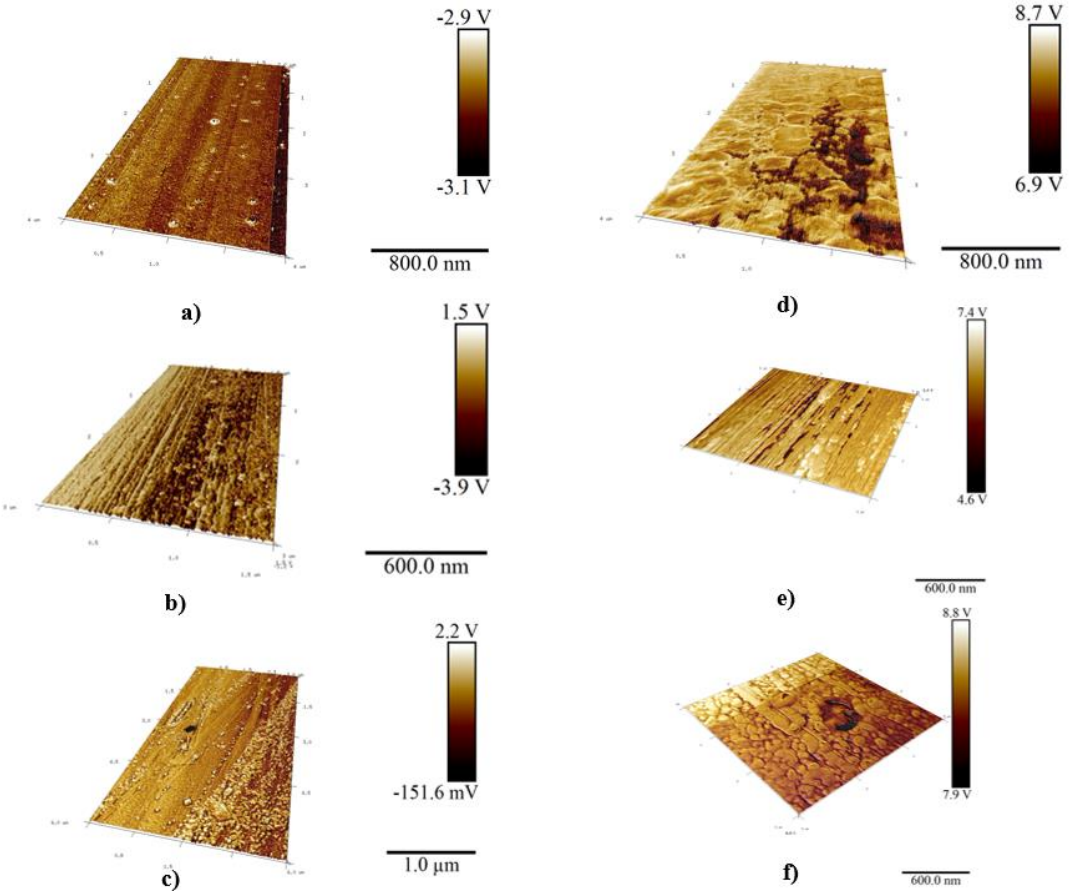

Figure 4-37 AFM phase scans of fibre surfaces before and post the microbond test. Images present a) glass fibre b) carbon fibre and c) PET fibre before silica aerogel application and d), e) and f) following the microbond test.

4.3.4.2 Polyimide aerogel

In the case of polyimide aerogel, substantially different force vs displacement behaviour was recorded, and an exemplary graph has been presented in Figure 4-38.

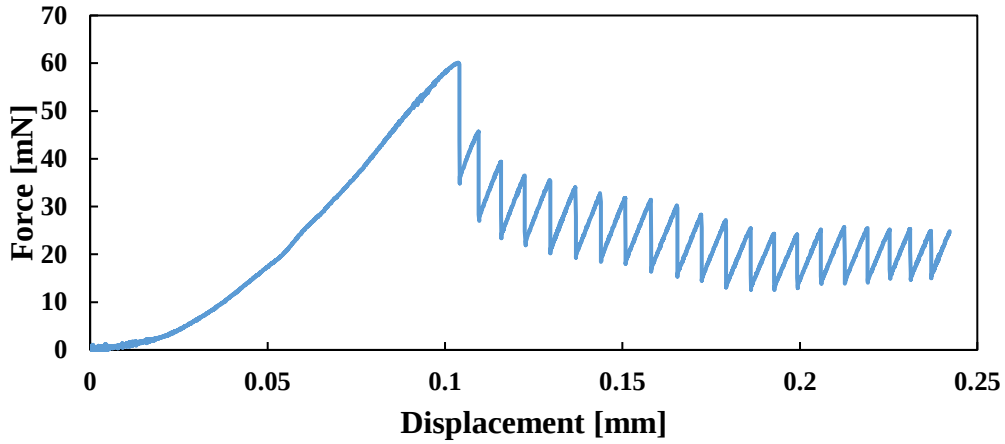

Figure 4-38 Example of load vs extension plots of polyimide aerogel samples.

Firstly, Figure 4-38 indicates that the linear relation between force and displacement is present until reaching the debonding force in the case of polyimide aerogel samples. Afterwards, a sharp drop in force was observed, followed by a fairly constant triangular wave fluctuation, indicating the existence of friction force between aerogel and the fibre. The SEM image in Figure 4-39 presents that in the case of polyimide aerogel droplets, the blade indentations are also present. Nevertheless, the post testing droplet presents a more cohesive structure without cracks and meniscus separation.

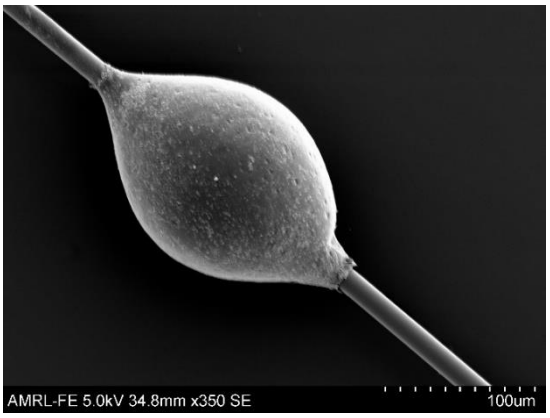

Figure 4-39 SEM image of post microbond polyimide aerogel droplets.

Figure 4-40 presents a plot of peak force vs interfacial area for the data set obtained with glass, carbon, and PET fibres in polyimide aerogel via the microbond method.

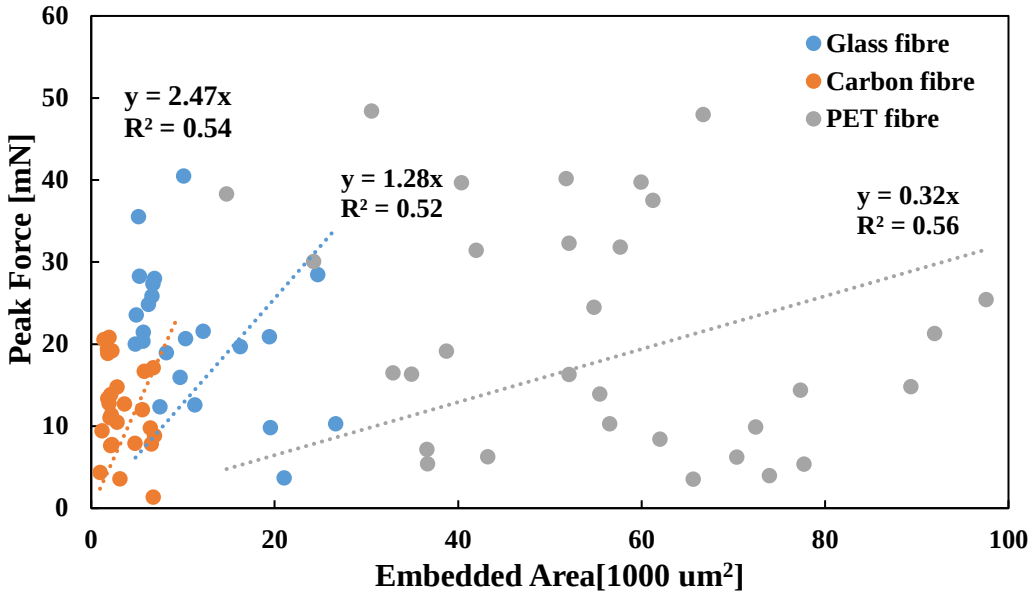

Figure 4-40 Plot of peak force vs embedded area measured for polyimide aerogel on glass, carbon and PET fibres using microbond test.

Similarly, as in the case of silica aerogel samples, linear trendlines have been fitted to the data and forced to go through the origin, the IFSS values of 1.28, 2.47 and 0.32 MPa have been measured for the combination of polyimide aerogel with respective glass, carbon, and PET fibres. The R^2 values for all data sets are significantly lower than in the previous case and only slightly exceeding 0.5, with the datapoints presenting a large scatter. Finally, due to the significantly varying fibre diameter, the datasets for respective fibre types cover different regions of the embedded area spectrum, with PET forming the largest interfacial regions and carbon fibre the smallest. Following the microbond testing, the samples have been inspected under the SEM and the images of fibre surfaces post the microbond test can be seen in Figure 4-41.

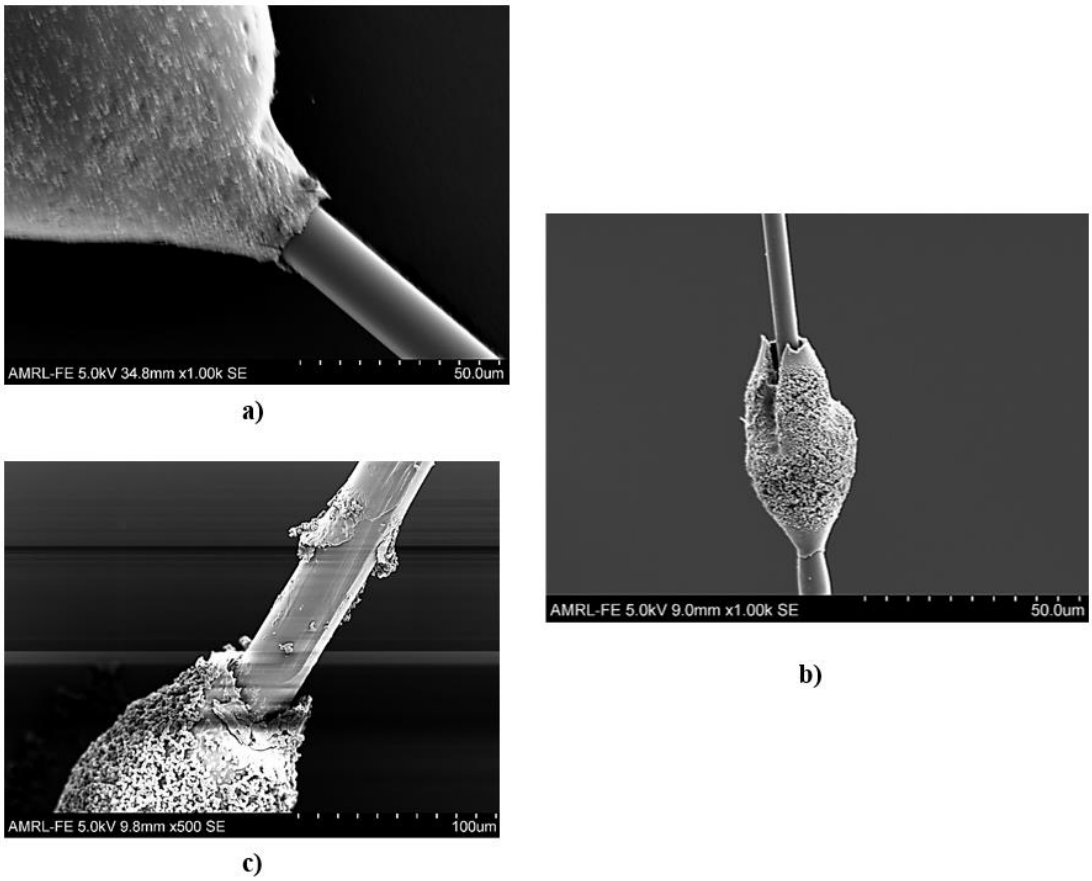

Figure 4-41 SEM images of fibre surfaces post the microbond test. Images presents a) glass fibre b) carbon fibre and c) PET fibre.

The SEM images of polyimide aerogel samples reveal that there was no aerogel residue left following the droplet shearing in most cases. Only Figure 4-41 c) presents a droplet meniscus and some aerogel pieces attached to the fibre post droplet displacement. The images with a larger magnification of fibres surfaces are presented in Appendix A. Nevertheless, the elemental analysis performed alongside SEM imagining revealed a presence of carbon and elevated presence of oxygen on the post-testing surface of glass fibre, which could imply certain residues. In addition, in the case of PET fibre surface, no oxygen was detected following the aerogel removal. The complete results of an elemental analysis can be seen in Appendix A. The post microbond fibres have also been subjected to AFM scanning, as shown in Figure 4-42. The scans present post microbond surfaces, which still carry a feature similar to the initial fibre surfaces. However, the increase in phase voltage is observed for silica and PET fibre, indicating that there might be residual material left to post the droplet displacement. Additionally, the surface roughness of tested fibres increased significantly with the average surface roughness of 0.59, 8.85 and 9.66 μm for respective glass, carbon fibres and PET. The AFM topography images can be seen in Appendix A. Even though such change could be

caused by mechanical damage to the fibre surface by the shearing blades, it could also support the idea of residue presence on the fibre surfaces.

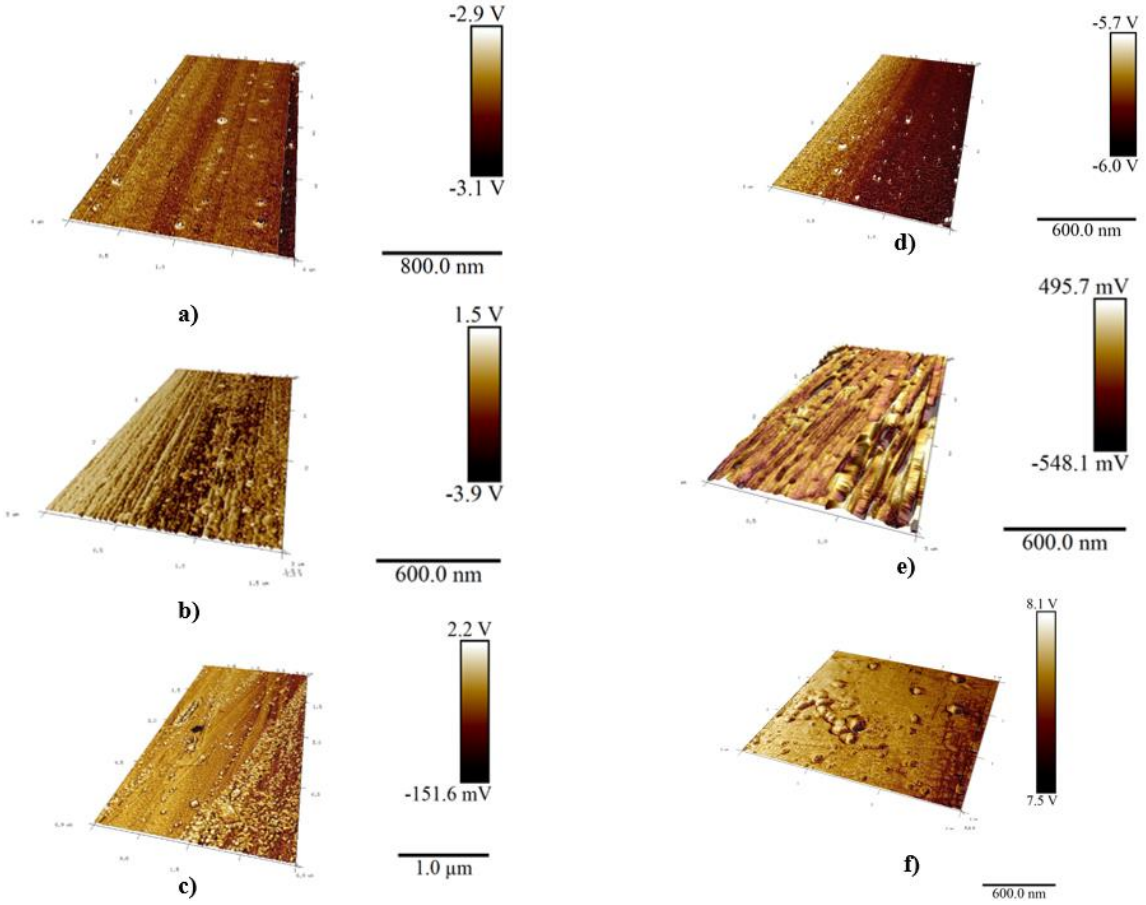

Figure 4-42 AFM phase scans of fibre surfaces before and post the microbond test. Images present a) glass fibre b) carbon fibre and c) PET fibre before polyimide aerogel application and d), e) and f) following the microbond test.

4.3.4.3 Discussion

Even though the results presented in previous sections provide an indication regarding the strength of aerogel and fibres interfacial interactions, they do not answer the question of how the extremely porous internal structure of the matrix influence such interface. Figure 4-43 presents the silica aerogel droplet after separation from the fibre, implying the different nature of the interfacial region from the rest of the droplet. The PI aerogel droplet was not inspected mainly due to the extremely difficult handling of small and brittle droplets the author was unable to prepare an adequate SEM sample.

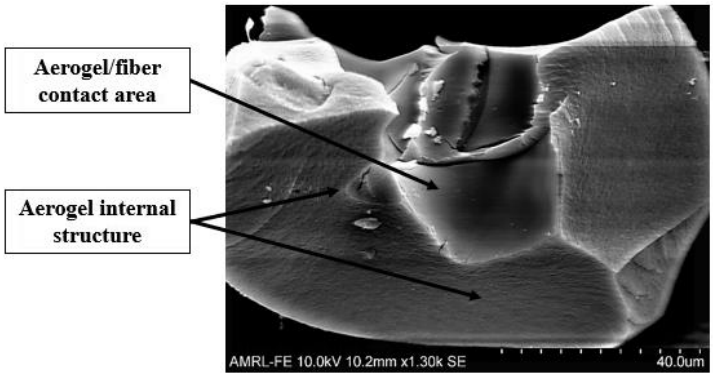

Figure 4-43 SEM image of silica aerogel droplet after separation from the fibre.

The visual inspection reveals a relatively smooth surface in the region where the aerogel was in contact with the fibre. On the contrary, the remaining portion of the droplet still indicates the porous nature of the material. Even though it is the only speculation, such behaviour would indicate the densification of the aerogel at the interfacial region providing pore-less contact between the fibre and the aerogel droplet. This, in return, could imply that the pores would not directly impact the adhesion properties by reducing the contact area between composite constituents but rather on the mechanical performance of the matrix further away from the fibre. The comparison of both aerogel type could still yield meaningful results. Figure 4-44 presents the IFSS values for polyimide and silica aerogels with various fibres achieved via the microbond test.

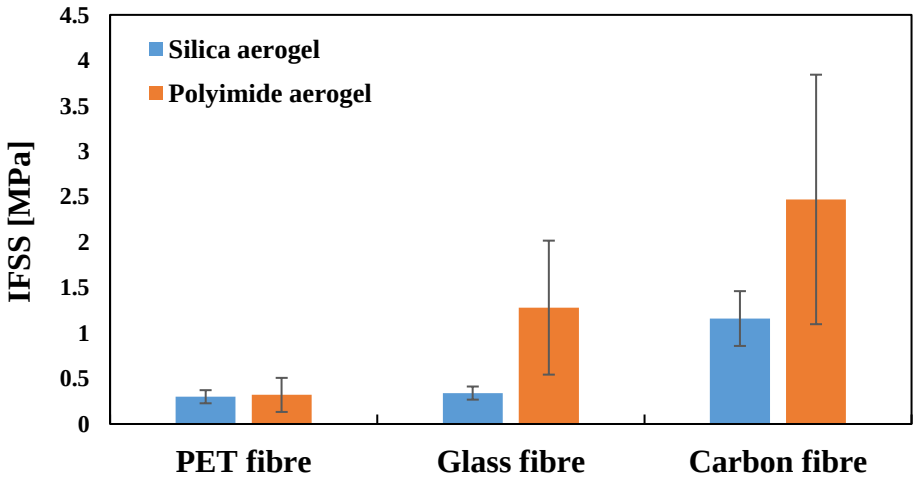

Figure 4-44 IFSS values for various aerogel and fibre combinations achieved via microbond test.

Figure 4-44 indicates that both aerogel types achieve relatively weak adhesion on average, not exceeding 2.5 MPa across all tested fibres. Such a finding was anticipated mainly due to both materials' porous internal structure. In addition, a large scatter was observed for each dataset

presented, which is mostly attributed to the complicated and hard to control aerogel synthesis process resulting in significant droplet diameter discrepancies.

The polyimide aerogel seems to achieve better adhesion than silica aerogel, especially when combined with glass or carbon fibre, nevertheless due to only single dataset being measured for each fibre type further analysis would be necessary to confirm such findings. The primary reason for such behaviour could be the higher porosity of silica aerogel, deteriorating the mechanical properties of the matrix. However, as presented in 4.3.3, both materials are highly porous, and the difference between 93% porosity of silica aerogel and 80% porosity of polyimide aerogel, would probably not yield such distinctive differences in the interfacial adhesion. As a result, it is suspected that other factors could also influence the fibres and aerogels interactions. Residual stresses could be other factors responsible for the superior adhesion of the polyimide aerogel. As shown by Thomason et al., in the case of epoxy composites, a combination of residual radial compressive stress and static friction at the fibre/matrix interface can be responsible for a significant portion of interfacial shear strength [284]. Their work shows that the residual stresses are mainly induced by the mismatch in the thermal expansion coefficients of fibre and matrix or a curing shrinkage of the matrix. In order to calculate the radial stresses due to thermal shrinkage, Raghava has proposed a following equation [349]:

$$\sigma_R = \frac{(\alpha_m - \alpha_f)(T_s - T_t)E_f E_m}{(1 + v_f + 2V_f)E_f + (1 + v_m)E_m} \qquad \text{Eq. 42}$$

where f and m are subscripts for the fibre and matrix respectively, α is the thermal expansion coefficient, T_s is the stress free temperature where matrix solidification begins, T_t is the testing temperature, ν is the Poisson ratio, V_f is the fibre volume fraction and E is the modulus. It is quite frequently assumed that for multiple composites the $E_f >> E_m$, which allows then to approximate that the σ_R scales with magnitude of $\Delta\alpha \times \Delta T \times E_m$ [284]. When considering the mentioned simplification for both silica and polyimide aerogels, the couple of parameters seems to suggest larger residual stresses for the latter. Firstly, a polyimide tends to have a relatively high thermal expansion coefficient (14 – 64 ppm/°C), while silica aerogel coefficient (2 ppm/°C) is much closer to the values presented by all fibres used in this study [42, 350]. Secondly, for both aerogel types the previous studies strongly correlated the Young's modulus with aerogel's density. As such due to the higher density of polyimide aerogel (as presented in Table 4-2) it can be expected that it's modulus can be even up to an order of magnitude higher than the modulus of silica aerogel [351]. Finally, as presented in 4.3.2, the cure shrinkage following the droplet deposition on the fibre is significantly larger for the polyimide

aerogel than silica aerogel. The combination of mentioned factors could suggests larger residual stresses for the polyimide aerogel samples, which would, in return, increase the IFSS values. On the other hand, it was previously presented that higher internal stresses could result in the severe deformations of the droplets during curing or drying. Nevertheless, lower porosity and less brittle structure of polyimide aerogel could prevent it from happening. Matrix failure could also be responsible for lower IFSS values of the silica aerogel. As presented by AFM and SEM analysis, there are residues left on the fibre surface following the microbond test, especially in silica aerogel. Such residues could imply that the silica aerogel undergoes a cohesive matrix failure. In that case, the measured IFSS value would not reflect the true adhesion between silica aerogel and the fibres but only on the matrix shear yielding strength. On the other hand, the lack of residues in the case of polyimide testing would suggest the adhesive interfacial failure with IFSS values truly representing the adhesion interactions.

When analysing the impact of fibrous reinforcement on the IFSS values as presented in Figure 4-44, the clear advantage of using carbon fibre can be noticed. In both silica and polyimide aerogel, droplets deposited on the carbon fibre have the highest IFSS values, followed in decreasing order by glass and PET fibres. Again, the combination of multiple factors can explain such results. Firstly, as indicated in the fibre surface analysis presented in 4.3.1, carbon fibre has an extremely rough surface composing of fine striated wrinkles and grooves with a height difference of around 20 nm. Those surface features could improve the aerogel adhesion as upon penetration of groves by liquid aerogel, the interlocking mechanism could be developed. Similar behaviour would not be possible in either glass or PET fibres, mainly due to the smoothness of both surfaces. Even though the PET had the highest average roughness value, it was mainly caused by wide groves stretching along the sample, contributing to the largest height variation among tested fibres exceeding 100 nm but results in little impact on the adhesion. The impact of surface roughness on the composite adhesion properties presented by Nganga et al., who have combined porous E-glass-fibre tissue and photopolymerisable resin system [330]. The resulting push-out forces were almost doubled when the porosity was increased from 10% to 60%, and the higher level of mechanical interlocking between the composite constituents was given as the main reason for such occurrence [330]. Chemical interaction can also be responsible for the difference in aerogel/fibre adhesion. However, very limited research has been performed in this area so far. Only a handful of up to date studies have shown that in order to create a strong chemical bond between silica aerogel and fibre, the latter should be able to form Si–O–Si chemical bonds [352]. As a result, Bangi et al. have treated the carbon nanotubes with a surfactant providing OH groups and reported silica particles tightly attached to their walls [353, 354]. Nevertheless, no research was looking into

such aspect of polyimide aerogel. Due to the scarce availability of data in this field, a limited discussion can be presented. In order to confirm the creation of chemical bonds between aerogels and fibres used in this study, a separate FTIR investigation would be required.

Regardless of all previously mentioned interactions, different fibres with substantially different diameters resulted in a lack of consistency among the droplet size. Figure 4-45 presents the IFSS as afunction of an average droplet size for all aerogel and fibre combinations prepared for the microbond test.

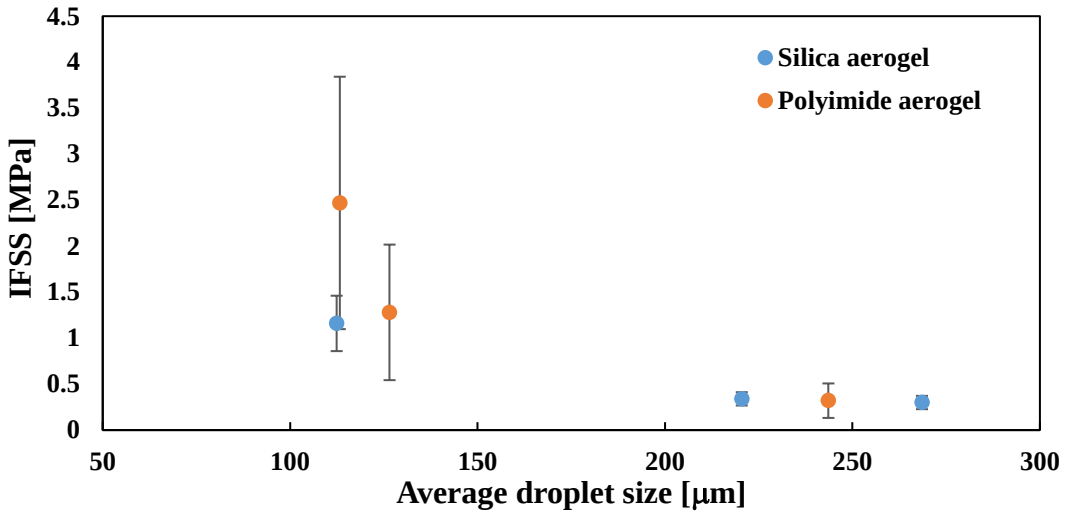

Figure 4-45 Average droplet size for various aerogel and fibre samples prepared for the microbond test.

By analysing Figure 4-45, it can be noticed that the IFSS values are directly related to the droplet size used, with the IFSS values increasing with decreasing droplet size for both aerogel types used. Such dependency can be explained in a twofold way. Firstly, it was previously shown by Rao et al. that the droplet size could affect the chemistry of the matrix system. In their case, a strong correlation between droplet size and the amount of curing agent was found, resulting in varying matrix properties [355]. The material property dependency on the droplet size would be even more severe for the aerogel samples as the droplet size could dictate the chemical composition of the material and the effects of each synthesis step. For example, smaller droplets size would facilitate through solvent exchange and increase the ratio of material subjected to the surface treatment. Such a thesis could also be supported by the finding from 4.3.2, which presented that smaller silica aerogel droplets maintained their translucent properties and experienced lower drying shrinkage compared to larger counterparts. It is highly likely that by influencing the aerogel's internal structure, the droplet size difference could easily impact its adhesion properties. Secondly, the difference in IFSS values could also be caused by test behaviour changes due to the wide embedded area range. As previously

reported by Zinck et al., interfacial shear stress is not constant across the whole interface but rather presents the peak values located at a distance from 1/10 to 1 fibre diameter from the gripped end of the droplet. The interfacial debonding occurs when the local shear stress reaches its critical value controlled by multiple parameters such as matrix Young's modulus, residual shrinking stress or fibre diameter, and embedded length [289]. Zhandarov and Mäder have investigated the impact of specimen geometry on the peak force during the microbond test and reported decreasing apparent IFSS values with increasing embedded length [356]. The impact of both phenomena would undermine the purpose of direct comparison of IFSS values between various fibres and further studies investigating IFSS of different fibre materials with the same fibre diameter would be necessary to finally conclude if these differences result from the aerogel properties or should be considered a test artefact. Overall, this study proves the possibility of performing the micromechanical testing on the aerogel composites. As such following further analysis this method might be used to compare the impact of different aerogel manufacturing techniques, chemical compositions and other variables on the adhesion between the aerogel and fibre materials.

4.4 Summary

In this chapter, the first-ever attempt to characterise the silica and polyimide aerogel adhesion to various fibrous reinforcements have been undertaken. To achieve it, a method was developed allowing for the deposition of microdroplets of silica and polyimide aerogels on the surfaces of glass, carbon, and PET fibres.

The visual observation of microdroplet formation indicated a large shrinkage of polyimide aerogel in a curing phase followed by little size changes in the subsequent steps of the aerogel synthesis. On the contrary, during the silica aerogel droplet formation, the largest shrinkage was associated with the drying process resulting in extremely high capillary forces and pore collapse. In addition, due to the translucent nature of the aerogel, a formation of crystalline zeolite inside the sample was also noticeable. Alongside the microbond sample preparation, the bulk silica and polyimide aerogel samples have also been created. The investigation of aerogels' internal structure via BET and MIP methods have proved the good quality of both aerogels with porosity exceeding 80% and other properties in a similar range as commercially available products. The micromechanical analysis was conducted following the microbond test procedure with samples subjected to visual inspection and AFM scanning upon test completion. As a result, the microbond test revealed superior adhesion of polyimide aerogel to all tested fibre types, mainly attributed to larger shrinkage during curing and more significant difference in heat expansion coefficient, which both contributed to larger residual stresses. In addition, in the case of silica aerogel, the material shear properties could be a

limiting factor leading to cohesive matrix failure and not reflecting on the true nature of the adhesion strength. Finally, the samples prepared with carbon fibre were characterised with the largest IFSS values. Such behaviour can be attributed to its geometrical features, such as high surface roughness and small diameter. In addition, certain chemical reactions could facilitate the adhesion. Nevertheless, those results should be treated with caution as the superior adhesion of aerogels to carbon fibre could also result from the difference in the sample size, which would be responsible for different internal structure and sample test behaviour across the samples.

Above all, this work indicates that the micromechanical testing of aerogel adhesion to fibrous reinforcements is possible using the microbond test. The deposition of droplets around the fibres required for this technique has proven to produce a consistent and easy to handle samples which was specially challenging due to the low porosity and high brittleness of the aerogel materials. Additionally, the shape and positioning of the droplets on the fibre enabled easy measurement of all parameters required for the IFSS calculations. Mentioned advantages of the microbond technique makes it probably the most suitable testing method to investigate the adhesion of aerogel composites. The other micromechanical methods require larger samples and clamping of the matrix material which would be extremely difficult to achieve without damaging the aerogel structure before commencing the test. However, even though the microbond presents an advantage over the other techniques a further analysis is required to evaluate the impact of test parameters and droplet size on the IFSS values. Following such investigation, it might be possible to use the microbond test to fully understand the impact of aerogels' properties, manufacturing techniques and composition on the adhesion with the fibre materials.

5 Nanoscale interface analysis

In this chapter a nanoscale investigation of thermal and mechanical properties of low density silica and polyimide using Large-scale Atomic/Molecular Massively Parallel Simulator (LAMMPS) has been conducted.

By simulating a range of silica and polyimide samples with varying densities a correlation between density and thermal, tensile, and compressive properties has been derived. Achieved results have proven to be in a close correlation with values achieved from previous studies and experimental tests. This investigation also allowed for the detailed assessment of interatomic potentials used for simulation of silica aerogels proving the superiority of Vashishta potential under tested conditions.

In addition, the low density samples have been combined with two reinforcement systems including amorphous silica and epoxy resin. Such combinations allowed nanoscale investigation to focus on quantifying the thermal and mechanical properties of interfaces between silica or polyimide and mentioned reinforcement systems. As a result, for the first time the effect of materials' density upon both interfacial thermal resistance and interfacial shear strength was calculated with both values increasing with increasing silica or polyimide densities.

5.1 Literature review

In the following section an overview of previous molecular dynamics simulations in the aerogel and interface testing filed has been summarised.

5.1.1 An overview of molecular dynamics simulations

5.1.1.1 Low density silica

5.1.1.1.1 Sample preparation

In the past, many attempts were undertaken to investigate the structure of silica aerogel by means of molecular dynamics. Initially, the greatest effort focussed on achieving correct porous structure and fractal nature of silica aerogels. In general, two main categories of simulations resulting in creation of silica aerogel structures has been identified. In the "mimetic" simulations an attempt to replicate the experimental synthesis process through molecular dynamics means is undertaken. On the other hand, second category relay on direct creation of silica aerogel models incorporating as much detail from available experimental data as possible. Regardless of the method used, created samples are latter validated by

comparison of geometrical features such as fractal dimensions, bond length and bond angle distributions and pore size distribution [357].

An example of the first category is given by Garofalini et al., who have investigated the solutions of water, silicic acid monomers, and silicic acid dimer [358-360]. The series of studies resulted in replication of experimental sol-gel systems achieving similar degrees of chain formation, the activation energy for branching, and relative time evolution [358-360]. The reactive molecular dynamics studies have also been used by Bhattacharya and Kieffer who improved the gelation process simulations by additionally considering transfer of charges [361, 362]. In their studies thy have compared fractal dimensions of silica structures created by reactive simulations and negative pressure rupturing method proving that this feature is most likely process-dependent and should not be correlated with the gel density and porosity [361, 362]. Overall, studies have proved that "mimetic" simulations can successfully crate silica aerogel structures, nevertheless they do require much larger computational resources than other silica aerogel simulations [357].

The more statistical approach has been firstly used by Kieffer and Angell who has simulated silica aerogel using a negative pressure rupture method with Born–Mayer potential [363]. Such approach requires gradual expansion, heating and quenching of the amorphous silica sample resulting in breakage of Si-O bonds until the required density is achieved. Obtained silica aerogel structures presented dependency of fractal dimensions upon sample density however, other geometrical features such as the neutron-scattering static structure factor, bond statistics, and pore size distribution corresponded well with experimental values [357]. This method seems to be the most popular among molecular dynamics studies of silica aerogel and many authors including Nakano, Murillo, Patil, Gonçalves and Liu used a similar technique and further focused on characterisation of mechanical and thermal properties of aerogels using wide range of potentials such as BKS or Vashishta [95, 238, 364-367].

5.1.1.1.2 Mechanical characterisation

Successfully created silica aerogel samples enabled the analysis of material's nanomechanical properties such as the bulk, shear and Young's moduli. In general, three different techniques have been incorporated in these studies including molecular dynamics, coarse grain simulations and combination of MD and analytical-numerical models.

One of the first of MD studies has been conducted by Campbell et al., who investigated the mechanical properties of xerogels with densities between 1.67 and 2.2 g/cm^3 [368]. They have found that silica aergoels Young's modulus is correlated with sample density and increases

following a power trend with an exponent of 3.5 ± 0.2 [368]. Similar investigation but for aerogels with lower densities (between 0.23 and 2.2 g/cm^3), has been conducted by both Murillo et al. and Patil et al. [369, 370]. The former one use the tension test in order to investigate the elastic modulus and strength of silica aerogel samples correlating them with density by a power law with exponents of respectively 3.11 ± 0.21 and 2.53 ± 0.15 [369]. On the other hand, Patil et al. have not only used much larger scale for their simulations (192,000 atoms used) but also incorporated both tensile and compressive deformation mode [95]. Resulting data indicated a power law correlation between density and both Young's modulus and strength to have an exponent of respectively 3.25 ± 0.1 and 2.79 ± 0.1 [95]. Finally, Gonçalves et al. investigated the largest volumes among all studies (20^3–100^3 nm^3) and have achieved similar results with elastic modulus following a power law with a 3.84 ± 0.22 exponent [367]. Additionally, their study has also analysed the asymmetry in tension-compression behaviour which was believed to originate from the substantial pre-existing compressive stress from the surface stress effect [367]. It is worth mentioning that all mentioned studies presented a relatively close match with experimental results acquired by Woignier regarding elastic moduli, nevertheless close correlation with strength data was not achieved [5, 23, 36, 95, 238, 357, 366, 371].

Slightly different approach has been used by Lei et al. who have used the two-level hierarchical model incorporating both characterization of the main backbone and secondary nanostructure [372]. The MD simulation has been used to investigate the mechanical properties of secondary nanostructure and presented correlation between Young's modulus and sample density with exponential factor of 3.17. Nominal Young's modulus of secondary nanostructure has been further incorporated in larger scale equations to determine Young's modulus of silica aerogel based on material features such as porosity [357, 372].

Finally, coarse grain simulations have also been utilised in predictions of silica aerogel properties at a higher length scale. Studies prepared by Gelb introduced the flexible reactive aerogel model and discovered much lower bulk modulus than one gathered from experimental work [373]. Further studies included more detailed analysis incorporating such features like particle sizes, densities, and size dispersity and resulted in the power law correlation between of the bulk moduli and density with an exponent of around 3.1 [373]. CG simulations has also been used in further studies by Ferreiro-Rangel and Gelb. By combing MD and hybrid Monte Carlo methods they have managed to reproduce the power law dependency with exponent of 3.0 and Poisson ratios between 0.17 and 0.23 [357, 374, 375].

5.1.1.1.3 Thermal characterisation

The experimental approach to evaluate thermal conductivity of silica aerogel is mainly used to describe the properties of commercially available products. However, studies by Fricke and Jain relate the thermal conductivity and density of the silica aerogel. Jain based his measurements on the 3-ω technique and the photothermal deflection method for porous silica xerogel films both sintered and prepared with the use of ethanol. His results presented a power law relationship between thermal conductivity and density with power law factors of 1.65 for aerogel made with ethanol and 1.04 for sintered ones [35]. Jain's results were in a close agreement with results obtained previously by Fricke who showed a power law relationship with a factor of 1.6 for monolith aerogels with density below 1 g/cm^3 [376]. On the other hand, many simulation-based approaches have been utilized in calculating the thermal conductivity of silica aerogel including pure molecular dynamics studies as well as a coupling model.

The example of silica aerogel study purely based on molecular dynamics approaches is presented by Ng and Yeo who both describe the relationship between thermal conductivity and density of silica aerogel [174, 377]. In order to achieve this, they used a negative pressure rupture method and two significantly different potentials, namely BKS and Tersoff potentials, which were previously successfully used to describe mechanical properties of the material. Both authors are using the Reverse Non-equilibrium Molecular Dynamics (RNEMD) in which the atoms with highest kinetic energy are selected and its energy is swapped with atoms with the lowest kinetic energy from the neighbouring piece [378]. As a result, a linear gradient across the sample is created allowing to calculate the thermal conductivity of investigated sample. Nevertheless, in both cases obtained results significantly overestimated the thermal conductivity of silica aerogel, presenting power law factors of 1.04 and 1.65. The discrepancies were explained by the lack of possibility to accurately simulate the porous structure of the material as the achieved porous regime was unable to break 5nm diameter [174, 377].

Second approach includes a coupling model which connects thermal conductivity to material features such as mean particle size, mean pore size, gaseous thermal conductivity and solid particle thermal conductivity all which can be obtained through molecular dynamics study [379]. Such study was conducted by Bi and Tang and aimed at calculating thermal conductivity of aerogel solid backbone. By including such a wide variety of material properties, the authors were able to closely replicate silica aerogel structure and obtain a close fit with regards to experimental results. The success of this model has been attributed to its

ability to take into account interfacial thermal resistance in between the particles of the aerogel backbone [357, 379].

5.1.1.2 Polyimide

Until now, no attempts have been undertaken to simulate polyimide aerogel via molecular dynamics techniques, however a broad range of studies have been conducted focusing on the synthesis and properties of polyimide.

By analysing literature, two main techniques used for creation of polyimide samples can be identified. First one includes introduction of already crosslinked PI monomers (with varying unit length) into investigated volume followed by volume shrinkage until reaching desired density and energy minimisation. This method has been used in many studies for example by Patil et al., Dong et al., Qi et al., and Min et al. [380-383]. Another method includes incorporation of desired diamines and dianhydrides followed by a volume shrinkage and the artificial imidization process until reaching desired crosslinking density. This more complex method has been incorporated in studies by Ravindranath, Vashisth et al. and Kumar et al. [384-386]. Using both methods the polyimide samples with acceptable level of details have been created allowing for further investigation of materials properties.

Current polyimide molecular dynamics studies focus on variety of material properties. Wen et al., have investigated glass transition temperature of polyimides while Hu et al., have developed coarse grained model and characterised thermomechanical properties (such as glass transition temperature and the coefficient of linear thermal expansion) as well as stress−strain behaviour under compression or tension. Both studies have achieved good correlation with experimental results [387, 388]. Additionally, often polyimide is used as a matrix system for various additives with those simulations focusing on interfacial properties. As a result, Kumar et al. investigated mixture of rutile and PI and Min et al. combined same polymer with silica glass [383, 386]. Finally, large quantity of studies has focused on graphene or carbon nanotube interactions with polyimide including works by Delozier et al., Patil et al., Dong et al. and Qi et al. [380-382, 389].

5.1.1.3 Epoxy

Epoxy resin has already been covered by a wide range of molecular dynamics simulations not only investigating its properties but also interactions with mostly fibrous reinforcements. Among various techniques allowing for creation of polymer structures which can be later used in molecular dynamics simulations the polymerization of seems to attract most of the attention mainly due to their ability to replicate complex topologies [390]. It includes crosslinking of

diglycidyl ether of bisphenol A (or other monomer) with curing agent of an interest. By opening up epoxides rings crosslinking process is commenced followed by creation of bonds between atoms within the cut-off distance [390]. Such approach has been widely used in the past with just a few examples including Fan et al, investigating the thermomechanical properties of an epoxy thermosetting polymer, Liu et al., analysing the mechanical properties and the glass transition temperature of the epoxy resin system and Li and Strachan characterising glass transition temperature, Young's modulus, and yield stress of the epoxy films [391-393]. Many other studies have focused on investigating thermal, mechanical and curing properties of created epoxy systems [390, 394-400]. Overall, conducted studies have highlighted the importance of achieving high crosslinking density in order to truly replicate the polymer system with conversion factor ranging between 0.7 and 1. In addition, the same technique has also been used in investigation of multiple epoxy-based composites and nanocomposites including graphene, carbon nanotubes and glass fibre [401-408].

5.1.1.4 Glass fibre

Similarly, as in case of epoxy, glass fibre is being often investigated via molecular dynamics techniques. Most frequently glass fibre samples are being created by a melt-quench procedure allowing to simulate the amorphous SiO_2, and latter apply required sizing (if non bare fibre is considered). This technique was used by Stoffels et al., who investigates the effect of water on interfacial adhesion in glass fibre-epoxy composites [406]. Similarly, Zhang et al., looked into the effect of temperature and strain rate on the interfacial behaviour of glass fibre reinforced polypropylene composites [409]. Other up to date, studies are often focusing on effect of applied sizing or fibre topological features on adhesion between glass fibre and various matrix systems such as polypropylene, polyamide or PEEK [408, 410-415]. Finally, of a particular interest for this study is an investigation carried by Patil et al., who have characterised the mechanical properties of silica aerogel reinforced with glass fibre [416]. Their work revealed 3.5, 9.5 and 11.5 times improvement in the axial loading of native silica aerogels when reinforced with glass fibres, graphene sheets, and carbon nanotubes respectively.

5.1.2 An overview of interface molecular dynamics simulations

At the moment of writing thesis, there was no previous molecular dynamics investigations regarding material interface carried for any aerogel type. However, multiple attempts have been made for other solid materials both looking into thermal and mechanical properties of the interface [417-430].

5.1.2.1 Thermal interfacial properties

Most investigations focusing on thermal properties of material interface use non-equilibrium molecular dynamics approach with heat source and heat sinks located on the opposite side of the material sample. The flow of energy between atom results in a temperature gradient, which most often is disrupted by the interface region. As a result, the discontinuity in the gradient is created and resulting temperature difference can be used for calculation of interface thermal resistance or thermal conductance [417-430].

Using this method multiple variation of materials interfaces has been described including non-organic structures analysed by Y. Chalopin et al. and E. S. Landry who have looked into Si/Ge composites and quantified interfacial thermal conductance in a range of 7.5 MW/m^2K^{-1} [420]. Similarly, Wang et al. investigated carbon nanotube/copper interface resulting in thermal resistance values of 0.18 ± 0.02 mm^2 K/W. Additionally, E. Lampin et al. quantified thermal boundary resistance at silicon-silica interfaces while Zhun-Yong Ong and Eric Pop did the same for carbon nanotubes and SiO_2 composite [425, 428]. Other works were used to measure thermal properties of interface of organic materials including mainly polymer composites. As a result, Luo and Lloyd measured the interfacial properties of graphene/graphite-polymer systems as a function of sample size and density resulting in average thermal conductance of 70 MW/m^2K [417]. Additionally, Hua et al. tested silicon and amorphous polyethylene interface obtaining thermal conductance of 20 MW/m^2K at room temperature [431]. Finally, wide range of investigations has been carried to evaluate interface thermal resistant of carbon nanotubes added to different matrix systems [432-435]. Overall, many researches indicates that the usage of nanoscale for thermal investigation carries potential drawbacks such as lack of possibility of geometrical features implementation. Currently to limit required computational resources, simulations are carried using mainly flat surfaces which represent only small portion of the contact region. In general, the authors of previous studies have suggested implementation of obtained results into higher scale models (micromechanical models) in order to fully understand the impact of geometry on the energy transfer phenomenon [419].

5.1.2.2 Mechanical interfacial properties

Less of an agreement can be noticed in terms of the interface mechanical characterisation techniques used in molecular dynamics studies. Three main deformation modes being pulling, peeling and sliding each characterised by different force/displacement application techniques. Pulling and peeling are similar methods with a constant displacement velocity being applied to the outward direction of all atoms (pulling) or selected group (peeling), while in sliding

mode displacement is applied parallel to the interface region. The schematical representation of methods is presented in Figure 5-1.

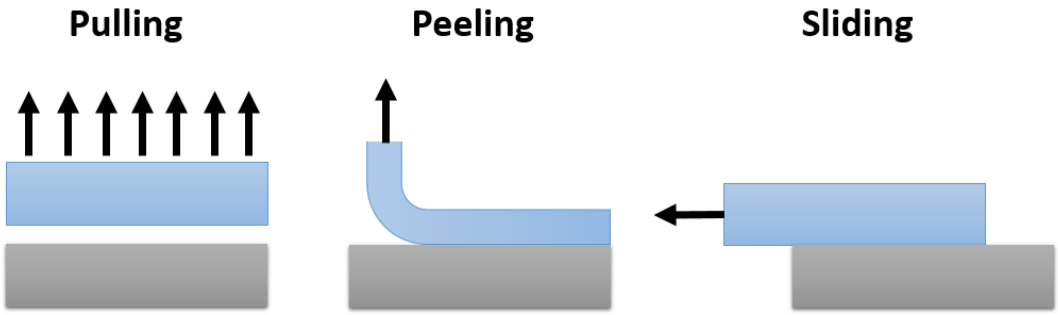

Figure 5-1 Modes of deformation used during molecular dynamics study to investigate mechanical properties of interface.

Each of the method has certain advantages over other and it is due to the user to select the most appropriate one. Pulling has high dependence on the pulling rate and requires greatest forces to be used due to the instantaneous detachment of the materials. It is often used in situations where geometrical characteristics of the sample cannot be introduced or are of a lesser importance. Such technique has been used by Johnston et al. for the multiscale analysis of carbon fibre/polymer interphase [148]. Peeling is the least displacement rate sensitive mode. Being similar to pulling it has been used by both Huang and Min et al. to investigate respectively peeling behaviour of single-walled carbon nanotubes off the gold surfaces and polyimide off the silica glass [88, 383, 436]. Finally, sliding requires large displacement distance due to the parallel separation of the materials. It is most often used in case of carbon nanotube pull-out investigations as the size of nanotube allows for simulation in which full submersion into matrix material occurs [383, 407, 437, 438]. As a result, Chawlaa et al. used such method for carbon nanotube pull-out from polyethylene matrix while Gou et al. did the same with epoxy matrix and Liao with polystyrene [148, 439-441].

Regardless of the mode of deformation used simulations allow to quantify the strength of adhesion between both materials and the property can be described using interfacial shear strength (IFSS) [286]. This numerical value can be calculated using two different approaches based on either force or potential energy difference recorded during simulation. The first one, “force” method calculate IFSS by dividing maximum force occurring during atom displacement by the initial surface area of the interface [148, 383, 440]. Second way include calculation of difference in potential energy of the system between combined and separate state of the materials, latter translated into IFSS [407, 441, 442]. No method present clear advantage and it is up to the judgement of the user which one to select. As a result of using

previously described simulation techniques many material combinations have been tested. Selected studies and their results are presented in Table 5-1.

Table 5-1 Selected molecular dynamics interface studies and IFSS values obtained.

Author	Materials	Test method	IFSS [MPa]
Jin et al. [438]	Graphene and polyethylene	Sliding	150 - 600
Demir et al. [443]	Carbon fibre and epoxy	Sliding	3000
Zhao et al. [444]	Graphene and copper	Sliding	234-1370
Singh et al. [445]	Carbon nanotube and polyethylene	Sliding	73-109
Li et al. [446]	Graphene and epoxy	Sliding	75-115
Xin et al. [447]	Graphene and poly (methyl methacrylate)	Sliding	145-265
Liu et al. [448]	Graphene and polyethylene	Pulling	150-900
Sun et al. [449]	Graphene and epoxy	Sliding	75-250
Peng et al. [450]	Carbon nanotube and epoxy	Sliding	175-275
Patil et al. [380]	Carbon nanotubes and polyimide	Pulling	204-237

5.1.3 Conclusion of literature review

Molecular dynamics techniques have been widely used in investigations of aerogel type of materials. Nevertheless, the scope of such studies is limited. Firstly, the majority of up to date work is investigating silica aerogel only. Due to large popularity of silica aerogel combined with the presence of well-established simulation techniques, other aerogel types have not been investigated in a many detail. Secondly, molecular dynamics aerogel studies mostly focus on aerogel internal structure as well as wide range of thermal and mechanical properties. Overall achieved results are in a good agreement with experimental results regardless of the scale difference. However, the interest in aerogel properties on a molecular level shall be broadened to incorporate interactions between aerogel and other materials. The analysis of previously conducted interfacial studies including mainly carbon-based materials revealed potential simulation techniques. To conclude, even though the wide range of molecular dynamics studies have been already investigating aerogels, most of them focuses on silica aerogel only. As a result, there is a significant need to investigate other aerogel types such as carbon or polyimide. In addition, the focus of study should not be solely placed on material thermal and mechanical properties but also expanded to investigate interactions between aerogel and other materials.

5.2 Molecular dynamics simulations

5.2.1 Sample preparation

5.2.1.1 Slow density silica samples

Silica samples were prepared using an altered method developed by Patil [95], which has been proven to create silica samples suitable in reproducing the mechanical properties of the material. This method varies from the most commonly used negative pressure rupturing of amorphous silica method. However, it also commences with the initial lattice configuration of ideal β-cristobalite, as it has density of 2.17 g/cm^3 which most accurately approximates the density of the amorphous silica. The parameters of β-cristobalite lattice were described by Wyckoff [451].

The generation of silica samples began with the creation of amorphous silica from initial the β-cristobalite structure. In order to achieve this, the periodic boundary conditions (PBC) were assigned to all dimensions and a time step of 0.5 fs was selected in order to solve the particles' equations of motion represented in velocity - Verlet algorithm. Initially, the temperature of the system was adjusted to be 7000K and thus particles were assigned with random velocities. Next, the sample was quenched to 300K using cooling rate of 30 K/ps and NVT ensemble. Further steps included energy minimisation via conjugate gradient method and finally amorphous silica was achieved after sample relaxation to 300 K and 1 bar (atmospheric conditions) using NPT ensemble [370].

Subsequently, the domain including amorphous silica was instantly enlarged to achieve expected density and temperature was gradually increased to 3000K using heating rate of 27 K/ps under NVT ensemble. The sample was then maintained at 3000K for 100 ps (NVT) and quenched to 0 K with cooling rate of 15 K/ps and again under NVT ensemble. The final steps leading to the formation of silica samples required energy minimization and relaxation of the sample to atmospheric conditions (NPT ensemble)[370].

The same procedure was used for creation of silica samples for all three potentials, each including 8 samples within a density range of 0.1 – 0.9 g/cm^3. The idea behind creation of such wide range of silica samples was to replicate the silica aerogel structure and investigate the impact of silica density on thermal, mechanical and interfacial properties of silica composites. All simulations incorporated 31940 atoms which was proven by previous researches to be number sufficient to simulate the behaviour of bulk material [238]. The

example of silica samples (0.9 g/cm^3) generated using Vahishta potential is presented in Figure 5-2.

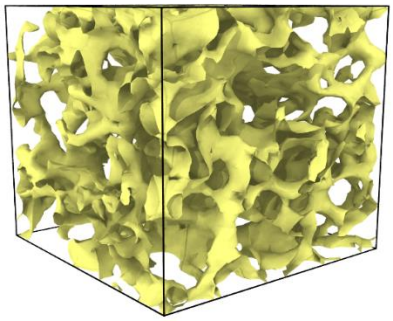

Figure 5-2 Mesh representing silica samples (0.9 g/cm^3) generated using Vahishta potential.

5.2.1.2 Low density polyimide samples

In order to simulate the low density polyimide samples, the polyimide itself has to be modelled first. The simulation has been based on the experimental work produced by Meador et al., who successfully synthesized PI aerogel using variety of diamines and dianhydrides [66]. Following her study biphenyl-3,3′,4,4′-tetracarboxylic dianydride (BPDA) and p-phenylene diamine (PPDA) has been chosen as a starting unit. It was reported polyimides formed such way present higher thermal stability at the same time maintaining brilliant insulating properties [66]. The imidization process is schematically represented in Figure 5-3.

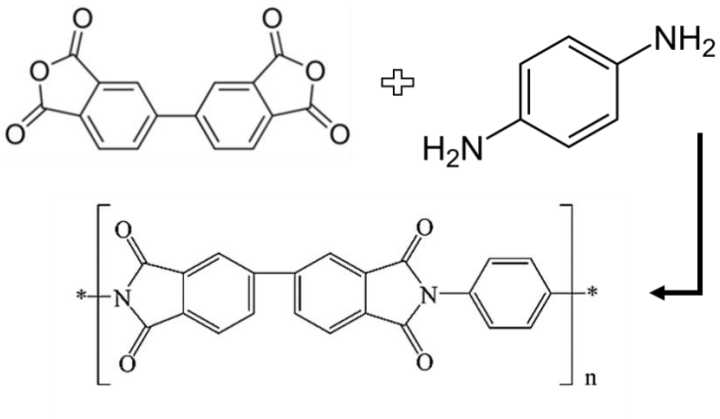

Figure 5-3 Schematical representation of PI imidization.

The polyimide crosslinking simulations were carried using Large-scale Atomic/Molecular Massively Parallel Simulator (LAMMPS) MD software package together with the OPLS – AA force field [169, 452]. BPDA and PPDA molecules were created in Avogadro advanced molecule editor. The energy minimization of monomers was conducted using UFF force field, with Conjugated-Gradient method terminating after reaching 1×10^{-4} energy tolerance. Afterwards, an randomly orientated distribution of both monomers was achieved with use of

Moltemplate and imported to LAMMPS [453, 454]. Finally, the outputs of LAMMPS simulations were visualised using Open Visualization Tool (OVITO) software package [455] and representation of BPDA and PPDA molecules are presented in Figure 5-4 .

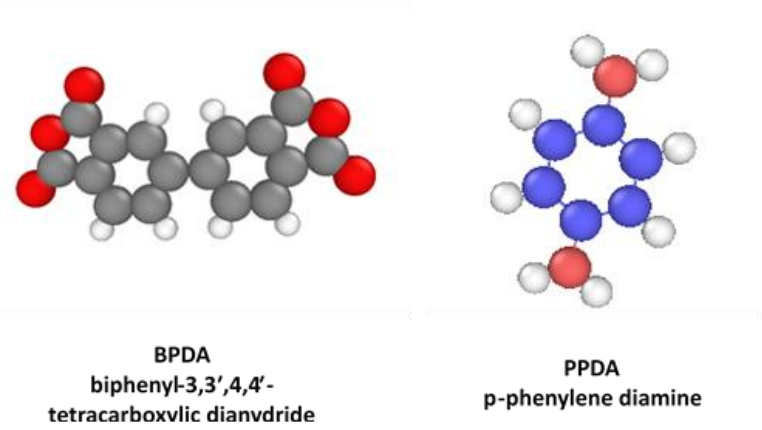

Figure 5-4 Representation of BPDA and PPDA molecules used during MD study.

During all simulations a time step of 0.1 fs was selected in order to solve the particles' equations of motion represented in velocity - Verlet algorithm. Additionally, room temperature condition together with periodic boundary conditions were introduced. To commence simulation, both oligomers have been randomly distributed in the simulation volume using ration of 1:1. Initially the molecules has been placed in a large volume to avoid unphysical behaviour. The first simulation step included energy minimization via conjugate gradient method with the energy tolerance of 1×10^{-4} Kcal/mole. Following, the temperature of the system was adjusted to 300K by assigning particles with random velocities using NVT ensemble. After achieving steady state, the volume box was shrunken at a rate of 1 Å/fs, as such rate allowed monomers to displace without breaking their chains. Then, the sample was relaxed and again its energy minimised using NPT ensemble under atmospherics conditions. This process was conducted in an increments allowing better monomers cohesion until reaching required density of 1.4 g/cm^3 [456]. Afterwards the sample underwent relaxation process lasting 100fs.

To commence the crosslinking process the temperature of the system was raised to 500K using canonical ensemble. Later, the hydrogen atoms connected to nitrogen and oxygen atoms at the end of BPDA molecule were removed and the bonds between free atoms were created using LAMMPs command "bond/create". Every step of the simulation a distance between crosslinking atoms was measured and if it was within cut-off range (6Å) the bond was established. Next, the energy minimization and system relaxation were conducted to lower the stresses generated during crosslinking process. Such procedure was repeated until almost all

possible bonds were created and the cross-linking density reached almost 100% rate. Finally, prepared polyimide samples were further equilibrated to atmospheric conditions in the NVT ensemble.

Upon completion of the synthesis of the polyimide the aerogel type of structure had to be achieved. As a result, similar procedure as in case of silica aerogel was implemented. Thus, the domain including polyimide was gradually enlarged to achieve required density without disturbing the polymer chain. In addition, the temperature of the system was gradually increased to 3000K using heating rate of 27 K/fs under NVT ensemble. The sample was then maintained at 3000K for 100 fs and further quenched to 0 K with cooling rate of 15 K/ps. The final steps leading to the formation of low density PI samples required energy minimization and relaxation of the sample to atmospheric conditions (NPT ensemble). The idea behind creation of such wide range of silica samples was to replicate the PI aerogel structure and investigate the impact of silica density on thermal, mechanical and interfacial properties of PI composites. An example of low density PI sample structure created with use of MD is presented in Figure 5-5

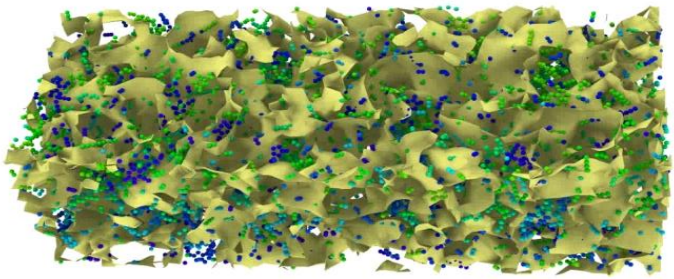

Figure 5-5 Low density PI sample structure created with use of MD.

5.2.1.3 Epoxy resin

The first step leading to simulation of epoxy sample was modelling of uncrosslinked monomers of DETA (diethylenetriamine) curing agent and DGEBA (diglycidyl ether of bisphenol-A) resin. It was latter followed with the crosslinking process and system equilibration before further analysis and usage. Required simulations were conducted using LAMMPS (large-scale atomic/molecular massively parallel simulator) using OPLS-AA potential.

As mentioned before the epoxy samples were created by crosslinking the DGEBA resin ($C_{21}H_{24}O_4$) with DETA curing agent ($C_4H_{13}N_3$). DGEBA is a reactant with epoxide group at each end (bi-functional), and DETA incorporate both primary and secondary amine groups

providing in total five reactive sites, and being multi-functional (fivefold-functional) reactant [457]. The schematical representation of both molecules can be seen below.

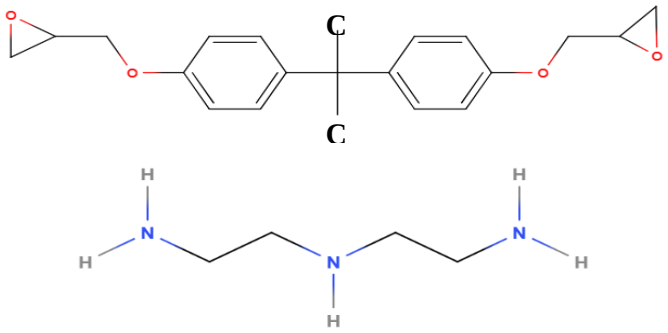

Figure 5-6. DGEBA (top), DETA (bottom) molecules.

The curing reaction commence when active hydrogen atoms in the amine groups of DETA molecule reacts with the epoxide groups in the DGEBA molecules. Afterwards, epoxides rings open up leading to crosslinking process and creation of covalent bonds. As a result, a 3D networked molecule is being created, however rarely reaching 100% conversion rate [458]. Entire crosslinking process is presented in the Figure 5-7.

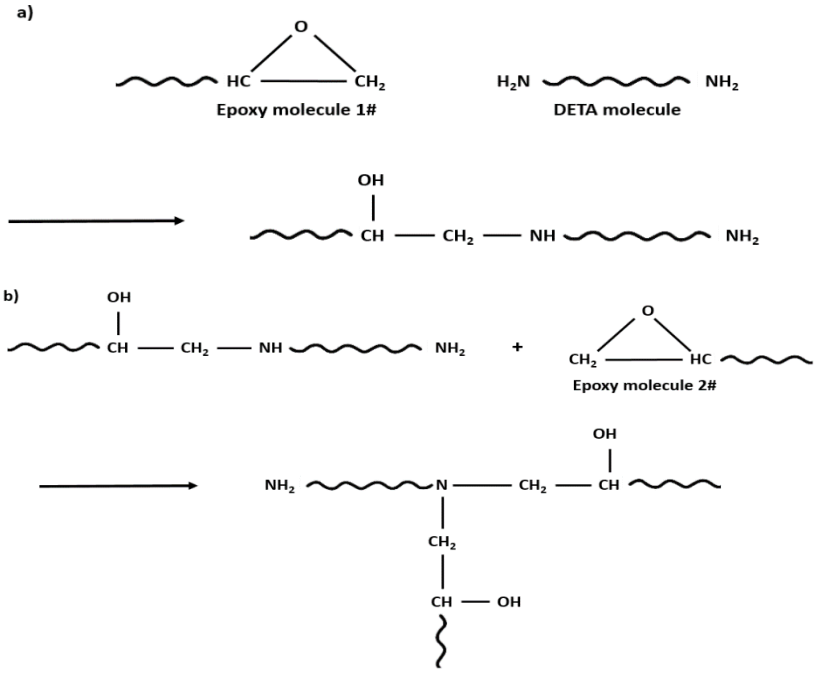

Figure 5-7. Schematic representation of DEGBA and DETA curing reaction. Top drawing presents opening of the epoxide rings, while bottom one creation of crosslinks [458].

In order to provide a proper ratio of both molecules within simulated epoxy sample a stoichiometric quantity was calculated using following calculations requiring to calculate

AEW (amine hydrogen equivalent weight), EEW (epoxide equivalent weight) and finally phr (parts per hundred) [458]:

$$AEW = \frac{molecular\ weight\ of\ amine}{number\ of\ active\ hydrogen\ atioms\ in\ amine} \quad \text{Eq. 43}$$

$$EEW = \frac{molecular\ weight\ of\ the\ epoxy\ molecule}{number\ of\ epoxide\ groups\ in\ the\ epoxy\ molecule} \quad \text{Eq. 44}$$

$$phr = \frac{AEW * 100}{EEW} \quad \text{Eq. 45}$$

For the example used during simulations following calculations were performed. DETA molecular weight was calculated to be 103 g/mol (4 carbon, 3 nitrogen and 13 hydrogen atoms) and possess 5 active hydrogens leading to:

$$AEW = \frac{103\ g/mol}{5} = 20.6\ g/mol$$

$$EEW = \frac{340\ g/mol}{2} = 170\ g/mol$$

$$phr = \frac{2060\ g/mol}{170\ g/mol} = 12.1$$

The results indicate that for every 100g of DGEBA 12.1g of DETA shall be added thus, stoichiometric ratio used was 89.2:10.8.

The epoxy crosslinking simulations were carried using Large-scale Atomic/Molecular Massively Parallel Simulator (LAMMPS) MD software package together with the OPLS – AA force field [169, 452]. DETA and DGEBA molecules were created in Avogadro advanced molecule editor as presented in Figure 5-8. The energy minimization of monomers was conducted using UFF force field, with Conjugated-Gradient method terminating after reaching 1×10^{-4} energy tolerance. Afterwards, an randomly orientated distribution of both monomers was achieved with use of Moltemplate and imported to LAMMPS [453, 454]. Finally, the outputs of LAMMPS simulations were visualised using Open Visualization Tool (OVITO) software package [455].

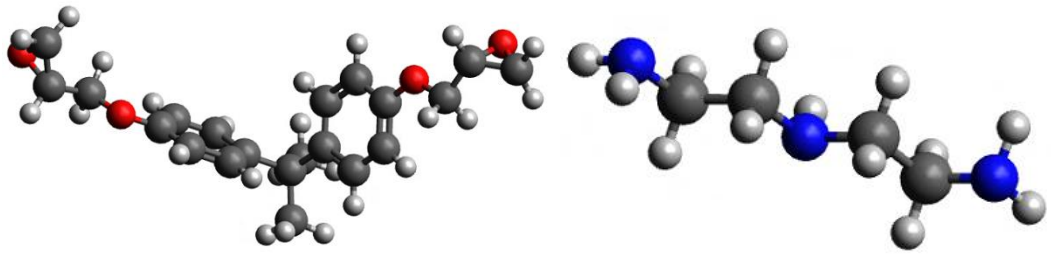

Figure 5-8. DGEBA (left) and DETA (right) monomers molecular models. Dark grey: carbon, light grey: hydrogen, red: oxygen, blue: nitrogen.

In order to perform a crosslinking process a procedure previously used by Shokuhfar and Arab with additional alterations was utilised [457].Randomly oriented monomers of DEGBA and DETA were placed in simulation box using composition ratio of 92:8. Initially the simulation volume was kept large leading to low density values of 0.1 g/cm^3. Additionally, room temperature condition together with periodic boundary conditions were introduced. The first simulation step included energy minimization via conjugate gradient method with the energy tolerance of 1×10^{-4} Kcal/mole.

During all simulations, a time step of 0.1 fs was selected in order to solve the particles' equations of motion represented in velocity - Verlet algorithm. Initially, the temperature of the system was adjusted to be 300K and particles were assigned with random velocities using NVT ensemble. After achieving equilibrium conditions with little fluctuations, the investigated volume was shrunken at a rate of 1 A/fs, as such rate allowed monomers to displace without disrupting their chains. Further steps included relaxation and energy minimisation of the volume using NPT ensemble and atmospherics conditions. This procedure was repeated until reaching required density of 1.2 g/cm^3. Afterwards the sample underwent relaxation process lasting 100fs to bring it to atmospheric conditions.

In order to increase a mobility of atoms for this step the temperature of the system was raised to 500K using canonical ensemble. Afterwards, the covalent bonds between selected atoms were created using LAMMPs command "bond/create". Every step of the simulation a distance between crosslinking atoms was measured and if it was within cut-off range (6Å) the bond was created. It was latter followed with energy minimization (to lower the stresses generated during crosslinking process) and relaxation of the system at 300K. This procedure was repeated until almost all possible bonds were created, and the cross-linking density reached almost 100% rate. Since further research was focusing on utilisation of epoxy sample for interface simulations, only samples with high curing density were generated. Samples with created covalent bonds were further equilibrated to atmospheric conditions in the NVT ensemble and the epoxy structure is presented in Figure 5-9.

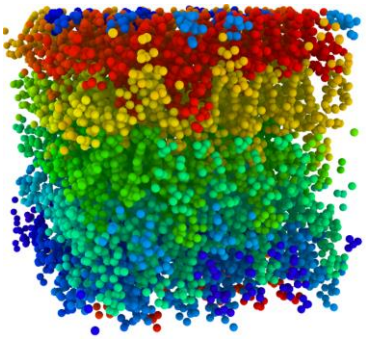

Figure 5-9 MD model of epoxy resin. The colour coding indicates molecule identification numbers used to make sure molecular structure is maintained.

5.2.1.4 Glass fibre

In the following simulations, glass fibre has been represented by amorphous silica as previously done by Stoffels or Min [406, 437]. Sample creation commences with the initial lattice configuration of ideal β-cristobalite, as it has density of 2.17 g/cm^3 which is the closest to the density of the amorphous silica. The parameters of β-cristobalite lattice were obtained from Wyckoff [451]. In order to achieve amorphous silica, the periodic boundary conditions were used for all dimensions and the temperature of the system was adjusted to be 7000K by assigning atoms with random velocities. Following the annealing step, the sample was quenched to 300K using cooling rate of 30 K/ps and NVT ensemble. Further steps included energy minimisation via conjugate gradient method and finally amorphous silica was achieved (Figure 5-10) after sample relaxation to 300 K and 1 bar (atmospheric conditions) using NPT ensemble [370].

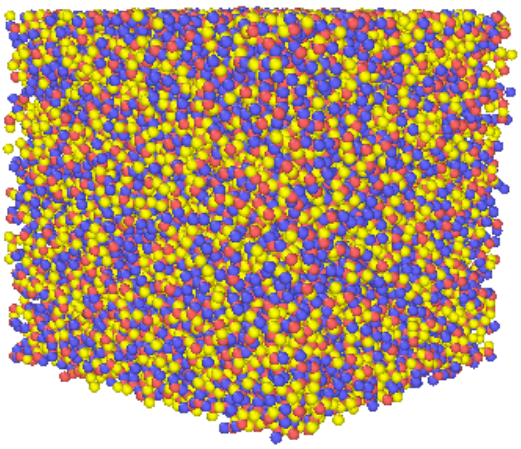

Figure 5-10 Amorphous silica sample. Silica atoms are represented by red spheres while blue and yellow represents oxygen atoms.

5.2.1.5 Interface

Following creation of low densities silica and polyimide, fibres and epoxy samples the combined models had to be simulated in order to progress with interface investigation. As a result, desired combination of materials was placed next to each other in a single simulation volume and relaxed under canonical ensemble and atmospheric conditions for 1000 fs. Such time was expected to allow atoms to form bond between both materials at the same time not interfering with material internal structure further away from boundary region. An example of interface model between low density silica sample and epoxy resin is preseted in Figure 5-11

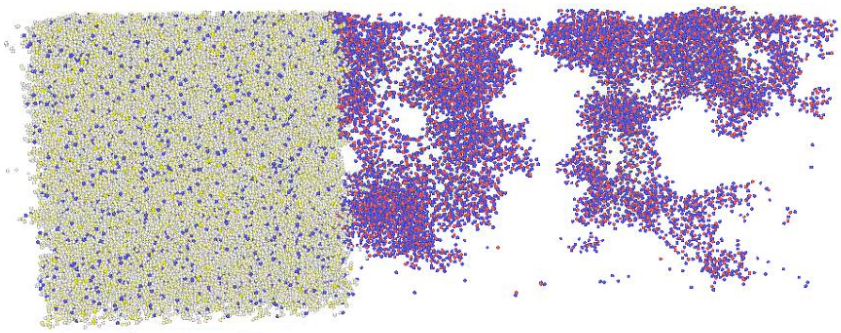

Figure 5-11 Interface model between low density silica (right) and epoxy resin (left).

5.2.2 Sample validation

5.2.2.1 Geometrical Characterisation

The Radial Distribution Function (RDF), describes how density changes in respect to the distance from a reference atom and its values can be easily calculated in LAMMPS and plotted as presented in Figure 5-12. In addition, the distance value corresponding to the highest value of RDF describes the bond length between atoms [361].

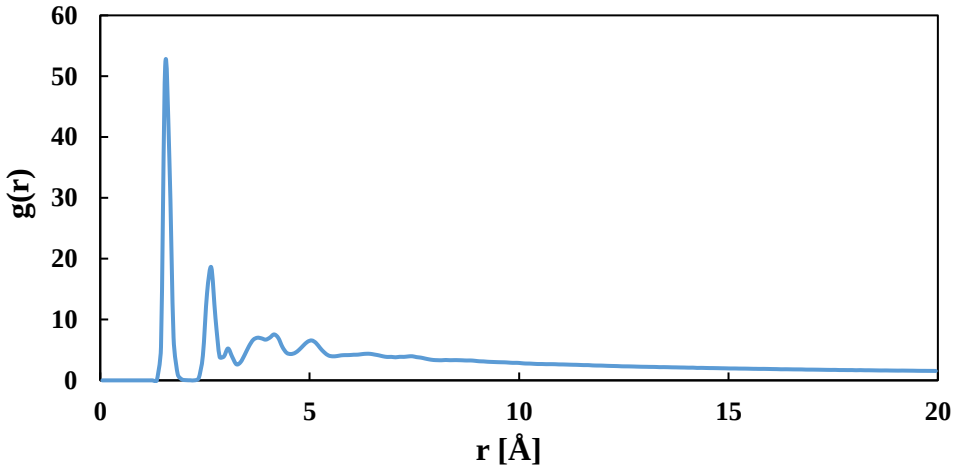

Figure 5-12 Pair distribution function of a 0.9 g/cm^3 sample determined using Tersoff potential.

Furthermore, using the RDF function for high values of atom separations (above 5A), it was possible to calculate the fractal dimension using method previously introduced by Kieffer's [361]:

$$d_f = 3 + \frac{d\ ln[g(r)]}{d\ ln(r)} \qquad \text{Eq. 46}$$

5.2.2.2 Pore Size Distribution

Pore size distribution (PSD) is an important feature able to describe the internal structure of created samples by supplying details regarding the fraction of void space that is occupied by pores of particular radius. The PSD was calculated using Zeo++ software which incorporates Voronoi decomposition and accessibility analysis to produce the histogram identifying the probability density function of certain size pores occurrence [459]. The pore size was calculated using a probe size of 2.3A approximately corresponding to a CO_2 molecule size. The typical graph describing distribution is presented in Figure 5-13:

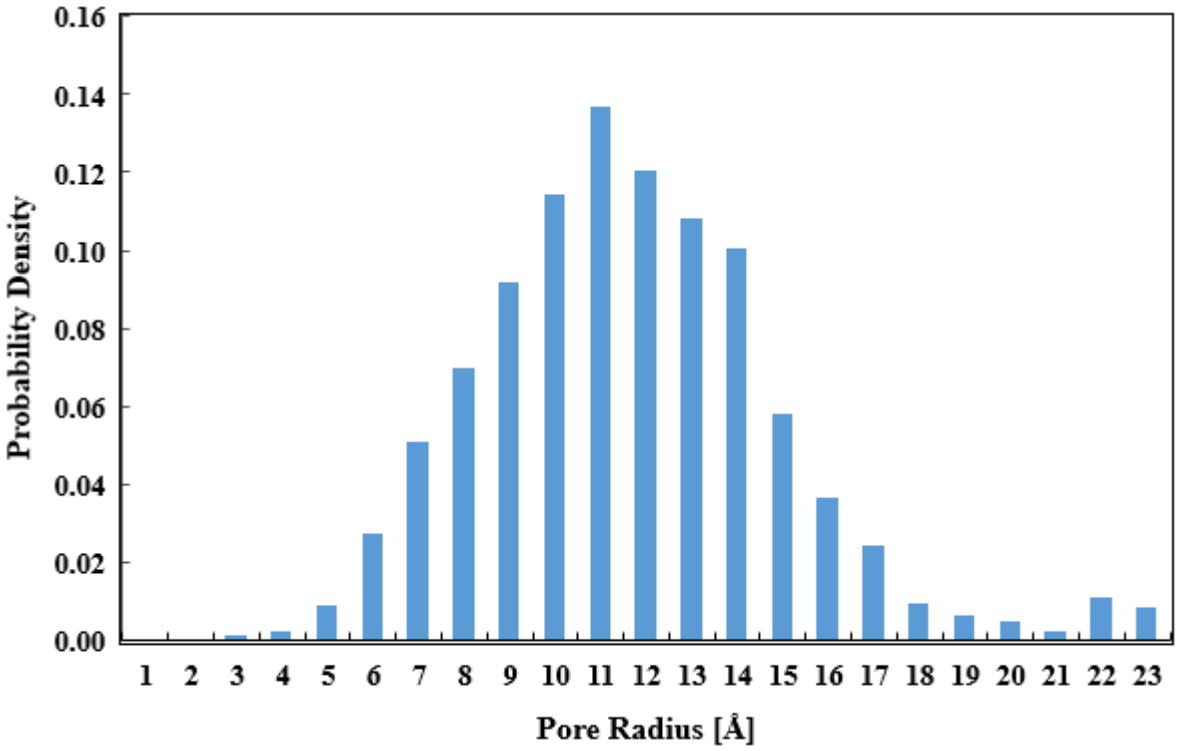

Figure 5-13 Pore Size Distribution of a 0.9 g/cm^3 sample created with Vashishta potential. Values calculated using Zeo++ software [459].

5.2.2.3 Density measurement

One of the simplest methods to investigate structure of solid materials is to determine local density across simulation volume. It was calculated using "fix ave/spatial" command for

simulation box equally divided across X, Y and Z axes. The mass of each atom included within such division was added and divided by division volume providing localised density.

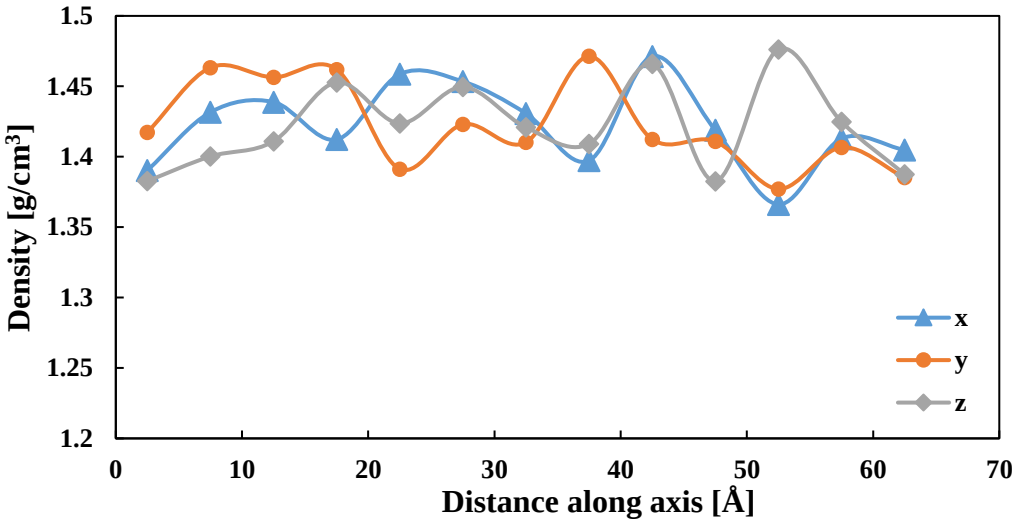

Figure 5-14 Results of localised density analysis.

Figure 5-14 presents the results of the analysis of cross-linked polyimide model. For solid materials the uniformity of those results is of a particular importance as it indicates lack of pores or local densifications. Nevertheless, the presence of small fluctuations can occur especially for the cross-linked systems. It is caused by a different number of atoms being included into divided sections due to the high quantity of cross-linked chains, which reduce mobility of atoms and limit molecular movement.

5.2.2.4 FTIR simulation

The Fourier transform infrared spectroscopy (FTIR) is used for investigation of infrared absorption and emission spectra allowing identification of chemical composition of tested samples. For the purpose of sample validation, the LAMMPS calculations has been conducted generating such spectrum for modelled samples and them compared with experimentally obtained results [460]. The calculations are divided into two steps. During the first one the instantaneous net dipole moment of the system versus time is being calculated. For this purpose, relaxed sample is being kept under atmospheric conditions and canonical ensemble for 10,000 fs in order to achieve required accuracy of the results. During second step the IR spectrum is being calculated using previously calculated dipole moments and linear response theory [461]. Python code calculates the spectra average for the initial coordinates and moments applicable to the desired experimental conditions such as particular temperature and pressure. Finally, the quantum correction function is calculated and being incorporated when

required to converge toward quantum reality [460, 462]. Figure 5-15 represents an example of results obtained by molecular dynamics FTIR analysis.

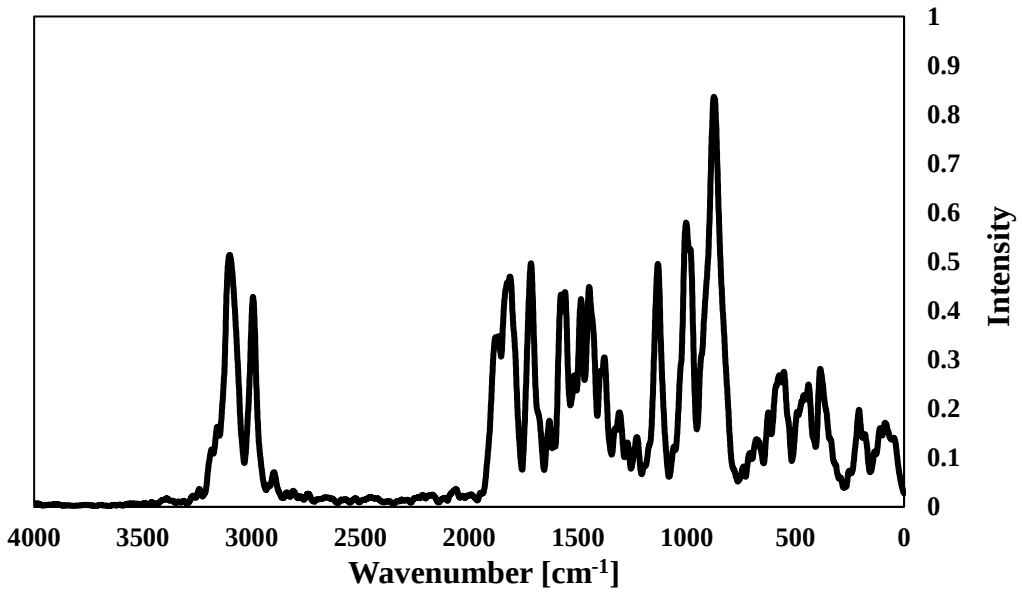

Figure 5-15 FTIR spectrum calculated for low density PI samples.

5.2.3 Testing

5.2.3.1 Tensile testing

Figure 5-16 presents the low density silica sample undergoing tensile testing.

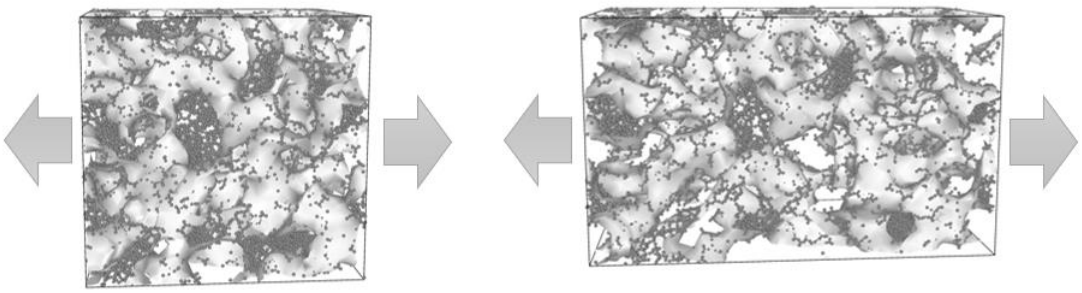

Figure 5-16 Tensile testing. Figure on the left presents 0.4 g/cm^3 silica sample while figure on the right presents the same sample at 0.3 compressive strain.

The mechanical properties of simulated materials have been investigated using uniaxial tension and compression test. For tension testing (Figure 5-16), the sample kept under atmospheric conditions and canonical ensemble has been exposed to the deformation along x axis at a strain rate of 0.0005 ps^{-1} for low density silica and 0.005 fs^{-1} for low density polyimide. During deformation, the force and displacement has been recorded allowing creation of stress-strain graph and thus calculation of Young's modulus and fracture strength. In order to remove the force fluctuations an exponential smoothing method has been used.

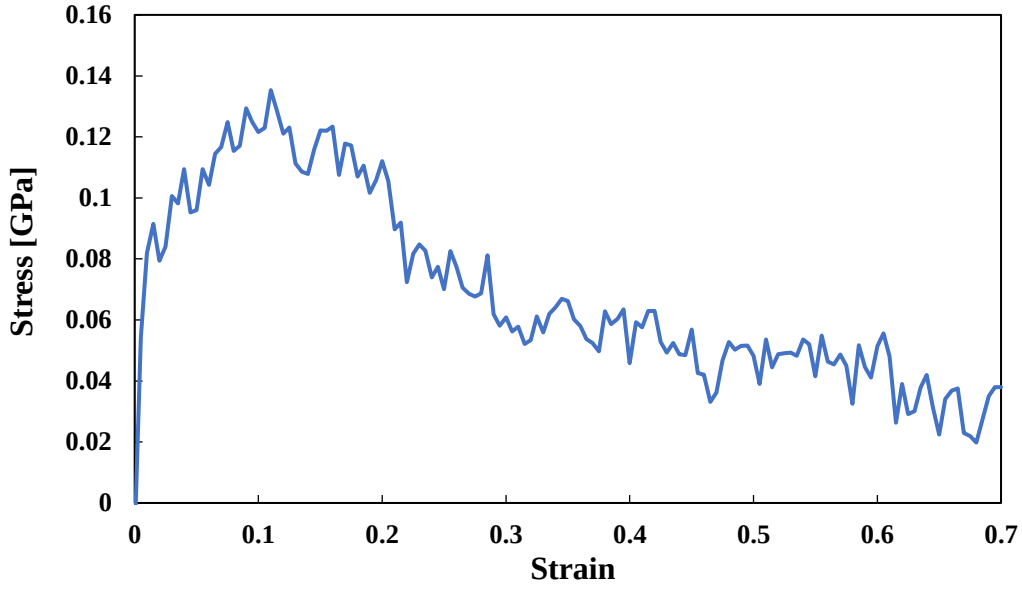

Figure 5-17 Example of stress/ strain curve produced during uniaxial tensile simulation.

5.2.3.2 Compression testing

Figure 5-17 presents the low density silica sample undergoing compression testing.

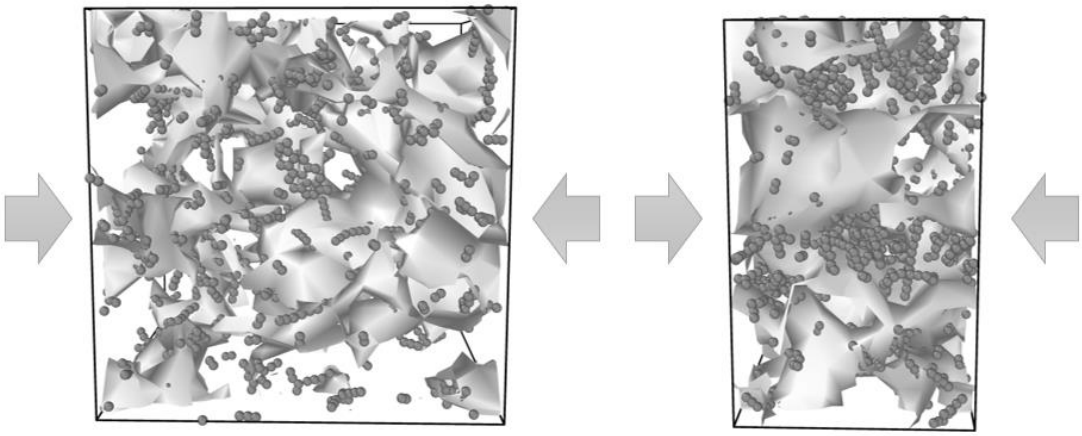

Figure 5-18 Compression testing. Figure on the left presents 0.4 g/cm^3 polyimide sample while figure on the right presents the same sample at 0.5 compressive strain.

For compression testing as presented in Figure 5-18, the sample kept under atmospheric conditions and canonical ensemble has been exposed to the deformation along x axis at a strain rate of -0.0005 ps^{-1} for low density silica and -0.005 fs^{-1} for low density polyimide. During deformation, the force and displacement has been recorded allowing creation of stress- strain graph and thus calculation of Young's modulus and fracture strength. In order to remove the force fluctuations an exponential smoothing method has been used and example stress vs strain graph is presented in Figure 5-19.

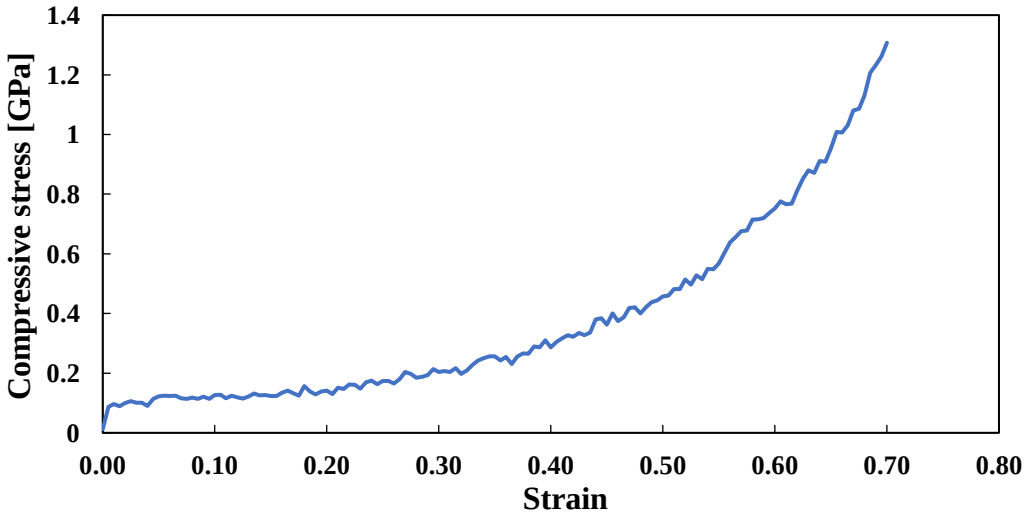

Figure 5-19 Example of stress/ strain curve produced during uniaxial compression simulation.

5.2.3.3 Interface mechanical characterisation

Figure 5-20 presents the snapshot of the debonding simulation.

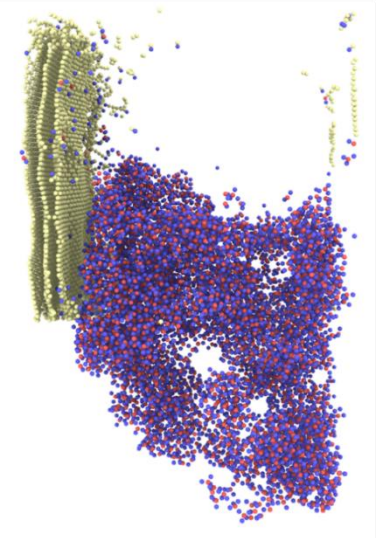

Figure 5-20 Snapshot of the debonding simulation.

The adhesion between simulated materials has been calculated using steered molecular dynamics (SMD) simulations. SMD is a simulation process which equates the non-equilibrium work done on the system to the equilibrium potential of mean force (PMF) with means of the Jarzynski inequality [383, 437, 463-465]. The method operates by addition of imaginary particles which is connected by a factious spring to all atoms of pulled materials. Latter, those particles are being displaced with a uniform velocity, in return applying a force on the matrix material resulting in debond of the surfaces [463]. The force resulting from atom displacement is calculated using following equations [463]:

$$U_{spring} = \frac{1}{2}k[vt - (R(t) - R_0) \times n)^2 \quad \text{Eq. 47}$$

$$F_{spring} = -\nabla U_{spring} \quad \text{Eq. 48}$$

where, k is the spring constant of the fiction spring, ν is the velocity of the particle displacement, R(t) is the position of the centre of mass of the pulled atoms at the given time step, R_0 is the starting centre of mass of pulled atoms, and n is a unit vector along the displacement. Then the work done during process is calculated as follow:

$$W = \int_{r=R_0}^{r=R_f} \nabla U_{spring}\, d\vec{r} \quad \text{Eq. 49}$$

where, R_f is the end position of the displaced material centre of mass. After calculation of an ensemble average the Jarzynski's equality is used to relate work and PMF:

$$\langle \exp(-\beta W) \rangle_{ensemble} = \exp(-\beta U_{omf}) \quad \text{Eq. 50}$$

$$\beta = \frac{1}{k_B T} \quad \text{Eq. 51}$$

With, k_B being Boltzmann constant, and T temperature of the simulation [440]. Interfacial shear strength is latter calculated by dividing maximum force during the atom displacement by the contact area between materials (A):

$$\tau = \frac{F_{max}}{A} \quad \text{Eq. 52}$$

The resulting displacement of atoms can be seen in Figure 5-21. In order to remove the force fluctuations an exponential smoothing method has been used.

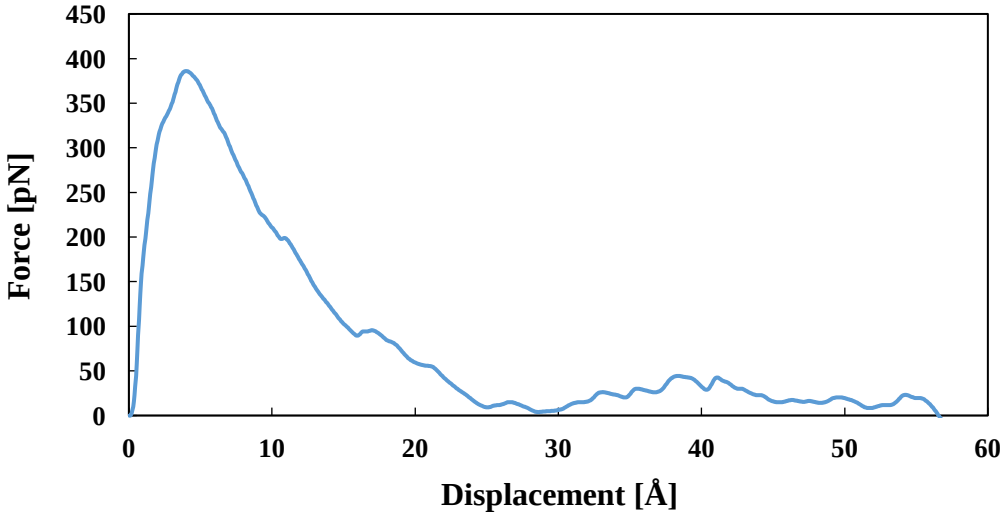

Figure 5-21 Example of force/ displacement curve produced during uniaxial compression simulation.

The alternative method involves calculation of the energy of the atom bonds broken during the atom displacement. In order to achieve it, the total energy of the system was measured during simulation and pull-out energy was defined as a:

$$\Delta E = E_{assembly} - (E_{aerogel} - E_{reinforcenment}) \quad \text{Eq. 53}$$

where, $E_{assembly}$ was total energy of combined samples and $E_{aerogel}$ and $E_{reinforcenment}$ were total energies of respectively aerogel and reinforcement sample in separate state. Interfacial shear strength is latter calculated by dividing total energy difference during the atom displacement by the contact area between materials (A) and pull-out distance (l):

$$\tau = \frac{\Delta E}{A * l} \quad \text{Eq. 54}$$

5.2.3.4 Material Thermal Testing

In order to calculate the thermal conductivity of created samples the Reverse Non-Equilibrium Molecular Dynamics (RNEMD) was used. During this approach, the simulation volume was split into equal fragments of width 1 Å (Figure 5-22) and the temperature of the central piece was increased imposing a heat gradient in the sample.

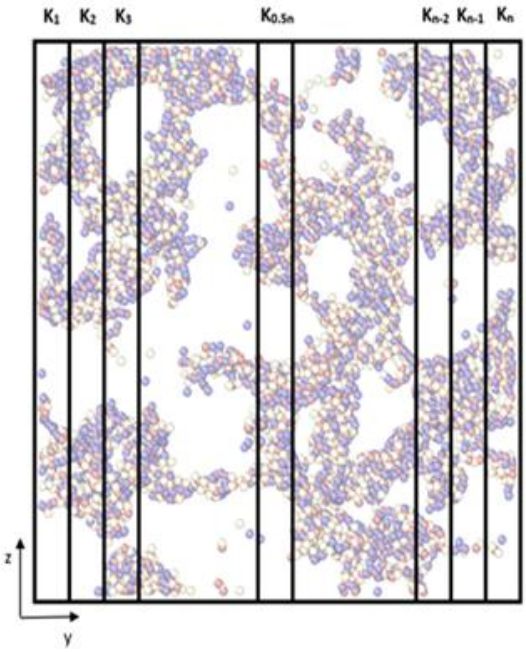

Figure 5-22 Representation of RNEMD method with hot slab being located at the middle of the simulation volume and cold slabs at both ends.

In order to achieve the heat gradient within every piece, the atoms with highest kinetic energy ("highest temperature" atoms) are selected and its energy is swapped with atoms with the lowest kinetic energy from the neighbouring piece [466]. The energy exchanges are repeated

every 10 time steps until the linear gradient across the sample was achieved. The amount of energy exchanged between pieces is calculated and recorded using:

$$j = \frac{1}{2tA} \sum_{Nswap} \left(\frac{m}{2}\right)\left(V_{hot}^2 - V_{cold}^2\right) \quad \text{Eq. 55}$$

where: t is total simulation time, A is the cross-sectional area of the sample in the direction of heat flow, N_{swap} is the cumulative number of atom swaps, m is the atomic mass of swapped atoms and v_{hot} and v_{cold} are, respectively, the velocities of highest energy and lowest energy atoms that have been exchanged. Following system stabilisation, the temperature of each piece was calculated by Equation:

$$T_{slab} = \frac{2}{3k_b N_{atom}} \sum_{i}^{N_{atoms}} \left(\frac{m_i}{2} v_i^2\right) \quad \text{Eq. 56}$$

where: N_{piece} is the number of atoms in the piece and k_B is the Stefan-Boltzmann constant. Following this, the calculation of the temperature within every piece and the temperature profile of the sample was achieved. Due to the fact that temperature presents a linear relationship with the distance as presented in Figure 5-23, it was possible to determine the temperature gradient of the system by implementing a linear regression method [467].

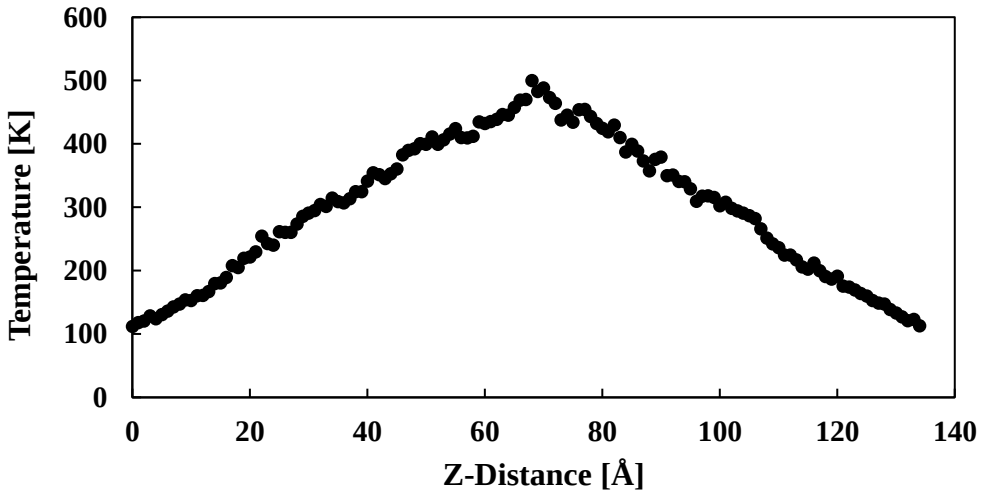

Figure 5-23 Plot of example temperature distribution occurring after RNEMD analysis.

Determining both values allowed the thermal conductivity of the material to be calculated using Fourier's law [468]:

$$\lambda = \frac{-j}{dT/dx} \quad \text{Eq. 57}$$

Even though alternative approaches for thermal conductivity calculations exist, the RNEMD method was selected for this study due to several advantages. Firstly, it is considered one of the simplest methods, thus limiting required computational resources. Secondly, RNEMD conserves total linear momentum and total energy of the system [467]. As a result, the microcanonicity of Newton's equation of motion is not violated and no thermostatting is necessary in order to perform calculations [467]. When studying material thermal properties, the RNEMD method provides a serious advantage over other methods as the heat flux is clearly defined. The velocity swaps allow precise calculation of transferred energy without taking into consideration its form and flow mechanism, significantly reducing the complexity of the approach [467].

5.2.3.5 Interface thermal testing

Figure 5-24 includes the representation of the simulation of interface thermal testing.

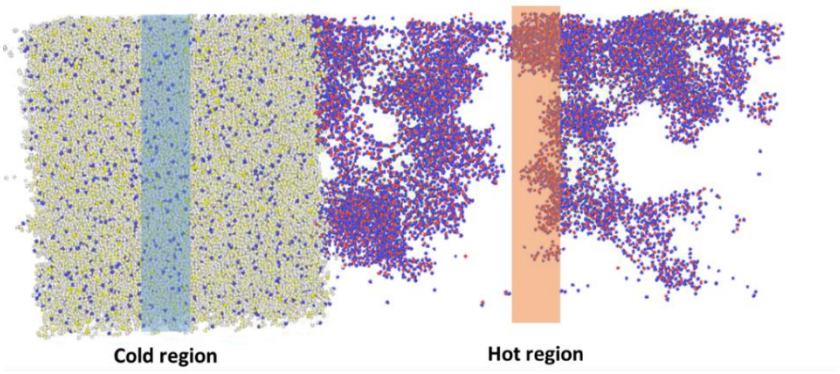

Figure 5-24 Representation of interface testing simulation with cold (blue) and hot (red) regions marked.

The interface thermal testing had to be modelled in a slightly different manner due to the interfacial region being often located in the middle of the sample. As a result, the heat source and sink had to be positioned in different materials and with sufficient distance away from interface to avoid interference. In order to achieve it "fix ehex" has been used which introduces asymmetric version of the enhanced heat exchange algorithm [452, 469]. In this algorithm specified kinetic energy is being swapped between defined regions effectively imposing a heat flux through the system. The simulations have been carried under NVE ensemble and using periodic boundary conditions [469]. The amount of energy exchanged between reservoirs is calculated and recorded using:

$$j = \frac{Q_{in}}{2L_x L_y} \qquad \text{Eq. 58}$$

where, Q_{in} is a fixed energy flux specified in the command and L_x and L_y represent dimensions of the simulation box perpendicular to the direction of the energy flow. Temperature gradient achieved through exchange of kinetic energy is then used to calculate the interfacial thermal conductivity using Fourier's law [468]:

$$\lambda = \frac{j}{\Delta T} \qquad \text{Eq. 59}$$

where, ΔT is a resulting temperature difference occurring on the interface between both materials as presented in Figure 5-25.

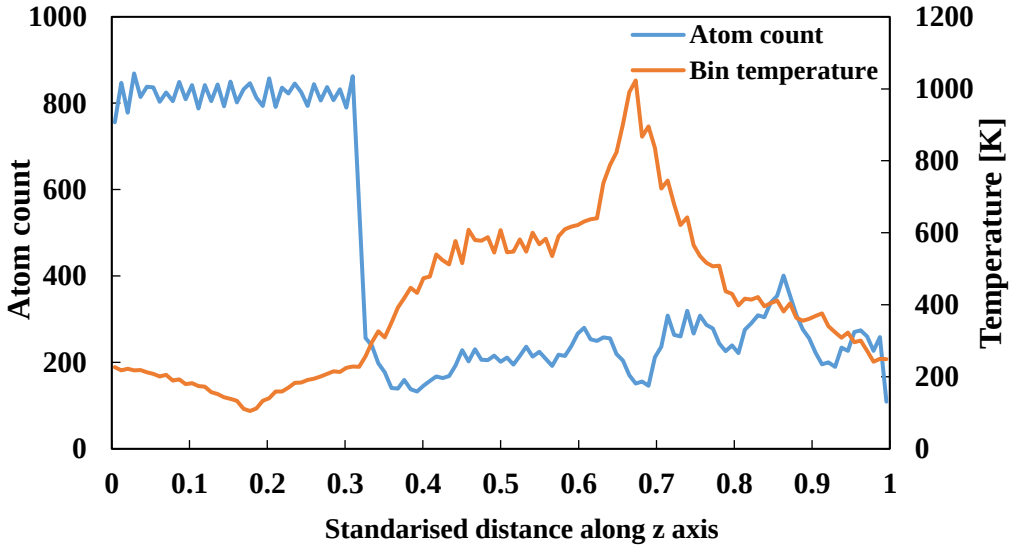

Figure 5-25 Graph presenting example results of interface thermal analysis. The figure includes both atoms count as well as temperature allowing to clearly identify the temperature variation at the materials border.

5.3 Results and discussion

The following section will focus on presentation of results starting with validation of created samples. It will be later followed by thermal and mechanical properties of individual materials, finally presenting results of the interface analysis.

5.3.1 Model validation

5.3.1.1 Low density silica

To select best atomistic potential to simulate low density silica various samples have been created using three different potentials. As a result, validation as well as thermal results will present results for all created samples. The analysis of low radial values of Radial Distribution Function were able to identify the bond length for all atoms used and results presented in Table 5-2.

Table 5-2 Bond lengths obtained for low density silica samples created using LAMMPS.

Bond Type	Bond Length [Å]		
	Vashishta	**Tersoff**	**BKS**
Si-Si	3.01 ± 0.05	3.04 ± 0.12	3.06 ± 0.10
Si-O	1.58 ± 0.08	1.58 ± 0.06	1.62 ± 0.03
O-O	2.63 ± 0.03	2.62 ± 0.10	2.58 ± 0.02

As it can be noticed, all three potentials were able to produce extremely similar bond length values. In addition, they do correspond to experimentally obtained values for silica samples which were as follows: 3.08 ± 0.10 Å for Si−Si, 1.61 ± 0.05 Å for Si−O and 2.632 ± 0.089 Å for O−O [166]. Finally, obtained results are also in close agreement with bond lengths of silica aerogel samples created during previous molecular dynamics investigations conducted using all three potentials by Murillo, Yeo or Ng [174, 238, 377]. Following analysis of radial distribution function, the coordination number of the same samples was also calculated. Values of 2.45, 2.46 and 2.48 were obtained for respectively Vashishta, Tersoff and BKS models. Again all the samples presented an agreement with experimental results, especially the one produced by Cai and Shan which ranged between 2.452 to 2.778 [470]. Additionally, the fractal dimension analysis has been conducted as obtained low density silica samples include regions of high density and sizable pores. Such variation in structure might lead to long-range density correlations and affected in fractal structures. In order to investigate this phenomenon, the fractal dimension as a function of density was plotted in Figure 5-26. In addition to values obtained in this study the fractal dimension calculated by Murillo et al., have also been incorporated for comparison purposes [369].

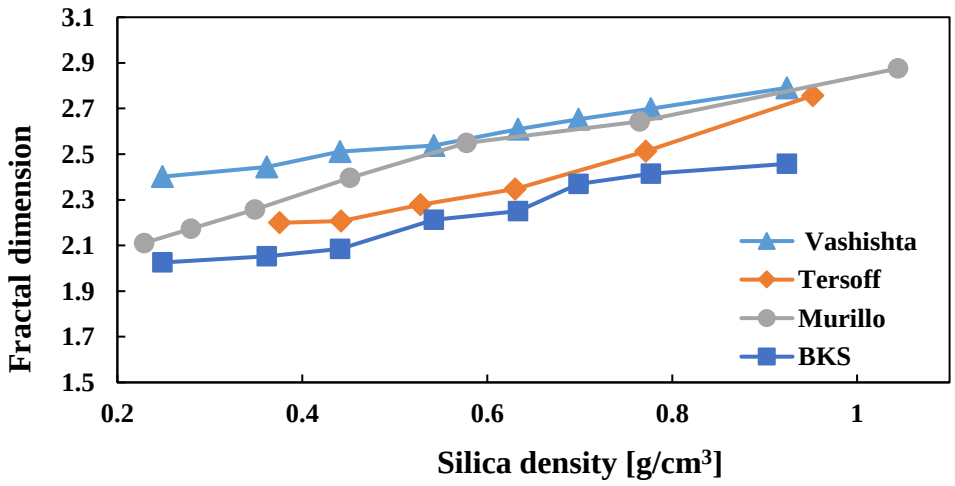

Figure 5-26 Fractal dimension of silica samples with varying densities and potentials. Results obtained by Murillo were included for comparison purposes [369].

As presented in Figure 5-26, generated results are in excellent agreement with results produced by Murillo, who in his studies has used Vashishta potential. Even though a different sample preparation method was used the fractal dimension for Vashishta potential closely follows the Murillo trend [369]. Tersoff and BKS potentials produced samples with slightly lower fractal dimension but still within the experimental range, indicating that fractal dimension values as low as 1.8 for basic processing conditions and values of 2.2 and 2.4 for, respectively, acidic and neutral condition [471]. Furthermore, all created samples follow the same trend, of increasing fractal dimension values with density approaching the limiting value of 3 presented by bulk silica [166].

Following the analysis of atomistic features of created low density samples, the analysis of geometrical properties has been conducted, as a result, pore size distribution was investigated. This feature was selected as it has been previously proven to significantly affect thermal properties of the silica aerogel. Recent studies have proved that it is possible to control the pore mean size during manufacturing process and thus alter the properties of material itself [40]. Figure 5-27 presents the pores size distribution for simulated low density silica samples with varying densities.

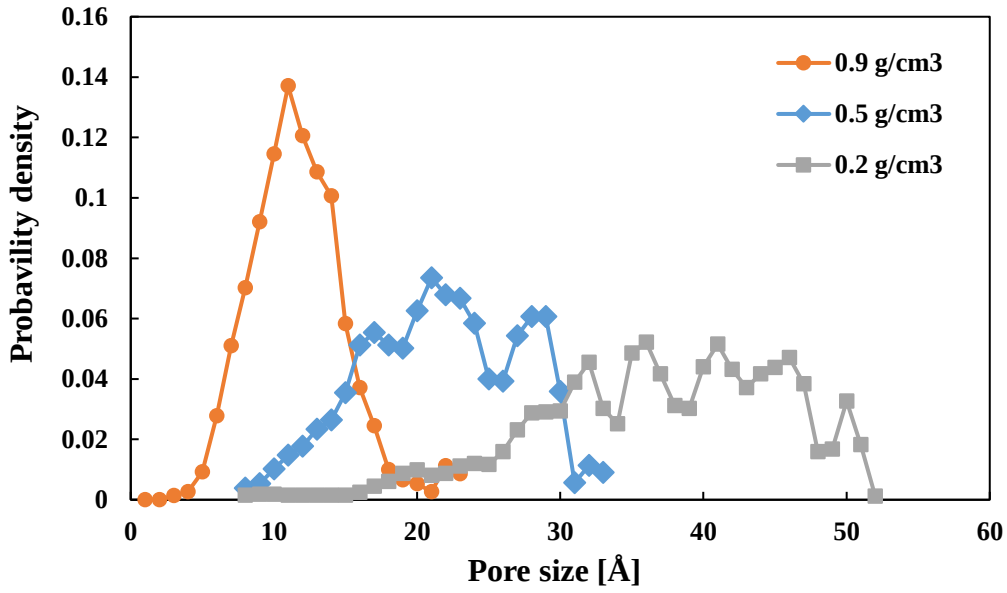

Figure 5-27 Probability density vs pore radius of silica with varying density created with use of Tersoff potential.

As it can be observed in Figure 5-27, lower density samples tend to produce wider pore distribution. Such behaviour is totally expected mainly due to the expansion process used for sample preparation, which allows higher stretching forces for lower density samples. By introduction of higher forces acting on the silica a higher chance of merging multiple pores

within the material occurs resulting in creation of a material with fewer pores but higher radius values. Following the analysis of all created samples Figure 5-28 was created presenting low density silica sample average pore size as a function of sample density.

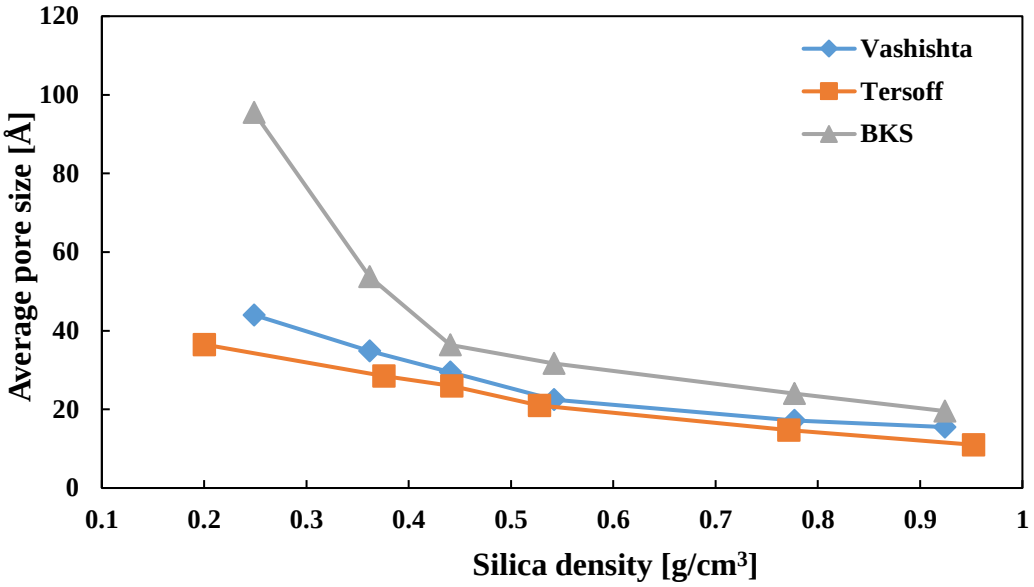

Figure 5-28 Average Pore diameter found in created low density silica samples with varying density. The values were calculated using Zeo++ software.

It can be seen that the Tersoff and Vashishta potentials produce samples with rather similar pore distribution, however it is the BKS potential for which the pores within samples are substantially larger. The difference in pore mean size increases with a reduction in density. Regardless of the potential used, all samples follow the same trend with pore mean size shifting to larger value but smaller occurrence probability, with lower density. Such dependency could be a consequence of higher stretching forces acting on the material leading to a higher chance of merging of large pores within the material with low densities. Such a phenomenon would produce fewer pores with higher radius values. The pore size distribution of Vashishta and Tersoff samples correlate with previously conducted studies by W. Gonçalves [366]. In his research, the average pore radius for samples with density between 250 kg m^{-3} and 450 kg m^{-3} oscillated between 35 and 50 Å. Furthermore, obtained results are also confirmed by experimental research conducted by Roiban et al., with use of electron tomography [472]. On the other hand, samples created using BKS potential present almost double pore size for low densities and are correspond to research presented by Deng, who managed to synthesize silica aerogel from E-40 achieving pore diameter of 20 nm range [473]. In addition to pore size distribution, geometrical analysis was also used to produce pore volume of modelled low density silica samples with the results presented in Figure 5-29.

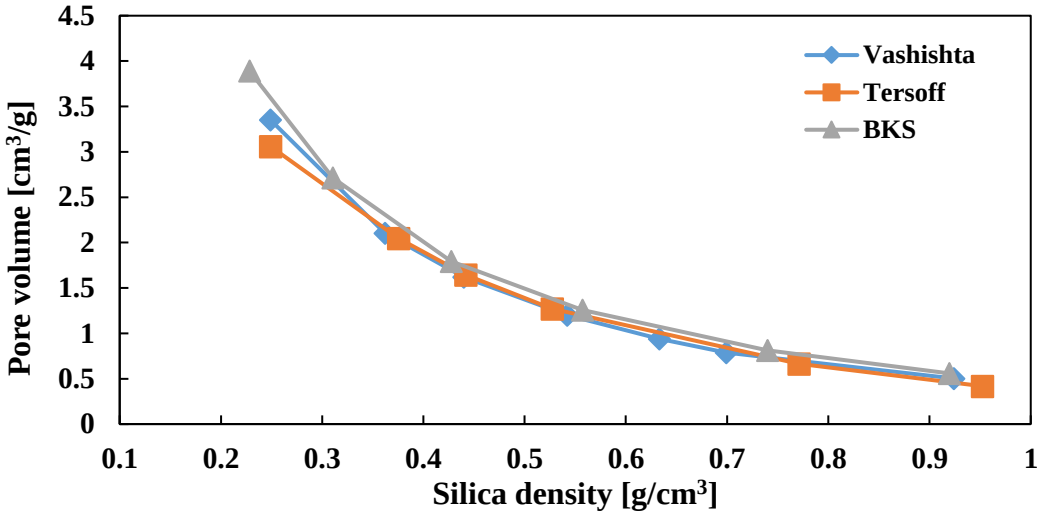

Figure 5-29 Pore volume of low density silica samples as a function of sample density. Pore volume has been measured for samples produced with different potentials.

As presented in Figure 5-29, all the samples follow the same trend with pore volume increasing exponentially as density decreases. Again, this behaviour is expected as by expanding amorphous silica lower density samples incorporated larger quantity of pores. In addition, when comparing all potentials used for sample preparation the results are extremely close even though pore size distribution was vastly different. The largest difference can be noticed at lowest sample density as pore volume of 3.9, 3.35 and 3.06 cm^3/g has been calculated for samples prepared with respectively BKS, Vashishta and Tersoff potentials. Similarly, as in case of pore distribution larger pore volume values achieved by BKS potential can be attributed to higher stretching forces acting during expansion process leading to a higher chance of merging of large pores within the material with low densities. Extremely close match was also achieved with experimental results produced by Iswar et al., who have investigated the effect of drying on material properties. In their work they have synthesized samples with densities between 0.088 and 0.354 g/cm^3 and pore volume of 10.7 and 2.3 cm^3/g [474]. Finally, when comparing the simulated low density silica samples with experimental results presented in previous chapters the close correlation can be found for cumulative pore volume which ranged between 3.47 and 3.88 cm^3/g for low density silica aerogel samples. However, the BET experimental results provided significantly larger pore size in a range between 16.44 and 19.63 nm. Significantly larger pore size could be attributed to the aerogel samples having lower density than simulated models and thus increasing an empty space between silica atoms.

5.3.1.2 Low density polyimide

Due to the fact that low density polyimide does not comprise of well-defined inorganic structures slightly different approach to its validation was undertaken. Firstly, before

validating the creation of low density polyimide samples, the analysis of the polyimide sample has been conducted in a first place in order to confirm proper starting material. As a result, the density measurements followed by FTIR analysis of crosslinked polyimide sample were conducted. The density of the polyimide was calculated along all axis (Figure 5-30) to confirm uniformity of the sample and lack of pores within.

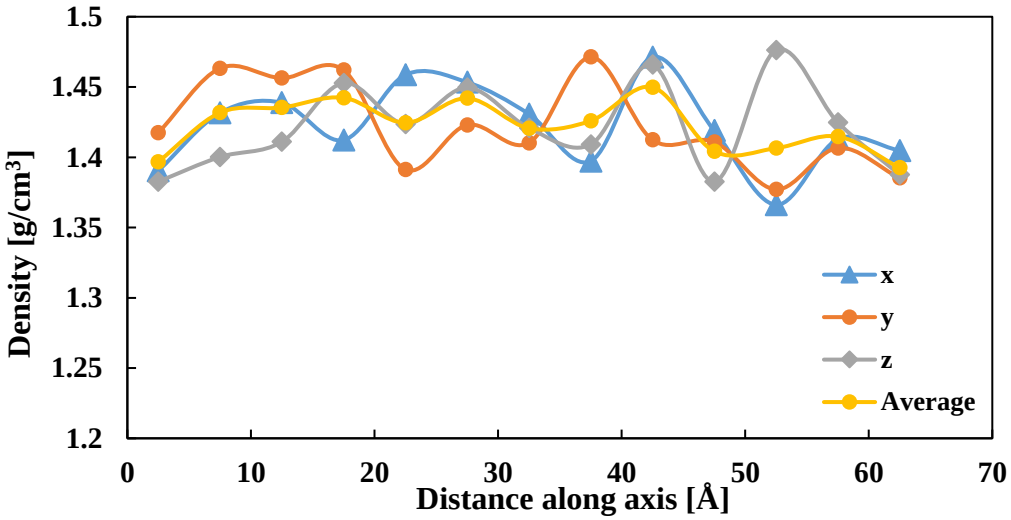

Figure 5-30 Density of PI sample along x, y and z axis.

Indicated by the results of the analysis in Figure 5-30, the even distribution of mass within created sample was achieved with average density value of 1.42 g/cm^3. Such value is an excellent match to range of commercially available DuPont™ Kapton® polyimides presenting the same density values [475]. Additionally, lack of pores and uniformity of the sample was confirmed as the density variation in all dimensions has not exceeded 0.05 g/cm^3 from the average. Such finding was of a particular importance as uniform sample following further expansion was more likely to produce aerogel like form.

Next step of the polyimide analysis included the FTIR spectrum measurements in order to confirm the correct chemical composition of modelled samples. Obtained FTIR spectrum is presented in Figure 5-31.

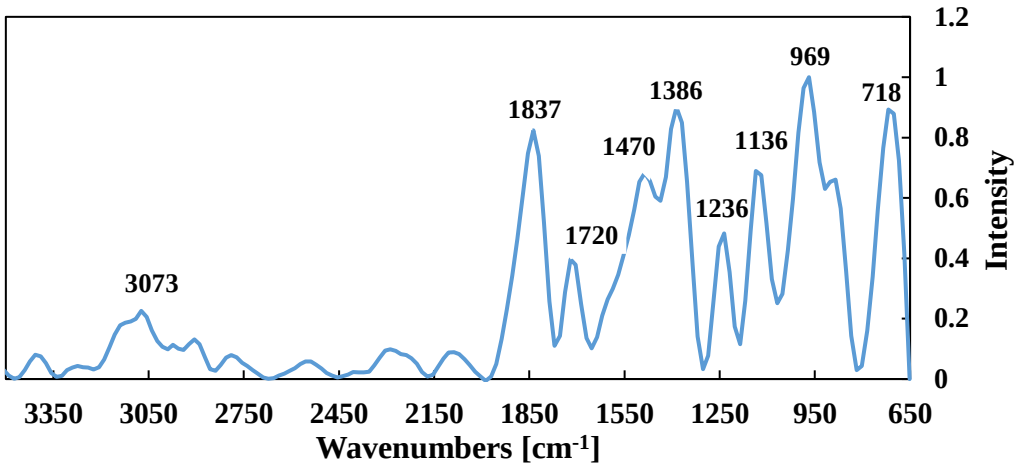

Figure 5-31 FTIR spectrum of simulated PI sample.

Calculated FTIR has confirmed simulation of polyimide sample by including the intensity bands characteristic for polyimide as presented by experimental work of Diaham and Locatelli [476]. Firstly, the spectrum includes the symmetric C=O stretch (imide I) peaks at 1837 cm^{-1} followed by asymmetric one at 1720 cm^{-1}. Also, the C–N stretch (imide II), C–H bend (imide III) and C=O bend (imide IV) peaks are present in the ranges around respectively 1386 cm^{-1}, 1136 cm^{-1} and 720 cm^{-1}. Furthermore, the presence of peak at 3073 cm^{-1} is corresponding to the C–H stretch bonds [476, 477]. The only outstanding peaks are present at 1470 cm^{-1} and 969 cm^{-1}, with the first one possibly associated with symmetric stretch of carboxylate ion COO– and the latter one with atom vibrations (due to the simulation scale) causing out of plane bending of aromatic rings [476, 478]. Following, expansion of polyimide sample to the low density form the attempt was made to geometrically characterise low density PI samples. As a result, using Zeo++ code the pore size distribution has been calculated and presented in the figure below.

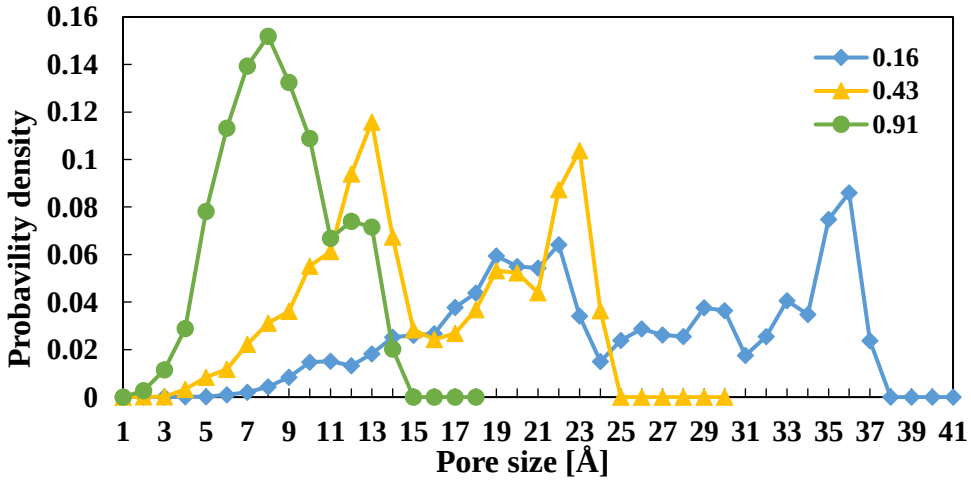

Figure 5-32 Pore size distribution of PI samples with density in g/cm^3.

As a result, the samples with lower density include pores with higher pore diameter than denser samples, resulting in maximum pore size of 37 Å for 0.16 g/cm^3 sample. Interestingly the pore size does not exceed this limit leading to results slightly different to those obtained through experiments. Such behaviour can be caused by the size of simulated volume being too small and not being able to incorporate larger voids within material structure. Following this analysis, the average pore size and pore volume has been also plotted as a functions of sample density in Figure 5-33.

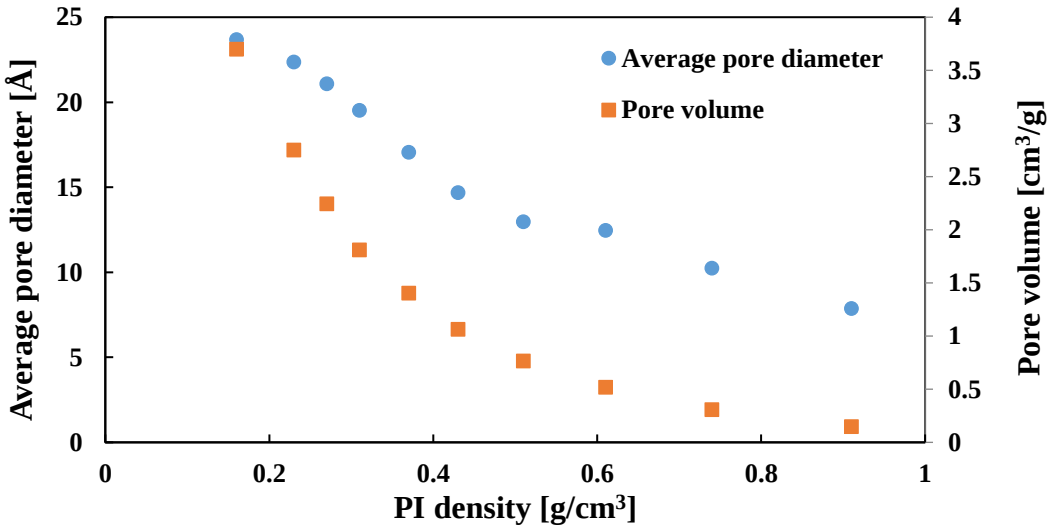

Figure 5-33 Average pore size and pore volume of created PI samples.

As presented in Figure 5-33 pore volume of created low density polyimide samples presents exponential trend with increasing pore volume as density decreases with maximum pore volume of 3.6 cm^3/g for lowest density sample. Those results are in line with experimental results from literature with highest recorded pore volume reaching even up to 8 cm^3/g, however most samples still achieving lower values [60, 66, 479]. Similar behaviour is presented by average pore diameter which also follows exponential trend with increasing pore size as density decreases. However, in this case less of an agreement is reached with experimental results which derive polyimide aerogel samples with average pore size in a range between 30 and 50 nm [480]. When comparing the simulated pore size and cumulative pore volume with previously presented experimental results significant discrepancies in both parameters can be noticed. The experimental BET measurements of polyimide aerogel suggested average pore size of 18.35 nm and cumulative pore volume of 0.012 cm^3/g. The differences might be resulting from too small simulation volume not allowing to create required pore size and in order to overcome this issue a larger computational power would be required. Despite such difference the pore volume still suggest that required quantity of pores has been achieved in

simulated material. As a result, the geometrical analysis together with previously conducted FTIR and density check, enough evidence has been gathered to assume that simulated low density polyimide samples are suitable for further investigation.

5.3.1.3 Epoxy

Similarly, as in case of polyimide validation of created epoxy resin will also be conducted through the means of density analysis and FTIR measurements. As a result, density of the epoxy resin was calculated along all axis to confirm uniformity of the sample and the results are presented in Figure 5-34.

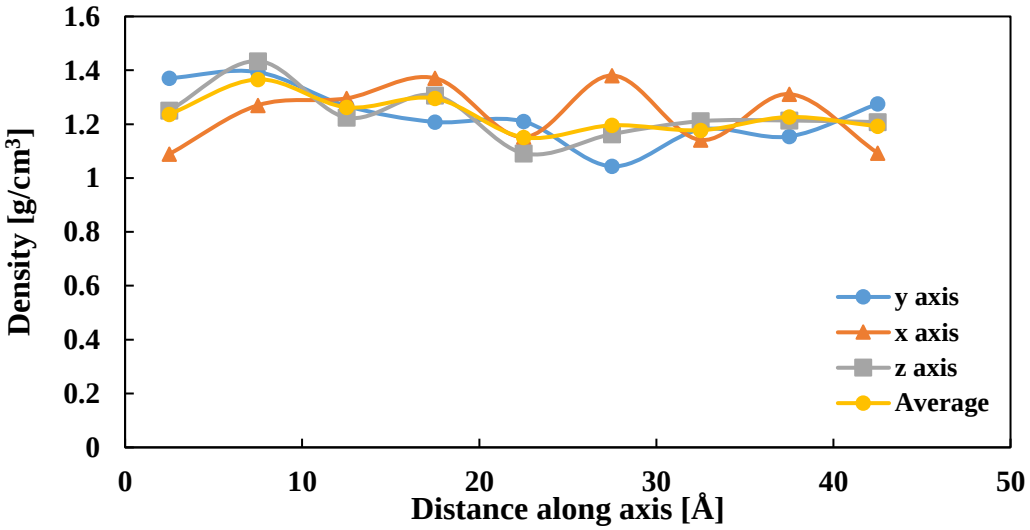

Figure 5-34 Density of simulated epoxy resin sample along x, y and z axis.

As shown by Figure 5-34 the even distribution of mass within created sample was achieved with average density value of 1.19 g/cm^3. Such value is an good match to most commercially available epoxy resin systems presenting density value around 1.2 g/cm^3 [481]. Additionally, lack of pores and uniformity of the sample was confirmed as the density variation in all dimensions has not exceeded 0.1 g/cm^3 from the average.

Next step of the epoxy analysis included the FTIR spectrum measurements in order to confirm the correct chemical composition of created samples. Obtained FTIR spectrum is presented in Figure 5-35.

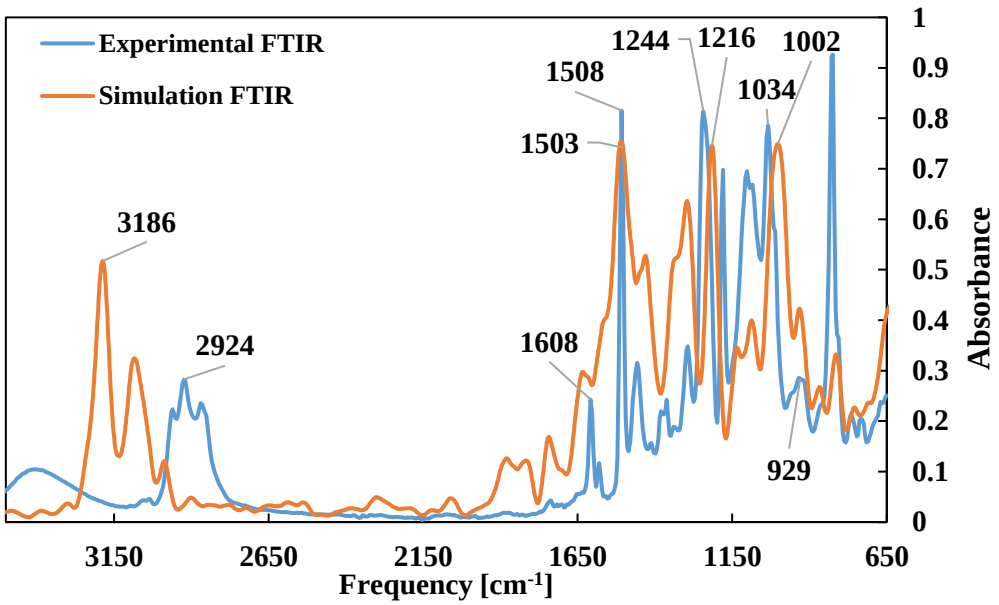

Figure 5-35 Experimental and simulated FTIR spectrum of epoxy sample.

When analysing Figure 5-35 a significant similarity between FTIR spectra obtained through experimental and simulation methods can be noticed. Firstly, standard peaks around 1200 cm^{-1}, 1509 cm^{-1} and 1609 cm^{-1} are present within both spectra and they represent respectively C – O aromatic ring stretching, C – C stretching of aromatic ring and C = C stretching aromatic ring [482]. In addition, both spectra are presenting a good cure degree as they both lack a peak at 915 cm^{-1}. This peak represents the epoxy ring which opens and cross links during cure so significant peak is for unreacted epoxy resin. Similar conclusion can be drawn from the presence of peak at 1100 cm^{-1} which increases with increased etherification during curing. Finally, both spectra have peaks around 3000-3400 cm^{-1} which can be associated with hydroxyl groups which form as the epoxy ring opens and increases with cure [482]. The slight shift in this region between experimental and simulated results can be attributed to the lack of model capability to recognise out of plane vibrations of atoms. As a result, of match of main parts of simulated FTIR spectra with experimental one, the epoxy resin sample was assessed to be suitable for further investigations.

5.3.1.4 Amorphous silica

The analysis of low radial values of Radial Distribution Function were able to identify the bond length for all atoms used in the simulation of amorphous silica and results presented in Table 5-3.

Table 5-3 Bond lengths obtained for amorphous silica sample.

Bond Type	Bond Length [Å]
Si-Si	3.01 ± 0.05
Si-O	1.58 ± 0.08
O-O	2.63 ± 0.03

As it can be noticed, bond length values, correspond to experimentally obtained values for silica samples which were as follows: 3.08 ± 0.10 Å for Si−Si, 1.61 ± 0.05 Å for Si−O and 2.632 ± 0.089 Å for O−O [166]. In addition, simulated sample achieved fractal dimension of 2.98, presenting extremely closely fit with experimental results of 3 presented by bulk silica [166]. Finally, the density distribution along all axis has been plotted in Figure 5-36 to check the uniformity of the sample.

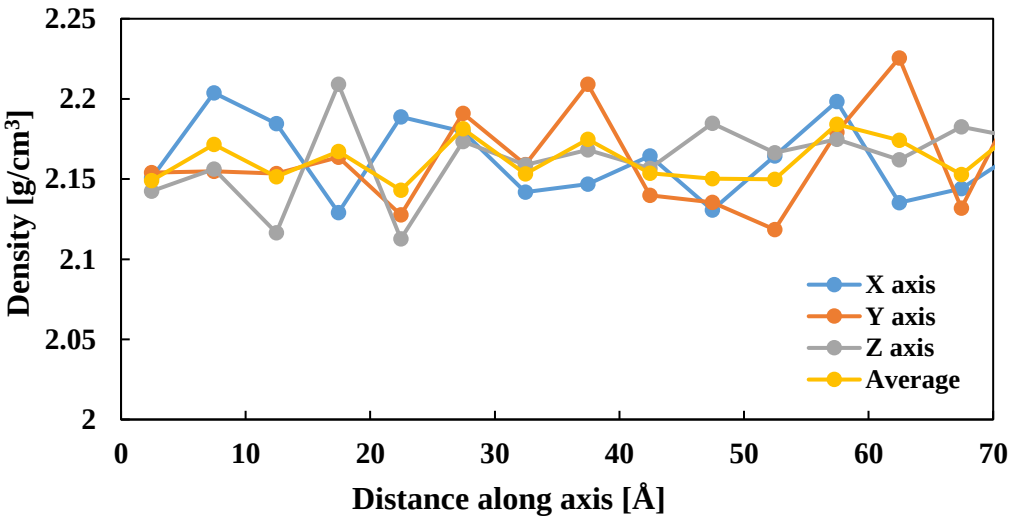

Figure 5-36 Density of simulated amorphous silica sample along x, y and z axis.

As shown by Figure 5-36 the even distribution of mass within created sample was achieved with average density value of 2.13 g/cm^3. Such value is an good match to experimental results presenting density value around 2.19 g/cm^3 [483]. Additionally, lack of pores and uniformity of the sample was confirmed as the density variation in all dimensions has not exceeded 0.1 g/cm^3 from the average.

5.3.2 Thermal conductivity

5.3.2.1 Low density silica

Temperature distribution for low density silica with varying density is presented in Figure 5-37.

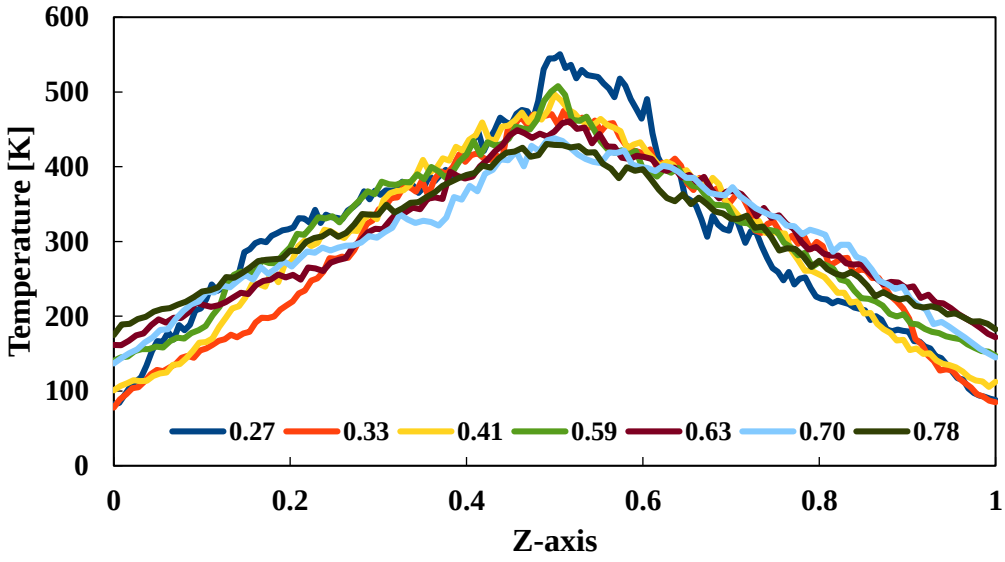

Figure 5-37 Temperature distribution at RNEMD simulation for silica samples with varying density [g/cm^3].

As it can be noticed, the temperature distribution for all the low density silica samples follows the same trend with highest temperature in the middle of the investigated volume and almost linear decrease of temperature with increasing distance from the centre. This situation is well expected and results from accumulation of the kinetic energy at the centre of investigated volume mainly due to the restriction of energy transfer through the sample. It is important to highlight the effect of sample density on the temperature distribution as, with decreasing density of the sample's temperature gradient is increasing. Again, this situation is expected and is caused by significantly higher pore volume within low density samples effectively restricting the energy transfer via means of conduction. Following analysis of temperature distribution thermal conductivity values of all the samples has been calculated are presented in Figure 5-38 together with error bars and a comparison to experimental results achieved by Jain et all. [35]. Error bars were obtained by considering fluctuations of thermal conductivity values after achieving a steady state RNEMD situation.

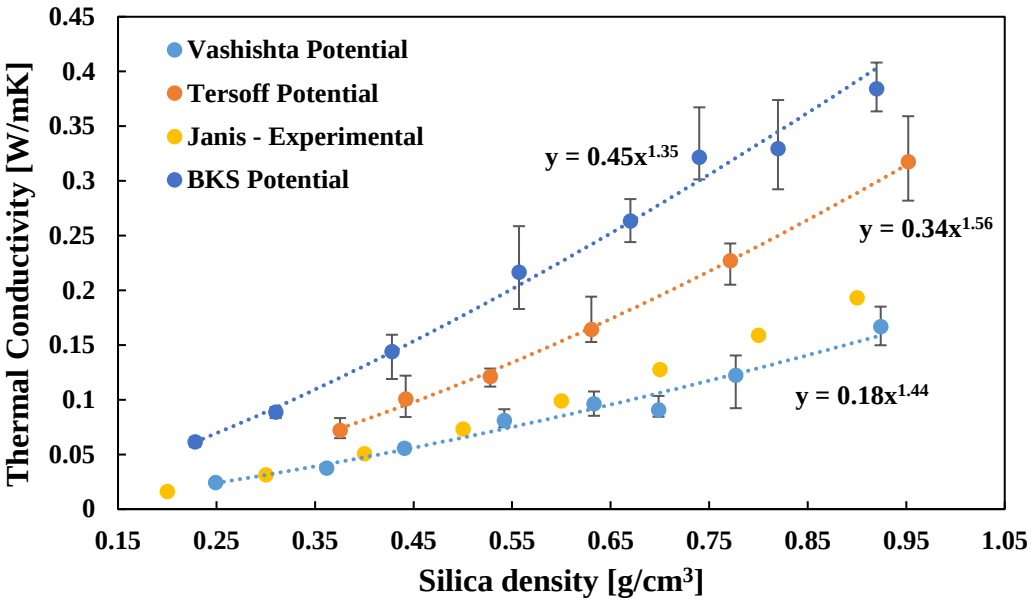

Figure 5-38 Thermal Conductivity Values vs density of the samples. Power law fit for analysed potentials was also included in order to facilitate the comparison.

All three potentials were investigated for densities between 0.1 and 1 g/cm^3 and present a similar trend with decreasing thermal conductivity as the density of the analysed sample decrease. The results present power law variation with exponents of 1.35, 1.56 and 1.44 for BKS, Tersoff and Vashishta potentials respectively. Thermal conductivity values achieved in the current study match the results obtained in previous research in which Yeo, using the Tersoff potential, introduced a power law fit of 1.61 while, Ng using, BKS potential achieved exponent of 1.01. It must be highlighted that the power law exponent for BKS potential is unlike the one presented by Ng, but the produced absolute values of thermal conductivity are within the same range and in the selected density spectrum present a similar trend. On the other hand, the values gathered with Tersoff potential are almost identical with previous studies both in terms of exponent and absolute values, almost replicating Yeo's studies[174, 377]. However, it should be noticed that both BKS and Tersoff potentials produced values significantly higher than experimental results. Similarly, observed in other research, the values obtained for low density silica samples were up to 10 times higher than experimental ones and presented rather poor prediction of the thermal properties of low density silica samples. As explained by previous studies, the main reason for such discrepancy was lack of possibility to reproduce the actual aerogel structure with use of the mentioned potentials [174, 377]. Finally, the Vashishta potential was used for the first time to simulate thermal properties of low density silica samples and was able to reproduce the experimental values with relatively small error and closely followed the experimental trend obtained by Jain where films created with ethanol were investigated [35]. However, it should be noted that the power law exponent was slightly

lower than the value obtained by Jain (1.44 vs 1.65 in Jain's work). As a result, the potential produced more adequate thermal conductivity values for low density samples and presenting slight deviation from the results in the higher density region.

5.3.2.2 Low density polyimide

Similarly, as in case of silica aerogel a RNEMD method was used in order to impose heat flow through the sample. As a result of energy swaps within the system the temperature gradient through the samples has been created and presented in Figure 5-39.

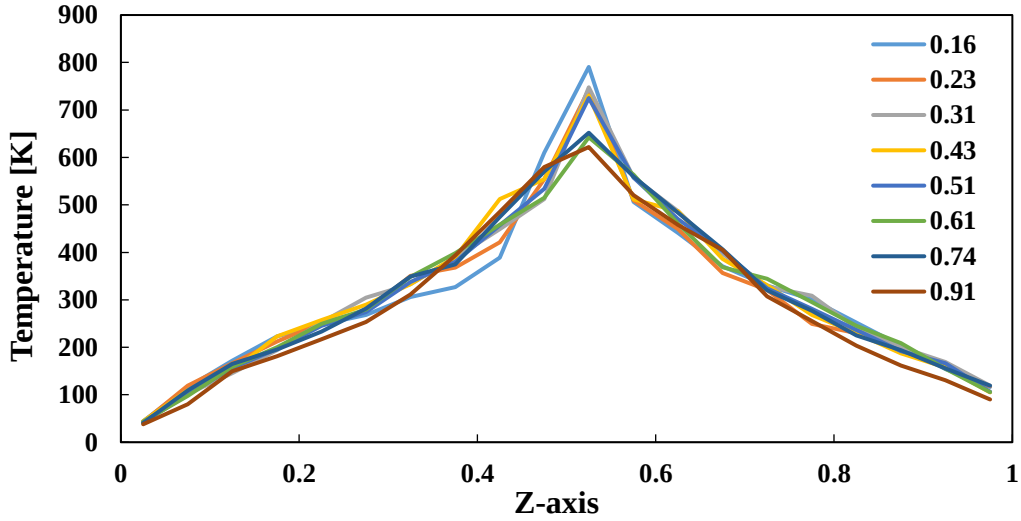

Figure 5-39 Temperature gradient created by RNEMD method for samples with density in g/cm^3.

Similarly, as in case of low density silica samples, Figure 5-39 also presents linear temperature distribution with highest temperature achieved in the centre of investigated volume and lowest temperature values at the volume's edges. One might also notice slight lack of symmetry between both sides, however its appearance is a result of uneven distribution of atoms during polyimide expansion process. In addition, larger central temperatures (and thus temperature gradients) have been achieved for samples with lower densities, as a result of lower quantity of material being able to conduct the energy through the sample. By recording the quantity of energy transferred during energy swaps it was possible to calculate the thermal conductivity values for each sample and they are presented in Figure 5-40.

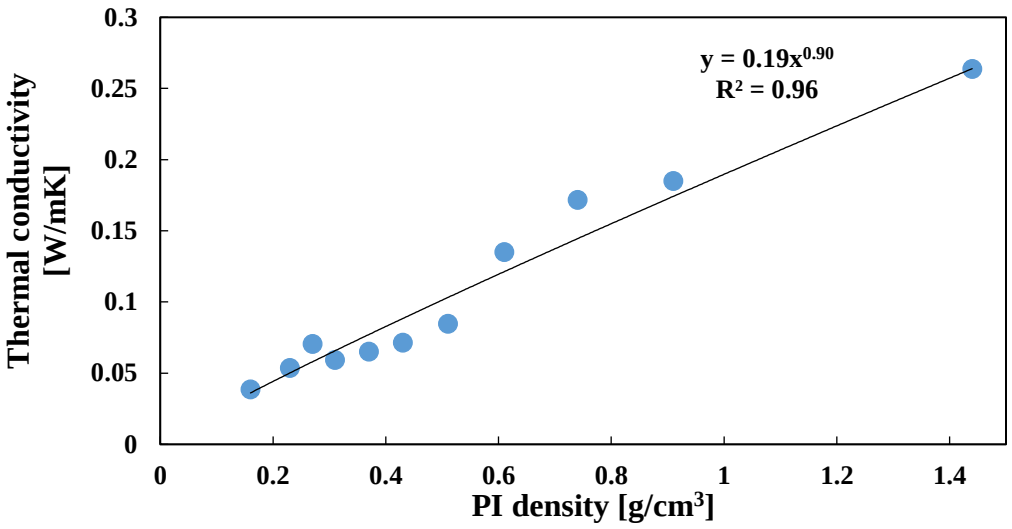

Figure 5-40 Thermal conductivity versus density of low density polyimide samples.

Figure 5-40 presents the effect of polyimide density on material's thermal conductivity and as it can be expected decreasing density led to lower thermal conductivities values of the PI samples. Again, lower thermal conductivity is achieved by restricting free energy transfer paths through material by incorporation of larger pore quantities with decreasing densities. As a result, the lowest thermal conductivity of 39 mW/mK has been achieved by a sample with density of 0.16 g/cm^3. Similarly, as in case of low density silica samples power trend-line was fitted through the data points and superscript of 0.9 was achieved.

Since low density polyimide has not been investigated through molecular dynamics means the comparison with only experimental results will be conducted. As a result, Feng et al., have synthesised polyimide aerogel using ODA and BPDA. He achieved thermal conductivity ranging from 30 to 31 mW/mK for samples with density between 0.08 and 0.14 g/cm^3 [484]. Furthermore, Wu et al., derived polyimide samples with varying BAPP content and for samples with density between 0.12 and 0.246 has found thermal conductivities in-between of 32 and 59 mW/mK [485]. Similar results have been achieved by many other studies which have also focused on polyimide aerogel [63, 65, 99, 456, 476]. Even though when comparing with literature it is possible to find data only for low density samples (below 0.3 g/cm^3), they do present quite close match with simulation results and suggest proper replication of polyimide aerogel in molecular dynamics environment.

5.3.2.3 Discussion

The following discussion on thermal properties of created low density samples will be divided into two distinct sections. Firstly, the difference in thermal conductivity of low density silica

samples created with various potential systems will be discussed. Followed by a comparison of results between low density silica and polyimide samples.

All previously described geometrical characterisations (described in 5.3.1) have proven the differences between potentials utilised for the simulation of silica aerogel. In order to fully understand how potentials affected the internal structure of aerogel samples, both two-body and three-body potential functions are presented in Figure 5-41. As it can be noted from analysis of the two-body constituents, the potentials presented have rather similar behaviour with similar depth and location (1.58 for Vashishta and 1.72 for BKS). Only the regime after achieving the minimum energy developed differently, mainly due to varying approaches to the cut-off distance. This observation is reflected in both bond length and fractal dimension measurements which presented comparable results. As proven by previous research, those values would have more substantial influence on measurement of vibrational frequency and bulk elastic constants [486].

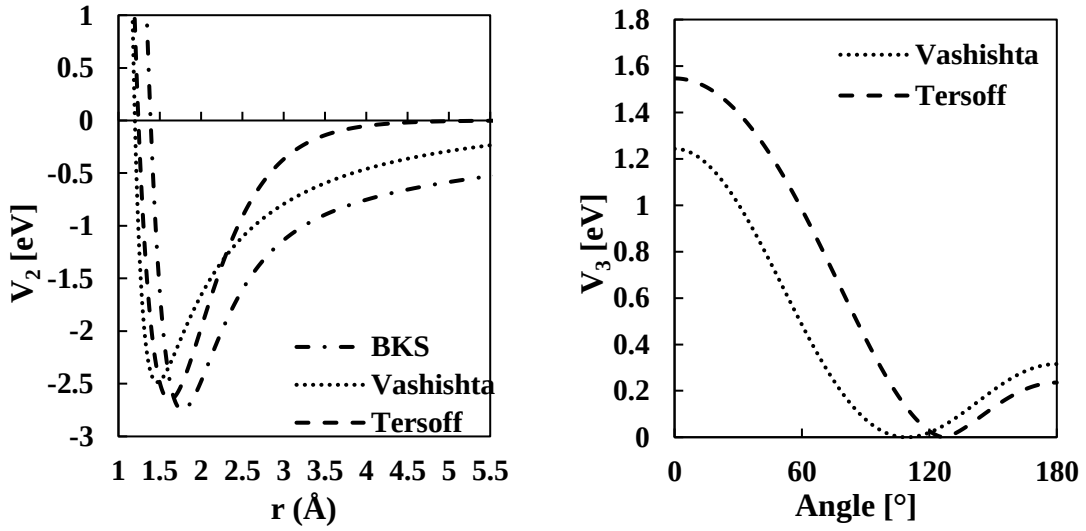

Figure 5-41 On the left: Comparison of the two body potential functions. On the left: Comparison of the three body potential functions. The BKS potential is not included as it's a pair potential.

Nevertheless, Tersoff and Vashishta potentials representing a group of multi-body potentials were also taken into consideration and the influence of other neighbouring atoms. Presented in Figure 5-41, three-body energy as a function of angle between three atoms i, j and k, calculated for an isosceles triangle fixed at the equilibrium bond length previously calculated for aerogel structures. Both potentials present a similar trend with higher energy at low angles subsequently decreasing until reaching the apex bond angle between the two equal bond lengths. Even though potentials exhibit some similarities, the values they present are slightly different with Tersoff potential being more repulsive and having slightly higher apex angle of

127° in comparison to 109° in the case of Vashishta potential. Occurring differences can be explained by an entirely different approach to calculating three-body energy. In the case of Tersoff potential, three-body influence is taken into account by the bond order parameter affecting the attractive element of two-body relations. The parameter is a monotonically decreasing function of the position of i and j atoms and defines the atom's local environment introducing angular dependencies [167]. Vashishta presents rather different approach as this potential includes implicitly a three-body interaction function which clearly defines all parameters affecting atoms such as angular or spatial dependencies [166]. The presence of three-body energy in Tersoff and Vashishta potentials is clearly reflected in pore size distribution graph (see Figure 5-28), presenting that silica aerogel structures created by BKS potential achieved much higher pore size. The pore size was directly affected by attractive and repulsive forces which are governed by potentials. Even though the two-body energy for all potentials seems similar the addition of three-body energy makes Vashishta and Tersoff potentials less attractive and thus stop them from aggregating atoms and preventing the creation of more voluminous pores. On the other hand, BKS potential based on only two-body energy presented much higher attractive forces (even though they were reduced by addition of 24-6' Lennard–Jones terms) which led to silica aerogel samples with larger pore diameters.

Except different internal structure of the samples, other factors were affecting the thermal conductivity of the materials. In order to discuss the thermal characterisation results the limitations of molecular dynamics in this regard should be mentioned alongside the discussion. Firstly, only limited electrical properties of the simulated materials are included and thus the electron kinetics are neglected, resulting in lack of contribution from free electrons toward the overall thermal conductivity values [487]. Remaining electrical interactions are best described by the Vashishta potential, which by including steric, Coulombic charge-dipole and van der Walls effects it is possible to simulate electric effects more accurately and thus more accurately represent the shape and reactivity of molecules [488]. Other potentials include only limited electrical interactions. BKS takes into account a Coulomb term and a covalent (short-range) contribution [170], while the Tersoff potential is strongly limited by the inclusion of only short range forces resulting in lack of compatibility between vibrational and elastic properties (phonon frequencies and their dispersions). The most important effect of such negligence is incorrect calculation of coefficient of thermal expansion which is directly dependent on the derivation of the phonon frequencies with respect to deformation [489, 490]. One can claim, that due to the fact that electrical insulators, such as bulk SiO_2, predominantly transfer heat through atom vibration, this limitation may not significant impact directly on thermal

conductivity values. However, due to the internal structure of aerogels, it might become important to the other means of heat transport into consideration [487].

Moreover, the differences in thermal conductivity results between potentials comes from different approaches to their parametrisation. BKS is a mixed ab initio empirical force field which indicates that its parameters were obtained by iterating between ab initio calculations and trying to optimise the values of bulk parameters in order to obtain match of elastic constant and unit-cell dimension with experimental values of quartz [170]. On the other hand, Tersoff parameters were established by analysis of a wide range of databases including energies obtained through the ab initio methods for abundance of atomic structures [167]. The Vashishta used a different approach and based part of the parameters on previous molecular dynamics studies regarding superionic conductors and glasses. The remaining constants were established by analysis of melting temperature and pressure at the experimental density [166]. It became clear that in order to achieve correct thermal conductivity values all required physics and parameters has to be correctly determined. By analysis of thermal characterisation of other materials, it can be noted that certain parameters sets are more suitable than the others and in our case, it can be assumed Vashishta potential fulfil this role slightly better than Tersoff and BKS. Nevertheless, it should be noted that few attempts were conducted for all discussed parameters in order to deliver more suitable parameters, however providing only slight improvements to the model [175, 177]. Overall, the analysis of geometrical features in conjunction with thermal results has indicated that Vashishta potential is predicting silica aerogel properties much more accurately. As a result, it will be used in all of the following simulations including aerogel mechanical investigation, interface simulations and following thermal conductivity comparison between both aerogel types.

In order to further discuss thermal conductivity within aerogels the comparison between both material types was conducted. As a result, Figure 5-42 presents thermal conductivity values for both silica and polyimide samples as a function of sample density.

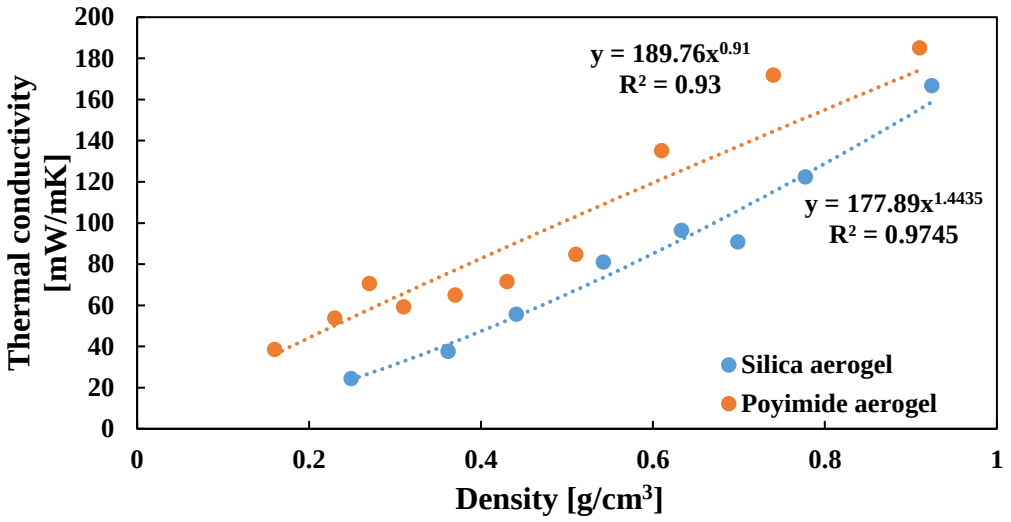

Figure 5-42 Comparison of thermal conductivity values between low density silica and polyimide samples with varying densities. Low density silica sample values has been calculated using Vashishta potential.

By analysing Figure 5-42, it can be noticed that both low density silica and polyimide are exceptionally low thermal conductivity materials and follows exponential trend line. However, silica samples tend to produce lower thermal conductivity values across the whole density range. From experimental point of view such behaviour seems natural as many previous studies has produced silica aerogel samples with lower thermal conductivity values that any polyimide aerogel and initial study by Kistler produced a silica aerogel samples with thermal conductivity of 10 mW/mK after air evacuation [2]. The difference in experimental values of thermal conductivity of both aerogels is often associated with different internal structure. Silica aerogel tends to produce smaller pores and achieve higher values of pore volume than polyimide aerogel [474]. Even though the geometrical analysis of both types of modelled low density samples has revealed that both materials have similar internal structure, other reason for higher thermal conductivity of low density polyimide can be found by analysing potentials and process used during sample modelling. As a result, during the expansion (used in a sample modelling process) different situations appears for both materials. In case of the low density polyimide the intramolecular forces are maintaining the molecular structure of polyimide oligomers effectively preventing its' breakage. As a result, most atoms incorporated within PI structure are interlinked and energy transfer path through the sample is always maintained. The situation is vastly different for low density silica. The expansion of amorphous silica is more random and as a result it can produce gaps within the material structure and cause higher resistance to energy transfer.

5.3.3 Mechanical properties

5.3.3.1 Low density silica

5.3.3.1.1 Compression

Following thermal analysis an attempt was made to evaluate compressive properties of created low density silica samples. As a result, each of the samples was subjected to uniaxial compression test, during which, the sample kept under atmospheric conditions and canonical ensemble has been exposed to the deformation along x-axis. The stress vs strain graph has been produced for each sample and presented in Figure 5-43.

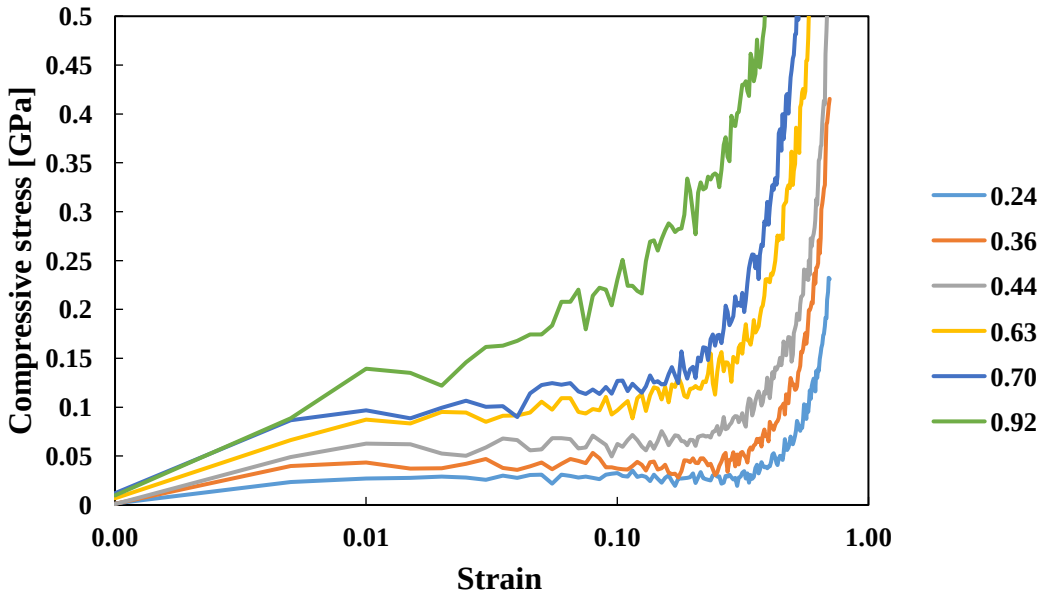

Figure 5-43 Compressive stress vs strain graph for silica samples with varying densities [g/cm^3].

Figure 5-43 indicates that all low density silica samples follow the compressive trend as expected from experimental setup with an initial linear behaviour until reaching distinct yield point, followed by a strain hardening at large deformation. However, the density of silica sample is a factor significantly affecting its' mechanical behaviour. Firstly, the samples with lower density tend to fail at lower stress values also, strain hardening commence much quicker for denser samples Such behaviour is directly linked with interatomic forces present within the sample, as in low-density samples the atom movement is relatively unobstructed regardless of strong atomic interactions. With increasing samples density, the interactions become much stronger effectively restricting atom movement and causing stiffer stress–strain response. To investigate the effect of silica density on mechanical performance Figure 5-44 and Figure 5-45

were produced and incorporate the compressive stress at yield and modulus against samples' density.

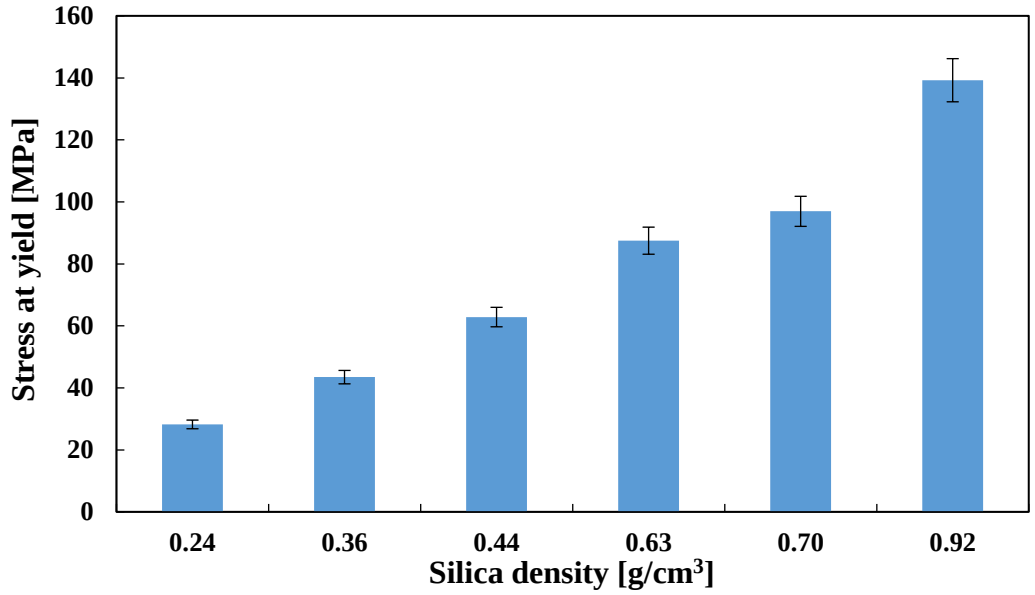

Figure 5-44 Compressive stress at yield vs silica density.

The analysis of Figure 5-44 reveals that the yield stress of low density silica samples increases with increasing density and the relationship follows exponential trend (with the exponent of 0.87). Similar relationship was also observed for elastic modulus as presented in Figure 5-45, however in this case the exponent of 1.27 was achieved. Both behaviours as expected and can be again increasing attributed to increasing interatomic forces with increasing samples density. In addition, yield stress and elastic modulus are in the same range as the results of similar molecular dynamics study conducted by Patil et al. In their work, they have simulated silica aerogel using Vashistha potential and conducted compressive testing resulting in elastic modulus of 109.1, 691.6 and 1586.1 MPa for samples with respective densities of 0.28, 0.42, and 0.62 g/cm^3 [95]. Experimental results also seem to support results obtained in this study. Alaoui et al., have prepared set of silica aerogels and tested them using both 3-point bending and uniaxial compression methods. Thier work mainly focused on low density aerogels, however they achieved 24 MPa yield strength for a 0.25 g/cm^3 sample, compared to 28 MPa in this study. In addition, their relation between Young's modulus and sample density has also followed power-law correlation with exponent of 2.89 as opposed to 1.27 in this study. However, the difference might result from incorporation of aerogel samples with density below 0.1 g/cm^3 into Alaoui's study [351].

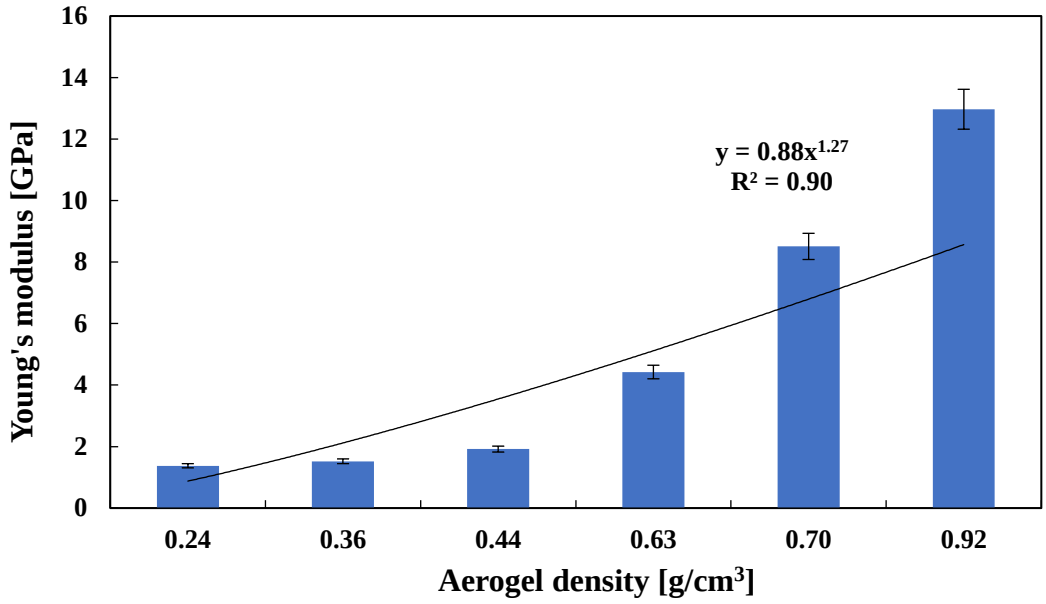

Figure 5-45 Young's modulus of silica vs density.

5.3.3.1.2 Tension

Following compressive investigation same low density silica samples has been subjected to the uniaxial tensile testing and resulting stress/strain graphs has been presented in Figure 5-46.

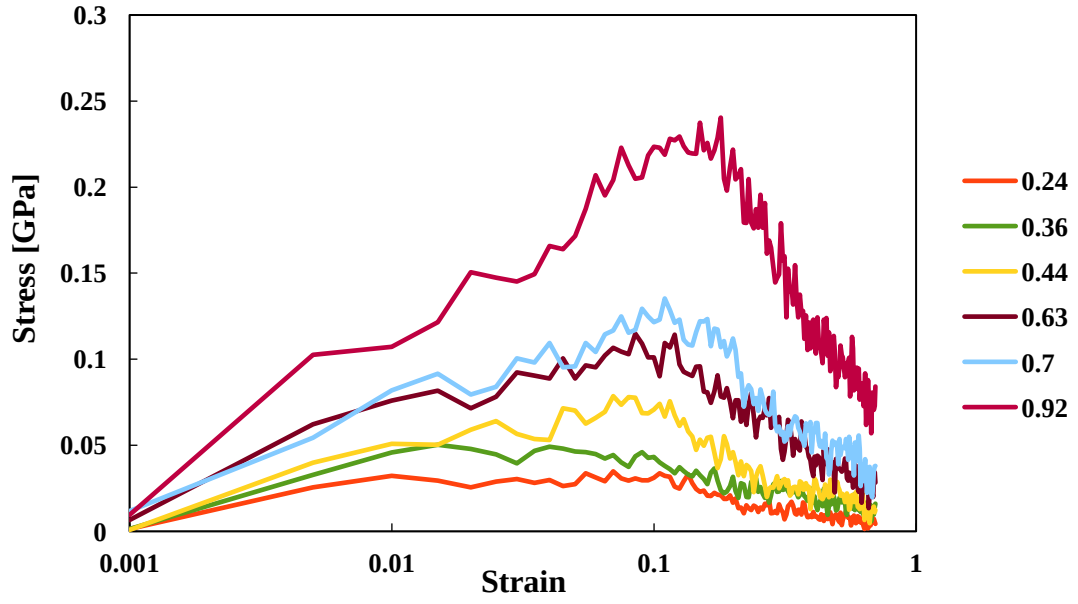

Figure 5-46 Tensile stress vs strain graph for silica samples with varying densities [g/cm^3].

The analysis of stress/strain graphs reveals that all simulated low density silica samples follow similar behaviour as experimental setup. Even though there is no sudden drop in stress value at yield (associated with brittle materials), the two most important regions including linear elastic region and yielding region are still present. In addition, it can be noticed that silica

density impact tensile properties of the material to the great extent. As with decreasing density, the material become more brittle and less stiff simultaneously. In order to further investigate tensile properties of low density silica samples Figure 5-47 and Figure 5-48 were created presenting both silica's tensile stress at yield and modulus against density.

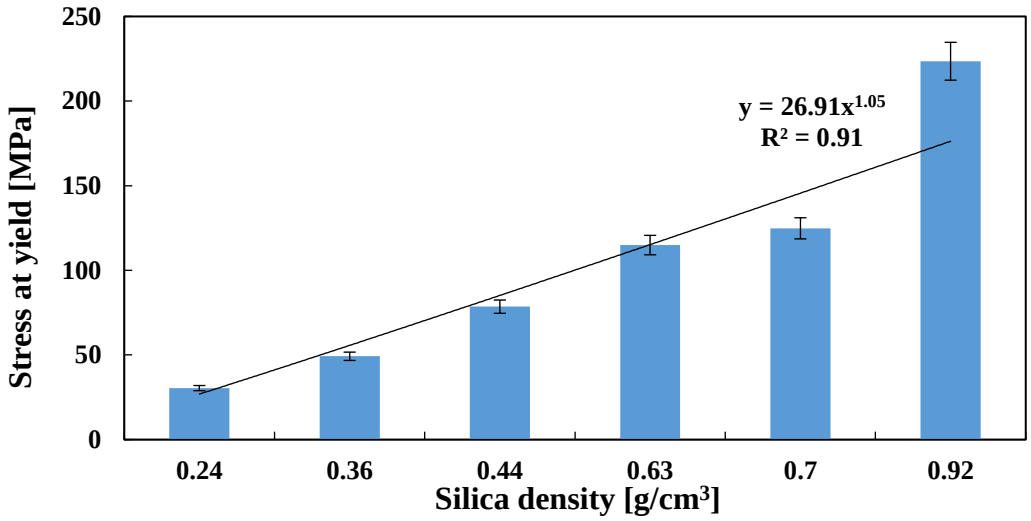

Figure 5-47 Tensile stress at yield as a function of silica density.

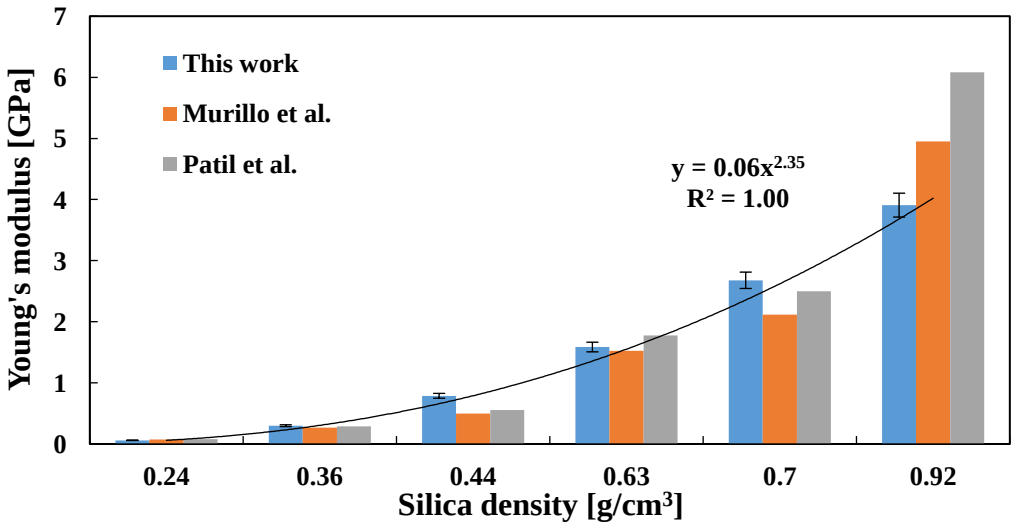

Figure 5-48 Young's modulus as a function of silica density. For comparison purposes elastic modulus observed by Murillo et al. and Patil et al. have also been incorporated [238, 370].

By investigating both Figure 5-47 and Figure 5-48, it can be noticed that tensile properties of low density silica samples increase exponentially with increasing density. Similarly, as in case of compression, the main reason for such behaviour is larger interatomic forces in higher density samples, this time however such forces are preventing atoms from being separated. The exponential value for both relations were estimated to be 1.05 and 2.35 for respectively yield stress and elastic modulus. Due to larger popularity of tensile testing among MD

simulations, there is a substantial number of previous works investigating tensile properties of silica aerogel. As a result, Patil et al., have subjected silica aerogel with varying density to uniaxial tension. In their work he has observed the yield strength of 44.2 MPa for sample with density of 0.28 g/cm^3. In addition, they have proposed a power relationship between elastic modulus and density with exponential value of 3.25 [370]. Similarly, Murillo et al., have also investigated silica aerogel in tension. Their work also suggested the exponential relationship between density and both elastic modulus and strength. In their case the exponential values of 3.11 and 2.53 have been observed for respectively modulus and strength [369]. Even though in both cases the trend is slightly different from the one obtained in this work, the difference in investigated density range should be highlighted. Both Patil and Murillo incorporated high density glasses into their studies, however when comparing elastic modulus and strength values for similar density samples a close match is obtained as presented in Figure 5-48 [238, 370]. On the other hand, when comparing with experimental results provided by Woignier et al. and Groß et al. simulated values seems to fit well especially for elastic modulus [5, 23, 36, 37, 371].

5.3.3.2 Low density polyimide

5.3.3.2.1 Compression

In order to investigate the compressive properties of low density polyimide samples , each of the samples was subjected to uniaxial compression test, during which, the sample kept under atmospheric conditions and canonical ensemble has been exposed to the deformation along x axis. The stress vs strain graph has been produced for each sample and presented in Figure 5-49.

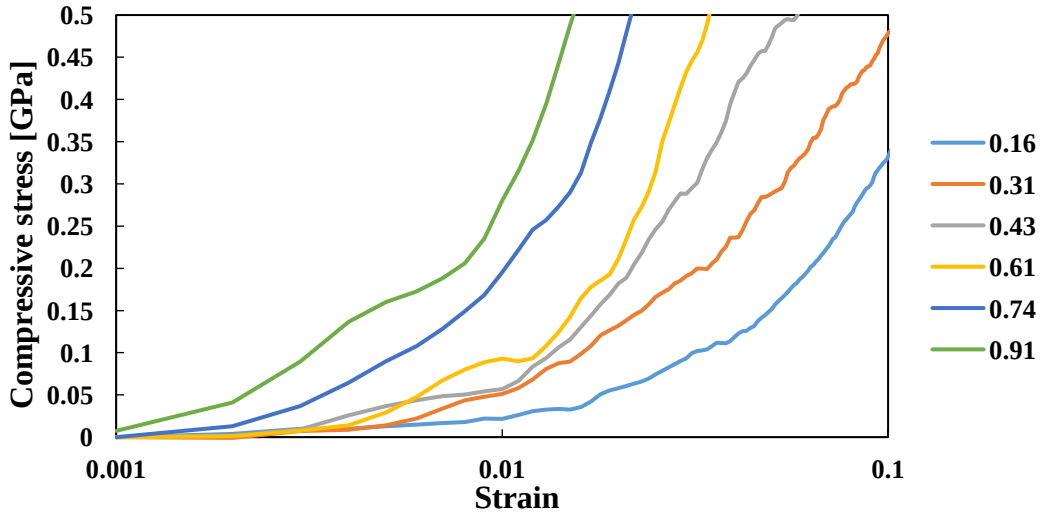

Figure 5-49 Compressive stress vs strain graph for polyimide samples with varying densities [g/cm^3].

By analysing Figure 5-49 it can be noticed that low density polyimide samples also follow expected compression stress strain curve with initial linear behaviour until reaching yield point, then followed by a strain hardening at large deformation. In addition, polyimide samples' density become a factor significantly affecting its' compressive behaviour. As a result, samples with higher density present much stiffer response to deformation with higher stress required to yield.

To further investigate the effect of polyimide density on mechanical performance Figure 5-50 and Figure 5-51 were produced and incorporate the compressive stress at yield and modulus against density.

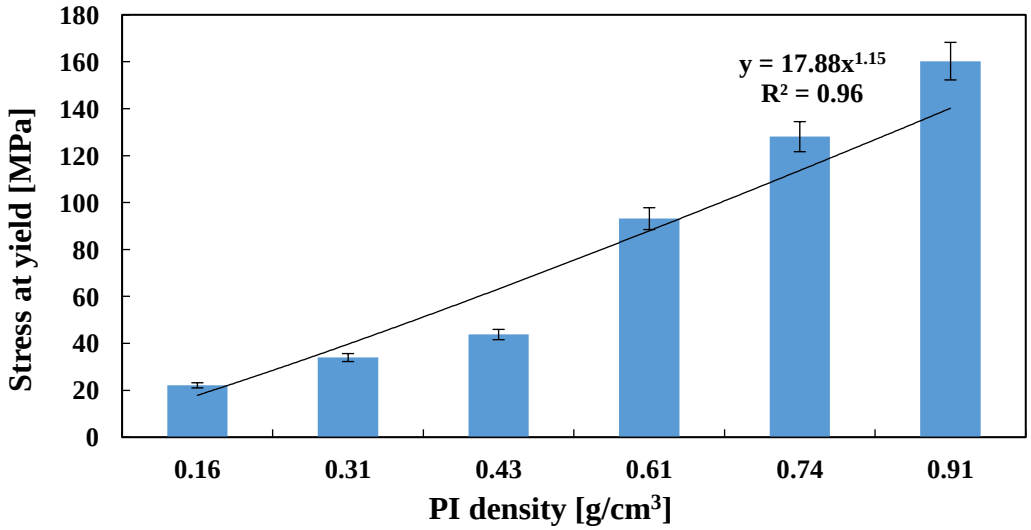

Figure 5-50 Compressive stress at yield vs polyimide density.

As indicated by Figure 5-50, the yield stress of low density polyimide samples increases with increasing density following power trend with an exponent of 1.15. The lowest value of yield stress of 22 MPa has been measured for sample with the density of 0.16 g/cm^3 and highest of 280 MPa for 0.91 g/cm^3 sample. In case of compressive modulus of created samples, they do also follow power trend as presented in Figure 5-51, however in this case the exponent of 1.77 is achieved. It is also worth noticing rather high values of modulus with the lowest one being 1.6 GPa for a 0.16 g/cm^3 sample. By analysing the literature, it can be noticed that both yield stress and compressive modulus of simulated samples are significantly higher than experimental values available. For example, Meador et al., have synthesized the polyimide aerogels by cross-linking anhydride capped polyamic acid oligomers with aromatic triamine. In her work the samples with density between 0.13 to 0.33 g/cm^3 were subjected to compressive testing and presented modulus values in a range of 1 - 100 MPa and yield stress 1 - 2 MPa [66]. Similarly, Nguyen et al., have prepared a set of PI aerogel samples by cross-

linking amine end-capped polyimide oligomers with the triisocyanate. Their samples presented density between 0.068 and 0.198 g/cm^3 with compression modulus and yield stress reaching up to respectively 228 MPa and 1.24 MPa [491].

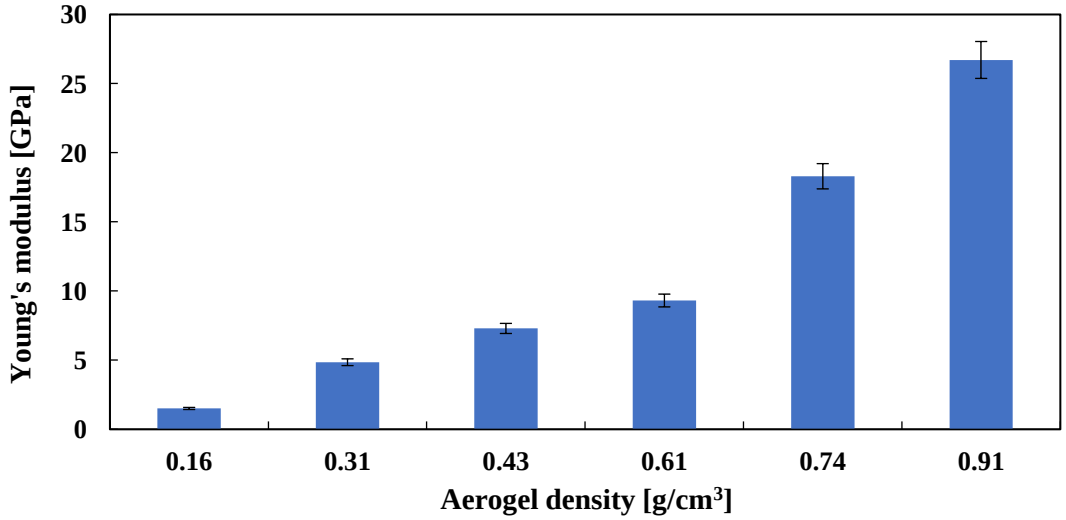

Figure 5-51 Compressive modulus of polyimide samples vs density.

5.3.3.2.2 Tension

Following compressive investigation same low density polyimide samples has been subjected to the uniaxial tensile testing and resulting stress/strain graphs has been presented in Figure 5-52.

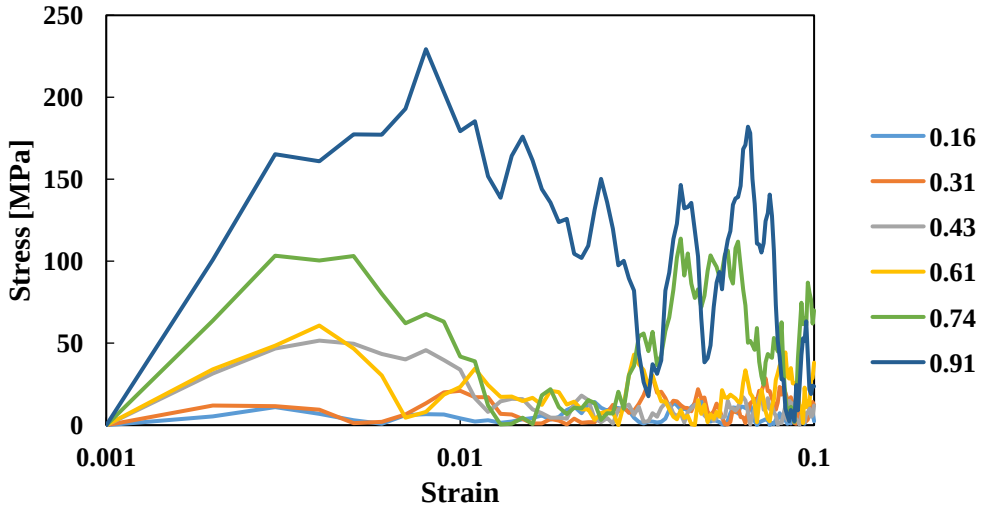

Figure 5-52 Tensile stress vs strain graph for polyimide samples with varying densities [g/cm^3].

Figure 5-52 indicates that PI samples subjected to tensile testing present expected behaviour with linear elastic region and distinctive yield point followed by a breakage of remaining bonds with progressing atom displacement. In addition, significant discrepancies between samples with varying densities has been noticed with the material becoming more brittle and less stiff

as density decreases. As a result, Figure 5-53 and Figure 5-54 have been created presenting tensile yield stress and Young's Modulus as a function of polyimide density.

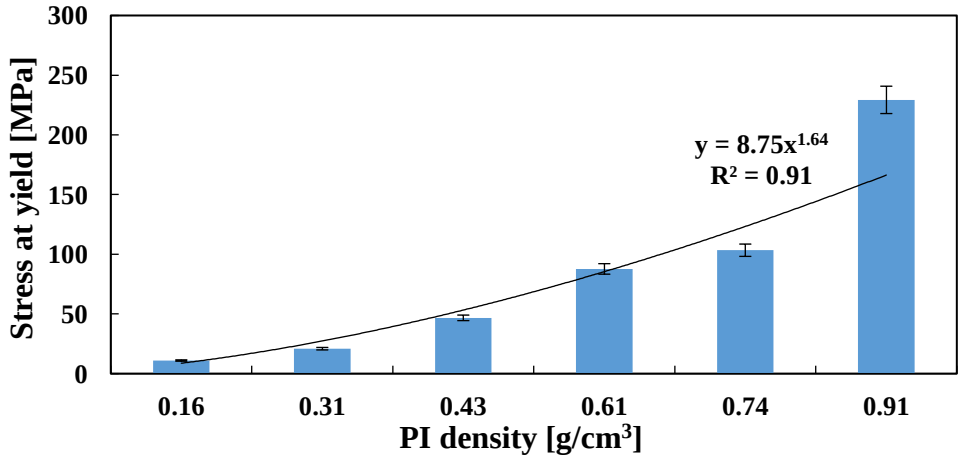

Figure 5-53 Tensile stress at yield as a function of density.

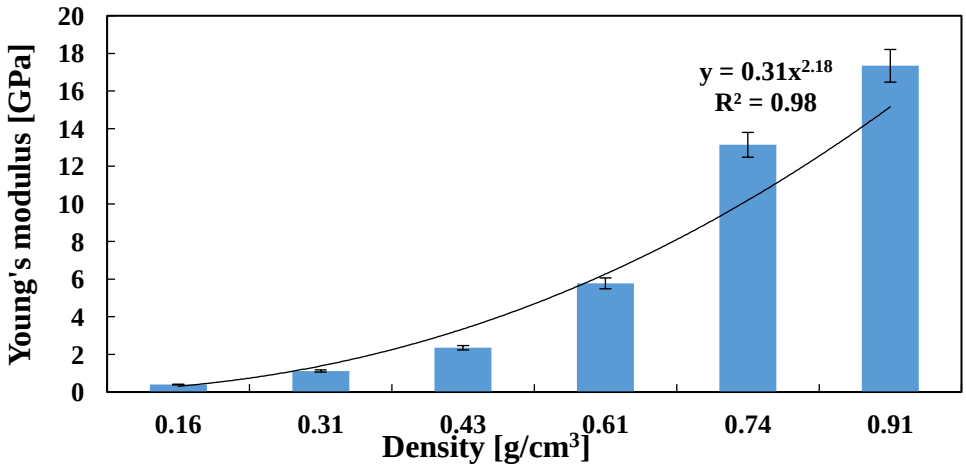

Figure 5-54 PI samples Young's modulus as a function of their density.

By investigating both Figure 5-53 and Figure 5-54, it can be noticed that both tensile yield stress and modulus of polyimide increase exponentially with increasing density. Similarly, as in case of compression, the larger interatomic forces in higher density samples are the main reason for such behaviour as they are preventing atoms from being separated. The power exponent value for both relations were estimated to be 1.65 and 2.18 for respectively yield stress and elastic modulus. When analysing the experimental data presented in literature a better match can be noticed that in case of compressive properties. Firstly, Meador et al., have achieved a tensile stress at yield of 10 MPa for a sample synthesized with DMBZ and BPDA while Qiao et al. used 6FAPB and BPDA achieving yield stress of 8 MPa [66, 492]. Both values closely correlate with 11 MPa simulated for 0.16 g/cm^3 sample. Nevertheless, simulated

modulus values are still significantly higher with 100 MPa presented in Meador study and 17 MPa in Qiao one [66, 492].

5.3.3.3 Discussion

Following the presentation of simulation results and comparison to previous molecular dynamics studies it can be noticed that low density silica samples seems to produce results which are in good agreement with current state of molecular dynamics studies. On the other hand, a significant discrepancy can be noticed for low density polyimide samples for which especially modulus values are few orders higher than data presented in experimental studies [60, 66]. Such discrepancies can be caused by too small, simulated volume of polyimide samples used in order to match available computational resources. As previously shown by pore size analysis the samples fail to precisely replicate the internal structure of polyimide aerogel. Under experimental conditions polyimide aerogels can incorporate pores with a few μm diameter, which for available computational resources are significantly too large to be included within MD model. As shown by previous studies at low strain rate the material with a large number of small pores exhibits higher strengths than the same material with small number of large pores [493]. In other words, by simulating nanometre size pores in polyimide samples their strength was increased beyond the experimental values. This issue does not seem to affect low density silica samples as they naturally incorporate much smaller pores, which are easily replicated in created MD samples. By taking the discrepancies into account, only yield stress values will be used in a comparison between mechanical properties of low density silica and polyimide samples. As a result, Figure 5-55 has been created to present compressive and tensile stress at yield of both material types.

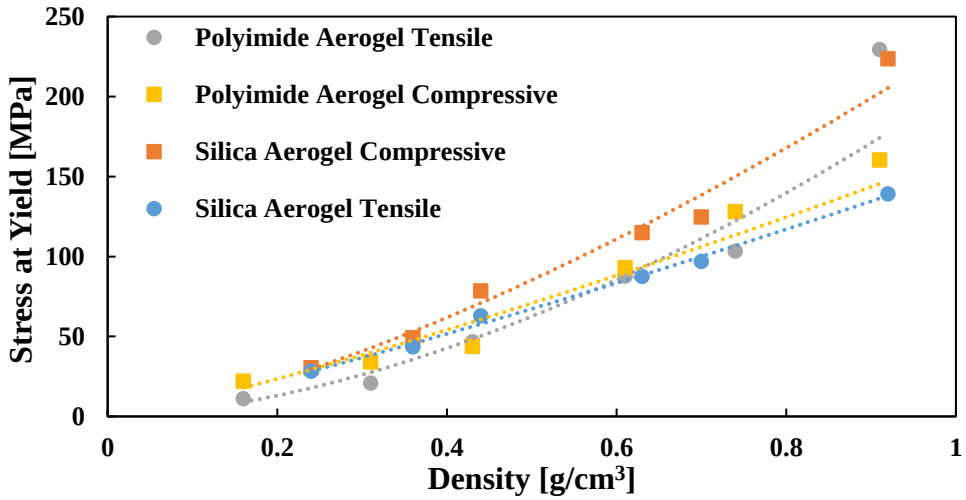

Figure 5-55 Comparison of tensile and compressive stress at yield of silica and polyimide as a function of their density.

By analysing Figure 5-55 it can be noticed that the compressive yield strength of both silica and polyimide is higher than tensile yield strength across the whole density range. This behaviour is well expected and can be easily associated with the testing method used. From the molecular point of view, in case of tensile testing the atom displacement results in constant bonds breakage reducing the number of interatomic interactions even before the yield occurs. On the other hand, the compression tends to constantly push the atoms into each other thus creating new bond which might resist atom displacement. When analysing both modes of deformation at higher scale the lack of flaw propagation is the main reason between higher compressive properties of brittle materials.

Focusing more on only compressive behaviour of both materials the low density silica samples tends to produce higher values than low density polyimide samples. Such behaviour is directly linked with interatomic forces present within the sample, as in low density silica samples the presence of many small pores results in unobstructed atom movement in the initial deformation period regardless of strong atomic interactions (more ductile behaviour). On the other hand, low density polyimide atoms are more clustered due to larger pores present in the structure. As a result, the interactions become much stronger effectively restricting atom movement and causing earlier material failure. On macroscale, such behaviour can result from two main factors including higher compressive strength of parent material and different internal structure. By analysing literature, the silica can reach compressive strength of 1350 MPa, significantly higher than 570 MPa for polyimide [351, 494]. In addition, as discussed before the low density polyimide samples incorporates larger pores. Once a crack emerge at a large flaw, the sample fails almost immediately, while in case of structure incorporating smaller pores loading in this range might resemble static loading [493]. On the other hand, by analysing the results of tensile testing, the low density silica samples produce higher yield stress at low density values below 0.6 g/cm^3 with low density polyimide surpassing it afterwards. Again, from MD point of view the reason for such behaviour can be found by analysing created samples. In low density samples the polyimide network within samples is less intertwined due to the larger pores than in silica structure. As a result, when subjecting polyimide samples to uniaxial atom displacement a fewer number of stronger bonds is required to be broken for the failure to happen. With increasing density, the number of bonds between polyimide molecules increases and their higher strength results in larger yield stress than in silica case. On a microscale level, it can be deducted that the same factors as in case of compressive properties are responsible for this behaviour. In this case it is the silica with lower tensile strength of about 45 MPa, while polyimide can reach even up to 90 MPa. It might be the internal structure of polyimide to cause the low-density samples to perform weaker than

silica counterparts. Nevertheless, with increasing sample density pore size is being significantly reduced resulting in decrease of the weakening effect and higher yield stress of the PI samples.

5.3.4 Interfacial thermal resistance

Following the combination of low density silica or polyimide samples with epoxy or amorphous silica reinforcement, thermal properties of created interface were measured by imposing the heat flux though the sample. The example of resulting temperature distribution is presented in Figure 5-56. Additionally, an atom distribution was also included allowing to identify the interfacial region.

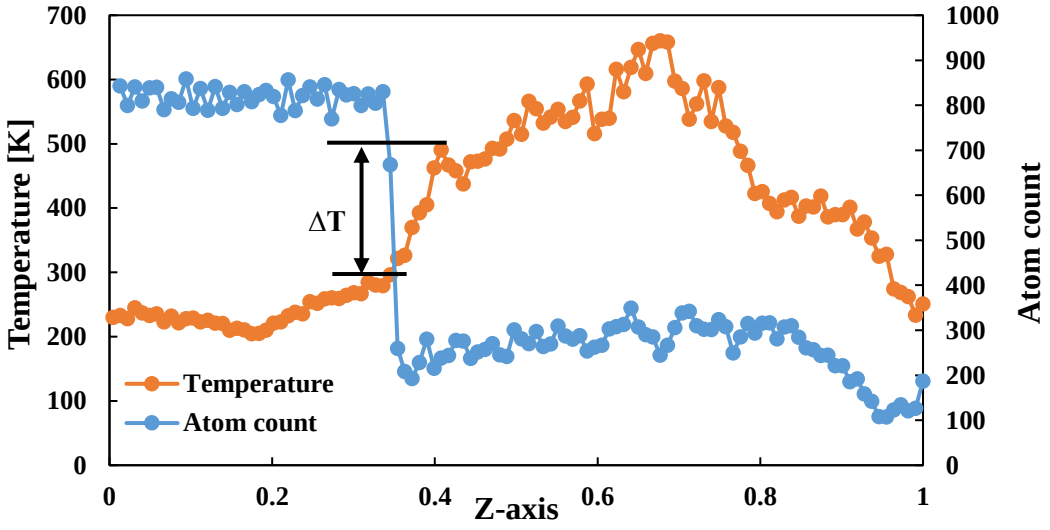

Figure 5-56 Example of temperature and atom distribution across combined sample. ΔT indicates the temperature difference occurring at the materials interface. Data obtained for silica sample with density of 0.24 g/cm^3 and amorphous silica.

Firstly, by analysing the atom count in Figure 5-56 two regions might be quickly identified. The region with significantly larger number of atoms within each bin represents the reinforcement, while low atom density can be attributed to the aerogel type sample. A sharp drop between atom count values indicates the interfacial region between both materials. In addition, Figure 5-56 presents that because of an energy transfer the temperature gradient with hot region in the middle of aerogel sample and cold region in the middle of reinforcement sample was created. Nevertheless, a significant discontinuity in temperature gradient can be observed appearing just around the interface region (defined by ΔT). Such behaviour is expected as due to the difference in material composition, as well as pores occurring at the interfacial region the energy transfer is disturbed. As a result, an energy accumulation occurs within the material incorporating hot region effectively elevating its temperature. On the other hand, a lack of energy input into the cold region results in decrease in temperature of the

reinforcement. Finally, when the steady state is achieved the two distinctive temperature gradients are created and linked by a temperature discontinuity, which is used to calculate the interfacial thermal resistance. In order to identify when the sample reaches steady state the total energy of the whole system is being monitored through the simulation time as presented in Figure 5-57.

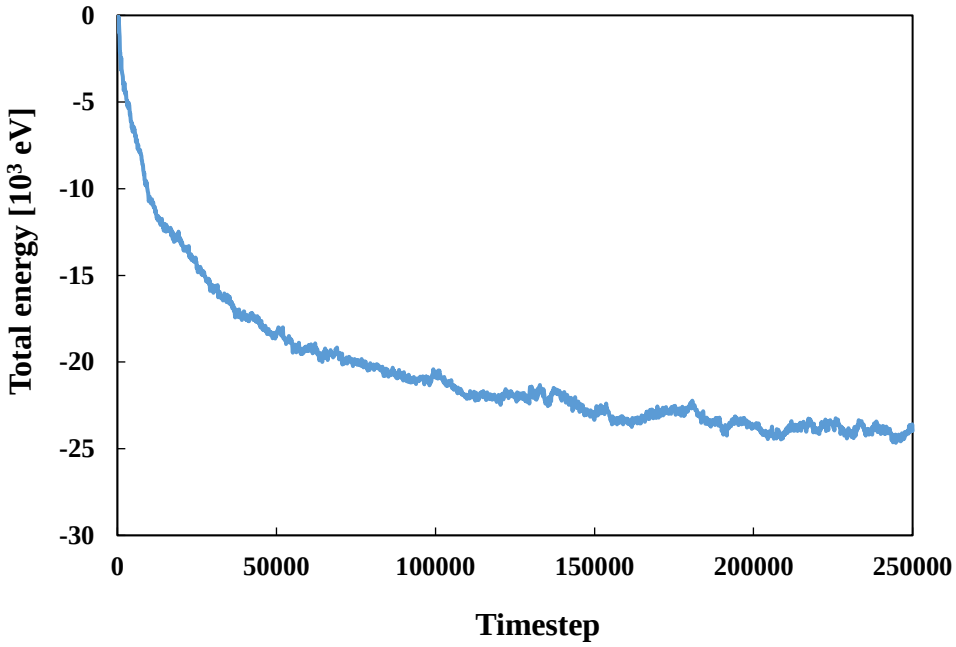

Figure 5-57 Total energy of the low density silica and amorphous silica system as a function of time step.

As presented in Figure 5-57 total energy of the system rapidly drops in the initial stage of the simulation to later stabilise. This situation is primarily caused by imposing the energy flux through the sample and constantly accumulating the energy on the material boundary. Similar energy behaviour has been previously seen in molecular dynamics simulations by Yang et al. and Yang et al. who investigated respectively aluminium/silicon and graphene/boron nitride interface [417, 495]. The temperature measurements have been taken following the energy stabilisation and the sample density has been identified as a major factor affecting thermal resistance. The example of temperature distribution with varying density has been presented in Figure 5-58.

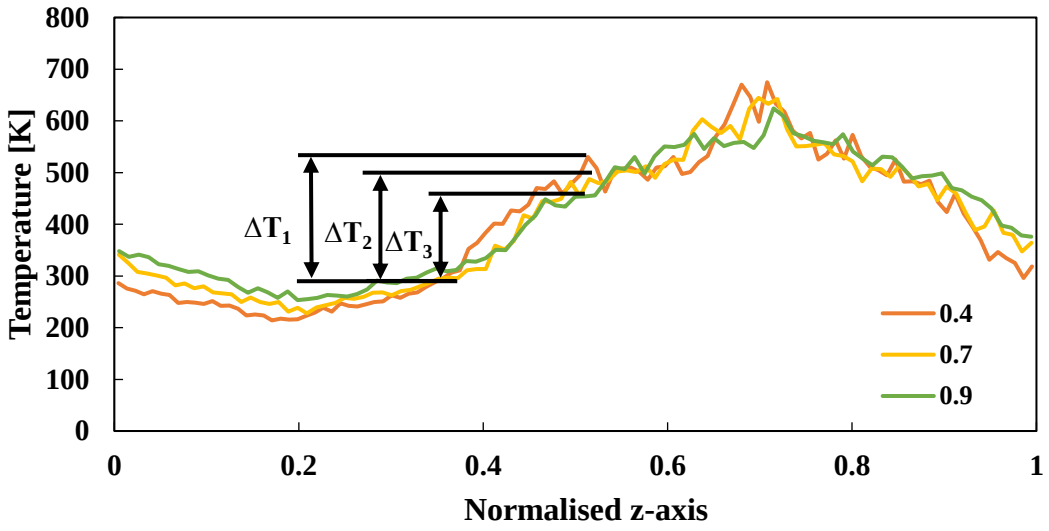

Figure 5-58 Temperature distribution of amorphous silica and silica samples with varying densities.

Temperature distributions in Figure 5-58 clearly indicates the impact of sample density on temperature occurring through the sample. Even though the temperature gradient in relatively similar for all samples, in reinforcement part the sample combined with lower density silica achieve substantially lower cold region temperature values. On the other hand, corresponding additive samples presents much higher temperatures that their counterparts with higher density. Such differences on both sides of the interface affect the magnitude of temperature disruption occurring at the interface, leading to increasing temperature difference with decreasing silica density. As presented in Figure 5-58, $\Delta T_1 > \Delta T_2 > \Delta T_3$ as those values has been achieved using silica samples with respectively 0.4, 0.7 and 0.9 g/cm^3. The results presented above are rather similar regardless of the type of the additive and reinforcement used as a result in order to avoid being repetitive only interfacial temperature differences and interfacial thermal resistance will be presented in the following sections.

5.3.4.1 Low density silica and amorphous silica

Following thermal analysis of the low density silica samples and amorphous silica interface the temperature discontinuity was found between reinforcement and each silica sample and results are presented in Figure 5-59.

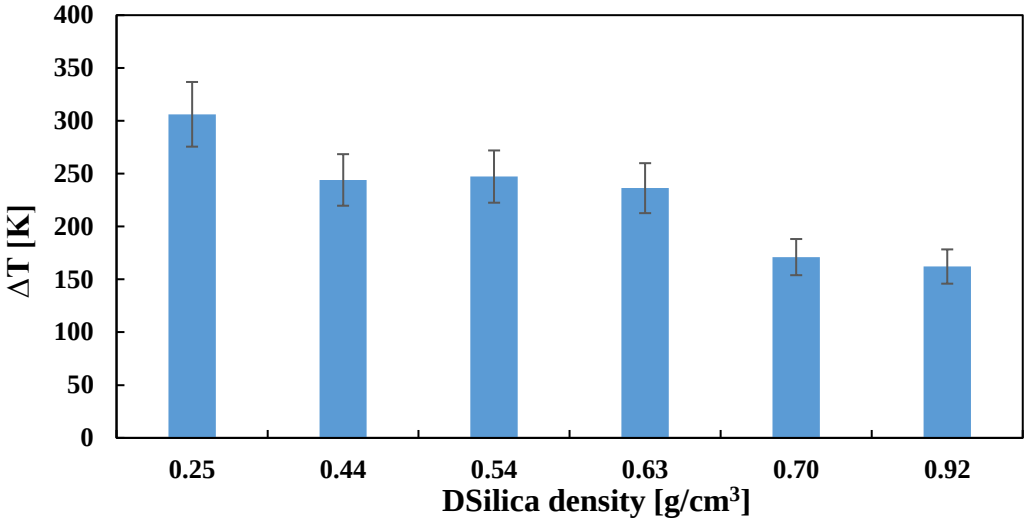

Figure 5-59 Temperature difference occurring at the interface between amorphous silica and silica samples with varying density.

As it can be noticed a significantly different discontinuity temperature has been found for low density silica samples with different densities. The highest value was measured for the silica sample with density of 0.25 g/cm^3, while the sample with density of 0.92 g/cm^3 experienced only half of that value. By incorporating geometrical features and simulation values such as sample size or heat flux the values of interfacial thermal resistance has been calculated and presented in Figure 5-60. Similarly, as in case of temperature the interfacial thermal resistance is decreasing with increasing density of the silica sample used and the relation follows the exponential trend with an exponent of -0.12.

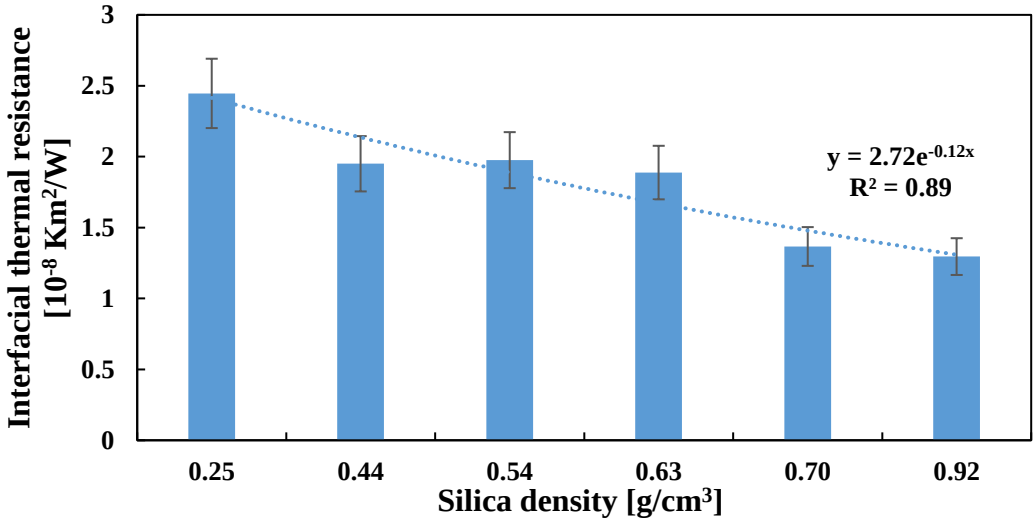

Figure 5-60 Interfacial thermal resistance between amorphous silica and silica with varying density.

5.3.4.2 Low density silica and epoxy

Following thermal analysis of the low density silica samples and epoxy interface the temperature discontinuity was found between reinforcement and each silica sample and results are presented in Figure 5-61.

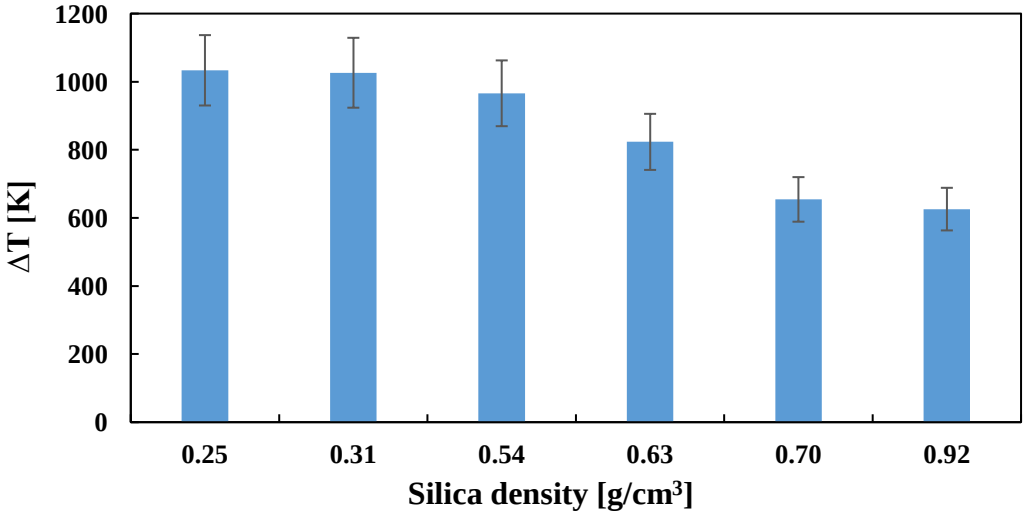

Figure 5-61 Temperature difference occurring at the interface epoxy and silica with varying density.

Presented by Figure 5-61 temperature difference follows decreasing trend with increasing silica density. Nevertheless, this time only small discrepancies can be noticed between interfacial temperature differences of silica with densities below 0.63 g/cm^3. With further increasing silica density a significant decrease was noticed leading to 625 K difference when using silica with density of 0.92 g/cm^3. The temperature results can be directly translated into interfacial thermal resistance as presented in Figure 5-62. Even though the minor changes are present at low silica density values, thermal resistance and silica density are correlated following exponential trend with the exponent of -0.115.

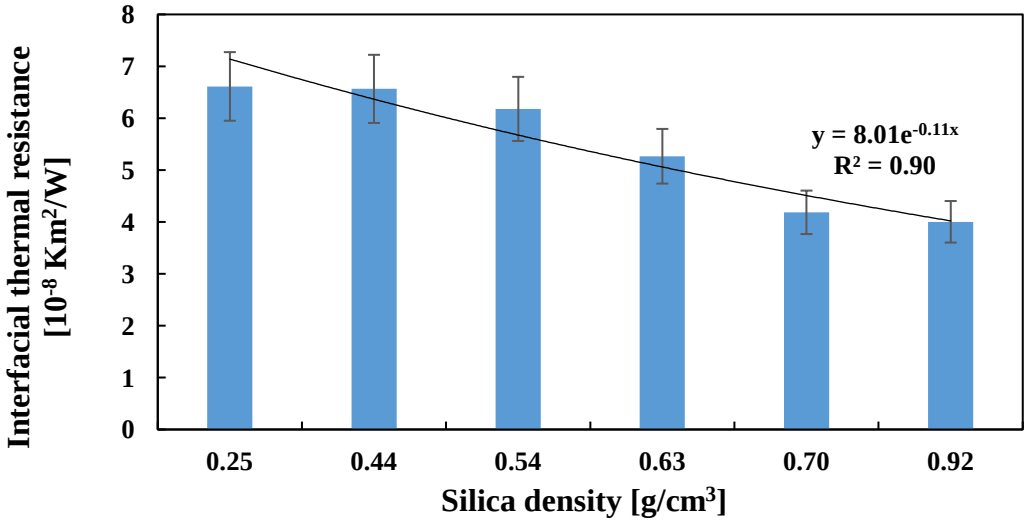

Figure 5-62 Interfacial thermal resistance between epoxy and silica with varying density.

5.3.4.3 Low density polyimide and amorphous silica

Using same thermal analysis as in case of the low density silica samples, polyimide samples have also been combined with amorphous silica. Temperature discontinuity was found between reinforcement and each sample and results are presented in Figure 5-63.

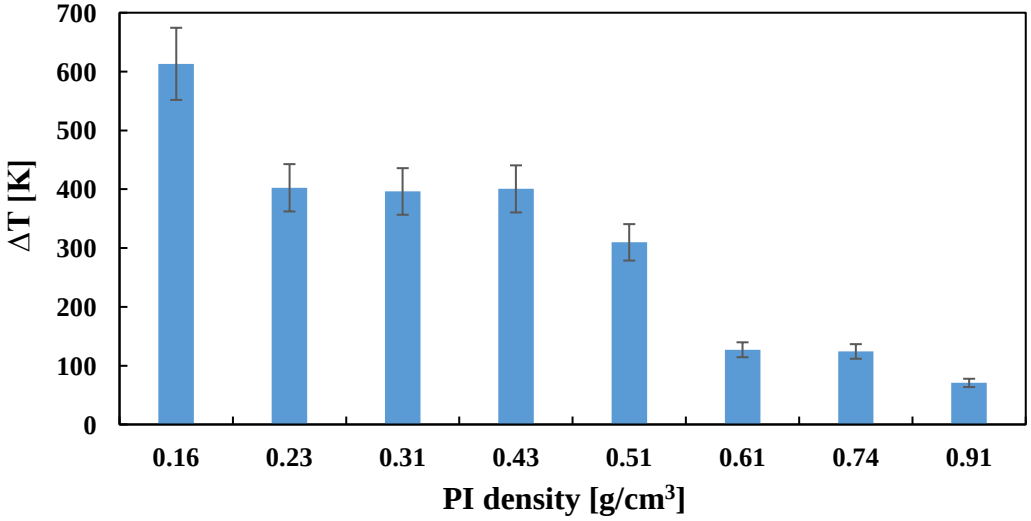

Figure 5-63 Temperature difference occurring at the interface between amorphous silica and polyimide with varying density.

Low density polyimide samples seems to follow similar trend to the one previously obtained for silica. As a result, by increasing the polyimide density the temperature difference occurring at the materials interface decreases. A major change in investigated temperature can be noticed at the transition from 0.16 to 0.23 g/cm^3 and 0.51 to 0.61 g/cm^3 polyimide. Correspondingly the interfacial thermal resistance follows the same pattern with highest value of 8.82 $\times 10^{-8}$ Km^2/W and lowest of 1 $\times 10^{-8}$ Km^2/W for respectively 0.16 and 0.91 g/cm^3 samples. The trend

relating interfacial thermal resistance and polyimide density follows exponential trend with the exponent of -0.29.

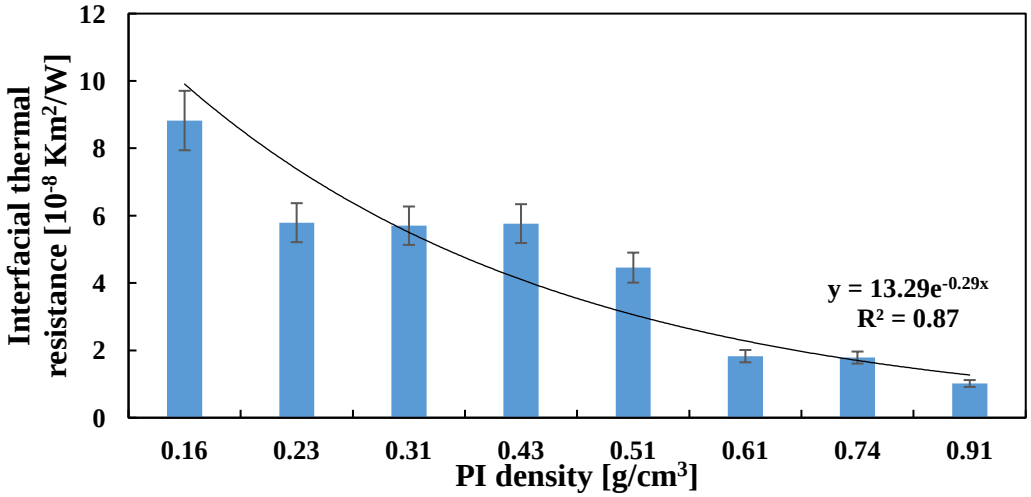

Figure 5-64 Interfacial thermal resistance between amorphous silica and polyimide with varying density.

5.3.4.4 Low density polyimide and epoxy

Again, following thermal analysis of the low density polyimide samples and epoxy interface the temperature discontinuity was found and results are presented in Figure 5-65.

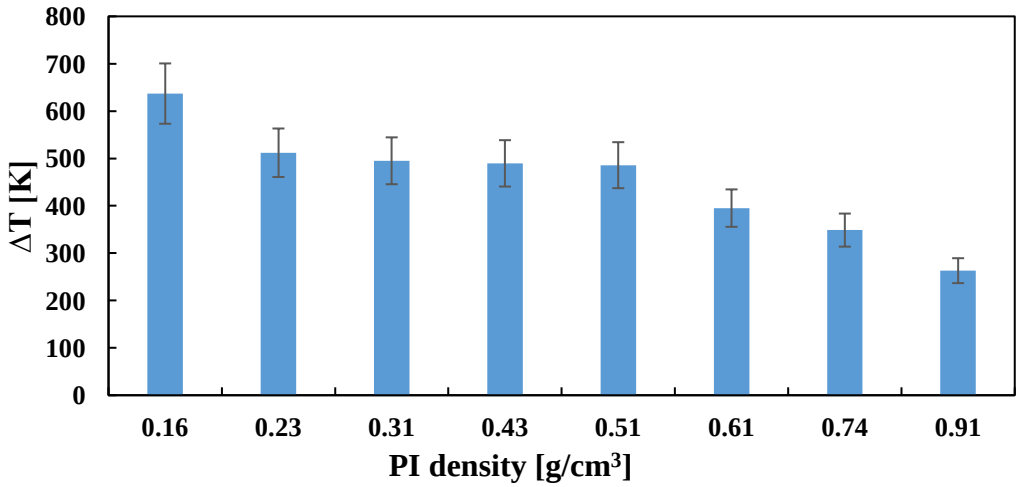

Figure 5-65 Temperature difference occurring at the interface between epoxy and polyimide with varying density.

The combination of low density polyimide samples with epoxy yields similar behaviour as previously simulated samples with decreasing temperature difference with increasing polyimide density. This time however, following sharp drop of ΔT value at 0.21 g/cm^3 a relative steady value is achieved until reaching 0.61 g/cm^3 when further decrease occurs. Same as previously, temperature values have been used to evaluate interfacial thermal resistance and

the results are presented in Figure 5-66. Again, as in the case of all previous combination an exponential trend is being fitted into collected data with an exponent of -0.105.

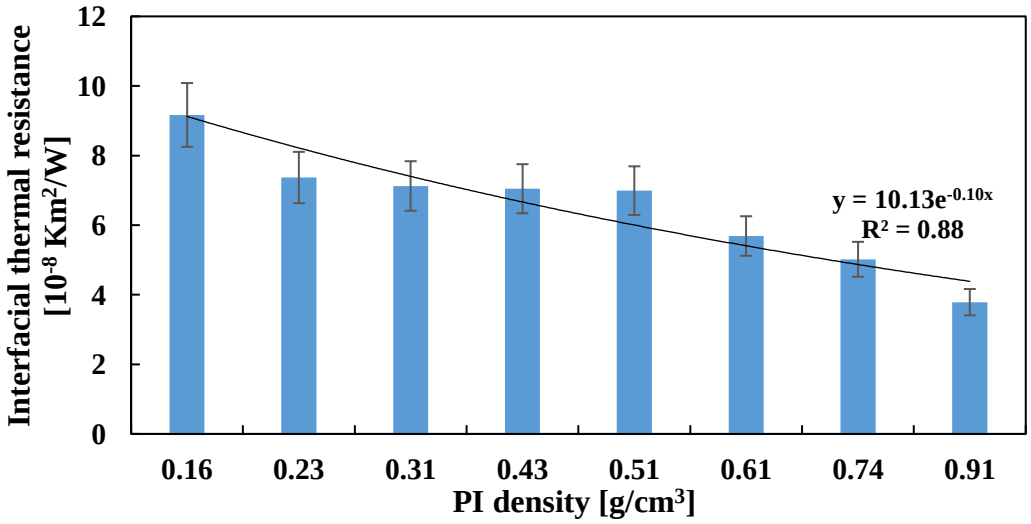

Figure 5-66 Interfacial thermal resistance between epoxy and polyimide with varying density.

5.3.4.5 Discussion

Following the presentation of results for each investigated combination the discussion of the results and comparative study will be conducted in the following section.

Firstly, as it can be noticed the interface thermal resistance values calculated in this study present extremely small values in a range of 10^{-8} Km^2/W. Even though there has not been an interface study conducted for any aerogel type on a molecular level which could be used for comparison purposes a broad range of other material types has been investigated and can assist in evaluating the accuracy of the results. As a result, Y. Chalopin et al. and E. S. Landry have investigated Si/Ge composites and achieved interfacial thermal resistance in a range of 13×10^{-8} Km^2/W [420]. Similarly, E. Lampin et al. quantified thermal boundary resistance at silicon-silica interfaces and achieved values between 1 and 8×10^{-9} Km^2/W [428]. Ong and Pop did the same for carbon nanotubes and SiO_2 composite resulting in interfacial thermal resistance of 58×10^{-8} Km^2/W. Other works were used to measure thermal properties of interface of organic materials including mainly polymer composites. As a result, Pan et al. tested silicon and amorphous polyethylene interface obtaining thermal conductance of 5×10^{-8} Km^2/W at room temperature [410]. All mentioned studies proves that the values obtained for low density silica and polyimide composites are within expected range and are in a good correlation with the literature. In addition, Figure 5-67 has been created combining interfacial thermal resistances between all investigated materials.

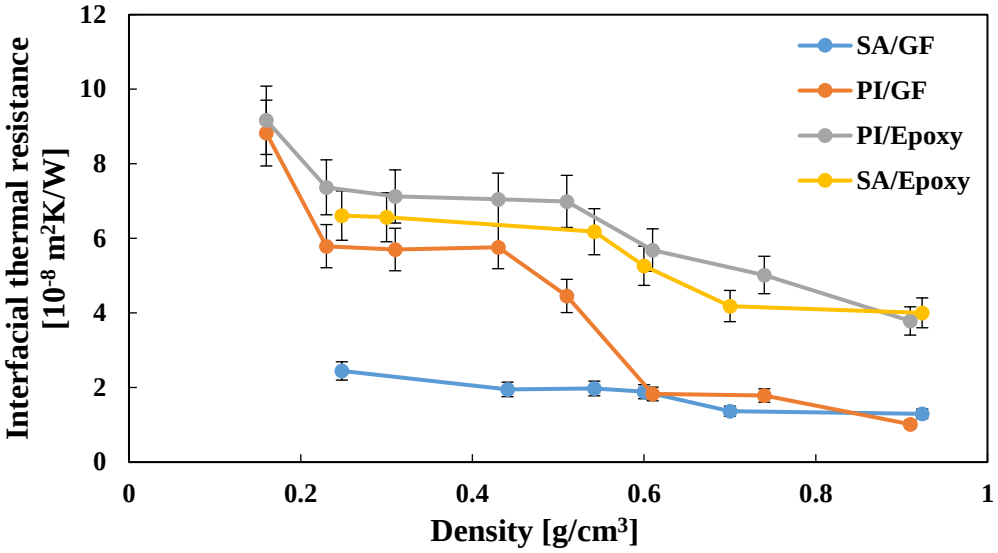

Figure 5-67 Comparison of interfacial thermal resistance between investigated materials.

By analysing Figure 5-67 it can be noticed that all the interfaces follow the same trend of decreasing interfacial thermal resistance with increasing inclusion density. Even without visible defects in the vicinity of the contact surfaces, it does create an impedance to thermal transport based mainly upon the differences in materials densities and phonon propagation speeds [496]. However, in this study a large quantity of pores has been modelled at the interfacial region. As a result, with increasing silica or polyimide density a larger number of atoms are being in direct contact with the atoms from reinforcement sample resulting in much greater energy transfer through lattice vibrations. Effectively by increasing contact area between both materials, a higher interfacial thermal conductance is achieved reducing thermal resistance at the border.

Another observation from Figure 5-67 implies that the silica samples present lower interfacial thermal resistance than polyimide samples when combined with same reinforcement. Especially when comparing the samples combined with amorphous silica a huge discrepancy can be noticed. The reason for such behaviour is a similarity of combined materials in case of SA/GF composites. From atomistic point of view silica prepared for this study is just an amorphous silica with large number of pores included within. As a result, when analysing heat flow through the interface the only disruption is the density change between both sides of the interface, while other chemical and physical factors (such as photon speed or overlap of their vibrational density of states) remain the same. Similar values of the interfacial thermal resistance have been previously achieved by E. Lampin et al. who have evaluated thermal boundary resistance at silicon-silica interfaces to be 8×10^{-9} Km^2/W. The value obtained in their study is even smaller than the one presented in this study because of lack of geometrical

features (pores) in their samples [428]. When considering the low density samples combined with epoxy a value is much more alike, with polyimide still presenting superior thermal resistance. In this case two factors should be considered including the geometrical features on the interface and thermal conductivity of parent materials. As polyimide samples incorporates larger pores in internal structure it might indicate that lesser number of atoms will be in a direct contact with the epoxy sample than in case of silica samples. As stated previously lower number of atoms in direct contact between both materials reduces energy transfer through lattice vibrations. Additionally, as presented by Zhang et al., the amorphous silica structures can improve the energy transport across interfaces [497]. Since, disordered atomic structures significantly improves the phonon scatterings in the amorphous system. As a result, phonon mean free path is shortened and the high frequency phonons are decomposes into multiple low frequency photons, which improves interfacial thermal transport and lower interfacial resistance [497]. It might be concluded that the combination of mentioned factors might be responsible for higher interfacial thermal resistance of composites prepared with polyimide and epoxy.

To conclude, it should be highlighted that that the usage of nanoscale for thermal investigation carries potential drawbacks such as lack of possibility of geometrical features implementation. Currently to limit required computational resources, simulations are carried using mainly flat surfaces which represent only small portion of the contact region. Overall many previous studies have suggested implementation of obtained results into higher scale models (micromechanical models) in order to fully understand the impact of geometry on the energy transfer phenomenon [419].

5.3.5 Interfacial shear stress

The interface between combined samples have also been tested mechanically by replicating the microbond test allowing to evaluate their interfacial shear strength. To do so, the reinforcement sample has been displaced at a steady rate and the resulting force imposed on displaced atoms as well as the energy of the whole assembly has been carefully measured over the whole time. As a result, the example force versus displacement graph is presented in Figure 5-68.

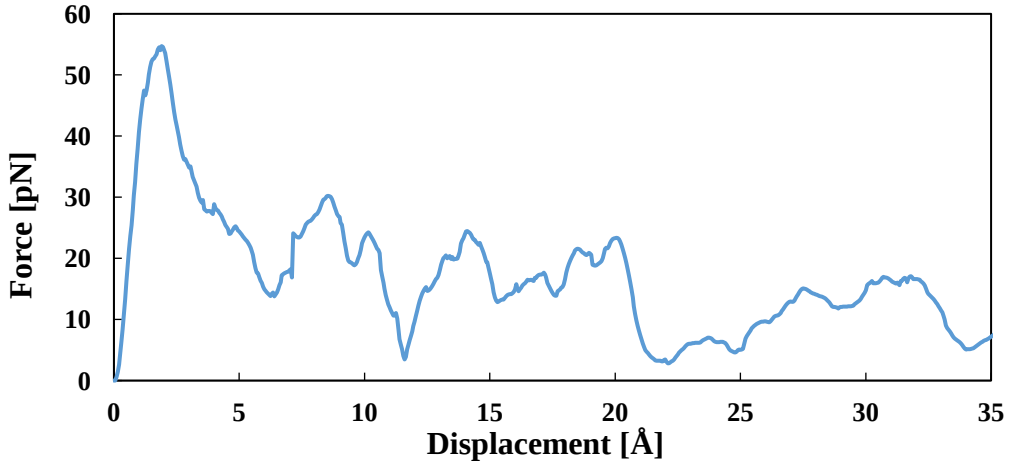

Figure 5-68 Example force/displacement graph achieved from microbond simulation. Sample used was amorphous silica and polyimide sample with density of 0.4 g/cm^3.

As it can be noticed the graph presented in Figure 5-68 closely replicates the graphs obtained by an experimental microbond testing with three distinctive regions identified. Firstly, in the initial stage of the atom displacement the force ramp can be noticed until the failure of the interface occurs. Such behaviour is expected as the relative sliding does not happen at the interface between low density material and the reinforcement. At that point, the atoms neighbouring with the interface are experiencing elastic deformation until the maximum shear force is achieved and relative sliding commence at the interface. Afterwards, a debonding process commences during which the force is steadily decreasing as increasing number of bonds between the atoms is being broken. Finally, the near zero force values as being obtained when complete separation of both materials is achieved. The breakage of the interface between both materials has a substantial impact on total energy of the system as indicated by Figure 5-69.

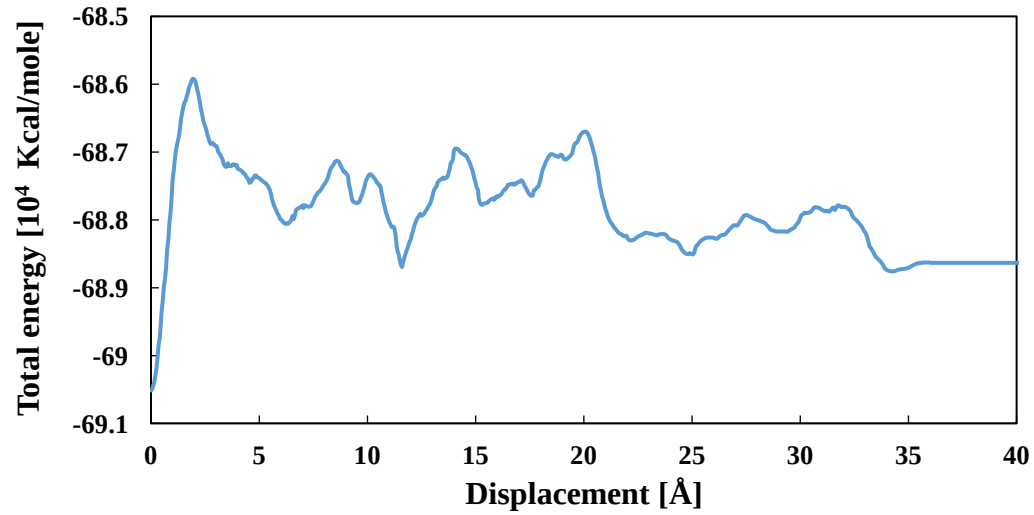

Figure 5-69 Example of total energy behaviour during microbond simulation. Sample used was amorphous silica and low density polyimide (0.4 g/cm^3).

Total energy of the ensemble is following similar path to the one presented by the imposed force. In the initial stages of the microbond test an increase in the total energy of the system is being recorded until the interface failure is achieved. Afterwards, the energy fluctuations are being recorded as a result of creation and breakage of bond between displaced atoms. Finally, the energy stabilises at a value corresponding to the energy of both materials in their separated states. The pull-out energy used for calculation of interfacial shear strength is equal to the difference between initial and final total energy of the system.

5.3.5.1 Low density silica and amorphous silica

The samples consisting of amorphous silica and low density silica (simulating aerogel) with different densities have been subjected to the microbond testing with the amorphous silica being displaced at a constant rate. As a result, the series of the force and displacement graphs have been created and presented in Figure 5-70.

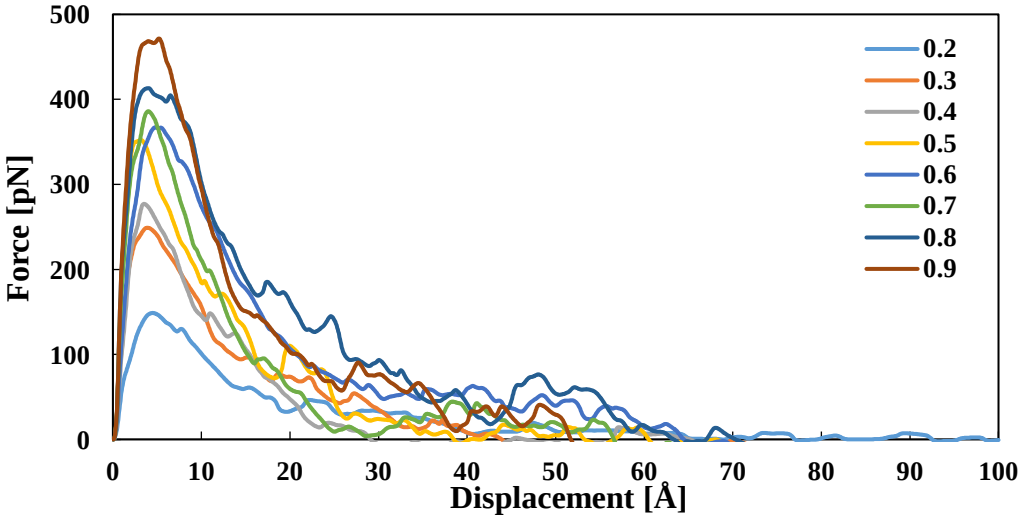

Figure 5-70 Force versus displacement graph obtained from microbond test of silica samples with varying densities [g/cm^3].

All the simulated samples follow the previously presented trend with force increase until the interface failure occurs. Nevertheless, a significant impact of silica density on the force behaviour can be noticed. With increasing silica density, a larger force is required for an interface failure to happens. The difference is rather substantial as the sample prepared with 0.2 g/cm^3 silica requires only 144 pN to break the interface while when using 0.9 g/cm^3 silica the same force increases up to 460 pN. Together with increase in the force required to break the atom bonds the silica density is also affecting pull-out force as presented in Figure 5-71.

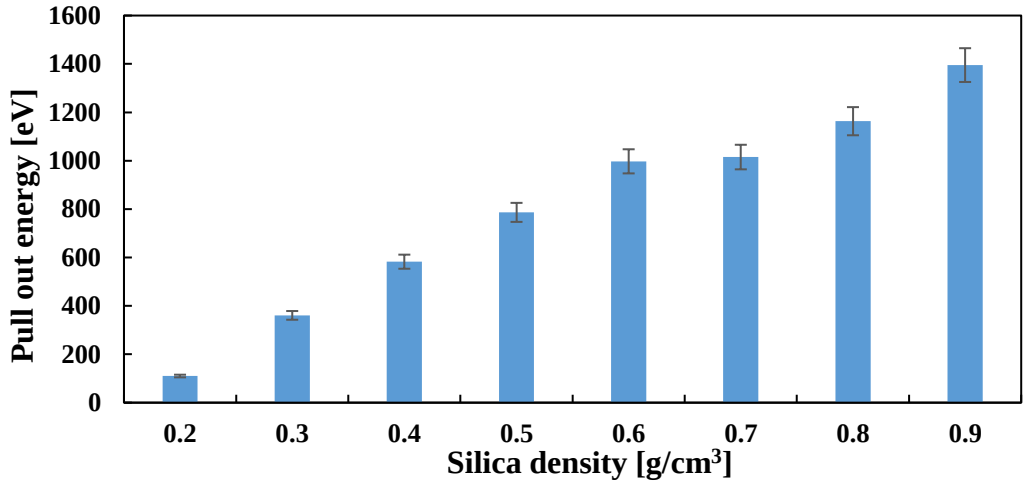

Figure 5-71 Pull out energy recorded during the interface breakage between amorphous silica and silica samples with varying density.

As discussed before, the pull-out energy represents the energy of bonds between atoms from both materials which has been broken during the atom displacement. Not surprisingly with increasing silica density the pull-out energy also increases. The relation between both properties follows the power trend with an exponent of 1.16. By incorporating some geometrical features of the sample and a pull-out energy an interfacial shear strength between both materials has been calculated and presented in Figure 5-72. Due to the face that pull-out energy and IFSS are directly related same trend of increasing IFSS with increasing silica density can be observed.

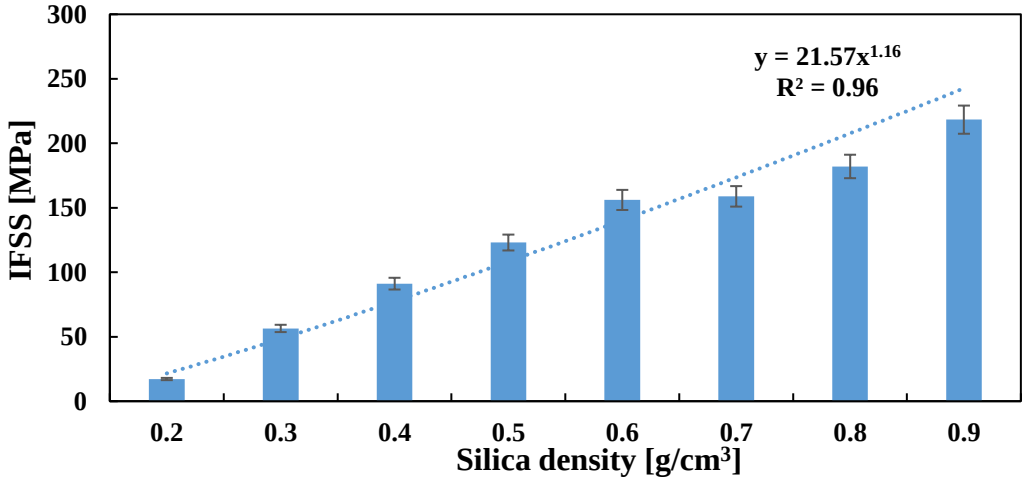

Figure 5-72 IFSS of the interface between amorphous silica and silica with varying density.

5.3.5.2 Low density silica and epoxy

Following previously described microbond procedure the epoxy atoms have been subjected to the uniaxial displacement in the presence of silica samples with varying densities. As a result, the force and displacement graphs have been created and presented in Figure 5-73.

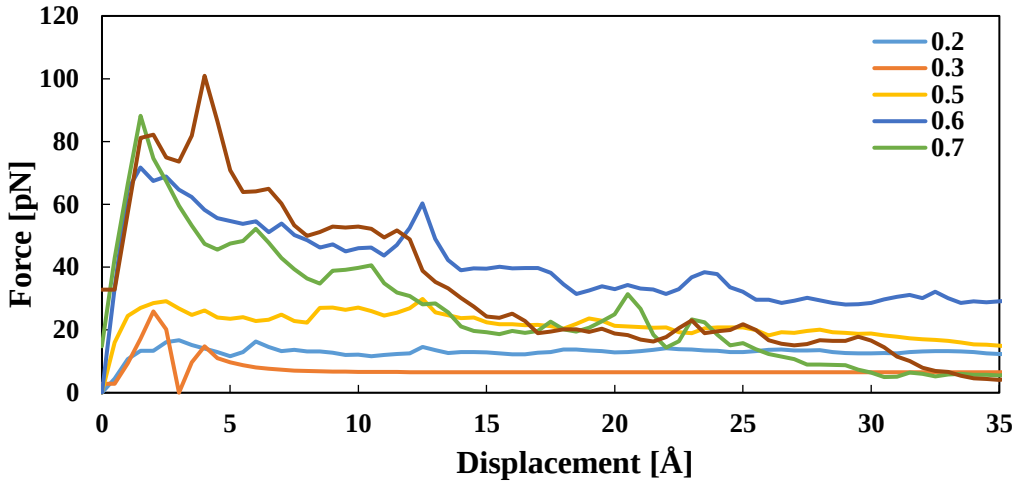

Figure 5-73 Force versus displacement graph obtained from microbond test of epoxy and silica samples with varying densities [g/cm^3].

The graphs presented in Figure 5-73, clearly indicates that all epoxy and silica samples followed the anticipated trend and has experienced elastic deformation until the maximum shear force was achieved. Nevertheless, the density of silica sample was a major factor affecting the force/displacement behaviour as with increasing density the interfaces presented stiffer response to atom movement. As a result, a 17 pN is required to break the interface between epoxy and 0.2 g/cm^3 silica, while when utilising 0.9 g/cm^3 silica required shear force increases to 101 pN. The density of silica sample affected not only force required to interface failure but also the pull-out energy. Figure 5-74 and Figure 5-75 are presenting respectively pull-out energy and interfacial shear strength of epoxy and silica samples.

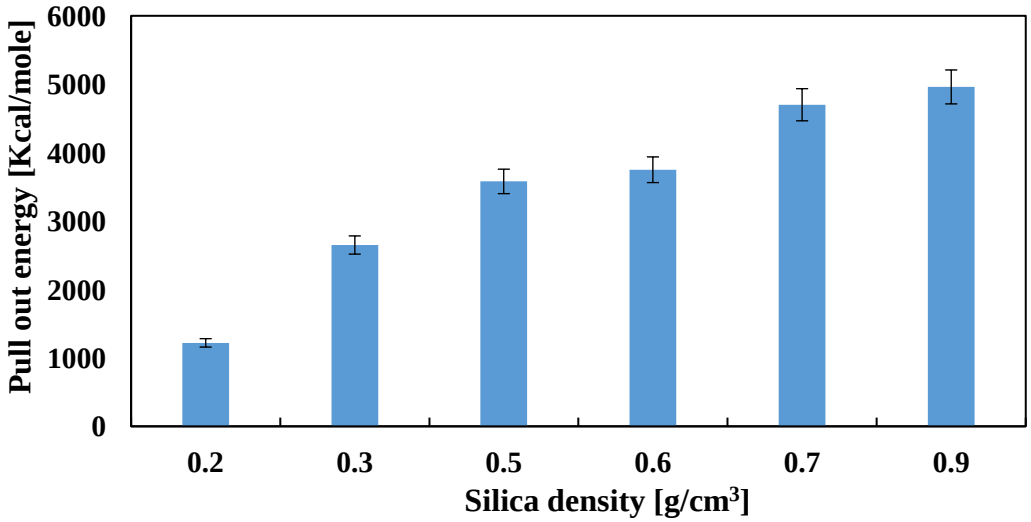

Figure 5-74 Pull out energy recorded during the interface breakage between epoxy and silica samples with varying density.

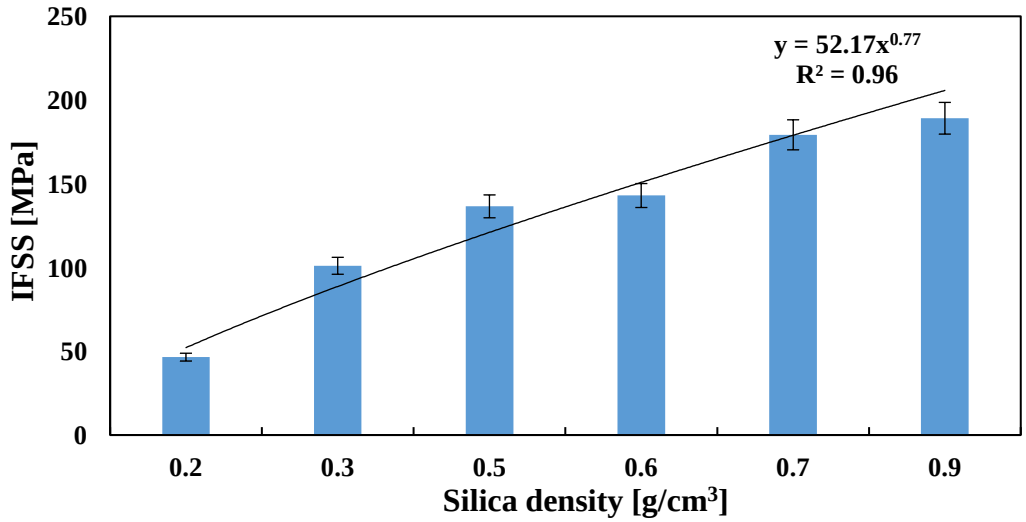

Figure 5-75 IFSS of the interface between amorphous silica and silica samples with varying density.

Since both properties are directly related, they both follow the same trend and increases with increasing density following the power law with an exponent of 0.77. As a result, a significant difference in interfacial shear strength can be noticed with an IFSS of 46.5 MPa simulated for the lowest density sample while almost 190 MPa for the highest density used.

5.3.5.3 Low density polyimide and amorphous silica

When analysing the mechanical properties of low density polyimide and amorphous silica interface the atoms of the latter material has been displaced along z-axis and the following force and displacement graphs have been created and presented in Figure 5-76.

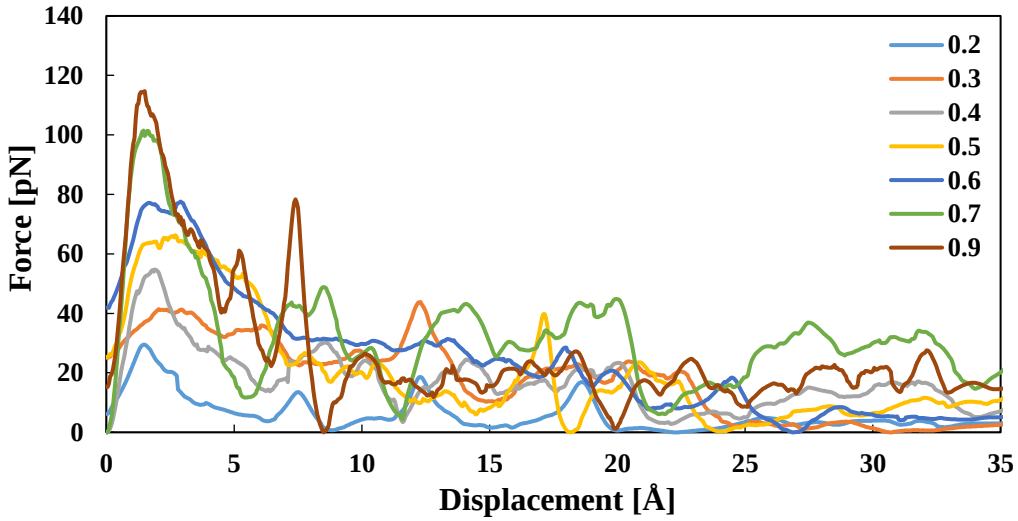

Figure 5-76 Force versus displacement graph obtained from microbond test of polyimide samples with varying densities [g/cm^3].

Polyimide and amorphous silica composites follow expected force/displacement trend when subjected to atom displacement. The initial force increase followed by an interface failure and steady shear force decrease can be easily noticed across samples with all polyimide densities used. Nevertheless, the samples incorporating higher density polyimide requires larger shear force in order to break the interface and commence atom sliding. As a result, a 33 pN are required to break the interface between amorphous silica and 0.2 g/cm^3 polyimide, while when using 0.9 g/cm^3 polyimide required shear force increases to 112 pN. Similar impact of polyimide density on pull-out energy can be noticed in Figure 5-77.

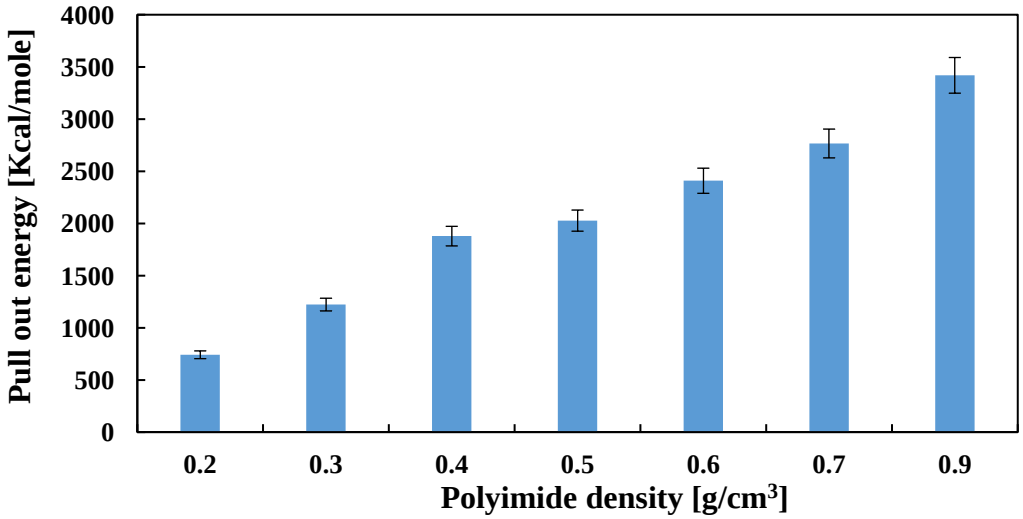

Figure 5-77 Pull out energy recorded during the interface breakage between amorphous silica and polyimide samples with varying density.

As presented in Figure 5-77, the pull-out energy increases with increasing polyimide density following the power trend with the exponent of 0.76. This behaviour is mainly attributed to the higher number of bonds between higher density polyimide and amorphous silica. In order to compare mechanical properties of this interface a interfacial shear strength values have been calculated and presented in Figure 5-78. Due to the direct correlation between pull-out force and IFSS the same power trend is being observed when correlated with density with lowest IFSS of 40 MPa obtained for 0.2 g/cm^3 polyimide and highest of 186 MPa achieved when using 0.9 g/cm^3 polyimide sample.

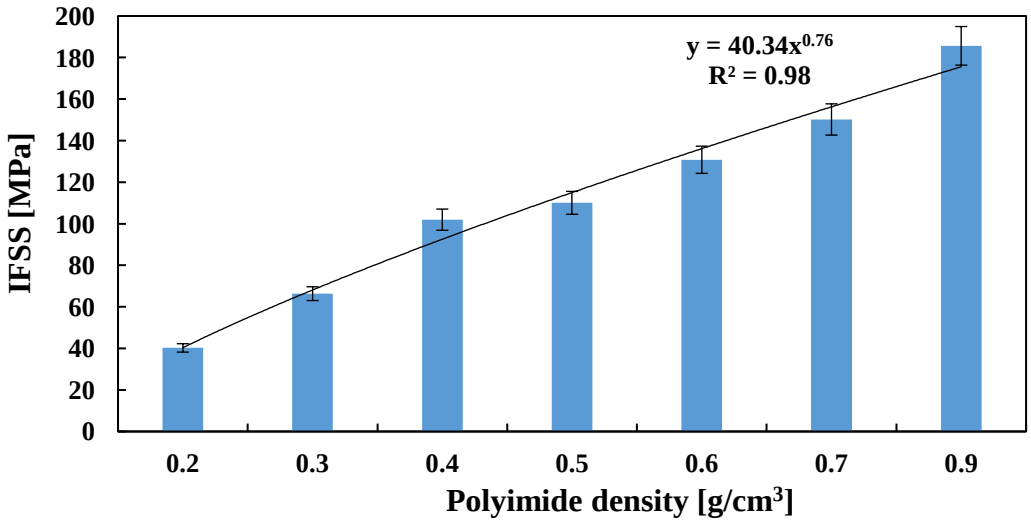

Figure 5-78 IFSS of the interface between amorphous silica and polyimide samples with varying density.

5.3.5.4 Low density polyimide and epoxy

Finally, the epoxy and low density polyimide samples has been also tested using the pull-out technique. Corresponding force and displacement graphs have been presented in Figure 5-79.

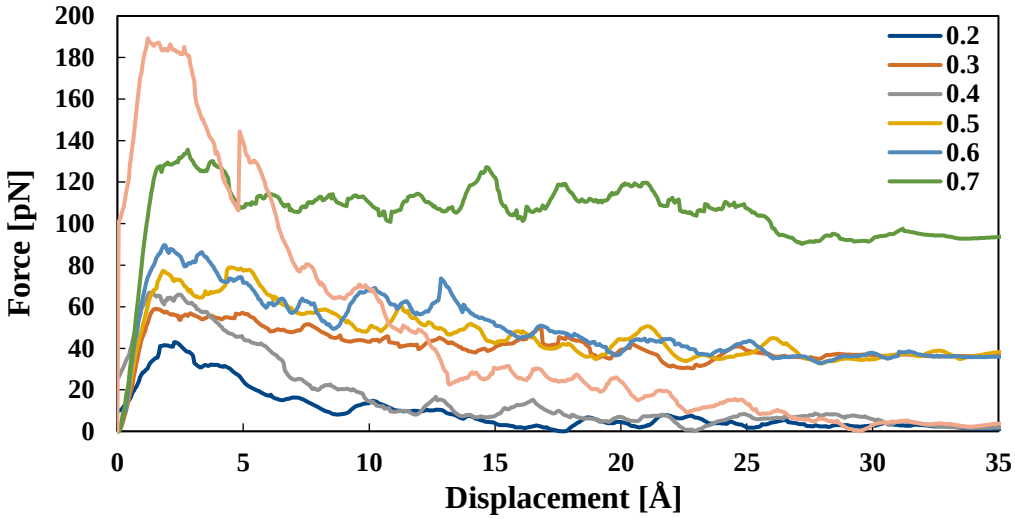

Figure 5-79 Force versus displacement graph obtained from microbond test of polyimide samples with varying densities [g/cm^3].

Again force-displacement graphs presented in Figure 5-79 presents a behaviour expected from the pull-out test with initial force ramp, failure of the interface and finally force decrease until reaching full debond. In addition, a significant impact of polyimide density on the force behaviour can be noticed, as with increasing polyimide density a larger force is required for an interface failure to occurs. Together with increase in the force required to break the atom bonds the polyimide density is also affecting pull-out force as presented in Figure 5-80.

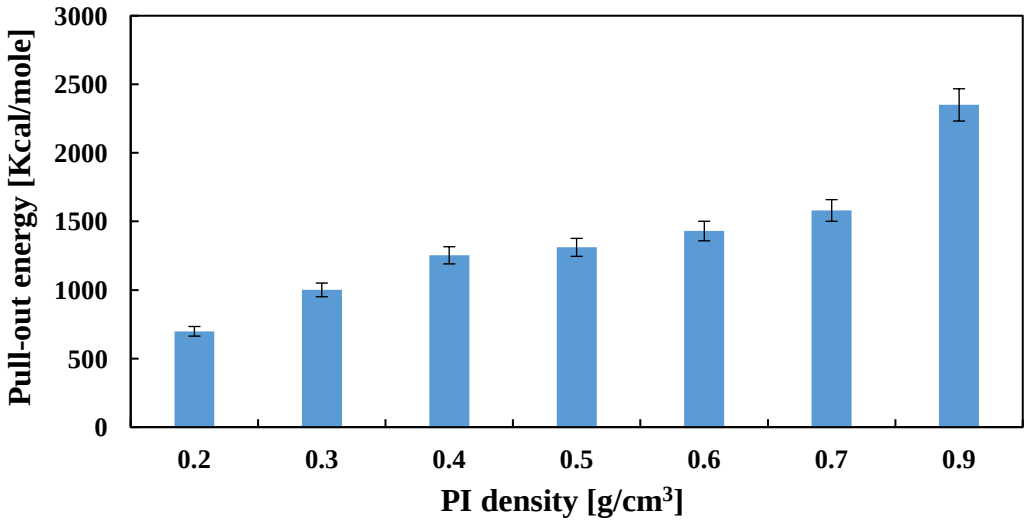

Figure 5-80 Pull out energy recorded during the interface breakage between epoxy and polyimide samples with varying density.

As indicated by Figure 5-80, the pull-out energy increases with increasing polyimide sample density as a result of increasing number of bonds between higher density polyimide and epoxy. The relation between both properties follows the power trend with an exponent of 0.53. In addition, an interfacial shear strength between both materials has been calculated and presented in Figure 5-81 allowing for further comparison of mechanical properties of various interfaces. Resulting IFSS values presented a wide range starting with lowest IFSS of 38 MPa obtained for 0.2 g/cm^3 polyimide and highest of 128 MPa achieved when using 0.9 g/cm^3 polyimide sample.

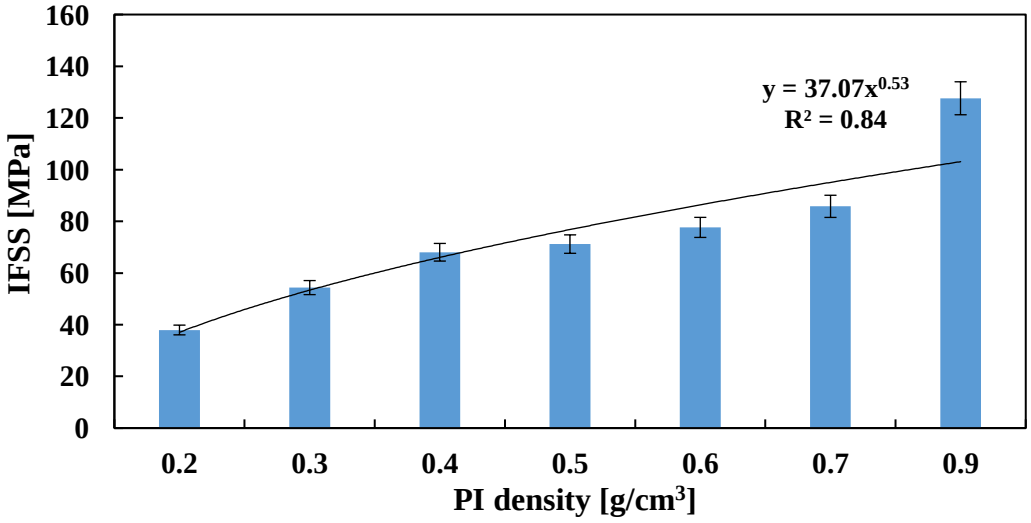

Figure 5-81 IFSS of the interface between epoxy and polyimide samples with varying density.

5.3.5.5 Discussion

Following the presentation of results for each investigated material combination the discussion of obtained results and the comparative study will be conducted in the following section.

When analysing presented results regarding interface mechanical simulations a huge difference between IFSS values for varying densities of silica and polyimide samples can be noticed. Especially for the high-density materials the IFSS values can reach as high as 220 MPa. Nevertheless, such values are not against results previously reported in the literature. Numerous studies investigating the interfacial strength of epoxy provided a wide range of IFSS values between 75 MPa and 3000 MPa [286, 406, 415, 498, 499]. However, when comparing the molecular dynamics results with experimental data presented in previous chapters a poor correlation was found. For silica (0.1 g/cm^3) and polyimide (0.19 g/cm^3) deposited onto the glass fibre the IFSS values were respectively 1.3 MPa and 4 MPa. As such the MD results are at least one order of magnitude too large with IFSS values of 17 MPa and 40 MPa for respectively silica and polyimides with density of 0.2 g/cm^3. When using the power trend equations for mixture of amorphous silica with silica and polyimide and material density values approaching the 0.02 g/cm^3 the IFSS values as low as 0.67 MPa for silica and 4.54 MPa for polyimide has been identified which might indicate better agreement at low aerogel density values. Furthermore, by calculating an interfacial shear strength value (presented in Figure 5-82) a direct comparison between all four systems can be conducted.

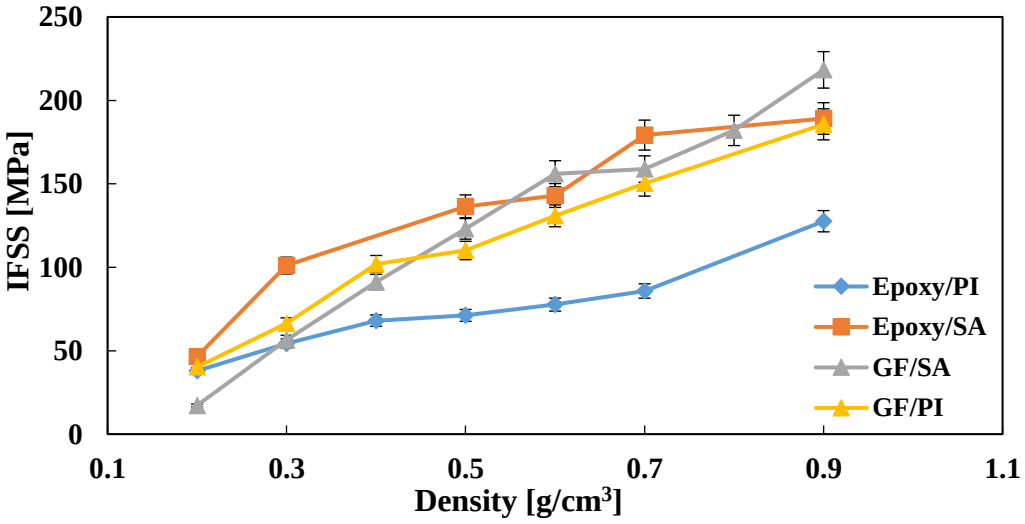

Figure 5-82 Comparison of interfacial shear strength of composites modelled with varying density silica and polyimide.

Firstly, by analysing Figure 5-82 it can be noticed that all four interfaces follow the same trend of decreasing IFSS values with decreasing silica or polyimide density. The explanation of this

behaviour simply comes down to increasing number of bonds created between reinforcement and silica or polyimide atoms when higher density material samples have been used. By incorporating larger number of atoms in direct contact with reinforcement sample a greater number of bonds is created during relaxation process. In return, an increasingly higher shear force is required in order to achieve an interface failure and higher pull-out energy is being recorded. Nevertheless, especially for high density silica or polyimide samples the IFSS values reach rather unphysical values as high as 219 MPa. There are few reasons which should be considered when analysing those results. Firstly, the time scale difference is substantial. Typical microbond test runs at a constant rate in the time scale of microseconds. On the other hand, molecular dynamics simulations are limited to time scales of pico or nano seconds to match required computational resources [500, 501]. Secondly issue is the size-effects. Since MD simulation can only reproduce a small representative group of atoms of the material a simulated volume might fail to capture the internal structure of the material or even its bulk behaviour. To reduce this issue, the periodic boundaries are being introduced, replicating simulated volume across all boundaries. Nevertheless, by incorporating this solution a true effect of the surrounding media is being removed. Especially for the pull-out simulations incorporating fibrous materials a numerous geometrical feature is missing including curvature of the fibre surface or even fibre roughness resulting in overestimated results [500]. Finally, the molecular dynamics simulations capture idealistic image of the material without any pre-existing defects or dislocations. As the crack creation and propagation is one of the most common reasons for material failure, its lack in molecular dynamics simulations significantly improves simulated mechanical properties [500, 501]. Especially this phenomenon is scaling substantially with increasing density of silica or polyimide samples, as by reducing the number of pores within the sample, more homogeneous and stronger material is being tested.

Finally, when comparing both low density materials used in this study overall polyimide is reporting lower interfacial shear strength values than silica counterpart (especially at high density values). Similarly, as in previously discussed interface features there are chemical or physical parameters of materials responsible for such behaviour. Firstly, it is the simulated internal structure of both materials. In silica samples the presence of many small pores results in unobstructed atom movement in the initial deformation period regardless of strong atomic interactions (more ductile behaviour). On the other hand, polyimide atoms are more clustered due to larger pores present in the structure. As a result, the interactions become much stiffer effectively restricting atom movement and causing earlier interface failure. Additionally, as low density polyimide incorporates larger pores it might indicate that lesser number of atoms will be in a direct contact with the reinforcement sample than in case of low density silica. As

stated previously lower number of atoms in direct contact between both materials reduces number of bonds created and thus the IFSS value. With decreasing silica or polyimide density, all mentioned reasons become less important as further expansion of samples results in creation of large pores in silica structure as well. Second reason for lower polyimides' IFSS lies in the interactions between atoms. In case of SA/GF composite the potential used recognised both materials as an amorphous silica with large number of pores included within. As a result, strong covalent bonds are simulated across the interface and contribute to the high IFSS values. Since strength of such bonds strongly depends on distance between the atoms, the decrease in material density significantly reduces IFSS values resulting in the lowest IFSS value when using silica or polyimide sample below 0.2 g/cm^3 [16, 351, 502]. Epoxy/silica and amorphous silica/ polyimide composites are both an example of polymer-silica interaction. As shown in previous studies such interfaces are connected via weak interaction such as: hydrogen bonds, non-bonded van der Waals, and columbic interactions. Even though those bonds are weaker than covalent bonds, they act on a longer distance and provide higher IFSS values at low silica or polyimide density than covalent bonds [406, 503]. Epoxy/polyimide composite is the only example of polymer-polymer interface and similar interactions as in case polymer-silica interface are responsible for their bonding [504]. Nevertheless, comparison study between works presented by Clark et al. who characterised wide range of polymer-polymer interface and Stoffels et al., who focused on silica-epoxy interface reveals significant discrepancies in terms of work adhesion [406, 504]. For simple SiO_2/epoxy interface the total work of adhesion was found to be 207.85 mJm^{-2}, while wide range of polymer interface investigated by Clark resulted in significantly lower total work of adhesion between 40 and 117 mJm^{-2} [406, 504]. It should be highlighted that Clark et al., was investigating mainly hydrocarbon polymers including polypropylene and polyethylenepropylene, however by analysing Figure 5-82 one might assume the interaction between epoxy and polyimide might yield similar work of adhesion energy and results in significantly lower IFSS values than other investigated interfaces. Finally, it needs to be highlighted, that such mechanical results are in good agreement with previously reported interfacial thermal resistance results as it is widely accepted that mechanically weaker interfaces present higher thermal resistance values.

5.4 Summary

In this chapter a nanoscale simulation of thermal and mechanical properties of low density silica and polyimide using Large-scale Atomic/Molecular Massively Parallel Simulator has been conducted.

Following the sample validation, a range of low density silica and polyimide samples with varying densities were created and a correlation between density and thermal, tensile, and compressive properties has been derived. In terms of thermal conductivity, low density silica has proved to have better insulating properties than polyimide counterpart. The internal structure of both materials has been identified as main reason for such behaviour with closely interlinked polyimide molecules maintaining the energy transfer path through the sample. Overall, achieved results have proven to be in a close correlation with values achieved from previous studies and experimental tests. This investigation also allowed for the detailed assessment of interatomic potentials used for simulation of silica aerogels proving the superiority of Vashishta potential under tested conditions. When simulating the tensile and compressive properties of both materials a good correlation between simulated and experimental results has been identified for low density silica. On the other hand, a significant discrepancy can be noticed for low density polyimide samples for which especially modulus values were a few orders higher than data presented in experimental studies. Such discrepancies were mainly caused by too small, simulated volume of polyimide used. By trying to match computational resources the samples failed to precisely replicate the internal structure of low density polyimide resulting in overestimating its modulus.

Furthermore, the silica and polyimide samples have been combined with amorphous silica and epoxy resin. Such combinations allowed nanoscale simulations to focus on quantifying the thermal and mechanical properties of interfaces between low density materials and mentioned reinforcement systems. As a result, for the first time the effect of silica and polyimide density upon both interfacial thermal resistance and interfacial shear strength was calculated.

When imposing the heat flux through the simulated interfaces an extremely small values of interfacial thermal resistance (in a range of 10^{-8} Km^2/W) have been achieved. Nevertheless, obtained values were still within expected range and were in a good correlation with the values obtained from literature. In addition, all the interfaces have followed similar trend with decreasing thermal interfacial resistance with increasing silica or polyimide density. Such behaviour was associated, with increasing number of atoms being in direct contact with the atoms of reinforcement sample when denser samples were utilised. This effectively allowed for a greater energy transfer through lattice vibrations and reducing thermal resistance at the border. The investigation has also suggested that the low density silica samples present lower interfacial thermal resistance than polyimide samples when combined with same reinforcement. Finally, it was highlighted that that the usage of nanoscale for thermal

investigation carries potential drawbacks such as lack of possibility of geometrical features implementation.

The interfacial mechanical properties of created interfaces have been simulated by shearing two parallel surfaces of different materials. The comparison of results reported in this study presented a good fit with previously reported molecular dynamics studies, however they were an order of magnitude larger than experimental values presented in Chapter 4. It was found that all four interfaces follow the same trend of decreasing IFSS values with decreasing silica or polyimide density mainly due to the decreasing number of bonds created between reinforcement and silica or polyimide samples when lower density samples have been used. Nevertheless, there was a significant discrepancy in IFSS values of various interfaces with silica-silica interface providing highest IFSS values when high density materials were used. The polymer-silica interface was predicted to be stronger at low density value while, the polymer-polymer interface provided lowest value across almost whole density range. Resulting IFSS discrepancies have been attributed to the interface type and associated interactions strength and length.

Following the simulation of various thermal, mechanical and interfacial properties of silica and polyimide samples, the MD has proven to be much more suitable for the analysis of materials' thermal behaviour. When able to properly replicate the internal structure and composition of the material the molecular dynamics studies predicted the thermal conductivity values similar to the experimental ones. Similarly, the interfacial thermal resistance predictions were also in the range expected by the current state of knowledge. However, the method still yields certain limitations and quite often the molecular dynamics simulations fail to capture the dimensional features (for example fibre curvature) due to the large quantity of computational resources required to replicate such shapes. On the other hand, the molecular dynamic simulations are unable to correctly model the mechanical response of the materials and their interfaces. As a result, the predicted tensile and compressive properties were couple of magnitudes higher than the experimental results. This can be associated with the dimensional and time scale mismatch resulting in significantly quicker atom displacement during simulations than during the experimental measurement. Secondly issue is the size-effects. Since MD simulation can only reproduce a small representative group of atoms of the material a simulated volume might fail to capture the internal structure of the material or even its bulk behaviour. Finally, the molecular dynamics simulations capture idealistic image of the material without any pre-existing defects or dislocations. As such to use the molecular dynamics studies in the future, there is a need for more detailed coupling mechanisms to

connect the nanoscale mechanical behaviour with the macroscale properties. Overall, the MD simulations require further expansion of the database of atomistic potentials enabling simulation of wider range of materials and lowering the computational resources needed. However, following the study in this thesis it can be concluded that in the current form the molecular dynamics is still a developing tool and cannot be easily implemented in the material analysis.

6 Microscale analysis of polymer-based particulate composites

Microscale modelling of epoxy composites filled with low density silica and polyimide particles is conducted via the finite element analysis (FEA) in this chapter. The model can generate spherical particles randomly inside the resin cube in order to mimic the internal structure of the materials. The incorporation of thermal and mechanical properties, obtained from the molecular dynamics, of both low density silica and polyimide allowed for the investigation of the energy and load transfer mechanisms inside particulate composites. Model verification and validation revealed good accuracy when predicting thermal conductivity of the composites and a compressive modulus. As a result, further studies are conducted to investigate the effects of particle size and silica and polyimide density on thermal and mechanical properties of composites.

6.1 Literature review

In this section, the most common models predicting particle-filled composites properties are presented. The main focus is on thermal and mechanical properties, including thermal conductivity, elastic modulus and strength. Additionally, the overview of FEA models used for micromechanical simulation of particulate composites is included to provide a basis for further FEA of aerogel filled polymers.

6.1.1 Constitutive modelling

In order to predict the properties of particulate composite materials, a number of constitutive models have been established in the literature. In most cases, they combine the properties of constituent materials to derive an 'averaged' physical property of composite materials. In general, these models are relatively simple and do not require considerable computational power. However, they rarely incorporate interface properties between constituent materials or geometrical features of dispersed materials (e.g. fillers). This may significantly decrease the uncertainty of predicted values. In this chapter, the most popular constitutive models for thermal and mechanical properties of particulate composites are presented.

6.1.1.1 Thermal properties

The currently available models for calculating the thermal conductivity of two-component systems are typically best suited for high thermal conductivity filler particles and low volume fractions. Despite this, an attempt was made to compare experimental data with six theoretical and empirical models. Firstly, the parallel (Eq.49) and series (Eq.50) model was utilised in order to obtain upper and lower boundaries of thermal conductivity of two-component systems (λ_c) [93, 242].

$$\lambda_c = v * \lambda_f + (1 - v) * \lambda_m \quad \text{Eq. 60}$$

$$\lambda_c = \frac{1}{\frac{v}{\lambda_f} + \frac{(1-v)}{\lambda_m}} \quad \text{Eq. 61}$$

where v stands for the volume fraction of silica aerogel particles, and $\lambda_m and\ \lambda_f$ are thermal conductivities of matrix and aerogel fillers, respectively. Additionally, the geometric mean model was also used to calculate thermal conductivity using the equation below [505]:

$$\log(\lambda_c) = v * \log(\lambda_f) + (1 - v) * \log(\lambda_m) \quad \text{Eq. 62}$$

Furthermore, the Maxwell model derived from the Laplace equation for randomly distributed and homogeneous spheres was used [506]:

$$\lambda_c = \lambda_m * \frac{\lambda_f + 2\lambda_m + 2v(\lambda_f - \lambda_m)}{\lambda_f + 2\lambda_m - v(\lambda_f - \lambda_m)} \quad \text{Eq. 63}$$

Next, the empirical model by Agari and Uno was introduced, incorporating both parallel and series models with additional constants determined experimentally [241]:

$$\log(\lambda_c) = vC_2 \log(\lambda_f) + (1 - v) * \log(C_1 \lambda_m) \quad \text{Eq. 64}$$

where, C_1 is the coefficient of the effect on crystallinity and crystal size of a polymer and C_2 is a factor of ease in forming conductive chains of particles. Both values have been calculated by Agari and Uno based on gathered experimental data. In case of systems investigated in this study the values used were C_1 = 1.0638 and C_2 = 1.0017.

Finally, a Nielsen model was used as it incorporates the shape of particles as well as their orientation and packing type within composite [507]:

$$\lambda_c = \lambda_m \frac{1 + A\beta v}{1 - A\omega v} \text{ for } \beta = \frac{\frac{\lambda_f}{\lambda_m} - 1}{\frac{\lambda_f}{\lambda_m} + A} \text{ and } \omega = 1 + \frac{1 - \lambda_m}{{v_m}^2} v$$

In our case, the randomly orientated spherical particles resulted in A = 1.5 and v_m = 00637. In order to compare mentioned models, thermal conductivities for epoxy and silica aerogel composite (silica density of 75 kg/m^3) were calculated and presented in Figure 6-1.

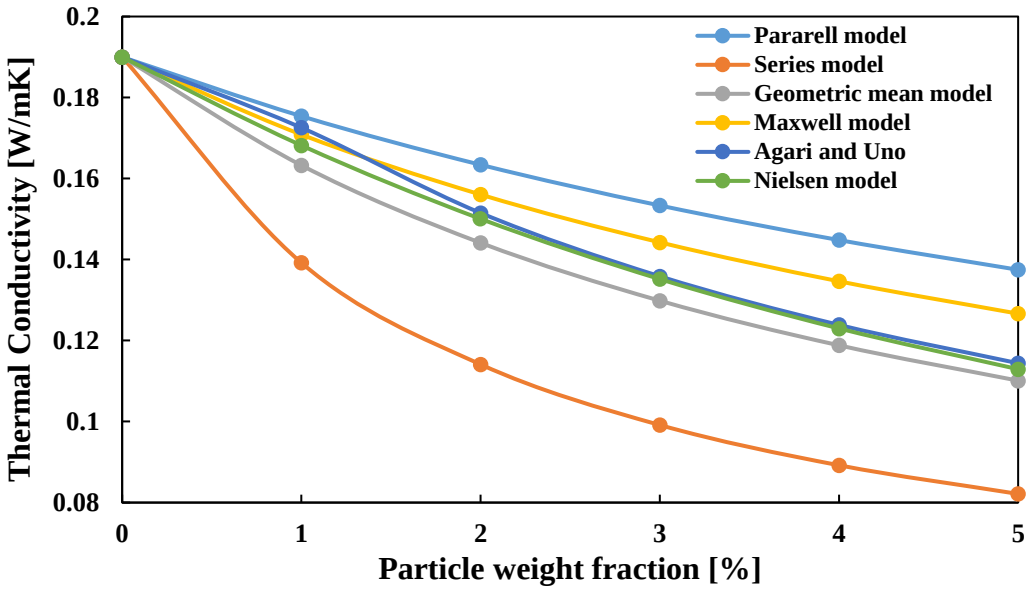

Figure 6-1 Thermal conductivity values obtained through various constitutive models in the literature. Values obtained for epoxy and silica aerogel (aerogel density of 75 kg/m^3) composite.

Figure 6-1 demonstrates that the series model provides the lowest results out of all investigated models, with the parallel model providing the highest values. Both models can be used to provide an upper and lower boundary value for the thermal conductivity of particulate composites. The remaining models seem to provide quite close values, especially in low particle weight fractions. Such behaviour can be explained by the fact that the Maxwell and parallel models do not include the interface between particle and the matrix in any form. Other models incorporate interface details to some extent as they incorporate coefficients based or calculated from the experimental data. Additionally, with the increase in the number of particles a higher interface area between epoxy and filler particles is achieved. This in return, enlarges the corresponding model error and reveals the superiority of models incorporating interface features.

6.1.1.2 Mechanical properties

The addition of particle fillers significantly affects the internal structure of matrix material and alters its load yielding capabilities as shown in Chapter 3. Three effects of filler addition on the parenting material has been seen:

- Beneficial – strengthening effect by creating an interpenetrating network [67].
- Neutral –no impact on matrix material [508].
- Detrimental – reducing the load-bearing area of the matrix material by acting closely as voids [509].

In order to predict the properties of the resulting composite material, various analytical approaches have been derived, with most of the models focusing on elastic modulus. The first model is often attributed to Einstein and relates the elastic modulus of composite material to elastic modulus of matrix material and volume fraction of particles inside [510]:

$$E_c = E_m(1 + 2.5\theta V_p) \quad \text{Eq. 65}$$

where E_c and E_m are elastic moduli of respectively composite and matrix material and V_p is a volume fraction of particles used. θ represents sensitivity factor and quite often is equal to 1. This model is designed only for low filler content and was proven unsatisfactory for filler content above 20 vol%. An alteration of this model has also been derived by including a volume fraction squared term, which accounts for the interactions between the grains of filler material [511].

$$E_c = E_m(1 + 2.5\theta V_p + 14.1{V_p}^2) \quad \text{Eq. 66}$$

Nevertheless, both models do not incorporate any filler properties and purely focus on its relative quantity in the material.

A completely different approach had to be used for particulate composites with high filler content, resulting in two main models, isostrain and isostress. In the isostrain model, it is assumed that both phases of the composites carry the same strain, however, with varying stress due to varying stiffness in dissimilar materials in particulate composites. The opposite view is presented by the isostress model, which implies the same stress but varying strain for the same reason. The simplest examples of the isostrain model include a rule of mixture [78, 512]:

$$E_c = \sum V_i E_i \quad \text{Eq. 67}$$

where V_i and E_i represent the volume fraction and Young's modulus of material phase i, respectively. On the other hand, the inverse rule of mixtures belongs to the isostress models [78, 512]:

$$\frac{1}{E_c} = \sum \frac{V_i}{E_i} \quad \text{Eq. 68}$$

Both models provide an extremely high and low value of elastic modulus of for particle filled composites, with the actual value falling in between them. In addition, multiple models have been created to account for the impact of porosity inside the composite on the elastic modulus. De to the fact that aerogel particles are extremely highly porous such models could still provide a good approximation of elastic modulus of for aerogel particle filled composites. Among all of them, the power law is the simplest one [67]:

$$E_c = E_m f^Y \quad \text{Eq. 69}$$

where E_m is an elastic modulus of the matrix material, f is a fractional density of composite material, and Y is an empirical exponent usually in the range between 3 and 4 obtained by fitting to experimental data. In this study a value of 3 has been selected for Y coefficient as it provided the most accurate fit with the previously obtained experimental data. Other models have been also developed and are based on fitting to experimental data obtained from various closed pore composites [513]:

$$E_c = E_m e^{-B(1-f)} \quad \text{Eq. 70}$$

In this case, B is a material property of how sensitive to porosity the material is and the value is obtained by fitting to experimental data.

Figure 6-2 was created to compare the above models, presenting the elastic modulus of the composite comprising of epoxy and silica (silica density of 75 kg/m^3). The modulus values for low density silica have been previously measured by Aloui et al. [351]. As expected, the rule of mixture and inverse rule of mixture provides respectively upper and lower boundaries for particulate composites elastic modulus values. The remaining models do fit in between them. However, it should be highlighted that to utilise those models; multiple factors have to be calculated or derived from experimental results to obtain accurate results.

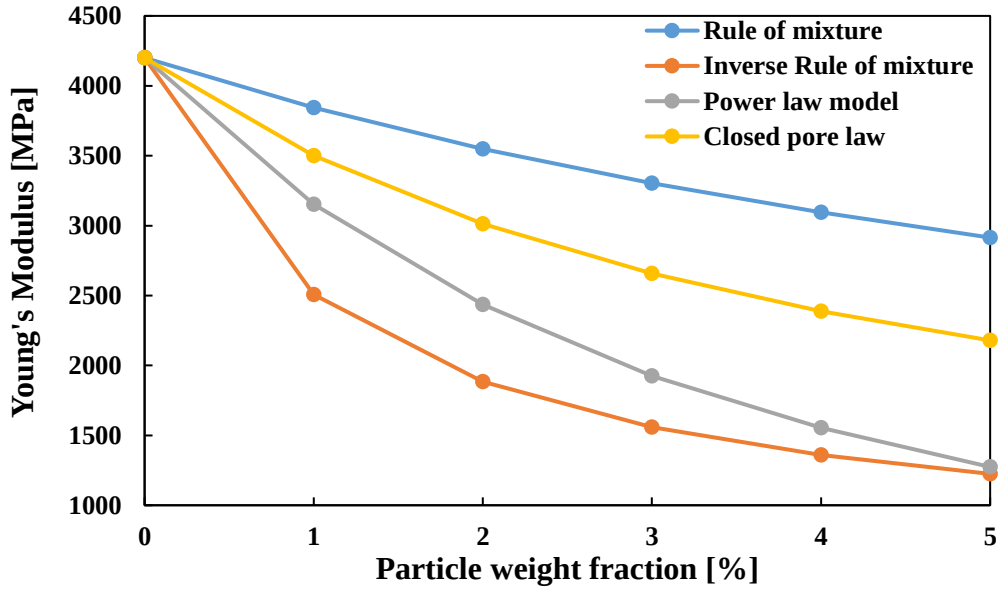

Figure 6-2 Comparison of elastic modulus obtained through various analytical models. Values calculated for epoxy and silica (silica density of 75 kg/m^3) composite. The pure epoxy modulus values have been obtained through compressive testing in the Chapter 3.

Strength is another mechanical property often calculated in the case of particulate composites. The first model used for strength prediction is called particulate composite strength models [510, 514]:

$$\sigma_c = \sigma_m(1 - 1.21V_p^{\frac{2}{3}})\chi \quad \text{Eq. 71}$$

where σ_c and σ_m are respectively strength of composite and matrix material, while V_p is the volume fraction of particles and χ is an interface cohesion term (varies between 0.2 and 1). As in many previously presented models, the particulate composite strength model does not incorporate the properties of second phase material but only its' quantity. Similarly, as in the elastic modulus, the power-law can predict the strength of composite material with pores inside [67].

$$\sigma_c = \sigma_m k f^p \quad \text{Eq. 72}$$

where k is a stress concentration factor depending on the particle shape and manufacturing conditions, and p is an exponent, which accounts for high-stress concentration effects at the pores. Usually, such exponent falls in values between 3 and 6, with higher values indicating cracks bridging between pores. Finally, the last model is used to relate the composites strength and fractional density of the composite [513].

$$\sigma_c = \sigma_m e^{-a(1-f)} \quad \text{Eq. 73}$$

where a is a sensitivity factor (value around 6) and f is representing fractional density of the composite. Again, to compare the models, Figure 6-3 was created, presenting the strength of the composite comprising epoxy and silica (density of 75 kg/m^3).

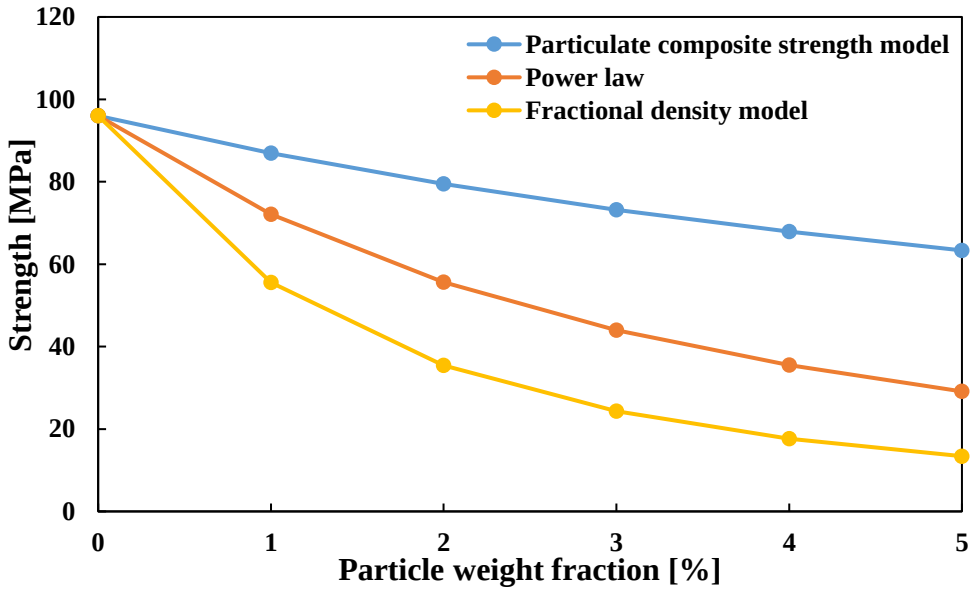

Figure 6-3 Comparison of strength obtained through various calculation models for epoxy and silica (density of 75 kg/m^3) composite.

By analysing Figure 6-3, it can be noticed that the particulate composite strength model provides the highest strength values and can be used to predict the upper bound of the composite strength. The power law and fractional density models predict lower strength values of the composites, however similar to the case of elastic modulus models, they also incorporate a significant number of variables that require to be derived from theoretical calculations or experimental measurements, thus significantly reducing the flexibility of their use [67].

Overall, when comparing the calculation models for thermal and mechanical properties, the models used to predict thermal properties are more flexible and require fewer input values. They incorporate the properties of a second-phase material and are only dependent on the particle loading and less on their shape or other geometrical properties. On the other hand, the models predicting mechanical properties often do not incorporate second-phase material properties and require a significant quantity of additional experimental or theoretical parameters to accurately predict the resulting mechanical properties of the composites.

6.1.2 FEA method

FEA has also been used to predict the properties of particle-filled composites on the microscale. It provides a particular advantage over previously described models as it allows to incorporate a geometrical feature of particulate composites such as particle size, shape or filler content. By incorporating the properties of constituent materials, the FEA user can derive a singular value of the investigated properties and look into the process of load or heat transfer through the composite structure. The following literature overview will present an overview of previous FEA work regarding various particulate filled composites and how they were used to predict thermal and mechanical properties of such materials.

6.1.2.1 Thermal properties

The FEA can evaluate the impact of particle additives on the thermal properties and have a control of particle geometrical or physical features for an iterative study. Among the current FEA investigations, thermal conductivity seems to be the most important parameter for material design and analysis.

Firstly, to investigate material thermal conductivity, the appropriate geometrical model of the material must be created. There have been multiple approaches to perform it, the simplest one including random distribution of the spherical inclusions inside the rectangular region. Such a method was used by Ramani et al., Moghaddam et al., Nayak et al., or Sanada et al. [515-518]. In order to increase the flexibility of the models, Chen et al., Park et al., and Yang et al. have altered the method slightly and focused on incorporating irregularly shaped particles into the

investigated matrix [519-521]. Finally, other authors have modelled the particles and incorporated the thin interface region around the particle inclusion. By altering the properties of the interfacial regions, the authors could achieve more accurate thermal conductivity results and capture better heat flux pattern. Examples of such work include studies carried out by Qian et al. and Porfiri et al. [214, 522]. Once the computational model is realised, the heat flux across the model must be induced to obtain the thermal conductivity values. The most popular method to achieve it is the modelling of isothermal boundary conditions for the top and bottom surface of the cubic model while insulating the remaining sides of the cube. Such boundary conditions allow to measure the heat flux across the sample only in one direction and comply with Fourier's law in 1D. Such an approach was used by all previously mentioned FEA investigations [515, 516, 519, 520, 523].

Ramani et al. used the FEA to investigate thermal properties of polymeric composites [515] and was able to measure the impact of multiple particle features (e.g. particle geometry)on the matrix thermal conductivity. Also included in that study is the microstructure of the composite, particle shape, filler aspect ratio, and interfacial thermal resistance between the matrix and the filler. The authors claim that their work provides a kind of design tool to select appropriate combinations of particles and matrix to fit the different needs [515]. Similar work has been performed by Moghaddam et al., who have also modelled the thermal conductivity of particle modified polymers [516]. By explicitly modelling the combination of the PEEK matrix and Ag particles, the authors provided a stochastic FEA framework. In addition, by comparing modelling and experimental results, a close correlation was achieved, assuring FAE suitability in particular composite modelling [516]. Nayak et al., who focused on specifically pine wood dust (PWD) and epoxy composites [26], have used a similar mixture of experimental and modelling techniques. They successfully lower the thermal conductivity of epoxy resin by almost 60% by the addition of 36 vol% of PWD. Additionally, the simulation results have been compared with both experimental results and other thermal conductivity prediction techniques. The results indicated the superiority of FEA, which provided a much closer match with experimental data [517]. Similar investigations have also been conducted for non-polymer-based composites, with Qian et al. looking into PPS/$CaCO_3$ and SiC_pAl composites, Porfiri et al. investigating synthetic foams, and Yang et al. analysing diamond/aluminium composites [520, 522-525].

6.1.2.2 Mechanical properties

The FEA has also been used to investigate the mechanical properties of the particulate composites and focused on such material properties as elastic modulus, strength or hardness.

The material modelling approach is almost identical, as is the case of previously described thermal investigations. However, to replicate the real-life experimental methods quite often, the sample shape according to the ISO or ASTM standards is modelled. In addition, across the FEA material mechanical investigations, a greater agreement regarding testing procedures has been achieved than in case of thermal measurements. As a result, for both the tensile and compression testing, one of the sample surfaces is being constrained (fixed) while the opposite face is subjected to displacement or external force in the direction according to the testing procedure. The resulting material response allows for a calculation of material mechanical properties and provides insight into the load bearing behaviour of the material.

Ghassemieh et al. developed a model to predict the mechanical properties of polymer-based composites [526]. The authors investigated various constraints and displacements modes in order to select the most suitable approach. The resulting micro-mechanical model presented a close agreement with experimental results and can be used to investigate stress distribution inside the particle-filled composite. Nevertheless, the authors highlighted that the presence of flaws or impurities within the composite structure or the interface region was ignored [526]. Another study was carried by Tsui et al., who investigated the effects of interphase-coated glass beads onto Young's modulus, maximum stress concentration factor and stress distribution of polycarbonate composites [527]. The results were in good agreement with experimental results. In addition, this study revealed the importance of modelling the interfacial region. By altering the filler content and the stiffness, thickness, and Poisson's ratio of the interphase, the authors were able to reduce the material stress concentration [527]. Similar work has been conducted by Sun et al., who modelled the BISGMA/TEGDMA composites reinforced with E-glass particles [528]. In addition to the FEA, authors also incorporated other mathematical models such as Hashin or Mori-Tanaka models for comparison purposes. The study revealed that the addition of E-glass particles improves the mechanical properties of investigated composites. However, the FEA model provided superior results, especially for the high loading scenarios [528]. The same particle filler has also been investigated by Guild et al., who simulated the E-glass particles and epoxy composites [529]. However, this work focused on the fracture behaviour of particulate composites, and the comparison between predictions and experimental measurements has been used to validate the model. Furthermore, the study investigated the stress distributions inside the microstructure of the material, allowing for a better understanding of their fracture behaviour [529]. Several other works have been devoted to the FEA analysis of polymer matric particulate composites [207, 210, 217, 218, 221, 508, 516, 528, 530-535].

In addition, a significant number of FEA has also been conducted to understand the impact of particles onto metal or ceramics-based composites. Sozhamannan et al. developed a model to predict the mechanical properties of metal matrix composites [536]. Other studies include the hardness investigation of the Ag-Ni composites conducted by Kim, the measurement of mechanical properties of glass-filled aluminium by Agarwal et al., and SiC and aluminium mixtures by Chen et al. [521, 537, 538]. Finally, Prabu et al. has used an FEA to describe the impact of particle clusters on mechanical properties of metal matrix composites [539, 540].

6.1.3 Conclusion of literature review

Multiple models predict both mechanical and thermal properties of particulate filled composites based on the constituents' properties. The property models require low number of input values and computational resources. Especially for the thermal properties, such models incorporate the properties of both phase materials. However, they are only dependent on the particle loading and not on their shape or other geometrical properties. Additionally, property models focusing on material mechanical response often omit the properties of second phase material and require a significant quantity of additional experimental or theoretical parameters to predict the resulting composites' mechanical properties.

Finite element analysis models have also been used in the prediction of the properties of particulate filled composites. Opposite to parameter models, they incorporate both geometrical and physical features of the additives and, on many occasions, have been proven to provide a close match with experimental results. FEA models also allow for incorporation of the interface properties resulting in even higher prediction accuracy. Overall, such models can be used to understand the load-bearing behaviour of the material and perform an iterative study to find the most desirable material mixture.

6.2 Modelling

In this section, the simulation techniques used to model the behaviour of particle-filled polymers will be described. It commences with thermal and mechanical properties of constituent materials, followed by an explanation of the geometry generating model. Furthermore, this section will present the meshing technique and the setups used for thermal and compressive investigation of particle filled polymers.

6.2.1 Materials and geometry

This study is specifically focusing on investigating the impact of low density silica and polyimide particles on epoxy resin. In the case of epoxy resin, the properties of IN2 Epoxy

Infusion Resin manufactured by Easy Composites were obtained from the manufacturer website and ANSYS repositories and are presented in Table 6-1.

Table 6-1 Property of epoxy resin used in the current model.

Property	Value
Density [kg/m^3]	1160
Young's Modulus [GPa]	3.15
Poisson's ratio	0.35
Bulk Modulus [GPa]	3.5
Shear modulus [GPa]	1.66
Tensile yield strength [MPa]	54.6
Compressive yield strength [MPa]	95.14
Thermal conductivity [W/mK]	0.19

Both polyimide and silica properties as a function of their density have been investigated via Molecular Dynamics in the previous chapter. As a result, a new material entry has been created in the ANSYS material library for each investigated material density. Those entries related the density of the silica or polyimide with thermal conductivity and compressive properties of the bulk material. Afterwards, during material modelling those library inputs have been used to describe the mAaterial composition of modelled filler particles. Only the polyimide compressive modulus values have been scaled down due to the molecular dynamics study providing unphysical modulus values. As a result, the relationship between modulus and density was maintained, but the values were adjusted to fit the solid polyimide modulus values presented in the work by Rubehn [541]. On the other hand, the interfacial properties have been directly implemented into the model by defining the contact region between the particles and the matrix. In case of thermal conductivity simulations, the bonded contact with pure penalty formulation and manually specified interface thermal conductance values from MD simulations have been used. Similarly, for compressive modelling the bonded contact region has been used.

The method of material samples generation has been previously established by Webley [542]. It was achieved using iterative MATLAB codes that initially generated the simulation volume filled with particles with a defined radius located in the random initial position. Afterwards, the distance between the particle edge and each side of the bounding region was measured to ensure that the particle was not in contact with model surfaces. If no contact has been detected, the model then inspected the distance between the newly generated particle and all previously generated particles to ensure no particle overlapping. When both conditions were approved,

the particle was saved, and the loop added another particle until reaching (or exceeding) the requested volume ratio when the ANSYS script was generated. In order to visually represent created geometry, the MATLAB code generated the scatter plot with all generated particles, as presented in Figure 6-4.

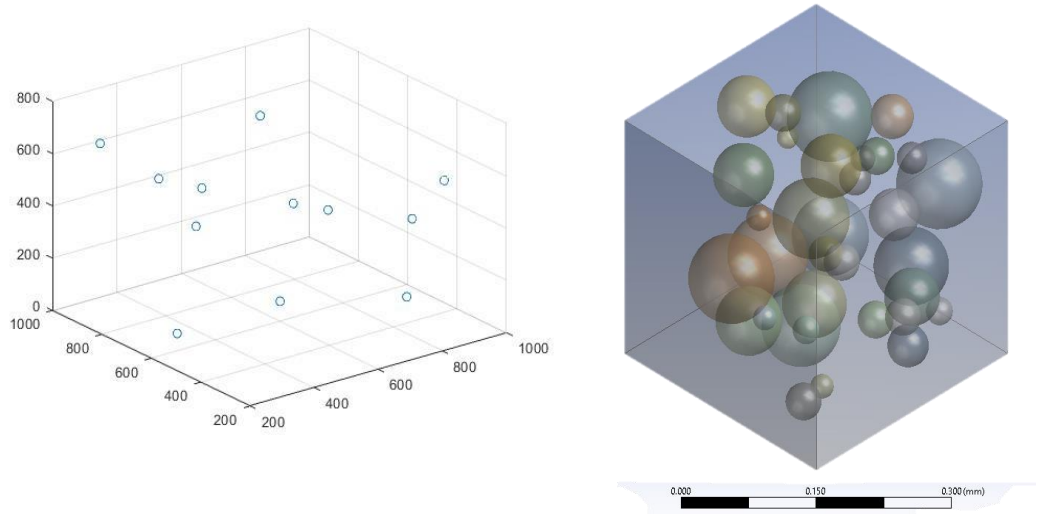

Figure 6-4 Left: Location of 100 µm particles in a 1 wt% composite. The x, y and z axes of the 3D scatter plot represents the external boundaries of generated composite model.
Right: Particle filled composite sample of epoxy filled with 2 wt% of 100 µm particles simulated with ANSYS Design Modeller.

Afterwards, the MATLAB generated script was imported into ANSYS Design Modeller, which created a 3D representation of the particulate composite. It was achieved by drawing a circle in the centre of the particle and revolving them to generate a complete sphere. This, combined with a "slice material" operation, generated a cube of matrix material with spherical inclusions, which can be treated as hollow or solid particles depending on the assigned properties. The example of generated sample is presented in Figure 6-4. The size of particles is not uniform, as the normal distribution of particle diameter was used centring around a pre-determined value. Such an approach has been introduced to facilitate model generation and produce more realistic models. Without introducing such an approach, higher volume fractions using larger particles would be unattainable. Even though this solution carries significant advantages, it also presents certain issues. Since the smaller diameter particles are easier to be incorporated into high particle content composites (by the MATLAB code), the normal distribution can also lead to bias in the particle distribution towards smaller diameters. As a result, the careful investigation of generated model is required to ensure that the acceptable balance between volume fraction and particle size range is obtained.

6.2.2 Meshing

The model meshing was accomplished using the Ansys inbuild meshing system. By utilising the tetrahedron method, it was possible to perfectly capture the spherical shape of particles, as presented in Figure 6-5. The remaining meshing settings include adaptive size function, medium relevance centre, slow transition, medium span angle centre and default defeature size. Additionally, a body sizing method with a 25% smaller element size was applied to the particles to ensure their shape was appropriately captured. It was found that inappropriate particle meshing can significantly affect the size of the contact regions between particles and epoxy resin. The number of elements increased with increasing the number of the particles and varied between 50,000 and 600,000 elements.

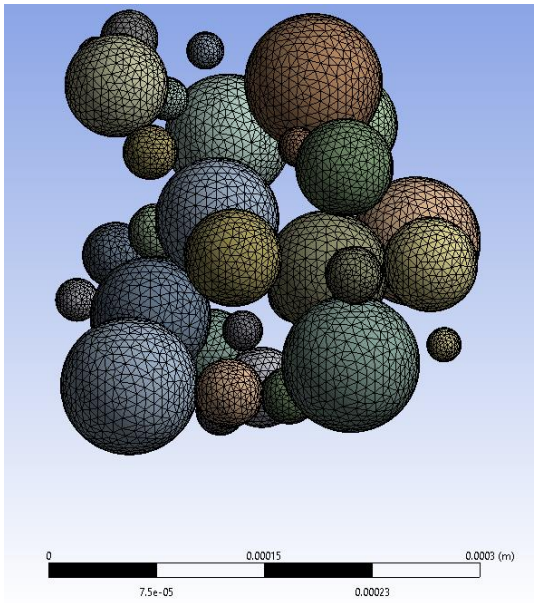

Figure 6-5 3D meshed particles with the surrounding epoxy resin hidden.

6.2.3 Testing setup

Following the sample generation and meshing, the samples were subjected to thermal and mechanical testing to calculate thermal conductivity and compressive properties.

6.2.3.1 Thermal Testing

Thermal analysis has been conducted using Transient Thermal analysis. In order to induce the heat flow through the samples, two opposing surfaces have been selected (left and right), and the heat flow of 1e-3 W was entering the sample through one of them and leaving through the other one as presented by blue arrows in Figure 6-6. The remaining surfaces of the rectangular sample have been modelled to be adiabatic surface with no heat transfer through them (grey surfaces). Furthermore, all the contact regions were assigned the interface thermal conductivity according to the results from the molecular dynamics study. Following the heat

flow application, the temperature of left and right surfaces has been measured by averaging the values across the surface nodes and further used to calculate the thermal conductivity. In addition to the thermal conductivity values, the heat flux through the model was captured as presented to investigate the heat transfer ability of the material further.

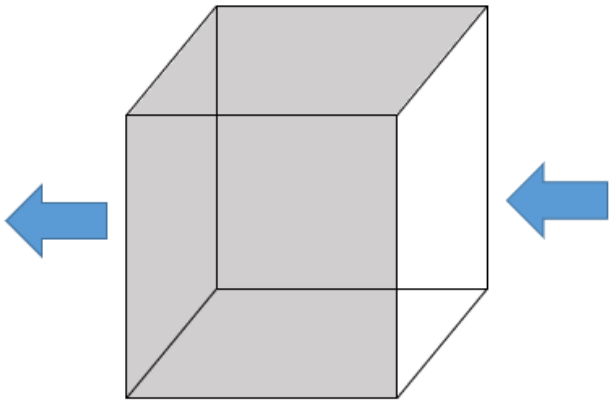

Figure 6-6 Schematical representation of thermal analysis performed in this study.

6.2.3.2 Mechanical Testing

Compression testing simulations have been conducted using Static Structural analysis. As presented in Figure 6-7, the material's top surface (blue) has been subjected to the displacement boundary conditions while the bottom surface (grey) is fixed, preventing it from any movement. The displacement of 1e-6 m was selected, allowing to measure material's compressive properties within the elastic region. In addition, the contact region between particles and epoxy matrix was set to bonded. A reactive force was recorded following the displacement, allowing to calculate the composite's strength and elastic modulus. In addition, the stress and strain distributions have also been captured, allowing for a better understanding of particle impact upon epoxy resin.

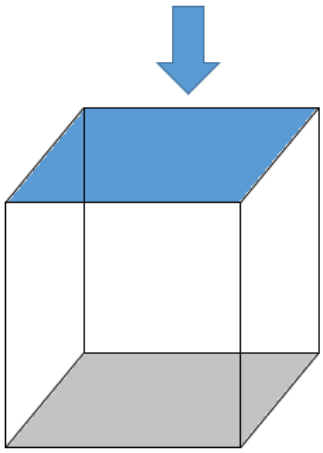

Figure 6-7 Schematical representation of mechanical analysis performed in this study.

6.3 Results

This section focuses on the impact of particles size and density on the thermal and compressive properties of epoxy resin. Before the model is incorporated into such a study, validation and verification will be conducted to confirm model accuracy.

6.3.1 Model validation and verification

Model validation and verification are essential steps to confirm whether the created model accurately represents the investigated situation. As a result, this section will commence with mesh analysis later, followed by comparing simulated results with property models and experimental results from previous chapters. The following validation will be conducted for the composites comprising of 100 µm silica particles and epoxy resin due to model efficiency.

6.3.1.1 Mesh analysis

The mesh analysis is crucial in finding out to extent the measured property depends on the mesh quality. As a result, it is possible to determine the lowest number of elements required to obtain stable results by conducting such an analysis. As a result, by running the same simulation with varying meshing parameters, the simulation accuracy can be significantly increased, and the required computation time can be reduced. Figure 6-8 was plotted in order to discover the dependency of thermal conductivity on mesh quality. The varying element number was achieved by adjusting the relevance factor.

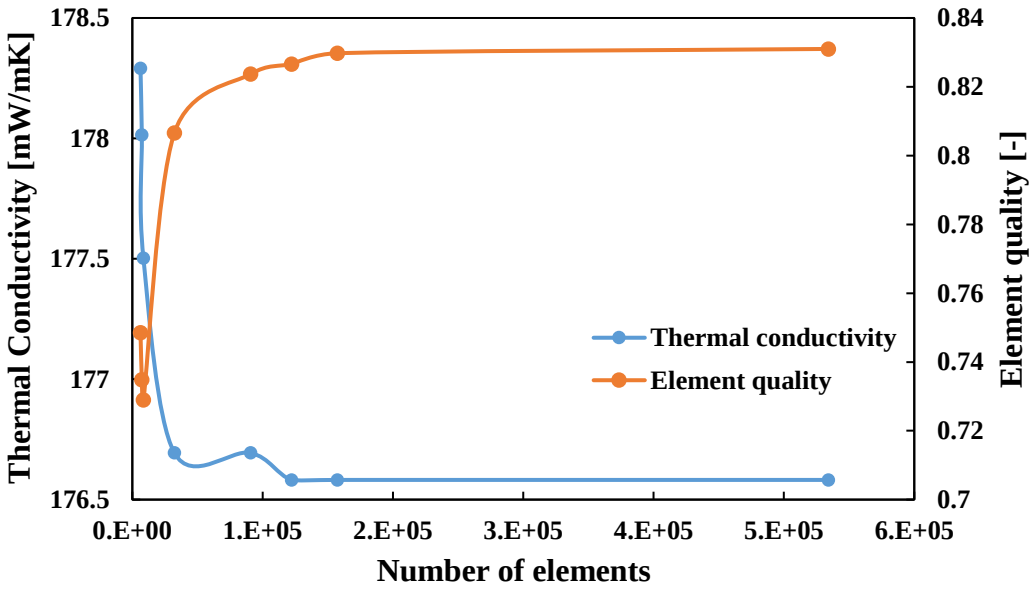

Figure 6-8 Thermal conductivity and element quality of 1 wt% 100 µm silica and epoxy composite as a function of element number.

By analysing Figure 6-8, it can be discovered that thermal conductivity significantly decreases with increasing elements number until around 150,000 elements are achieved, and the results

stabilise. This behaviour is strictly correlated with the fact that the mesh model could not correctly represent the spherical shape of particles at low element numbers. As a result of the particle deformation, a varying contact area between particle and epoxy was modelled, resulting in a significantly altered heat flux. Nevertheless, after reaching 150,000 elements, the results stabilise, and a further increase in mesh accuracy yields no results upon composite thermal properties. The elements' quality factor also supports such conclusions and as shown in Figure 6-8, it drastically increases with increasing element number. However similarly to thermal conductivity, it stabilises at around 150,000 elements with no significant improvement afterwards.

A similar analysis has also been conducted for compressive testing. In this case, an elastic modulus has been selected as material property which dependency on mesh quality was analysed and presented in Figure 6-9.

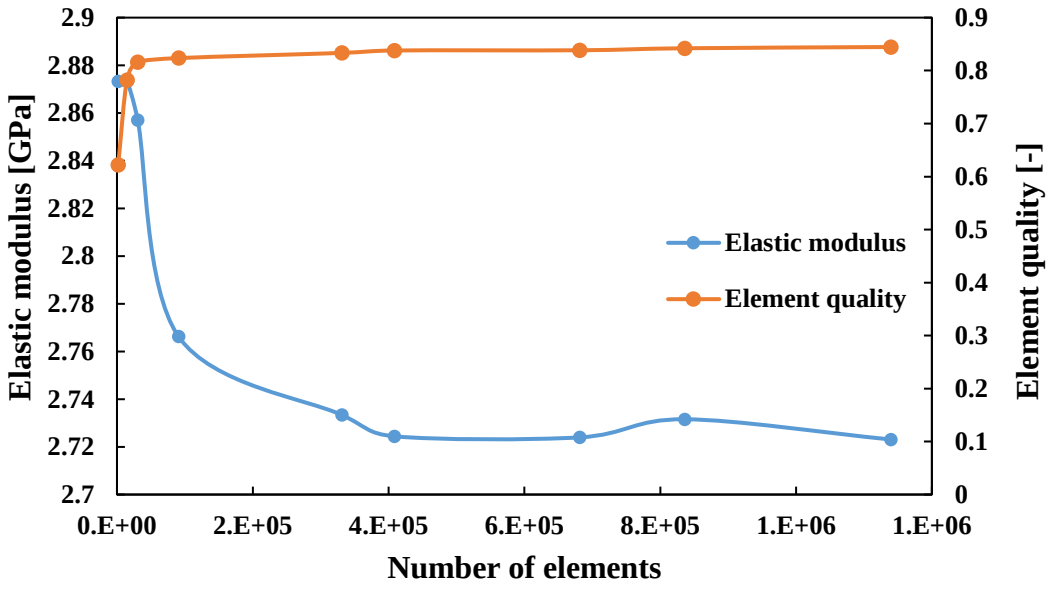

Figure 6-9 Elastic modulus and element quality of 1 wt% 100 µm silica and epoxy composite as a function of element number.

Figure 6-9 presents a similar behaviour as in the case of thermal analysis. It indicates that the elastic modulus value decreases sharply with increasing elements' number until reaching 400,000 elements when it stabilises. It is believed that again the mesh with low elements' number failed at capturing the microstructure of the composite. In addition, it should be highlighted that the elements' number required for the compressive property to stabilise is more than doubled of what is required from the thermal analysis. It might indicate that overall mechanical properties are much more dependent on mesh quality, and a smaller element size will be required to capture the material's load-bearing behaviour. The element quality factor

increases with increasing elements' number. Nevertheless, it stabilises when the mesh was constructed with at least 30,000 elements.

Finally, the mesh analysis has allowed us to determine the minimum element number required for mechanical and thermal testing of particulate composites using the model presented in this work. As a result, all the following simulations will comply with the findings of mesh analysis, allowing to avoid results fluctuations without utilising excessive computational resources.

6.3.1.2 Thermal analysis

Following the mesh analysis, the thermal model has been subjected to further validation to ensure that the physical behaviour of the model complies with a real-life scenario. Initially, it was necessary to validate whether the simulation is capable of achieving a steady state. In order to do so, the temperature of the top and bottom surfaces over simulation time was recorded and presented in Figure 6-10.

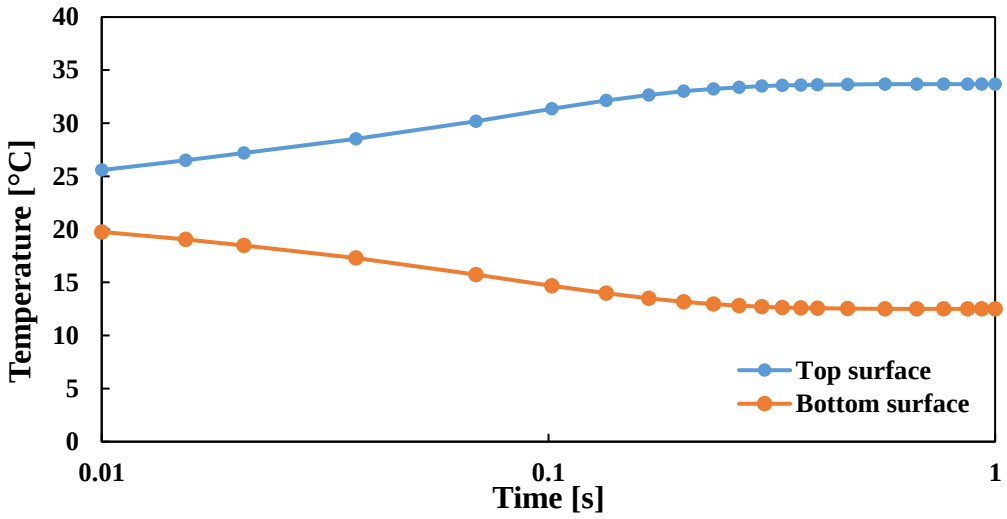

Figure 6-10 The temperature of the top and bottom surfaces of the analysed sample over emulation time.

As presented in Figure 6-10, both surfaces' temperature changes over time, with top and bottom surfaces' temperature respectively increasing and decreasing over time. Such a trend is caused by the presence of the material's internal energy, which, when the simulation commences, causes temperature fluctuations. Nevertheless, upon reaching the 0.5 s mark, the temperatures of both surfaces converge at a constant value, and the steady temperature gradient across the sample is achieved. Such steady-state is necessary in order to take the accurate temperature measurements required to calculate the thermal conductivity. A further step of the thermal model verification required to test the thermal conductivity dependency upon the heat flow imposed across the sample. As a result, a series of simulations were performed with

varying heat flow between 1e-6 and 1 W and resulting thermal conductivities are presented in Figure 6-11.

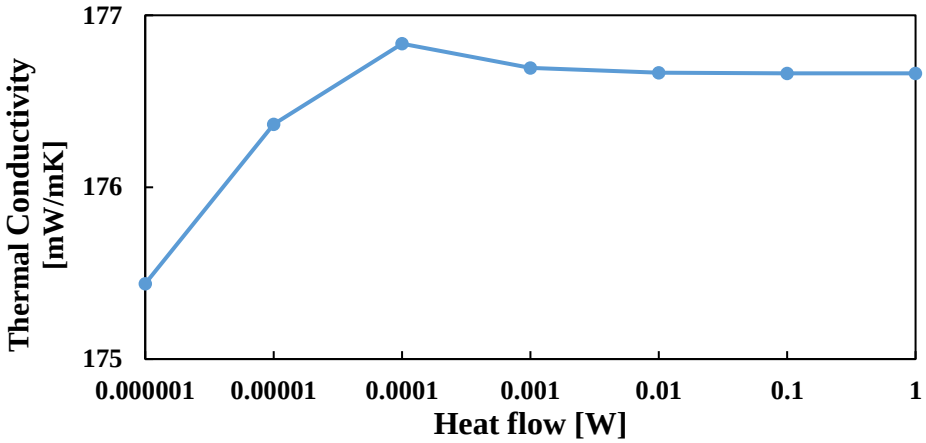

Figure 6-11 Thermal conductivity of 1 wt% 100 µm silica and epoxy samples with varying heat flow.

Figure 6-11 indicates that the thermal conductivity of silica and epoxy composites is slightly dependent upon the utilised heat flow, as an increase in conductivity value is observed with increasing heat flow. Such occurrence can be attributed to the insufficient simulation time for the low heat flow values, which prevent the simulation from achieving a stable temperature gradient and leading to lower thermal conductivity values. Nevertheless, the change in investigated value does not even reach 1%, and once heat flows larger than 0.001 W were used, the thermal conductivity completely stabilises. A further step of the verification included the thermal properties directionality investigation. As a result, the heat flow has been applied to the 100 µm particle samples across x, y and z axes to validate the homogeneity of the results. Obtained thermal conductivity values have been presented in Figure 6-12.

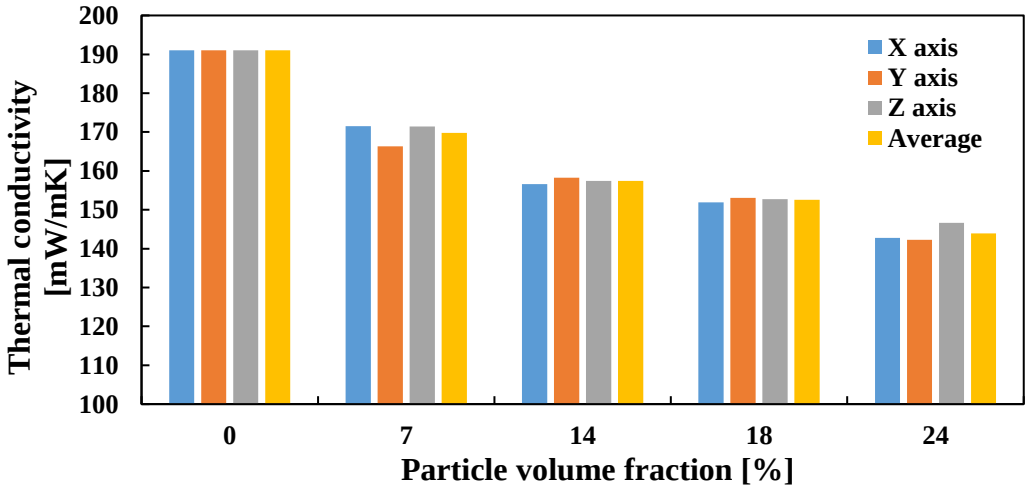

Figure 6-12 Thermal conductivity of 100 µm silica and epoxy composites with varying particle loading across x, y and z axes.

Thermal conductivity values included in Figure 6-12 presents a steady decrease with increasing particle volume fraction. Nevertheless, they are consistent regardless of the heat flow direction. Across the whole investigated particle volume fraction, the difference between directional and averaged thermal conductivities does not exceed 3.5 mW/mK. Additionally, there is a slight dependency of the particle content on the measured difference, as the 7 vol% samples present on average a 2.3 mW/mK difference from the averaged value. In comparison, 24 vol% samples present much more stable results, with the difference significantly decreasing to 0.43 mW/mK. Such results indicate the homogeneity of simulated particulate composites and are particularly important as they confirm the correct generation of material samples. In addition, it significantly reduces the simulation time, as due to the uniformity of thermal conductivity properties, there is no need to conduct thermal analysis in all three directions.

Following model verification, the obtained results are compared to experimental values presented in previous chapters of this thesis. For comparison consistency, the thermal conductivity values of the 100 µm silica particles and epoxy resin composites are presented in Figure 6-13. For the simulation results, thermal conductivity values obtained with and without the results from molecular dynamics are included to evaluate the impact of the thermal interfacial resistance between silica and epoxy resin. The FEA results reach only 2.5 wt% of particle loading mainly due to the high simulation time and significant computational resources required to generate sample with higher particle loading.

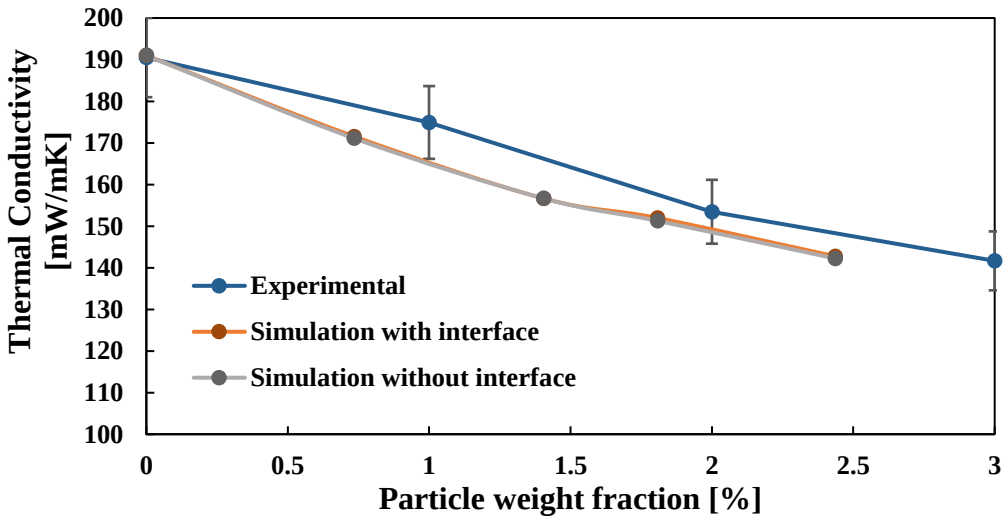

Figure 6-13 Comparison of experimental and simulated thermal conductivity values for 100 um low density silica and epoxy composites.

Figure 6-13 presents a good match between experimental and simulated results, with the current model slightly underestimating the thermal conductivity values of the composites.

Nevertheless, the difference between experimental and simulated values decreases with increasing particle content. Such a discrepancy between experimental and simulated results can be attributed to the idealistic representation of low density particles in the simulated model. It uses spherical particles unaffected by the manufacturing process and incorporating their full thermal resistance capabilities. On the other hand, during the composite manufacturing process certain quantity of pores can be infiltrated by the liquid resin. Such occurrence effectively limits particles' ability to reduce energy transfer and results in higher thermal conductivity values. Furthermore, particles used in the experimental investigation are irregular in their shape, leading to varying heat transfer patterns through the composite. Regardless of all those issues, the model accurately predicts the thermal conductivity of epoxy composites with an error not exceeding 5%. What is more, Figure 6-13 also presents that incorporation of detailed information regarding particle and epoxy interface yield little effects on the thermal conductivity values of the particulate composites within investigated range. Across the whole particle content range, the incorporation of interface thermal conductance values obtained from molecular dynamics increases the thermal conductivity by 0.3%. Nevertheless, it is essential to highlight that the thermal conductivity difference increases slightly with the incorporation of larger particle quantities. It is believed that such behaviour is related to an increase in the interface area and might yield even more significant differences when reaching much higher loading scenarios. Even though the thermal conductivity value is relatively similar, different heat transfer behaviour between the two models can be noticed. An example heat flux distribution for a 2% 100 µm silica and epoxy composites is presented in Figure 6-14. Please note this section plane is a part of a larger model and was produced for illustration purposes only.

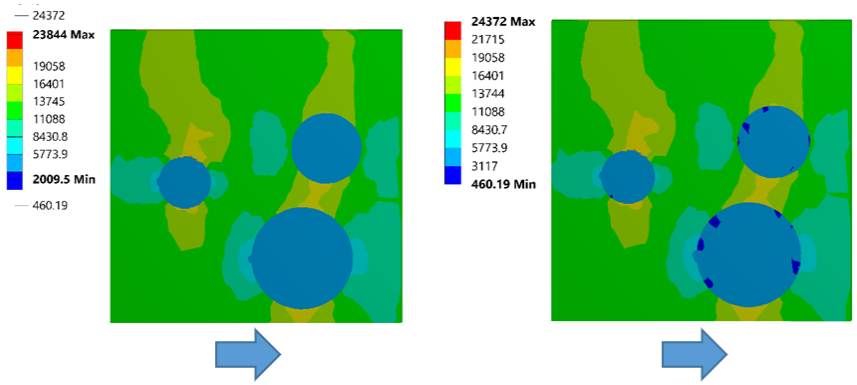

Figure 6-14 An example of heat flux distribution for a 2% 100 µm low density silica and epoxy composites. Section plane of the model on the left was obtained without interface details, while the section plane on the right incorporated thermal interface details. The arrows under images indicates the direction of heat flux.

Figure 6-14 indicates that in both cases, the heat transfer is primarily happening through the epoxy matrix since the low density silica particles have much lower thermal conductivity values. The energy is travelling around silica particles which also imply that the particle location plays an important role. By placing the particles close to each other, a barrier for the energy flow is created with only a few bottleneck areas reducing the heat transfer even further. However, a variation in heat flux can be spotted by a different approach to the thermal interface. Firstly, the model incorporating the interface details presents a wider heat flux range for the same modelled situation. Secondly, by incorporating the interface details, the heat flux through the low density silica particles become less uniform and incorporate extremely low heat flux regions. Those behaviours can be explained by the lower values of interfacial thermal conductance introduced from molecular dynamics. As presented by Ramani et al., the thermal conductivity of composites with high values of interfacial thermal resistance are more susceptible to changes due to the microstructure [515]. Thus, when altering the interfacial thermal conductance values, the model becomes more susceptible to the particle location and due to energy accumulation results in higher maximum heat flux values across the model. Also, by increasing interfacial thermal conductance, more heat conductance occurs through the interfacial region. This, in return, further limits the energy transport through the particles and creates low heat flux regions within particles. In order to provide a complete picture, the obtained results are also compared to previously described property models. As a result, thermal conductivity values obtained with and without detailed interface analysis along various models are presented in Figure 6-15.

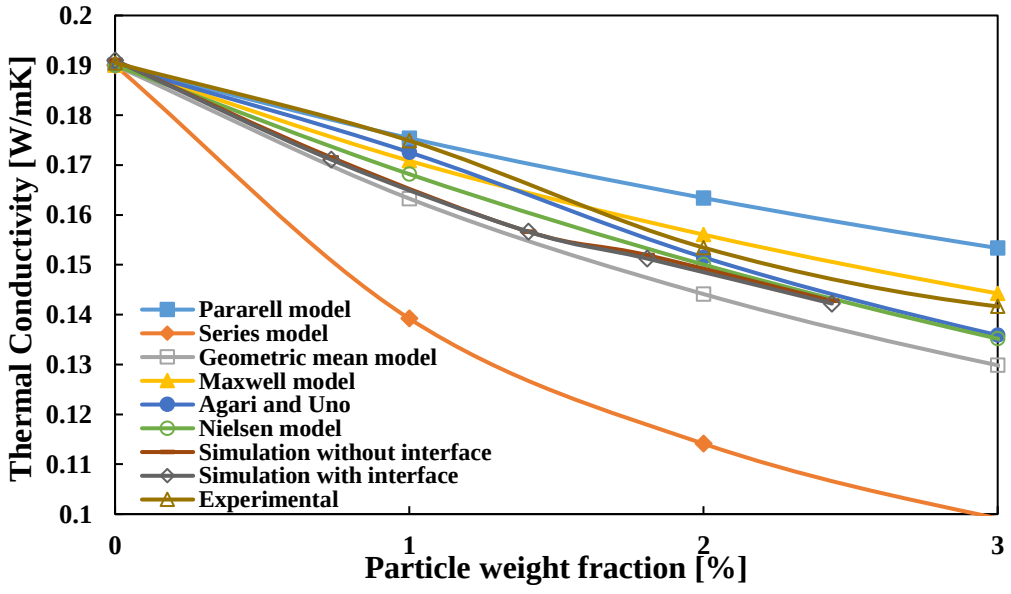

Figure 6-15 Thermal conductivity values obtained in this study and predicted by property models.

Analysis of Figure 6-15 demonstrates that the series model is the least accurate method utilised, providing values far out with the simulation data obtained in this work. On the contrary, all remaining models seem to provide values much closer to measured thermal conductivities. Maxwell and parallel models providing the best match in lower loading scenarios, while Nielsen, geometric mean and Agari and Uno models best represent higher loadings. Such behaviour can be explained by the fact that the Maxwell and parallel models do not include the interface in any form, while the other models incorporate such details due to their experimental nature. The increase in the number of particles leads to a higher interface area between epoxy and particles. This in return, enlarges the corresponding error and reveals the superiority of models incorporating interface features. Finally, when comparing the property models' results with current work, it was concluded that the geometric mean model best matches experimental data at lower loading scenarios. However, Nielsen, geometric mean and Agari and Uno models are more accurate at higher particle loading, which may be attributed to the inclusion of particle-polymer interface features present in these models.

By analysing previous verification and validation, it can be noticed that the model used in this study accurately describes the heat transfer through simulated epoxy and low density silica/polyimide samples. As such the decision was undertaken to use it in further parts of the analysis and incorporate the interfacial properties obtained through molecular dynamics simulations.

6.3.1.3 Mechanical analysis

A similar investigation was conducted in order to validate the compressive model. Firstly, the stress and strain distributions for a 2 wt% 100 µm low density silica and epoxy composites has been recorded and presented in Figure 6-16.

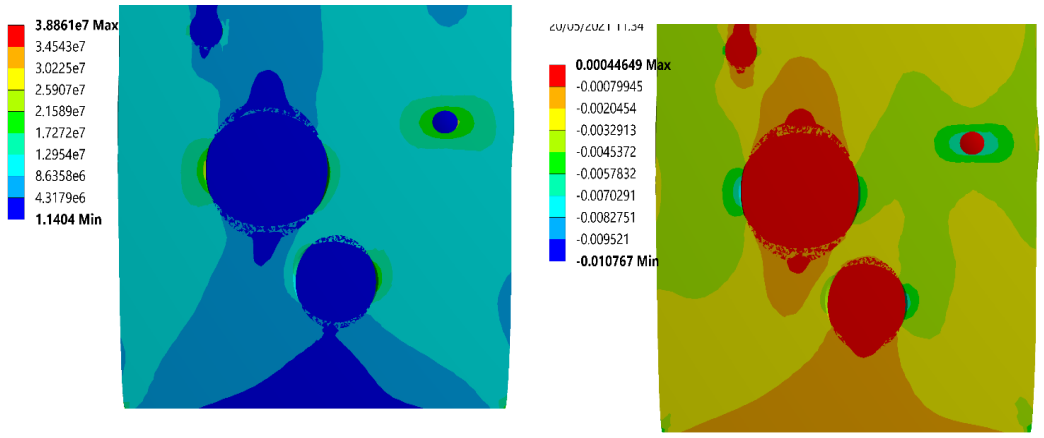

Figure 6-16 An example of von Mises stress (left) and strain (right) distribution for a 2 wt% 100 µm low density silica and epoxy composites.

As expected, the stress distribution presented in Figure 6-16 indicates that most of the load is transferred through the epoxy resin, with particles presenting negligible load-bearing capabilities. It is mainly caused by the high porosity of low density silica and its extremely low compressive properties. The spherical inclusions also act as stress concentration points with high-stress locations present on the sphere ends perpendicular to the load direction. Such stress distribution is expected from the weakening additives and was previously observed by Chen et al. [265]. Additionally, the strain distribution also yields features characteristic of particulate composites. With the strain being very inhomogeneous and the matrix strain higher at the load-carrying direction ends of particles and is significantly lower at the regions perpendicular to that direction. Again, a similar pattern was observed by Paknia et al. [543]. Following initial step required to test the elastic modulus dependency upon the surface displacement imposed. As a result, a series of simulations were performed with varying surface displacement between 0.1 and 100 µm and the resulting elastic modules are presented in Figure 6-17.

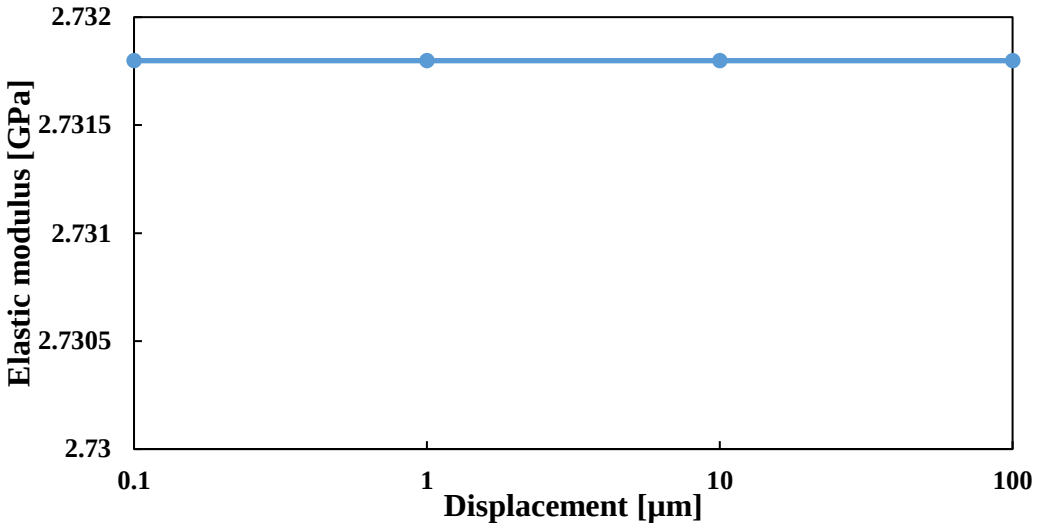

Figure 6-17 Elastic modulus of 1 wt% 100 µm low density silica and epoxy samples with varying surface displacement.

As indicated by Figure 6-17, the displacement value has no impact on the elastic modulus of the particulate composite. Such behaviour results from a static structural analysis resulting in a linear relation between displacement and reactive force. The further step of the verification included the directionality investigation. As a result, the surface displacement has been applied to the 100 µm particle samples across x, y and z axes to validate the homogeneity of the results. Obtained elastic modulus values have been presented in Figure 6-18.

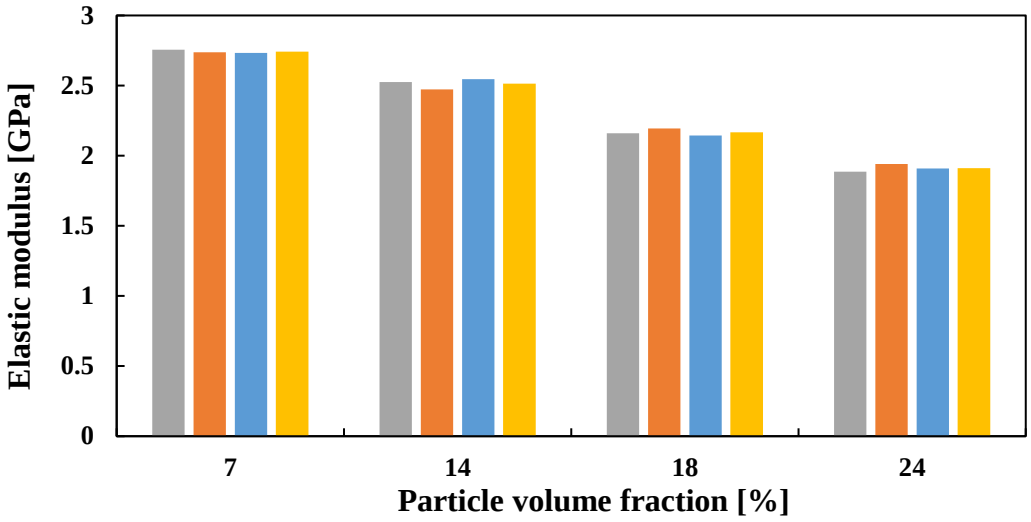

Figure 6-18 Elastic modulus of 100 µm low density silica and epoxy composites with varying particle loading across x, y and z axes.

Elastic modulus values presented in Figure 6-18 decrease steadily with increasing particle volume fraction. Nevertheless, they are consistent regardless of the displacement direction. Across the whole loading scenarios, the difference between directional and averaged elastic modulus barely exceeds 30 MPa. Additionally, there is no direct dependency of the particle loading on the measured difference, as the most considerable variation is presented by a 14 vol% sample with an average variation of 28 MPa. At the same time, the most stable results are achieved for 7 vol% loading samples with only 9 MPa average variation. Similarly, as in the thermal conductivity case, such results indicate the homogeneity of simulated particulate composites and are particularly important as they confirm the correct generation of material samples.

Following model verification, the obtained elastic modulus values are compared to experimental values presented in previous chapters of this thesis. For comparison consistency, an elastic modulus values of the 100 µm low density silica particles and epoxy resin composites are presented in Figure 6-19.

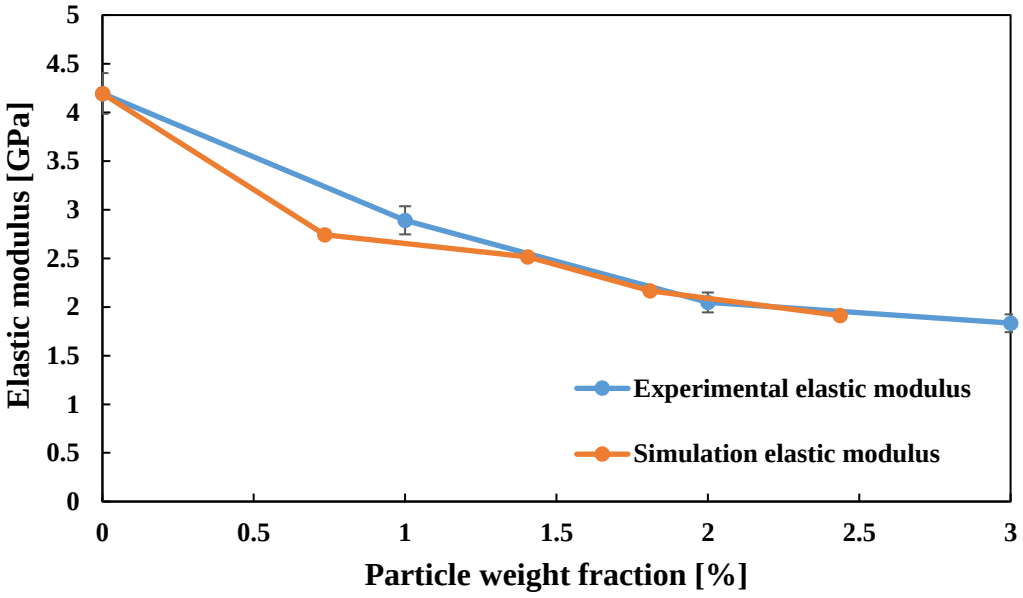

Figure 6-19 Comparison of experimental and simulated elastic modulus values for 100 μm low density silica and epoxy composites.

As indicated by Figure 6-19, simulated and experimental values of elastic modulus present an excellent agreement. Following the initial discrepancy at low partile loading, the model tightly follows the experimental result. As a result, it is accepted that the model presented in this study excels in predicting the elastic modulus values. Nevertheless, to validate results even further, the elastic modulus values are also compared to previously described property models and presented in Figure 6-20.

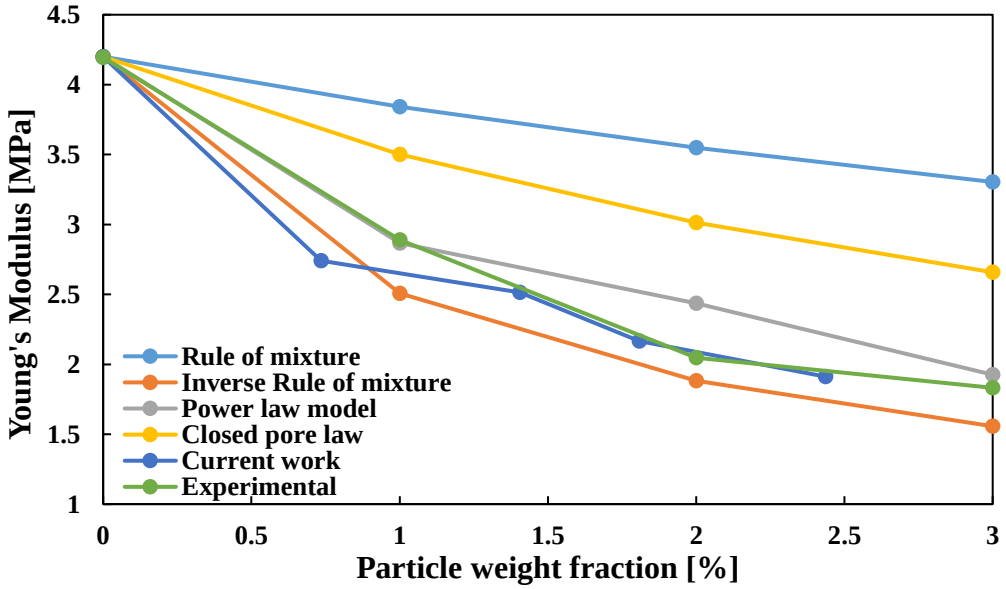

Figure 6-20 Elastic modulus values obtained in this study and predicted by property models.

As indicated by Figure 6-20, the property models do not predict the elastic modulus values accurately. Firstly, the rule of the mixture and closed pore law are significantly overestimating the compressive properties of particulate composites, with the difference reaching even up to 40%. The inverse rule of mixture and power-law model provides a much better fit, which provides a respectively lower and upper boundary for obtained results. Such significant discrepancies can be attributed to the simplicity of used property models. In most cases, the models predicting mechanical properties do not incorporate properties of second phase material or geometrical features, including particle shape or size. Additionally, they require a significant quantity of additional experimental or theoretical parameters to accurately predict the mechanical properties of resulting composites [67].To further verify the compressive model used in this study, the comparison of experimental and simulated values of low density silica and epoxy resin compressive strength has been conducted in Figure 6-21.

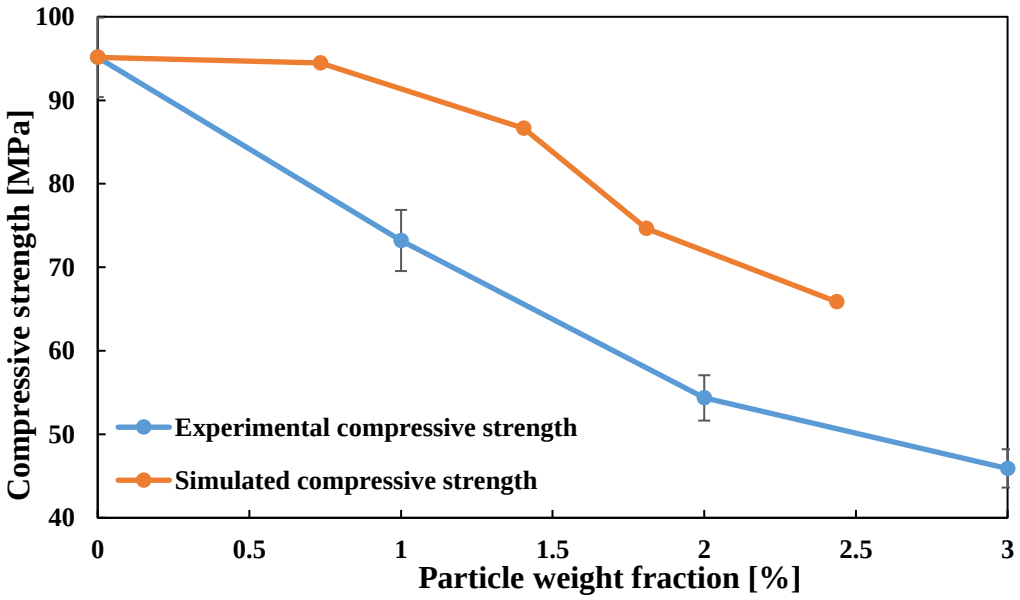

Figure 6-21 Comparison of experimental and simulated compressive strength values for 100 μm low density silica and epoxy composites.

The compressive strength values presented in Figure 6-21 indicates a significant discrepancy between experimental and simulated results. The model fails to capture a significant drop in compressive strength at low particle loading, and over the whole loading range overestimates the composites' strength value. Such behaviour is expected as static structural analysis applies the "linear law" regardless of the strain being outside the elastic region [207]. As a result, it does not detect material failure and produces stresses that can be much higher than the material's yield stress. Overall a careful investigation of obtained strength values is recommended [207]. In order to check the results even further, the compressive strength values

are also compared to previously described property models and presented in Figure 6-22. Opposite to the elastic modulus results, the property models are significantly more accurate in predicting the compressive strength values of particulate composites than the current model. Mainly the power law seems to replicate the experimental results quite well. On the other hand, the strength model, similarly to current work, tend to overestimate the compressive strength while the fractional density model underestimated the same property. Such discrepancies in compressive strength predictions only prove the difficulty in creating an accurate model.

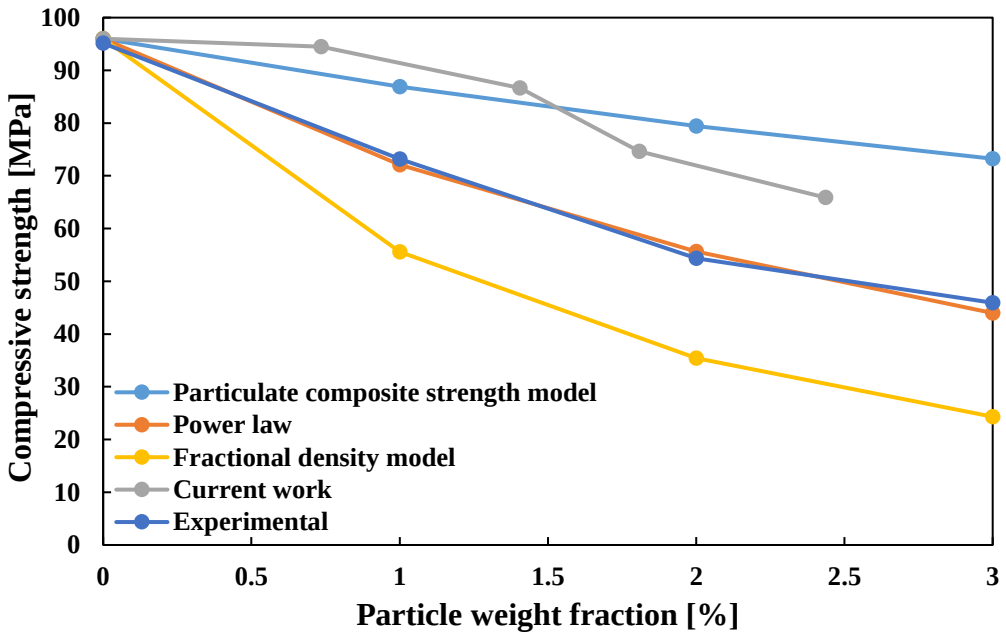

Figure 6-22 Compressive strength values obtained in this study and predicted by property models for 100 μm low density silica and epoxy composites.

Overall, the validation and verification of thermal and compressive models presented in this work revealed their suitability to predict the thermal conductivity and compressive modulus of particles filled polymer composites. The simulated results for both properties presented a close match with experimental results, allowing for a detailed analysis of the microscale behaviour of the material. Less of an agreement has been achieved between experimental and simulation results for a compressive strength with the current model overestimating this property. Nevertheless, following successful validation, discussed models will be used in the further part of this study, focusing on investigating the effects of particle size and silica or polyimide density upon thermal and mechanical properties of composite material prepared with epoxy resin and low density silica or polyimide.

6.3.2 Effect of particle size on composite thermal behaviour

6.3.2.1 Low density silica

Figure 6-23 presents thermal conductivity values of composites modelled with epoxy resin and varying size of low density silica particles as a function of different particle weight fractions.

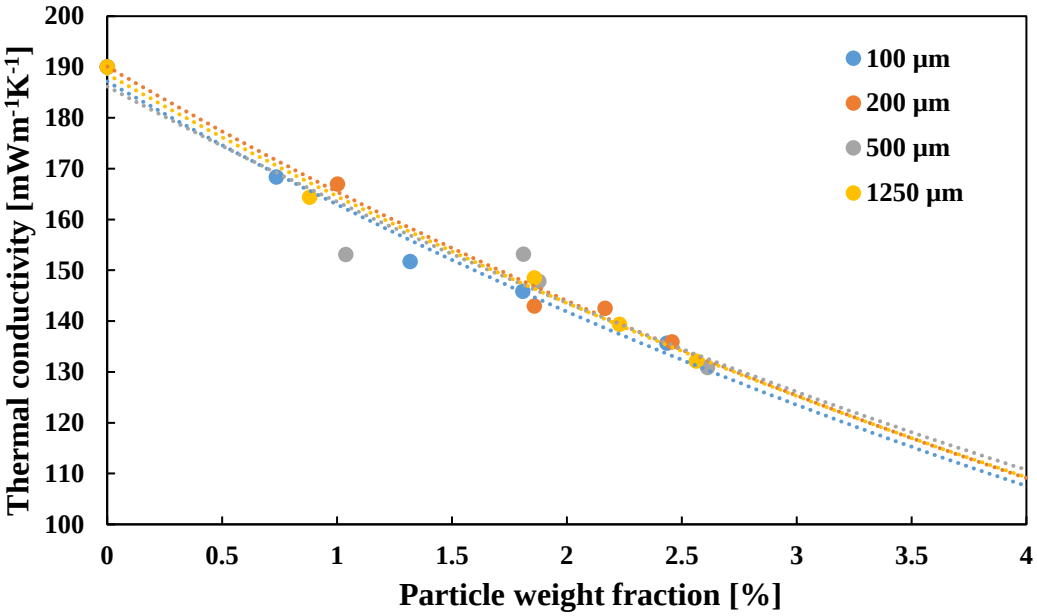

Figure 6-23 Thermal conductivity of low density silica / epoxy composites with varying particle size and loading.

When analysing Figure 6-23, it can be noticed that the particulate composites' thermal conductivity varies with both the quantity of low density silica as well as the particle size. Across the whole particle size range, a common trend emerges with epoxy matrix thermal conductivity being reduced by incorporating larger quantities of low density silica particles. On average, the addition of 1 wt% of particles results in a 14% reduction in thermal conductivity and increases to 30% when 2.5 wt% of silica particles are incorporated. Figure 6-23 also reveals little impact of particle size on the Tc values across the investigated loading range with all the composites converging at a similar thermal conductivity value at higher particle loading.

6.3.2.2 Low density polyimide

Figure 6-24 presents thermal conductivity values of composites manufactured with epoxy resin and varying size of low density polyimide particles as a function of different particle weight fractions.

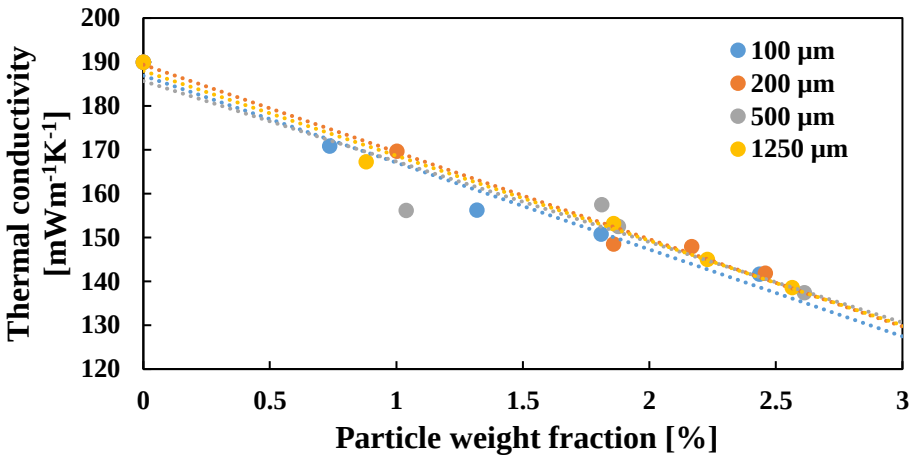

Figure 6-24 Thermal conductivity of low density polyimide / epoxy composites with varying particle size and loading.

The analysis of Figure 6-24 reveals that the addition of low density polyimide affects the thermal conductivity of epoxy resin similarly to low density silica. As a result, the addition of low density polyimide reduced the composites' thermal conductivity with increasing material loading. In this case, however, 1 wt% of low density polyimide provides an average of 12.6% thermal conductivity reduction, increasing to up to 26.3% reduction with the addition of 2.5 wt%. Overall, across the investigated loading range, the correlation between thermal conductivity and particle loading seems linear for all the different particle sizes and similarly as in the previous case the little impact of particle size on the Tc values across the investigated loading range can be noticed with all the composites converging at a similar thermal conductivity value at higher particle loading.

6.3.2.3 Discussion

The results strongly indicate that the addition of low density silica and polyimide particles to epoxy resin reduces its thermal conductivity. Similarly, as in experimental results, such behaviour can be explained by analysing the energy transfer through the material.

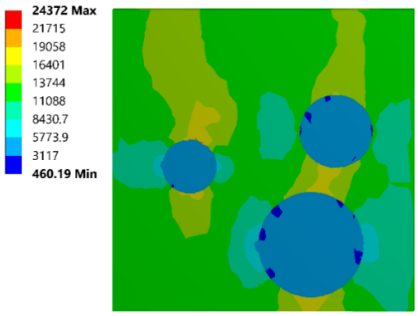

Figure 6-25 An example of heat flux distribution for a 2% 100 µm low density silica and epoxy composites.

As a result, the most significant difference comes from the reduction in solid conduction of the material, which is reduced by adding extremely low thermal conductivity regions of low density silica and polyimide particles. Both polyimide and silica are poor conductors of heat and combined with the high porosity, they provide even better insulation. In addition, dispersed particles create a barrier for energy transfer and create a bottleneck region, effectively limiting the heat transfer area. Both phenomena can be observed in Figure 6-25, with the low density particles presenting significantly lower heat flux values than surrounding epoxy. Additionally, the high flux regions can be identified in regions in between the particles as the energy accumulate there sue to not being able to travel through neighbouring particles. The remaining modes of heat transfer, including gas convection and radiation, can be neglected, as shown by previous studies. In order to compare both particle types Figure 6-26 were prepared and plots, the average reduction in epoxy thermal conductivity as a particle loading function for all particle size investigated.

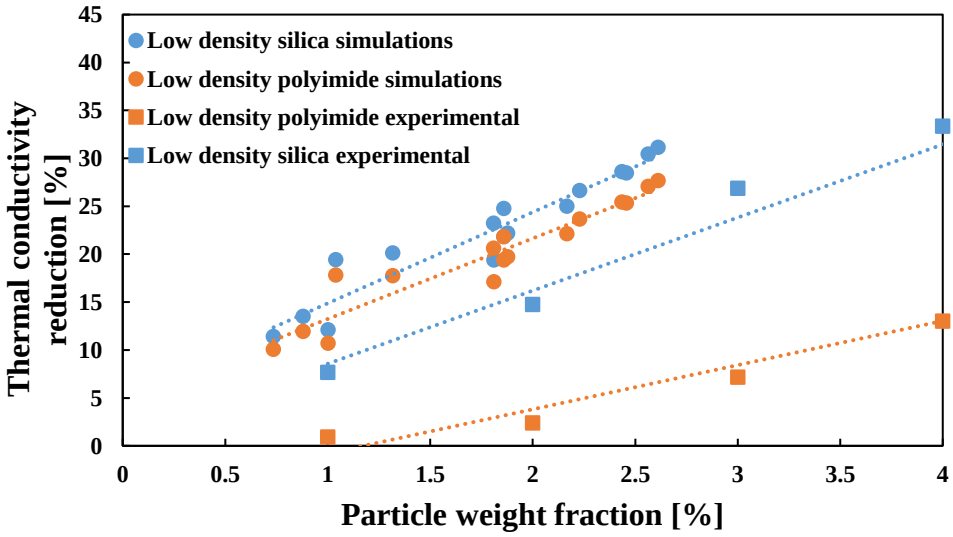

Figure 6-26 The comparison of experimental and simulated average reduction in epoxy thermal conductivity as a function of low density silica and polyimide particle loading.

Figure 6-26 indicates that the correlation between thermal conductivity and low density particle loading seems linear for both material types. Nevertheless, low density polyimide particles reduce epoxy thermal conductivity to a lesser extent when compared with the silica counterpart. Such phenomena can be attributed to higher thermal conductivity values of the low density polyimide, as presented by the molecular dynamics study. Additionally, the difference in thermal conductivity reduction between both composites is increasing with increasing particle loading. Even though the interfacial thermal resistance is higher between polyimide and epoxy, its effects seem outweighed by the difference in thermal conductivity of

constituent materials. As a result, low density PI cannot introduce the same degree of a barrier for energy transfer and reduce direct paths through the composite. When comparing a simulated thermal conductivity reduction with the experimental results from Chapter 3 a discrepancy can be noticed, however different for each particle type. In case of low density silica particles both predicted and measured results follow similar trend with increasing T_c reduction when higher particle weight fraction is used. However, the experimental results present around 5% lower reduction of epoxy thermal conductivity values with the difference increasing with higher particle loading used. Again, such difference might be attributed to the destruction of the aerogel internal pores during the sample manufacturing ether by filling them with liquid resin or by crushing them during mixing stage. Significantly larger differences (reaching even up to 20%) can be observed between the simulated and experimental thermal conductivity reduction values for the epoxy samples with low density polyimide particles. In this case the reason for such discrepancies is the model's lack of ability to capture the open pore structure of the polyimide aerogel used in the experimental research. Such structure enabled the significant pore infiltration and as presented by the experimental results limited impact on the heat transfer capability of the epoxy resin. The FEA model assumed the ideal manufacturing conditions which enabled complete preservation of the aerogels' interna structure and suggested that further reduction in T_c values of epoxy resin can be achieved by further improving the manufacturing techniques of aerogel particulate composites.

By simulating different particle size within a polymer matrix, it is possible to investigate particle size's effect on thermal conductivity reduction. Figure 6-27 includes the average reduction in polymer thermal conductivity as an particle loading function for composites manufactured with both low density silica and polyimide.

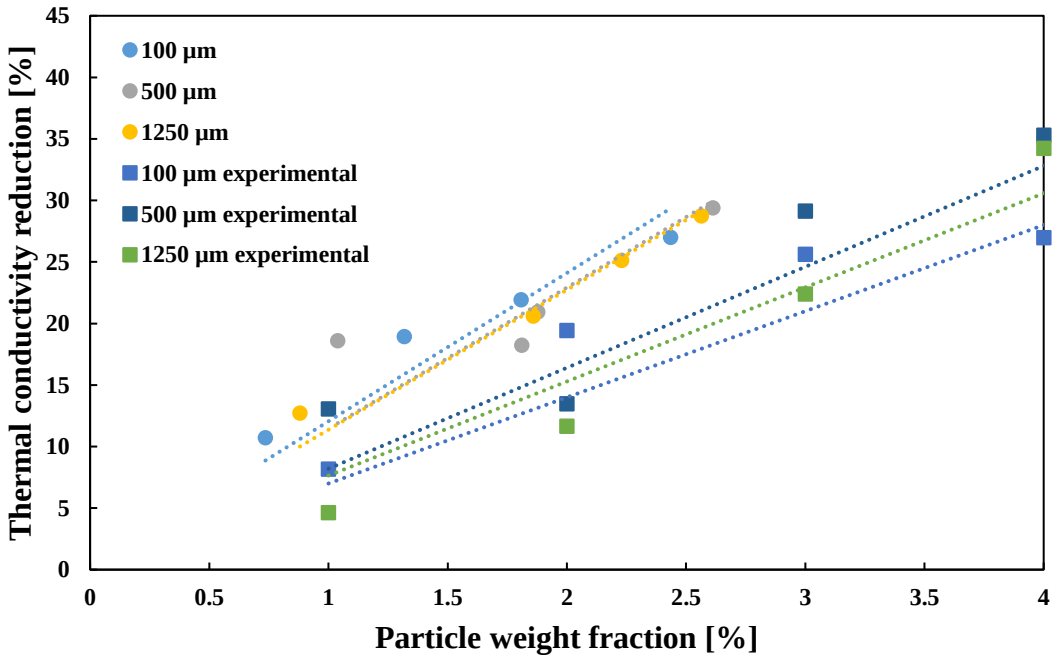

Figure 6-27 Average reduction in polymer thermal conductivity as a function of low density particle loading for varying particle size. Values have been calculated for composites manufactured with both silica and polyimide.

Figure 6-27 indicates that the for the simulated composites the particle size has a little effect on the thermal conductivity reduction with all modelled samples predicting similar values regardless of the particle size used. This however presents a difference form the experimental results which indicate a variation in thermal conductivity values between epoxy samples prepared with different size of aerogel particles. Additionally, the modelled samples always predict higher T_c reduction with the difference being exacerbated with increasing particle loading. It can be speculated that similarly as in previous figure the ANSYS model failed to capture the changes happening to the internal structure of the low density materials during manufacturing stage and thus was not able to reflect them in the T_c values. The lack of difference in modelled values could also imply that the difference in thermal conductivities obtained in the experimental research was more likely due to the different response of particles with different diameters to the physical phenomena occurring during sample manufacturing (such as pore infiltration or particle crushing) rather than to the changes in heat transfer through the epoxy resin imposed by the particles. However, further studies are required to verify this thesis.

6.3.3 Effect of particle density on composite thermal behaviour

The synthesis of aerogel materials is complicated, and the production of materials with consistent densities pose significant challenges. As a result, the subsequent investigation will

focus on the impact of silica and polyimide density upon epoxy thermal conductivity. However, with changing density, a range of other parameters, including thermal conductivity, interfacial thermal resistance or heat capacity, are also being altered.

6.3.3.1 Low density silica

Figure 6-28 presents thermal conductivity values of composites manufactured with epoxy resin and varying density silica particles as a function of different silica weight fractions. For this investigation, 100 μm particles have been modelled as an epoxy filler.

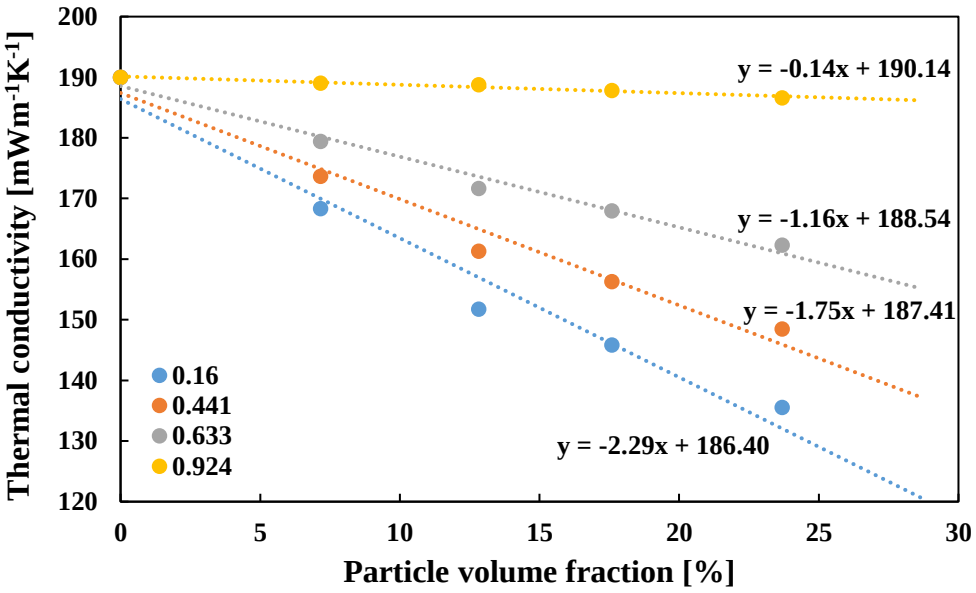

Figure 6-28 Thermal conductivity of 100 μm silica / epoxy composites with varying particle density and loading. All densities are given in g/cm^3.

Figure 6-28 indicates that the usage of higher density silica increases the thermal conductivity of the resulting composite. Nevertheless, regardless of the silica density, the correlation between thermal conductivity and particle volume fraction follows linear relation of decreasing thermal conductivity with increasing particle content. As a result, with the addition of the 25 vol% of silica, the thermal conductivity has been reduced by approximately 29, 22, 14 and 2% when using silica articles with densities of respectively 0.16, 0.44, 0.63 and 0.92 g/cm^3.

6.3.3.2 Low density polyimide

Figure 6-29 presents thermal conductivity values of composites manufactured with epoxy resin and varying density polyimide particles as a function of different polyimide weight fractions. For this investigation, 100 μm particles have been modelled as an epoxy filler.

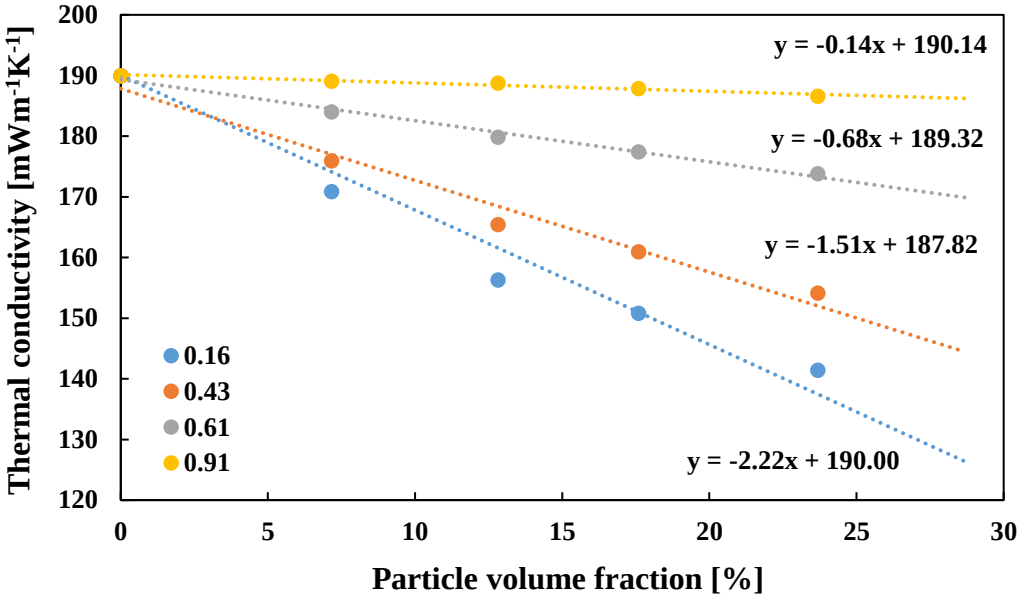

Figure 6-29 Thermal conductivity of low density polyimide / epoxy composites with varying polyimide density and loading. All densities are given in g/cm^3.

As shown in Figure 6-29, the density of polyimide used in epoxy composites impacts the final thermal conductivity of the composite. The most significant reduction in T_c of 26% is achieved by incorporating 15 vol% of 0.16 g/cm^3 polyimide particles. At the same particle volume fraction, remaining investigated polyimide densities results in thermal conductivity decrease of 19, 9 and 2% for respectively 0.43, 0.61 and 0.91 g/cm^3 polyimides. Similarly, as in the case of silica particles, the relationship between composites' thermal conductivity and particles volume fraction follows a linear trend regardless of the density used.

6.3.3.3 Discussion

The increase in thermal conductivity values when using higher density silica or polimide particles is an expected phenomenon explained by the analysis of heat flux distribution as presented in Figure 6-30.

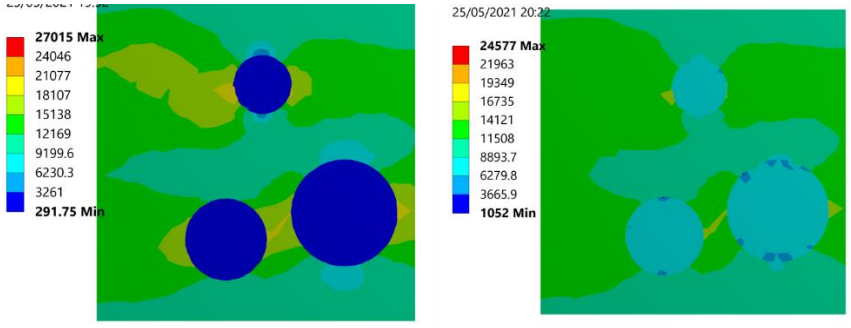

Figure 6-30 An example of heat flux distribution for a 2% 100 µm silica and epoxy composites when using 0.16 g/cm^3 (left) and 0.91 g/cm^3 (right) particles.

As presented in Figure 6-30, the low-density particles create an obstacle for the energy transfer through the material. However, with increasing particle density, those obstacles become less effective insulators, and larger heat flux values can be noticed across particles. This is mainly caused by the changes happening inside the silica or polyimide structure when increasing its density. As a result of densification, the porosity of particles is significantly decreasing, resulting in less quantity of air being encapsulated inside pores. In addition, denser material is providing more direct paths for the energy transfer through the conduction model. Finally, the lower interfacial thermal resistance for denser particles negates the potential benefits of particle introductions for polymer matrices. All those issues are effectively responsible for improving thermal conductivity of particles with their increasing density and further diminishing the created composites' thermal resistance properties. In order to better understand the impact of silica and polyimide density on thermal conductivity of epoxy, Figure 6-31 has been plotted presenting thermal conductivity of epoxy and polyimide or silica composites as a function of composites density.

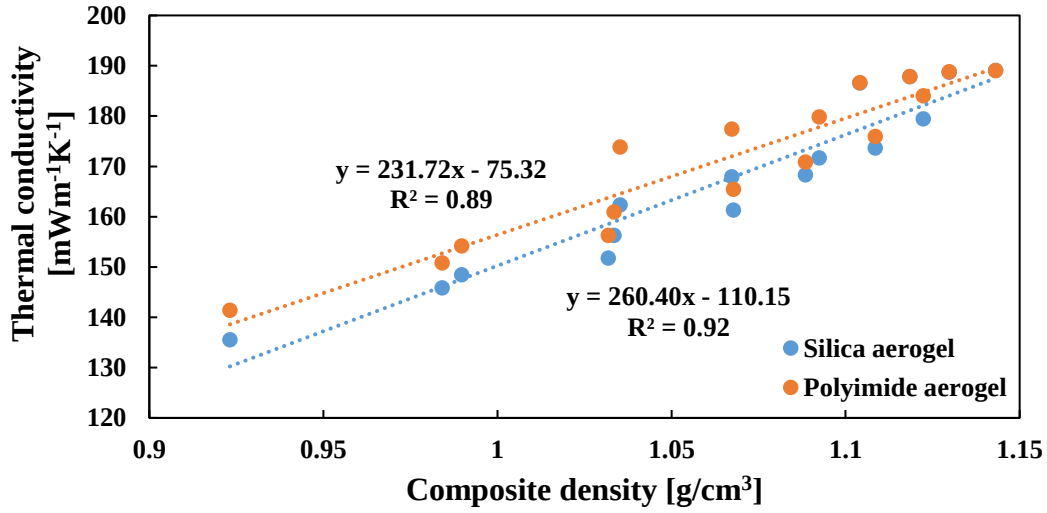

Figure 6-31 Thermal conductivity of epoxy and polyimide or silica composites as a function of composites density.

Figure 6-31 presents the thermal conductivity of the epoxy composites as a function of their density. As expected, for both types of particles, the conductivity rises as the density increases, and they correlate well in a linear fashion with an r-squared value of 0.92 and 0.89 for respective silica and PI. The slope of discussed trend lines also indicates that the silica has a more considerable impact on composite thermal conductivity with a slope gradient of 260.4 compared to 231.7 in polyimide. Again, it is suspected that the lower thermal conductivity of low density silica particles is responsible for the superior thermal resistance of epoxy and silica composites. Finally, to fully appreciate the impact of varying silica and polyimide densities

on epoxy thermal conductivity, Figure 6-32 has been plotted. It presents the average reduction in epoxy thermal conductivity as a function of particle loading when using varying silica or polyimide densities. The values have been averaged across both silica and polyimide composites.

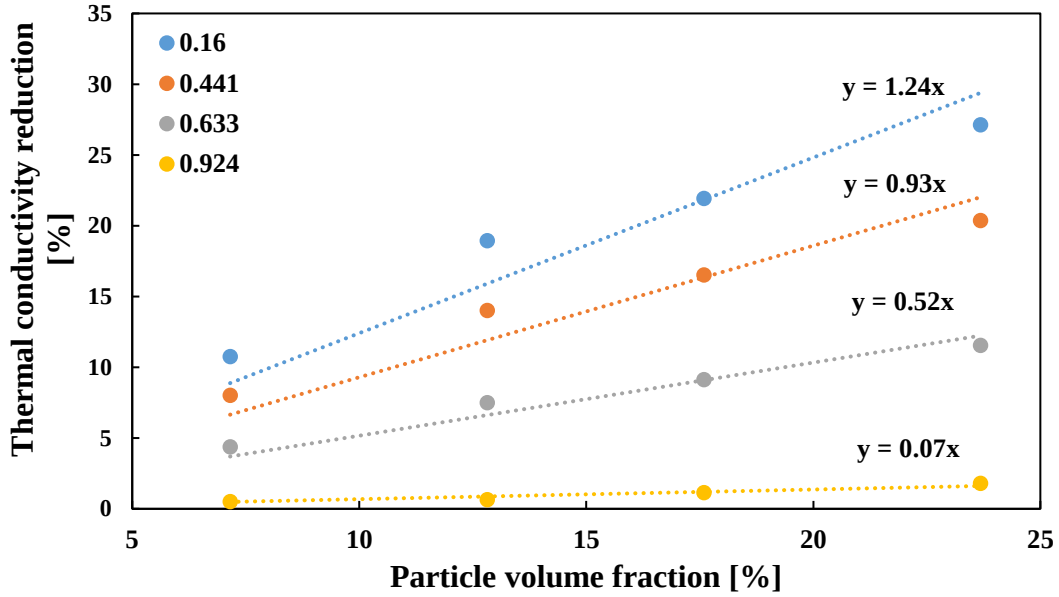

Figure 6-32 Average reduction in epoxy thermal conductivity as a function of particle loading. Values have been calculated for composites simulated with both material types.

Figure 6-32 again confirms that the incorporation of low-density silica and polyimide particles yields the most significant thermal conductivity reductions. Additionally, the difference in thermal conductivity reduction between varying particle densities is only increasing with increasing particle volume fraction. Nevertheless, this graph also indicates that with increasing particle density, the incremental impact on the material's thermal property is decreasing. For example, the difference in thermal conductivity reduction for the 25 vol% samples prepared with 0.924 and 0.63 g/cm^3 particles is equal to 9.76%. When analysing similar density changes between samples prepared with 0.44 and 0.16 g/cm^3 particles, the same difference equals only 6.76% (almost 45% difference). Such results suggest that the external phenomena which might affect the density (or porosity) of the additive particles (such as pore infiltration during the manufacturing process) are more severe for the high density materials and their more careful application is required.

6.3.4 Effect of particle size on composite compressive properties

As presented in the experimental part of this thesis, the addition of aerogel particle can significantly affect the mechanical behaviour of epoxy resin. Additionally, the impact of particle size on the composites' compressive properties has been identified. In order to further

investigate the effect of composites microstructure on mechanical properties, the FEA compressive testing simulations has been carried on epoxy composites incorporating varying silica and polyimide particle size and particle loading.

6.3.4.1 Low density silica

Figure 6-33 presents the compressive modulus of composites manufactured with epoxy resin and varying size low density silica particles as a function of different particle weight fractions. For this study, the silica particle with a density of 0.16 g/cm^3 has been used.

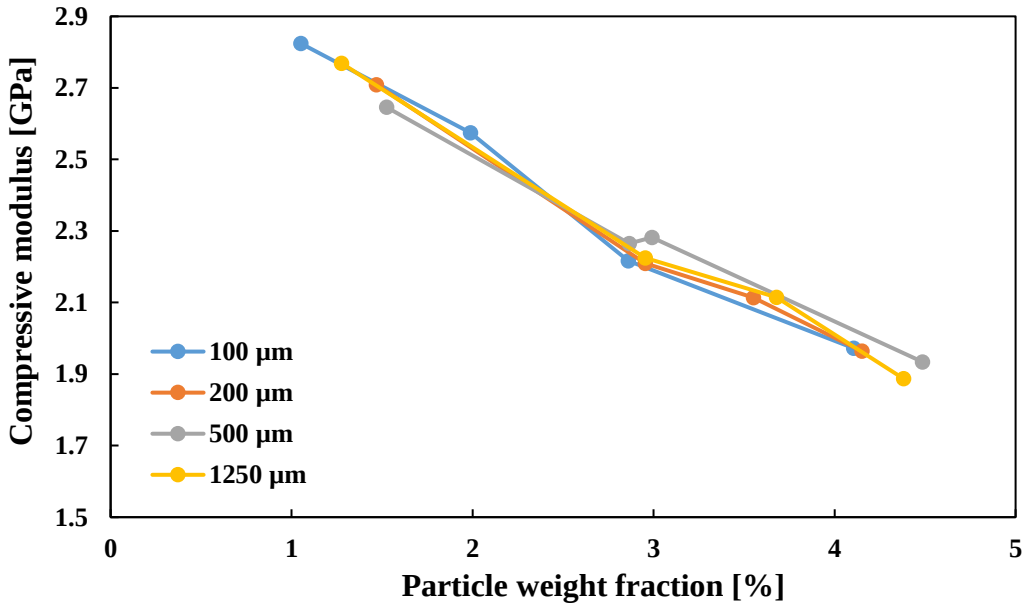

Figure 6-33 Compressive modulus of low density silica/ epoxy composite with varying particle size and loading.

Figure 6-33 implies that the compressive modulus of epoxy resin decreases after the addition of silica particles. Low density silica particles cause a constant, linear decrease in compressive modulus, presenting an average drop of 53% with the addition of 4.25 wt% of particles. Moreover, it should be highlighted that the particle size carries little effect on the compressive modulus, with all the composites producing relatively close results for the same particle weight fraction. Nevertheless, by analysing the current trend, it can be speculated that larger particles would produce lower compressive properties at higher loadings. Somewhat similar behaviour can be noticed for the composites' compressive strength values presented in Figure 6-34.

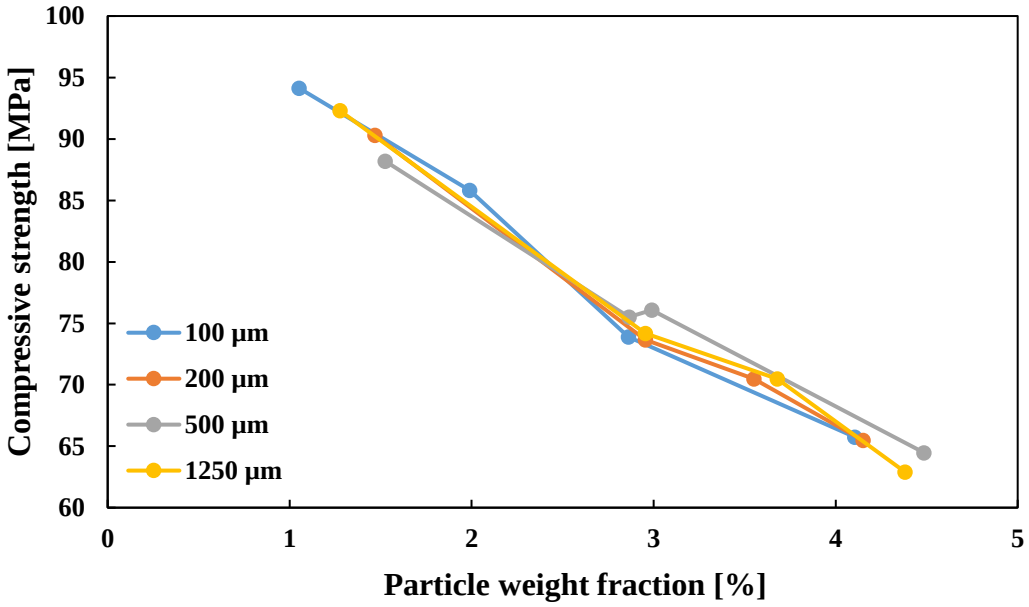

Figure 6-34 Compressive yield strength of low density silica/ epoxy composite with varying silica content and particle sizes.

Figure 6-34 shows that compressive strength decreases with increasing loading of the low density silica particles following the linear fashion regardless of the particle size. The addition of 1, 2, 3 and 4 wt% of particles yield the decrease in compressive strength of respectively 4, 19, 23 and 32%, much lower than in the case of compressive modulus. Especially a minor difference from initial 95 MPa compressive strength of pure epoxy achieved with the addition of 1% particle weight fraction, highlighted the model's inability to correctly capture the compressive strength of the composite. Additionally, it is difficult to identify the impact of particle size upon the compressive strength of silica and epoxy composites. However, similarly, as in compressive modulus, the trend lines suggest that increasing particle loading more significant decrease in compressive strength can be expected for larger particles.

6.3.4.2 Low density polyimide

Figure 6-35 presents the compressive modulus of composites manufactured with epoxy resin and varying size low density polyimide particles as a function of different particle weight fractions. For this study, the low density polyimide with a density of 0.16 g/cm^3 has been used.

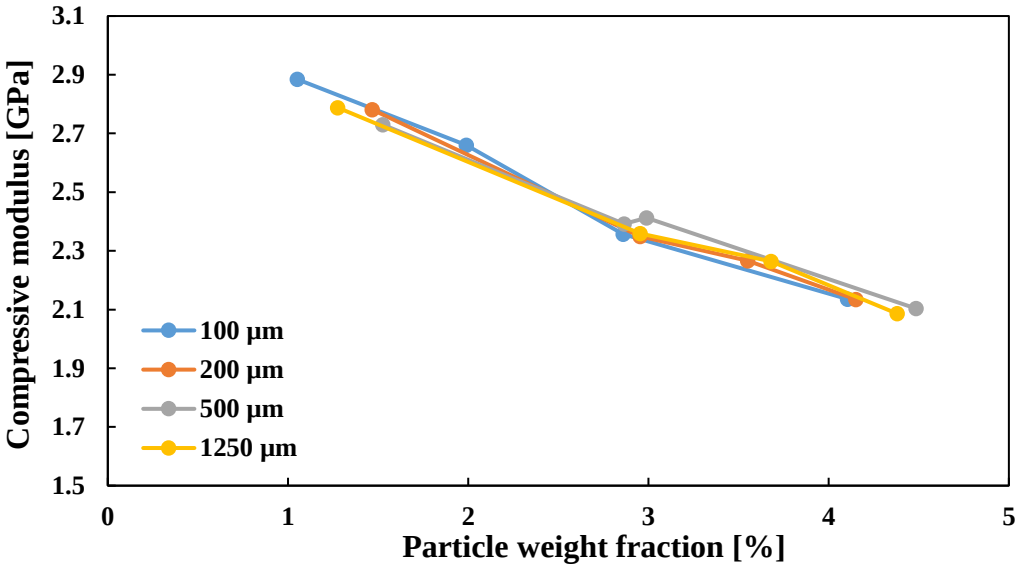

Figure 6-35 Compressive modulus of low density polyimide/ epoxy composite with varying particle size and loading.

Figure 6-35 indicates that incorporating low density polyimide particles into epoxy resin results in a significant decrease of compressive modulus. Regardless of the particle size, the compressive modulus decreases with increasing particle loading following the linear trend and results in a 33% reduction in epoxy's elastic modulus with the addition of 4.25 wt% of polyimide particles. Similarly, as in low density silica composites, particle size has little impact upon compressive modulus reduction. Following the presentation of the impact of low density polyimide loading on the composite compressive modulus, Figure 6-36 has been created to correlate compressive strength with particle weight fraction.

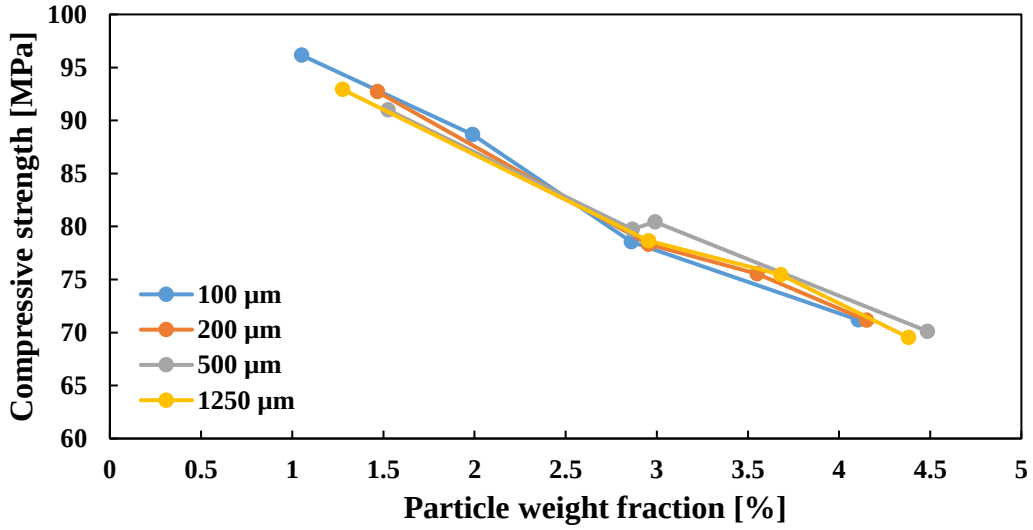

Figure 6-36 Compressive yield strength of low density polyimide/ epoxy composite with varying particle content and sizes.

The analysis of Figure 6-36 reveals that the addition of low density polyimide affects the compressive yield strength of epoxy resin similarly to low density silica. As a result, the addition of low density polyimide reduced the composites' compressive yield strength with particle loading increasing. In this case, however, 1 wt% of low density polyimide provides an average of 1.9% reduction, increasing to up to 26% reduction with the addition of 4.25 wt%. Overall, across the investigated loading range, the correlation between compressive yield strength and particle loading seems linear for all the different particle sizes.

6.3.4.3 Discussion

The presented results suggest that the addition of low density particles hinders the compressive properties of epoxy resin. Such behaviour is anticipated mainly because both low density silica and polyimide have much lower mechanical properties than epoxy resin systems [246, 247]. As a result, the introduction of air-filled porous particles into a coherent structure of a matrix decreases its' compressive properties. In addition, due to the entirely different physical properties of inclusions, the additive particles can be classified as irregularities in otherwise coherent matrix geometry. Effectively, they became the stress concentration locations that block the load transfer mechanism and further hamper composites' compressive properties. In order to compare both material types, Figure 6-37 was prepared, which plots the average reduction in composites' compressive modulus as a particle loading function for all particle size investigated. The elastic modulus was selected for further analysis as during model validation it presented a much closer match with experimental values.

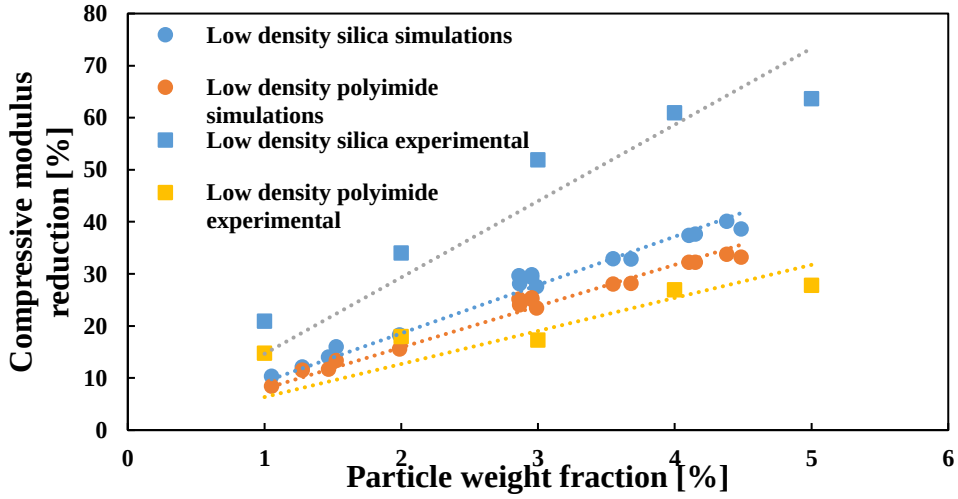

Figure 6-37 Average reduction in epoxy compressive strength as a function of particle loading. Values have been averaged between all particle sizes used.

Similarly, as in thermal conductivity, the composites created with low density PI particles present a much smaller reduction in compressive modulus than silica ones. Such behaviour

can be explained by the superior compressive properties of PI particles used in this model, which again results from lower porosity when compared with low density silica. As a result of higher elastic modulus and yield strength, low density polyimide has much better stress bearing properties and thus impact the composites compressive properties to a lesser extent. On the other hand, due to the brittle nature and extremely high porosity of low density silica, its impact on the epoxy's compressive properties can be almost compared to an empty void inside the resins' structure. Similarly, as in the case of thermal conductivity the compressive values have also been compared with experimental results previously presented in Chapter 3. As it can be noticed the compressive modulus reduction of simulated epoxy composites with low density polyimide particles presents a good fit with the experimental results, however the difference between both is increasing with increasing particle loading. A significantly larger differences are present in case of low density silica composites with experimental results suggesting significantly more detrimental impact of silica particles on the compressive properties of the epoxy resin. One of the reasons for such finding might be the use of the spherical particles in the FEA model (in comparison to sharp and irregular particles used in the experimental research) which reduce the stress concentration factor and thus suggest much lower impact of the silica particles on epoxy’s mechanical properties during modelling. Additionally, the model does not introduce any manufacturing defects which might occur in real life which further reduce the impact of the additives. Even though the previous results have shown the negligible impact of particle size upon compressive properties of composites, Figure 6-38 has been created. It includes the average reduction in polymer compressive modulus as an particle loading function for composites manufactured with both low density silica and polyimide.

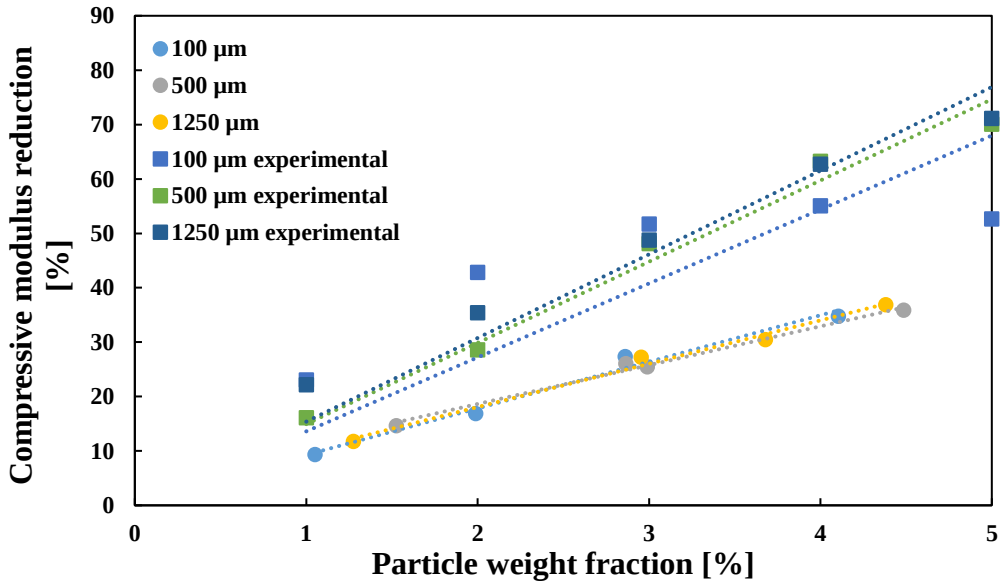

Figure 6-38 Average reduction in polymer elastic modulus as a function of particle loading for varying particle size. Values have been calculated for composites manufactured with both low density silica and polyimide.

By analysing Figure 6-38, it can be noticed that the particle size has little effect on the compressive modulus of simulated composites. Such a finding contradicts the experimental results presented in this thesis, which indicated a little effect of the smallest particles on the compressive strength at high particle content (> 3 wt%). All remaining particle sizes reduced yield strength and modulus monotonically up to 5 wt%, however with the most considerable reduction caused by particles with the highest diameter. A few factors can explain such discrepancies. Firstly, Inglis et al., who have investigated mechanical properties of particulate composites using Mori-Tanka and FEA solution, have also investigated similar behaviour. In their work, authors simulated composites with particles between 20 and 50 µm and discovered the little effect on the elastic region of the stress/strain curve. A much more significant impact has been discovered for an elastic region, where particle size dictated the slope of the transitional stage. This could indicate that the significant difference in the compressive performance of particulate composites prepared with different size of particles originates from their response to the displacement after reaching the elastic region. In this case, the current steady-state model would not capture such phenomena as it only operates in the plastic region. Secondly, the variation between simulated and experimental result is also caused by the idealistic approach of the FEA model. By assuming ideal, spherical particles, a wide range of external factors such as particle shape or the degree of pore infiltration is neglected. However, it is suspected that their effect on compressive properties is related to particle size used but would not be reflected in the current model. The possible approach to increase the accuracy of

the FEA model would be to perform a transient investigation and incorporate elastic properties of investigated materials. Finally, to directly compare the effects of low density particle addition on mechanical and thermal properties of epoxy resin, Figure 6-39 has been created.

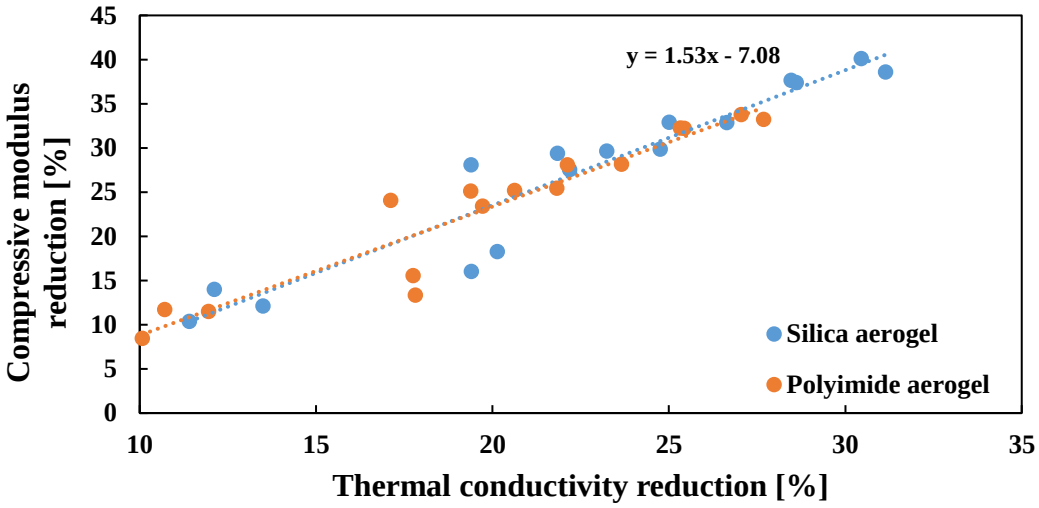

Figure 6-39 Correlation between average reduction in epoxy compressive modulus and a reduction in thermal conductivity. Values have been calculated for all particle size.

Figure 6-39 indicates the possibility of enhancing the thermal insulating properties of epoxy resin by introducing both low density silica and polyimide particles. Simultaneously, the addition of particles deteriorates the compressive properties of epoxy resin, and those materials are more likely to be used in scenarios with limited external loading applied to them. Both types of particles seem to provide a similar relation between compressive modulus and thermal conductivity reduction at low particle loadings. Nevertheless, with increasing presence, low density polyimide particles result in superior mechanical properties for the same thermal conductivity reduction. On the other hand, due to the highly porous internal structure, low density silica can produce much more significant overall thermal conductivity reductions. By simulating the impact of low density particles on both thermal and mechanical properties, as presented in this work, the opportunity for careful balancing of those properties has been created. Also, by incorporating the details of particulate composites microstructure into higher scale simulations, it would be possible to identify a combination best suiting investigated design, hopefully leading to greater usage of this lightweight insulation material.

6.3.5 Effect of particle density on composite compressive properties

Similarly, as in the case of thermal properties, the particle density also affects the load-bearing properties of composites. Thus, the subsequent investigation will focus on the impact of silica and polyimide density upon epoxy compressive modulus and strength.

6.3.5.1 Slow density silica

Figure 6-40 presents compressive modulus values of composites manufactured with epoxy resin and varying density silica particles as a function of different particle volume fractions. For this investigation, 100 μm particles have been modelled as an epoxy filler.

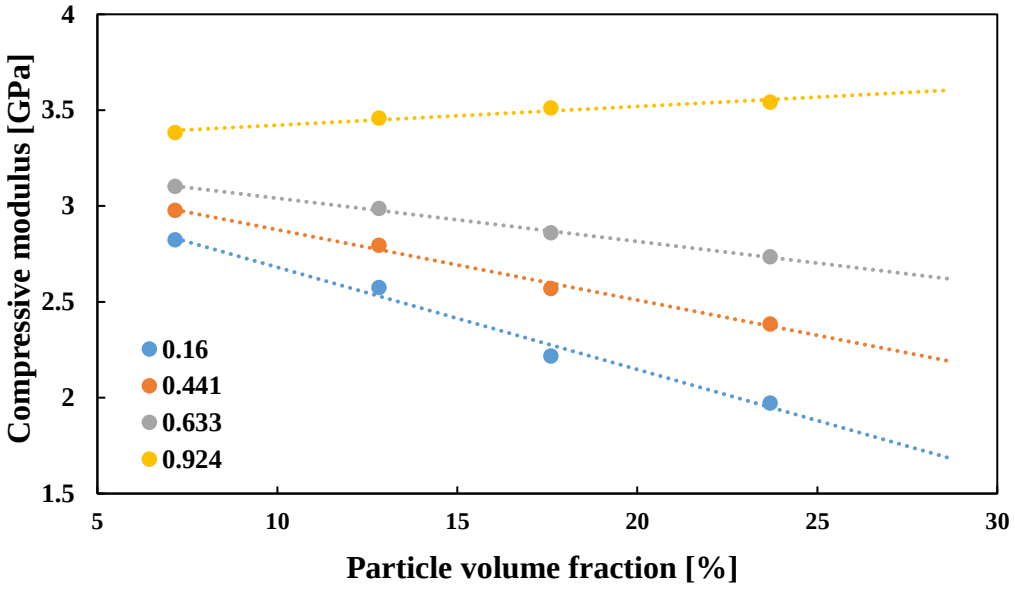

Figure 6-40 Compressive modulus of low density silica/ epoxy composite with varying particle density and loading. Particle density values are given in g/cm^3.

Figure 6-40 imply that the addition of low-density silica particles negatively affects the compressive modulus of epoxy resin. By incorporating 25 vol% of silica particles with densities of 0.16, 0.44 and 0.63 g/cm^3, the decrease in compressive modulus of respectively 37, 24, and 13% has been measured. On the contrary, the incorporation of 0.92 g/cm^3 density particles had a positive impact on the compressive properties of epoxy resin with an almost 12% increase in modulus value. Almost identical behaviour can be noticed for the composites' compressive strength values presented in Figure 6-41.

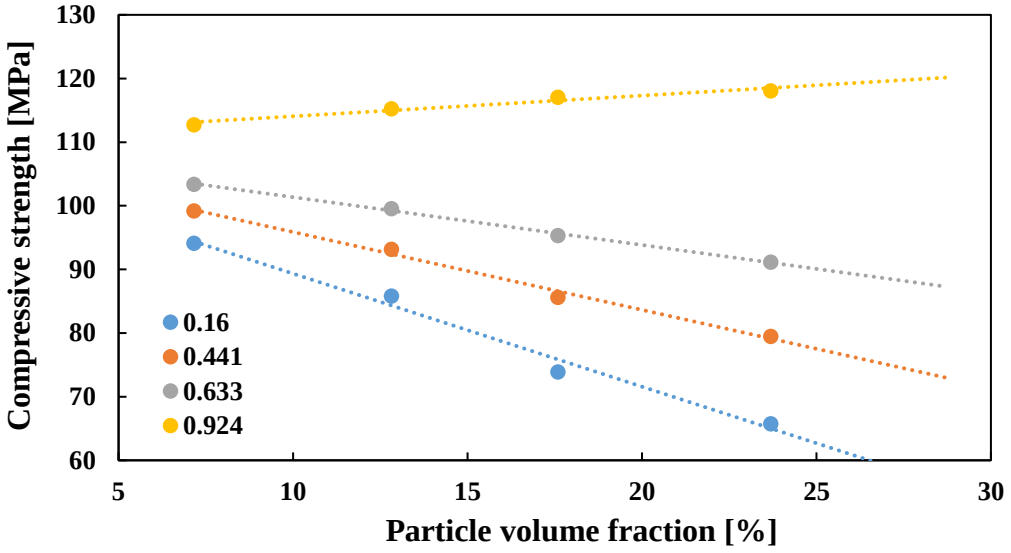

Figure 6-41 Compressive strength of low density silica/ epoxy composite with varying particle density and loading. Particle density values are given in g/cm^3.

6.3.5.2 Low density polyimide

Figure 6-42 presents compressive modulus values of composites manufactured with epoxy resin and varying density polyimide particles as a function of different particle weight fractions. For this investigation, 100 μm particles have been modelled as an epoxy filler.

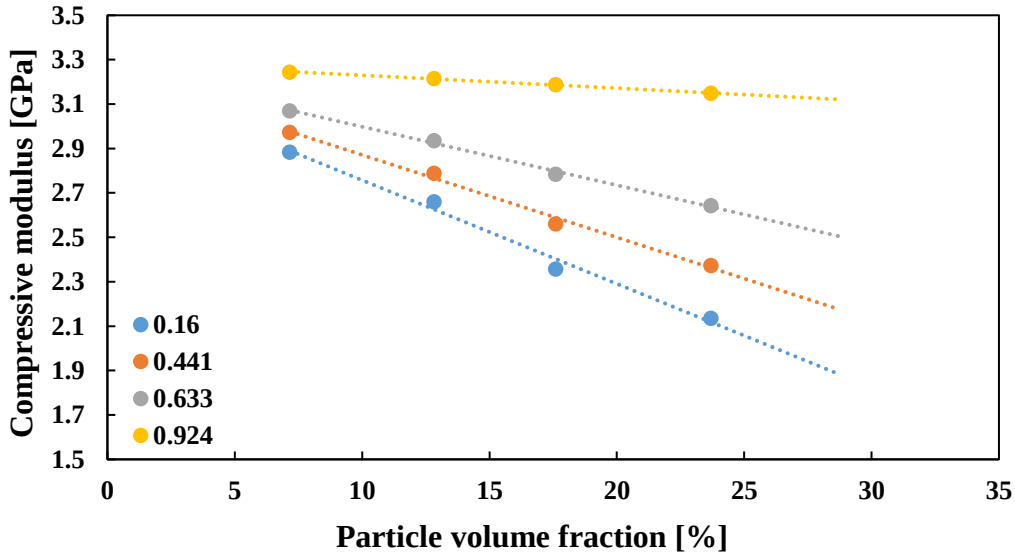

Figure 6-42 Compressive modulus of low density polyimide/ epoxy composite with varying particle density and loading. Particle density values are given in g/cm^3.

By analysing Figure 6-42, it can be noticed that similarly to silica particles, polyimide particles also hinder the mechanical properties of epoxy resin. Nevertheless, with increasing polyimide density, the load-bearing properties of composites are improved, resulting in 32, 25, 16 and 0.05 % reduction of compressive modulus when adding 25 vol% of particles with density of

respectively 0.16, 0.44, 0.63 and 0.92 g/cm^3. However, in this case, no strengthening mechanism is observed when adding a high-density particle to epoxy resin. The decrease in compressive properties was also indicated in Figure 6-43, which presents the composites' compressive strength values as a function of low density polyimide volume fraction. It supports the findings from the analysis of compressive modulus and indicates that lower density polyimide yield a much more significant reduction in materials' compressive strength.

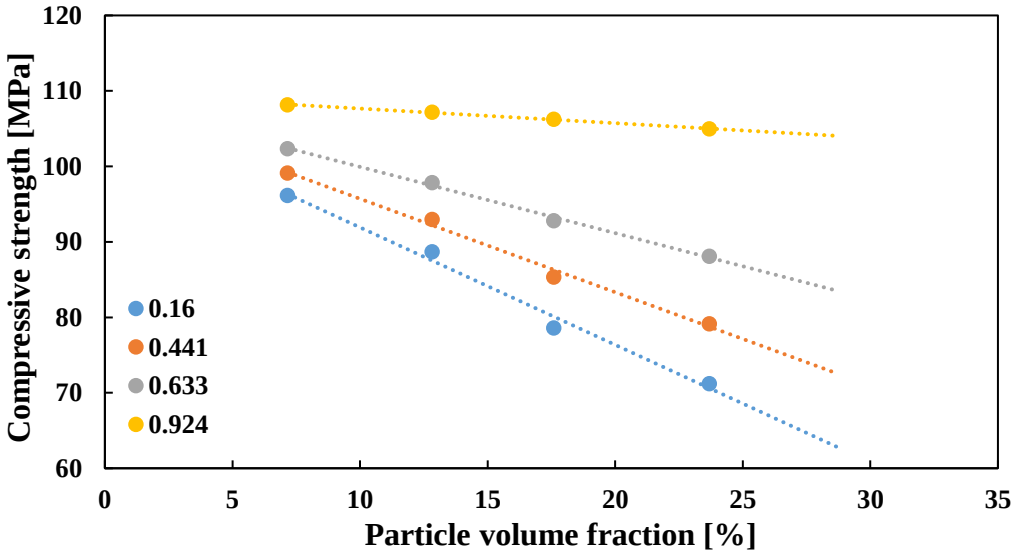

Figure 6-43 Compressive strength of low density polyimide/ epoxy composite with varying particle density and loading. Particle density values are given in g/cm^3.

6.3.5.3 Discussion

Lower degradation of compressive properties of epoxy resin when using higher density particles is an expected phenomenon that can be explained by the analysis of stress distribution graphs as presented in Figure 6-44.

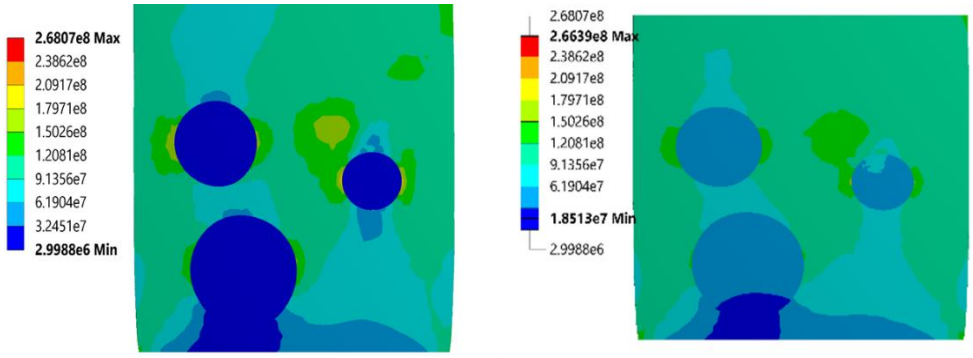

Figure 6-44 An example of von Mises stress distribution for a 2% 100 µm low density silica and epoxy composites using 0.16 g/cm^3 (left) and 0.63 g/cm^3 (right) particles.

As indicated by Figure 6-44, the low-density particles provide a minimum load-bearing capability, highlighted by low-stress values across the 0.16 g/cm^3 particles. With increasing

density, the particles become capable of carrying more significant stresses. Similarly, to thermal properties, this behaviour can be attributed to the changes happening inside the paticle structure when increasing density. As a result of particle densification, the porosity of particles is significantly decreasing, and the previously air-filled material become a more coherent structure. Such material provides much better paths for a load transfer and increases materials' compressive strength. In addition, the high-density particles do not introduce the same degree of stress concentration compared with lighter counterparts. Again, comparing both composites in Figure 6-44, much lower stress values can be noticed at particles' edges parallel to the load direction. Such a decrease in localised stress values can prevent the premature failure of the composite material. In order to better understand the impact of silica or polyimide density on epoxy' compressive modulus, Figure 6-45 has been plotted, presenting reduction in compressive modulus of epoxy and low density polyimide or silica composites as a function of composites density.

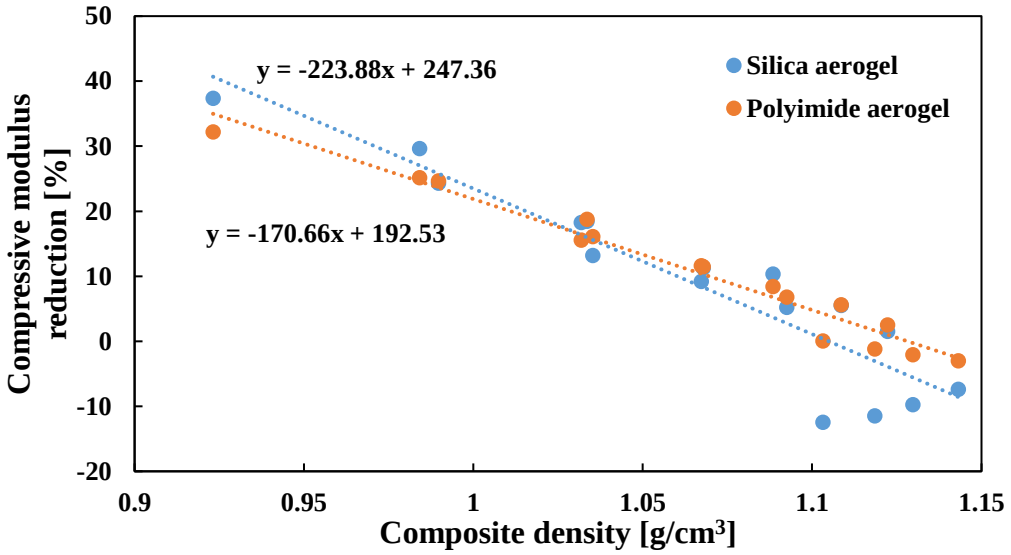

Figure 6-45 Compressive modulus of epoxy and low density polyimide or silica composites as a function of composites density.

Figure 6-45 indicates that composites prepared with silica and polyimide particles present slightly different compressive modulus values at the same density. As a result, the silica composite is more susceptible to compressive modulus degradation when using low-density particles. Nevertheless, when increasing particle density beyond 1.03 g/cm^3, the silica composites commence presenting superior compressive modulus, further increasing above the pure matrix modulus values. On the other hand, the composites prepared with polyimide particles are superior in low-density scenarios. Nevertheless, they barely affect the compressive modulus values when high-density particles are used. Such phenomena can be explained by analysing the internal structure of both particle types at various densities. As

discussed in Chapter 6.3.4.3, at low particle density, silica presents much lower compressive modulus and strength values mainly due to higher porosity and brittleness of parent material. The addition of such particles blocks the load transfer mechanism and hamper composites' compressive properties. A similar impact is achieved with polyimide. However, with better mechanical properties at low densities, it is not as detrimental. With the increasing density of particles, their internal structure changes and starts to resemble the internal structure of parental materials. In the case of silica, the increase in density rapidly increases compressive modulus and strength of the material even up to 160 GPa when pure amorphous silica is reached [544]. On the other hand, the polyimide is a much more ductile material and presents a modulus between 2.5 and 9.3 GPa [541]. As a result, the increase in particle density yields a much more significant impact on composites prepared with low density silica, finally leading to the strengthening mechanism. The improvement in mechanical properties of epoxy resin with the addition of silica particles behaviour has been observed in the experimental work by Yamamoto et al., who incorporated crystalline and amorphous silica particles into epoxy resin and achieved significant improvement in both values [545]. Preghenella et al. used fumed silica particles and found out almost 25% improvement in tensile modulus of epoxy resin when adding 30 vol% of particles [249]. Nevertheless, a decrease in modulus values was noticed when using lower volume fraction of silica particles [249]. Hamid et al. investigated the mechanical properties of epoxy composites reinforced with amorphous and crystalline silica using a 3-point bending test. The results indicated significant improvement in epoxy modulus of elasticity and modulus of rupture when amorphous silica particles were added [546].

6.4 Summary

This chapter presents the microscale characterisation of epoxy composites prepared with low density silica and polyimide particles via finite element analysis.

Firstly, the MATLAB script was used to randomly distribute spherical particles inside the resin cube, and the results were imported into ANSYS software to replicate the materials' internal structure. Afterwards, the material properties were assigned to composites' constituents as achieved from the molecular dynamics study. Finally, modelled material samples have been subjected to thermal flux and compressive displacement, allowing replicating thermal and mechanical testing techniques. Model verification and validation were conducted by analysing the dependency of investigated properties upon mesh quality or testing parameters. Furthermore, the comparison with experimental results presented in previous sections of this thesis has also been performed. Overall, validation revealed the model's good accuracy when predicting composites' thermal conductivity and a compressive modulus. However, due to the

steady-state mechanical analysis performed, the model could not accurately capture changes in compressive strength. The incorporation of thermal and mechanical properties of both particle types from molecular dynamics study allowed to investigate further the energy and load transfer mechanisms inside particulate composites. As a result, the impact of particle size and density on composites' thermal and mechanical properties has been analysed.

As a result, the analysis of particle size impact on thermal conductivity of epoxy composites revealed lower thermal conductivity values achieved when incorporating low density silica particles regardless of their size. Such finding was mainly attributed to better thermal insulating properties of low density silica when compared with polyimide counterpart. Additionally, the smallest particles were the most effective in reducing thermal conductivity values mainly due to the larger number of particles incorporated, creating a barrier for energy transfer and reducing the number of direct paths through the composite. Particles' density was also found to be an important factor affecting the thermal conductivity of epoxy composites. With increasing particle density, the particles become less effective insulators, and larger heat flux values across them are noticed. The results also indicate that with increasing particle density, the incremental impact on the material's thermal property is decreasing. Such results suggest that the external phenomena that might affect the density (or porosity) of the particles (such as pore infiltration during manufacturing) are more severe to low-density particles. The mechanical results obtained in this study strongly suggest that the addition of low density particles hinders the compressive properties of epoxy resin. This behaviour is attributed to the much lower mechanical properties of particles than the epoxy resin. Nevertheless, the composites created with low density PI particles present a much smaller reduction in compressive modulus than one created with low density silica. Such behaviour was explained by higher elastic modulus and yield strength of polyimide particles resulting in much better stress bearing properties. Overall, the particle size had little effect on the compressive modulus of simulated composites. On the other hand, the particle density was found to substantially affect the compressive properties of epoxy composites with denser particles producing composites with higher compressive modulus and strength values. The density analysis has also revealed that low density silica composites are more susceptible to compressive modulus degradation at lower particle loading but provide superior compressive properties in comparison to epoxy and polyimide composites at higher densities. Finally, the simulated values have also been compared to the experimental results from Chapter 3 revealing some discrepancies between them. As a result, the model tends to overestimate the impact of low density particles on epoxy thermal conductivity while underestimating their impact on epoxy compressive properties. Both phenomena were attributed to the inability of the model to

capture the effects of the physical phenomena occurring during sample manufacturing such as pore infiltration or particle crushing as well as the idealistic approach of the FEA model in regards to the particle shape.

7 Conclusions and Future work

In the following chapter, an overview of conclusions drawn from this thesis is present. Additionally, the outline of future work allowing further improvement of aerogel composites based on a conducted investigation is proposed.

7.1 Conclusion of the thesis

The aerogel composites are facing significant challenges before they can be broadly incorporated into real-life applications. They are substantially hindered by the lack of understanding of interactions between comprising materials. Therefore, the primary goal of this thesis was to provide a better insight into the interactions between aerogels and the most common reinforcement materials with the use of multiscale modelling and micromechanical testing. Additionally, the aerogel influence on the various properties of polymer matrices is investigated, allowing for the broader incorporation of aerogel type materials into future projects. To fulfil the goal of this thesis, the following objectives have been formulated:

1. To experimentally investigate the effect of aerogel particles on the mechanical and thermal properties of epoxy and vinyl ester.
2. To investigate the interfacial adhesion of aerogel fibrous composites using micromechanical testing methods.
3. To use the multiscale modelling approach to study silica and polyimide aerogels' thermal and mechanical properties and their interactions with reinforcement materials.

7.1.1 Thermomechanical characterisation of aerogel particulate composites

This work had revealed that the addition of silica aerogel particles facilitated a significant reduction in epoxy and vinyl ester thermal conductivity, providing approximately a 40% reduction in thermal conductivity of both when a particle loading of 5 wt% was applied. Additionally, it was also found that the largest particles tend to reduce thermal conductivity the most, while polyimide aerogel particles had negligible effects. The superior performance of large particles has been attributed to their lower surface-to-volume ratio resulting in lower pore infiltration when compared with smaller particles. Nevertheless, the superior thermal properties were also associated with a decrease in composites' compressive properties. It was found that the compressive yield strength and compressive modulus of the aerogel filled composites decrease with increasing aerogel content resulting in as much as 56% reduction in compressive properties of epoxy and 42% of vinyl ester. Additionally, no significant differences in compressive properties has been found between composites manufactured with

varying sizes of silica aerogel particles. On the other hand, the composites created with polyimide aerogel particles presented a much smaller reduction in composites' compressive properties when compared with silica aerogel particles.

Thermomechanical properties of aerogel filled composites have also been under investigation. It was revealed that in the case of both epoxy and vinyl ester resin, their coefficients of thermal expansion decrease with increasing particle content. The main reason behind such behaviour was low intrinsic CTEs of the aerogels and the interface region between resin and aerogel, restricting the mobility of polymers chains surrounding aerogel particles. What is more, the size and type of aerogel particles used yielded no impact on the CTE values of created composites materials.

When analysing the glass transition temperature both TMA and DMA have been used, with TMA indicating that the addition of low quantities of aerogel particles can increase the glass transition temperature of both epoxy and vinyl ester while the DMA results suggesting that the aerogel particles can only decrease T_g. After initial difference, the results obtained through both methods followed the same trend with decreasing glass transition temperature with increasing aerogel content. The initial difference between both techniques was attributed to uneven heating rates, various arrangement of temperature sensors and the influence of sample sizes leading to lag in the measured temperature of the sample. In case of polyimide aerogel both TMA and DMA indicated increase in T_g following the addition of particles. Regardless of aerogel type the addition of particles reduced the storage modulus of polymer resins.

Finally, the impact of aerogel particles on the heat distortion temperature of both resins was investigated. As a result, for both epoxy and vinyl ester the HDT increase at low loading scenarios and further addition of particles leading to a linear decrease in HDT. Since HDT is principally a function of sample stiffness and T_g, it is suspected that initial increase in HDT values might correspond to the increase in polymers' T_g values as presented by TMA. Further, linear decrease in the HDT values with addition of more aerogel particles might results from decreasing stiffness of the composites manufactured with high aerogel loading. On the other hand, PI aerogel particles' introduction has achieved different results with much larger increase in heat distortion temperature recorded than for any of the silica aerogel composites.

7.1.2 Mechanical characterisation of aerogel and fibre interface

In this work, the visual observation of microdroplet formation indicated a large shrinkage of polyimide aerogel in a curing and silica aerogel in the drying phase. Alongside the microbond sample preparation, the bulk silica and polyimide aerogel samples have also been created. The

investigation of aerogels' internal structure via BET and MIP methods have proved the good quality of both aerogels with porosity exceeding 80% and other properties in a similar range as commercially available products. The micromechanical analysis was conducted following the microbond test procedure with samples subjected to visual inspection and AFM scanning upon test completion. As a result, the microbond test revealed that both silica and polyimide aerogel present relatively poor adhesion to various fibres with average IFSS not exceeding 2.5 MPa. In addition, polyimide aerogel presented superior adhesion to all tested fibre types, which was mainly attributed to larger shrinkage during curing and more significant difference in heat expansion coefficient, which both contributed to larger residual stresses. In the case of silica aerogel, the material shear properties could be a limiting factor leading to cohesive matrix failure. Finally, the samples prepared with carbon fibre were characterised with the largest IFSS values. Such behaviour can be attributed to its geometrical features, such as high surface roughness and small diameter. Nevertheless, the superior adhesion of aerogels to carbon fibre could also result from the difference in the sample size, which would be responsible for different internal structure and sample test behaviour.

7.1.3 Nanoscale interface simulation

Following the sample validation, a range of silica and polyimide samples with varying densities has been created and a correlation between density and thermal, tensile, and compressive properties has been derived. The low density silica has proved to have better insulating properties than the polyimide counterpart in terms of thermal conductivity. The internal structure of both materials has been identified as the main reason for such behaviour. When analysing low density silica and polyimide tensile and compressive properties, a good correlation between simulated and experimental results has been identified for low density silica. On the other hand, a significant discrepancy can be noticed for low density polyimide samples for which especially modulus values were a few orders higher than data presented in experimental studies. Such discrepancies were mainly caused by utilisation of too small simulation volume for polyimide. By creating the model matching computational resources, the samples failed to precisely replicate the internal structure of low density polyimide resulting in overestimating the material’s modulus.

Furthermore, the low density silica and polyimide samples have been combined with two reinforcement systems, including amorphous silica and epoxy resin. As a result, for the first time, the effect of silica and polyimide density upon both interfacial thermal resistance and interfacial shear strength was calculated. When imposing the heat flux through the simulated interfaces an extremely small thermal resistance values in a range of 10^{-8} Km^2/W have been

achieved. Such values were still within the expected range and were in a good correlation with the values obtained from the literature. In addition, all the interfaces have followed a similar trend with decreasing thermal interfacial resistance with increasing density. Such behaviour was associated with an increasing number of silica and polyimide atoms being in direct contact with the atoms of the reinforcement sample when denser samples were utilised. The investigation has also suggested that the low density silica samples present lower interfacial thermal resistance than polyimide samples when combined with the same reinforcement.

Finally, the interfacial mechanical properties of created interfaces have been simulated by shearing two parallel surfaces of different materials. The comparison of results reported in this study presented a good fit with previously simulated interfaces, but not with the experimental results obtained through the microbond experiments. The results suggested that all four interfaces follow the same trend of decreasing IFSS values with decreasing aerogel density. This was mainly associated with the decreasing number of bonds created between reinforcement and silica or polyimide atoms when lower density samples have been used. Nevertheless, there was a significant discrepancy in IFSS values of various interfaces with a silica-silica interface providing the highest IFSS values when high-density samples were used. The polymer-silica interface was simulated to be stronger at a low-density value, while the polymer-polymer interface provided the lowest value across almost the whole density range. The resulting IFSS discrepancies have been attributed to the current state of the molecular dynamic simulations being unable to correctly model the mechanical response of the materials and their interfaces.

7.1.4 Microscale modelling of polymer-based particulate composites

The nanoscale results have been incorporated into finite element analysis of epoxy composites prepared with low density silica and polyimide particles. The model was created by using MATLAB script to distribute spherical particles inside the resin cube randomly. Upon importing into ANSYS, the material properties were assigned to composites' constituents as the molecular dynamics study achieved. Modelled material samples have been subjected to thermal flux and compressive displacement, allowing replicating thermal and mechanical testing techniques. Model verification and validation revealed good accuracy when predicting composites' thermal conductivity and a compressive modulus. However, due to the steady-state mechanical analysis performed, the model could not accurately capture changes in compressive strength.

The created model allowed the investigation of the impact of particle size and density on composites' thermal and mechanical properties. As a result, the analysis of particle size impact

on thermal conductivity of epoxy composites revealed lower thermal conductivity values achieved when incorporating low density silica rather than polyimide particles regardless of their size. Additionally, the smallest particles were the most effective in reducing thermal conductivity values mainly due to the larger number of particles incorporated, creating a barrier for energy transfer and reducing the number of direct paths through the composite. Particles' density was also found to be an important factor affecting the thermal conductivity of epoxy composites. With increasing particle density, the particles became less effective insulators, and larger heat flux values were noticed across the samples.

The results of modelling of mechanical results obtained in this study strongly suggest that the addition of low density silica or polyimide particles hinders the compressive properties of epoxy resin. Nevertheless, the composites created with low density PI particles present a much smaller reduction in compressive modulus than one created with low density silica. Overall, the particle size had little effect on the compressive modulus of simulated composites. On the other hand, the particle density was found to substantially affect the compressive properties of epoxy composites, with denser particles producing composites with higher compressive modulus and strength values. The density analysis has also revealed that low density silica composites are more susceptible to compressive modulus degradation. Finally, the simulated values have also been compared to the experimental results from Chapter 3 revealing some discrepancies between them. As such, the model tends to overestimate the impact of low density particles on epoxy thermal conductivity while underestimating their impact on epoxy compressive properties.

7.2 Future Work

This study was focusing on tackling the issues facing aerogel composites. Regardless of the progress made, a wide range of improvements can be introduced, facilitating the use of those type of materials. As a result, the following chapters highlight the future work that the author believes might help increase the understanding of aerogel composites.

7.2.1 Thermomechanical characterisation of aerogel particulate composites

Even though this investigation has defined a wide range of thermal, mechanical and thermomechanical properties of epoxy and vinyl ester-based composites, there is still much uncertainty regarding aerogel-filled polymers.

Firstly, a better understanding of the internal structure of such composites should be achieved. As a result, a series of transition electron microscopy, FTIR, elemental mapping, or micro-computed tomography should be conducted. It would be interesting to combine such

investigations with the matrix viscosity investigation performed in this study, allowing to understand the pore infiltration phenomena. Additionally, a more detailed characterisation of the internal structure could improve the current understanding of the aerogel-filled composites' load and heat transfer behaviour. Finally, the FTIR spectrums could identify the chemical interactions between composites constituents and possibly relate them to the bulk material properties.

Secondly, a comparison between various aerogel filled polymer composites manufacturing processes could be undertaken. By comparing an already wide range of manufacturing techniques, identifying the most effective one could broaden the usage of aerogel composites. Such a study would have to consider a wider range of parameters, including the easiness of application, preservation of aerogel pores, and resulting composite properties. In addition, a more comprehensive range of material combinations could be investigated. This study was only limited to polymer-based matrices; nevertheless, very little study has been performed to understand the impact of aerogel particles on ceramics or metal matrix systems. In terms of aerogels the organic, carbon or single element aerogels could also be used. Finally, regardless of the aerogel type, the particle geometrical features' impact should also be further investigated. This study has only focused on varying particle size, however other features such as particle shape or surface roughness could also impact the bulk material properties.

7.2.2 Mechanical characterisation of aerogel and fibre interface

Since it was the first time the micromechanical investigation of aerogel adhesion was conducted, a wide range of improvements and future work can be suggested.

Firstly, this investigation suggested that similar samples have to be prepared to use microbond results for comparison purposes. As a result, future studies could focus on deriving the sample manufacturing methods to prepare samples with identical external geometries and internal structures. Even though the lengthy and complicated process of silica aerogel synthesis is extremely hard to control, only with uniform samples the impact of investigated factors on interfacial adhesion can be measured. This could even imply using the different micromechanical testing procedure, allowing for a different sample shape.

Secondly, the impact of fibre surface chemistry on the aerogel adhesion properties could be evaluated. Even though this study focused on various fibres, the possibility of enhancing aerogel adhesion properties by means of fibre sizing has not been examined at all. The future study in the initial stages could focus on utilising commercially available fibres with pre-applied sizing with further aspects of developing the sizing specifically for aerogel type of

materials. Such investigation could also be applied to a wider range of aerogel and fibre combinations than presented in this study. The silica aerogel is currently the most popular aerogel type for the production of aerogel blankets. However, the interfacial study of other aerogel types such as carbon, polyimide and other oxide aerogels used could promote their incorporation into aerogel composites.

Finally, the future study could also focus on relating the aerogel interfacial adhesion with the mechanical performance of aerogel blankets. Since the measurement of aerogel interfacial properties yields minimal impact on understanding the mechanical performance of the whole composite. In addition, further investigation into the physical nature of the aerogel interface could also be related to understanding the interfacial mechanism of other porous matrices such as cement.

7.2.3 Nanoscale interface analysis

The conducted nanoscale investigation focused on the impact of aerogel density and thus porosity on the mechanical, thermal, and interfacial properties of aerogel.

Firstly, future work should focus on more accurate replication of the polyimide aerogel. The simulated volume used in this study has proven to be too small to capture the polyimide aerogel internal structure adequately. As a result, the incorporation of larger computational resources could allow for a more accurate investigation of polyimide aerogel properties. Additionally, future work could focus on the validation of molecular dynamics results via experimental means. The incorporation of increasingly popular nanoscale techniques could provide results much more applicable to the simulated length scale. The comparison between experimental and simulation results could also suggest a potential area of improvement for created MD models.

Secondly, the future study could evaluate the impact of the material temperature on composites' properties as those materials are widely used in extreme temperature condition. The understanding of the temperature influence on especially interfacial properties could allow for better aerogel and reinforcement combinations. In addition, future work could also be focusing on the investigation of the fibre/ particle sizing on the interfacial properties of the aerogel composites. By incorporation of a layer of sizing atoms on the reinforcement surface, the impact of various chemical sizing could be evaluated before introducing experimental testing.

Finally, a better correlation of nanoscale results with higher scale simulations should also be established. Currently, molecular dynamics simulations can be useful to investigate a wide

range of effects on the nanoscale. Nevertheless, there is no straightforward coupling mechanism allowing for the direct incorporation of MD results into higher scale models. The derivation of such mechanisms could potentially increase the usefulness of nanoscale simulations to a wider range of engineering community.

7.2.4 Microscale characterisation of polymer-based particulate composites

This study has created a microscale model that estimates the thermal conductivity and compressive modulus of aerogel filled polymers. Nevertheless, the overshooting of composites' yield strength was also noticed. As a result, the micromechanical model could be improved by incorporating a transient compressive test or the nonlinear material analysis to capture the material's yield point. In addition, upon introducing such changes, the same model could be used to investigate the tensile properties of aerogel and polymer composites. In addition, this model has been only validated for the most studied epoxy and silica aerogel composites. However, to prove its' versatility, the additional validation incorporating other types of aerogels and the matrices should be conducted. Such study could incorporate organic, carbon or single element aerogels and consider non-polymeric matrix types, including ceramics or hybrid matrices.

Besides overcoming the limitations of the current model, further study could also look into the effects of the interface volume. In the current study, the interface was assumed as a surface of the particle with certain properties. However, by altering the thickness of the interface region, a more detailed investigation of the interface impact on the aerogel filled composites could be measured. In addition, with the incorporation of a few more material properties or changes in sample geometry, the model could be used to evaluate other properties of aerogel composites. Except for previously mentioned tensile properties, the model could focus on a wider range of mechanical properties such as shear or bending and some thermomechanical properties, including coefficient of thermal expansion. Finally, the material properties achieved from the micromechanical model should be transferred to higher scale models. The bulk material properties could be directly inputted into the macroscale simulations without explicitly modelling the internal structure of the composite material. Such an approach would require less computational resources to complete simulations and further progress the idea of multiscale modelling.

References

[1] H. Maleki, "Recent advances in aerogels for environmental remediation applications: a review," *Chemical Engineering Journal,* vol. 300, pp. 98-118, 2016.

[2] S. Kistler, "Coherent expanded-aerogels," *The Journal of Physical Chemistry,* vol. 36, no. 1, pp. 52-64, 1932.

[3] T. Graham, "On the properties of silicic acid and other analogous colloidal substances," *Journal of the Chemical Society,* vol. 17, pp. 318-327, 1864.

[4] G. Pajonk, "Transparent silica aerogels," *Journal of Non-Crystalline Solids,* vol. 225, pp. 307-314, 1998.

[5] T. Woignier, J. Phalippou, and J. Zarzycki, "Monolithic aerogels in the systems SiO_2/B_2O_3, SiO_2/P_2O_5, $SiO_2/B_2O_3/P_2O_5$," *Journal of Non-Crystalline Solids,* vol. 63, no. 1-2, pp. 117-130, 1984.

[6] S. Teichner, "Aerogels of inorganic oxides," in *Aerogels*: Springer, 1986, pp. 22-30.

[7] R. Pekala, "Organic aerogels from the polycondensation of resorcinol with formaldehyde," *Journal of materials science,* vol. 24, no. 9, pp. 3221-3227, 1989.

[8] R. Pekala, S. Mayer, J. Kaschmitter, and F. Kong, "Carbon aerogels: an update on structure, properties, and applications," in *Sol-Gel Processing and Applications*: Springer, 1994, pp. 369-377.

[9] I. Mejri, M. K. Younes, and A. Ghorbel, "Comparative study of the textural and structural properties of the aerogel and xerogel sulphated zirconia," *Journal of sol-gel science and technology,* vol. 40, no. 1, pp. 3-8, 2006.

[10] Y. Suzuki *et al.*, "Synthesis and Microstructure Of A Novel TiO_2 Aerogel–TiO_2 Nanowire Composite," *Nano,* vol. 3, no. 05, pp. 373-379, 2008.

[11] Q. Yao, I. U. Arachchige, and S. L. Brock, "Expanding the repertoire of chalcogenide nanocrystal networks: Ag_2Se gels and aerogels by cation exchange reactions," *Journal of the American Chemical Society,* vol. 131, no. 8, pp. 2800-2801, 2009.

[12] M. Aegerter, N. Leventis, and M. M. Koebel, *Aerogels handbook*. Springer Science & Business Media, 2011.

[13] V. Morales-Flórez, J. Toledo-Fernández, N. De la Rosa-Fox, M. Piñero, and L. Esquivias, "Percolation of the organic phase in hybrid organic–inorganic aerogels," *Journal of sol-gel science and technology,* vol. 50, no. 2, pp. 170-175, 2009.

[14] V. Drach, M. Wiener, G. Reichenauer, H. P. Ebert, and J. Fricke, "Determination of the anisotropic thermal conductivity of a carbon aerogel–fiber composite by a non-contact thermographic technique," *International Journal of Thermophysics,* vol. 28, no. 5, pp. 1542-1562, 2007.

[15] E. Baudrin, G. Sudant, D. Larcher, B. Dunn, and J.-M. Tarascon, "Preparation of nanotextured VO_2 [B] from vanadium oxide aerogels," *Chemistry of materials,* vol. 18, no. 18, pp. 4369-4374, 2006.

[16] H. Lu, H. Luo, S. Mulik, L. Sotiriou-Leventis, and N. Leventis, "Compressive behavior of crosslinked mesoporous silica aerogels at high strain rates," *Conference proceedings of 11th International Congress and Exhibition on Experimental and Applied Mechanics,* 2008.

[17] S. S. Latthe, D. Y. Nadargi, and A. V. Rao, "TMOS based water repellent silica thin films by co-precursor method using TMES as a hydrophobic agent," *Applied Surface Science,* vol. 255, no. 6, pp. 3600-3604, 2009.
[18] D. L. Plata *et al.*, "Aerogel-platform optical sensors for oxygen gas," *Journal of Non-crystalline solids,* vol. 350, pp. 326-335, 2004.
[19] S. Steinbach and L. Ratke, "The microstructure response to fluid flow fields in Al-cast alloys," *Trans. Indian Inst. Metals,* vol. 60, pp. 167-171, 2007.
[20] H. Nagahara, T. Suginouchi, and M. Hashimoto, "P1M-8 Acoustic Properties of Nanofoam and its Applied Air-Borne Ultrasonic Transducers," in *2006 IEEE Ultrasonics Symposium*, 2006, pp. 1541-1544: IEEE.
[21] J. Long, A. Fischer, T. McEvoy, M. Bourg, J. Lytle, and D. Rolison, "Self-limiting electropolymerization en route to ultrathin, conformal polymer coatings for energy storage applications," *PMSE Prepr,* vol. 99, pp. 772-773, 2008.
[22] A. Santos, M. Ajbary, J. A. Toledo-Fernández, V. Morales-Flórez, A. Kherbeche, and L. Esquivias, "Reactivity of CO_2 traps in aerogel–wollastonite composites," *Journal of sol-gel science and technology,* vol. 48, no. 1-2, pp. 224-230, 2008.
[23] T. Woignier *et al.*, "The use of silica aerogels as host matrices for chemical species: Different ways to control the permeability and the mechanical properties," *Journal of non-crystalline solids,* vol. 350, pp. 299-307, 2004.
[24] U. Bauer *et al.*, "Aerogel particles and methods of making same," ed: Google Patents, 2012.
[25] A. C. Pierre, "History of aerogels," in *Aerogels Handbook*: Springer, 2011, pp. 3-18.
[26] J. K. Lee, G. L. Gould, and W. Rhine, "Polyurea based aerogel for a high performance thermal insulation material," *Journal of sol-gel Science and Technology,* vol. 49, no. 2, pp. 209-220, 2009.
[27] Z. Li, X. Cheng, S. He, X. Shi, L. Gong, and H. Zhang, "Aramid fibers reinforced silica aerogel composites with low thermal conductivity and improved mechanical performance," *Composites Part A: Applied Science and Manufacturing,* vol. 84, pp. 316-325, 2016.
[28] J. Jaxel, G. Markevicius, A. Rigacci, and T. Budtova, "Thermal superinsulating silica aerogels reinforced with short man-made cellulose fibers," *Composites Part A: Applied Science and Manufacturing,* vol. 103, pp. 113-121, 2017.
[29] J. I. Gurav JL, Park H, Kang ES, Nadargi DY, "Silica Aerogel: Synthesis and Applications," *Journal of nanomaterials,* vol. 2010, 2010.
[30] H. Lee *et al.*, "Super-insulating, flame-retardant, and flexible poly (dimethylsiloxane) composites based on silica aerogel," *Composites Part A: Applied Science and Manufacturing,* vol. 123, pp. 108-113, 2019.
[31] R. Yin, H. Cheng, C. Hong, and X. Zhang, "Synthesis and characterization of novel phenolic resin/silicone hybrid aerogel composites with enhanced thermal, mechanical and ablative properties," *Composites Part A: Applied Science and Manufacturing,* vol. 101, pp. 500-510, 2017.
[32] H. M. Kim, Y. J. Noh, J. Yu, S. Y. Kim, and J. R. Youn, "Silica aerogel/polyvinyl alcohol (PVA) insulation composites with preserved aerogel pores using interfaces between the superhydrophobic aerogel and hydrophilic

PVA solution," *Composites Part A: Applied Science and Manufacturing,* vol. 75, pp. 39-45, 2015.
[33] N. Gupta and W. Ricci, "Processing and compressive properties of aerogel/epoxy composites," *Journal of materials processing technology,* vol. 198, no. 1-3, pp. 178-182, 2008.
[34] J. Fricke, *Aerogels: Proceedings of the First International Symposium, Würzburg, Fed. Rep. of Germany September 23–25, 1985*. Springer Science & Business Media, 2012.
[35] A. Jain *et al.*, "Processing dependent thermal conductivity of nanoporous silica xerogel films," *Journal of applied physics,* vol. 91, no. 5, pp. 3275-3281, 2002.
[36] T. Woignier, J. Reynes, A. H. Alaoui, I. Beurroies, and J. Phalippou, "Different kinds of structure in aerogels: relationships with the mechanical properties1," *Journal of Non-Crystalline Solids,* vol. 241, no. 1, pp. 45-52, 1998.
[37] J. Groβ and J. Fricke, "Scaling of elastic properties in highly porous nanostructured aerogels," *Nanostructured Materials,* vol. 6, no. 5-8, pp. 905-908, 1995.
[38] A. A. Anappara, S. Rajeshkumar, P. Mukundan, P. Warrier, S. Ghosh, and K. Warrier, "Impedance spectroscopic studies of sol–gel derived subcritically dried silica aerogels," *Acta Materialia,* vol. 52, no. 2, pp. 369-375, 2004.
[39] A. V. Rao, M. M. Kulkarni, D. Amalnerkar, and T. Seth, "Superhydrophobic silica aerogels based on methyltrimethoxysilane precursor," *Journal of Non-Crystalline Solids,* vol. 330, no. 1-3, pp. 187-195, 2003.
[40] J. Fricke and A. Emmerling, "Aerogels—Preparation, properties, applications," in *Chemistry, Spectroscopy and Applications of Sol-Gel Glasses*: Springer, 1992, pp. 37-87.
[41] N. Ishizuka *et al.*, "Performance of a monolithic silica column in a capillary under pressure-driven and electrodriven conditions," *Analytical Chemistry,* vol. 72, no. 6, pp. 1275-1280, 2000.
[42] A. S. Dorcheh and M. Abbasi, "Silica aerogel; synthesis, properties and characterization," *Journal of materials processing technology,* vol. 199, no. 1-3, pp. 10-26, 2008.
[43] H. Tamon, T. Sone, and M. Okazaki, "Control of mesoporous structure of silica aerogel prepared from TMOS," *Journal of colloid and interface science,* vol. 188, no. 1, pp. 162-167, 1997.
[44] B. Karmakar, G. De, and D. Ganguli, "Dense silica microspheres from organic and inorganic acid hydrolysis of TEOS," *Journal of non-crystalline solids,* vol. 272, no. 2-3, pp. 119-126, 2000.
[45] F. Kirkbir, H. Murata, D. Meyers, and S. R. Chaudhuri, "Drying of aerogels in different solvents between atmospheric and supercritical pressures," *Journal of non-crystalline solids,* vol. 225, pp. 14-18, 1998.
[46] P. Dieudonné, A. H. Alaoui, P. Delord, and J. Phalippou, "Transformation of nanostructure of silica gels during drying," *Journal of non-crystalline solids,* vol. 262, no. 1-3, pp. 155-161, 2000.
[47] J. Chandradass, S. Kang, and D. S. Bae, "Synthesis of silica aerogel blanket by ambient drying method using water glass based precursor and glass wool modified by alumina sol," *Journal of Non-Crystalline Solids,* vol. 354, no. 34, pp. 4115-4119, 2008.

[48] M. Titulaer, J. Jansen, and J. Geus, "Fluid composition effects on silica gel aging," *Journal of non-crystalline solids,* vol. 170, no. 1, pp. 11-20, 1994.
[49] S. Hæreid, E. Nilsen, and M. A. Einarsrud, "Properties of silica gels aged in TEOS," *Journal of Non-Crystalline Solids,* vol. 204, no. 3, pp. 228-234, 1996.
[50] K. Chou and B. Lee, "Solvent effect on ageing of silica gels," *Journal of materials science,* vol. 29, no. 13, pp. 3565-3571, 1994.
[51] S. Smitha, P. Shajesh, and K. Warrier, "Investigations on the effect of experimental parameters on the porosity features of silica aerogels synthesized at ambient drying conditions," *Materials Chemistry and Physics,* vol. 131, no. 1-2, pp. 507-511, 2011.
[52] C. García-González, M. Camino-Rey, M. Alnaief, C. Zetzl, and I. Smirnova, "Supercritical drying of aerogels using CO_2: Effect of extraction time on the end material textural properties," *The Journal of Supercritical Fluids,* vol. 66, pp. 297-306, 2012.
[53] J. Alemán *et al.*, "Definitions of terms relating to the structure and processing of sols, gels, networks, and inorganic-organic hybrid materials (IUPAC Recommendations 2007)," *Pure and Applied Chemistry,* vol. 79, no. 10, pp. 1801-1829, 2007.
[54] D. M. Smith, D. Stein, J. M. Anderson, and W. Ackerman, "Preparation of low-density xerogels at ambient pressure," *Journal of Non-Crystalline Solids,* vol. 186, pp. 104-112, 1995.
[55] R. Kocklenberg *et al.*, "Texture control of freeze-dried resorcinol–formaldehyde gels," *Journal of Non-Crystalline Solids,* vol. 225, pp. 8-13, 1998.
[56] M. PERRUT and E. FRANÇAIS, "Aerogel Drying," *State of the art book on Supercritical Fluids,* vol. 4, pp. 129-134, 2004.
[57] Y. Tao, M. Endo, and K. Kaneko, "A review of synthesis and nanopore structures of organic polymer aerogels and carbon aerogels," *Recent Patents on Chemical Engineering,* vol. 1, no. 3, pp. 192-200, 2008.
[58] C. Simón-Herrero, X. Y. Chen, M. L. Ortiz, A. Romero, J. L. Valverde, and L. Sánchez-Silva, "Linear and crosslinked polyimide aerogels: synthesis and characterization," *Journal of Materials Research and Technology,* vol. 8, no. 3, pp. 2638-2648, 2019.
[59] P. A. Farrar, "Low dielectric constant shallow trench isolation," ed: Google Patents, 2004.
[60] M. A. B. Meador *et al.*, "Polyimide aerogels with amide cross-links: a low cost alternative for mechanically strong polymer aerogels," *ACS applied materials & interfaces,* vol. 7, no. 2, pp. 1240-1249, 2015.
[61] J. G. Liu, X. M. Zhang, F. X. Chen, W. S. Tong, and Y. H. Zhang, "A Review on Recent Progress of Research and Application for Polyimide Aerogels," *Synthesis, Application and Research* p. 105, 2017.
[62] S. G. Mosanenzadeh, Z. Saadatnia, S. Karamikamkar, C. B. Park, and H. E. Naguib, "Polyimide aerogels with novel bimodal micro and nano porous structure assembly for airborne nano filtering applications," *RSC Advances,* vol. 10, no. 39, pp. 22909-22920, 2020.
[63] C. Chidambareswarapattar, Z. Larimore, C. Sotiriou-Leventis, J. T. Mang, and N. Leventis, "One-step room-temperature synthesis of fibrous polyimide aerogels from anhydrides and isocyanates and conversion to isomorphic

carbons," *Journal of Materials Chemistry,* vol. 20, no. 43, pp. 9666-9678, 2010.
[64] H. Guo *et al.*, "Tailoring Properties of Cross-Linked Polyimide Aerogels for Better Moisture Resistance, Flexibility, and Strength," *ACS Applied Materials & Interfaces,* vol. 4, no. 10, pp. 5422-5429, 2012.
[65] H. Guo *et al.*, "Polyimide aerogels cross-linked through amine functionalized polyoligomeric silsesquioxane," *ACS applied materials & interfaces,* vol. 3, no. 2, pp. 546-552, 2011.
[66] M. A. B. Meador *et al.*, "Mechanically strong, flexible polyimide aerogels cross-linked with aromatic triamine," *ACS applied materials & interfaces,* vol. 4, no. 2, pp. 536-544, 2012.
[67] R. M. German, *Particulate Composites*. Springer, 2016.
[68] J. R. Kelly, I. Nishimura, and S. D. Campbell, "Ceramics in dentistry: historical roots and current perspectives," *The Journal of prosthetic dentistry,* vol. 75, no. 1, pp. 18-32, 1996.
[69] J. P.-S. Elorz, J. Verdeja-González, J. Sancho-Martinez, and N. Vilela, "Melting and sintering platinum in the 18th Century: the secret of the Spanish," *JOM,* vol. 51, no. 10, pp. 9-13, 1999.
[70] M. Balasubramanian, *Composite materials and processing*. CRC press, 2013.
[71] W. D. Kingery, "Sintering from prehistoric times to the present," in *Solid State Phenomena*, 1992, vol. 25, pp. 1-10: Trans Tech Publ.
[72] J. V. Milewski and H. S. Katz, "Handbook of reinforcements for plastics," 1987.
[73] D. Bigg and S. Bhattacharya, "Metal filled polymers," *ed. Bhattacharya SK, Marcel Dekker, New York,* vol. 615, 1986.
[74] F. Carmona, "Conducting filled polymers," *Physica A: Statistical Mechanics and its Applications,* vol. 157, no. 1, pp. 461-469, 1989.
[75] F. Hussain, M. Hojjati, M. Okamoto, and R. E. Gorga, "Polymer-matrix nanocomposites, processing, manufacturing, and application: an overview," *Journal of composite materials,* vol. 40, no. 17, pp. 1511-1575, 2006.
[76] K. K. Chawla, *Composite materials: science and engineering*. Springer Science & Business Media, 2012.
[77] C. A. Harper, *Handbook of plastics, elastomers, and composites*. McGraw-Hill New York, 2002.
[78] T. Clyne and P. Withers, *An introduction to metal matrix composites*. Cambridge university press, 1995.
[79] K. K. Chawla, "Metal matrix composites," in *Composite Materials*: Springer, 2012, pp. 197-248.
[80] I. Ibrahim, F. Mohamed, and E. Lavernia, "Particulate reinforced metal matrix composites—a review," *Journal of materials science,* vol. 26, no. 5, pp. 1137-1156, 1991.
[81] K. K. Chawla, *Ceramic matrix composites*. Springer Science & Business Media, 2013.
[82] A. G. Evans and D. B. Marshall, "The mechanical behavior of ceramic matrix composites," in *Proceedings of The 7th International Conference On Fracture (ICF7)*, 1989, pp. 3593-3641: Elsevier.

[83] J. P. Zhao, D. T. Ge, S. L. Zhang, and X. L. Wei, "Studies on thermal property of silica aerogel/epoxy composite," in *Materials science forum*, 2007, vol. 546, pp. 1581-1584: Trans Tech Publ.

[84] C. Venkata Prasad, P. Sudhakara, M. N. Prabhakar, A. Ur Rehman Shah, and J. I. Song, "An Investigation on the Effect of Silica Aerogel Content on Thermal and Mechanical Properties of Sisal/PLA Nano Composites," *Polymer Composites,* vol. 39, no. 3, pp. 835-840, 2018.

[85] S. Salimian, W. J. Malfait, A. Zadhoush, Z. Talebi, and M. Naeimirad, "Fabrication and evaluation of silica aerogel-epoxy nanocomposites: fracture and toughening mechanisms," *Theoretical and Applied Fracture Mechanics,* vol. 97, pp. 156-164, 2018.

[86] S. Salimian, A. Zadhoush, M. Naeimirad, R. Kotek, and S. Ramakrishna, "A review on aerogel: 3D nanoporous structured fillers in polymer-based nanocomposites," *Polymer Composites,* vol. 39, no. 10, pp. 3383-3408, 2018.

[87] K. Maghsoudi and S. Motahari, "Mechanical, thermal, and hydrophobic properties of silica aerogel–epoxy composites," *Journal of Applied Polymer Science,* vol. 135, no. 3, p. 45706, 2018.

[88] S. Krishnaswamy, D. Bhattacharyya, H. Abhyankar, V. Marchante, Z. Huang, and J. Brighton, "Morphological, optical and thermal characterisation of aerogel-epoxy composites for enhanced thermal insulation," *Journal of Composite Materials,* vol. 53, no. 7, pp. 909-923, 2019.

[89] Y. G. Kim *et al.*, "Thermally insulating, fire-retardant, smokeless and flexible polyvinylidene fluoride nanofibers filled with silica aerogels," *Chemical Engineering Journal,* vol. 351, pp. 473-481, 2018.

[90] H. S. Kim *et al.*, "Thermal Management in Polymer Composites: A Review of Physical and Structural Parameters," *Advanced Engineering Materials,* vol. 20, no. 10, 2018.

[91] H. M. Kim, H. S. Kim, S. Y. Kim, and J. R. Youn, "Silica aerogel/epoxy composites with preserved aerogel pores and low thermal conductivity," *e-Polymers,* vol. 15, no. 2, pp. 111-117, 2015.

[92] S. Y. Kim, Y. J. Noh, J. Lim, and N. H. You, "Silica aerogel/polyimide composites with preserved aerogel pores using multi-step curing," *Macromolecular Research,* vol. 22, no. 1, pp. 108-111, 2014.

[93] D. Ge, L. Yang, Y. Li, and J. Zhao, "Hydrophobic and thermal insulation properties of silica aerogel/epoxy composite," *Journal of Non-Crystalline Solids,* vol. 355, no. 52-54, pp. 2610-2615, 2009.

[94] Z. A. Abdul Halim, M. A. Mat Yajid, M. H. Idris, and H. Hamdan, "Effects of silica aerogel particle sizes on the thermal–mechanical properties of silica aerogel – unsaturated polyester composites," *Plastics, Rubber and Composites,* vol. 46, no. 4, pp. 184-192, 2017.

[95] S. P. Patil, A. Rege, M. Itskov, and B. Markert, "Mechanics of nanostructured porous silica aerogel resulting from molecular dynamics simulations," *The Journal of Physical Chemistry B,* vol. 121, no. 22, pp. 5660-5668, 2017.

[96] H. B. Chen and D. A. Schiraldi, "Flammability of Polymer/Clay Aerogel Composites: An Overview," *Polymer Reviews,* vol. 59, no. 1, pp. 1-24, 2019.

[97] T. Pojanavaraphan and R. Magaraphan, "Prevulcanized natural rubber latex/clay aerogel nanocomposites," *European Polymer Journal,* vol. 44, no. 7, pp. 1968-1977, 2008.

[98] L. Wang, M. Sanchez-Soto, and M. L. Maspoch, "Polymer/clay aerogel composites with flame retardant agents: Mechanical, thermal and fire behavior," *Materials & Design (1980-2015)*, vol. 52, pp. 609-614, 2013.
[99] J. Guo, B. N. Nguyen, L. Li, M. A. B. Meador, D. A. Scheiman, and M. Cakmak, "Clay reinforced polyimide/silica hybrid aerogel," *Journal of Materials Chemistry A*, vol. 1, no. 24, pp. 7211-7221, 2013.
[100] W. Luecha and R. Magaraphan, "A Novel and Facile Nanoclay Aerogel Masterbatch toward Exfoliated Polymer-Clay Nanocomposites through a Melt-Mixing Process," *Advances in Materials Science and Engineering*, vol. 2018, p. 8106189, 2018.
[101] T. Horikawa, J. i. Hayashi, and K. Muroyama, "Size control and characterization of spherical carbon aerogel particles from resorcinol–formaldehyde resin," *Carbon*, vol. 42, no. 1, pp. 169-175, 2004.
[102] C. Moreno-Castilla and F. Maldonado-Hódar, "Carbon aerogels for catalysis applications: An overview," *Carbon*, vol. 43, no. 3, pp. 455-465, 2005.
[103] N. Liu, S. Zhang, R. Fu, M. S. Dresselhaus, and G. Dresselhaus, "Carbon aerogel spheres prepared via alcohol supercritical drying," *Carbon*, vol. 44, no. 12, pp. 2430-2436, 2006.
[104] T. Y. Ying, K. L. Yang, S. Yiacoumi, and C. Tsouris, "Electrosorption of ions from aqueous solutions by nanostructured carbon aerogel," *Journal of colloid and interface science*, vol. 250, no. 1, pp. 18-27, 2002.
[105] J. Li, X. Wang, Q. Huang, S. Gamboa, and P. Sebastian, "Studies on preparation and performances of carbon aerogel electrodes for the application of supercapacitor," *Journal of Power Sources*, vol. 158, no. 1, pp. 784-788, 2006.
[106] S. W. Hwang and S. H. Hyun, "Capacitance control of carbon aerogel electrodes," *Journal of non-crystalline solids*, vol. 347, no. 1-3, pp. 238-245, 2004.
[107] V. Palmre *et al.*, "Electroactive polymer actuators with carbon aerogel electrodes," *Journal of Materials Chemistry*, vol. 21, no. 8, pp. 2577-2583, 2011.
[108] T. H. Hsieh, Y. S. Huang, and M. Y. Shen, "Mechanical properties and toughness of carbon aerogel/epoxy polymer composites," *Journal of Materials Science*, vol. 50, no. 8, pp. 3258-3266, 2015.
[109] H. Zhuo, Y. Hu, Z. Chen, and L. Zhong, "Cellulose carbon aerogel/PPy composites for high-performance supercapacitor," *Carbohydrate polymers*, vol. 215, pp. 322-329, 2019.
[110] H. An *et al.*, "Polypyrrole/carbon aerogel composite materials for supercapacitor," *Journal of Power Sources*, vol. 195, no. 19, pp. 6964-6969, 2010.
[111] R. J. Young and P. A. Lovell, *Introduction to polymers*. CRC press, 2011.
[112] F. Zhao, W. Bi, and S. Zhao, "Influence of crosslink density on mechanical properties of natural rubber vulcanizates," *Journal of Macromolecular Science, Part B*, vol. 50, no. 7, pp. 1460-1469, 2011.
[113] R. M. Wang, S. R. Zheng, and Y. G. Zheng, *Polymer matrix composites and technology*. Elsevier, 2011.
[114] J. Nicholson, *The chemistry of polymers*. Royal Society of Chemistry, 2017.

[115] F. L. Jin, X. Li, and S. J. Park, "Synthesis and application of epoxy resins: A review," *Journal of Industrial and Engineering Chemistry,* vol. 29, pp. 1-11, 2015.
[116] A. C. Loos and G. S. Springer, "Curing of epoxy matrix composites," *Journal of composite materials,* vol. 17, no. 2, pp. 135-169, 1983.
[117] S. Kocaman and G. Ahmetli, "A study of coating properties of biobased modified epoxy resin with different hardeners," *Progress in Organic Coatings,* vol. 97, pp. 53-64, 2016.
[118] F. Wu, X. Zhou, and X. Yu, "Reaction mechanism, cure behavior and properties of a multifunctional epoxy resin, TGDDM, with latent curing agent dicyandiamide," *RSC advances,* vol. 8, no. 15, pp. 8248-8258, 2018.
[119] Y. Kwon, B. S. Yim, J. M. Kim, and J. Kim, "Mechanical and wetting properties of epoxy resins: Amine-containing epoxy-terminated siloxane oligomer with or without reductant," *Microelectronics Reliability,* vol. 51, no. 4, pp. 819-825, 2011.
[120] C. May and H. Newey, "Epoxy-Acrylic Resins for FRP Structures, 20th ANTEC," *SPI. Feb,* 1965.
[121] W. D. Cook, G. P. Simon, P. J. Burchill, M. Lau, and T. J. Fitch, "Curing kinetics and thermal properties of vinyl ester resins," *Journal of Applied Polymer Science,* vol. 64, no. 4, pp. 769-781, 1997.
[122] M. B. Launikitis, "Vinyl ester resins," in *Handbook of composites*: Springer, 1982, pp. 38-49.
[123] H. Li III, "Synthesis, characterization and properties of vinyl ester matrix resins," Virginia Tech, 1998.
[124] C. Alía, J. A. Jofre-Reche, J. C. Suárez, J. M. Arenas, and J. M. Martín-Martínez, "Influence of post-curing temperature on the structure, properties, and adhesion of vinyl ester adhesive," *Journal of Adhesion Science and Technology,* vol. 29, no. 6, pp. 518-531, 2015.
[125] J. J. Cain *et al.*, "Post-curing effects on marine VARTM FRP composite material properties for test and implementation," *Journal of Engineering Materials and Technology,* 2006.
[126] M. G. Knight, "Numerical modelling of particulate and fibre reinforced composites," Brunel University, 2002.
[127] P. K. Hari, "1 - Types and properties of fibres and yarns used in weaving," in *Woven Textiles*, K. L. Gandhi, Ed.: Woodhead Publishing, 2012, pp. 3-34.
[128] S. M. Sapuan, "Chapter 3 - Composite Materials," in *Composite Materials*, S. M. Sapuan, Ed. Boston: Butterworth-Heinemann, 2017, pp. 57-93.
[129] R. Bauri and D. Yadav, "Chapter 1 - Introduction to Metal Matrix Composites," in *Metal Matrix Composites by Friction Stir Processing*, R. Bauri and D. Yadav, Eds.: Butterworth-Heinemann, 2018, pp. 1-16.
[130] D. B. Marshall and A. G. Evans, "Failure mechanisms in ceramic-fiber/ceramic-matrix composites," *Journal of the American Ceramic Society,* vol. 68, no. 5, pp. 225-231, 1985.
[131] M. A. Hasan, R. Sangashetty, A. C. M. Esther, S. B. Patil, B. N. Sherikar, and A. Dey, "Prospect of thermal insulation by silica aerogel: a brief review," *Journal of The Institution of Engineers : Series D,* vol. 98, no. 2, pp. 297-304, 2017.

[132] A. Hoseini, C. McCague, M. Andisheh Tadbir, and M. Bahrami, "Aerogel blankets: From mathematical modeling to material characterization and experimental analysis," *International Journal of Heat and Mass Transfer*, vol. 93, pp. 1124-1131, 2016.
[133] U. Berardi, "Aerogel-enhanced systems for building energy retrofits: Insights from a case study," *Energy and Buildings*, vol. 159, pp. 370-381, 2018.
[134] N. Bheekhun, A. Talib, A. Rahim, and M. R. Hassan, "Aerogels in aerospace: an overview," *Advances in Materials Science and Engineering*, vol. 2013, 2013.
[135] S. Grishanov, "2 - Structure and properties of textile materials," in *Handbook of Textile and Industrial Dyeing*, vol. 1, M. Clark, Ed.: Woodhead Publishing, 2011, pp. 28-63.
[136] L. Mishnaevsky, K. Branner, H. N. Petersen, J. Beauson, M. McGugan, and B. F. Sørensen, "Materials for wind turbine blades: an overview," *Materials*, vol. 10, no. 11, p. 1285, 2017.
[137] D. Hull and T. Clyne, *An introduction to composite materials*. Cambridge university press, 1996.
[138] A. Cevahir, "5 - Glass fibers," in *Fiber Technology for Fiber-Reinforced Composites*, M. Ö. Seydibeyoğlu, A. K. Mohanty, and M. Misra, Eds.: Woodhead Publishing, 2017, pp. 99-121.
[139] A. Shrivastava, "4 - Additives for Plastics," in *Introduction to Plastics Engineering*, A. Shrivastava, Ed.: William Andrew Publishing, 2018, pp. 111-141.
[140] M. A. Masuelli, "Introduction of fibre-reinforced polymers− polymers and composites: concepts, properties and processes," in *Fiber Reinforced Polymers-The Technology Applied for Concrete Repair*: IntechOpen, 2013.
[141] K. Acatay, "6 - Carbon fibers," in *Fiber Technology for Fiber-Reinforced Composites*, M. Ö. Seydibeyoğlu, A. K. Mohanty, and M. Misra, Eds.: Woodhead Publishing, 2017, pp. 123-151.
[142] B. Fei, "2 - High-performance fibers for textiles," in *Engineering of High-Performance Textiles*, M. Miao and J. H. Xin, Eds.: Woodhead Publishing, 2018, pp. 27-58.
[143] J. Militký, "13 - Tensile failure of polyester fibers," in *Handbook of Properties of Textile and Technical Fibres (Second Edition)*, A. R. Bunsell, Ed.: Woodhead Publishing, 2018, pp. 421-514.
[144] J. A. Elliott, "Novel approaches to multiscale modelling in materials science," *International Materials Reviews*, vol. 56, no. 4, pp. 207-225, 2011.
[145] H. D. Espinosa, T. Filleter, and M. Naraghi, "Multiscale experimental mechanics of hierarchical carbon‐based materials," *Advanced Materials*, vol. 24, no. 21, pp. 2805-2823, 2012.
[146] C. R. Weinberger and G. J. Tucker, "Multiscale materials modeling for nanomechanics," 2016.
[147] S. Schmauder and I. Schäfer, *Multiscale materials modeling: approaches to full multiscaling*. Walter de Gruyter GmbH & Co KG, 2016.
[148] J. P. Johnston, B. Koo, N. Subramanian, and A. Chattopadhyay, "Modeling the molecular structure of the carbon fiber/polymer interphase for multiscale analysis of composites," *Composites Part B: Engineering*, vol. 111, pp. 27-36, 2017.

[149] S. Chandra, M. Samal, V. Chavan, and S. Raghunathan, "Hierarchical multiscale modeling of plasticity in copper: From single crystals to polycrystalline aggregates," *International Journal of Plasticity*, vol. 101, pp. 188-212, 2018.
[150] T. D. Scheibe *et al.*, "An Analysis Platform for Multiscale Hydrogeologic Modeling with Emphasis on Hybrid Multiscale Methods," vol. 53, no. 1, pp. 38-56, 2015.
[151] C. Y. Wang and X. Zhang, "Multiscale modeling and related hybrid approaches," *Current Opinion in Solid State and Materials Science*, vol. 10, no. 1, pp. 2-14, 2006.
[152] E. Van Der Giessen *et al.*, "Roadmap on multiscale materials modeling," *Modelling and Simulation in Materials Science and Engineering*, vol. 28, no. 4, 2020.
[153] E. Lidorikis, M. E. Bachlechner, R. K. Kalia, A. Nakano, P. Vashishta, and G. Z. Voyiadjis, "Coupling length scales for multiscale atomistics-continuum simulations: atomistically induced stress distributions in Si/Si 3 N 4 nanopixels," *Physical review letters*, vol. 87, no. 8, p. 086104, 2001.
[154] S. Sharma, *Molecular Dynamics Simulation of Nanocomposites Using BIOVIA Materials Studio, Lammps and Gromacs*. Elsevier, 2019.
[155] D. C. Rapaport, *The art of molecular dynamics simulation*. Cambridge university press, 2004.
[156] T. Hansson, C. Oostenbrink, and W. van Gunsteren, "Molecular dynamics simulations," *Current opinion in structural biology*, vol. 12, no. 2, pp. 190-196, 2002.
[157] I. Omelyan, I. Mryglod, and R. Folk, "Optimized Verlet-like algorithms for molecular dynamics simulations," *Physical Review E*, vol. 65, no. 5, p. 056706, 2002.
[158] H. Grubmüller, H. Heller, A. Windemuth, and K. Schulten, "Generalized Verlet algorithm for efficient molecular dynamics simulations with long-range interactions," *Molecular Simulation*, vol. 6, no. 1-3, pp. 121-142, 1991.
[159] Q. Spreiter and M. Walter, "Classical molecular dynamics simulation with the Velocity Verlet algorithm at strong external magnetic fields," *Journal of Computational Physics*, vol. 152, no. 1, pp. 102-119, 1999.
[160] D. Fincham, "Leapfrog rotational algorithms," *Molecular Simulation*, vol. 8, no. 3-5, pp. 165-178, 1992.
[161] K. Binder, *Monte Carlo and molecular dynamics simulations in polymer science*. Oxford University Press, 1995.
[162] G. Ciccotti, M. Ferrario, and C. Schuette, "Molecular Dynamics Simulation," *Entropy*, vol. 16, p. 233, 2014.
[163] M. P. Allen, "Introduction to molecular dynamics simulation," *Computational soft matter: from synthetic polymers to proteins*, vol. 23, pp. 1-28, 2004.
[164] Y. W. Kwon, D. H. Allen, and R. Talreja, *Multiscale modeling and simulation of composite materials and structures*. Springer, 2008.
[165] A. C. Van Duin, S. Dasgupta, F. Lorant, and W. A. Goddard, "ReaxFF: a reactive force field for hydrocarbons," *The Journal of Physical Chemistry A*, vol. 105, no. 41, pp. 9396-9409, 2001.

[166] P. Vashishta, R. K. Kalia, J. P. Rino, and I. Ebbsjö, "Interaction potential for SiO_2: a molecular-dynamics study of structural correlations," *Physical Review B*, vol. 41, no. 17, p. 12197, 1990.
[167] J. Tersoff, "New empirical approach for the structure and energy of covalent systems," *Physical Review B*, vol. 37, no. 12, p. 6991, 1988.
[168] W. L. Jorgensen and J. Tirado-Rives, "The OPLS [optimized potentials for liquid simulations] potential functions for proteins, energy minimizations for crystals of cyclic peptides and crambin," *Journal of the American Chemical Society*, vol. 110, no. 6, pp. 1657-1666, 1988.
[169] W. L. Jorgensen, D. S. Maxwell, and J. Tirado-Rives, "Development and testing of the OPLS all-atom force field on conformational energetics and properties of organic liquids," *Journal of the American Chemical Society*, vol. 118, no. 45, pp. 11225-11236, 1996.
[170] B. Van Beest, G. J. Kramer, and R. Van Santen, "Force fields for silicas and aluminophosphates based on ab initio calculations," *Physical Review Letters*, vol. 64, no. 16, p. 1955, 1990.
[171] R. W. Hockney and J. W. Eastwood, *Computer simulation using particles*. crc Press, 1988.
[172] S. S. Mahajan, G. Subbarayan, and B. G. Sammakia, "Estimating thermal conductivity of amorphous silica nanoparticles and nanowires using molecular dynamics simulations," *Physical Review E*, vol. 76, no. 5, p. 056701, 2007.
[173] A. McGaughey and M. Kaviany, "Thermal conductivity decomposition and analysis using molecular dynamics simulations: Part II. Complex silica structures," *International Journal of Heat and Mass Transfer*, vol. 47, no. 8-9, pp. 1799-1816, 2004.
[174] T. Y. Ng, J. J. Yeo, and Z. Liu, "A molecular dynamics study of the thermal conductivity of nanoporous silica aerogel, obtained through negative pressure rupturing," *Journal of Non-Crystalline Solids*, vol. 358, no. 11, pp. 1350-1355, 2012.
[175] K. Matsunaga, C. Fisher, and H. Matsubara, "Tersoff potential parameters for simulating cubic boron carbonitrides," *Japanese Journal of Applied Physics*, vol. 39, no. 1A, p. L48, 2000.
[176] R. Saito, R. Matsuo, T. Kimura, G. Dresselhaus, and M. Dresselhaus, "Anomalous potential barrier of double-wall carbon nanotube," *Chemical physics letters*, vol. 348, no. 3-4, pp. 187-193, 2001.
[177] P. S. Branicio, J. P. Rino, C. K. Gan, and H. Tsuzuki, "Interaction potential for indium phosphide: a molecular dynamics and first-principles study of the elastic constants, generalized stacking fault and surface energies," *Journal of Physics: Condensed Matter*, vol. 21, no. 9, p. 095002, 2009.
[178] W. L. Jorgensen, J. D. Madura, and C. J. Swenson, "Optimized intermolecular potential functions for liquid hydrocarbons," *Journal of the American Chemical Society*, vol. 106, no. 22, pp. 6638-6646, 1984.
[179] W. L. Jorgensen and C. J. Swenson, "Optimized intermolecular potential functions for amides and peptides. Hydration of amides," *Journal of the American Chemical Society*, vol. 107, no. 6, pp. 1489-1496, 1985.
[180] B. R. Brooks *et al.*, "CHARMM: the biomolecular simulation program," *Journal of computational chemistry*, vol. 30, no. 10, pp. 1545-1614, 2009.

[181] S. J. Weiner, P. A. Kollman, D. T. Nguyen, and D. A. Case, "An all atom force field for simulations of proteins and nucleic acids," *Journal of computational chemistry,* vol. 7, no. 2, pp. 230-252, 1986.
[182] K. Chenoweth, A. C. Van Duin, and W. A. Goddard, "ReaxFF reactive force field for molecular dynamics simulations of hydrocarbon oxidation," *The Journal of Physical Chemistry A,* vol. 112, no. 5, pp. 1040-1053, 2008.
[183] G. Shchygol, A. Yakovlev, T. Trnka, A. C. T. van Duin, and T. Verstraelen, "ReaxFF Parameter Optimization with Monte-Carlo and Evolutionary Algorithms: Guidelines and Insights," *Journal of Chemical Theory and Computation,* vol. 15, no. 12, pp. 6799-6812, 2019.
[184] D. A. Newsome, D. Sengupta, H. Foroutan, M. F. Russo, and A. C. Van Duin, "Oxidation of silicon carbide by O_2 and H_2O: a ReaxFF reactive molecular dynamics study, Part I," *The Journal of Physical Chemistry C,* vol. 116, no. 30, pp. 16111-16121, 2012.
[185] M. J. Buehler, A. C. T. van Duin, and W. A. Goddard, "Multiparadigm Modeling of Dynamical Crack Propagation in Silicon Using a Reactive Force Field," *Physical Review Letters,* vol. 96, no. 9, p. 095505, 2006.
[186] K. D. Nielson, A. C. T. van Duin, J. Oxgaard, W. Q. Deng, and W. A. Goddard, "Development of the ReaxFF Reactive Force Field for Describing Transition Metal Catalyzed Reactions, with Application to the Initial Stages of the Catalytic Formation of Carbon Nanotubes," *The Journal of Physical Chemistry A,* vol. 109, no. 3, pp. 493-499, 2005.
[187] B. J. Alder and T. E. Wainwright, "Studies in molecular dynamics. I. General method," *The Journal of Chemical Physics,* vol. 31, no. 2, pp. 459-466, 1959.
[188] S. Nosé, "A molecular dynamics method for simulations in the canonical ensemble," *Molecular physics,* vol. 52, no. 2, pp. 255-268, 1984.
[189] S. Nosé, "An extension of the canonical ensemble molecular dynamics method," *Molecular Physics,* vol. 57, no. 1, pp. 187-191, 1986.
[190] J. R. Ray, "Microcanonical ensemble monte carlo method," *Physical Review A,* vol. 44, no. 6, p. 4061, 1991.
[191] G. J. Martyna, D. J. Tobias, and M. L. Klein, "Constant pressure molecular dynamics algorithms," *The Journal of chemical physics,* vol. 101, no. 5, pp. 4177-4189, 1994.
[192] G. C. Lynch and B. M. Pettitt, "Grand canonical ensemble molecular dynamics simulations: Reformulation of extended system dynamics approaches," *The Journal of chemical physics,* vol. 107, no. 20, pp. 8594-8610, 1997.
[193] P. H. Hünenberger, "Thermostat algorithms for molecular dynamics simulations," in *Advanced computer simulation*: Springer, 2005, pp. 105-149.
[194] A. Lemak and N. Balabaev, "On the Berendsen thermostat," *Molecular Simulation,* vol. 13, no. 3, pp. 177-187, 1994.
[195] V. Rühle, "Berendsen and nose-hoover thermostats," *Am. J. Phys,* 2007.
[196] D. J. Evans and B. L. Holian, "The nose–hoover thermostat," *The Journal of chemical physics,* vol. 83, no. 8, pp. 4069-4074, 1985.
[197] M. T. E. Kio, "Molecular Dynamics of Kapitza Resistance at the Solid-Liquid Interface of Nanofluidic Channels," 2014.
[198] O. N. de Souza and R. L. Ornstein, "Effect of periodic box size on aqueous molecular dynamics simulation of a DNA dodecamer with particle-mesh Ewald method," *Biophysical journal,* vol. 72, no. 6, pp. 2395-2397, 1997.

[199] S. Namilae, D. M. Nicholson, P. Nukala, C. Y. Gao, Y. Osetsky, and D. J. Keffer, "Absorbing boundary conditions for molecular dynamics and multiscale modeling," *Physical Review B,* vol. 76, no. 14, p. 144111, 2007.
[200] D. Passerone and M. Parrinello, "Action-derived molecular dynamics in the study of rare events," *Physical review letters,* vol. 87, no. 10, p. 108302, 2001.
[201] J. Z. Yang and X. Li, "Comparative study of boundary conditions for molecular dynamics simulations of solids at low temperature," *Physical Review B,* vol. 73, no. 22, 2006.
[202] S. Plimpton, "Fast parallel algorithms for short-range molecular dynamics," Sandia National Labs., Albuquerque, NM (United States)1993.
[203] T. W. Sirk, S. Moore, and E. F. Brown, "Characteristics of thermal conductivity in classical water models," *The Journal of chemical physics,* vol. 138, no. 6, p. 064505, 2013.
[204] A. P. Thompson, S. J. Plimpton, and W. Mattson, "General formulation of pressure and stress tensor for arbitrary many-body interaction potentials under periodic boundary conditions," *The Journal of chemical physics,* vol. 131, no. 15, 2009.
[205] Z. Bi, *Finite element analysis applications: A systematic and practical approach*. Academic Press, 2017.
[206] R. M. Pidaparti, "Engineering finite element analysis," *Synthesis Lectures on Mechanical Engineering,* vol. 1, no. 1, pp. 1-267, 2017.
[207] N. S. Gokhale, *Practical finite element analysis*. Finite to infinite, 2008.
[208] S. Bhavikatti, *Finite element analysis*. New Age International, 2005.
[209] R. I. Mackie, "Advantages of object-oriented finite-element analysis," *Proceedings of the Institution of Civil Engineers-Engineering and Computational Mechanics,* vol. 162, no. 1, pp. 23-29, 2009.
[210] Z. Bi, "Chapter 1 - Overview of Finite Element Analysis," in *Finite Element Analysis Applications*, Z. Bi, Ed.: Academic Press, 2018, pp. 1-29.
[211] M. Gyimesi and D. Ostergaard, "Inductance computation by incremental finite element analysis," *IEEE transactions on magnetics,* vol. 35, no. 3, pp. 1119-1122, 1999.
[212] D. V Hutton, *Fundamentals of finite element analysis*. McGraw-Hill Education, 2003.
[213] B. Szabó and I. Babuška, *Finite element analysis*. John Wiley & Sons, 1991.
[214] S. McCaslin, "Validation and Verification in Finite Element Analysis (FEA)," *Control Automation,* 2021.
[215] T. Chung, "Finite element analysis in fluid dynamics," *NASA STI/Recon Technical Report A,* vol. 78, p. 44102, 1978.
[216] D. Roylance, "Finite element analysis," *Department of Materials Science and Engineering, Massachusetts Institute of Technology, Cambridge,* 2001.
[217] L. J. Segerlind and H. Saunders, "Applied finite element analysis," 1987.
[218] Y. You, X. Kou, and S. Tan, "Adaptive meshing for finite element analysis of heterogeneous materials," *Computer-Aided Design,* vol. 62, pp. 176-189, 2015.
[219] G. Nikishkov, "Basics of the domain decomposition method for finite element analysis," *Mesh Partitioning Techniques and Domain Decomposition Methods,* pp. 119-142, 2007.

[220] D. Ulrich, B. van Rietbergen, H. Weinans, and P. Rüegsegger, "Finite element analysis of trabecular bone structure: a comparison of image-based meshing techniques," *Journal of biomechanics*, vol. 31, no. 12, pp. 1187-1192, 1998.
[221] S. E. Benzley, E. Perry, K. Merkley, B. Clark, and G. Sjaardama, "A comparison of all hexagonal and all tetrahedral finite element meshes for elastic and elasto-plastic analysis," in *Proceedings, 4th international meshing roundtable*, 1995, vol. 17, pp. 179-191: Citeseer.
[222] R. Glowinski, E. Y. Rodin, and O. C. Zienkiewicz, *Energy methods in finite element analysis*. Wiley New York, 1979.
[223] C. Brebbia, "Weighted residual classification of approximate methods," *Applied Mathematical Modelling*, vol. 2, no. 3, pp. 160-164, 1978.
[224] O. C. Zienkiewicz, "A new look at the Newmark, Houbolt and other time stepping formulas. A weighted residual approach," *Earthquake Engineering Structural Dynamics*, vol. 5, no. 4, pp. 413-418, 1977.
[225] B. Szabó, *Introduction to finite element analysis: formulation, verification and validation*. John Wiley & Sons, 2011.
[226] N. Amaral, J. J. Rencis, and Y. K. Rong, "Development of a finite element analysis tool for fixture design integrity verification and optimisation," *The International Journal of Advanced Manufacturing Technology*, vol. 25, no. 5-6, pp. 409-419, 2005.
[227] T. Stolarski, Y. Nakasone, and S. Yoshimoto, *Engineering analysis with ANSYS software*. Butterworth-Heinemann, 2018.
[228] E. Madenci and I. Guven, *The finite element method and applications in engineering using ANSYS®*. Springer, 2015.
[229] P. Kohnke, "Ansys," in *Finite Element Systems*: Springer, 1982, pp. 19-25.
[230] N. Mazlan, N. Termazi, S. Abdul Rashid, and S. Rahmanian, "Investigations on composite flexural behaviour with inclusion of CNT enhanced silica aerogel in epoxy nanocomposites," in *Applied Mechanics and Materials*, 2015, vol. 695, pp. 179-182: Trans Tech Publ.
[231] M. Basri, N. Mazlan, and F. Mustapha, "Effects of stirring speed and time on water absorption performance of silica aerogel/epoxy nanocomposite," *ARPN J Eng Appl Sci*, vol. 10, no. 21, pp. 9982-9991, 2015.
[232] J. Cho, H. G. Jang, S. Y. Kim, and B. Yang, "Flexible and coatable insulating silica aerogel/polyurethane composites via soft segment control," *Composites Science and Technology*, vol. 171, pp. 244-251, 2019.
[233] J. M. Allan, M. A. Mumin, J. A. Wood, W. Z. Xu, W. Wu, and P. A. Charpentier, "Silica aerogel–poly (ethylene-co-vinyl acetate) composite for transparent heat retention films," *Journal of Polymer Science Part B: Polymer Physics*, vol. 52, no. 14, pp. 927-935, 2014.
[234] G. Kim and S. Hyun, "Effect of mixing on thermal and mechanical properties of aerogel-PVB composites," *Journal of materials science*, vol. 38, no. 9, pp. 1961-1966, 2003.
[235] R. W. B. Guptaa N, "Processing and compressive properties of aerogel/epoxy composites," *ournal of materials processing technology*, vol. 198, pp. 178-182, 2008.
[236] A. Du *et al.*, "Aerogel: a potential three-dimensional nanoporous filler for resins," *Journal of reinforced plastics and composites*, vol. 30, no. 11, pp. 912-921, 2011.

[237] S. Fu *et al.*, "Accurate characterization of full pore size distribution of tight sandstones by low-temperature nitrogen gas adsorption and high-pressure mercury intrusion combination method," *Energy Science & Engineering,* vol. 9, no. 1, pp. 80-100, 2021.
[238] J. S. R. Murillo, M. E. Bachlechner, F. A. Campo, and E. J. Barbero, "Structure and mechanical properties of silica aerogels and xerogels modeled by molecular dynamics simulation," *Journal of Non-Crystalline Solids,* vol. 356, no. 25-27, pp. 1325-1331, 2010.
[239] M. Bhambhani, P. Cutting, K. Sing, and D. Turk, "Analysis of nitrogen adsorption isotherms on porous and nonporous silicas by the BET and αs methods," *Journal of Colloid and Interface Science,* vol. 38, no. 1, pp. 109-117, 1972.
[240] X. Cao and L. J. Lee, "Control of shrinkage and final conversion of vinyl ester resins cured in low-temperature molding processes," *Journal of Applied Polymer Science,* vol. 90, no. 6, pp. 1486-1496, 2003.
[241] Y. Agari, A. Ueda, and S. Nagai, "Thermal conductivity of a polymer composite," *Journal of Applied Polymer Science,* vol. 49, no. 9, pp. 1625-1634, 1993.
[242] Y. Agari and T. Uno, "Estimation on thermal conductivities of filled polymers," *Journal of Applied Polymer Science,* vol. 32, no. 7, pp. 5705-5712, 1986.
[243] R. Yang, G. Chen, and M. S. Dresselhaus, "Thermal conductivity modeling of core− shell and tubular nanowires," *Nano letters,* vol. 5, no. 6, pp. 1111-1115, 2005.
[244] H. Zhang, C. Zhang, W. Ji, X. Wang, Y. Li, and W. Tao, "Experimental Characterization of the Thermal Conductivity and Microstructure of Opacifier-Fiber-Aerogel Composite," *Molecules,* vol. 23, no. 9, p. 2198, 2018.
[245] M. Sachithanadam and S. C. Joshi, "Superhydrophobic and Ultralow Thermal Insulation," in *Silica Aerogel Composites: Novel Fabrication Methods*Singapore: Springer Singapore, 2016, pp. 81-108.
[246] J. C. Wong, H. Kaymak, S. Brunner, and M. M. Koebel, "Mechanical properties of monolithic silica aerogels made from polyethoxydisiloxanes," *Microporous and mesoporous materials,* vol. 183, pp. 23-29, 2014.
[247] K. E. Parmenter and F. Milstein, "Mechanical properties of silica aerogels," *Journal of Non-Crystalline Solids,* vol. 223, no. 3, pp. 179-189, 1998.
[248] L. Khoun and P. Hubert, "Cure shrinkage characterization of an epoxy resin system by two in situ measurement methods," *Polymer composites,* vol. 31, no. 9, pp. 1603-1610, 2010.
[249] M. Preghenella, A. Pegoretti, and C. Migliaresi, "Thermo-mechanical characterization of fumed silica-epoxy nanocomposites," *Polymer,* vol. 46, no. 26, pp. 12065-12072, 2005.
[250] J. Gross and J. Fricke, "Thermal expansion of carbon and silica aerogels above room temperature," *Journal of non-crystalline solids,* vol. 186, pp. 301-308, 1995.
[251] C. Wong and R. S. Bollampally, "Thermal conductivity, elastic modulus, and coefficient of thermal expansion of polymer composites filled with ceramic particles for electronic packaging," *Journal of applied polymer science,* vol. 74, no. 14, pp. 3396-3403, 1999.

[252] Y. X. He, Y. F. Sang, L. Zhang, D. H. Yao, K. B. Sun, and Y. Q. Zhang, "Coefficient of thermal expansion and mechanical properties at cryogenic temperature of core–shell rubber particle modified epoxy," *Plastics, Rubber and Composites,* vol. 43, no. 3, pp. 89-97, 2014.
[253] K. J. Soderholm, "Influence of silane treatment and filler fraction on thermal expansion of composite resins," *Journal of dental research,* vol. 63, no. 11, pp. 1321-1326, 1984.
[254] H. H. Hamama, "Recent advances in posterior resin composite restorations," *Applications of Nanocomposite Materials in Dentistry,* pp. 319-336, 2019.
[255] J. S. Jang, B. Bouveret, J. Suhr, and R. F. Gibson, "Combined numerical/experimental investigation of particle diameter and interphase effects on coefficient of thermal expansion and young's modulus of SiO2/epoxy nanocomposites," *Polymer composites,* vol. 33, no. 8, pp. 1415-1423, 2012.
[256] G. Elsner, J. Kempf, J. Bartha, and H. Wagner, "Anisotropy of thermal expansion of thin polyimide films," *Thin Solid Films,* vol. 185, no. 1, pp. 189-197, 1990.
[257] D. Cho, S. Lee, G. Yang, H. Fukushima, and L. T. Drzal, "Dynamic mechanical and thermal properties of phenylethynyl‐terminated polyimide composites reinforced with expanded graphite nanoplatelets," *Macromolecular Materials and Engineering,* vol. 290, no. 3, pp. 179-187, 2005.
[258] K. Backfolk, R. Holmes, P. Ihalainen, P. Sirviö, N. Triantafillopoulos, and J. Peltonen, "Determination of the glass transition temperature of latex films: Comparison of various methods," *Polymer Testing,* vol. 26, no. 8, pp. 1031-1040, 2007.
[259] W. Jiang, F.-L. Jin, and S.-J. Park, "Thermo-mechanical behaviors of epoxy resins reinforced with nano-Al2O3 particles," *Journal of Industrial and Engineering chemistry,* vol. 18, no. 2, pp. 594-596, 2012.
[260] O. Startsev, Y. M. Vapirov, M. Lebedev, and A. Kychkin, "Comparison of glass-transition temperatures for epoxy polymers obtained by methods of thermal analysis," *Mechanics of Composite Materials,* vol. 56, pp. 227-240, 2020.
[261] B. Cassel and B. Twombly, "Glass transition determination by thermomechanical analysis, a dynamic mechanical analyzer, and a differential scanning calorimeter," in *Materials Characterization by Thermomechanical Analysis*: ASTM International, 1991.
[262] Y. L. Liu, C. Y. Hsu, W. L. Wei, and R. J. Jeng, "Preparation and thermal properties of epoxy-silica nanocomposites from nanoscale colloidal silica," *Polymer,* vol. 44, no. 18, pp. 5159-5167, 2003.
[263] H. Zhang, Z. Zhang, K. Friedrich, and C. Eger, "Property improvements of in situ epoxy nanocomposites with reduced interparticle distance at high nanosilica content," *Acta Materialia,* vol. 54, no. 7, pp. 1833-1842, 2006.
[264] T. Mahrholz, J. Stängle, and M. Sinapius, "Quantitation of the reinforcement effect of silica nanoparticles in epoxy resins used in liquid composite moulding processes," *Composites Part A: Applied Science and Manufacturing,* vol. 40, no. 3, pp. 235-243, 2009.

[265] Y. Chen *et al.*, "Superior mechanical enhancement of epoxy composites reinforced by polyimide nanofibers via a vacuum-assisted hot-pressing," *Composites Science and Technology*, vol. 174, pp. 20-26, 2019.
[266] J. K. Kim and Y. W. Mai, *Engineered interfaces in fiber reinforced composites*. Elsevier, 1998.
[267] L. Yang, "A physical approach to interfacial strength in fibre reinforced thermoplastic composites," University of Strathclyde, 2011.
[268] R. F. Minty, "The influence of matrix stoichiometry on interfacial adhesion in composites for wind turbine applications," University of Strathclyde, 2018.
[269] F. Bartell and H. Osterhof, "Colloid Symposium " *Monograph*, vol. 19, p. 1277, 1927.
[270] T. Young, "III. An essay on the cohesion of fluids," *Philosophical transactions of the royal society of London*, no. 95, pp. 65-87, 1805.
[271] L. T. Drzal, "The interphase in epoxy composites," *Epoxy resins and composites II*, pp. 1-32, 1986.
[272] K. Van de Velde and P. Kiekens, "Wettability and surface analysis of glass fibres," *NISCAIR Online Periodicals Repository*, 2000.
[273] K. Szymczyk, A. Zdziennicka, J. Krawczyk, and B. Jańczuk, "Wettability, adhesion, adsorption and interface tension in the polymer/surfactant aqueous solution system. I. Critical surface tension of polymer wetting and its surface tension," *Colloids and Surfaces A: Physicochemical and Engineering Aspects*, vol. 402, pp. 132-138, 2012.
[274] S. Rebouillat, B. Letellier, and B. Steffenino, "Wettability of single fibres–beyond the contact angle approach," *International journal of adhesion and adhesives*, vol. 19, no. 4, pp. 303-314, 1999.
[275] M. Giraud, T. Nguyen, X. Gu, and M. R. VanLandingham, "Effects of stoichiometry and epoxy molecular mass on wettability and interfacial microstructures of amine-cured epoxies," in *Proc. Adhesion Society Meeting*, 2001, vol. 260.
[276] P. Chen, C. Lu, Q. Yu, Y. Gao, J. Li, and X. Li, "Influence of fiber wettability on the interfacial adhesion of continuous fiber‐reinforced PPESK composite," *Journal of applied polymer science*, vol. 102, no. 3, pp. 2544-2551, 2006.
[277] J. L. Thomason, "The interface region in glass fibre-reinforced epoxy resin composites: 3. Characterization of fibre surface coatings and the interphase," *Composites*, vol. 26, no. 7, pp. 487-498, 1995.
[278] J. Williams, M. Donnellan, M. James, and W. Morris, "Properties of the interphase in organic matrix composites," *Materials Science and Engineering: A*, vol. 126, no. 1-2, pp. 305-312, 1990.
[279] E. P. Plueddemann, "Reminiscing on silane coupling agents," *Journal of adhesion science and technology*, vol. 5, no. 4, pp. 261-277, 1991.
[280] X. Gao, R. Jensen, W. Li, J. Deitzel, S. McKnight, and J. Gillespie Jr, "Effect of fiber surface texture created from silane blends on the strength and energy absorption of the glass fiber/epoxy interphase," *Journal of Composite Materials*, vol. 42, no. 5, pp. 513-534, 2008.
[281] A. Firas, G. Michael, K. Georgina, F. Bronwyn, and P. Paul, "Adhesion of polymers," *Progress in Polymer Science*, vol. 34, no. 9, pp. 948-968, 2009.

[282] L. Yang and J. L. Thomason, "The thermal behaviour of glass fibre investigated by thermomechanical analysis," *Journal of Materials Science,* vol. 48, no. 17, pp. 5768-5775, 2013.
[283] J. L. Thomason and L. Yang, "Temperature dependence of the interfacial shear strength in glass–fibre polypropylene composites," *Composites Science Technology,* vol. 71, no. 13, pp. 1600-1605, 2011.
[284] J. L. Thomason and L. Yang, "Temperature dependence of the interfacial shear strength in glass–fibre epoxy composites," *Composites science and technology,* vol. 96, pp. 7-12, 2014.
[285] J. L. Thomason, U. Nagel, L. Yang, and D. Bryce, "A study of the thermal degradation of glass fibre sizings at composite processing temperatures," *Composites Part A: Applied Science and Manufacturing,* vol. 121, pp. 56-63, 2019.
[286] L. Yang and J. L. Thomason, "Interface strength in glass fibre–polypropylene measured using the fibre pull-out and microbond methods," *Composites Part A: Applied Science and Manufacturing,* vol. 41, no. 9, pp. 1077-1083, 2010.
[287] R. F. Minty, L. Yang, and J. L. Thomason, "The influence of hardener-to-epoxy ratio on the interfacial strength in glass fibre reinforced epoxy composites," *Composites Part A: Applied Science and Manufacturing,* vol. 112, pp. 64-70, 2018.
[288] B. Miller, P. Muri, and L. Rebenfeld, "A microbond method for determination of the shear strength of a fiber/resin interface," *Composites Science and Technology,* vol. 28, no. 1, pp. 17-32, 1987.
[289] P. Zinck, H. Wagner, L. Salmon, and J. Gerard, "Are microcomposites realistic models of the fibre/matrix interface? II. Physico-chemical approach," *Polymer,* vol. 42, no. 15, pp. 6641-6650, 2001.
[290] H. Heilhecker, W. Cross, R. Pentland, C. Griswold, J. Kellar, and L. Kjerengtroen, "The vice angle in the microbond test," *Journal of materials science letters,* vol. 19, no. 23, pp. 2145-2147, 2000.
[291] C. Chou, U. Gaur, and B. Miller, "The effect of microvise gap width on microbond pull-out test results," *Composites science and technology,* vol. 51, no. 1, pp. 111-116, 1994.
[292] J. Craven, R. Cripps, and C. Viney, "Evaluating the silk/epoxy interface by means of the microbond test," *Composites Part A: Applied Science and Manufacturing,* vol. 31, no. 7, pp. 653-660, 2000.
[293] B. Liu, Z. Liu, X. Wang, G. Zhang, S. Long, and J. Yang, "Interfacial shear strength of carbon fiber reinforced polyphenylene sulfide measured by the microbond test," *Polymer testing,* vol. 32, no. 4, pp. 724-730, 2013.
[294] A. Wada and H. Fukuda, "Microbond test for the fiber/matrix interfacial shearing strength," in *ICCM12 Conference*, 1999, p. 347.
[295] H. Wang, H. Wang, W. Li, D. Ren, and Y. Yu, "An improved microbond test method for determination of the interfacial shear strength between carbon fibers and epoxy resin," *Polymer testing,* vol. 32, no. 8, pp. 1460-1465, 2013.
[296] P. Herrera-Franco and L. Drzal, "Comparison of methods for the measurement of fibre/matrix adhesion in composites," *Composites,* vol. 23, no. 1, pp. 2-27, 1992.
[297] L. Yang and J. L. Thomason, "Development and application of micromechanical techniques for characterising interfacial shear strength in

fibre-thermoplastic composites," *Polymer Testing,* vol. 31, no. 7, pp. 895-903, 2012.
[298] S. F. Zhandarov and E. V. Pisanova, "The local bond strength and its determination by fragmentation and pull-out tests," *Composites Science and Technology,* vol. 57, no. 8, pp. 957-964, 1997.
[299] Y. A. Gorbatkina and V. Ivanova-Mumjieva, "Adhesion of polymers to fibers: Further elaboration of pull-out method," *Polymer Science. Series D,* vol. 2, no. 4, pp. 214-216, 2009.
[300] J. K. Kim, C. Baillie, and Y. W. Mai, "Interfacial debonding and fibre pull-out stresses," *Journal of materials science,* vol. 27, no. 12, pp. 3143-3154, 1992.
[301] S. Zhandarov and E. Mäder, "Analysis of a pull-out test with real specimen geometry. Part I: matrix droplet in the shape of a spherical segment," *Journal of adhesion science technology,* vol. 27, no. 4, pp. 430-465, 2013.
[302] W. Beckert and B. Lauke, "Finite element calculation of energy release rate for single-fibre pull-out test," *Computational Materials Science,* vol. 5, no. 1-3, pp. 1-11, 1996.
[303] L. M. Zhou, J. K. Kim, and Y. W. Mai, "On the single fibre pull-out problem: effect of loading method," *Composites science technology,* vol. 45, no. 2, pp. 153-160, 1992.
[304] C. Wang, "Fracture mechanics of single-fibre pull-out test," *Journal of materials science,* vol. 32, no. 2, pp. 483-490, 1997.
[305] D. Tripathi, T. Turton, F. Chen, and F. Jones, "A new method to normalize the effect of matrix properties on the value of interfacial shear strength obtained from the fragmentation test," *Journal of Materials Science*
[306] P. Feillard, G. Desarmot, and J. Favre, "A critical assessment of the fragmentation test for glass/epoxy systems," *Composites science and technology,* vol. 49, no. 2, pp. 109-119, 1993.
[307] A. Awal, G. Cescutti, S. Ghosh, and J. Müssig, "Interfacial studies of natural fibre/polypropylene composites using single fibre fragmentation test (SFFT)," *Composites Part A: Applied Science and Manufacturing,* vol. 42, no. 1, pp. 50-56, 2011.
[308] R. Joffe, J. Andersons, and L. Wallström, "Strength and adhesion characteristics of elementary flax fibres with different surface treatments," *Composites Part A: Applied Science and Manufacturing,* vol. 34, no. 7, pp. 603-612, 2003.
[309] J. Zhang, D. He, H. Wagner, E. Wiesel, and J. Bai, "Interfacial studies of carbon fiber/epoxy composites using single fiber fragmentation test," *Composite Interfaces,* vol. 20, no. 6, pp. 421-429, 2013.
[310] R. Sager *et al.*, "Effect of carbon nanotubes on the interfacial shear strength of T650 carbon fiber in an epoxy matrix," *Composites Science and Technology,* vol. 69, no. 7-8, pp. 898-904, 2009.
[311] J. H. You *et al.*, "Fiber push-out study of a copper matrix composite with an engineered interface: Experiments and cohesive element simulation," *International Journal of Solids Structures,* vol. 46, no. 25-26, pp. 4277-4286, 2009.
[312] K. Goto, I. Kawahara, H. Hatta, Y. Kogo, and I. Shiota, "Measurement of fiber/matrix interface properties of C/C composites by single fiber and fiber

bundle push-out methods," *Composite Interfaces,* vol. 12, no. 7, pp. 603-616, 2005.
[313] A. Kalton, D. Miracle, and T. Clyne, "The effect of interfacial strength on the response of Ti MMCs to single fibre push-out and transverse tensile testing," in *Key Engineering Materials*, 1997, vol. 127, pp. 659-670: Trans Tech Publ.
[314] A. Battisti, D. Esqué-de los Ojos, R. Ghisleni, and A. J. Brunner, "Single fiber push-out characterization of interfacial properties of hierarchical CNT-carbon fiber composites prepared by electrophoretic deposition," *Composites science and technology,* vol. 95, pp. 121-127, 2014.
[315] M. Rodríguez, J. M. Molina-Aldareguía, C. González, and J. LLorca, "A methodology to measure the interface shear strength by means of the fiber push-in test," *Composites Science and Technology,* vol. 72, no. 15, pp. 1924-1932, 2012.
[316] J. M. Molina-Aldareguía, M. Rodríguez, C. González, and J. LLorca, "An experimental and numerical study of the influence of local effects on the application of the fibre push-in test," *Philosophical Magazine,* vol. 91, no. 7-9, pp. 1293-1307, 2011.
[317] C. Medina M, J. M. Molina-Aldareguía, C. González, M. F. Melendrez, P. Flores, and J. LLorca, "Comparison of push-in and push-out tests for measuring interfacial shear strength in nano-reinforced composite materials," *Journal of Composite Materials,* vol. 50, no. 12, pp. 1651-1659, 2016.
[318] M. Piggott, "Why the fibre/polymer interface can appear to be stronger than the polymer matrix," *Composites science and technology,* vol. 57, no. 8, pp. 853-857, 1997.
[319] M. Piggott, "Why interface testing by single-fibre methods can be misleading," *Composites Science and Technology,* vol. 57, no. 8, pp. 965-974, 1997.
[320] A. Mouritz, "Ultrasonic and interlaminar properties of highly porous composites," *Journal of composite materials,* vol. 34, no. 3, pp. 218-239, 2000.
[321] Y. Zhang, L. Zhang, X. Yin, Y. Liu, Z. He, and J. Zhang, "Effects of porosity on in-plane and interlaminar shear strengths of two-dimensional carbon fiber reinforced silicon carbide composites," *Materials & Design,* vol. 98, pp. 120-127, 2016.
[322] M. L. Costa, S. f. M. De Almeida, and M. C. Rezende, "The influence of porosity on the interlaminar shear strength of carbon/epoxy and carbon/bismaleimide fabric laminates," *Composites Science and Technology,* vol. 61, no. 14, pp. 2101-2108, 2001.
[323] M. Mehdikhani, L. Gorbatikh, I. Verpoest, and S. V. Lomov, "Voids in fiber-reinforced polymer composites: A review on their formation, characteristics, and effects on mechanical performance," *Journal of Composite Materials,* vol. 53, no. 12, pp. 1579-1669, 2019.
[324] J. L. Thomason, "The interface region in glass fibre-reinforced epoxy resin composites: 1. Sample preparation, void content and interfacial strength," *Composites,* vol. 7, no. 26, pp. 467-475, 1995.
[325] J. M. Whitney and R. J. Nuismer, "Stress fracture criteria for laminated composites containing stress concentrations," *Journal of composite materials,* vol. 8, no. 3, pp. 253-265, 1974.

[326] E. de Azevedo Soriano and S. F. M. de Almeida, "Notch sensitivity of carbon/epoxy fabric laminates," *Composites science and technology,* vol. 59, no. 8, pp. 1143-1151, 1999.
[327] S. F. M. de Almeida and Z. d. S. N. Neto, "Effect of void content on the strength of composite laminates," *Composite structures,* vol. 28, no. 2, pp. 139-148, 1994.
[328] M. Ali and B. Singh, "The effect of porosity on the properties of glass fibre-reinforced gypsum plaster," *Journal of Materials Science,* vol. 10, no. 11, pp. 1920-1928, 1975.
[329] S. Sarıdağ, D. Helvacıoğlu-Yiğit, M. Özcan, E. Avcu, and G. Kızıltaş, "Micro-computerized tomography analysis of cement voids and pull-out strength of glass fiber posts luted with self-adhesive and glass-ionomer cements in the root canal," *Journal of adhesion science and Technology,* vol. 30, no. 14, pp. 1585-1595, 2016.
[330] S. Nganga, A. Ylä-Soininmäki, L. V. Lassila, and P. K. Vallittu, "Interface shear strength and fracture behaviour of porous glass-fibre-reinforced composite implant and bone model material," *Journal of the mechanical behavior of biomedical materials,* vol. 4, no. 8, pp. 1797-1804, 2011.
[331] G. Jia, Z. Li, P. Liu, and Q. Jing, "Preparation and characterization of aerogel/expanded perlite composite as building thermal insulation material," *Journal of Non-Crystalline Solids,* vol. 482, pp. 192-202, 2018.
[332] J. Song, Q. Zhao, C. Meng, J. Meng, Z. Chen, and J. Li, "Hierarchical Porous Recycled PET Nanofibers for High-Efficiency Aerosols and Virus Capturing," *ACS Applied Materials & Interfaces,* vol. 13, no. 41, pp. 49380-49389, 2021.
[333] N.-J. Lee and J. Jang, "The effect of fibre content on the mechanical properties of glass fibre mat/polypropylene composites," *Composites Part A: Applied Science and Manufacturing,* vol. 30, no. 6, pp. 815-822, 1999.
[334] F. Mesquita, S. Bucknell, Y. Leray, S. V. Lomov, and Y. Swolfs, "Single carbon and glass fibre properties characterised using large data sets obtained through automated single fibre tensile testing," *Composites Part A: Applied Science and Manufacturing,* vol. 145, p. 106389, 2021.
[335] J. Thomason, L. Yang, and R. Meier, "The properties of glass fibres after conditioning at composite recycling temperatures," *Composites Part A: Applied Science and Manufacturing,* vol. 61, pp. 201-208, 2014.
[336] D. Bryce, L. Yang, and J. L. Thomason, "An investigation of fibre sizing on the interfacial strength of glass-fibre epoxy composites," in *ECCM18-18th European Conference on Composite Materials*, 2018.
[337] D. Thorne, "Distribution of internal flaws in acrylic fibers," *Journal of applied polymer science,* vol. 14, no. 1, pp. 103-113, 1970.
[338] P. Li and H. Shan, "Study on polymerization of acrylonitrile with methylacrylate and itaconic acid in mixed solvent," *Journal of applied polymer science,* vol. 56, no. 7, pp. 877-880, 1995.
[339] Y. Xu, W. Xu, F. Huang, and Q. Wei, "Preparation and Photocatalytic Activity of TiO_2-deposited fabrics," *International Journal of Photoenergy,* vol. 2012, 2012.
[340] Y. Sun, C. Yang, and Y. Lu, "Weak layer exfoliation and an attempt for modification in anodic oxidation of PAN-based carbon fiber," *Journal of Materials Science,* vol. 55, no. 6, pp. 2372-2379, 2020.

[341] Q. Huo, "Chapter 16 - Synthetic Chemistry of the Inorganic Ordered Porous Materials," in *Modern Inorganic Synthetic Chemistry*, R. Xu, W. Pang, and Q. Huo, Eds. Amsterdam: Elsevier, 2011, pp. 339-373.
[342] R. Yang, X. Wang, Y. Zhang, H. Mao, P. Lan, and D. Zhou, "Facile synthesis of mesoporous silica aerogels from rice straw ash-based biosilica via freeze-drying," *BioResources*, vol. 14, no. 1, pp. 87-98, 2019.
[343] G. Wu, Y. Yu, X. Cheng, and Y. Zhang, "Preparation and surface modification mechanism of silica aerogels via ambient pressure drying," *Materials Chemistry and Physics*, vol. 129, no. 1-2, pp. 308-314, 2011.
[344] G. W. Scherer and D. M. Smith, "Cavitation during drying of a gel," *Journal of Non-Crystalline Solids*, vol. 189, no. 3, pp. 197-211, 1995.
[345] J. Kwon, J. Kim, T. Yoo, D. Park, and H. Han, "Preparation and Characterization of Spherical Polyimide Aerogel Microparticles," *Macromolecular Materials and Engineering*, https://doi.org/10.1002/mame.201400010 vol. 299, no. 9, pp. 1081-1088, 2014.
[346] G. W. Scherer, D. M. Smith, and D. Stein, "Deformation of aerogels during characterization," *Journal of Non-Crystalline Solids*, vol. 186, pp. 309-315, 1995.
[347] A. Ayral, J. Phalippou, and T. Woignier, "Skeletal density of silica aerogels determined by helium pycnometry," *Journal of materials science*, vol. 27, no. 5, pp. 1166-1170, 1992.
[348] H. Guo, M. A. B. Meador, L. S. McCorkle, D. A. Scheiman, J. D. McCrone, and B. Wilkewitz, "Poly(maleic anhydride) cross-linked polyimide aerogels: synthesis and properties," *RSC Advances*, 10.1039/C6RA01013J vol. 6, no. 31, pp. 26055-26065, 2016.
[349] R. Raghava, "Thermal expansion of organic and inorganic matrix composites: A review of theoretical and experimental studies," *Polymer Composites*, vol. 9, no. 1, pp. 1-11, 1988.
[350] S. I. Numata, S. Oohara, K. Fujisaki, J. I. Imaizumi, and N. Kinjo, "Thermal expansion behavior of various aromatic polyimides," *Journal of applied polymer science*, vol. 31, no. 1, pp. 101-110, 1986.
[351] A. H. Alaoui, T. Woignier, G. W. Scherer, and J. Phalippou, "Comparison between flexural and uniaxial compression tests to measure the elastic modulus of silica aerogel," *Journal of non-crystalline solids*, vol. 354, no. 40-41, pp. 4556-4561, 2008.
[352] X. Li, Q. Wang, H. Li, H. Ji, X. Sun, and J. He, "Effect of sepiolite fiber on the structure and properties of the sepiolite/silica aerogel composite," *Journal of Sol-Gel Science and Technology*, vol. 67, no. 3, pp. 646-653, 2013.
[353] U. K. H. Bangi, M. S. Kavale, S. Baek, and H. H. Park, "Synthesis of MWCNTs doped sodium silicate based aerogels by ambient pressure drying," *Journal of Sol-Gel Science and Technology*, vol. 62, no. 2, pp. 201-207, 2012.
[354] T. Linhares, M. T. Pessoa de Amorim, and L. Durães, "Silica aerogel composites with embedded fibres: a review on their preparation, properties and applications," *Journal of Materials Chemistry A*, 10.1039/C9TA04811A vol. 7, no. 40, pp. 22768-22802, 2019.
[355] V. Rao, P. Herrera-Franco, A. Ozzello, and L. Drzal, "A direct comparison of the fragmentation test and the microbond pull-out test for determining the

interfacial shear strength," *The Journal of Adhesion,* vol. 34, no. 1-4, pp. 65-77, 1991.
[356] S. Zhandarov and E. Mäder, "Peak force as function of the embedded length in pull-out and microbond tests: effect of specimen geometry," *Journal of adhesion science and technology,* vol. 19, no. 10, pp. 817-855, 2005.
[357] J. Yeo, Z. Liu, and T. Y. Ng, "Silica Aerogels: A Review of Molecular Dynamics Modelling and Characterization of the Structural, Thermal, and Mechanical Properties," *Handbook of Materials Modeling: Applications: Current and Emerging Materials*, pp. 1575-1595, 2020.
[358] B. Feuston and S. Garofalini, "Oligomerization in silica sols," *Journal of Physical Chemistry,* vol. 94, no. 13, pp. 5351-5356, 1990.
[359] S. H. Garofalini and G. Martin, "Molecular simulations of the polymerization of silicic acid molecules and network formation," *The Journal of Physical Chemistry,* vol. 98, no. 4, pp. 1311-1316, 1994.
[360] G. E. Martin and S. H. Garofalini, "Sol-gel polymerization: analysis of molecular mechanisms and the effect of hydrogen," *Journal of non-crystalline solids,* vol. 171, no. 1, pp. 68-79, 1994.
[361] S. Bhattacharya and J. Kieffer, "Fractal dimensions of silica gels generated using reactive molecular dynamics simulations," *The Journal of chemical physics,* vol. 122, no. 9, p. 094715, 2005.
[362] S. Bhattacharya and J. Kieffer, "Molecular dynamics simulation study of growth regimes during polycondensation of silicic acid: from silica nanoparticles to porous gels," *The Journal of Physical Chemistry C,* vol. 112, no. 6, pp. 1764-1771, 2008.
[363] J. Kieffer and C. A. Angell, "Generation of fractal structures by negative pressure rupturing of SiO_2 glass," *Journal of Non-Crystalline Solids,* vol. 106, no. 1-3, pp. 336-342, 1988.
[364] A. Nakano, L. Bi, R. K. Kalia, and P. Vashishta, "Structural correlations in porous silica: Molecular dynamics simulation on a parallel computer," *Physical review letters,* vol. 71, no. 1, p. 85, 1993.
[365] Z. Lu, Z. Yuan, Q. Liu, Z. Hu, F. Xie, and M. Zhu, "Multi-scale simulation of the tensile properties of fiber-reinforced silica aerogel composites," *Materials Science and Engineering: A,* vol. 625, pp. 278-287, 2015.
[366] G. Gonçalves, M. Lenzi, O. Santos, and L. Jorge, "Preparation and characterization of nickel based catalysts on silica, alumina and titania obtained by sol–gel method," *Journal of Non-Crystalline Solids,* vol. 352, no. 32-35, pp. 3697-3704, 2006.
[367] W. Gonçalves, J. Morthomas, P. Chantrenne, M. Perez, G. Foray, and C. L. Martin, "Molecular dynamics simulations of amorphous silica surface properties with truncated Coulomb interactions," *Journal of Non-Crystalline Solids,* vol. 447, pp. 1-8, 2016.
[368] T. Campbell *et al.*, "Structural correlations and mechanical behavior in nanophase silica glasses," *Physical review letters,* vol. 82, no. 20, p. 4018, 1999.
[369] J. S. R. Murillo, M. E. Bachlechner, F. A. Campo, and E. J. Barbero, "Structure and mechanical properties of silica aerogels and xerogels modeled by molecular dynamics simulation," *Journal of Non-Crystalline Solids,* vol. 356, no. 25, pp. 1325-1331, 2010.

[370] S. P. Patil, A. Rege, M. Itskov, and B. Markert, "Mechanics of Nanostructured Porous Silica Aerogel Resulting From Molecular Dynamics Simulations," *The Journal of Physical Chemistry B,* 2017.
[371] T. Woignier, J. Primera, A. Alaoui, P. Etienne, F. Despestis, and S. Calas-Etienne, "Mechanical Properties and Brittle Behavior of Silica Aerogels," *Gels,* vol. 1, no. 2, pp. 256-275, 2015.
[372] J. Lei, Z. Liu, J. Yeo, and T. Y. Ng, "Determination of the Young's modulus of silica aerogels–an analytical–numerical approach," *Soft Matter,* vol. 9, no. 47, pp. 11367-11373, 2013.
[373] L. D. Gelb, "Simulating silica aerogels with a coarse-grained flexible model and langevin dynamics," *The Journal of Physical Chemistry C,* vol. 111, no. 43, pp. 15792-15802, 2007.
[374] C. A. Ferreiro-Rangel and L. D. Gelb, "Computational study of uniaxial deformations in silica aerogel using a coarse-grained model," *The Journal of Physical Chemistry B,* vol. 119, no. 27, pp. 8640-8650, 2015.
[375] C. A. Ferreiro-Rangel and L. D. Gelb, "Investigation of the bulk modulus of silica aerogel using molecular dynamics simulations of a coarse-grained model," *The Journal of Physical Chemistry B,* vol. 117, no. 23, pp. 7095-7105, 2013.
[376] J. Fricke, "Aerogels—highly tenuous solids with fascinating properties," *Journal of non-Crystalline solids,* vol. 100, no. 1-3, pp. 169-173, 1988.
[377] J. J. Yeo, Z. Liu, and T. Y. Ng, "Enhanced thermal characterization of silica aerogels through molecular dynamics simulation," *Modelling and Simulation in Materials Science and Engineering,* vol. 21, no. 7, p. 075004, 2013.
[378] J. J. Yeo, Z. Liu, and T. Y. Ng, "Enhanced thermal characterization of silica aerogels through molecular dynamics simulation," *Modelling and Simulation in Materials Science and Engineering,* vol. 21, no. 7, 2013.
[379] C. Bi, G. Tang, and Z. Hu, "Heat conduction modeling in 3-D ordered structures for prediction of aerogel thermal conductivity," *International Journal of Heat and Mass Transfer,* vol. 73, pp. 103-109, 2014.
[380] S. U. Patil *et al.*, "Interfacial characteristics between flattened CNT stacks and polyimides: A molecular dynamics study," *Computational Materials Science,* vol. 185, p. 109970, 2020.
[381] Y. Dong, S. C. Rismiller, and J. Lin, "Molecular dynamic simulation of layered graphene clusters formation from polyimides under extreme conditions," *Carbon,* vol. 104, pp. 47-55, 2016.
[382] D. Qi, J. Hinkley, and G. He, "Molecular dynamics simulation of thermal and mechanical properties of polyimide–carbon-nanotube composites," *Modelling and Simulation in Materials Science and Engineering,* vol. 13, no. 4, p. 493, 2005.
[383] K. Min *et al.*, "Computational approaches for investigating interfacial adhesion phenomena of polyimide on silica glass," *Scientific reports,* vol. 7, no. 1, pp. 1-11, 2017.
[384] F. P. K. Ravindranath, "Molecular Modeling of PMR-15 Polyimide," Citeseer, 2013.
[385] A. Vashisth, C. Ashraf, C. E. Bakis, and A. Van Duin, "Reactive Molecular Dynamics Simulation of Accelerated Cross-linking and Disintegration of Bisphenol F/DETDA Polymer using ReaxFF," in *American Society for*

Composites (ASC) 33rd Annual Technical Conference, the 18th US-Japan Conference on Composite Materials, and the ASTM D30, 2018.
[386] A. Kumar *et al.*, "Adhesion between a rutile surface and a polyimide: a coarse grained molecular dynamics study," *Modelling and Simulation in Materials Science and Engineering,* vol. 26, no. 3, p. 035012, 2018.
[387] C. Wen, B. Liu, J. Wolfgang, T. E. Long, R. Odle, and S. Cheng, "Determination of glass transition temperature of polyimides from atomistic molecular dynamics simulations and machine-learning algorithms," *Journal of Polymer Science,* vol. 58, no. 11, pp. 1521-1534, 2020.
[388] C. Hu, T. Lu, and H. Guo, "Developing a transferable coarse-grained model for the prediction of thermodynamic, structural, and mechanical properties of polyimides at different thermodynamic state points," *Journal of chemical information and modeling,* vol. 59, no. 5, pp. 2009-2025, 2019.
[389] D. M. Delozier, K. A. Watson, J. G. Smith, T. C. Clancy, and J. W. Connell, "Investigation of aromatic/aliphatic polyimides as dispersants for single wall carbon nanotubes," *Macromolecules,* vol. 39, no. 5, pp. 1731-1739, 2006.
[390] K. S. Khare and R. Khare, "Directed diffusion approach for preparing atomistic models of crosslinked epoxy for use in molecular simulations," *Macromolecular theory and simulations,* vol. 21, no. 5, pp. 322-327, 2012.
[391] J. Fan, A. Anastassiou, C. W. Macosko, and E. B. Tadmor, "Molecular dynamics predictions of thermomechanical properties of an epoxy thermosetting polymer," *Polymer,* vol. 196, p. 122477, 2020.
[392] H. Liu, M. Li, Z. Y. Lu, Z. G. Zhang, C. C. Sun, and T. Cui, "Multiscale simulation study on the curing reaction and the network structure in a typical epoxy system," *Macromolecules,* vol. 44, no. 21, pp. 8650-8660, 2011.
[393] C. Li and A. Strachan, "Effect of thickness on the thermo-mechanical response of free-standing thermoset nanofilms from molecular dynamics," *Macromolecules,* vol. 44, no. 23, pp. 9448-9454, 2011.
[394] G. M. Odegard, B. D. Jensen, S. Gowtham, J. Wu, J. He, and Z. Zhang, "Predicting mechanical response of crosslinked epoxy using ReaxFF," *Chemical Physics Letters,* vol. 591, pp. 175-178, 2014.
[395] J. L. Tack and D. M. Ford, "Thermodynamic and mechanical properties of epoxy resin DGEBF crosslinked with DETDA by molecular dynamics," *Journal of Molecular Graphics and Modelling,* vol. 26, no. 8, pp. 1269-1275, 2008.
[396] C. Li, G. A. Medvedev, E. W. Lee, J. Kim, J. M. Caruthers, and A. Strachan, "Molecular dynamics simulations and experimental studies of the thermomechanical response of an epoxy thermoset polymer," *Polymer,* vol. 53, no. 19, pp. 4222-4230, 2012.
[397] A. Bandyopadhyay, P. K. Valavala, T. C. Clancy, K. E. Wise, and G. M. Odegard, "Molecular modeling of crosslinked epoxy polymers: The effect of crosslink density on thermomechanical properties," *Polymer,* vol. 52, no. 11, pp. 2445-2452, 2011.
[398] L. H. Tam and D. Lau, "Moisture effect on the mechanical and interfacial properties of epoxy-bonded material system: An atomistic and experimental investigation," *Polymer,* vol. 57, pp. 132-142, 2015.
[399] V. Varshney, S. S. Patnaik, A. K. Roy, and B. L. Farmer, "A molecular dynamics study of epoxy-based networks: cross-linking procedure and

prediction of molecular and material properties," *Macromolecules*, vol. 41, no. 18, pp. 6837-6842, 2008.
[400] T. Okabe, Y. Oya, K. Tanabe, G. Kikugawa, and K. Yoshioka, "Molecular dynamics simulation of crosslinked epoxy resins: curing and mechanical properties," *European Polymer Journal*, vol. 80, pp. 78-88, 2016.
[401] C. Li, A. R. Browning, S. Christensen, and A. Strachan, "Atomistic simulations on multilayer graphene reinforced epoxy composites," *Composites Part A: Applied Science and Manufacturing*, vol. 43, no. 8, pp. 1293-1300, 2012.
[402] H. Al Mahmud, M. S. Radue, S. Chinkanjanarot, W. A. Pisani, S. Gowtham, and G. M. Odegard, "Multiscale modeling of carbon fiber-graphene nanoplatelet-epoxy hybrid composites using a reactive force field," *Composites Part B: Engineering*, vol. 172, pp. 628-635, 2019.
[403] S. M. Rahimian-Koloor, S. M. Hashemianzadeh, and M. M. Shokrieh, "Effect of CNT structural defects on the mechanical properties of CNT/Epoxy nanocomposite," *Physica B: Condensed Matter*, vol. 540, pp. 16-25, 2018.
[404] N. Fasanella and V. Sundararaghavan, "Atomistic modeling of thermomechanical properties of SWNT/Epoxy nanocomposites," *Modelling and Simulation in Materials Science and Engineering*, vol. 23, no. 6, p. 065003, 2015.
[405] C. M. Hadden *et al.*, "Mechanical properties of graphene nanoplatelet/carbon fiber/epoxy hybrid composites: Multiscale modeling and experiments," *Carbon*, vol. 95, pp. 100-112, 2015.
[406] M. T. Stoffels, M. P. Staiger, and C. M. Bishop, "Reduced interfacial adhesion in glass fibre-epoxy composites due to water absorption via molecular dynamics simulations," *Composites Part A: Applied Science and Manufacturing*, vol. 118, pp. 99-105, 2019.
[407] S. C. Chowdhury and T. Okabe, "Computer simulation of carbon nanotube pull-out from polymer by the molecular dynamics method," *Composites Part A: Applied Science and Manufacturing*, vol. 38, no. 3, pp. 747-754, 2007.
[408] S. C. Chowdhury, R. Prosser, T. W. Sirk, R. M. Elder, and J. W. Gillespie Jr, "Glass fiber-epoxy interactions in the presence of silane: A molecular dynamics study," *Applied Surface Science*, vol. 542, p. 148738, 2021.
[409] M. Zhang, B. Jiang, C. Chen, D. Drummer, and Z. Zhai, "The effect of temperature and strain rate on the interfacial behavior of glass fiber reinforced polypropylene composites: a molecular dynamics study," *Polymers*, vol. 11, no. 11, 2019.
[410] L. Pan, H. Guo, L. Zhong, M. Wang, P. Xue, and X. Yuan, "Influence of surface-modified glass fibers on interfacial properties of GF/PEEK composites using molecular dynamics," *Computational Materials Science*, vol. 188, p. 110216, 2021.
[411] S. C. Chowdhury, E. A. Wise, and J. W. Gillespie Jr, "Modeling of Glass Fiber with Surface Cracks—A Molecular Dynamics Simulation Study," in *Proceedings of the American Society for Composites—Thirty-second Technical Conference*, 2017.
[412] S. Chowdhury, E. Wise, R. Elder, T. Sirk, D. Hartman, and J. Gillespie Jr, "Molecular Dynamics Simulations of Fiber-Sizing Interphase," in *Proceedings of the American Society for Composites—Thirty-third Technical Conference*, 2018.

[413] S. Curgul, K. J. Van Vliet, and G. C. Rutledge, "Molecular dynamics simulation of size-dependent structural and thermal properties of polymer nanofibers," *Macromolecules,* vol. 40, no. 23, pp. 8483-8489, 2007.
[414] L. Adkins and A. Cormack, "A Study of Silica Glass Fiber Structure and Elastic Properties, using Molecular Dynamics Simulations," *Processing, Properties and Applications of Glass and Optical Materials: Ceramic Transactions,* vol. 231, pp. 115-123, 2012.
[415] V. Tan, M. Deng, and T. Tay, "Molecular Dynamics Simulation of glass/epoxy interfaces," *Proceedings of the ICCM 2009,* 2009.
[416] S. P. Patil, P. Shendye, and B. Markert, "Molecular dynamics simulations of silica aerogel nanocomposites reinforced by glass fibers, graphene sheets and carbon nanotubes: A comparison study on mechanical properties," *Composites Part B: Engineering,* vol. 190, p. 107884, 2020.
[417] N. Yang *et al.*, "Thermal Interface Conductance Between Aluminum and Silicon by Molecular Dynamics Simulations," *Journal of Computational and Theoretical Nanoscience,* vol. 12, no. 2, pp. 168-174, 2015.
[418] H. Zhong and J. R. Lukes, "Interfacial thermal resistance between carbon nanotubes: Molecular dynamics simulations and analytical thermal modeling," *Physical Review B,* vol. 74, no. 12, 2006.
[419] T. Luo and J. R. Lloyd, "Enhancement of Thermal Energy Transport Across Graphene/Graphite and Polymer Interfaces: A Molecular Dynamics Study," *Advanced Functional Materials,* vol. 22, no. 12, pp. 2495-2502, 2012.
[420] Y. Chalopin, K. Esfarjani, A. Henry, S. Volz, and G. Chen, "Thermal interface conductance in Si/Ge superlattices by equilibrium molecular dynamics," *Physical Review B,* vol. 85, no. 19, p. 195302, 2012.
[421] Y. Wang, X. Ruan, and A. K. Roy, "Two-temperature nonequilibrium molecular dynamics simulation of thermal transport across metal-nonmetal interfaces," *Physical Review B,* vol. 85, no. 20, p. 205311, 2012.
[422] R. J. Stevens, L. V. Zhigilei, and P. M. Norris, "Effects of temperature and disorder on thermal boundary conductance at solid–solid interfaces: Nonequilibrium molecular dynamics simulations," *International Journal of Heat and Mass Transfer,* vol. 50, no. 19, pp. 3977-3989, 2007.
[423] J. Diao, D. Srivastava, and M. Menon, "Molecular dynamics simulations of carbon nanotube/silicon interfacial thermal conductance," *The Journal of chemical physics,* vol. 128, no. 16, p. 164708, 2008.
[424] E. Landry and A. McGaughey, "Thermal boundary resistance predictions from molecular dynamics simulations and theoretical calculations," *Physical Review B,* vol. 80, no. 16, p. 165304, 2009.
[425] Z. Y. Ong and E. Pop, "Molecular dynamics simulation of thermal boundary conductance between carbon nanotubes and SiO_2," *Physical Review B,* vol. 81, no. 15, p. 155408, 2010.
[426] Y. Wang, C. Yang, Y. Cheng, and Y. Zhang, "A molecular dynamics study on thermal and mechanical properties of graphene–paraffin nanocomposites," *RSC Advances,* vol. 5, no. 101, pp. 82638-82644, 2015.
[427] K. Zhang, H. Fan, and M. M. Yuen, "Molecular dynamics study on thermal performance of CNT-array-thermal interface material," in *2006 International Conference on Electronic Materials and Packaging*, 2006, pp. 1-4: IEEE.

[428] E. Lampin, Q. H. Nguyen, P. Francioso, and F. Cleri, "Thermal boundary resistance at silicon-silica interfaces by molecular dynamics simulations," *Applied Physics Letters,* vol. 100, no. 13, p. 131906, 2012.
[429] A. Yu, P. Ramesh, M. E. Itkis, E. Bekyarova, and R. C. Haddon, "Graphite nanoplatelet− epoxy composite thermal interface materials," *The Journal of Physical Chemistry C,* vol. 111, no. 21, pp. 7565-7569, 2007.
[430] M. Barisik and A. Beskok, "Boundary treatment effects on molecular dynamics simulations of interface thermal resistance," *Journal of Computational Physics,* vol. 231, no. 23, pp. 7881-7892, 2012.
[431] M. Hu, S. Shenogin, and P. Keblinski, "Molecular dynamics simulation of interfacial thermal conductance between silicon and amorphous polyethylene," *Applied Physics Letters,* vol. 91, no. 24, p. 241910, 2007.
[432] V. Varshney, S. S. Patnaik, A. K. Roy, and B. L. Farmer, "Modeling of thermal conductance at transverse CNT− CNT interfaces," *The Journal of Physical Chemistry C,* vol. 114, no. 39, pp. 16223-16228, 2010.
[433] Y. Wang and Y. Zhang, "Superior thermal conductivity of carbon nanoscroll based thermal interface materials," in *2015 IEEE 65th Electronic Components and Technology Conference (ECTC)*, 2015, pp. 1234-1239: IEEE.
[434] M. Wang, N. Hu, L. Zhou, and C. Yan, "Enhanced interfacial thermal transport across graphene–polymer interfaces by grafting polymer chains," *Carbon,* vol. 85, pp. 414-421, 2015.
[435] A. K. Vallabhaneni, B. Qiu, J. Hu, Y. P. Chen, A. K. Roy, and X. Ruan, "Interfacial thermal conductance limit and thermal rectification across vertical carbon nanotube/graphene nanoribbon-silicon interfaces," *Journal of Applied Physics,* vol. 113, no. 6, p. 064311, 2013.
[436] P. H. Huang, "Molecular dynamics for lateral surface adhesion and peeling behavior of single-walled carbon nanotubes on gold surfaces," *Materials Chemistry and Physics,* vol. 131, no. 1-2, pp. 297-305, 2011.
[437] K. Min *et al.*, "Interfacial adhesion behavior of polyimides on silica glass: A molecular dynamics study," *Polymer,* vol. 98, pp. 1-10, 2016.
[438] Y. Jin, F. Duan, and X. Mu, "Functionalization enhancement on interfacial shear strength between graphene and polyethylene," *Applied Surface Science,* vol. 387, pp. 1100-1109, 2016.
[439] J. Gou, B. Minaie, B. Wang, Z. Liang, and C. Zhang, "Computational and experimental study of interfacial bonding of single-walled nanotube reinforced composites," *Computational Materials Science,* vol. 31, no. 3, pp. 225-236, 2004.
[440] R. Chawla and S. Sharma, "Molecular dynamics simulation of carbon nanotube pull-out from polyethylene matrix," *Composites Science and Technology,* vol. 144, pp. 169-177, 2017.
[441] K. Liao and S. Li, "Interfacial characteristics of a carbon nanotube–polystyrene composite system," *Applied Physics Letters,* vol. 79, no. 25, pp. 4225-4227, 2001.
[442] Q. Zheng, D. Xia, Q. Xue, K. Yan, X. Gao, and Q. Li, "Computational analysis of effect of modification on the interfacial characteristics of a carbon nanotube–polyethylene composite system," *Applied Surface Science,* vol. 255, no. 6, pp. 3534-3543, 2009.

[443] B. Demir, K. M. Beggs, B. L. Fox, L. Servinis, L. C. Henderson, and T. R. Walsh, "A predictive model of interfacial interactions between functionalised carbon fibre surfaces cross-linked with epoxy resin," *Composites Science and Technology,* vol. 159, pp. 127-134, 2018.
[444] S. Zhao, Y. Zhang, J. Yang, and S. Kitipornchai, "Significantly improved interfacial shear strength in graphene/copper nanocomposite via wrinkles and functionalization: A molecular dynamics study," *Carbon,* vol. 174, pp. 335-344, 2021.
[445] A. Singh and D. Kumar, "Temperature effects on the interfacial behavior of functionalized carbon nanotube–polyethylene nanocomposite using molecular dynamics simulation," *Proceedings of the Institution of Mechanical Engineers, Part N: Journal of Nanomaterials, Nanoengineering and Nanosystems,* vol. 233, no. 1, pp. 3-15, 2019.
[446] M. Li, H. Zhou, Y. Zhang, Y. Liao, and H. Zhou, "The effect of defects on the interfacial mechanical properties of graphene/epoxy composites," *RSC advances,* vol. 7, no. 73, pp. 46101-46108, 2017.
[447] Y. Xin, F. Duan, and X. Mu, "Effects of defects on the interfacial shear characteristics between graphene and poly (methyl methacrylate)," *Polymer Composites,* vol. 41, no. 10, pp. 4297-4306, 2020.
[448] F. Liu *et al.,* "The interfacial mechanical properties of functionalized graphene–polymer nanocomposites," *RSC advances,* vol. 6, no. 71, pp. 66658-66664, 2016.
[449] R. Sun, L. Li, H. Zhang, and J. Yang, "Effect of hydrogen functionalization on interfacial behavior of defective‐graphene/polymer nanocomposites," *Polymer Composites,* vol. 41, no. 4, pp. 1291-1298, 2020.
[450] X. Peng and S. Meguid, "Molecular simulations of the influence of defects and functionalization on the shear strength of carbon nanotube-epoxy polymer interfaces," *Computational Materials Science,* vol. 126, pp. 204-216, 2017.
[451] R. W. Wyckoff, *Crystal structures. vol. 1*. Interscience Publ., 1971.
[452] "LAMMPS," *available at: http:/lammps. sandia. gov,* 2013.
[453] M. D. Hanwell, D. E. Curtis, D. C. Lonie, T. Vandermeersch, E. Zurek, and G. R. Hutchison, "Avogadro: an advanced semantic chemical editor, visualization, and analysis platform," *Journal of cheminformatics,* vol. 4, no. 1, p. 17, 2012.
[454] A. I. Jewett, Z. Zhuang, and J.-E. Shea, "Moltemplate a coarse-grained model assembly tool," *Biophysical Journal,* vol. 104, no. 2, p. 169a, 2013.
[455] A. Stukowski, "Visualization and analysis of atomistic simulation data with OVITO–the Open Visualization Tool," *Modelling and Simulation in Materials Science and Engineering,* vol. 18, no. 1, p. 015012, 2009.
[456] C. Feger, *Advances in polyimide: science and technology*. CRC Press, 1993.
[457] A. Shokuhfar and B. Arab, "The effect of cross linking density on the mechanical properties and structure of the epoxy polymers: molecular dynamics simulation," *Journal of Molecular Modeling,* journal article vol. 19, no. 9, pp. 3719-3731, September 01 2013.
[458] P. Mallick, *Processing of Polymer Matrix Composites*. CRC Press, 2017.
[459] T. F. Willems, C. H. Rycroft, M. Kazi, J. C. Meza, and M. Haranczyk, "Algorithms and tools for high-throughput geometry-based analysis of

crystalline porous materials," *Microporous and Mesoporous Materials,* vol. 149, no. 1, pp. 134-141, 2012.
[460] E. Braun, " Open Source Code: Calculating an IR Spectra from a LAMMPS Simulation (Version v1.0.0)," 2016.
[461] H. Eyring, D. Henderson, and W. Jost, "Physical chemistry: an advanced treatise," Academic Press1967.
[462] P. H. Berens and K. R. Wilson, "Molecular dynamics and spectra. I. Diatomic rotation and vibration," *The Journal of Chemical Physics,* vol. 74, no. 9, pp. 4872-4882, 1981.
[463] S. Goyal *et al.*, "Characterizing the fundamental adhesion of polyimide monomers on crystalline and glassy silica surfaces: A molecular dynamics study," *The Journal of Physical Chemistry C,* vol. 120, no. 41, pp. 23631-23639, 2016.
[464] S. Izrailev *et al.*, "Computational Molecular Dynamics: Challenges, Methods," in *Ideas*, 1998, vol. 4, p. 39.
[465] C. Jarzynski, "Nonequilibrium equality for free energy differences," *Physical Review Letters,* vol. 78, no. 14, p. 2690, 1997.
[466] S. Kuang and J. D. Gezelter, "A gentler approach to RNEMD: nonisotropic velocity scaling for computing thermal conductivity and shear viscosity," *The Journal of chemical physics,* vol. 133, no. 16, p. 164101, 2010.
[467] F. Müller-Plathe and P. Bordat, "Reverse non-equilibrium molecular dynamics," in *Novel methods in soft matter simulations*: Springer, 2004, pp. 310-326.
[468] T. L. Bergman, F. P. Incropera, D. P. DeWitt, and A. S. Lavine, *Fundamentals of heat and mass transfer*. John Wiley & Sons, 2011.
[469] P. Wirnsberger, D. Frenkel, and C. Dellago, "An enhanced version of the heat exchange algorithm with excellent energy conservation properties," *The Journal of chemical physics,* vol. 143, no. 12, p. 124104, 2015.
[470] L. Cai and G. Shan, "Elastic silica aerogel using methyltrimethoxysilane precusor via ambient pressure drying," *Journal of Porous Materials,* vol. 22, no. 6, pp. 1455-1463, 2015.
[471] E. Courtens and R. Vacher, "Porous silica," *Amorphous Insulators and Semiconductors, NATO ASI Series,* vol. 3, pp. 255-288, 1997.
[472] L. Roiban *et al.*, "Advanced three dimensional characterization of silica-based ultraporous materials," *RSC Advances,* vol. 6, no. 13, pp. 10625-10632, 2016.
[473] Z. Deng, J. Wang, J. Wei, J. Shen, B. Zhou, and L. Chen, "Physical properties of silica aerogels prepared with polyethoxydisiloxanes," *Journal of Sol-Gel Science and Technology,* vol. 19, no. 1-3, pp. 677-680, 2000.
[474] S. Iswar, W. J. Malfait, S. Balog, F. Winnefeld, M. Lattuada, and M. M. Koebel, "Effect of aging on silica aerogel properties," *Microporous and Mesoporous Materials,* vol. 241, pp. 293-302, 2017.
[475] A. C. Lua and J. Su, "Isothermal and non-isothermal pyrolysis kinetics of Kapton® polyimide," *Polymer Degradation and Stability,* vol. 91, no. 1, pp. 144-153, 2006.
[476] S. Diaham, M. Locatelli, and R. Khazaka, "BPDA-PDA polyimide: synthesis, characterizations, aging and semiconductor device passivation," *High Performance Polymers-Polyimides Based-From Chemistry to Applications,* pp. 15-36, 2012.

[477] G. D. Hietpas and D. L. Allara, "The molecular structure of poly (biphenyl dianhydride-p-phenylenediamine) polyimide thin films by infrared spectroscopy: Thickness dependence of structure in the nano-to micrometer range," *Journal of Polymer Science Part B: Polymer Physics*, vol. 36, no. 7, pp. 1247-1260, 1998.
[478] Y. Yang *et al.*, "FTIR and dielectric studies of electrical aging in polyimide under AC voltage," *IEEE Transactions on Dielectrics and Electrical Insulation*, vol. 19, no. 2, pp. 574-581, 2012.
[479] S. L. Vivod, M. A. B. Meador, C. Pugh, M. Wilkosz, K. Calomino, and L. McCorkle, "Toward Improved Optical Transparency of Polyimide Aerogels," *ACS applied materials and interfaces*, vol. 12, no. 7, pp. 8622-8633, 2020.
[480] H. Guo *et al.*, "Polyimide aerogels cross-linked through amine functionalized polyoligomeric silsesquioxane," *ACS applied materialsand interfaces*, vol. 3, no. 2, pp. 546-552, 2011.
[481] G. Qianming, L. Dan, L. Zhi, Y. Xiao-Su, and L. Ji, "Tribology properties of carbon nanotube-reinforced composites," in *Tribology and Interface Engineering Series*, vol. 55: Elsevier, 2008, pp. 245-267.
[482] S. T. Cholake *et al.*, "Quantitative analysis of curing mechanisms of epoxy resin by mid-and near-fourier transform infra red spectroscopy," *Defence Science Journal*, vol. 64, no. 3, p. 314, 2014.
[483] W. M. Haynes, *CRC handbook of chemistry and physics*. CRC press, 2014.
[484] J. Feng, X. Wang, Y. Jiang, D. Du, and J. Feng, "Study on thermal conductivities of aromatic polyimide aerogels," *ACS applied materials and interfaces*, vol. 8, no. 20, pp. 12992-12996, 2016.
[485] S. Wu, A. Du, S. Huang, W. Sun, Y. Xiang, and B. Zhou, "Solution-processable polyimide aerogels with high hydrophobicity," *Materials Letters*, vol. 176, pp. 118-121, 2016.
[486] H. Balamane, T. Halicioglu, and W. Tiller, "Comparative study of silicon empirical interatomic potentials," *Physical Review B*, vol. 46, no. 4, p. 2250, 1992.
[487] W. Kassem, "Direct molecular dynamics simulation of piezoelectric and piezothermal couplings in crystals," Ecole Centrale Paris, 2015.
[488] S. Munetoh, T. Motooka, K. Moriguchi, and A. Shintani, "Interatomic potential for Si–O systems using Tersoff parameterization," *Computational Materials Science*, vol. 39, no. 2, pp. 334-339, 2007.
[489] U. Monteverde, M. Migliorato, J. Pal, and D. Powell, "Elastic and vibrational properties of group IV semiconductors in empirical potential modelling," *Journal of Physics: Condensed Matter*, vol. 25, no. 42, p. 425801, 2013.
[490] U. Monteverde, M. Migliorato, and D. Powell, "Atomistic modelling of elasticity and phonons in Diamond and Graphene," in *Numerical Simulation of Optoelectronic Devices (NUSOD), 2013 13th International Conference on*, 2013, pp. 79-80: IEEE.
[491] B. N. Nguyen, M. A. B. Meador, D. Scheiman, and L. McCorkle, "Polyimide aerogels using triisocyanate as cross-linker," *ACS applied materials and interfaces*, vol. 9, no. 32, pp. 27313-27321, 2017.
[492] S. Qiao, S. Kang, Z. Hu, J. Yu, Y. Wang, and J. Zhu, "Moisture-resistance, mechanical and thermal properties of polyimide aerogels," *Journal of Porous Materials*, vol. 27, no. 1, pp. 237-247, 2020.

[493] C. Katcoff and L. Graham-Brady, "Modeling dynamic brittle behavior of materials with circular flaws or pores," *International Journal of Solids and Structures,* vol. 51, no. 3-4, pp. 754-766, 2014.
[494] M. Guerette *et al.*, "Structure and properties of silica glass densified in cold compression and hot compression," *Scientific reports,* vol. 5, no. 1, pp. 1-10, 2015.
[495] H. Yang, Z. Zhang, J. Zhang, and X. C. Zeng, "Machine learning and artificial neural network prediction of interfacial thermal resistance between graphene and hexagonal boron nitride," *Nanoscale,* vol. 10, no. 40, pp. 19092-19099, 2018.
[496] G. Balasubramanian and I. K. Puri, "Heat conduction across a solid-solid interface: Understanding nanoscale interfacial effects on thermal resistance," *Applied Physics Letters,* vol. 99, no. 1, p. 013116, 2011.
[497] J. Zhang, Y. Hong, Z. Tong, Z. Xiao, H. Bao, and Y. Yue, "Molecular dynamics study of interfacial thermal transport between silicene and substrates," *Physical Chemistry Chemical Physics,* vol. 17, no. 37, pp. 23704-23710, 2015.
[498] K. Min *et al.*, "Interfacial adhesion behavior of polyimides on silica glass: A molecular dynamics study," *Polymer,* vol. 98, pp. 1-10, 2016.
[499] Y. L. Yaphary, Z. Yu, R. H. Lam, D. Hui, and D. Lau, "Molecular dynamics simulations on adhesion of epoxy-silica interface in salt environment," *Composites Part B: Engineering,* vol. 131, pp. 165-172, 2017.
[500] G. S. Camprubí, "Mechanical properties at nano-level," Universitat Politècnica de Catalunya. Escola Tècnica Superior d'Enginyeria …, 2010.
[501] G. C. Schatz, "Using theory and computation to model nanoscale properties," *Proceedings of the National Academy of Sciences,* vol. 104, no. 17, pp. 6885-6892, 2007.
[502] D. R. Ferrier, *Biochemistry*. Lippincott Williams & Wilkins, 2014.
[503] O. Hölck, E. Dermitzaki, B. Wunderle, J. Bauer, and B. Michel, "Basic thermo-mechanical property estimation of a 3D-crosslinked epoxy/SiO_2 interface using molecular modelling," *Microelectronics Reliability,* vol. 51, no. 6, pp. 1027-1034, 2011.
[504] T. Clancy and W. Mattice, "Computer simulation of polyolefin interfaces," *Computational and Theoretical Polymer Science,* vol. 9, no. 3-4, pp. 261-270, 1999.
[505] B. Troschke and H. Burkhardt, "Thermal conductivity models fro two-phase systems," *Physics and Chemistry of the Earth,* vol. 23, no. 3, pp. 351-355, 1998.
[506] W. Yu and S. Choi, "The role of interfacial layers in the enhanced thermal conductivity of nanofluids: a renovated Maxwell model," *Journal of nanoparticle research,* vol. 5, no. 1-2, pp. 167-171, 2003.
[507] T. B. Lewis and L. E. Nielsen, "Dynamic mechanical properties of particulate-filled composites," *Journal of applied polymer science,* vol. 14, no. 6, pp. 1449-1471, 1970.
[508] J. Segurado and J. LLorca, "A new three-dimensional interface finite element to simulate fracture in composites," *International journal of solids and structures,* vol. 41, no. 11-12, pp. 2977-2993, 2004.

[509] J. Segurado and J. LLorca, "Computational micromechanics of composites: the effect of particle spatial distribution," *Mechanics of materials,* vol. 38, no. 8-10, pp. 873-883, 2006.
[510] S. Ahmed and F. Jones, "A review of particulate reinforcement theories for polymer composites," *Journal of materials science,* vol. 25, no. 12, pp. 4933-4942, 1990.
[511] M. Phillips, "Simple geometrical models for Young's modulus of fibrous and particulate composites," *Composites science and technology,* vol. 43, no. 1, pp. 95-100, 1992.
[512] P. Kwon and C. Dharan, "Effective moduli of high volume fraction particulate composites," *Acta metallurgica et materialia,* vol. 43, no. 3, pp. 1141-1147, 1995.
[513] R. W. Rice, *Porosity of ceramics: properties and applications*. CRC Press, 2017.
[514] M. Waldron, "The production of cermets containing a relatively large amount of dispersed phase," *Powder Metallurgy,* vol. 10, no. 20, pp. 288-306, 1967.
[515] K. Ramani and A. Vaidyanathan, "Finite element analysis of effective thermal conductivity of filled polymeric composites," *Journal of Composite Materials,* vol. 29, no. 13, pp. 1725-1740, 1995.
[516] H. A. Moghaddam and P. Mertiny, "Stochastic finite element analysis framework for modelling thermal conductivity of particulate modified polymer composites," *Results in Physics,* vol. 11, pp. 905-914, 2018.
[517] R. Nayak, D. P. Tarkes, and A. Satapathy, "A computational and experimental investigation on thermal conductivity of particle reinforced epoxy composites," *Computational Materials Science,* vol. 48, no. 3, pp. 576-581, 2010.
[518] K. Sanada, Y. Tada, and Y. Shindo, "Thermal conductivity of polymer composites with close-packed structure of nano and micro fillers," *Composites Part A: Applied Science and Manufacturing,* vol. 40, no. 6-7, pp. 724-730, 2009.
[519] H. K. Park, J. Jung, and H. S. Kim, "Three-dimensional microstructure modeling of particulate composites using statistical synthetic structure and its thermo-mechanical finite element analysis," *Computational Materials Science,* vol. 126, pp. 265-271, 2017.
[520] W. Yang, K. Peng, L. Zhou, J. Zhu, and D. Li, "Finite element simulation and experimental investigation on thermal conductivity of diamond/aluminium composites with imperfect interface," *Computational materials science,* vol. 83, pp. 375-380, 2014.
[521] C. Chen, S. Qin, S. Li, and J. Wen, "Finite element analysis about effects of particle morphology on mechanical response of composites," *Materials Science and Engineering: A,* vol. 278, no. 1-2, pp. 96-105, 2000.
[522] M. Porfiri, N. Nguyen, and N. Gupta, "Thermal conductivity of multiphase particulate composite materials," *Journal of materials science,* vol. 44, no. 6, pp. 1540-1550, 2009.
[523] L. Qian, X. Pang, J. Zhou, J. Yang, S. Lin, and D. Hui, "Theoretical model and finite element simulation on the effective thermal conductivity of particulate composite materials," *Composites Part B: Engineering,* vol. 116, pp. 291-297, 2017.

[524] D. Kumlutas and I. H. Tavman, "A numerical and experimental study on thermal conductivity of particle filled polymer composites," *Journal of thermoplastic composite materials*, vol. 19, no. 4, pp. 441-455, 2006.
[525] L. Davis and B. Artz, "Thermal conductivity of metal-matrix composites," *Journal of applied physics*, vol. 77, no. 10, pp. 4954-4960, 1995.
[526] E. Ghassemieh and V. Naseehi, "Prediction of failure and fracture mechanisms of polymeric composites using finite element analysis. Part 1: Particulate filled composites," *Polymer composites*, vol. 22, no. 4, pp. 528-541, 2001.
[527] C. P. Tsui, C. Y. Tang, and T. Lee, "Finite element analysis of polymer composites filled by interphase coated particles," *Journal of Materials Processing Technology*, vol. 117, no. 1-2, pp. 105-110, 2001.
[528] C. Sun, P. Saffari, R. Ranade, K. Sadeghipour, and G. Baran, "Finite element analysis of elastic property bounds of a composite with randomly distributed particles," *Composites Part A: Applied Science and Manufacturing*, vol. 38, no. 1, pp. 80-86, 2007.
[529] F. Guild and R. Young, "A predictive model for particulate-filled composite materials," *Journal of materials science*, vol. 24, no. 1, pp. 298-306, 1989.
[530] Y. Wu and Z. Dong, "Three-dimensional finite element analysis of composites with coated spherical inclusions," *Materials Science and Engineering: A*, vol. 203, no. 1-2, pp. 314-323, 1995.
[531] A. Levy and J. M. Papazian, "Tensile properties of short fiber-reinforced SiC/Al composites: Part II. Finite-element analysis," *Metallurgical transactions A*, vol. 21, no. 1, pp. 411-420, 1990.
[532] G. Stefanou, D. Savvas, and M. Papadrakakis, "Stochastic finite element analysis of composite structures based on mesoscale random fields of material properties," *Computer Methods in Applied Mechanics and Engineering*, vol. 326, pp. 319-337, 2017.
[533] G. Stefanou, D. Savvas, and M. Papadrakakis, "Stochastic finite element analysis of composite structures based on material microstructure," *Composite Structures*, vol. 132, pp. 384-392, 2015.
[534] L. Brassart, I. Doghri, and L. Delannay, "Homogenization of elasto-plastic composites coupled with a nonlinear finite element analysis of the equivalent inclusion problem," *International Journal of Solids and Structures*, vol. 47, no. 5, pp. 716-729, 2010.
[535] W. Wang, K. Sadeghipour, and G. Baran, "Finite element analysis of the effect of an interphase on toughening of a particle-reinforced polymer composite," *Composites Part A: Applied Science and Manufacturing*, vol. 39, no. 6, pp. 956-964, 2008.
[536] G. Sozhamannan, S. B. Prabu, and R. Paskaramoorthy, "Failures analysis of particle reinforced metal matrix composites by microstructure based models," *Materials and Design*, vol. 31, no. 8, pp. 3785-3790, 2010.
[537] H. S. Kim, "On the rule of mixtures for the hardness of particle reinforced composites," *Materials Science and Engineering: A*, vol. 289, no. 1-2, pp. 30-33, 2000.
[538] B. Agarwal and L. Broutman, "Three-dimensional finite element analysis of spherical particle composites," *Fibre Science and Technology*, vol. 7, no. 1, pp. 63-77, 1974.

[539] S. B. Prabu and L. Karunamoorthy, "Microstructure-based finite element analysis of failure prediction in particle-reinforced metal–matrix composite," *Journal of materials processing technology,* vol. 207, no. 1-3, pp. 53-62, 2008.
[540] S. B. Prabu, L. Karunamoorthy, and G. Kandasami, "A finite element analysis study of micromechanical interfacial characteristics of metal matrix composites," *Journal of materials processing technology,* vol. 153, pp. 992-997, 2004.
[541] B. Rubehn and T. Stieglitz, "In vitro evaluation of the long-term stability of polyimide as a material for neural implants," *Biomaterials,* vol. 31, no. 13, pp. 3449-3458, 2010.
[542] A. Webley, L. Yang, and D. Nash, "Simulation of the heat transfer through fibrous insulation," in *17th European Conference on Composite Materials*, 2016.
[543] A. Paknia, A. Pramanik, A. Dixit, and S. Chattopadhyaya, "Effect of size, content and shape of reinforcements on the behavior of metal matrix composites (MMCs) under tension," *Journal of Materials Engineering and Performance,* vol. 25, no. 10, pp. 4444-4459, 2016.
[544] V. Kulikovsky, V. Vorlíček, P. Boháč, M. Stranyánek, R. Čtvrtlík, and A. Kurdyumov, "Mechanical properties of amorphous and microcrystalline silicon films," *Thin solid films,* vol. 516, no. 16, pp. 5368-5375, 2008.
[545] I. Yamamoto, T. Higashihara, and T. Kobayashi, "Effect of silica-particle characteristics on impact/usual fatigue properties and evaluation of mechanical characteristics of silica-particle epoxy resins," *JSME International Journal Series A Solid Mechanics and Material Engineering,* vol. 46, no. 2, pp. 145-153, 2003.
[546] N. H. Hamid, W. S. I. W. B. Hisan, U. H. Abdullah, A. A. A. Azim, and P. M. Tahir, "Mechanical properties and moisture absorption of epoxy composites mixed with amorphous and crystalline silica from rice husk," *BioResources*, vol. 14, no. 3, pp. 7363-7374, 2019.

Appendix

Appendix A The remaining results of post microbond fibre surface analysis

In this section, the additional results achieved during the course of the macromechanical testing of the aerogel and fibres interface are presented. It includes additional SEM images, results of elemental analysis and remaining AFM spectra. Firstly, the additional SEM images will be presented. Figure A-0-1 and Figure A-0-2 capture the silica aerogel residues on the surface of the respective glass and PET fibre, with a 10k magnification highlighting the typical spherical structure of silica aerogel.

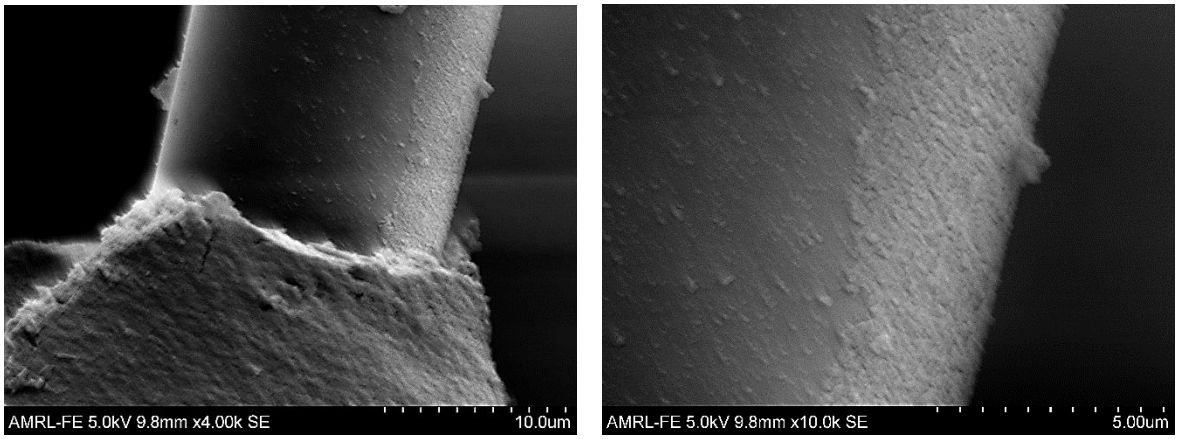

Figure A-0-1 The SEM images of silica aerogel residues on the surface of glass fibre.

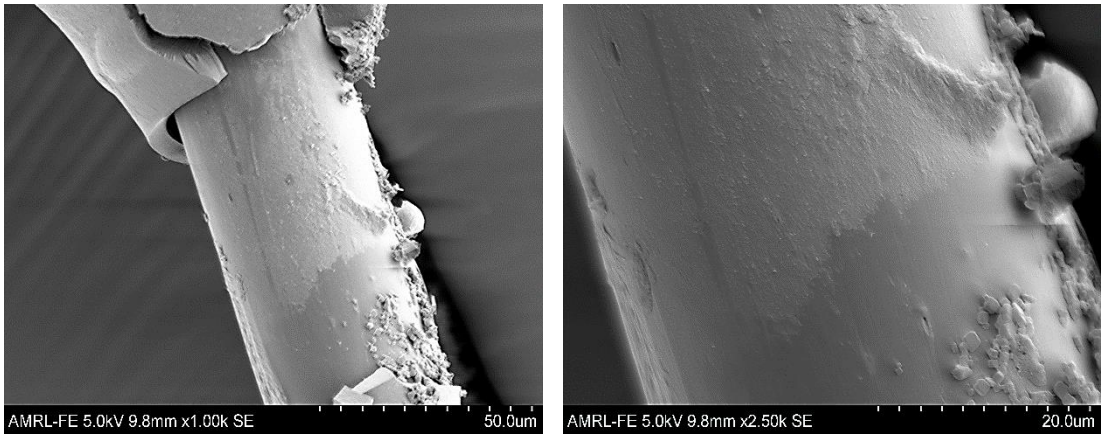

Figure A-0-2 The SEM images of silica aerogel residues on the surface of PET fibre.

Much less residue can be noticed in the case of polyimide aerogel as presented in Figure A-0-3, Figure A-0-4 and Figure A-0-5, which provides a magnification at the surfaces of respectively glass, carbon and PET fibres post microbond. This is because the little residue left on those fibres are agglomerated in larger lumps rather than evenly spread across the fibre surface.

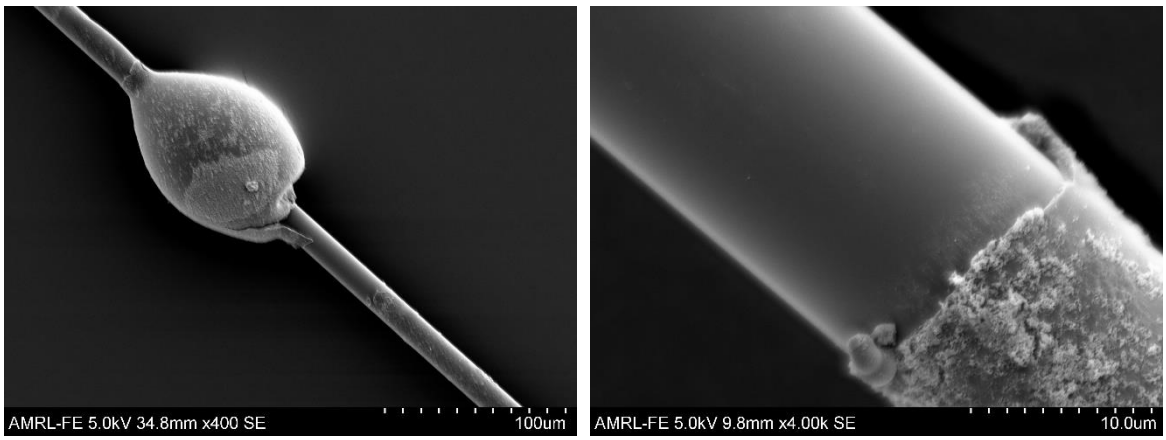

Figure A-0-3 The SEM images of polyimide aerogel residues on the surface of glass fibre.

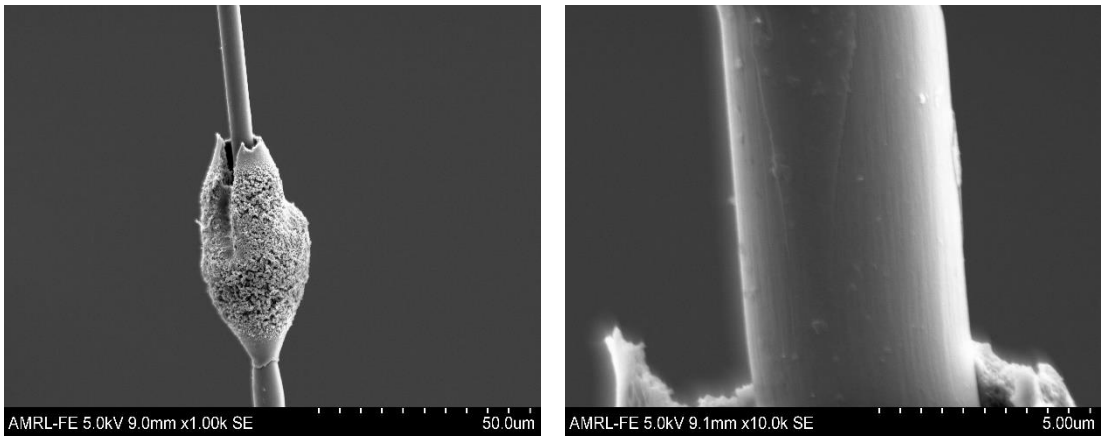

Figure A-0-4 The SEM images of polyimide aerogel residues on the surface of carbon fibre.

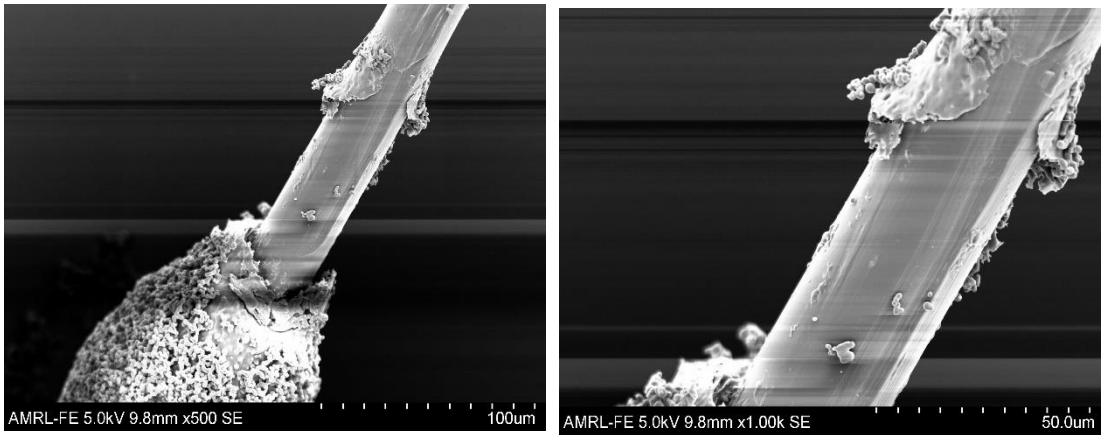

Figure A-0-5 The SEM images of polyimide aerogel residues on the surface of PET fibre.

The results of the elemental analysis are presented in Table A-0-1 and Table A-0-2. They include the average chemical composition of fibre surfaces regions for virgin and post microbond fibres. Each value was achieved as an average of the results for at least two regions.

Table A-0-1 Results of elemental analysis of virgin fibres and fibres post shearing of silica aerogel droplets.

	Element Content [%]						
Sample	**C**	**O**	**Mg**	**Al**	**Si**	**Ca**	**Total**
Glass Fibre	-	40.4	1.7	7.5	32.7	17.6	100
GF/SA	-	38.78	-	6.4	41.1	13.7	100
Carbon Fibre	100	-	-	-	-	-	100
CF/ SA	91.3	7.3	-	-	1.4	-	100
PET Fibre	69.7	30.3	-	-	-	-	100
PET/SA	68.8	28.8	-	-	2.4	-	100

Table A-0-2 Results of elemental analysis of virgin fibres and fibres post shearing of polyimide aerogel droplets.

	Element Content [%]						
Sample	**C**	**O**	**Mg**	**Al**	**Si**	**Ca**	**Total**
Glass Fibre	-	40.4	1.7	7.5	32.7	17.6	100
GF/PI	11.7	54.7	-	6.6	27.0	-	100
Carbon Fibre	100	-	-	-	-	-	100
CF/ PI	100	-	-	-	-	-	100
Pet Fibre	69.7	30.3	-	-	-	-	100
PET/PI	100	-	-	-	-	-	100

Finally, the topographies of glass, carbon, and PET fibre post microbond test of silica and polyimide aerogel droplets are included in Figure 0-6 and Figure 0-7.

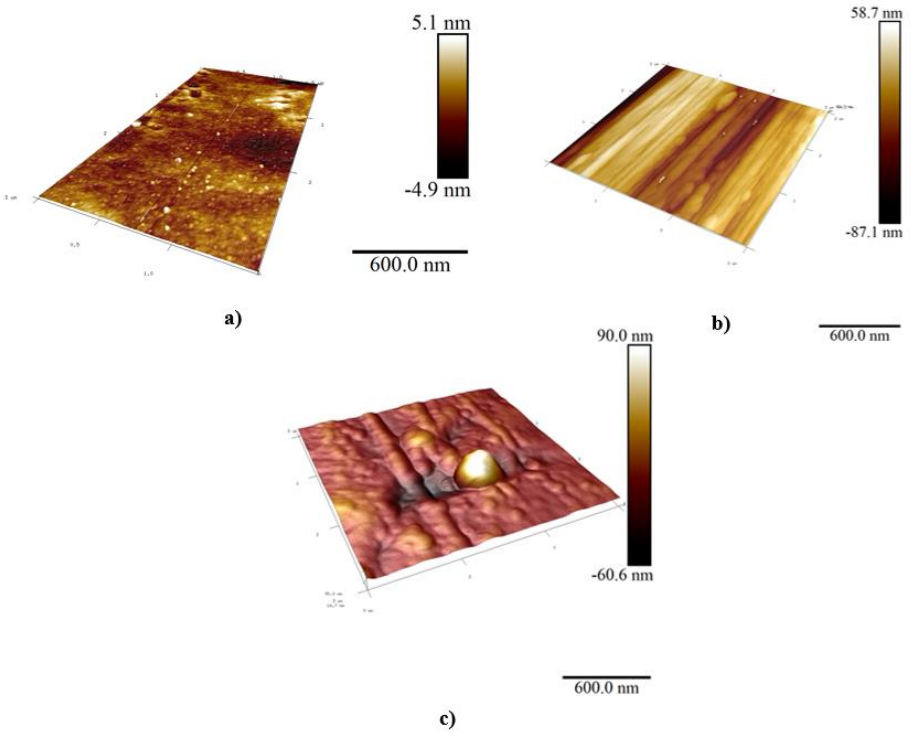

Figure 0-6 AFM topography scans of fibre surfaces post the silica aerogel microbond test. Images presents a) glass fibre b) carbon fibre and c) PET fibre.

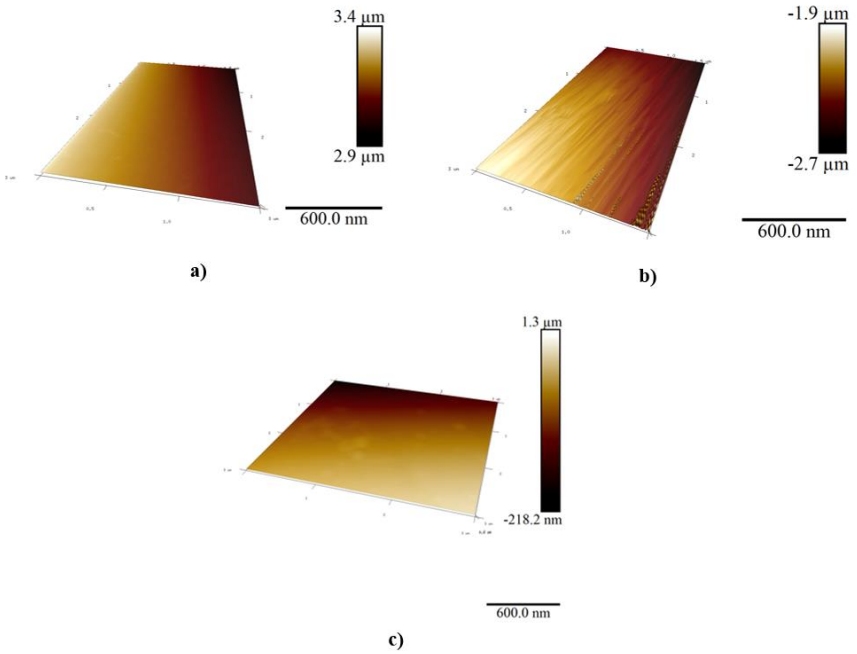

Figure 0-7 AFM topography scans of fibre surfaces post the polyimide aerogel microbond test. Images presents a) glass fibre b) carbon fibre and c) PET fibre.